MODERN ANTENNA DESIGN

THOMAS A. MILLIGAN
Martin Marietta Denver Aerospace

McGRAW-HILL BOOK COMPANY
New York St. Louis San Francisco Auckland Bogotá
Hamburg Johannesburg London Madrid
Mexico Montreal New Delhi Panama
Paris São Paulo Singapore
Sydney Tokyo Toronto

Library of Congress Cataloging in Publication Data

Milligan, Thomas.
Modern antenna design.

Includes bibliographical references and index.
1. Antennas (Electronics)—Design and construction.
I. Title.
TK7871.6.M54 1985 621.38'028'3 84-17131
ISBN 0-07-042318-0

Copyright © 1985 by McGraw-Hill, Inc.

1234567890 DOC/DOC 8987654

ISBN 0-07-042318-0

The editors for this book were Roy Mogilanski
and Galen H. Fleck; the designer was Naomi Auerbach;
and the production supervisor was Thomas G. Kowalczyk.
It was set in Caledonia by Beacon Graphics Corporation.

Printed and bound by R.R. Donnelley & Sons Company.

To Mary, Jane, Margaret,
and to the memory of my father, James

CONTENTS

Preface xiii

Chapter 1 PROPERTIES OF ANTENNAS 1

- 1-1 Antenna Radiation 2
- 1-2 Gain 4
- 1-3 Effective Area 6
- 1-4 Path Loss 6
- 1-5 Why Use an Antenna 8
- 1-6 Directivity 9
- 1-7 Directivity Estimates 10
- 1-8 Beam Efficiency 14
- 1-9 Polarization 15
- 1-10 Impedance 22

References 23

Chapter 2 ANTENNA TYPES 24

Radiation Structures 24

- 2-1 Radiation from Currents 25
- 2-2 Radiation from Magnetic Currents 29
- 2-3 Apertures 31
- 2-4 Discontinuities 35

Catalog of Antennas 35

- 2-5 Small Resonant Antennas 36
- 2-6 Conformal Antennas 38
- 2-7 End-Fire Antennas 38
- 2-8 Leaky Wave Antennas 40

2-9 Long Wire Antennas 41
2-10 Self-scaling Antennas 41
2-11 Horn Antennas 42
2-12 Reflector Antennas 44
2-13 Lens Antennas 45
2-14 Relation between Beamwidths 47
References 47

Chapter 3 ARRAYS 48

3-1 Two-Element Array 49
3-2 Mutual Impedance 51
3-3 Linear Array of *N* Elements 55
3-4 Hansen and Woodyard End-Fire Array 59
3-5 Phased Arrays 60
3-6 Multiple Beams 63
References 65

Chapter 4 DIPOLES AND SLOTS 66

4-1 Standing Wave Currents 66
4-2 Radiation Resistance (Conductance) 68
4-3 Babinet-Booker Principle 70
4-4 Monopole 72
4-5 Cavity-Backed Slots 72
4-6 Dipoles Located Over Ground Planes 72
Feeding Methods 74
4-7 Baluns 74
4-8 Offset Feed 83
4-9 Sleeve Antenna 84
4-10 Folded Dipole 85
4-11 Resonant Loop 86
4-12 Shunt Feeding 86
4-13 Waveguide-Fed Slots 87
4-14 Rectangular-Waveguide Wall Slots 89
4-15 Circular-Waveguide Slots 92
4-16 Waveguide Slot Arrays 93
References 93

Chapter 5 CONFORMAL ANTENNAS 95

5-1 Stripline Series Slots 96
5-2 Microstrip Patch Antennas 99
5-3 Rectangular Microstrip Patch Antenna 100
5-4 Circular Microstrip Patch 105
5-5 Patch Antenna Feed Networks 107
5-6 Microstrip Transmission Line 109
5-7 Circularly Polarized Patch Antennas 111
5-8 Series-Fed Array 115
5-9 Half-Patch Antenna 117
5-10 Microstrip Dipole 119

5-11 Microstrip Franklin Array 120
5-12 Microstrip Antenna Mechanical Properties 122
5-13 Shallow-Cavity Crossed-Slot Antenna 123
5-14 T-Bar-Fed Slot Antenna 124
5-15 Cavity-Mounted Dipole Antenna 126
References 127

Chapter 6 RADIATION FROM APERTURES 129

6-1 Fourier Transform in k Space 129
6-2 Amplitude Taper and Phase Error Efficiencies 134
Linear Distributions 137
6-3 Uniform Distribution 137
6-4 Other Simple Geometrical Distributions 139
6-5 Taylor Line Distribution 141
6-6 Taylor Line Distribution with Edge Nulls 146
6-7 Bayliss Line Source Distribution 148
6-8 Line Sources with Arbitrary Sidelobe Levels 153
6-9 Woodward Line Source Synthesis 154
Circular Apertures 157
6-10 Parabolic^N Circular-Aperture Distribution 158
6-11 Circular Gaussian Distribution 161
6-12 Hansen Single-Parameter Circular Distribution 163
6-13 Taylor Circular-Aperture Distribution 164
6-14 Bayliss Circular-Aperture Distribution 166
6-15 Aperture Blockage 169
6-16 Quadratic Phase Error 173
6-17 Beam Efficiency of Circular Apertures with Axisymmetric Distributions 175
References 178

Chapter 7 HORN ANTENNAS 179

7-1 Rectangular Horn (Pyramidal) 181
7-2 Circular-Aperture Horn 190
7-3 Overmoded Circular-Aperture Horns 196
7-4 Circular (Conical) Corrugated Horn 201
7-5 Box Horn 208
7-6 Multimode Circular Horn 210
7-7 Biconical Horn 211
References 213

Chapter 8 REFLECTOR ANTENNAS 214

8-1 Geometric Optics 215
8-2 Parabolic Reflector Geometry 220
8-3 Paraboloidal Reflector Aperture Distribution Losses 222
8-4 Approximate Spillover and Amplitude Taper Trade-offs 224
8-5 Phase Error Losses and Axial Defocusing 226
8-6 Astigmatism 228
8-7 Feed Scanning 228

8-8 Random Phase Errors 232
8-9 Physical Optics 234
8-10 Focal Plane Fields 236
8-11 Feed Mismatch Due to the Reflector 237
8-12 Reflections from Conic Sections 239
8-13 Dual-Reflector Antennas 239
8-14 G/T (Gain/Noise Temperature) 248
8-15 Offset-Fed Reflector 249
8-16 Spherical Reflector 252
8-17 Corrector Subreflector for a Spherical Reflector 254
8-18 Shaped Reflectors 256
8-19 Reflectors Made from Flat Plates 266
References 271

Chapter 9 LENS ANTENNAS 273

9-1 Single Refracting Surface Lenses 274
9-2 Zoned Lenses 278
9-3 Metal-Plate Lenses 281
9-4 Surface Mismatch and Dielectric Losses 284
9-5 Feed Scanning of Hyperboloidal Lens 286
9-6 Dual-Surface Lenses 286
9-7 Bootlace Lens 293
9-8 Luneburg Lens 294
References 295

Chapter 10 ARRAY SYNTHESIS 297

10-1 Schelkunoff's Unit Circle Method 298
10-2 Dolph-Chebyshev Linear Array 302
10-3 Other Chebyshev Array Techniques 305
10-4 Planar Arrays 308
10-5 Zero Sampling of Continuous Distributions 315
10-6 Shaped Beam Methods 315
References 318

Chapter 11 TRAVELING WAVE ANTENNAS 320

11-1 General Traveling Waves 321
11-2 Long Wire Antennas 327
11-3 Yagi-Uda Antennas 332
11-4 Corrugated-Rod, or Cigar, Antenna 345
11-5 Dielectric Rod (Polyrod) Antenna 346
11-6 Helical Wire Antenna 348
11-7 Planar Surface Wave Structures 354
11-8 Leaky Wave Structures 357
11-9 Measurement of Traveling Wave Parameters 363
11-10 Waveguide Slot Array 365
References 369

Chapter 12 SELF-SCALING ANTENNAS 372
12-1 Archimedian Spiral 373
12-2 Equiangular Spiral 375
12-3 Infinite Balun 377
12-4 Conical Log Spiral Antenna 377
12-5 Mode 2 Conical Log Spiral Antenna 381
12-6 Feeding Conical Log Spirals 382
Log-Periodic Antennas 383
12-7 Log-Periodic Dipole Antenna 384
12-8 Other Log-Periodic Types 393
References 396
Index 397

PREFACE

I wrote this book, from my perspective as a designer, for users and designers of antennas. The two groups have similar needs. Each must thoroughly understand the properties of antennas and the limits of design. The initial part of design is the selection of the proper antenna type. To enable a quick selection of antenna type and approximate size without performing a detailed design, the book stresses the limitations and summarizes the characteristics of antennas. The use of this material will minimize the costly misdirection of effort. Beyond providing that help in selecting the design approach, the book reduces antenna theory to a few basic ideas and presents concepts that I myself have found useful when designing and troubleshooting antenna systems.

Because antenna theory is a mature subject, it is easy to become lost in the mathematics and lose sight of what is happening. Ideas are presented with a minimum of mathematical development except in areas where it is necessary for understanding. Expositions of analytical techniques, such as the method of moments and the geometric theory of diffraction, have been excluded to maximize the space for design methods. The results of analytical techniques are included, but only the basic ideas of the methods are given. The book presents many design methods that start with the usual specifications and end with dimensions. Methods that are applicable to all antennas do not exist, but the basic concepts developed in the first few chapters will help with starting any antenna design. Because there is always a place for empirically derived designs, dimensions of successful designs are listed.

The book arose from a set of notes used in a three-semester in-house continuing education course given a number of times to combinations of designers, users, recent graduates, and other interested persons. Each group had special needs, but all wanted a basic understanding and a unified approach useful for meeting real-world problems. The variety of interests, questions, and initial misconceptions of the members of the classes helped define the book.

Although the material was initially presented at a variety of levels, the following knowledge is needed to achieve full benefit from the material: an understanding of electromagnetics in the relation of fields and boundary conditions, an ability to add signals expressed as amplitude and phase, and some understanding of the vector nature of fields. If a section is beyond your mathematical level, skip it. You can continue without it because there are no long mathematical developments which build on earlier sections. Most of the design methods use only algebra; the exceptions are the design of shaped reflectors and two-surface lenses, which require a knowledge of integral and differential equations. The material is suitable for a graduate-level course stressing the practical aspects of design, but it will then require the addition of supplemental problems.

Many of the results are presented in tables. Graphical presentations give broad trends, but tables contain better information. The tables are ideal in computer programs when combined with an interpolation algorithm. Simple programs can be written on small machines to produce designs quickly. Explicit computer routines have not been included because I feel that each person should understand the design method and write his or her own program in a language which fits the machine in use.

The first few chapters comprise the introduction. Chapter 1 lists basic definitions and approaches the subject in terms of a communication link, that is, from the user's point of view. Chapter 2 touches lightly on electromagnetics by describing the three basic radiation sources: electric currents, magnetic currents developed from duality, and the combination of the two in the radiation from apertures. The ideas exceed the importance of the mathematics. The second part of Chap. 2 summarizes antenna types and gives methods for simple analyses of expected performance as a starting point for antenna selection. Chapter 3, on arrays, introduces the idea of radiation from an extended source as the summation of phasors from a finite number of radiation points. Array synthesis is not covered until after aperture distributions have been discussed because many large arrays are designed by sampling a continuous distribution. Chapter 4 is a transition between introductory material and the design of particular antennas. It develops the duality of dipoles and slots. Both the importance and the design descriptions of baluns are presented so the reader will understand the problems of feed line radiation and stray currents on support structures.

The remaining chapters either discuss design methods of particular antennas or develop general ideas, such as aperture distributions and array synthesis, more thoroughly. The choice of topics reflects the author's experience with microwave antennas, although many of the concepts apply to lower-frequency antennas. The chapters may be considered in almost any order. Although some topics build on preceding ideas, quick reference to earlier sections will let the reader jump around. Sections 6-2, on amplitude taper and phase error efficiencies, and 6-16, on quadratic phase error, are exceptions. The sections following those two make extensive use of the idea of the separation of directivity into distribution losses (Sec. 6-2) and quadratic phase error (Sec. 6-16). On first reading, the rest of Chap. 6, on aperture distributions, can be skipped.

The chapters on the design of particular antennas are summarized as follows. Chapter 5, on conformal antennas, presents the practical aspects of microstrip and stripline antennas, together with methods for quick design of these thin convenient antennas, and tables of limitations allow rapid determination of their possible uses. The general aperture distributions of Chap. 6 can be applied to many antennas without undertaking detailed analysis. Chapter 7, on horns, not only covers analysis techniques but gives design methods that produce dimensions from specifications. Chapter 8, on reflectors, covers all aspects of design and analysis extensively and includes examples to demonstrate design methods from both mechanical and electrical performance points of view. Chapter 9, on lenses, stresses the increasing importance of lens antennas above microwave frequencies, although lower-frequency types such as metal plate and bootlace designs are covered. Chapter 10 discusses the usual Chebyshev methods for equal sidelobe array synthesis, shaped beam methods using Fourier series and Woodward methods, and planar array synthesis through convolution of simple arrays. Chapter 11, on traveling wave antennas, uses both aperture theory and specific antennas, such as Yagi-Uda, helical wire, and dielectric antennas, to demonstrate design methods and a generalized approach to surface wave and leaky-wave antennas. Chapter 12, on self-scaling antennas, combines a discussion of structural requirements for broadband antennas with design details of log-periodic and spiral antennas.

My special thanks go to Manuel R. Moreno, who not only reviewed the entire manuscript and made many suggestions on its unclear sections but also encouraged me while I was writing it. I would also like to acknowledge the useful criticisms of Loren K. DeSize, who suggested changes in emphasis. My students provided invaluable help through their questions, which arose not only from misconceptions but from experience in the design of particular antennas and which identified areas of possible misunderstanding. In conclusion, I must express my gratitude to Mary Wright Milligan, who supported and encouraged me throughout this project and who read and proofread the various manuscripts and detected many wording problems. I have enjoyed writing this book, which clarified my own thinking, and I hope the book will be useful to the reader.

Thomas A. Milligan

CHAPTER

1

PROPERTIES OF ANTENNAS

An antenna converts bound circuit fields into propagating electromagnetic waves and, by reciprocity, removes power from passing electromagnetic waves. Maxwell's equations predict that any time-varying electric or magnetic field produces the other field and forms an electromagnetic wave. In an electromagnetic wave, the pair of fields are orthogonally placed and propagate in the direction of the normal to the plane defined by the perpendicular electric and magnetic fields. The electric field, the magnetic field, and the direction of propagation form a right-hand coordinate system. The propagating wave field intensity decreases by $1/R$ away from the source, whereas a static field drops off by $1/R^2$. Any circuit with time-varying fields has the capability of radiating to some degree. Many circuit designers have discovered this radiation by running their fingers around the circuit while observing the response. Antenna designers are also fond of running their hands over an antenna while monitoring the input match, but we are looking for changes in the response indicating radiation. How do antennas radiate and how do we keep circuits from radiating?

The retarded potential concept explains radiation. Simply stated, a change in a circuit is not detected until it has had time to propagate to the detection point. The propagating velocity is the speed of light in the medium, a consequence of the theory of special relativity limiting the speed of information propagation. We will only consider time-harmonic fields and will use the phasor notation with the time dependence $e^{j\omega t}$. An outward-propagating wave is given by

$$e^{-j(kR-\omega t)}$$

where k, the wave number, is given by $2\pi/\lambda$. λ is the wavelength of the wave given by c/f, where c is the velocity of light (3×10^8 m/s in free space) and f is the frequency. Increasing the distance from the source decreases the phase of the wave.

Consider a two-wire transmission line with fields bound to it. The currents on one wire will radiate; but as long as the ground return is near, its radiation will nearly cancel the other line's radiation because the two are 180° out of phase and the waves travel about the same distance. As the lines become farther and farther apart, in terms of wavelengths, the fields produced by the two currents will no longer cancel in all directions. The phase delay is different for each field, and power escapes from the line. We keep circuits from radiating by providing close ground returns. Hence, high-speed logic requires ground planes to reduce radiation and its unwanted cross talk.

Consider a conical transmission line made from two cones with a common vertex and different cone angles. The characteristic impedance between the cones is constant. If the line is fed from the center, the power will spread out in spherical waves between the cones. The waves will reach the ends of the cones and be reflected by the open circuit. Because the distance between the cones has grown to be a significant part of a wavelength, the field halfway between the cones cannot know until sometime later (retarded potential) that the transmission line is open-circuited. We could say that the power just flies off into space because it forgot it was part of the transmission line mode. This is not very rigorous, but it has a good physical feel to it. The power reflected by the open boundary is out of phase with the fields reflected by the ends because of the retardation time finding out about the open circuit. Since this center reflection is out of phase, the total reflected field is reduced and the difference is radiated. Dipoles and horns can also be considered as diverging transmission lines radiating for the same reason as the biconical horn. The impedance along the biconical horn is constant, but the dipole transmission line impedance rises rapidly [1].*

1-1 Antenna Radiation

Antennas radiate spherical waves propagating in the radial direction with the center of the coordinate system on the antenna. At large distances spherical waves can be approximated by plane waves. Plane waves are useful because they simplify the problem. They are not physical, however, because they require infinite energy.

*Numbers in brackets indicate references listed at ends of chapters.

The Poynting vector describes both the direction of propagation and the power density of the electromagnetic wave. It is found from the vector cross product of the electric and magnetic fields and is denoted **S**.

$$\mathbf{S} = \mathbf{E} \times \mathbf{H}^* \qquad \mathrm{W/m^2}$$

Root mean square (rms) values are used to express the magnitude of the fields. $\mathbf{H}^*$ is the complex conjugate of the magnetic field phasor. The magnetic field is proportional to the electric field in the far field. The constant of proportion is η, the impedance of free space (376.7 Ω).

$$|\mathbf{S}| = S = \frac{|\mathbf{E}|^2}{\eta} \qquad \mathrm{W/m^2} \tag{1-1}$$

Because the Poynting vector is the vector product of the two fields, it is orthogonal to both fields and the triplet defines a right-hand coordinate system: (**E**, **H**, **S**).

Consider a pair of concentric spheres centered on the antenna. The fields around the antenna decrease as $1/R$, $1/R^2$, $1/R^3$, etc. Constant-order terms would require that the power radiated grow with distance and power would not be conserved. The power density, due to field terms proportional to $1/R^2$, $1/R^3$, and higher, decreases with distance faster than the area increases. The energy on the inner sphere is larger than that on the outer sphere. The energies are not radiated but are instead concentrated around the antenna; they are near-field terms. Only the $1/R^2$ term of the Poynting vector ($1/R$ field terms) represents radiated power because the sphere area grows as R^2 and gives a constant product. All the radiated power on the inner sphere will propagate to the outer sphere.

The sign of the input reactance depends on the near-field predominance of field type: electric (capacitive) or magnetic (inductive). At resonance (zero reactance) the stored energies due to the near fields are equal. Increasing the stored fields increases the circuit Q and narrows the impedance bandwidth.

Far enough from the antenna we consider only the radiated fields and power density. The power is the same through each sphere.

$$4\pi R_1^2 S_{1,\mathrm{avg}} = 4\pi R_2^2 S_{2,\mathrm{avg}}$$

The average power density is proportional to $1/R^2$. Consider differential areas on the two spheres at the same coordinate angles. The antenna radiates only in the radial direction; therefore, no power may travel in the θ or ϕ direction. Power travels in flux tubes between areas, and it follows that not only the average Poynting vector but also every part of the power density is proportional to $1/R^2$.

$$S_1 R_1^2 \sin\theta\, d\theta\, d\phi = S_2 R_2^2 \sin\theta\, d\theta\, d\phi$$

Since in a radiated wave S is proportional to $1/R^2$, E is proportional to $1/R$.

It is convenient to define radiation intensity to remove the $1/R^2$ dependence

$$U(\theta, \phi) = S(R, \theta, \phi)R^2 \qquad \text{W/solid angle}$$

Radiation intensity depends only on the direction of radiation and makes the pattern the same at all distances. A probe antenna measures the relative radiation intensity (pattern) by rotating in a circle (constant R) around the antenna. Often, of course, the antenna rotates and the probe is stationary.

Some patterns have established names. Patterns along constant angles of the spherical coordinates are called either conical (constant θ) or great circle (constant ϕ). The great circle cuts when $\phi = 0°$ or $\phi = 90°$ are the principal plane patterns. Other cuts also are used, but their names are dependent on the measurement positioners and cause confusion. Annotate these patterns carefully to avoid confusion between people measuring patterns on different positioners. Patterns are measured by using three scales: (1) linear (power), (2) square root (field intensity), and (3) decibels. The dB scale is used most because it reveals more of the low-level responses (sidelobes).

Figure 1-1 demonstrates many characteristics of patterns. The half-power beamwidth is sometimes called just the beamwidth. The tenth-power and null beamwidths are used in some applications. The pattern comes from a parabolic reflector whose feed is not located on the axis. The vestigial lobe occurs when the first sidelobe becomes joined to the main beam and forms a shoulder. When the feed is located on the axis of the parabola, the first sidelobes will be equal.

1-2 Gain

Gain is a measure of the ability of the antenna to direct the power delivered to the input into radiation in a particular direction. It is measured at the peak radiation intensity. Consider the power density radiated by an isotropic antenna at a distance R and input power P_0:

$$S = \frac{P_0}{4\pi R^2}$$

An isotropic antenna radiates equally in all directions, and the power density S is found by dividing the radiated power by the area of the sphere with radius R. The isotropic radiator is considered to be 100 percent efficient. The gain of a real antenna increases the power density in the direction of the peak radiation.

$$S = \frac{P_0 g}{4\pi R^2}$$

Gain is achieved by directing the radiation so that other parts of the radiation

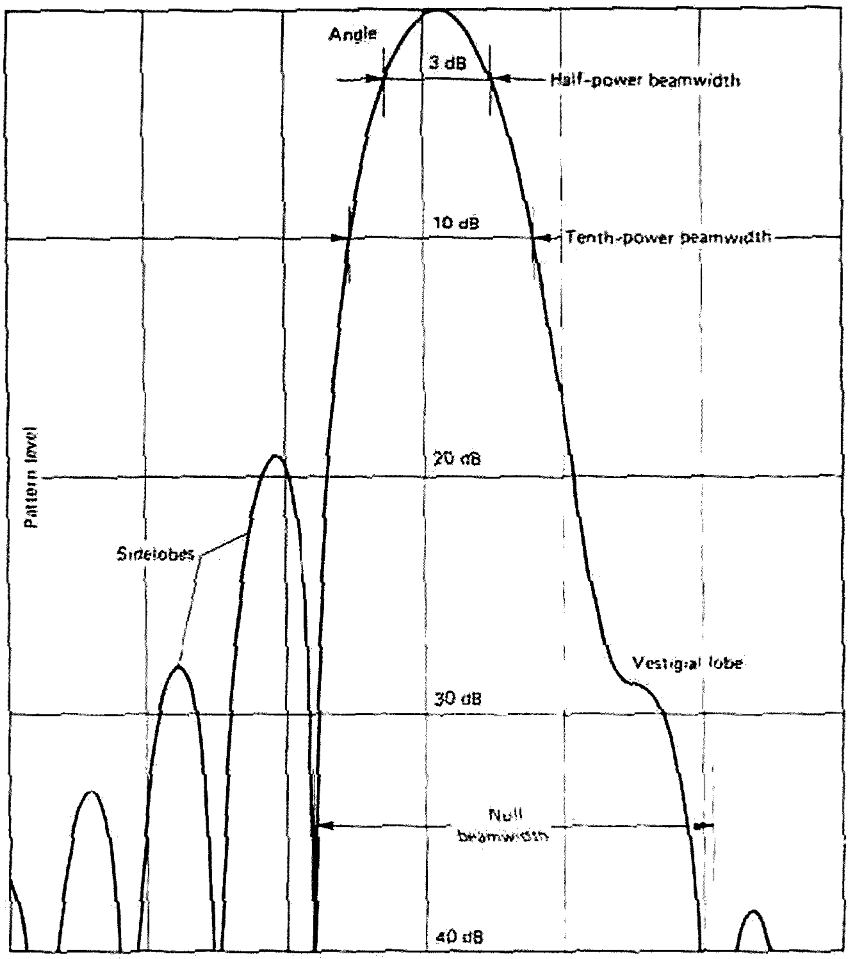

Figure 1-1 Antenna pattern characteristics.

sphere will have fields less than the isotropic radiator. In general, gain is defined as the gain-biased pattern of the antenna

$$S(\theta, \phi) = \frac{P_0 g(\theta, \phi)}{4\pi R^2} \qquad \text{power density} \tag{1-2}$$

$$U(\theta, \phi) = \frac{P_0 g(\theta, \phi)}{4\pi} \qquad \text{radiation intensity}$$

The surface integral of the radiation intensity over the radiation sphere divided by the input power P_0 is a measure of the relative power radiated by the antenna, or the antenna efficiency.

$$\frac{P_r}{P_0} = \int_0^{2\pi} \int_0^{\pi} \frac{g(\theta, \phi)}{4\pi} \sin\theta \, d\theta \, d\phi = \eta_e \qquad \text{efficiency}$$

where P_r is the radiated power. Material losses in the antenna reduce the radiated power.

In a system the transmitter output impedance or the receiver input impedance may not conjugate-match the antenna. Peak gain occurs for a conjugate match. Precision gain measurements require a tuner between the antenna and receiver to conjugate-match the two together. Alternatively, the mismatch loss must be removed by calculation after the measurement. The effects of mismatches are considered separately for a given system. Many antennas are measured into the system impedance, and mismatch loss is considered to be part of the efficiency.

Example Find the peak power density at 10 km of an antenna with an input power of 3 W and a gain of 15 dB.
First convert dB gain to a ratio.

$$g = 10^{15/10} = 31.62$$

The area of the sphere with radius 10 km is $4\pi(10^4)^2$ m^2. The power density is

$$S = \frac{(3\ \mathrm{W})(31.62)}{4\pi \times 10^8\ \mathrm{m}^2} = 75.5\ \mathrm{nW/m}^2$$

We find the electric field intensity by rearranging Eq. (1-1).

$$|\mathbf{E}| = \sqrt{S\eta} = \sqrt{(75.5 \times 10^{-9})(376.7)} = 5333\ \mu\mathrm{V/m}$$

Gain is relative to an isotropic antenna. Some antenna gains are with reference to a half-wavelength dipole, which has a gain of 2.14 dB.

1-3 Effective Area

Antennas capture power from passing waves and deliver some of it to the terminals. Given the power density of the incident wave and the effective area of the antenna, the power delivered to the terminals is the product.

$$P_d = SA_{\mathrm{eff}} \tag{1-3}$$

For an aperture antenna such as a horn, parabolic reflector, or flat-plate array, the effective area relates to the physical area by the aperture efficiency. Antennas with infinitesimal physical areas, such as dipoles, have effective areas because they remove power from passing waves. Losses due to material, distribution, and mismatch reduce the ratio of the effective area to the physical area. A typical value for a parabolic reflector is 55 percent aperture efficiency.

1-4 Path Loss

We combine the gain of the transmitting antenna with the effective area of the receiving antenna to find the delivered power and path loss. The power density at the receiving antenna is given by Eq. (1-2), and the received power is given by Eq. (1-3). By combining the two, we obtain the path loss:

$$\frac{P_d}{P_t} = \frac{A_2 g_1(\theta, \phi)}{4\pi R^2}$$

Antenna 1 transmits, and antenna 2 receives.

If the materials in the antennas are linear and isotropic, then the transmit and receive responses are identical (reciprocal) [2]. Consider antenna 2 as the transmitting antenna and antenna 1 as the receiving one. The path loss is

$$\frac{P_d}{P_t} = \frac{A_1 g_2(\theta, \phi)}{4\pi R^2}$$

Since the responses are reciprocal, the path losses are equal and we have

$$\frac{g_1}{A_1} = \frac{g_2}{A_2} = \text{constant}$$

Because the antennas are arbitrary, this quotient must equal a constant. The constant is found by considering the radiation between large apertures [3]:

$$\frac{g}{A} = \frac{4\pi}{\lambda^2} \tag{1-4}$$

By this equation, path loss is found in terms of the gains or effective areas

$$\frac{P_d}{P_t} = g_1 g_2 \left(\frac{\lambda}{4\pi R}\right)^2 = \frac{A_1 A_2}{\lambda^2 R^2} \tag{1-5}$$

The following formulas give the path loss for various units of distance and for frequency in megahertz.

$$\text{Path loss (dB)} = 32.45 + 20 \log (FR) - G_1 \text{ (dB)} - G_2 \text{ (dB)} \tag{1-6a}$$

where R is in kilometers.

$$\text{Path loss (dB)} = 37.80 + 20 \log (FR) - G_1 \text{ (dB)} - G_2 \text{ (dB)} \tag{1-6b}$$

where R is in nautical miles.

Example Find the gain of a 3-m-diameter parabolic reflector at 4 GHz assuming 55 percent aperture efficiency. Gain is related to effective area by Eq. (1-4)

$$g = \frac{4\pi A}{\lambda^2}$$

The area of a circular aperture is found by $A = \pi[(D/2)^2]$. By combining these equations, we have

$$g = \left(\frac{\pi D}{\lambda}\right)^2 \eta_a = \left(\frac{\pi D F}{c}\right)^2 \eta_a \tag{1-7}$$

where D is the diameter and η_a is the aperture efficiency. On substituting the above values, we obtain the gain.

$$g = \left(\frac{\pi(3)(4) \times 10^9}{0.3 \times 10^9}\right)^2 0.55 = 8685 \quad (39.4 \text{ dB})$$

Example Find the path loss of a 50-km communication link at 2.2 GHz using a transmitter antenna with a gain of 25 dB and a receiver antenna with a gain of 20 dB.

$$\text{Path loss} = 32.45 + 20 \log (2200 \cdot 50) - 25 - 20 = 88.3 \text{ dB}$$

What happens to transmission between two apertures as the frequency is increased? If we assume that the effective area remains constant, as in a parabolic reflector, then the transmission increases as the square of frequency:

$$\frac{P_d}{P_t} = \frac{A_1 A_2}{R^2} \frac{1}{\lambda^2} = \frac{A_1 A_2}{R^2} \left(\frac{F}{c}\right)^2 = BF^2$$

where B is a constant for a fixed range. The receiving aperture captures the same power regardless of frequency, but the gain of the transmitting antenna increases as the square of frequency. Hence, the received power also increases as frequency squared. Only for fixed gain antennas does the path loss increase as the square of frequency.

1-5 Why Use an Antenna?

We use antennas when nothing else is possible, as in communication with a missile or over rugged mountain terrain. Cables are expensive and take a long time to install. Are there times when we would use antennas over level ground? The large path losses of antenna systems make us feel that cable runs are better.

Example Suppose we must choose between using a low-loss waveguide run and using a pair of antennas at 3 GHz. Each antenna has 10 dB of gain. The low-loss waveguide has only 19.7 dB/km loss. The following table is a comparison of losses over various distances.

Distance, km	*Waveguide loss, dB*	*Antenna path loss, dB*
2	39.4	88
4	78.8	94
6	118.2	97.6
10	197	102

The waveguide link starts out with lower loss, but the antenna system soon overtakes it. When the path length doubles, the cable link loss also doubles in dB, but an antenna link increases by only 6 dB. As distance is increased, antennas eventually have lower losses than any cable.

Example A 200-m outside antenna range was set up to operate at 2 GHz using a 2-m-diameter reflector as a source. The receiver required a sample of the transmitter signal to phase-lock the local oscillator and signal at a 45-MHz difference. It was proposed to run an RG/U 115 cable through the power and control cable conduit, since the run was short. The cable loss was 36 dB per 100 m, giving a total cable loss of 72 dB. A 10-dB coupler was used on the transmitter to pick off the reference signal, so the total loss was 82 dB. Since the source transmitted 100 mW (20 dBm), the signal was −62 dBm at the receiver, sufficient for phase lock.

A second proposed method was to place a standard-gain horn (15 dB gain) within the beam of the source on a small stand out of the way of the measurement and next to the receiver. If we assume that the source antenna had only 30 percent aperture efficiency, we find the gain from Eq. (1-7).

$$\lambda = 0.15 \text{ m}$$

$$g = \left(\frac{2\pi}{0.15}\right)^2 0.3 = 526 \quad (27.2 \text{ dB})$$

The path loss is found from Eq. (1-6) for a range of 0.2 km.

$$32.45 + 20 \log [2000(0.2)] - 27.2 - 15 = 42.3 \text{ dB}$$

The power out of the horn is 20 dBm − 42.3 dB = −22.3 dBm. A 20-dB attenuator must be put on the horn to prevent saturation of the receiver (−30 dBm). Even with a short run, it is sometimes better to transmit the signal by using antennas instead of cables.

1-6 Directivity

Directivity is a measure of the concentration of the radiation in the direction of the maximum.

$$\text{Directivity} = \frac{\text{maximum radiation intensity}}{\text{average radiation intensity}} = \frac{U_{\max}}{U_0} \tag{1-8}$$

Directivity and gain differ only by the efficiency, but directivity is easily estimated from patterns. Gain—directivity times efficiency—must be measured.

The average radiation intensity can be found from a surface integral on the radiation sphere of the radiation intensity divided by 4π, the area of the sphere in steradians.

$$\text{Average radiation intensity} = \frac{1}{4\pi}\int_0^{2\pi}\int_0^{\pi} U(\theta, \phi) \sin\theta \, d\theta \, d\phi \tag{1-9}$$

This is the radiated power divided by the area of a unit sphere. We will find that there are co- and cross-polarization components to the radiation intensity dividing $U(\theta, \phi)$ into a sum.

$$U_0 = \frac{1}{4\pi}\int_0^{2\pi}\int_0^{\pi} [U_c(\theta, \phi) + U_x(\theta, \phi)] \sin\theta \, d\theta \, d\phi \tag{1-10}$$

Both co- and cross-polarization directivities can be defined.

$$\text{Directivity}_c = \frac{U_{c,\max}}{U_0} \qquad \text{Directivity}_x = \frac{U_{x,\max}}{U_0} \tag{1-11}$$

Directivity can be defined for an arbitrary direction $D(\theta, \phi)$ as radiation intensity divided by the average radiation intensity. When the coordinate angles are not specified, we take directivity at $U_{\max}$.

1-7 Directivity Estimates

Because a ratio of radiation intensities is used, the pattern may be referred to any convenient level. The most accurate estimate is based on measurements at equal angle increments over the whole radiation sphere. The average may be found from coarse measurements by using numerical integration, but the directivity measured is directly affected by whether the maximum is found.

The directivity of antennas with well-behaved patterns can be estimated from one or two patterns. Either the integral over the pattern is approximated or the pattern is approximated with a function whose integral is found exactly.

Kraus [4] devised a method for pencil beam patterns, peaks centered on $\theta = 0°$, by estimating the integral. Given the half-power beamwidths of the principal plane patterns, the integral is approximately the product of the beamwidths. In circuit theory the integral of a time pulse is approximately the pulse width (3 dB points) times the pulse peak.

$$U_0 = \frac{\theta_1\theta_2}{4\pi}$$

where θ_1 and θ_2 are the 3-dB beamwidths, in radians, of the principal plane patterns.

$$\text{Directivity} = \underset{\text{radians}}{\frac{4\pi}{\theta_1\theta_2}} = \underset{\text{degrees}}{\frac{41{,}253}{\theta_1\theta_2}} \tag{1-12}$$

Example Estimate the directivity of an antenna with E- and H-plane (principal plane) pattern beamwidths of 24° and 36°.

$$\text{Directivity} = \frac{41{,}253}{24(36)} = 47.75 \quad (16.8 \text{ dB})$$

An analytical function, $\cos^{2N}(\theta/2)$, approximates a broad pattern centered on $\theta = 0°$ with a null at $\theta = 180°$. The directivity of such a pattern can be found exactly. The characteristics of the approximation are

$$\text{Half-power beamwidth (HPBW)} = 4\cos^{-1} 0.5^{1/2N} \tag{1-13a}$$

$$N = \frac{\log 0.5}{2 \log \cos (\text{HPBW}/4)} \tag{1-13b}$$

$$\text{Directivity} = N + 1 \qquad \text{ratio} \tag{1-13c}$$

This pattern approximation requires equal principal plane beamwidths. An elliptic approximation is used with unequal beamwidths.

$$U(\theta, \phi) = \cos^{2N_e} \frac{\theta}{2} \cos^2 \phi + \cos^{2N_h} \frac{\theta}{2} \sin^2 \phi \tag{1-14}$$

where N_e and N_h are found from the principal plane beamwidths. These relations are combined in a nomograph for directivity estimates from beamwidths (Fig. 1-2).

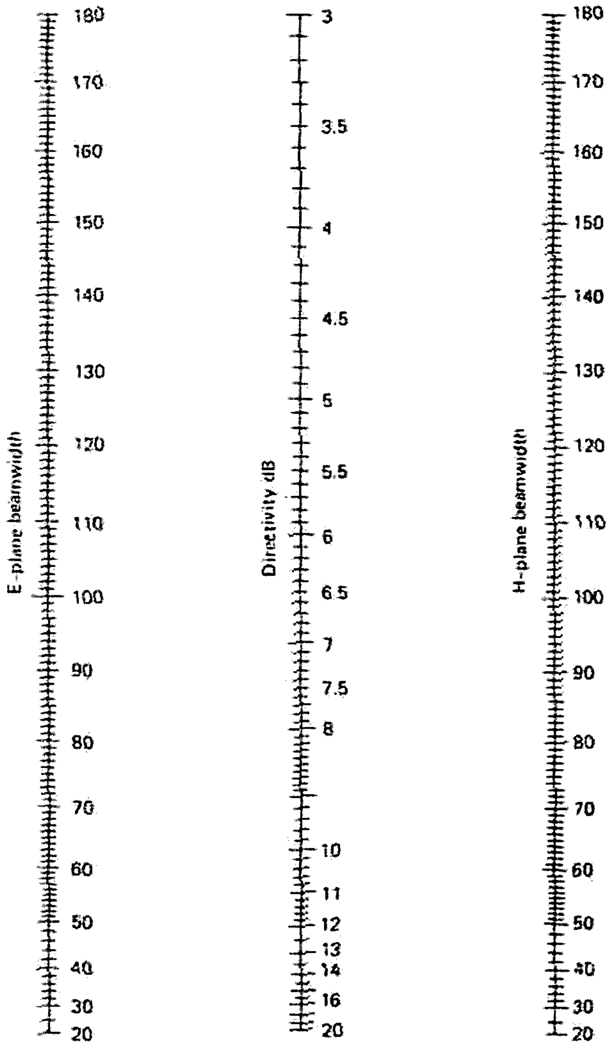

Figure 1-2 Nomograph for directivity estimates from beamwidths.

Example Estimate the directivity of an antenna with E- and H-plane pattern beamwidths of 98° and 140°. A line is drawn between the 98° and 140° points on the scales of Fig. 1-2, and the directivity is read on the center scale. It is 5.4 dB.

Butterfly Patterns Many antennas have nulls at $\theta = 0°$ with rotational symmetry about the z axis. Neither of the above directivity estimates can be used with such patterns because the patterns require the beam peak to be at $\theta = 0°$. Such patterns are generated by mode 2 log-periodic conical spirals, shaped reflectors, some higher-order-mode waveguide horns, biconical horns, and traveling wave antennas. A formula similar to Kraus's can be found if we assume that all the power is between the 3-dB beamwidth angles, θ_1 and θ_2.

$$U_0 = \tfrac{1}{2}\int_{\theta_1}^{\theta_2} \sin\theta\, d\theta = \frac{\cos\theta_1 - \cos\theta_2}{2}$$

Rotational symmetry removes the requirement of integration over ϕ.

$$\text{Directivity} = \frac{U_{\max}}{U_0} = \frac{2}{\cos\theta_1 - \cos\theta_2} \tag{1-15}$$

Example A pattern with rotational symmetry has half-power points at 35° and 75°. Estimate directivity.

$$\text{Directivity} = \frac{2}{\cos 35° - \cos 75°} = 3.57 \quad (5.5\text{ dB})$$

If the pattern also has symmetry about $\theta = 90°$, the integral for the average radiation intensity has limits from 0 to $\pi/2$. Equation (1-15) reduces to

$$\text{Directivity} = \frac{1}{\cos\theta_1}$$

Example A rotationally symmetric pattern with a maximum at 90° has a 45° beamwidth. Estimate directivity.

$$\theta_1 = 90° - \frac{45°}{2} = 67.5°$$

$$\text{Directivity} = \frac{1}{\cos 67.5°} = 2.61 \quad (4.2\text{ dB})$$

The pattern can be approximated by the function

$$U(\theta) = B\sin^{2M}\frac{\theta}{2}\cos^{2N}\frac{\theta}{2}$$

but the directivity estimates found by integrating this function show only minor improvements over the Kraus-like formula [Eq. (1-15)].

The directivity of butterfly patterns with unequal beamwidths in the principal planes cannot be estimated directly from the above formulas. Similarly, some pencil beam patterns have large sidelobes which decrease the directivity and cannot be accurately estimated from Eq. (1-12). Both problems are solved by considering the directivity as an estimate of the average radiation intensity.

Example A butterfly pattern peak is at 50° in both principal planes, but the beamwidths are 20° and 50°. Estimate directivity. The 3-dB pattern points are given by

Cut 1: 40° and 60°

$$U_{01} = \frac{\cos 40^\circ - \cos 60^\circ}{2} = 0.133$$

Cut 2: 25° and 75°

$$U_{02} = \frac{\cos 25^\circ - \cos 75^\circ}{2} = 0.324$$

Average the two pattern integral estimates.

$$U_0 = \frac{0.133 + 0.324}{2} = 0.228$$

$$\text{Directivity} = \frac{U_{\max}}{U_0} = \frac{1}{0.228} = 4.38 \quad (6.4\ \text{dB})$$

Suppose the beams are at different levels on the same pattern. For example, the lobe on the right of the first pattern is the peak and the left lobe is reduced by 3 dB. The peaks of the second pattern are reduced by 1 dB. We can average on one pattern alone. Each lobe contributes $U_{\max}(\cos\theta_1 - \cos\theta_2)/4$ to the integral. The integral of the first pattern is approximated by

$$\frac{0.266 + 0.266 \times 10^{-3/10}}{4} = 0.100$$

The integral of the second pattern is reduced 1 dB from the peak. The average radiation intensity is found by averaging between the two pattern averages.

$$U_0 = \frac{0.100 + 0.324 \times 10^{-0.1}}{2} = 0.178$$

$$\text{Directivity} = \frac{1}{U_0} = 5.602 \quad (7.5\ \text{dB})$$

Pencil beam patterns with large sidelobes can be averaged in a similar manner.

$$U_p = \frac{1}{\text{directivity}}$$

By using Eq. (1-12) and assuming equal beamwidths, we have

$$U_p = \frac{(\text{HPBW})^2}{41{,}253}$$

where U_p is the portion of the integral due to the pencil beam and HPBW is the beamwidth in degrees.

Example Consider a pencil beam antenna with pattern beamwidths of 50° and 70° in the principal planes. The second pattern has a sidelobe at $\theta = 60°$ down 5 dB from the peak and a 30° beamwidth below the 5 dB. What is the effect of the sidelobe on the directivity estimate?

Without the sidelobe the directivity estimate is

$$\text{Directivity} = \frac{41{,}253}{50(70)} = 11.79 \qquad 10.7 \text{ dB}$$

Consider each pattern separately.

$$U_{p1} = \frac{50^2}{41{,}253} = 0.0606$$

$$U_{p2} = \frac{70^2}{41{,}253} = 0.1188$$

The sidelobe adds to the second integral

$$U_{ps2} = \frac{(\cos 45° - \cos 75°)10^{-5/10}}{4} = 0.0354$$

Averaging the integrals of the parts gives us 0.1074.

$$\text{Directivity} = \frac{1}{U_0} = 9.31 \quad (9.7 \text{ dB})$$

If there had been a sidelobe on each side, each would have added to the integral.

Estimating integrals in this manner has limited value. Remember that these are only approximations. More accurate results can be obtained by digitizing the pattern and performing numerical integration on each pattern by using Eq. (1-9) or (1-10).

1-8 Beam Efficiency

Radiometer system designs [5] specify the antenna in terms of beam efficiency. For a pencil beam antenna, boresight at $\theta = 0$, beam efficiency is the ratio (or percent) of the pattern power within a specified cone centered on boresight to the total pattern power. In terms of the radiation intensity U,

$$\text{Beam efficiency} = \frac{\int_0^{\theta_1}\int_0^{2\pi} U(\theta, \phi) \sin\theta \, d\phi \, d\theta}{\int_0^{\pi}\int_0^{2\pi} U(\theta, \phi) \sin\theta \, d\phi \, d\theta} \tag{1-16}$$

where U includes both polarizations if necessary. Extended noise sources, such as radiometry targets, radiate noise into sidelobes of the antenna. Beam efficiency measures the probability of the detected target being located within the main beam ($\theta \leq \theta_1$).

Sometimes, as in the case of a paraboloidal reflector, we can find directivity more easily than the pattern everywhere required by the denominator of Eq. (1-16). We use Eqs. (1-8) and (1-9) to find the denominator integral.

$$\int_0^{\pi}\int_0^{2\pi} U(\theta, \phi) \sin \theta \, d\phi \, d\theta = \frac{4\pi U_{\max}}{\text{directivity}}$$

This reduces Eq. (1-16) to

$$\text{Beam efficiency} = \frac{\text{directivity} \int_0^{\theta_1}\int_0^{2\pi} U(\theta, \phi) \sin \theta \, d\phi \, d\theta}{4\pi U_{\max}} \tag{1-17}$$

Equation (1-17) greatly reduces the pattern calculation requirements to find beam efficiency when the directivity can be found without pattern evaluation over the whole radiation sphere.

1-9 Polarization

The polarization of a wave is the direction of the electric field. The spherical wave in the far field has only θ and ϕ components of the electric field.

$$\mathbf{E} = E_\theta \mathbf{a}_\theta + E_\phi \mathbf{a}_\phi$$

E_θ and E_ϕ are phasor components in the direction of the unit vectors $\mathbf{a}_\theta$ and $\mathbf{a}_\phi$. We can also express the direction of the electric field in terms of a plane wave propagating along the z axis.

$$\mathbf{E} = E_x \mathbf{a}_x + E_y \mathbf{a}_y$$

The direction of propagation confines the electric field to a plane. Polarization is concerned with methods of describing this two-dimensional space.

Both of the above are linear polarization expansions. We can rewrite them as

$$\mathbf{E} = E_\theta(\mathbf{a}_\theta + \hat{\rho}_L \mathbf{a}_\phi) \qquad \hat{\rho}_L = E_\phi / E_\theta \tag{1-18}$$

$$\mathbf{E} = E_x(\mathbf{a}_x + \hat{\rho}_L \mathbf{a}_y) \qquad \hat{\rho}_L = E_y / E_x$$

where $\hat{\rho}_L$ is the linear polarization ratio, a complex constant. If time is inserted into the expansions, then the tip of the electric field can be traced in space over time and appears as an ellipse with the electric field rotating either cw or ccw (Fig. 1-3). τ is the tilt of the polarization ellipse and the angle of maximum response. The ratio of the maximum to minimum responses on the ellipse is the axial ratio.

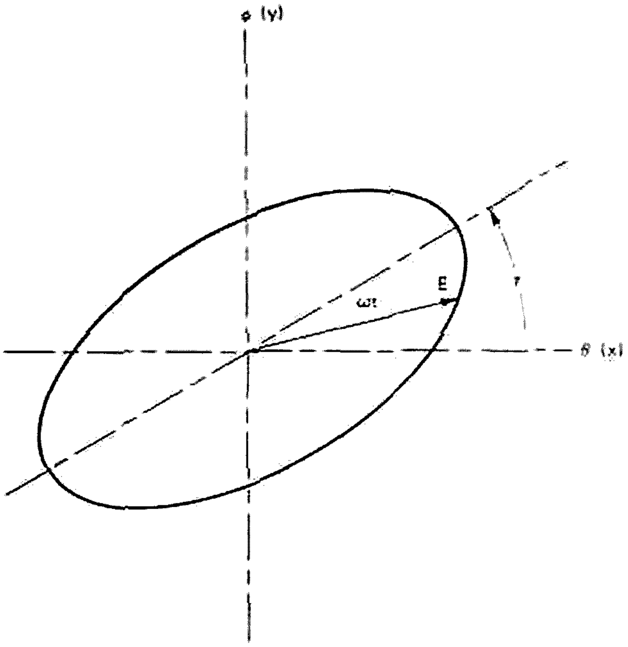

Figure 1-3 Polarization ellipse.

If $\hat{\rho}_L = e^{\mp j\pi/2}$, then the ellipse expands to a circle and gives the special case of circular polarization. The electric field is constant in magnitude but rotates either cw (left hand) or ccw (right hand) at the rate ωt. The direction of propagation is out of the paper.

Circular Polarization Components The two circular polarizations also span the two-dimensional space of polarization. The orthogonal unit vectors defined in terms of linear components are

$$\mathbf{a}_R = \frac{1}{\sqrt{2}}(\mathbf{a}_\theta - j\mathbf{a}_\phi) \qquad \text{or} \qquad \frac{1}{\sqrt{2}}(\mathbf{a}_x - j\mathbf{a}_y) \tag{1-19a}$$

$$\mathbf{a}_L = \frac{1}{\sqrt{2}}(\mathbf{a}_\theta + j\mathbf{a}_\phi) \qquad \text{or} \qquad \frac{1}{\sqrt{2}}(\mathbf{a}_x + j\mathbf{a}_y) \tag{1-19b}$$

The electric field in the polarization plane can be expressed in terms of these new unit vectors.

$$\mathbf{E} = E_L\mathbf{a}_L + E_R\mathbf{a}_R$$

When projecting a vector onto one of the unit vectors, it is necessary to use the complex conjugate.

$$E_L = \mathbf{a}_L^* \cdot \mathbf{E} \qquad E_R = \mathbf{a}_R^* \cdot \mathbf{E}$$

Project $\mathbf{a}_R$ onto itself:

$$\mathbf{a}_R^* \cdot \mathbf{a}_R = \tfrac{1}{2}(\mathbf{a}_\theta + j\mathbf{a}_\phi) \cdot (\mathbf{a}_\phi - j\mathbf{a}_\phi) = \tfrac{1}{2}(1 - j \cdot j) = 1$$

Similarly,

$$\mathbf{a}_R^* \cdot \mathbf{a}_L = \tfrac{1}{2}(\mathbf{a}_\theta + j\mathbf{a}_\phi) \cdot (\mathbf{a}_\theta + j\mathbf{a}_\phi) = \tfrac{1}{2}(1 + j \cdot j) = 0$$

The right- and left-hand circular (RHC and LHC) components are orthonormal.

A circular polarization ratio can be defined from the equation

$$\mathbf{E} = E_L(\mathbf{a}_L + \hat{\rho}_c \mathbf{a}_R) \qquad \hat{\rho}_c = \frac{E_R}{E_L} = \rho_c e^{j\delta_c} \tag{1-20}$$

Let us look at a predominately left-hand circularly polarized wave when time and space combine to a phase of zero for E_L. We draw the polarization as two circles (Fig. 1-4). The circles rotate at the rate ωt in opposite directions (Fig. 1-5) with the center of the right-hand circular polarization circle moving on the end of the vector of the left-hand circular polarization circle. The phase of the circular polarization ratio δ_c is the difference between the right- and left-hand circular components. Maximum and minimum electric fields occur when the circles alternately add and subtract as shown in Fig. 1-4.

$$E_{\max} = |E_R| + |E_L| \qquad E_{\min} = |E_L| - |E_R|$$

$$\begin{aligned} \text{Axial ratio} &= \frac{E_{\max}}{E_{\min}} = \frac{|E_L| + |E_R|}{|E_L| - |E_R|} = \frac{1 + |\hat{\rho}_c|}{1 - |\hat{\rho}_c|} \qquad \text{LHC} \\ &= \frac{|E_R| + |E_L|}{|E_R| - |E_L|} = \frac{|\hat{\rho}_c| + 1}{|\hat{\rho}_c| - 1} \qquad \text{RHC} \end{aligned} \tag{1-21}$$

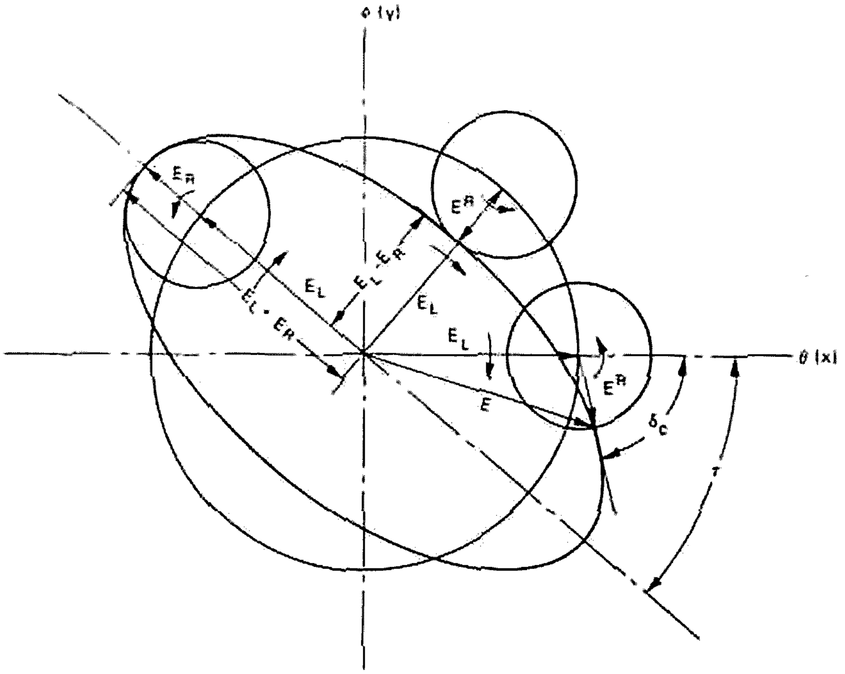

Figure 1-4 Polarization ellipse LHC and RHC components. (After J. S. Hollis, T. J. Lyon, and L. Clayton, *Microwave Antenna Measurements*, Scientific Atlanta, 1969, pp. 3–6. Adapted by permission.)

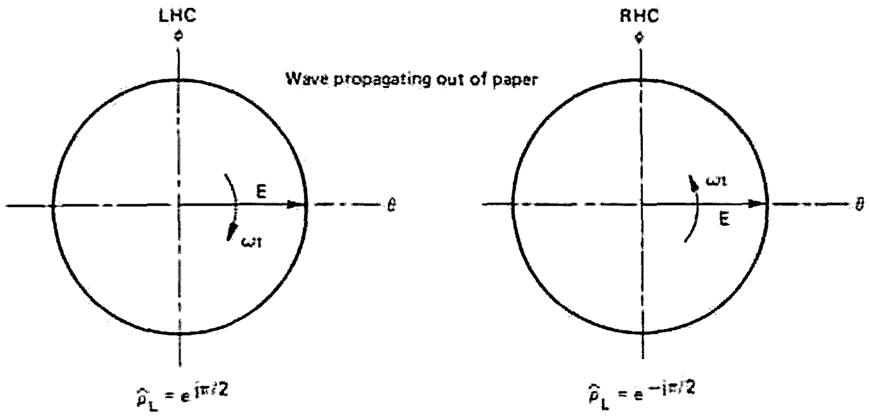
LHC
φ
RHC
φ
Wave propagating out of paper
E
ωt
θ
E
ωt
θ
$\hat{\rho}_L = e^{j\pi/2}$
$\hat{\rho}_L = e^{-j\pi/2}$

Figure 1-5 Circular polarization components. (After J. S. Hollis, T. J. Lyon, and L. Clayton, *Microwave Antenna Measurements*, Scientific Atlanta, 1969, pp. 3–5. Adapted by permission.)

$$0 \le |\hat{\rho}_c| < 1 \qquad \text{LHC}$$

$$0 \le \left|\frac{1}{\hat{\rho}_c}\right| < 1 \qquad \text{RHC}$$

$$\text{Axial ratio (dB)} = 20 \log \frac{E_{\max}}{E_{\min}}$$

The tilt angle of the polarization ellipse τ is one-half δ_c, the phase of $\hat{\rho}_c$. Imagine time moving forward in Fig. 1-4. When the LHC vector has rotated $\delta_c/2$ cw, the RHC vector has rotated $\delta_c/2$ ccw and the two align for a maximum.

Relations between Bases In problems with antennas at arbitrary orientations, circularly polarized components have an advantage over linear components. When the coordinate system is rotated, both the amplitude and phase of $\hat{\rho}_L$, the linear polarization ratio, change. The circular polarization ratio $\hat{\rho}_c$ magnitude is constant under rotations and only the phase changes. That is, the ratio of the diameters of the circles (Fig. 1-5) is constant.

The circular components can be found from linear polarization components by projection.

$$E_R = \mathbf{a}_R^* \cdot (E_\theta \mathbf{a}_\theta + E_\phi \mathbf{a}_\phi)$$

$$= \frac{1}{\sqrt{2}}(\mathbf{a}_\theta + j\mathbf{a}_\phi) \cdot (E_\theta \mathbf{a}_\theta + E_\phi \mathbf{a}_\phi)$$

$$E_R = \frac{1}{\sqrt{2}}(E_\theta + jE_\phi)$$

Similarly

$$E_L = \frac{1}{\sqrt{2}}(E_\theta - jE_\phi) \tag{1-22}$$

The linear polarizations can be found in terms of the circular components in the same manner.

$$E_\theta = \frac{1}{\sqrt{2}}(E_L + E_R) \qquad E_\phi = \frac{j}{\sqrt{2}}(E_L - E_R)$$

These relations enable the conversion between polarizations.

Good circularly polarized antennas over a wide bandwidth are difficult to build, but good linearly polarized antennas are easily obtained. If the phase and amplitude of a wave's E_θ and E_ϕ component phasors are measured, then the circular components can be found from Eqs. (1-22), the axial ratio [Eq. (1-21)], and the tilt angle of the polarization ellipse. By using a leveled phase-locked source, two patterns are recorded with orthogonal linear sources (or the same linear source is rotated between patterns) and polarization conversions are made to any desired polarization components.

Antenna Polarization Response The path loss formulas assume that the two antennas have matched polarizations. Polarization mismatch adds an extra loss. An antenna transmitting in the z direction has the linear components

$$\mathbf{E}_a = E_1(\mathbf{a}_x + \hat{\rho}_{L1}\mathbf{a}_y)$$

The incident wave on the antenna is given by

$$\mathbf{E}_i = E_2(\mathbf{a}_x + \hat{\rho}_{L2}\mathbf{a}_y)$$

where the wave is expressed in the coordinates of the source antenna. The z axis of the source is in the direction opposite that of the antenna. It is necessary to rotate the coordinates of the source antenna wave. Rotating about the x axis is equivalent to changing the sign of the tilt angle or taking the complex conjugate of E_i.

The response of the antenna to the incident wave is the scalar product

$$E_a E_i^*(1 + \hat{\rho}_{L1}\hat{\rho}_{L2}^*)$$

If we normalize the incident wave and antenna response, then the loss due to polarization mismatch is found.

$$E_i^* = \frac{\mathbf{a}_x + \hat{\rho}_{L2}^*\mathbf{a}_y}{\sqrt{1 + \hat{\rho}_{L2}\hat{\rho}_{L2}^*}} \qquad \mathbf{E}_a = \frac{\mathbf{a}_x + \hat{\rho}_{L1}\mathbf{a}_y}{\sqrt{1 + \hat{\rho}_{L1}\hat{\rho}_{L1}^*}}$$

The normalized voltage response is

$$\frac{1 + \hat{\rho}_{L1}\hat{\rho}_{L2}^*}{\sqrt{1 + \hat{\rho}_{L1}\hat{\rho}_{L1}^*}\sqrt{1 + \hat{\rho}_{L2}\hat{\rho}_{L2}^*}}$$

When we express it as a power response, we obtain the polarization efficiency Γ:

$$\Gamma = \frac{1 + |\hat{\rho}_{L1}|^2|\hat{\rho}_{L2}|^2 + 2|\hat{\rho}_{L1}||\hat{\rho}_{L2}|\cos(\delta_1 - \delta_2)}{(1 + |\hat{\rho}_{L1}|^2)(1 + |\hat{\rho}_{L2}|^2|} \tag{1-23}$$

This is the loss due to polarization mismatch. δ_1 and δ_2 are the phases of the polarization ratios. As expressed in terms of linear polarization ratios, the formula is awkward because, as the antenna is rotated to find the peak response, both the amplitudes and phases change. A formula using circular polarization ratios would be more useful.

Two polarizations are orthogonal ($\Gamma = 0$) only if

$$|\hat{\rho}_{L1}| = \frac{1}{|\hat{\rho}_{L2}|} \qquad \text{and} \qquad \delta_1 - \delta_2 = \pm 180^\circ \tag{1-24}$$

This can be expressed vectorially by using unit vectors:

$$\mathbf{a}_m^* \cdot \mathbf{a}_n = 0$$

$\mathbf{a}_m$ and $\mathbf{a}_n$ are the orthonormal generalized basis vectors for polarization. We can define polarization in terms of this basis with a polarization ratio $\hat{\rho}$. By paralleling the above analysis for linear polarizations, we obtain the polarization efficiency for an arbitrary orthonormal polarization basis.

$$\Gamma = \frac{1 + |\hat{\rho}_1|^2 |\hat{\rho}_2|^2 + 2|\hat{\rho}_1|\,|\hat{\rho}_2| \cos(\delta_1 - \delta_2)}{(1 + |\hat{\rho}_1|^2)(1 + |\hat{\rho}_2|^2)} \tag{1-25}$$

It has the same form as Eq. (1-23) derived for linear polarizations.

We can use Eq. (1-25) with circular polarizations whose polarization ratio ρ_c magnitudes are constant with rotations of the antenna. The maximum and minimum polarization efficiencies occur when $\delta_1 - \delta_2$ equals 0° and 180°, respectively. The polarization efficiency becomes

$$\Gamma_{\substack{\max \\ \min}} = \frac{(1 \pm |\hat{\rho}_1|\,|\hat{\rho}_2|)^2}{(1 + |\hat{\rho}_1|^2)(1 + |\hat{\rho}_2|^2)} \tag{1-26}$$

In all other bases for polarization the magnitude of the polarization ratio $\hat{\rho}$ changes under rotations.

Figure 1-6 expresses Eq. (1-26) as a nomograph. If we have fixed installations, we can rotate one antenna until the maximum response is obtained. We can realize the minimum polarization loss. In transmission between mobile antennas such as those of missiles or satellites, the orientation cannot be controlled in some cases and the maximum polarization loss must be used in the link analysis. Circularly polarized antennas are used in these cases.

Example A satellite telemetry antenna is RHC with an axial ratio of 7 dB. The ground station is RHC with a 1.5-dB axial ratio. Find the polarization loss. Because the orientation of the satellite is unknown, we must use the maximum polarization loss. To find it, use the RHC ends of the scales in Fig. 1-6. Draw a line from 7 on the leftmost scale to 1.5 on the center scale. Read the loss on the scale between: 0.9 dB.

The measured cross-polarization response of a linearly polarized antenna is the reciprocal of axial ratio, the same absolute magnitude in dB.

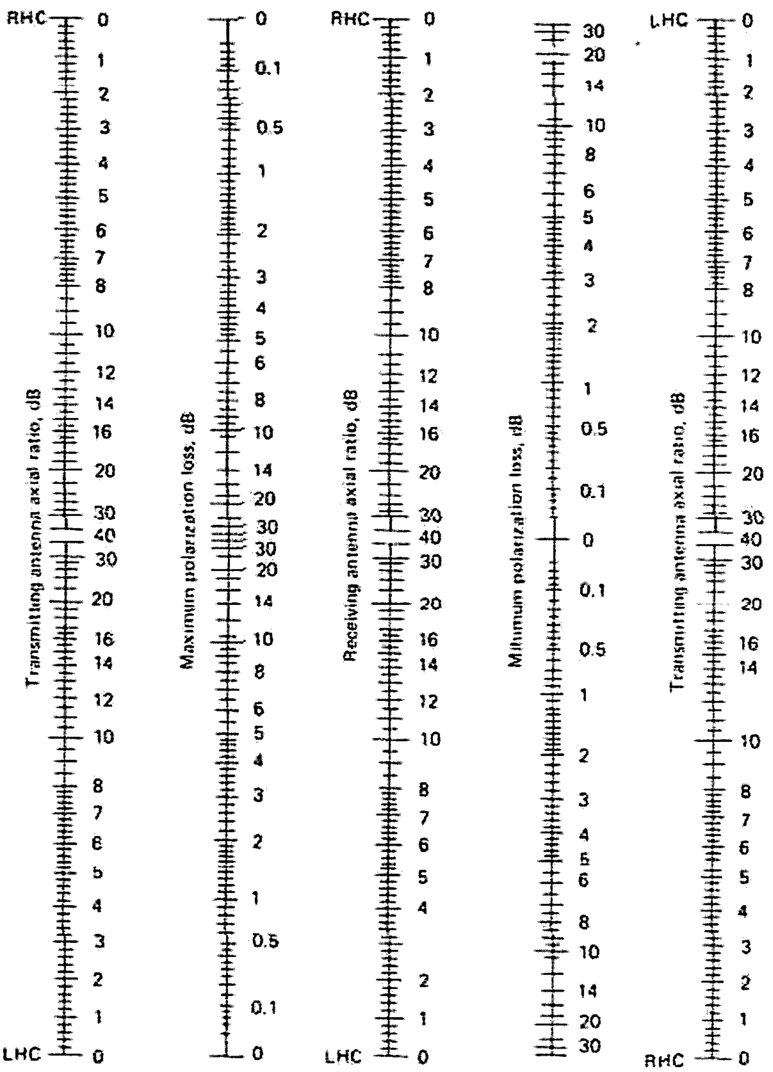

Figure 1-6 Maximum and minimum polarization loss. (After A. C. Ludwig, "A Simple Graph for Determining Polarization Loss," *Microwave J.*, vol. 19, no. 9, September 1976, p. 63.)

Example Suppose the linear cross-polarization responses of two antennas in a stationary link are given as 10 and 20 dB. Find the minimum polarization loss. Rotate one of the antennas until the maximum response is found. The cross-polarization response does not state whether an antenna is predominately left- or right-hand circularly polarized. It must be one or the other. Suppose the 20-dB cross-polarization antenna is LHC. If the other antenna also is LHC, draw a line from the lower portion of the center scale in Fig. 1-6 to the rightmost LHC scale and read 0.2 dB loss on the scale between the two. The second antenna could be predominately RHC. On drawing a line to the RHC (lower) scale, we read 0.7 dB on the center scale. When polarization is expressed in terms of linearly polarized components, it is ambiguous to give only magnitudes.

Phase Response of Rotating Antennas The polarization sense of an antenna can be determined from the phase slope of a rotating antenna. Before starting the phase measurement determine that it is proper. Some phase-amplitude receivers are ambiguous. We use the convention that increased distance between antennas gives decreased phase. Move the antenna away from the source and observe decreasing phase or correct the setup. A rotating linearly polarized source field is given by

$$\mathbf{E}_s = E_2(\cos\alpha\, \mathbf{a}_x + \sin\alpha\, \mathbf{a}_y)$$

where α is clockwise rotation viewed from the direction of propagation (forward). A horizontally polarized linear antenna has a response

$$\mathbf{E}_a = E_1\mathbf{a}_x$$

It responds to the rotating linear

$$E_1 E_2 \cos\alpha$$

The phase is constant under rotation until the null is passed; it rotates 180° through the null.

An RHC polarized antenna has a response

$$E_1(\mathbf{a}_x - j\mathbf{a}_y)$$

It responds to the rotating linear source field

$$E_1 E_2(\cos\alpha - j\sin\alpha) = E_1 E_2 e^{-j\alpha}$$

The magnitude remains constant, but the phase decreases with rotation. Phase increases when the antenna is LHC. By observing the phase slope, the sense of the predominant polarization can be determined.

RHC = negative phase slope

LHC = positive phase slope

It is easily remembered by considering the basis.

$$\mathbf{a}_R = \frac{1}{\sqrt{2}}(\mathbf{a}_x - j\mathbf{a}_y)$$

In rotation from the x axis to the y axis, the phase decreases 90°.

1-10 Impedance

The input impedance is measured with respect to some transmission line or source characteristic impedance. When the two are not the same, a voltage wave is reflected, ρV_i, where ρ is the voltage reflection coefficient.

$$\rho = \frac{Z_A - Z_0}{Z_A + Z_0}$$

where Z_A is the antenna impedance and Z_0 is the measurement characteristic impedance.

On a transmission line the two traveling waves, incident and reflected, will establish a standing wave.

$$V_{\max} = (1 + |\rho|)V_i \qquad V_{\min} = (1 - |\rho|)V_i$$

$$\text{VSWR} = \frac{V_{\max}}{V_{\min}} = \frac{1 + |\rho|}{1 - |\rho|}$$

where VSWR is the voltage standing wave ratio.

The reflected power is given by

$$\frac{V_i^2|\rho|^2}{Z_0}$$

The incident power is V_i^2/Z_0. The ratio of the reflected power to the incident power is $|\rho|^2$. It is the returned power ratio.

$$\text{Return loss} = -20 \log|\rho|$$

The power delivered to the antenna is the difference between the incident and the reflected power. Normalized, it is expressed as

$$1 - |\rho|^2$$

The source impedance which delivers the maximum power is the complex conjugate of the antenna impedance [6].

REFERENCES

1. S. A. Schelkunoff and H. Friis, *Antenna Theory and Practice*, Wiley, New York, 1952, p. 109.
2. R. F. Harrington, *Time-Harmonic Electromagnetic Fields*, McGraw-Hill, New York, 1961, p. 116.
3. H. Friis, "A Note on a Simple Transmission Formula," *Proc. IRE*, vol. 34, May 1946, pp. 254–256.
4. J. D. Kraus, *Antennas*, McGraw-Hill, New York, 1950.
5. W. F. Croswell and M. C. Bailey in R. C. Johnson and H. Jasik (eds.), *Antenna Engineering Handbook*, McGraw-Hill, New York, 1984, p. 31-6.
6. C. G. Montgomery, R. H. Dicke, and E. M. Purcell, *Principles of Microwave Circuits*, McGraw-Hill, New York, 1948, p. 94.

CHAPTER

2

ANTENNA TYPES

This chapter is an overview of antenna types and radiation structures. Only the creativity of the designer limits the number of possible antennas. Maintain an open mind when designing, and remember that the structure can solve the electromagnetic boundary value problem instantly. Designs can be founded on careful calculations, but we must accept empirical designs based on a willingness to try new ideas and risk failure. Before we can try new ideas, we need a knowledge of basic radiation structures.

Not all designs can be based on the empirical adjustment of the antenna. Large antennas and antenna systems must have careful design before building. There are elaborate analysis techniques, developed for these cases, which should be used. Simple antennas can be designed with straightforward procedures given in the following chapters. But keep in mind that too much analysis can stifle creativity.

RADIATION STRUCTURES

Waves radiate from four basic structures: (1) currents, (2) magnetic currents, (3) apertures, and (4) discontinuities in open transmission lines. This division is quite arbitrary. In some cases we can argue for more than one radiation cause. We judge between methods by the contribution to good design.

2-1 Radiation from Currents

The currents from which radiation occurs are the normal electron flow currents. The usual example is filamentary current on wire, but we include surface and volumetric current densities as well. We will analyze them by using the magnetic vector potential.* The far-field electric field is proportional to the magnetic vector potential **A**.

$$\mathbf{E} = -j\omega\mu\mathbf{A} \tag{2-1}$$

where μ is the permeability ($4\pi \times 10^{-7}$ H/m in free space). We find the magnetic field from

$$|\mathbf{E}| = \eta|\mathbf{H}| \tag{2-2}$$

and the knowledge that it is orthogonal to the electric field. Since the electric field direction defines polarization, we usually ignore the magnetic field.

We find the magnetic vector potential from a retarded volume integral over the current density **J**.

$$\mathbf{A} = \iiint \frac{\mathbf{J}(\mathbf{r}')e^{jk|\mathbf{r}-\mathbf{r}'|}}{4\pi|\mathbf{r} - \mathbf{r}'|}\,dV' \tag{2-3}$$

where **r** is the field measurement point radius vector, **r**′ is the source point radius vector, and k, the wave number, is $2\pi/\lambda$. As written, Eq. (2-3) finds the potential **A** everywhere—near and far field.

Radiation Approximation When we are interested only in the far-field response of an antenna, we can simplify the integral [Eq. (2-3)]. An antenna must be large in terms of wavelengths before it can radiate efficiently with gain, but at great distances, it still appears as a point source. Consider the radiation from two different parts of an antenna. Far away from the antenna the ratio of the two distances to the different parts will be nearly 1. The phase shift from each part will go through many cycles before reaching the observation point. When adding the response from each part, we need only the difference in phase shift.

The radiation approximation calls for us to pick a reference point on the antenna. We use the distance from that point to the far-field observation point for amplitudes, $1/R$, for all parts of the antenna. The direction of

---

*We will use the magnetic vector potential as defined by Roger Harrington, *Time-Harmonic Electromagnetic Fields*, McGraw-Hill Book Company, New York, p. 77. It avoids the use of flux densities and defines the potential directly in terms of the magnetic field.

radiation defines a plane through the reference point. This plane is defined by the radius normal vector, given in rectangular coordinates by

$$\mathbf{a}_r = \sin\theta\cos\phi\,\mathbf{a}_x + \sin\theta\sin\phi\,\mathbf{a}_y + \cos\theta\,\mathbf{a}_z$$

We find the phase difference to the far-field point by dropping a normal to the reference plane from each point on the antenna. This distance times k, the propagation constant, is the phase difference. Given a point on the antenna $\mathbf{r}'$, the phase difference is

$$k\mathbf{r}' \cdot \mathbf{a}_r$$

When we substitute these ideas into Eq. (2-3), the equation becomes

$$\mathbf{A} = \frac{e^{-jkr}}{4\pi r}\iiint \mathbf{J}' e^{jk\mathbf{r}'\cdot\mathbf{a}_r}\,dV' \tag{2-4}$$

In rectangular coordinates $k\mathbf{r}' \cdot \mathbf{a}_r$ becomes

$$k(x'\sin\theta\cos\phi + y'\sin\theta\sin\phi + z'\cos\theta)$$

We can combine k and $\mathbf{a}_r$ to form a $\mathbf{k}$ space:

$$\mathbf{k} = k\mathbf{a}_r = k\sin\theta\cos\phi\,\mathbf{a}_x + k\sin\theta\sin\phi\,\mathbf{a}_y + k\cos\theta\,\mathbf{a}_z$$

and the phase constant becomes

$$\mathbf{k} \cdot \mathbf{r}'$$

We find the $\mathbf{k}$ space convenient when dealing with apertures and arrays because we can normalize the results for any size.

Currents in filaments (wires) simplify Eq. (2-4) to a single line integral. Magnetic vector potentials and electric fields are in the same directions as the wires that limit the directions of current. A filamentary current along the z axis produces z-directed electric fields. Spherical waves (far field) have only $\mathbf{a}_\theta$ and $\mathbf{a}_\phi$ components found from the projection of E_z onto those axes.

$$\mathbf{a}_\theta \cdot \mathbf{a}_z = -\sin\theta \qquad \mathbf{a}_\phi \cdot \mathbf{a}_z = 0$$

Filamentary currents on the z axis produce only $\mathbf{a}_\theta$-directed electric fields with a null from $\mathbf{a}_\theta \cdot \mathbf{a}_z = -\sin\theta$ at $\theta = 0$. In turn, x- or y-directed currents produce electric fields depending on the scalar products (projections) of the $\mathbf{a}_x$ and $\mathbf{a}_y$ unit vectors onto the $\mathbf{a}_\theta$ and $\mathbf{a}_\phi$ vectors in the far field.

$$\mathbf{a}_\theta \cdot \mathbf{a}_x = \cos\theta\cos\phi \qquad \mathbf{a}_\phi \cdot \mathbf{a}_x = -\sin\phi$$

$$\mathbf{a}_\theta \cdot \mathbf{a}_y = \cos\theta\sin\phi \qquad \mathbf{a}_\phi \cdot \mathbf{a}_y = \cos\phi$$

Without knowing the exact pattern, we can estimate the polarization of the waves by examining the directions of the wires limiting the current density.

Consider various axes or planes of symmetry on an antenna, for example, a center-fed wire along the z axis. If we rotate it about the z axis, the problem remains the same. That is, all conical polar patterns (constant θ) must be circles; in other words, all great circle patterns must be the same. The antenna is the same below the xy plane as above; therefore, the pattern will be the same above and below the xy plane. Without any calculations we are able to discover some characteristics of the antenna pattern. Always look for axes and planes of symmetry to simplify the problem.

The magnetic vector potential can also find the near fields.

$$\mathbf{E} = -j\omega\mu\mathbf{A} + \frac{\nabla(\nabla \cdot \mathbf{A})}{j\omega\,\epsilon}$$

$$\mathbf{H} = \nabla \times \mathbf{A}$$

The electric field terms separate into far- and near-field terms as seen from Eq. (2-1). The equation for the magnetic field, the defining equation of the potential, does not separate.

Example Use the magnetic vector potential to find the far field of a short current element. Assume a constant current on the wire.

The current density is $I\ell\,\delta(r')\,\mathbf{a}_z$, where $\delta(r')$ is the Dirac delta distribution and ℓ is the length over which the far-field phase is constant. The integral in Eq. (2-4) quickly reduces to

$$A_z = \frac{I\ell e^{-jkr}}{4\pi r}$$

The current element is so short that the phase distances from all parts of the element are considered to be equal. e^{-jkr} is the retarded potential phase term.

The electric field is found from A_z by using Eq. (2-1):

$$E_z = -j\omega\mu\frac{I\ell}{4\pi r}e^{-jkr}$$

$$E_\theta = E_z\mathbf{a}_z \cdot \mathbf{a}_\theta = j\omega\mu\frac{I\ell}{4\pi r}e^{-jkr}\sin\theta$$

Evaluate ω as $2\pi F$; split μ in $\sqrt{\mu}\sqrt{\mu}$; and divide and multiply by $\sqrt{\epsilon}$.

$$E_\theta = \frac{jI\ell\,2\pi F\sqrt{\mu\epsilon}}{4\pi r}\sqrt{\frac{\mu}{\epsilon}}e^{-jkr}\sin\theta$$

The following terms can be recognized as

$$c = \frac{1}{\sqrt{\mu\epsilon}} \qquad \frac{F}{c} = \frac{\ell}{\lambda} \qquad \eta = \sqrt{\frac{\mu}{\epsilon}}$$

The far-field electric field becomes

$$E_\theta = \frac{jI\ell\eta}{2\lambda r}e^{-jkr}\sin\theta$$

The magnetic field is found from the electric field by using Eq. (2-2):

$$H_\phi = \frac{E_\theta}{\eta} = \frac{jI\ell}{2\lambda r} e^{-jkr} \sin\theta$$

The term j can be evaluated as $e^{j\pi/2}$, a phase shift term. The power density S_r is

$$S_r = E_\theta H_\phi^* = \frac{|I|^2\ell^2}{4\lambda^2 r^2}\, \eta \sin^2\theta$$

The normalized power pattern is equal to $\sin^2\theta$.
We can find the directivity by calculating the average radiation intensity, which is often normalized to the peak of the power pattern.

$$U_{\text{avg}} = \int_0^{\pi/2} \sin^2\theta \sin\theta\, d\theta = \tfrac{2}{3}$$

$$U_{\text{max}} = 1$$

$$\text{Directivity} = \frac{U_{\text{max}}}{U_{\text{avg}}} = 1.5 \quad (1.76 \text{ dB})$$

The total power radiated by the antenna is found by integrating the Poynting vector magnitude over a sphere.

$$\begin{aligned} P_r &= \int_0^{2\pi}\int_0^{\pi} S_r r^2 \sin\theta\, d\theta\, d\phi \\ &= \int_0^{2\pi}\int_0^{\pi} \left(\frac{|I|\ell}{2\lambda}\right)^2 \eta \sin^2\theta \sin\theta\, d\theta\, d\phi \\ &= \frac{2\pi}{3}\left(\frac{|I|\ell}{\lambda}\right)^2 \eta \end{aligned}$$

We represent the radiated power as a radiation resistance at the input of the antenna.

$$R_r = \frac{P_r}{|I|^2} = \frac{2\pi}{3}\eta\left(\frac{\ell}{\lambda}\right)^2$$

The input resistance of the antenna is the sum of the radiation resistance and the resistance due to material losses.

$$P_{\text{in}} = (R_r + R_l)|I|^2$$

The gain of an antenna is the ratio of the peak radiation intensity to the input power averaged over the radiation sphere.

$$\text{Gain} = \frac{S_{r,\text{peak}} r^2}{P_{\text{in}}/4\pi} = \frac{U_{\text{max}}}{P_{\text{in}}/4\pi}$$

By using the idea of radiation resistance, this is made

$$\text{Gain} = \frac{4\pi U_{\max}}{(R_r + R_l)|I|^2}$$

Efficiency is the ratio of radiated power to input power.

$$\eta_e = \frac{P_r}{P_{\text{in}}} = \frac{R_r|I|^2}{(R_r + R_l)|I|^2} = \frac{R_r}{R_r + R_l}$$

We can sometimes find the input power of the antenna from currents induced on the antenna elements by given voltage sources on various terminals of the antenna.

$$P_{\text{in}} = \text{Re}\,(V_1 I_1^*) + \text{Re}\,(V_2 I_2^*) + \text{Re}\,(V_3 I_3^*) + \cdots$$

The gain can be found from

$$\text{Gain}(\theta, \phi) = \frac{S_r(\theta, \phi)r^2}{P_{\text{in}}/4\pi} = \frac{U(\theta, \phi)}{P_{\text{in}}/4\pi}$$

This method is considerably easier than integrating the radiation intensity to find the directivity. The moment method of analysis will give us the currents for given input voltages.

2-2 Radiation from Magnetic Currents

Magnetic currents along the long axis of slots in ground planes replace the electric fields across the slots by application of the equivalence theorem. Current loops can be replaced by magnetic dipole elements to calculate the radiation. Magnetic currents are fictitious, but they enable slot radiation to be solved by the same methods as currents by using duality. Slot radiation could be calculated from the surface currents around it, but it is easier to use magnetic currents to replace the electric field in the slot.

We use the electric vector potential **F** with magnetic currents. The far-field magnetic field is proportional to the electric vector potential.

$$\mathbf{H} = -j\omega\epsilon\mathbf{F} \tag{2-5}$$

where ϵ is the permittivity (8.854×10^{-12} F/m in free space). We find the magnitude of the electric field from Eq. (2-2); it is perpendicular to **H**.

The electric vector potential is found from a retarded volume integral over the magnetic current density M. Applying the radiation approximation, it is

$$\mathbf{F} = \frac{e^{-jkr}}{4\pi r}\iiint \mathbf{M}' e^{j\mathbf{k}\cdot\mathbf{r}'}\, dV' \tag{2-6}$$

Equation (2-5) is the dual of Eq. (2-1), and Eq. (2-6) is the dual of Eq. (2-4). The dual of Eq. (2-3) is valid in both the near- and far-field regions.

The magnetic currents in a slot are perpendicular to the slot electric fields

$$\mathbf{M} = \mathbf{E} \times \mathbf{n}$$

where $\mathbf{n}$ is the normal to the plane with the slot. The filamentary currents of thin slots reduce Eq. (2-6) to a line integral. The magnetic current direction limits the direction of the electric vector potential and the magnetic field. Since the electric field (far field) is orthogonal to the magnetic field, the electric field is in the same direction as the field across the slots. We can use the direction of the electric field across the slots to estimate the polarization of the far field. As with filamentary electric currents, the far field is zero along the axis of the magnetic current.

The electric vector potential can also be used to find the near field.

$$\mathbf{H} = -j\omega\epsilon\mathbf{F} + \frac{\nabla(\nabla \cdot \mathbf{F})}{j\omega\mu}$$

$$\mathbf{E} = -\nabla \times \mathbf{F}$$

The magnetic field separates into near- and far-field terms; the electric field does not.

Example Find the fields from a small constant-current loop.

We could use the magnetic vector potential and calculate over the currents in the wire. Place the loop in the xy plane. The electric field radiated by the loop is in the ϕ direction because the currents in the loop can only be in the $\mathbf{a}_\phi$ direction. When solving the integral for the magnetic vector potential, note that the direction of the current on the loop, $\mathbf{a}'_\phi$, at a general point is not in the same direction as the field point, $\mathbf{a}_\phi$, unit vector. The integral must be solved with a constant vector direction, one component at a time.

Although the magnetic vector potential can be found, it is easier to replace the current loop with a magnetic current element. The equivalent magnetic current element is

$$I_m\ell = j\omega\mu IA$$

where A is the area of the loop. The magnetic current density is

$$\mathbf{M} = I_m\ell\delta(\mathbf{r}')\mathbf{a}_z = j\omega\mu IA\delta(\mathbf{r}')\mathbf{a}_z$$

By using Eq. (2-6), the electric vector potential is found.

$$F_z = \frac{j\omega\mu IA}{4\pi r}e^{-jkr}$$

The magnetic field is found from this electric vector potential by Eq. (2-5).

$$H_z = -j\omega\epsilon F_z = \frac{\omega^2\mu\epsilon IA}{4\pi r}e^{-jkr}$$

We find the H_θ component by projection.

$$H_\theta = H_z\mathbf{a}_z \cdot \mathbf{a}_\theta = \frac{-\omega^2\mu\epsilon IA}{4\pi r}e^{-jkr}\sin\theta$$

E_ϕ and H_θ are related in the far field.

$$E_\phi = -\eta H_\theta = \frac{\omega^2\mu\epsilon IA\eta}{4\pi r}e^{-jkr}\sin\theta$$

The small current loop and small current element have the same pattern shape, $\sin\theta$, but opposite polarizations. The directivity is 1.5 (1.76 dB).

2-3 Apertures

Antennas, such as horns or parabolic reflectors, can be analyzed as apertures. Equivalent electric and magnetic currents replace the incident fields. Using the vector potentials, the far fields are found as a superposition of each source. Most of the time, we assume that the incident field is a propagating free-space wave whose electric and magnetic fields are proportional to one another. This gives us the Huygens source approximation and allows us to use integrals of the electric field in the aperture. Each point in the aperture is considered to be a source of radiation. The far field is given by a Fourier transform of the aperture field.

$$\mathbf{f}(k_x, k_y) = \iint_S \mathbf{E}e^{j\mathbf{k}\cdot\mathbf{r}'}\,dS' \tag{2-7}$$

This uses the vector propagation constant

$$\mathbf{k} = k_x\mathbf{a}_x + k_y\mathbf{a}_y + k_z\mathbf{a}_z$$

$$k_x = k\sin\theta\cos\phi \qquad k_y = k\sin\theta\sin\phi \qquad k_z = k\cos\theta$$

where $\mathbf{f}(k_x, k_y)$ is the pattern in k space. To this, we multiply the pattern of the Huygens source.

$$\frac{je^{-jkr}}{2\lambda r}(1 + \cos\theta) \tag{2-8}$$

When apertures are large, we can ignore this pattern factor.

In Eq. (2-7) $\mathbf{f}(k_x, k_y)$ is a vector in the same direction as the electric field in the aperture. Each component is transformed separately. The far-field components E_θ and E_ϕ are found by projection (scalar products) from $\mathbf{f}(k_x, k_y)$ times the pattern factor of the Huygens source, Eq. (2-8).

If we have a rectangular aperture in which the electric field is expressed as a product of functions of x and y only, then the integral reduces to the product of two single integrals along each coordinate. The Fourier transform provides us with insight into the pattern shape along the two axes. Large apertures radiate patterns with small beamwidths. An antenna with long and short axes has a narrow beamwidth pattern in the plane containing the long dimension and a wide beamwidth in the plane containing the short dimension. This is the same as the time and frequency dual normally used with the Fourier transform.

A uniform amplitude and phase aperture distribution produces the maximum aperture efficiency and gain. An aperture collects power from a passing electromagnetic wave. The maximum collectible power occurs at the peak amplitude response of the aperture. If the amplitude response somewhere else in the aperture is reduced from the maximum, then that portion will collect less power. The amplitude response can be reduced only by adding loss or reflecting the power in reradiation. The antenna with the highest aperture efficiency reflects the least amount of power when illuminated by a plane wave. Similarly, if the phase shift from the collecting aperture to the antenna connector is different for different parts of the aperture, then the voltages from the various parts will not add in phase. Gain is directly proportional to aperture efficiency, Eq. (1-4). Therefore, a uniform amplitude and phase aperture distribution has maximum gain. All this assumes that the input match on various aperture distribution antennas is the same.

Example Find the pattern of a uniform aperture distribution in a rectangular aperture a by b.

Use the Fourier transform and ignore the polarization of the electric field in the aperture. (This assumes that the field has constant polarization.)

$$f(k_x, k_y) = E_0 \int_{-b/2}^{b/2} \int_{-a/2}^{a/2} e^{j\mathbf{k}\cdot\mathbf{r}}\, dx\, dy$$

$$= E_0 \int_{-b/2}^{b/2} \int_{-a/2}^{a/2} e^{jk_x x} e^{jk_y y}\, dx\, dy$$

We can separate the integral into a product of two integrals each of which has the form

$$\int_{-a/2}^{a/2} e^{jk_x x}\, dx = \frac{(e^{jk_x a/2} - e^{-jk_x a/2})}{jk_x}$$

$$= \frac{a \sin (k_x a/2)}{k_x a/2}$$

On combining the two similar integrals, we have

$$f(k_x, k_y) = ab \frac{\sin (k_x a/2)}{k_x a/2} \frac{\sin (k_y b/2)}{k_y b/2}$$

where $k_x = k \sin \theta \cos \phi$, $k_y = k \sin \theta \sin \phi$, and $k = 2\pi/\lambda$. The pattern in both planes is given by a k-space function

$$\frac{\sin u}{u}$$

The half-power points occur when

$$\frac{\sin u}{u} = \frac{1}{\sqrt{2}} \qquad \text{or} \qquad u = 1.39156$$

When we substitute for u, we have in the principal planes

$$\frac{\pi a}{\lambda} \sin \theta = 1.39156$$

By solving for θ, we can find the half-power beamwidth (HPBW).

$$\text{HPBW} = 2 \sin^{-1} \frac{0.4429\lambda}{a}$$

By using the approximation $u = \sin u$ for small angles, the half-power beamwidth can be estimated as

$$\text{HPBW} = 50.76° \frac{\lambda}{a}$$

Note that we have ignored the $(1 + \cos \theta)/2$ pattern of the Huygens source that will reduce the beamwidth for small apertures.

We can use the above result to find an estimate for the gain of a rectangular aperture from the beamwidths. The gain of a uniform distribution rectangular aperture is by Eq. (1-4),

$$\text{Gain} = \frac{4\pi ab}{\lambda^2}$$

We can solve for the aperture dimension divided by the wavelength

$$\frac{a}{\lambda} = \frac{50.76°}{\text{HPBW}}$$

By substituting in the gain formula, we obtain

$$\text{Gain} = \frac{32{,}375}{\theta_1 \theta_2} \tag{2-9}$$

where θ_1 and θ_2 are the half-power beamwidths in the principal planes. This is similar to Kraus's formula, Eq. (1-12), for directivity. Although it has been derived for an aperture with a uniform distribution, it can be used with other distributions for an approximation. Both formulas are about the same even though they differ by about 1 dB. Given the distribution in the aperture, the gain can be calculated more accurately than with the above formula.

The gain of a uniform amplitude and phase aperture distribution is given by Eq. (1-4), where A is the area of the aperture. The effects of nonuniform aperture amplitude distributions are accounted for by an amplitude taper efficiency. Phase anomalies are accounted for by a phase error efficiency. Each of these is found from the distribution of the aperture fields.

Example Find the length of the aperture with a uniform distribution that will give a 10° beamwidth.

$$\frac{a}{\lambda} = \frac{50.76^\circ}{\text{HPBW}} \qquad a \cong 5 \text{ wavelengths}$$

We can find the radiated power by integrating the Poynting vector magnitude over the radiation sphere, but there is an easier way. We assumed that the aperture fields are free-space waves. The total power radiated is in the aperture,

$$P_r = \iint_{\text{aperture}} \frac{|E|^2}{\eta} dS \qquad P_{\text{avg}} = U_{\text{avg}} = \frac{P_r}{4\pi} \tag{2-10}$$

where η is the impedance of free space. The radiated electric field is

$$\mathbf{E} = \frac{je^{-jkr}(1 + \cos\theta)}{2\lambda r} \mathbf{f}(k_x, k_y)$$

The Poynting vector magnitude is

$$S_r = \frac{|\mathbf{E}|^2}{\eta} = \frac{(1 + \cos\theta)^2}{4\lambda^2 r^2} |\mathbf{f}(k_x, k_y)|^2 \tag{2-11}$$

By combining Eqs. (2-10) and (2-11), we can find the directivity.

$$\text{Directivity}(\theta, \phi) = \frac{U(\theta, \phi)}{U_{\text{avg}}} = \frac{S_r r^2}{P_r/4\pi}$$

$$\text{Directivity} = \frac{\pi(1 + \cos\theta)^2}{\lambda^2} \frac{\left| \iint \mathbf{E} e^{j\mathbf{k}\cdot\mathbf{r}'} dS \right|^2}{\iint |\mathbf{E}|^2 dS} \tag{2-12}$$

Example Suppose E is uniform over the aperture, find the directivity at $\theta = 0$ by using Eq. (2-12).

$$\text{Directivity} = \frac{\pi(1 + 1)^2}{\lambda^2} \frac{|E_0|^2 \left| \iint dS \right|^2}{|E_0|^2 \iint dS}$$

The integral $\iint ds$ equals the area of the aperture.

$$\text{Directivity} = \frac{4\pi}{\lambda^2}\frac{A^2}{A} = \frac{4\pi A}{\lambda^2}$$

This is the same as Eq. (1-4) for a perfectly efficient antenna.

2-4 Discontinuities

Discontinuities in transmission lines excite higher-order modes to satisfy the boundary conditions. In a normal closed transmission line, such as waveguide or coax, the higher-order modes excited by discontinuities soon die out because they cannot propagate. The excess electric or magnetic fields in the region of the discontinuity appear as capacitive or inductive reactances to the transmission line. If the transmission line is open or is opened by a discontinuity (a slot or hole), then the higher-order modes can radiate their power. As a class, the surface wave transmission lines will radiate at discontinuities. They include dielectric slabs, dielectric rods, and corrugated metal surfaces. At the point of excitation and at the point of termination, the higher-order modes generated will radiate.

Like other methods of analysis, these structural changes can be used to explain radiation. It is not as easy to apply as the other methods, but it gives us a physical feeling for radiation and alerts us to possible radiation points. The geometric theory of diffraction (GTD) can be used with structures of the order of a wavelength or greater in size. In this method we find effects of diffractions off edges or around smooth surfaces. The idea is that shadow or reflection boundaries (field discontinuities) cannot exist in free space because fields must be continuous across nonmaterial boundaries. By combining ray tracing with diffractions, the patterns of large structures can be found. Space itself has become the open transmission line in GTD analysis.

Radiation structures will not always neatly fit into the division given here and will leave open the possible method of analysis. The true test of any method is its ability to predict measurements.

CATALOG OF ANTENNAS

Antennas can be made by combining different elements in configurations which will give us a seemingly limitless number of different antennas. A catalog of basic antenna types and their characteristics is presented as a quick reference. The list of major divisions of antenna types, along with common examples, will help in the selection of the right design. The definitions of pattern types are from IEEE STD 145-1983. Details of analysis and design will be given later.

Directional Antenna An antenna having the property of radiating or receiving more effectively in some directions than others.

Fan-Beam Antenna An antenna producing a major lobe whose transverse cross section has a large ratio of major to minor dimensions.

Omnidirectional Antenna An antenna having an essentially nondirectional pattern in a given plane of the antenna and a directional pattern in any orthogonal plane.

Pencil Beam Antenna An antenna whose radiation pattern consists of a single main lobe with narrow principal plane beamwidths and sidelobes having relatively low levels.

1. Small resonant. Omnidirectional: usually linear polarization.
Examples: Dipole (small, $\lambda/2$, sleeve, monopole), loop, slot

2. Conformal. Unidirectional: linear or circular polarization: narrow bandwidth.
Examples: Microstrip patch, slot, cavity-mounted elements.

3. End-fire. Pencil beam, slow-wave line structure.
Examples: Helical wire, cigar, Yagi-Uda, dielectric rod.

4. Long-wire. End-fire pencil beam except for polarization null on axis.
Examples: Beverage, vee, rhombic.

5. Leaky wave. Pencil or fan beam, fast-wave structure.
Examples: Waveguide with holes or slots.

6. Self-scaling. Unidirectional or bidirectional, wide bandwidths.
Examples: Spirals (equiangular, conical, Archimedian), log-periodics.

7. Horns. Unidirectional or fan-beam, bandwidth determined by feed waveguide.
Examples: Sectoral, pyramidal, conical, corrugated, biconical.

8. Reflector. Uses free space for feeding large aperture: bandwidth and polarization determined by feed antenna: pencil or fan beam.
Examples: Paraboloidal, parabolic cylinder, dual (Cassegrain, Gregorian, offset), offset-fed, corner.

9. Lens. Uses free space to feed large aperture with feed antenna mounted behind aperture: pencil or fan beam.
Examples: Dielectric, waveguide flat plate, artificial, bootlace.

2-5 Small Resonant Antennas

Small resonant antennas are small relative to a wavelength and have low gain. Both the dipole and its dual, the slot, are resonant antennas. Two straight rods make up the dipole, split near the middle, and fed from a balanced line. A narrow slot, cut in a ground plane, resonates with an equivalent magnetic current standing wave. If the slot radiates on both sides of the ground plane, then both the dipole and the slot have the same pattern magnitude with differing polarizations. The slot is replaced by an equivalent magnetic current, and then the antennas have dual symmetry. The pattern has a null in the direction of the dipole or slot axis and a broad beam everywhere else. Long elements ($>1\lambda$) give additional nulls. After the dipole is rotated about its axis, the problem remains the same: an operation showing the circular symmetry of the pattern. The polarization, the direction of the electric field, is in the same direction as the current (rod). The electric field across the narrow width of the slot establishes the polarization. Because the dipole and the slot have the same pattern, they have the same directivity for a given length. Given the input impedance of one, we find the input impedance of the other through the Babinet-Booker principle, since the dipole and slot are complementary antennas. When short, these antennas are difficult to match and suffer from low efficiency. But when they are a resonant length ($\approx\lambda/2$), the radiation resistance far exceeds the material loss resistance. The result is excellent efficiency and input match. Gain ranges from 1.7 to about 5 dB.

A closed loop resonates when it is approximately one wavelength in circumference and has an approximately sinusoidal current distribution. The feed point occurs at the split on the loop. The direction of the electric field across the gap establishes the far-field polarization and the direction of the null in the pattern. The loop's exact shape has only a minor effect on the pattern, and its gain is about the same as that of a one-wavelength dipole (3.8 dB). The bandwidth of the resonant loop antenna roughly equals that of the halfwave dipole.

A single rod, normal to a ground plane and fed from a coax center conductor, forms a monopole antenna. It radiates on only one side of the ground plane. Its dual is a cavity-backed slot limited to radiation on one side only. By using the method of images, an equivalent dipole is analyzed to find the pattern above the ground plane. The monopole gain is twice the gain of the equivalent dipole, and its impedance is half as great. The cavity-backed slot has twice the gain but double the input impedance of the slot radiating on both sides.

A sleeve around the input region and extending out the arms of the dipole or monopole increases the impedance bandwidth of the antenna. The pattern remains about the same. Because the standing wave current magnitude remains nearly constant with changing frequency at the feed, the end of the sleeve, so does the input impedance. The ratio of the highest to lowest frequency of operation can be from 2:1 to 3:1.

Most dipole, loop, and sleeve dipoles must be placed over a ground plane. The ground plane limits the radiation directions and increases the gain. The spacing over the ground plane determines the exact increase when the antenna is analyzed as a two-element array; the second element comes from the image. Because these antennas have wide beamwidths, they are greatly affected by nearby structures and antennas.

2-6 Conformal Antennas

Conformal antennas mount with low profiles on the outsides of vehicles. They must assume the shape of the object. The microstrip patch antenna has a large number of applications because it can radiate both linear and circular polarizations. Photoetching a variety of cavity shapes (rectangular and circular, most commonly) on one side of a dielectric slab forms the antenna. A metal ground plane remains intact on the second side of the slab. A microstrip line on the substrate or a coax probe from below feeds the antenna. A nonradiating feed circuit can be etched on the same dielectric slab. The ground plane limits the radiation to the half plane, and, combined with an effective two-slot radiation from adjacent edges, the patch has about 7 dB gain. The impedance bandwidth is very narrow, but the patch can meet the requirements of many systems.

A cavity-backed slot can also be made conformal by cutting a slot in one of the ground planes of stripline and forming a cavity by using plated-through holes or edge plating between the ground planes. It is fed below from stripline feed networks. The single slot radiator has a greater beamwidth in the E plane than the microstrip patch antenna because there is only one radiating slot. For a given volume both antennas (patch and stripline slot) have about the same bandwidth.

An annular slot radiates a pattern and a polarization similar to those of a monopole. The power spreads from a coax input with the center conductor connected across a cavity to the inner metal circle and the shield to the ground plane below. Shorting pins connect the two ground planes beyond the slot and impress a field across the ring slot.

Many other types of antennas, such as traveling wave antennas, can be made conformal, and that leaves open the number of possible conformal antennas. Because the volume of conformal antennas is limited, so will be the input impedance bandwidth.

2-7 End-Fire Antennas

An end-fire antenna radiates in the direction of a wave traveling along the structure away from the feed point. If the structure lies along the z axis, then the peak of the beam also will be in the z direction. Most end-fire antennas radiate from surface wave structures that slow the traveling wave velocity *below the speed of light* (that is, *they increase the effective propagation* constant). To achieve a single unidirectional beam centered on the z axis, the effective propagation constant must be matched to the length of the antenna. A wave propagating along the structure with the free-space velocity and radiating uniformly along the axis has a simple formula for directivity:

$$\text{Directivity} = \frac{4L}{\lambda} \tag{2-13}$$

To double the gain (directivity), it is necessary to double the length L. Any realizable radiation structure will impart some pattern from an incremental segment and increase gain. If the wave velocity is slowed, then the gain increases up to a point. Increased slowing starts increasing the sidelobes and decreasing the gain. The optimum slowing is found from the Hansen and Woodyard criterion [3], which gives a directivity $\approx 7.4L/\lambda$.

An end-fire helical antenna consists of a helical coil of wire each turn of which is approximately one wavelength long. A short helical antenna, by matching its modes to the length, adjusts its effective propagation constant over nearly a 1.7:1 range of frequencies so that a single end-fire beam is achieved. *The rotating traveling wave radiates a circular polarized wave in* the same sense as the winding. Matched pairs of helical antennas with opposite senses of windings provide circular polarization standards. These determine the polarization sense of test antennas by comparing the responses.

The helical antenna mode transition consists of a coax mounted to a small ground plane. The helix is fed from the center conductor of the coax. As the length increases, the helical antenna frequency bandwidth shrinks, but the gain increases. The antenna's directivity will exceed the Hansen and Woodyard criterion because the single-turn pattern narrows the beamwidth and reduces sidelobes.

The cigar or corrugated-rod antenna is a stack of alternating diameter disks. It supports a surface wave in a hybrid mode which maintains linear polarization. The response and design parameters for antennas using closely spaced circular disks can be found exactly, but antennas can be made by using other shapes as well. Empirical designs, using other shapes, start from a known solution, and the dimensions of the parts are adjusted to achieve the proper phase velocity for a given length. Good operation occurs only over a narrow bandwidth that decreases for increased gain (length). The maximum directivity is about $8L/\lambda$. The structure can be excited by a combination of a linearly polarized radiator (dipole or loop) and a reflector element to achieve a unidirectional wave in the direction of the rod.

A dielectric rod will support a hybrid mode (linear polarization) surface wave. Like the others, it produces an end-fire pattern when its effective propagation constant matches its length. It is usually fed by a circular waveguide operating in the TE_{11} mode. The rod could just as well be square or rectangular and be fed from a rectangular waveguide. Tapering the rod increases the bandwidth and establishes an amplitude taper on the rod.

A Yagi-Uda end-fire antenna couples energy from a fed element to a reflector element and a series of director elements. It can be analyzed as an array or as a surface wave device. Because it radiates linear polarization, the hybrid mode approximates its response and establishes an upper bound on directivity for a given length. The antenna elements consist of dipoles or loops adjusted to give the proper phasing through mutual coupling to approximate a surface wave response. Like the others, its bandwidth decreases with increased gain.

Flat structures, such as dielectric slabs on ground planes and corrugated surfaces, support surface waves. These surfaces shape the beams of antennas by capturing some of the radiated power and redirecting it into an end-fire pattern. The surfaces can have positive effects over narrow bandwidths, but they cause pattern distortion in other cases. All surface wave radiators capture power from some primary radiator, dipole or waveguide, and direct its radiation.

Simple periodic structures can be solved with boundary matching, but tapered and modulated structures can be used as well. Without waiting for solutions, antennas using them can be designed empirically. Do not be limited to regular structures matching coordinate systems.

2-8 Leaky Wave Antennas

Leaky wave antennas radiate from structures whose relative propagation constant is less than 1. The wave is no longer bound to the surface; instead, it constantly leaks power along its length and attenuates the traveling wave. The radiation maximum occurs at an angle to the direction of wave propagation determined by the relative propagation constant.

$$e^{-jPkz} \qquad \theta_{\max} = \cos^{-1} P \qquad P < 1$$

Waveguides are fast wave structures. When opened by holes or slots, the fast leaky waves radiate from the openings. Small openings have little effect on the internal wave and the unperturbed waveguide phase velocity determines the radiation direction. although radiation implies a changed phase velocity. A waveguide with a series of resonant-length slots in the walls can be analyzed as an array. Terminating the guide with a short circuit establishes a standing wave ($P = 0$) and gives a broadside pattern ($\theta = 90°$). A matched load on the end of the waveguide leads to a nonresonant design whose beam direction is determined by the waveguide propagation constant.

Waveguide structures with holes or nonresonant-length slots radiate leaky waves. Each opening radiates a small portion of the passing internal wave. The amplitude distribution can be controlled by varying the openings. To obtain uniform radiation along the length, the first opening can radiate only a small portion of the available power and the openings further along will then radiate more and more of the remaining power in the traveling wave.

If the antenna has circular symmetry about the z axis, we can estimate the directivity. For broadside radiation from a uniform distribution, directivity is

$$\frac{2L}{\lambda} \tag{2-14}$$

where L is the length. As the antenna beam is scanned off broadside, it broadens because the projected area shrinks. But because the pattern is multiplied by sin θ when the average radiation intensity is calculated, the product remains constant. The gain for a scanned linear aperture with circular symmetry remains constant. The pattern gain may drop because the pattern of the incremental radiator (slot or dipole) will decrease the off-broadside gain, but Eq. (2-14) remains a good estimate.

2-9 Long Wire Antennas

A long wire loaded on the end would radiate an end-fire beam except that the pattern of the incremental radiator, the current element, has a null along the axis. This null splits the beam around the wire. Long wire antennas have good directivity but poor gain, since some of the input power is lost in the load. The length of the wire determines the beam direction.

A single long wire high over a ground plane is called a *Beverage antenna*. Two Beverage antennas fed out of phase and so angled that their maximums are aligned form a V antenna. Two V antennas make up a rhombic antenna. The second V, attached to the ends of the first, brings the ends back to a point where a load connects them. These antennas are used to radiate sky waves for ionosphere hopping.

2-10 Self-scaling Antennas

Self-scaling antennas contain in themselves their own scale models. They divide into continuous scaling and log-periodic scaling types. Continuous scaling antennas depend only on angles for dimensions, and without any characteristic length, they can have large continuous bandwidths. The log-periodic antenna scales itself at discrete frequencies with response variations within the scaling period.

Both a flat equiangular (log) two-arm spiral and a conical equiangular two-arm spiral antenna (projection on a cone) depend only on angles for dimensions. They radiate circular polarization. The flat spiral radiates equally on both sides with opposite senses of polarization. Its directivity may be doubled by backing it with a cavity that eliminates the opposite-sense radiation. When a spiral is projected on a cone, its changed shape increases the radiation in the direction of the cone apex. Archimedian spirals exhibit wide bandwidths, as do the equiangular spirals, but they require loads on the ends of the arms to eliminate end reflections.

The log-periodic antenna is usually linearly polarized, although it can be used in a pair to obtain circular polarization. It scales itself at discrete frequencies, usually with dipoles, and its response varies between the scalings. A central transmission line feeds each dipole or other element. The mutual coupling between elements broadens the response between the resonant frequencies of the elements. The gain ranges from 7 to 12 dB.

Self-scaling antennas have limited gain because, at any one frequency, they radiate over a limited active region. Like all end-fire antennas, the length of the active region determines gain. The higher-frequency portion of the antenna must act as a transmission line between the feed and the active region. The transmission line portion is a slow-wave structure moving to a radiating fast-wave structure in the active region with its backfire radiation. Past the active region little power is left to radiate. Because of their ability to scale themselves, self-scaling antennas have bandwidths measured in octaves.

2-11 Horn Antennas

A horn is an aperture antenna fed from a waveguide mode in an expanded waveguide. If the expanded waveguide cross section increases slowly, the waveguide mode amplitude distribution translates to the aperture plane. The increased length along the slant walls compared with the direct path to the aperture causes a phase error in the aperture. The phase distribution is approximately quadratic. Given two horns with the same aperture, the horn with the longer slant length has the greater gain. The horn can achieve very pure linear polarization, which makes it useful in antenna measurements both as a source and as a gain standard.

The aperture efficiency is a product of the amplitude taper efficiency, determined by the amplitude distribution of the waveguide mode, and the phase error efficiency, determined by the quadratic phase distribution. In Table 2-1 the aperture efficiencies of different horns, each with a 0.3-wavelength maximum aperture phase error, are compared.

Increasing the phase deviation in the aperture will decrease the aperture efficiency at different rates for the various horns. The efficiency of a corrugated-wall horn decreases more slowly than that of a smooth-wall horn. The corrugated-wall horn will eventually have better efficiency for a given aperture phase deviation.

The pyramidal horn fulfills many requirements for antennas. It starts in a rectangular waveguide operating in the TE_{10} mode. The waveguide walls

TABLE 2-1 Aperture Efficiencies

Horn type	Wall type	Efficiency, %	Loss, dB
Pyramidal	Smooth	50.5	2.97
Pyramidal	Corrugated	48.8	3.12
Conical	Smooth	63.4	1.98
Conical	Corrugated	57.4	2.41

flare out to the aperture. The waveguide mode establishes a constant aperture amplitude distribution in the *E* plane. The *H* plane has a cosine distribution. Horns with greatly differing beamwidths are designed by varying the aperture plane dimensions. When a horn is flared only in the *H* plane, the *E*-plane pattern remains broad while the *H*-plane pattern narrows. Similarly, a horn flared only in the *E* plane retains a broad *H*-plane pattern as the *E*-plane pattern narrows. The Fourier transform relation, wide aperture lengths give narrow beamwidths (Sec. 2-4), is used to design the antenna. The usual horn has approximately equal beamwidths in both planes, but the pyramidal horn can provide controlled beamwidths in both planes.

A circular waveguide excited in the TE_{11} mode feeds the conical horn, a truncated circular cone attached to a circular waveguide. The horn has good aperture efficiency. Because the *E*- and *H*-plane dimensions are the same, the ratio of the beamwidths is fixed. For a maximum slant length deviation of 0.3 wavelength from the central length, the *H*-plane beamwidth is approximately 1.21 times the *E*-plane beamwidth. Dual polarized antennas are easily constructed because the circular waveguide can be fed from any polarization. Of course, the pyramidal horn can be fed from a square waveguide and achieve dual polarization.

Corrugated-wall horns have equal *E*- and *H*-plane amplitude distributions. The corrugations, cut normal to the direction of propagation, excite higher-order waveguide modes. A combination of the TE_{11} and TM_{11} modes, a hybrid HE_{11} mode, feeds the aperture of the corrugated-wall conical horn. The hybrid mode has circular symmetry and gives equal *E*- and *H*-plane beamwidths. The fields vanish on the walls when the corrugated surface is capacitive (slots $\lambda/4$ to $\lambda/2$ deep). Because the fields vanish on the walls, there is no edge diffraction to radiate sidelobes. Corrugations in the *E*-plane walls of a pyramidal horn taper the distribution to a cosine-like amplitude that produces *H*-plane beamwidths and sidelobe levels. Square corrugated horns have equal *E*- and *H*-plane beamwidths to both polarizations.

External corrugations around the aperture plane of the horn achieve the same effect as wall corrugations by forcing the fields to zero on the walls of the *E* plane. In a circular horn this is called a coaxial or choke horn. It is a good design for small apertures in which internal corrugations are expensive to machine. Over narrow bandwidths the corrugation depths can be varied to excite a series of modes to match the focal plane fields of a parabolic reflector. Rectangular horns may also use external corrugations along the *E*-plane walls.

In stepped multimode horns abrupt steps are used in the input waveguide to generate higher-order modes. The step discontinuity generates higher-order modes to satisfy the boundary conditions at the step. The increased waveguide dimensions and symmetry select the propagating higher-order mode. The distance between the step and the aperture establishes the phase shift between modes. Each mode travels with a different phase velocity. The rectangular stepped horn (box horn) steps in the *H* plane to generate the TE_{30} mode. The combination of the TE_{10} and TE_{30} modes flattens the *H*-plane amplitude distribution. A step in a circular waveguide excites the TM_{11} symmetrical mode from an input TE_{11} mode. When combined in the aperture with the right phase, the sum produces the HE_{11} of the corrugated-wall horn.

The bandwidth of a horn is determined by the input waveguide for large apertures. Central ridges increase the bandwidth of waveguide by lowering the cutoff frequency. Near-decade bandwidths are possible from horns with ridges. The ridges also serve as impedance transformers between the coax input and the radiating aperture impedance.

A biconical horn flares from the conductors of a coax line into two cones. The coax excites a spherical mode field between the cones that has circular symmetry. The distance between the cones at the aperture plane along with the phase error loss determines the gain of the antenna. Equation (2-14) puts an upper bound on the gain for long cones.

2-12 Reflector Antennas

A parabolic reflector is the cheapest large-aperture (gain) antenna. When fed from an antenna at its focus, it collimates the power into a large-aperture plane, the projected area of the reflector. The length of the aperture in various pattern planes and the amplitude distribution determine the beamwidth. Reflectors with elliptical edge shapes produce fan beams with the narrow beamwidth in the plane containing the major axis.

The feed for optimum gain has its 10-dB beamwidth approximately equal to the subtended angle of the reflector. The minimum sum of amplitude taper loss and feed spillover loss occurs nearly at this point. The gain can be estimated from Eq. (1-7) by using an aperture efficiency of 55 percent. The beamwidth is approximately

$$\mathrm{HPBW} = \frac{70^\circ\,\lambda}{D}$$

where D is the diameter.

A dual-reflector antenna increases the effective focal length of the main reflector. The Cassegrain has a hyperbolic subreflector to spread the feed energy out to the main reflector. One focus of the hyperbola is at the focus of the main reflector; the other focus is at the feed antenna. The Gregorian antenna uses an elliptical subreflector. Because of the added losses of the subreflector blockage, dual-reflector antennas become effective only when the main reflector is large.

A cylindrical reflector uses a parabola in one plane to form the beam. A line feed forms the beam in the other plane. A phased array feed can scan the beam in one plane while mechanical rotation scans the beam in the other plane.

The central blockage of the center-fed reflector reduces the gain and increases the sidelobe level of the antenna. An offset-fed reflector eliminates these problems. The reflector is formed out of a piece of an imaginary larger reflector. The feed is still located at the focus, but it is pointed toward the center of the reflector. Dual reflectors can also be offset. Large feed structures require offset designs to eliminate blockage problems.

Spherical reflectors can be scanned to large angles by moving the feed. Moving the feed to scan a parabolic reflector degrades the pattern. The wave no longer focuses to a point in a spherical reflector but instead focuses to a line. The feed must be a line source to match the incident fields.

Shaped reflectors are of two types. Cassegrain subreflector shaping coupled with minor main reflector shaping can increase the gain of the total antenna by improving the flatness of the aperture field. A parabolic reflector has a built-in amplitude taper because of the increased distance to the reflector from the feed as the angle increases off the axis. A shaped subreflector directs more power toward the edge of the main reflector to improve flatness. The second type of shaped reflector produces a prescribed pattern, such as cosecant squared, by distorting the reflector from a parabola. The gain decreases from the expected gain of the aperture as more of the power is spread out to shape the beam.

Flat plates are used as reflectors. A corner reflector gives an effective array of dipoles through images to increase the gain. It restricts the directions of possible radiation and reflects energy in the forward direction. By combining the direct radiation, reflections, and edge diffractions from the corners, we find the total pattern (GTD). A large corner reflector restricts the power to one- fourth of the radiation sphere and would increase the gain by 9 dB if diffraction effects were not present. The exact increase depends on the interaction of the dipole and its images. A ground plane increases the gain of an antenna by restricting radiation directions and reducing backlobe radiation.

2-13 Lens Antennas

Ever-increasing bandwidth requirements force the use of higher and higher frequencies. Mechanical tolerances and losses limit the choice of antennas. Optical methods become more attractive. The great amount of work in optics can be directly applied after the effects of the large wavelengths for optics are considered. Reflectors become impractical because of the tolerance requirements and the necessity of having large feed structures. The frequencies must be detected at the antenna to eliminate transmission line losses and to avoid the associated increased noise temperature of the system. The large blockage causes loss and high sidelobe levels. The feed of a lens remains out of the aperture.

Lenses divide into three types. A dielectric lens is designed directly from optics, and the aperture of the antenna is equal to the projection of the rim shape. Artificial dielectrics can be made by embedding small metal objects in a foam matrix; this allows for varying the effective dielectric constant by varying the density. In the third type metal strips are used as waveguides to increase the phase velocity by acting as parallel-plate waveguides when the electric field is parallel to the plates. The waveguide increases the phase velocity of the waves to produce an effective index of refraction less than 1.

The lens can be zoned by removing multiples of wavelengths from the thickness. Zoning narrows the frequency bandwidth and causes shadowing losses at the zone transitions.

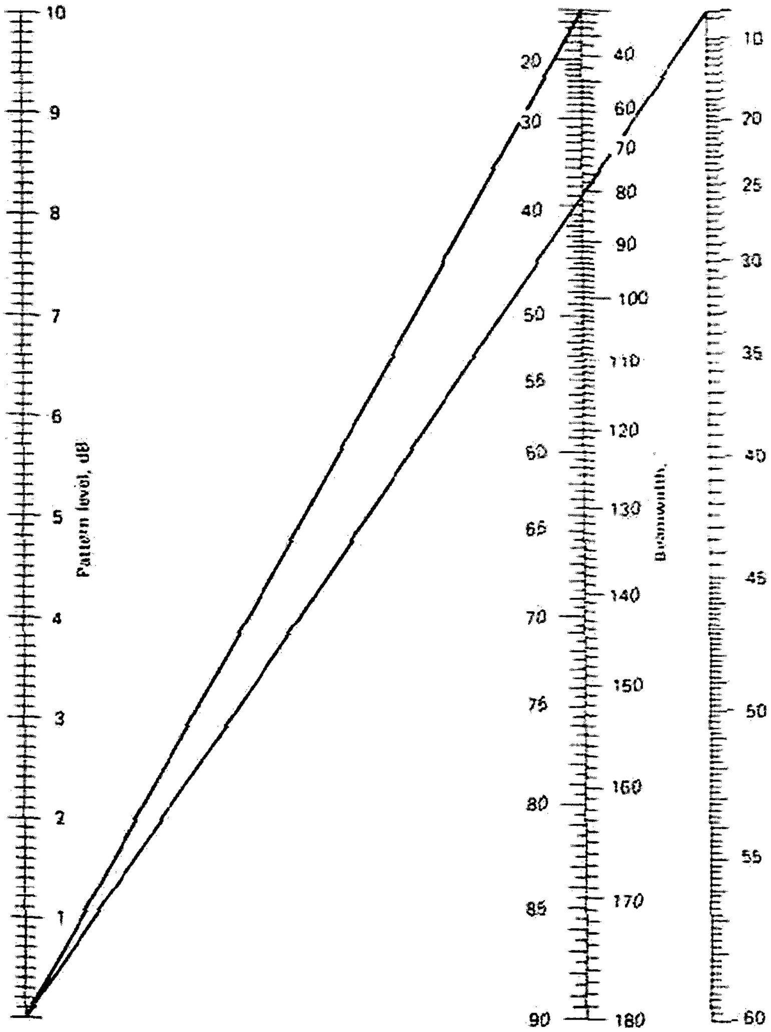

Figure 2-1 Approximate relation of beamwidths at different levels.

2-14 Relation between Beamwidths

The pattern approximation $\cos^{2N}(\theta/2)$ can be used to find a relation between beamwidths at different pattern levels. The exponent N for any beamwidth level is found from an expression similar to Eq. (1-13). By using this N and the new beamwidth level, the new beamwidth can be found. With a nomograph (Fig. 2-1) these expressions can be solved by drawing two lines. The left-hand scale is the pattern level in dB. The right-hand scale is the beamwidth. The unmarked diagonal scales are the exponent N. Draw a line from the pattern level to the beamwidth. Through the intersection of the diagonal N draw a second line from the new pattern level to the beamwidth scale (the right axis). Read the beamwidth at the new level. Multiply the left linear scale by any convenient factor to extend its range.

> **Example** An antenna has a 45° 3-dB beamwidth centered on $\theta = 0$ (a limitation of the approximation). Find the 10-dB beamwidth.
>
> Draw a line from the 3-dB point on the left-hand scale through the diagonal to the leftmost beamwidth scale at the 45° point. Draw a second line from the 10-dB pattern level scale (at the left) through the intersection of the first line and the diagonal to the beamwidth scale. Read the beamwidth, by using the same scale as with the first line, as 82°.

REFERENCES

1. R. F. Harrington, *Time-Harmonic Electromagnetic Fields*, McGraw-Hill, New York, 1961, p. 77.
2. IEEE STD 145-1983, "IEEE Standard Definitions of Terms for Antennas," *IEEE Trans. Antennas Propagat.*, vol. 31, no. 6, pt. II, November 1983.
3. W. W. Hansen and J. R. Woodyard, "A New Principle in Directional Antenna Design," *Proc. IRE*, vol. 26, March 1938, pp. 333–345.

CHAPTER

3

ARRAYS

An array radiates or receives from two or more antennas at the same frequency. Around the antennas we add the electric fields radiated from each antenna. The amplitudes and phases of each antenna give us extra degrees of freedom to shape the pattern of the combination. In some respects the design problem shifts from the radiating elements to the feed network.

A single antenna radiates an electric field with two polarization components.

$$\mathbf{E} = E_\theta(\theta, \phi)\mathbf{a}_\theta + E_\phi(\theta, \phi)\mathbf{a}_\phi$$

where E_θ and E_ϕ are the two components (amplitude and phase) referenced to some point on the antenna. If we move the antenna or the phase reference point, then the phase components are changed. We assume that the movement is small enough that the radiation approximation can still be used. Given $\mathbf{r}'$ as the location of the antenna relative to the phase reference point, the added phase component is

$$e^{j\mathbf{k}\cdot\mathbf{r}'}$$

where $\mathbf{k} = 2\pi/\lambda(\sin\theta\cos\phi\mathbf{a}_x + \sin\theta\sin\phi\mathbf{a}_y + \cos\theta\mathbf{a}_z)$ and $\mathbf{r}' = x'\mathbf{a}_x + y'\mathbf{a}_y + z'\mathbf{a}_z$, the location of the antenna. $\mathbf{k}\cdot\mathbf{r}'$ is the phase distance from the antenna to the reference plane through the reference point, and it is defined by the radiation (receiving) direction. The electric field radiated from the moved antenna becomes

$$[E_\theta(\theta, \phi)\mathbf{a}_\theta + E_\phi(\theta, \phi)\mathbf{a}_\phi]e^{j\mathbf{k}\cdot\mathbf{r}'}$$

We assume that nearby objects do not alter the patterns in the movement. These changes can be reflected in the components if necessary.

Suppose we have an array of antennas located at points $\mathbf{r}_1'$, $\mathbf{r}_2'$, etc. We obtain the total pattern by adding the electric fields radiated from each.

$$\mathbf{E} = \sum_{i=1}^{N}[E_{\theta i}(\theta, \phi)\mathbf{a}_\theta + E_{\phi i}(\theta, \phi)\mathbf{a}_\phi]e^{j\mathbf{k}\cdot\mathbf{r}_i'} \tag{3-1}$$

Bringing the antennas close together will change the patterns of each because every antenna will block the radiation of the others. The distribution of currents on the elements may be changed. The shape of small resonant antennas limits the possible distribution of currents, but the magnitude and phase may be changed.

Various approximations are made to Eq. (3-1). Changes in the patterns due to nearby antennas are ignored, and isolated element patterns are used. We can assume a certain amplitude and phase distribution on the elements and ignore the problem of the feed network. Polarization reduces to a single term for equally polarized elements, such as dipoles, slots, or horns. If the antennas have identical element patterns, then we can separate Eq. (3-1) into a product.

$$\mathbf{E} = [E_\theta(\theta, \phi)\mathbf{a}_\theta + E_\phi(\theta, \phi)\mathbf{a}_\phi]\sum_{i=1}^{N} E_i e^{j\mathbf{k}\cdot\mathbf{r}_i'} \tag{3-2}$$

where E_θ and E_ϕ are the normalized patterns of the single element. E_i is the electric field of the ith element including amplitude and phase of the feed distribution.

Equation (3-2) separates the pattern into an element pattern and an array factor. The general operation is called pattern multiplication. The method requires that all antennas have the same pattern and be orientated in the same direction. The element patterns themselves could be arrays. We can use pattern multiplication to synthesize planar and volumetric arrays from linear arrays. The array factor represents the pattern from an array of isotropic pattern antennas. Because array factors can be calculated by hand, we find them useful for gaining insight. We leave calculations with Eqs. (3-1) and (3-2) to the computer.

3-1 Two-Element Array

Consider two elements lying on the z axis and spaced some distance d around the origin (Fig. 3-1). If we rotate the isotropic pattern antennas

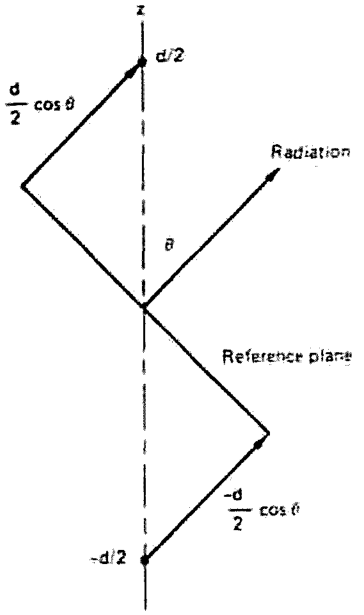

Figure 3-1 Two-element array on z axis.

around the z axis, then the problem remains unchanged. That is, all great-circle (constant-ϕ) patterns are identical. On the z axis, the phase constant becomes

$$e^{jkz'\cos\theta}$$

For simple line arrays we can find pattern nulls and peaks by simple arguments.

Example The two elements are spaced $\lambda/2$ and have equal amplitudes and phases. Find the nulls and peaks. The phase reference planes can be placed at any convenient point.
Consider the pattern at $\theta = 90°$. Place the reference plane through the axis of the array. The added phase factor is zero for both elements; we just add components. The equal element phases add to give a beam peak.
Place a second reference plane through the top element. The wave radiated from the bottom element travels across the array $\lambda/2$ to the reference plane. Increasing the distance propagated decreases the phase. The phase changes by $-180°$. The two out-of-phase signals cancel to produce a pattern null. The array has symmetry about the xy plane; the same pattern is above and below the plane. We denote this an even-mode array. Repeat the example for an odd-mode array (phases 0° and 180°) and convince yourself that the null occurs at $\theta = 90°$ and the beam peak is at $\theta = 0°$ (180°).

Example Suppose the two elements are spaced $\lambda/4$. The top element phase is $-90°$; the bottom element phase is 0°. Find the beam peak and pattern null. Place a reference plane through the top element. The wave radiated from the bottom element travels across the array, and its phase decreases by 90°. Both radiated waves have the same phase ($-90°$) at the reference plane and add for a beam peak. Consider a second plane through the bottom element. The wave from the top element loses 90° propagating across the array. The waves are 180° out of phase at the bottom reference plane and cancel for a null.

The second example is an end-fire array. The phases match those of a wave traveling in the direction of the maximum. In the examples unequal amplitudes would limit the null depth to the difference. Varying the element phasings, while maintaining equal amplitudes, moves the null directions.

Consider a general two-element array with equal amplitudes and a phase difference between them. We divide the phase shift into equal parts. The top-element phase is $-\delta/2$; the bottom-element phase is $\delta/2$. When we apply Eq. (3-2) with an isotropic element pattern, we obtain the following electric field by using Euler's identity.

$$E(\theta) = 2E_0 \cos\left(\frac{\pi d}{\lambda}\cos\theta - \frac{\delta}{2}\right)\frac{e^{-jkr}}{r} \tag{3-3}$$

Pattern maximums occur when the argument of the cosine is $n\pi$, the nulls when it is $(2n-1)\pi/2$.

$$\cos\theta_{\max} = \left(n\pi + \frac{\delta}{2}\right)\frac{\lambda}{\pi d}$$

$$\cos\theta_{\text{null}} = \left[(2n-1)\frac{\pi}{2} + \frac{\delta}{2}\right]\frac{\lambda}{\pi d}$$

We find the average radiation intensity by an integral

$$U_{\text{avg}} = \frac{4E_0^2}{\eta}\int_0^{\pi/2} \cos^2\left(\frac{\pi d}{\lambda}\cos\theta - \frac{\delta}{2}\right)\sin\theta\, d\theta$$

The directivity is

$$\frac{U_{\max}}{U_{\text{avg}}} = \frac{2|E_{\max}|^2}{1 + \dfrac{\sin(2\pi d/\lambda)\cos\delta}{2\pi d/\lambda}} \tag{3-4}$$

where $E_{\max} = \cos(\pi d/\lambda \cos\theta_{\max} - \delta/2)$. When $d \geq \lambda/2$, $E_{\max} = 1$.

Figure 3-2 shows the directivity versus spacing for the special cases $\delta = 0°$ and $\delta = 180°$ (even and odd modes). The directivity varies because each antenna receives power from the other. The combination of the input power and the power transferred between elements changes with spacing.

3-2 Mutual Impedance

We can use the mutual impedance concept to find the effective input power of every element and thereby avoid having to integrate the pattern to find the average radiation intensity. We represent the circuit relations of two antennas by a two-port impedance matrix.

$$\begin{bmatrix} V_1 \\ V_2 \end{bmatrix} = \begin{bmatrix} Z_{11} & Z_{12} \\ Z_{21} & Z_{22} \end{bmatrix} \begin{bmatrix} I_1 \\ I_2 \end{bmatrix}$$

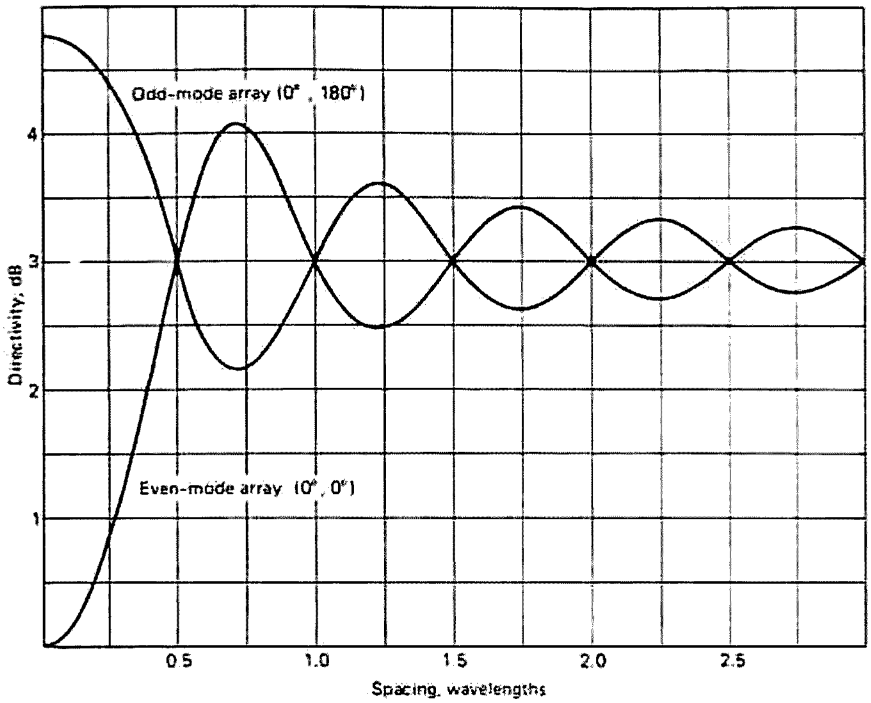

Figure 3-2 Directivity of even- and odd-mode two-isotropic-element arrays.

Symmetrical elements across the diagonal of the matrix are equal for antennas satisfying reciprocity. The total input power is given by

$$P_{\text{in}} = \operatorname{Re}(V_1 I_1^*) + \operatorname{Re}(V_2 I_2^*)$$

The general N-element array has an $N \times N$ matrix and N terms in the input power sum. Given the feed coefficients, we have a relation between different I_i. For our two elements

$$I_2 = I_1 e^{j\delta} \qquad \text{and} \qquad V_1 = (Z_{11} + Z_{12}e^{j\delta})I_1$$

The power into the first element is

$$\operatorname{Re}(Z_{11} + Z_{12}e^{j\delta})I_1 I_1^*$$

By symmetry, the power into the second antenna is the same. The total input power to the array is

$$P_{\text{in}} = 2\operatorname{Re}(Z_{11})I_1 I_1^* \left[1 + \frac{\operatorname{Re}(Z_{12}e^{j\delta})}{\operatorname{Re}(Z_{11})}\right]$$

The factor $\operatorname{Re}(Z_{11})I_1 I_1^*$ is the power into an isolated element: $4\pi E_0^2/\eta$. The average radiation intensity (100 percent efficient antenna) is $P_{\text{in}}/4\pi$.

$$\text{Gain} = \text{directivity} = \frac{2|E(\theta_{\max})|^2/\eta}{P_{\text{in}}/4\pi}$$

$$= \frac{2|E_{\max}|^2}{1 + [\operatorname{Re}(Z_{12}e^{j\delta})]/[\operatorname{Re}(Z_{11})]} \tag{3-5}$$

By comparing Eqs. (3-5) and (3-4), we can identify

$$\frac{\operatorname{Re}(Z_{12}e^{j\delta})}{\operatorname{Re}(Z_{11})} = \frac{R_{12}\cos\delta}{R_{11}} = \frac{\sin(2\pi d/\lambda)\cos\delta}{2\pi d/\lambda}$$

$$\frac{R_{12}(d)}{R_{11}} = \frac{\sin(2\pi d/\lambda)}{2\pi d/\lambda}$$

We can use this mutual impedance ratio to find the directivity of arrays of isotropic elements of any number.

Example Find the directivity of a linear array of three equally spaced isotropic elements with equal amplitudes and phases.

The powers into the elements are

$$P_1 = P_3 = \frac{4\pi E_0^2}{\eta}\left[1 + \frac{R_{12}(d)}{R_{11}} + \frac{R_{12}(2d)}{R_{11}}\right]$$

$$P_2 = \frac{4\pi E_0^2}{\eta}\left[1 + \frac{2R_{12}(d)}{R_{11}}\right] \qquad U_{\max} = \frac{3^2E_0^2}{\eta}$$

The total power into the array is found from the sum.

$$P_t = P_1 + P_2 + P_3 = \frac{4\pi E_0^2}{\eta}\left[3 + \frac{4R_{12}(d)}{R_{11}} + \frac{2R_{12}(2d)}{R_{11}}\right]$$

$$\text{Directivity} = \frac{U_{\max}}{P_t/4\pi} = \frac{9}{3 + [4R_{12}(d)/R_{11}] + [2R_{12}(2d)/R_{11}]}$$

The directivity of the general N-element equally spaced linear array, excited by equal-amplitude and -phase signals, is easily found by extending the development.

$$\text{Directivity} = \frac{N^2(\text{element directivity})}{N + 2\sum_{M=1}^{N-1}(N-M)[R_{12}(Md)/R_{11}]}$$

Figure 3-3 plots this for isotropic element pattern antennas.

The directivity attained in an array depends on the particular mutual impedance terms of the radiators. The directivity of a uniform array of broadside-coupled half-wave dipoles is similar to that shown in Fig. 3-3, but the peak values are shifted slightly higher and to the right.

The first element of an N-element array has the impedance equation

$$V_1 = Z_{11}I_1 + Z_{12}I_2 + Z_{13}I_3 + \cdots + Z_{1N}I_N$$

If we know the relation between the radiation amplitudes, we also know the ratio of the currents.

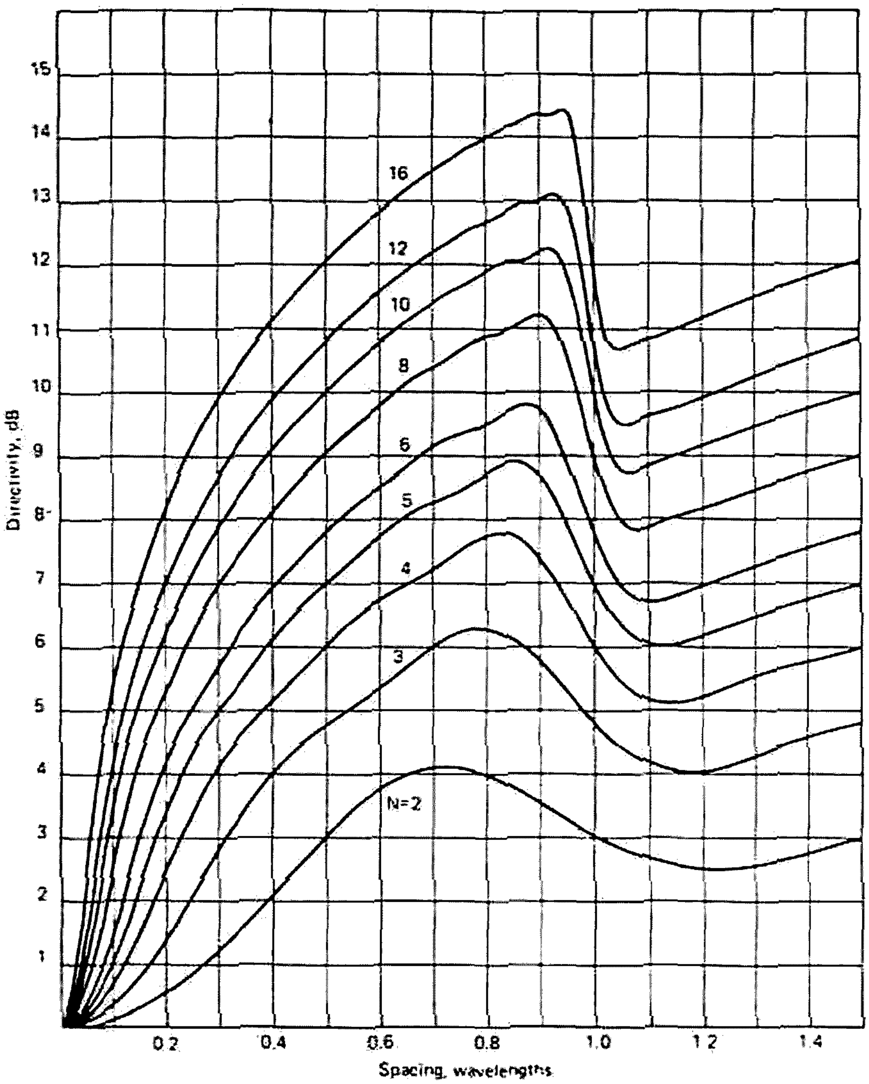

Figure 3-3 Directivity of a uniform array of isotropic antennas.

$$V_1 = I_1\left(Z_{11} + \frac{I_2}{I_1}Z_{12} + \frac{I_3}{I_1}Z_{13} + \cdots + \frac{I_N}{I_1}Z_{1N}\right)$$

The effective or active impedance of the first element is

$$Z_1 = \frac{V_1}{I_1} = Z_{11} + \frac{I_2}{I_1}Z_{12} + \frac{I_3}{I_1}Z_{13} + \cdots + \frac{I_N}{I_1}Z_{1N}$$

It depends on the self-impedance and the excitation of all the other antennas. The power into the first element is

$$P_1 = \mathrm{Re}\,(V_1 I_1^*) = I_1 I_1^* \,\mathrm{Re}\left(Z_{11} + \frac{I_2}{I_1}Z_{12} + \cdots + \frac{I_N}{I_1}Z_{1N}\right)$$

By knowing the feeding coefficients and the mutual impedances, we can find the total input power and gain. In general, every antenna in the array has a different input impedance. As the feeding coefficients change, so will the input impedances. A phased array changes the feeding coefficients to scan the beam. Hence, the active impedance, seen by the feed network, changes with scan angle.

We can repeat the same arguments for slots using mutual conductances, since magnetic currents are proportional to the voltage across each slot.

3-3 Linear Array of *N* Elements

Suppose there are N isotropic radiators equally spaced along the z axis and fed with equal amplitudes. We assume a fixed phase shift δ between progressive elements. The array factor field is

$$\frac{\sin (N\psi/2)}{N \sin (\psi/2)}$$

where $\psi = kd \cos \theta + \delta$ [1]. We use this to plot a universal radiation pattern for the array (Fig. 3-4) for two to ten elements. The abscissa ψ is plotted in degrees (360° is substituted for 2π in k). Both ends of the plot are lines of symmetry. The plot is periodic (period 360°). We see that the level of the first sidelobe ($N = 2$ has no sidelobe) decreases as N decreases but approaches a limit of 13.3 dB of the continuous aperture. Figure 3-5 demonstrates the periodic pattern for $N = 6$. We can plot similar curves for other array distributions; all have a period of 360°.

Since $\cos \theta$ is limited to ± 1, the region of the abscissa used (the visible region) is

$$\frac{-360^\circ d}{\lambda} + \delta \qquad \text{to} \qquad \frac{360^\circ d}{\lambda} + \delta$$

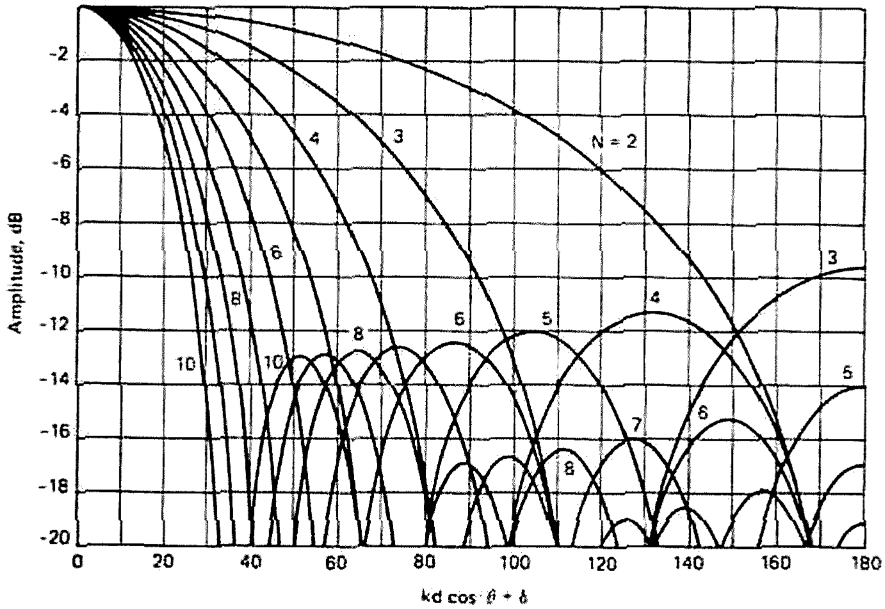

Figure 3-4 ψ-space pattern of linear arrays with a uniform amplitude distribution.

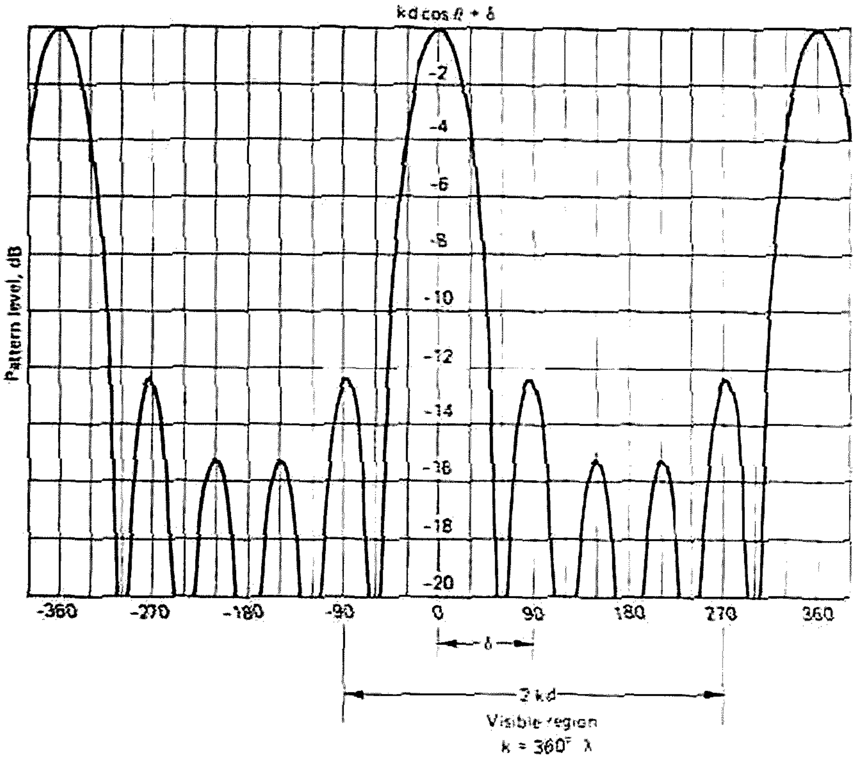

Figure 3-5 ψ-space pattern of a six-element linear array with a uniform amplitude distribution.

When the spacing between elements is greater than $\lambda/2$, the visible region can include more than one periodic main lobe and have multiple beams.

To have a beam centered at θ_1, set the progressive phase difference between elements

$$\delta = \frac{-360^\circ d}{\lambda} \cos \theta_1 \tag{3-6}$$

End fire ($\theta_1 = 0$) occurs when

$$\delta = \frac{-360^\circ d}{\lambda} \tag{3-7}$$

Phased arrays vary the progressive phase by Eq. (3-6) to scan the beam. When the spacings are greater than $\lambda/2$, the appearance of secondary beam peaks (grating lobes) limits the scan angle. The grating lobe attains full amplitude when

$$\frac{d}{\lambda}(1 + \cos \theta_{gr}) = 1 \qquad \theta_{gr} = \cos^{-1}\left(\frac{\lambda}{d} - 1\right)$$

Example The spacing of the elements of an array is 0.75 wavelength. Find the scan angle when the grating lobe is full amplitude.

$$\theta_{gr} = \cos^{-1}\left(\tfrac{4}{3} - 1\right) = 70.5^\circ$$

At this point the grating lobe is the same amplitude as the main beam. The lobe does not appear suddenly; it grows as the visible region shifts and starts including the second periodic main lobe.

Arrays with spacings greater than λ always have grating lobes (multiple main beams), but the pattern of the antenna elements may reduce the grating lobes to acceptable levels and allow wide spacings.

We can use Fig. 3-4 to find the beamwidth angles of arrays. Table 3-1 is a listing of the ψ-space angles of the 3- and 10-dB levels.

Example A six-element equally spaced uniform array has spacings of $\lambda/2$ and no progressive phase shift between elements ($\delta = 0°$). Find the 3-dB beamwidth.

From Table 3-1, $\psi_{3\,\mathrm{dB}} = 26.90°$. Because the pattern is symmetrical in ψ space (Fig. 3-5), the second $\psi_{3\,\mathrm{dB}}$ is $-26.90°$.

$$kd \cos \theta_{1,2} + \delta = \pm\psi_{3\,\mathrm{dB}}$$

$$\frac{360°}{\lambda}\frac{\lambda}{2} \cos \theta_{1,2} = \pm 26.90° \qquad \cos \theta_{1,2} = \frac{\pm 26.9°}{180°}$$

$$\theta_1 = 81.4° \qquad \theta_2 = 98.6°$$

Remember that θ is measured from the axis of the array (z axis). The 3-dB beamwidth is the difference (17.2°). On Fig. 3-5 the visible region ranges between −180° and +180°. There are four sidelobes in the visible region (Fig. 3-5). An array samples a continuous aperture distribution. The continuous distribution is Nd long. The beamwidth is estimated by using a uniform amplitude distribution.

$$\mathrm{HPBW} = 50.76° \frac{\lambda}{Nd} = 16.92°$$

It reasonably approximates the array beamwidth.

TABLE 3-1 ψ-Space Angles of 3- and 10-dB Levels of an Equal-Amplitude Distribution Array

N	3 dB	10 dB	N	3 dB	10 dB	N	3 dB	10 dB
2	90.00°	143.13°	11	14.55°	24.21°	20	7.980°	13.29°
3	55.90°	91.47°	12	13.33°	22.18°	24	6.649°	11.08°
4	40.98°	67.63°	13	12.30°	20.47°	28	5.698°	9.492°
5	32.46°	53.75°	14	11.42°	19.00°	32	4.985°	8.305°
6	26.90°	44.63°	15	10.65°	17.74°	36	4.431°	7.382°
7	22.98°	38.18°	16	9.98°	16.62°	40	3.988°	6.643°
8	20.07°	33.36°	17	9.39°	15.64°	50	3.190°	5.314°
9	17.81°	29.62°	18	8.87°	14.77°	64	2.492°	4.152°
10	16.02°	26.64°	19	8.40°	14.00°	100	1.595°	2.657°

Example A six-element array has a progressive phase shift δ of 90° between elements. Find the 10-dB beam edge angles for $\lambda/2$ spacings.

$$\psi_{10\,\mathrm{dB}} = \pm 44.63^\circ \qquad \text{Table 3-1}$$

$$kd\cos\theta_{1,2} = \pm\psi_{10\,\mathrm{dB}} - \delta$$

Solving for $\cos\theta_{1,2}$, we have

$$\cos\theta_{1,2} = \frac{\pm\psi_{10\,\mathrm{dB}} - \delta}{kd} = \frac{\pm 44.63^\circ - 90^\circ}{180^\circ}$$

$$\theta_1 = 104.6^\circ \qquad \theta_2 = 138.4^\circ \qquad \text{beamwidth} = 33.8^\circ$$

There are five sidelobes in the visible region (Fig. 3-5). Equation (3-6) gives the beam maximum direction.

$$\cos\theta_0 = \frac{-\delta}{kd} = \frac{-90^\circ}{180^\circ} \qquad \theta_0 = 120^\circ$$

The main beam is no longer symmetrical about the beam peak. The 3-dB pattern angles are 110.5° and 130.5°. The beamwidth (3-dB beamwidth = 20°) increases with scan angle. What element spacing would result in this beamwidth for broadside radiation ($\delta = 0^\circ$)?

$$\frac{360^\circ}{\lambda} d\cos\theta_1 = 26.90^\circ \qquad \text{Table 3-1}$$

On solving for spacing, we have

$$\frac{d}{\lambda} = \frac{26.9^\circ}{360^\circ\cos\theta_1}$$

Remember that the beam is centered on $\theta = 90^\circ$, so that $\theta_1 = 90 - 20/2 = 80^\circ$.

$$\frac{d}{\lambda} = \frac{26.9^\circ}{360^\circ\cos 80^\circ} = 0.431$$

The effective spacing has been reduced by approximately the cosine of the scan angle from $\theta = 90^\circ$, broadside.

$$\frac{d}{\lambda}\cos 30^\circ = 0.433$$

The accuracy of the cosine relation increases with more elements.

Example Determine the progressive phase shift between elements for an end-fire array with 0.3λ spacings. Find the beamwidth for a uniform distribution array with five elements.

End fire occurs when [Eq. (3-7)]

$$\delta = \frac{-360^\circ(0.3\lambda)}{\lambda} = -108^\circ$$

This is the progressive phase shift for all distributions with 0.3λ spacings for an end-fire pattern. Table 3-1 gives the ψ-space angle, $\psi_{3\,\text{dB}} = \pm 32.46°$. Substituting in the expression for ψ, we have

$$\frac{360°(0.3\lambda)}{\lambda}\cos\theta_{1,2} = \pm 32.46°$$

$$\cos\theta_{1,2} = \frac{\pm 32.46° + 108°}{360°(0.3)}$$

$$\cos\theta_1 = \frac{140.46}{108} = 1.301 \qquad \cos\theta_2 = \frac{75.46}{108} = 0.699$$

θ_1 is in invisible space, since $|\cos\theta| \le 1$; $\theta_2 = 45.6°$. The symmetry about the z axis supplies us with the second angle $\theta_1 = -45.6°$. The beamwidth is the difference: 91.2°. The end-fire array samples a traveling wave distribution. The continuous uniform distribution phased for end fire with the same length has a 90.4° beamwidth.

Remember we have been dealing with isotropic pattern antennas. Broad cast towers, seen from above, approximate isotropic antennas in the plane. The patterns of the individual antennas modify the results of isotropic antenna arrays. In small arrays the element pattern is quite significant, but the beamwidths of large arrays are determined mostly by the array. The beamwidths calculated for array factors only approximate the actual beamwidths when the elements have patterns. We must rely on computer solutions of specific cases, including the element pattern, if better results are needed.

3-4 Hansen and Woodyard End-Fire Array [2]

The directivity of an end-fire array increases if the sum of the progressive phase shifts between elements is decreased by π. That is, the traveling wave velocity slows in the structure relative to free space. The progressive phase shift between elements becomes

$$\delta = -kd - \frac{\pi}{N} \quad \text{radians} \tag{3-8}$$

where N is the number of elements in the array. The normal end-fire progressive phase shift between elements, $\delta = -kd$, places one edge of the visible region at the origin of ψ space. This method shifts the edge to a lower portion of the curve. The peak of the universal radiation curve (Fig. 3-5) shifts into invisible space. The sidelobes rise in proportion to the new beam peak, but the beamwidth narrows. The relation holds strictly only for arrays with large numbers of elements, but the directivity increases for all arrays when it is applied.

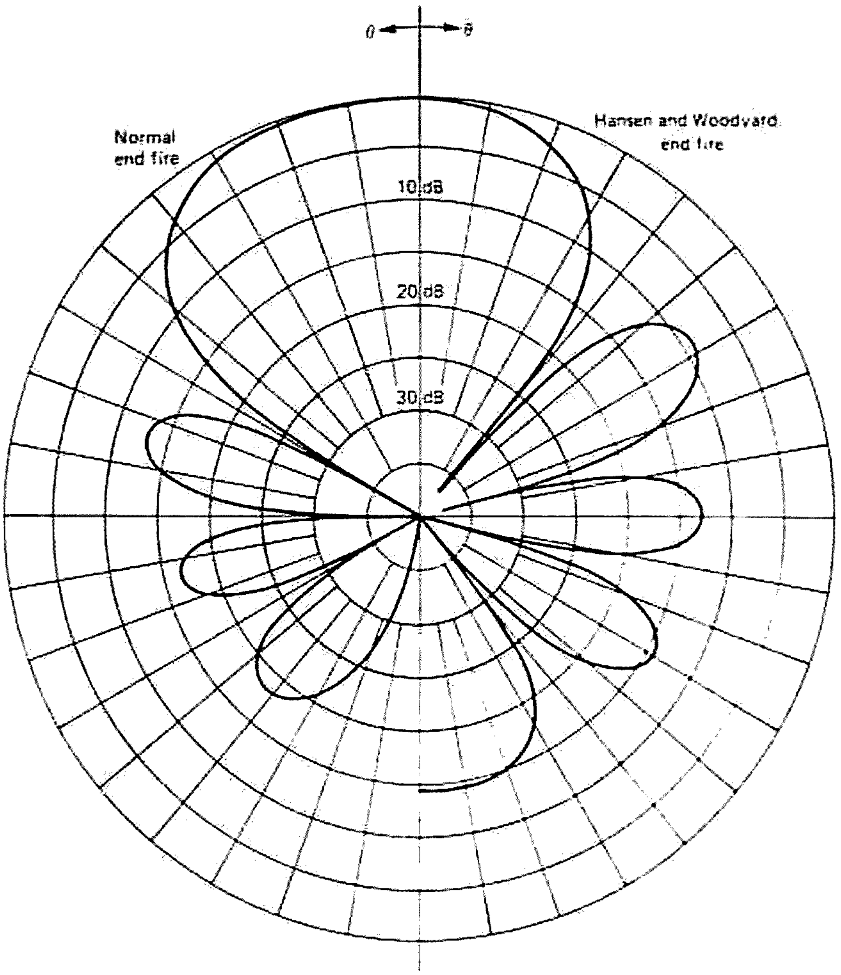

Figure 3-6 Patterns of a normal end-fire and a Hansen and Woodyard end-fire array of isotropic elements.

Example Suppose eight elements are spaced λ/4 apart with a uniform amplitude distribution. Compare the two end-fire designs. The results are as follows:

	Progressive phase shift, °	*HPBW,* °	*Directivity, dB*
Normal end fire	−90	80	9
Hansen & Woodyard end fire	−112.5	44	11.5

The two patterns are compared in Fig. 3-6. The beamwidth decreases, and the directivity increases by 2.5 dB. The sidelobes rise to 9 from 13 dB.

3-5 Phased Arrays

Suppose a wave approaches at an angle an array of elements located on the z axis (Fig. 3-7). The wave reaches the top element before the rest and progresses down the array in succession. If the signals are added directly, they will cancel each other to some extent because they have a progression

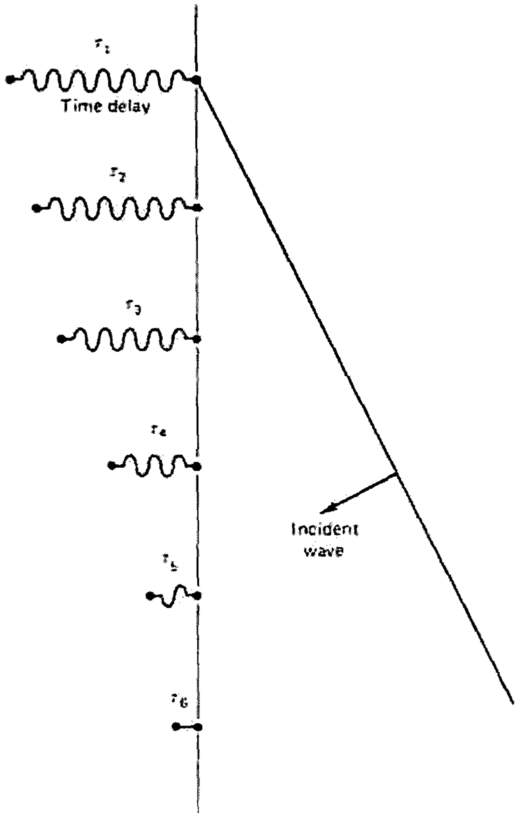

Figure 3-7 Linear array scanned with time delay networks.

of phases. Figure 3-7 shows a series of time delays to equalize the path lengths in the lines. Position along the axis determines the time delay τ_i

$$\tau_i = \frac{z_i}{c} \cos \theta_0 + \tau_0$$

where z_i is the position, θ_0 is the angle of the incident wave, c is the velocity of light, and τ_0 is an arbitrary time delay. τ_0 keeps all time delays τ_i positive. This feed network is frequency-independent. As we vary the progression of time delays, the beam scans.

Phase shifters replace the time delay networks in phased arrays. They provide equivalent beam scanning at a single frequency. To scan to an angle θ_0, the required phase shift is

$$-\frac{2\pi}{\lambda} z \cos \theta_0 \qquad \text{modulo } 2\pi \qquad \text{(radians)}$$

$$-\frac{360^\circ}{\lambda} z \cos \theta_0 \qquad \text{modulo } 360^\circ \qquad \text{(degrees)}$$

for elements located on the z axis. For a general space array we must counteract the phase difference to the reference plane, $e^{jk\cdot r'}$, for the direction of scan so that the phases of all elements are zero. To scan in the direction (θ_0, ϕ_0), we must add a phase factor to every element depending on its position. The phase factor on each element of a general space array is

$$e^{-j\mathbf{k}_0\cdot\mathbf{r}'} \tag{3-9}$$

where

$$\mathbf{k}_0 = \frac{2\pi}{\lambda}(\sin\theta_0\cos\phi_0\mathbf{a}_x + \sin\theta_0\sin\phi_0\mathbf{a}_y + \cos\theta_0\mathbf{a}_z)$$

is the vector propagation constant in the direction of the beam and $\mathbf{r}'$ is the element location. Adding this phase factor to the element phases causes the product of the exponential factors [Eq. (3-2)] to be 1 at the scan angle. The components E_i add in the scan direction.

Using phase shifters limits the frequency bandwidth. Given a fixed phase shift over a small frequency range, increasing the frequency scans the beam toward broadside

$$\Delta\theta = \frac{f_1 - f_2}{f_2}\tan\left(\frac{\pi}{2} - \theta_0\right) \quad \text{radians} \tag{3-10}$$

where θ_0 is the scan angle [3]. Limiting the allowable scanning with frequency to plus or minus one-fourth of the local beamwidth defines the bandwidth of the array. When the beam is scanned to 30° off the axis, the bandwidth is directly related to the beamwidth at broadside ($\theta = 90°$).

$$\text{Bandwidth (percent)} \cong \text{beamwidth (degrees)} \qquad \text{at } \theta_0 = 30°$$

The beam shifts less with frequency near broadside, since the tangent factor in Eq. (3-10) approaches zero. A general estimate is given by

$$\text{Bandwidth (percent)} \cong \frac{\text{beamwidth (degrees)}}{2\cos\theta_0} \tag{3-11}$$

where the broadside beamwidth is used.

Example Given an array with 100 elements spaced at $\lambda/2$, find the bandwidth when scanned to 45°.

The beamwidth is estimated from the aperture width

$$\text{HPBW} = \frac{50.76°}{100(\frac{1}{2})} \cong 1$$

$$\text{Bandwidth (percent)} \cong \frac{1}{2\cos 45°} = 0.7 \text{ percent}$$

Any radar antenna would have a broader beamwidth because the sidelobes need to be reduced, but this is a good first estimate.

The bandwidth can be increased by feeding subarrays with time delay networks. The subarrays continue to be scanned with phase shifters. Only a few time delay networks are needed, and the subarray beamwidth determines the bandwidth.

3-6 Multiple Beams

An array can form multiple beams. Equation (3-9) gives the phase coefficients to multiply each element feed voltage E_i to scan it to a given angle. The array will form a second beam if we add a second distribution

$$E_i e^{-jk_2 \cdot r_i}$$

The distribution E_i remains constant for both beams. We add the two distributions to obtain both beams.

$$E_i(e^{-jk_1 \cdot r_i} + e^{-jk_2 \cdot r_i}) \tag{3-12}$$

This multiplies the distribution E_i by a second distribution whose amplitudes and phases are functions of the antenna position and the scan angles of the two beams. Each beam uses the whole array to form its beam. In a phased array both phase and amplitude must be varied to achieve multiple beams. An array, which can only vary phase, must be divided into subarrays to form multiple beams. Its beamwidth sizes will depend on the subarray widths.

We can have unequal beams with different amplitude distributions and pattern shapes if they are needed. We can add as many beams as necessary by including the distribution element factors with the scanning phase coefficients in Eq. (3-12). The element feeding coefficients become the sum.

Example Find the feed coefficients of a 15-element array with $\lambda/2$ spacings and a uniform distribution scanned to 45° and 120° from the z axis.
Center the array on the z axis. The elements are located at

$$z_i = \frac{(-8+i)\lambda}{2}$$

To scan to 45°, the element phase factors are

$$\exp(-jk\cos 45^\circ z_i) = \exp\left[-j\frac{360^\circ}{\lambda}\frac{1}{\sqrt{2}}\frac{(-8+i)\lambda}{2}\right]$$

To scan to 120°, the element phase factors are

$$e^{j90^\circ(-8+i)}$$

The ninth element ($z_9 = \lambda/2$) phase factors are

$$e^{-j127.3^\circ} \qquad \text{and} \qquad e^{j90^\circ}$$

Assume a voltage magnitude of one-half for each uniform amplitude distribution beam so that the center element has a magnitude of 1. Sum the distributions to find the feeding coefficients of the ninth element: $0.32e^{j161.4^\circ}$. When converted to dB ratios, the feeding coefficients for the array become:

1.	−2.38 dB	130.48°	4.	−11.49 dB	74.56°
2.	−8.59 dB	111.84°	5.	−1.64 dB	55.92°
3.	−0.01 dB	−86.80°	6.	−1.99 dB	−142.72°

7.	−9.91 dB	−161.36°
8.	0.00 dB	0°
9.	−9.91 dB	161.36°
10.	−1.99 dB	142.72°
11.	−1.64 dB	−55.92°
12.	−11.49 dB	−74.56°
13.	−0.01 dB	86.80°
14.	−8.59 dB	−111.84°
15.	−2.38 dB	−130.48°

We can estimate both beamwidths from Table 3-1. $\psi_{3\text{ dB}} = 10.65°$.

$$\cos\theta_{1,2} = \frac{\pm 10.65 + 127.28}{180} \qquad \theta_1 = 40°,\ \theta_2 = 49.6°$$

$$\cos\theta_{1,2} = \frac{\pm 10.65 - 90}{180} \qquad \theta_1 = 116.2°,\ \theta_2 = 124°$$

The pattern (Fig. 3-8) has these beamwidth edges.

The gain of each beam depends on the feed network. If a single input supplies power to two beams, then each beam can receive only half the power and the gain is halved. Butler matrices and Blass beam-forming networks supply an input for each beam. The inputs are isolated from each other. The transmitter power in each port feeds only one beam, and therefore the

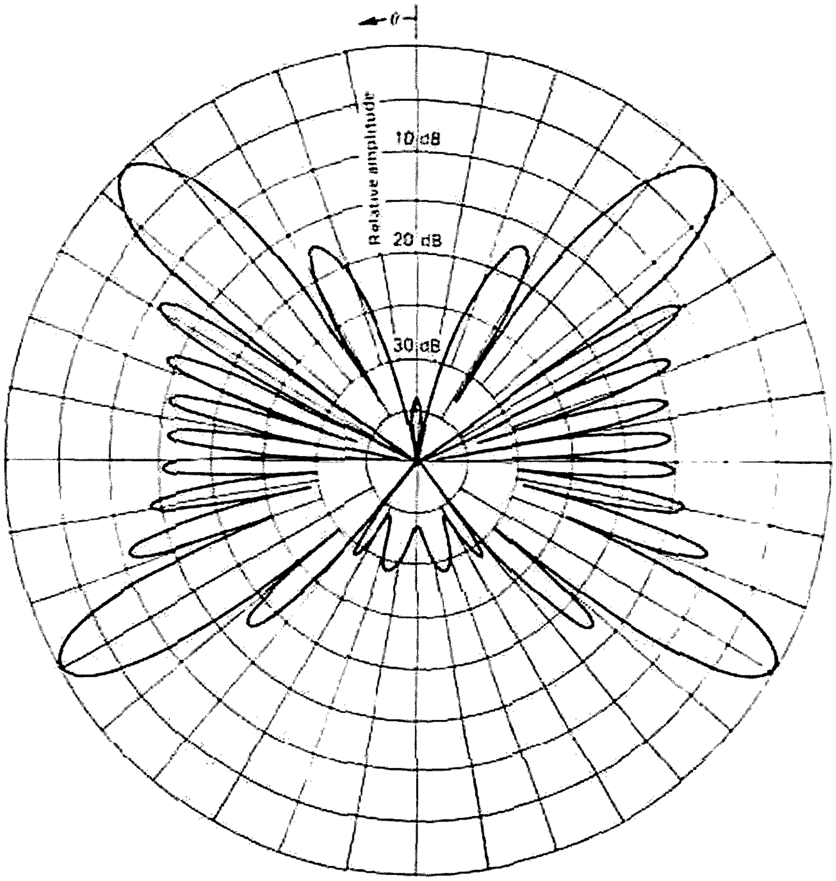

Figure 3-8 Fifteen-element linear array pattern with simultaneous beams at $\theta = 45°$ and 120°.

full array gain is available to each input. Similarly, we can place a receiver on each port and use the full effective area for each.

We will delay the important topics of array synthesis and sidelobe reduction until after we have discussed aperture distributions. A trade-off is made between the beamwidth and the sidelobe levels. The beamwidth narrows only by putting more power into the sidelobes.

REFERENCES

1. C. A. Balanis, *Antenna Theory, Analysis and Design*, Harper & Row, New York, 1982, p. 212.
2. W. W. Hansen and J. R. Woodyard, "A New Principle in Directional Antenna Design," *Proc. IRE*, vol. 26, March 1938, pp. 333–345.
3. T. C. Cheston and J. Frank, "Array Antennas," *Tech. Memo TG-956*, The Johns Hopkins University Applied Physics Laboratory, 1968, p. 80.
4. J. L. Butler, "Multiple Beam Antennas," Sanders Associates Internal Memo, RF 3849, 1960.
5. J. Blass, "The Multidirectional Antenna: A New Approach to Stacked Beams," IRE *Intern. Conv. Record*, vol. 8, pt. 1, 1960, pp. 48–50.

$$H_\theta = \frac{\pm jV_0}{\eta 2\pi r} e^{-jkr} \frac{\cos\,(kL/2\,\cos\,\theta) - \cos\,(kL/2)}{\sin\,\theta} \qquad \text{slot} \qquad (4\text{-}3)$$

where L is the total slot length. The upper sign is for $Y > 0$, and the lower sign is for $Y < 0$. The electric field of the slot is found from

$$E_\phi = -\eta H_\theta$$

Equations (4-2) and (4-3) have the same pattern amplitudes and directivities. We can integrate the magnitude squared of Eqs. (4-2) and (4-3) to find the average radiation intensity. Joined with the maximum radiation intensity, we find the directivity (Fig. 4-3) versus length.

4-2 Radiation Resistance (Conductance)

The far-field power densities, Poynting vectors, are given by

$$S_r = \frac{|E_\theta|^2}{\eta} \qquad \text{dipole}$$

$$S_r = |H_\theta|^2 \eta \qquad \text{slot}$$

where η is the impedance of free space (376.7 Ω). When these are integrated over the radiation sphere to find the power radiated, the results contain either $|I_0|^2$ (dipole) or $|V_0|^2$ (slot), the maximum sinusoidal current (voltage). We define the radiation resistance (conductance) as

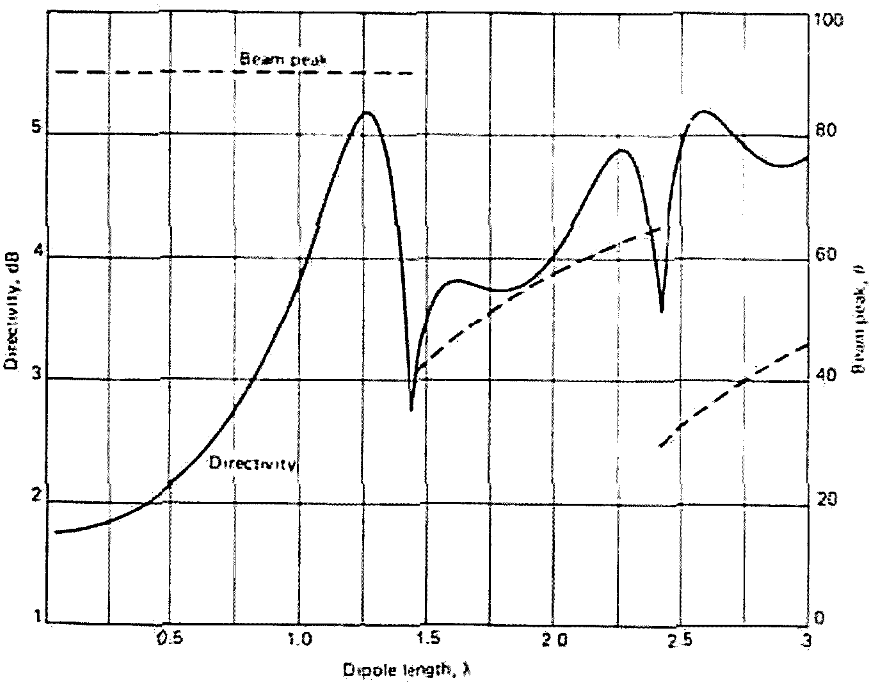

Figure 4-3 Dipole (slot) directivity and beam peak versus length.

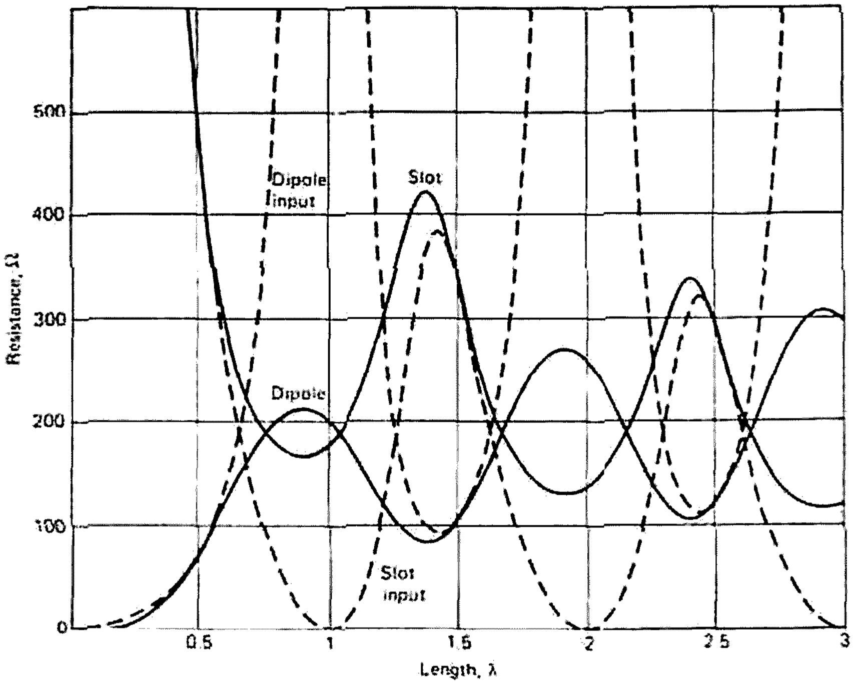

Figure 4-4 Dipole and slot radiation and center-fed input resistances.

$$R_r = \frac{P_r}{|I_0|^2} \qquad \text{dipole}$$

$$G_r = \frac{P_r}{|V_0|^2} \qquad \text{slot} \tag{4-4}$$

Figure 4-4 is a plot of the radiation resistance of each versus length [2].

The input resistance differs from the radiation resistance because it is the ratio of the input current (voltage) to the power radiated.

$$I_i = I_0 \sin\frac{kL}{2} \qquad \text{dipole}$$

$$V_i = V_0 \sin\frac{kL}{2} \qquad \text{slot} \tag{4-5}$$

On combining Eqs. (4-4) and (4-5), we find

$$R_i = \frac{R_r}{\sin^2(kL/2)} \qquad \text{dipole}$$

$$G_i = \frac{G_r}{\sin^2(kL/2)} \qquad \text{slot} \tag{4-6}$$

The input resistances (Fig. 4-4) differ from the radiation resistances by Eqs. (4-6). The input resistance of a one-wavelength dipole is large, but not infinite, as shown; it depends greatly on the diameter and input region. If we take the product of the radiation or input resistances, we find

$$R_{\text{dipole}} R_{\text{slot}} = \frac{\eta^2}{4} \tag{4-7}$$

one of the consequences of the Babinet-Booker principle [3].

The input resistance depends on the current at the input [Eq. (4-6)]. When the standing wave current is high and the voltage is low, the input resistance is low. A center-fed half-wavelength dipole has the same input resistance as radiation resistance, since the current maximum occurs as the input. On the other hand, a center-fed half-wavelength slot has a current minimum (voltage maximum) at its input, which gives it a high input resistance. When both are a full wavelength long, the dipole standing wave current is at a minimum and the slot standing wave current is at a maximum (Fig. 4-2). The dipole has a high input resistance and the slot has a low input resistance. We can lower the input resistance by feeding at a high current point, but we may excite a different distribution than expected.

A short dipole looks like a capacitor at the input. As the length increases, the radiation resistance grows and the capacitance decreases. Just before the length reaches $\lambda/2$, the capacitance becomes zero. The exact length at which the antenna resonates (zero reactance) depends on the diameter of the elements and the input gap. A good starting point is 95 percent of a half wavelength. Beyond the resonant length, the dipole becomes inductive. The impedance of a thin half-wavelength dipole is $73 + j42.2\ \Omega$, whereas the resonant length dipole impedance is about $67\ \Omega$. The slot looks like an inductor when short. Think of it as a short length short-circuited shunt stub. The inductance increases as the length increases and the slot resonates like the dipole, just short of $\lambda/2$. Additional resonances occur at longer lengths. Increasing the frequency is equivalent to increasing the length for the thin dipole.

4-3 Babinet-Booker Principle [3, 4]

A strip dipole and a slot are complementary antennas. The solution for the slot can be found from the solution to an equivalent dipole by an interchange of the electric and magnetic fields. Not only the pattern but also the input impedance can be found. Figure 4-5 shows two such complementary structures.

Babinet's principle of optical screens (scalar fields) states that given the solutions to the diffraction patterns of a screen, F_1, and the screen's complement, F_c, the sum equals the pattern without the screen. Booker extended Babinet's principle to vector electromagnetic fields. Strict complementation of an electric conductor requires a nonexistent magnetic conductor. Booker solved this problem by using only perfectly conducting infinitesimally thin

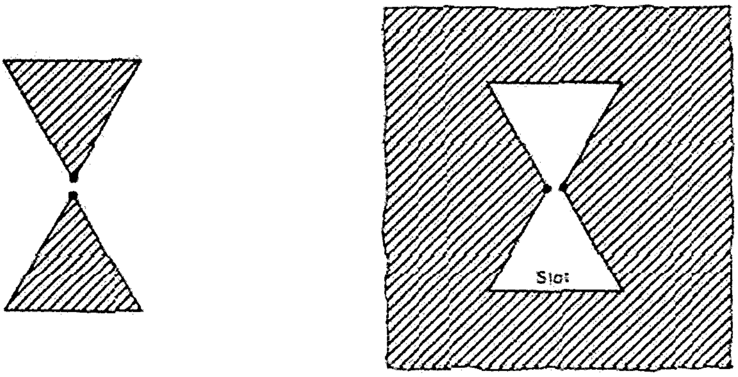

Figure 4-5 Complementary screens.

screens and by interchanging the electric and magnetic fields between the screen and its complement. If we take two such complementary screens and perform line integrals over identical paths to find the impedance of each, we obtain the result

$$Z_1 Z_c = \frac{\eta^2}{4} \tag{4-8}$$

where Z_1 is the input impedance of the structure, Z_c is the input impedance of the complementary structure, and η is the impedance of free space (376.7 Ω). Equation (4-8) extends Eq. (4-7) to the total impedance and includes mutual impedances as well as self-impedances.

Certain antennas, such as flat spirals, are self-complementary—an exchange of the spaces and conductors leaves the structure unchanged except for rotation. For a two-arm structure

$$Z_0^2 = \frac{\eta^2}{4} \quad \text{or} \quad Z_0 = 188\ \Omega$$

Rumsey [5] extended these ideas to antennas with more than two conductors to find the input impedances in various feeding modes.

We must relate flat-strip dipoles to normal round-rod dipoles to use the available results for round dipoles. The diameter of an equivalent round rod equals one-half the strip width of the flat structure. Consider a thin dipole with its near $\lambda/2$ resonance of 67 Ω. We find the equivalent slot impedance from Eq. (4-8)

$$Z_s = \frac{376.7^2}{4(67)} = 530\ \Omega$$

A half-wavelength slot has an impedance

$$Z_s = \frac{376.7^2}{4(73 + j42.5)} = 363 - j211\ \Omega$$

Whereas the $\lambda/2$ dipole is inductive when it is longer than a resonant length, the slot is capacitive.

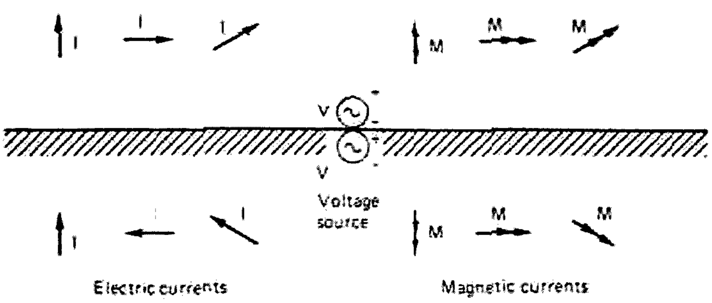

Figure 4-6 Ground plane images.

4-4 Monopole

A monopole consists of a single conductor fed out of a ground plane from the center conductor of a coax. Including its image (Fig. 4-6), the monopole equates to a dipole for analysis. The fields vanish below the ground plane. Restricting the fields to the upper hemisphere doubles the gain over a dipole, since only half the input power of the dipole is needed to produce the same field strength.

The input impedance decreases to half that of the equivalent dipole. We can form the image of the voltage source feeding the monopole in the ground plane. The voltage across the input of the equivalent dipole is twice that of the monopole to produce the same current. Therefore, the impedance of the monopole is half the impedance of the dipole.

4-5 Cavity-Backed Slots

A slot which radiates only on one side of the ground plane is the dual of a monopole. As in the case of the monopole, restricting the radiation to above the ground plane doubles the gain. The voltage across the slot determines the field strength. Since the radiated power is only half that of the slot radiating on both sides and having the same peak fields, the input impedance doubles. The already high slot impedance becomes even higher.

The cavity must present an open circuit at the slot, or its susceptance must combine with the slot susceptance to resonate. Normally, it is a quarter-wavelength deep. Since many cavities form a box, the waveguide mode determines the propagation constant (wavelength) used to find the depth.

4-6 Dipoles Located Over Ground Planes

We analyze a dipole over a ground plane as a two-element array: the dipole and its image. The ground plane more than doubles the gain of the element by limiting the radiation directions. We can expect a change in the input impedance as the dipole interacts with its image.

A vertical dipole excites currents in the ground plane when transmitting that are equivalent to its image. The image is vertical (Fig. 4-6) and has the same phase as the dipole (even mode). The impedance of the dipole becomes

$$Z = Z_{11} + Z_{12}$$

Z_{12} is the mutual impedance between the dipole and its image spaced $2H$, where H is the height of the dipole over the ground plane. The array radiates its maximum in the direction of the ground plane. The dipole also radiates greatest along the ground plane given by

$$U_{\max} = \frac{\eta |I_0|^2}{(2\pi)^2}\left[1 - \cos\left(\frac{kL}{2}\right)\right]^2 \tag{4-9}$$

where L is the dipole length. The radiated power of the single dipole is

$$P_{\text{in}} = R_{11}|I_0|^2\left(1 + \frac{R_{12}}{R_{11}}\right)$$

The two-element array increases the field over a single element by 2 and the radiation intensity by 4.

$$\text{Directivity} = \frac{4U_{d,\max}}{P_{\text{in}}/4\pi} = \frac{4\eta[1 - \cos(kL/2)]^2}{(R_{11} + R_{12})\pi}$$

We used only the power into the dipole since no source is connected to the image. Figure 4-7 is a plot of the directivity of a vertical dipole versus height over the ground plane.

A horizontal dipole and its image (Fig. 4-6) form an odd-mode two-element array. The input impedance of the dipole becomes

$$Z_{11} - Z_{12}$$

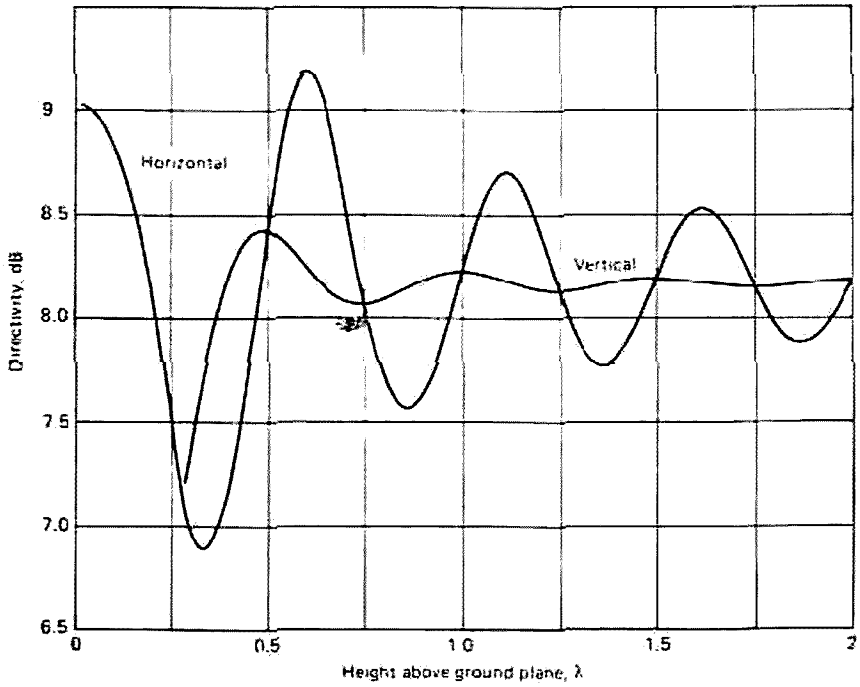

Figure 4-7 Directivity of half-wavelength dipoles over a ground plane.

for the odd-mode array. The value of the mutual impedance Z_{12} approaches that of the self-impedance Z_{11} as the two dipoles move close together. The input impedance nears zero as the distance from dipole to ground plane shrinks. The input impedance of all odd-mode array elements lessens as the elements approach each other.

The two-element odd-mode array produces a null along the ground plane. The beam peak occurs normal to the ground plane ($\theta = 0°$) when the distance between the dipole and its image is less than $\lambda/2$ or $H \le \lambda/4$. The pattern bifurcates after that height is exceeded. The maximum radiation from the array is

$$U_{A,\max} = 4 \sin^2 \frac{2\pi H}{\lambda} \qquad H \le \frac{\lambda}{4}$$

$$= 4 \qquad H \ge \frac{\lambda}{4} \qquad \theta_{\max} = \cos^{-1} \frac{\lambda}{4H}$$

The dipole pattern [Eq. (4.2)] increases the radiation intensity. The total input power into the single dipole becomes

$$P_{\text{in}} = |I_0|^2(R_{11} - R_{12})$$

$$\text{Directivity} = \frac{U_{A,\max}\, U_{d,\max}}{P_{\text{in}}/4\pi}$$

After inserting the various terms, we obtain the directivity of a horizontal dipole over ground.

$$\text{Directivity} = \frac{4\eta \sin^2 (2\pi H/\lambda)[1 - \cos (kL/2)]^2}{\pi(R_{11} - R_{12})} \qquad H \le \frac{\lambda}{4}$$

$$= \frac{4\eta[1 - \cos (kL/2)]^2}{\pi(R_{11} - R_{12})} \qquad H \ge \frac{\lambda}{4}$$

Its plot is included in Fig. 4-7.

FEEDING METHODS

4-7 Baluns [6, 7]

A balun properly connects a *bal*anced transmission line to an *un*balanced transmission line. Simple arguments about impedances to the balanced and unbalanced modes of the three-wire transmission lines explain the operation. Considering one of the lines of a transmission line as ground misleads us. A ground plane under the transmission line feeder becomes the third conductor of a three-wire line. Currents flowing in the ground plane can unbalance the currents in the feeder.

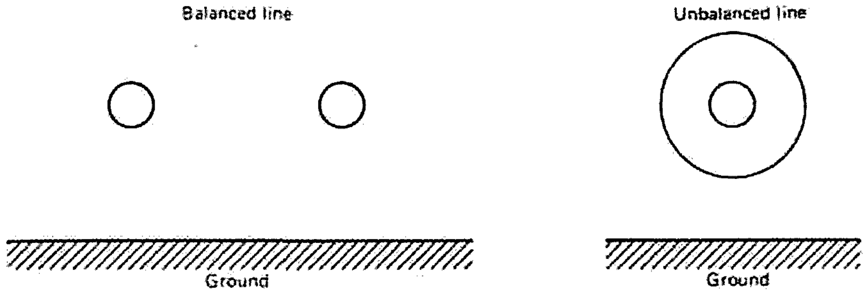

Figure 4-8 Physically balanced and unbalanced transmission lines.

A balanced three-wire transmission line mode carries equal and opposite currents in the feeder lines. The capacitances per unit length of the two lines to ground are the same. Coax is an example of an unbalanced line structure (Fig. 4-8). The inner conductor has no direct capacitance to ground. The two-wire line (Fig. 4-8) is a balanced line having equal capacitances to ground. Judge a balanced line by the currents and not just the physical structure.

Before we analyze baluns, we must consider the fundamental modes of a three-wire transmission line. Figure 4-9 shows circuit representations of the modes without showing the ground conductor. Equal loads terminate ports 3 and 4. The even mode applies equal voltages on ports 1 and 2 and forms a magnetic wall between the conductors. The magnetic field vanishes on the magnetic wall to produce a virtual open circuit. The unbalanced mode—equal current directions—is associated with the even mode. Equal and opposite voltages on ports 1 and 2 form the odd mode and set up an electric wall between the conductors. The electric wall is a virtual short circuit. The odd mode excites equal and opposite currents—balanced mode—on the two lines. When the loads on ports 3 and 4 are unequal, the modes separate according to the voltages, even and odd, or the currents, unbalanced and balanced. Dipoles present loads between the lines and not to ground.

Unbalanced mode circuits radiate. Only closely spaced equal and opposite currents, the balanced mode, cancel the far-field radiation from the currents. The radiating feeder line adds radiation components to the antenna. These components can radiate unwanted polarizations and redirect the beam peak of the antenna (squint). In reception, the unwanted currents excited on the feeder by passing electromagnetic waves reach the receiver

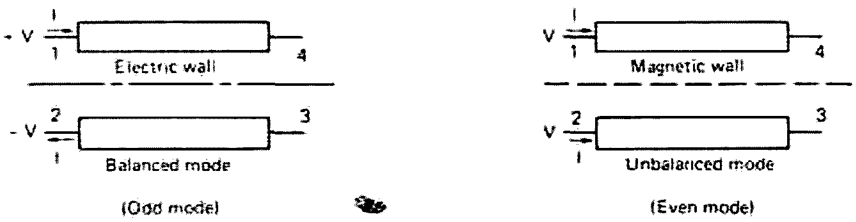

Figure 4-9 Balanced and unbalanced modes on three-wire transmission line.

terminals without a balun to block them. We analyze baluns by using either transmitting or receiving antennas depending on convenience. Reciprocity applies to baluns as well as antennas.

We can detect balance problems from pattern squint and polarization. An impedance-measuring setup can detect some balance problems. Radiating unbalanced currents cause changes in the impedance. The radiation shows when the impedance changes as fingers are run over the coax line from the equipment. If we feed a dipole from a coax without a balun, the current on the outer conductor splits between the dipole conductor and the outside of the conductor. Patterns and impedance measurements detect this current. Unbalanced currents on the arms of the dipole and feeder currents cause pattern squint.

Folded Balun A folded balun (Fig. 4-10) allows the direct connection of a coax line to the dipole. A dummy coax outer conductor is connected to the pole fed from the center conductor. It runs alongside the feeder coax for a quarter wavelength and connects to ground. The other pole connects directly to the shield of the feeder coax. The outer conductor of the coax and the extra line are two lines in a three-wire line with ground.

We analyze the structure by using balanced (odd) and unbalanced (even) modes. Unbalanced mode excitation at the dipole forms a magnetic wall through the ground connection between the two coax shields. The circuit reduces to a single line with an open circuit at the ground connection. The open circuit transforms through the quarter-wavelength line to a short circuit at the dipole. Any unbalanced currents induced on the dipole or the coax outer conductor are shorted at the input. Balanced mode excitation at the dipole forms an electric wall through the ground connection. The balanced mode circuit of the two coax shields is a quarter-wavelength short-circuited stub connected in shunt with the dipole (Fig. 4-11). We can analyze the

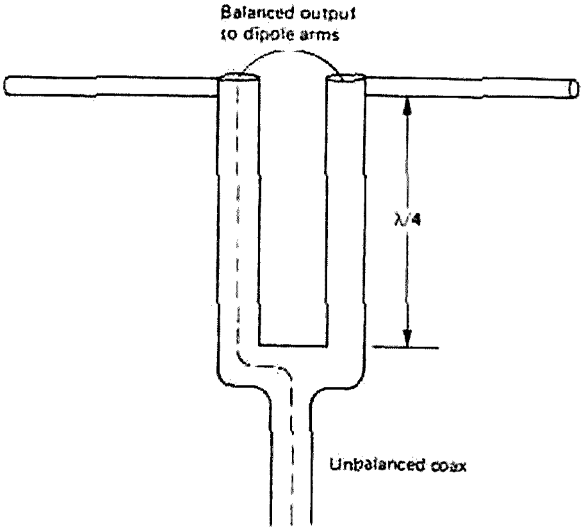

Figure 4-10 Folded balun.

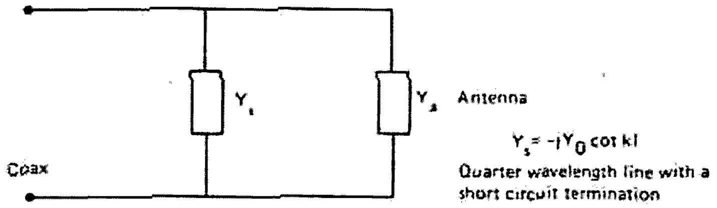

Figure 4-11 Folded balun equivalent circuit (balanced mode).

frequency response from Fig. 4-11. The bandwidth of the balun, although narrow, exceeds the bandwidth of the dipole.

Sleeve or Bazooka Baluns An outer jacket shields the outer conductor of the coax feeder in the sleeve balun (Fig. 4-12). The sleeve and the outer conductor of the coax form a series stub between the coax feeder and ground. The quarter-wavelength stub presents a high impedance to the unbalanced currents (Fig. 4-13). A second sleeve below the first one and directed away from the dipole further prevents currents excited on the coax from reaching the input. When the frequency changes, the connection to ground through the sleeve unbalances the transmission line. The balun is inherently narrowband.

Adding a stub to the center conductor (Fig. 4-14) increases the bandwidth because the stubs track each other when the frequency changes. Figure 4-13 demonstrates the circuit diagrams of the two types of sleeve baluns. The type II sleeve balun has matching series stubs on the outputs. The lines remain balanced at all frequencies, but the stubs limit the bandwidth of efficient operation.

Split Coax Balun [8] The split coax balun allows the connection of both arms of the dipole to the outer shield of the coax. The structure maintains symmetry to the dipole arms. Its rigidity helps to overcome vibration prob-

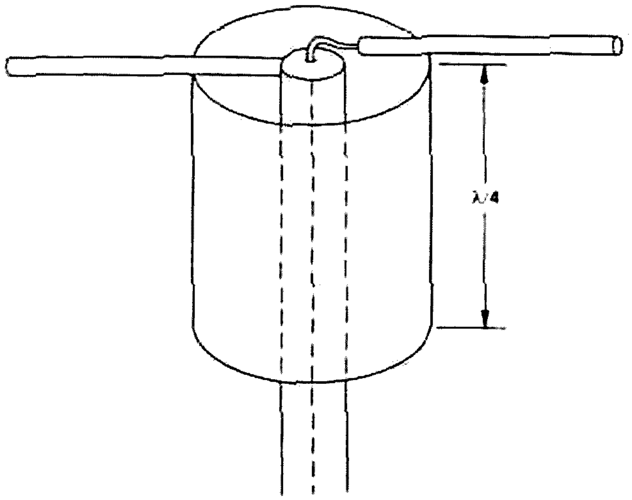

Figure 4-12 Sleeve or bazooka balun.

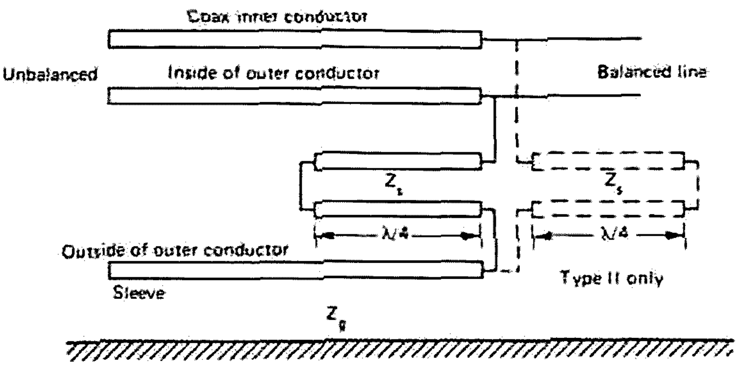

Figure 4-13 Schematic of types I and II sleeve or bazooka baluns.

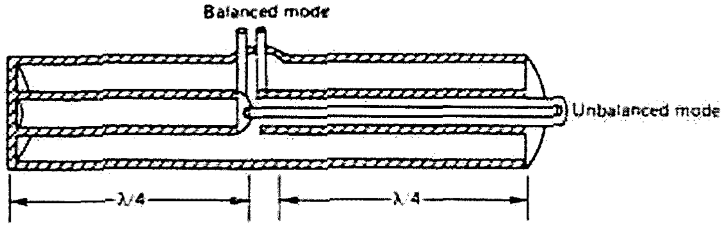

Figure 4-14 Type II sleeve balun.

lems. Slots cut in the outer shield (Fig. 4-15) enable the coax line to support two modes and make it equivalent to a three-wire line. A shorting pin excites the TE_{11} mode in the slotted coax (Fig. 4-16) to feed the dipole in the balanced mode.

Analysis of the split coax balun is similar to that of the folded balun. The ends of the slots are equivalent to the ground connection of the two coax shields of the folded balun. A virtual open circuit forms at the ends of the slots in the unbalanced (even) mode. It transforms to a short circuit at the dipole and shorts the unbalanced mode at the input. The virtual short circuit at the slot ends in the balanced mode transforms to an open circuit at the input. Figure 4-11 gives the circuit diagram.

Symmetry improves the performance of the split coax balun over the folded balun. The shorting pin is used only to excite the TE_{11} mode to feed the dipole arms. The extra wire length of the center conductor jumper of the

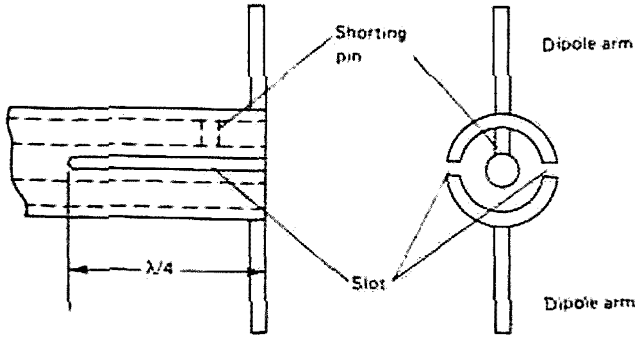

Figure 4-15 Split coax balun. (Source: S. Silver, ed., *Microwave Antenna Theory and Design*, McGraw-Hill, New York, 1949, p. 246. Used by permission.)

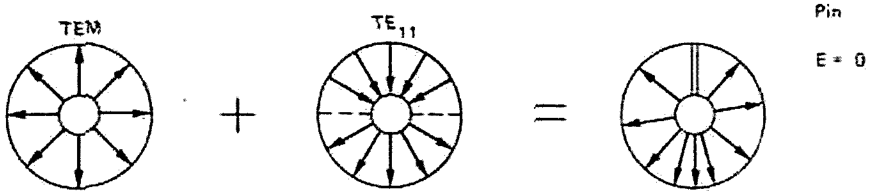

Figure 4-16 Coaxial transmission line modes in split coax balun. (Source: S. Silver, ed., *Microwave Antenna Theory and Design*, McGraw-Hill, New York, 1949, p. 247. Used by permission.)

folded balun introduces phase shift to the second arm and squints the beam. For that reason, the split coax balun is a better high-frequency balun. The phase shift problem of the jumper also occurs with the "infinite" balun of the log-periodic antenna.

Half-Wavelength Balun The half-wavelength balun (Fig. 4-17) works by cancellation of the unbalanced mode currents at the input to the coax. The impedance transforms by a factor of 4 from unbalanced- to balanced-mode ports. In the unbalanced (even) mode, equal voltages are applied to the two output ports. When the voltage wave on the upper line propagates through the half-wavelength line, its phase changes by 180°. This signal cancels the signal connected directly to the coax center conductor.

A load across a balanced-mode transmission line has a virtual short circuit halfway through it. The load on each balanced-mode line is $2Z_0$, where Z_0 is the coax characteristic impedance. The load on the end of the half-wavelength line is transformed by the line to the same impedance. The two loads, each $2Z_0$, are connected in shunt at the coax input and combine to Z_0. A balanced-mode impedance of $4Z_0$ transforms to Z_0 at the coax input. The half-wavelength cable can be rolled up for low frequencies. The balun transforms 300-Ω input impedances of folded dipoles to 75 Ω by using RG-59 cable (75 Ω).

Candelabra Balun The candelabra balun (Fig. 4-18) transforms the unbalanced-mode impedance by 4 times to the balanced-mode port. The coax cables on the balanced-mode side connect in series; those on the unbalanced-mode side connect in parallel. We can divide the balanced-mode

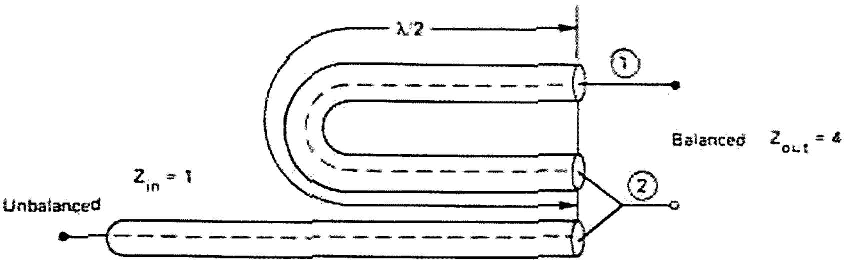

Figure 4-17 Half-wavelength balun.

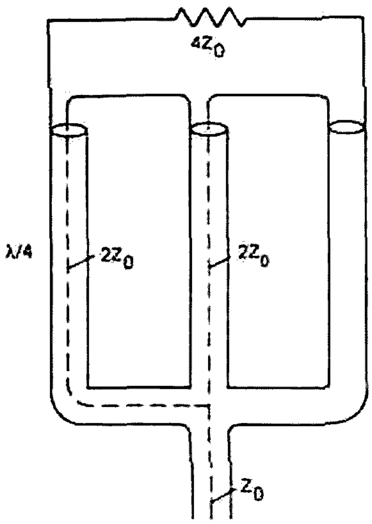

Figure 4-18 Candelabra balun.

impedance in two and connect each half to a $2Z_0$ impedance transmission line. These lines then connect in shunt at the unbalanced-mode port. The unbalanced-mode currents short out at the input to the $2Z_0$ coax lines in the same manner as the folded balun. More lines can be stacked in series and higher-impedance transformations obtained, but construction becomes more difficult.

Ferrite Core Baluns Ferrite can be used to increase the impedance to the unbalanced-mode currents and reduce them. At low frequencies (<100 MHz) ferrite has high permeability. As the frequency increases, the permeability drops but the losses to internal magnetic fields increase. The increased inductance of transmission lines is used at low frequencies, and the increased loss is used at high frequencies to inhibit currents.

Ferrite Bazooka or Sleeve Balun Ferrite cores, placed on the outside of a coax line (Fig. 4-19), increase the impedance to ground for currents on the outside of the shield. The ferrite cores inhibit unbalanced currents between the ground and the outer shield. The ferrite balun can work over many decades. The ferrite material provides the high impedance at low frequencies. As the ferrite material impedance drops when frequency increases, the transmission line approaches λ/4 of the bazooka balun. Any

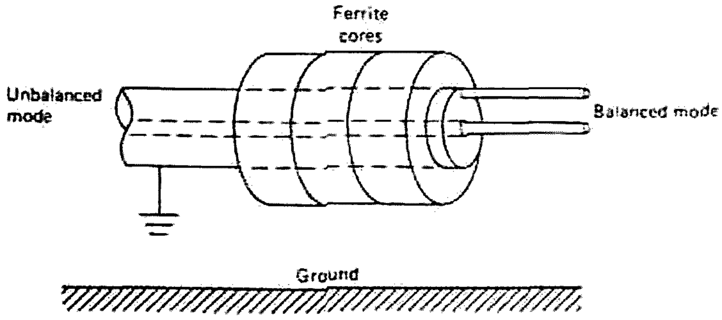

Figure 4-19 Ferrite core bazooka balun.

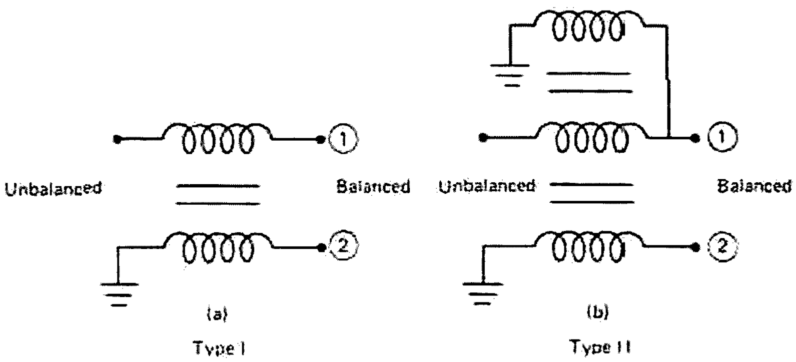

Figure 4-20 Bifilar wire ferrite core baluns: (*a*) type I; (*b*) type II.

ferrite core balun is a compromise design between the low-frequency response controlled by the amount of ferrite and the high-frequency response controlled by the length of transmission line.

Bifilar wire windings on a ferrite core form the 1:1 balun (Fig. 4-20*a*). The bifilar wire closely approximates 50- to 100-Ω characteristic impedance transmission lines. This balun can work satisfactorily from 100 kHz to 1 GHz. When there are balanced currents in the windings, there is no net magnetic field in the ferrite. In the unbalanced mode, the fields add in the core and give a high series impedance that is due to the high inductance (low frequency) or high resistance (high frequency).

The amplitude at port 2 (Fig. 4-20*a*) is lower than at port 1 because of the extra losses introduced in the ground lead by the ferrite core. This can be corrected by adding an extra winding to ground (Fig. 4-20*b*), which produces a type II bazooka balun. The extra winding balances the outputs by adding loss to port 1 without any increase in bandwidth.

Ferrite Candelabra Balun We can make a parallel-to-series ferrite balun that transforms the unbalanced-mode input impedance 4 times to the balanced-mode output (Fig. 4-21). As in the coax version, the characteristic impedance between the wires in the cores should be twice the unbalanced-mode input impedance. Point 3 (Fig. 4-21) is a virtual short. Connecting it to ground sometimes helps the balance. Both windings can be wound on the same core, such as a binocular core.

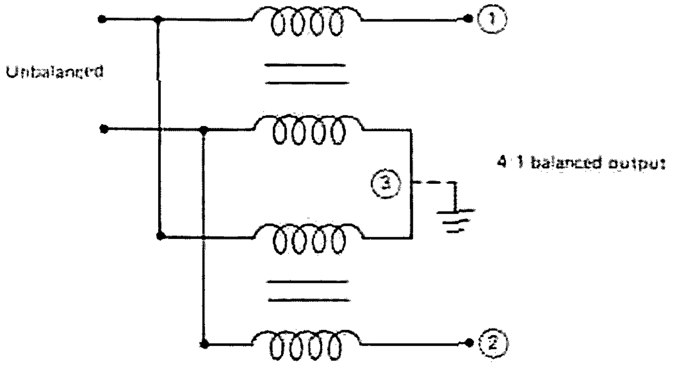

Figure 4-21 Ferrite core candelabra balun.

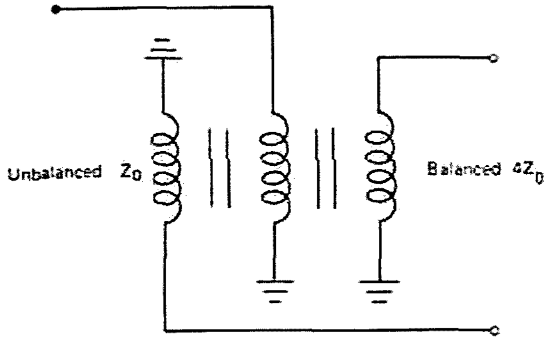

Figure 4-22 Ferrite transformer balun.

Transformer Balun The transformer balun has no transmission line equivalent; it is merely a transformer (Fig. 4-22). The balanced-mode output impedance is 4 times the input unbalanced mode. Wound with trifilar wire, the output has twice the turns of the input, and each output line has the same impedance to ground through the transformer. No transmission line effects extend the upper band edge beyond the transformer action of the windings and ferrite, but the transformer balun is a fine low-frequency device.

The use of No. 36 and 38 wires in ferrite core baluns limits the power-handling capability of the baluns to receive only levels. The ferrite bazooka balun (Fig. 4-19) carries the power in coax, which allows higher power levels.

Split Tapered Coax Balun [9] The split tapered coax balun starts with inherently unbalanced coax. Moving toward the balanced end, an outer conductor slot opens and exposes more and more of the center conductor (Fig. 4-23). At the point where the size of the outer conductor is reduced to that of the inner conductor, balanced twin line connects to the two conductors.

The impedance must be raised from input to output, since the two-wire line, spaced the radius of the coax, has a higher impedance than the input coax has. The balance depends on reducing the reflected wave in the transformer. Any suitable tapered transformer, such as Dolph-Chebyshev or exponential, can be used. Return loss is a measure of the unbalanced mode.

The balun can be constructed in microstrip. The ground plane tapers until it and the upper conductor are the same size. This balun can operate

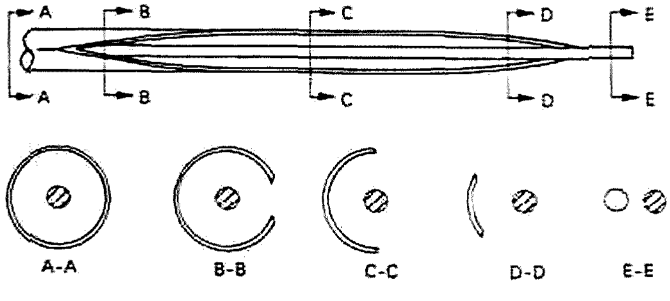

Figure 4-23 Split tapered coax balun. (Source: J. W. Duncan and V. P. Minerva, "100:1 Balun Transformer," *Proc. IRE*, vol. 48, no. 2, February 1960, p. 156. © 1960 IEEE.)

over decades of bandwidth, since the tapered transformer determines the bandwidth.

We have not exhausted the number of balun designs. The so-called "infinite" balun of log-periodic antennas will be discussed as a part of the construction of such antennas. When a broad-beam antenna is designed, sometimes a little squint in the beam and a little cross-polarization are acceptable and the antenna may be fed without a balun.

4-8 Offset Feed

We gain extra freedom by feeding a dipole (slot) off center. In most cases the length of the element determines the current (voltage) distribution so that offset feeding has little effect on the pattern, but we can change the input impedance level. Take a dipole whose center is at zero but is fed at $z = \xi$. We start at each end with zero current and move toward the center using a sinusoidal current distribution on each end

$$I(z) = I_1 \sin k\left(\frac{L}{2} - \xi\right) \qquad z > \xi$$

$$I(z) = I_2 \sin k\left(\frac{L}{2} + \xi\right) \qquad z < \xi$$

We find the ratio of I_1 to I_2 by matching the currents at $z = \xi$.

An antenna has a low input impedance level at high current points. Consider the half-wavelength dipole and slot. We raise the impedance of the dipole and lower the impedance of the slot as we move the feed point off center. The input resistance of the slot decreases approximately as

$$\sin^2 k\left(\frac{L}{2} - \xi\right)$$

as the feed is offset from the center of a half-wavelength slot.

Example Find the 50-Ω feed point of a resonant $\lambda/2$ slot ($L = 0.45\lambda$) that has a center feed point impedance of 510 Ω. We solve for the feed point

$$\xi = \frac{L}{2} - \frac{\lambda}{2\pi}\sin^{-1}\sqrt{\frac{Z_{in}}{Z_c}}$$

where Z_c is the center-fed resistance. By inserting values, we find $\xi = 0.174\lambda$, or a feed point 0.051λ from the end.

A slot does not need a balun because we can solder the outer shield of a coax to one side of the ground plane and jump the slot with the center conductor to apply the voltage. Any currents induced on the outside of the coax are just part of the ground plane currents.

If we offset-feed a one-wavelength dipole, we fail to get the current distribution shown in Fig. 4-2 because the current becomes a full si-

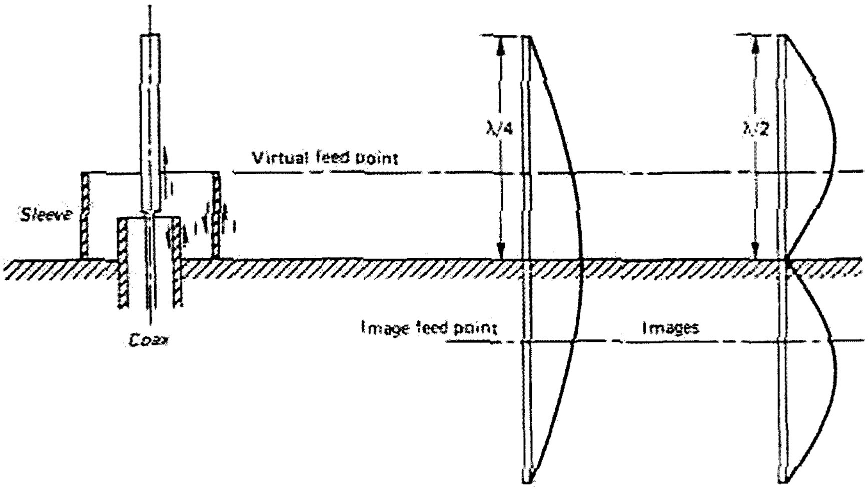

Figure 4-24 Sleeve monopole and current distributions.

nusoidal distribution instead of a rectified current pattern (Fig. 4-2) and develops a pattern null at $\theta = 90°$.

4-9 Sleeve Antenna [10, 11, 12, 13]

A sleeve around the monopole (Fig. 4-24) moves the virtual antenna feed up the monopole. The bandwidth increases because the current at the feed point remains nearly constant over a wide band. Currents at the input for when the monopole is a quarter wavelength long and when it is a half wavelength long are about the same (Fig. 4-24). The input resistance remains constant with changes in frequency.

The sleeve shields possible radiation from the internal currents while the currents on the outside of the sleeve radiate. The pattern changes little from the unshielded monopole. The internal structure is available as a series-matching stub and a transformer to broadband the antenna. The design consists of adjusting the parts until a suitable compromise input impedance match is achieved over the band.

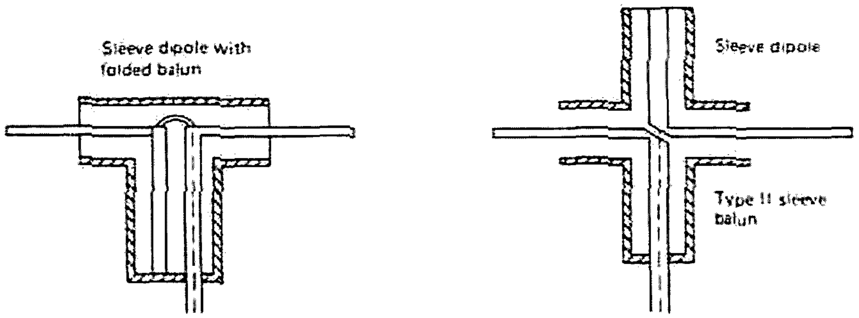

Figure 4-25 Sleeve dipoles.

Dipole sleeve antennas (Fig. 4-25) require symmetrical sleeves on the arms to maintain the symmetry of the currents. It is equivalent to feeding the antenna in two places. The balun is made an integral part of the base.

In both antennas, strips or rods can replace the total coaxial sleeve. The currents on the rods cancel the radiation from the currents on the internal feeder.

4-10 Folded Dipole

A half-wavelength folded dipole increases the input impedance of a normal dipole 4 times. It has about the same pattern as the dipole has. With the two elements closely coupled, we analyze the antenna by using even and odd modes (Fig. 4-26). The even mode divides the antenna into separate dipoles because the magnetic wall is a virtual open circuit. The input current to the even mode becomes

$$I_e = \frac{V}{2(Z_{11} + Z_{12})}$$

where Z_{11} is the self-impedance of one of the dipoles and Z_{12} is the mutual impedance between the closely coupled dipoles. The odd mode reduces the antenna to the series connection of two nonradiating quarter-wavelength stubs.

$$I_0 = \frac{V}{jZ_0 \tan(kL/2)}$$

where Z_0 is the characteristic impedance between the two rods. The input current is the sum of the even-mode and odd-mode currents. Near $L = \lambda/2$, the odd-mode current is quite small, since its input impedance is an open circuit. The input impedance is then determined by the even mode only.

$$Z_{in} = \frac{V}{I_e} = 2(Z_{11} + Z_{12})$$

For closely coupled lines $Z_{11} - Z_{12}$ and the input impedance becomes

$$Z_{in} = 4Z_{11}$$

where Z_{11} is the self-impedance of the dipole. Higher input impedance levels can be obtained by adding more elements.

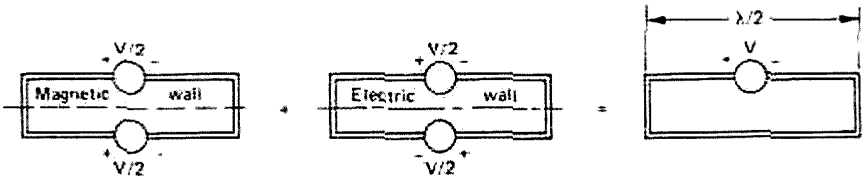

Figure 4-26 Folded dipole analysis modes.

4-11 Resonant Loop [14, 15]

A folded dipole has a perimeter of one wavelength and any shaped loop will resonate when its perimeter is near one wavelength. The sinusoidal current distribution of the folded dipole remains on the loop. The folded dipole has a dipole pattern with its null in the direction of the voltage across the feed. The loop retains this pattern property when it is symmetrical about the feed point. Opening the loop distorts the normal perfect-circle H-plane pattern of the dipole and gives 3- to 4-dB peaks in the directions normal to the loop compared with the directions in the plane of the loop. The E-plane null is filled in with a cross-polarized pattern at about 20 dB below the beam peak.

The current distribution is sinusoidal on the loop. Opposite the feed and halfway around the loop perimeter is a virtual short circuit point. The current reaches maximums at the virtual short circuit and at the feed. We can expect a low input resistance. A circular loop has an input resistance of about 130 Ω when the loop is 1.08 wavelengths in perimeter. If the loop is a parallelogram, the resonant input resistance depends on the angle between the wires at the feed. The resistance starts at about 300 Ω for the folded dipole and decreases for decreasing angles. At 120° between the lines, the resistance is about 250 Ω and drops to 50 Ω when the angle is 60°. Four common loop shapes are (1) circular, (2) square (quad), (3) parallelogram, and (4) triangle. Changes in the shape affect the input resistance at resonance and, to a slight degree, the resonant perimeter.

The Q of the antenna is about the same as that of a half-wavelength dipole. The gain equals that of the one-wavelength dipole, 3.8 dB.

4-12 Shunt Feeding [16]

Shunt feeding grows out of the folded dipole. The T match (Fig. 4-27) starts as a folded dipole when the taps are at the ends. As the taps move toward the center, the impedance of the dipole dominates at first, since the admittance of the shunt stub in the odd mode is small. The input impedance is capacitive. At some point, as the taps move toward the center, the inductive

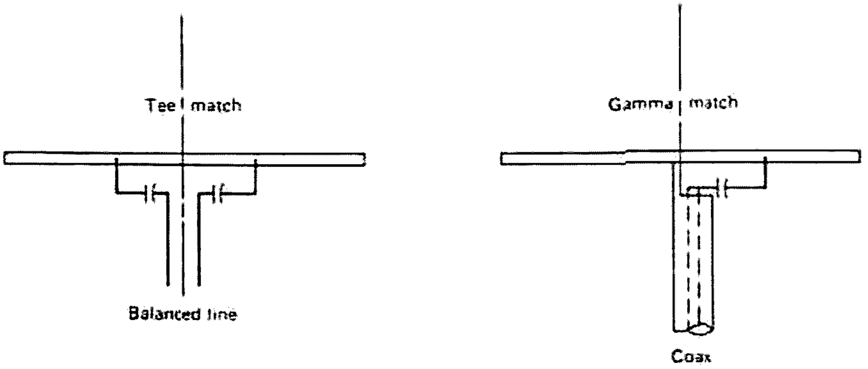

Figure 4-27 Shunt-fed dipoles.

admittance of the stub will cancel the capacitive admittance of the dipole and an antiresonance with its high input resistance will be reached. The location and magnitude of this peak resistance depend on the diameters of the rods in the T match section and the diameter of the radiator. The input resistance decreases as the tap point moves toward the center after the antiresonance point is reached. The input impedance is inductive, and match is achieved by using symmetrical series capacitors. The T match is fed from a balanced line.

The center short on the dipole allows the direct connection of the dipole to ground. Direct connection of broadcast towers (monopoles) to ground gives some lightning protection because the transmitter is capacitively connected to the tower. Shunt feeding with a T match enables solid conductors, such as the skin of an aircraft, to be excited as a dipole. Horizontal dipoles can be connected directly to vertical towers with a metal-to-metal contact to increase the strength of the antenna to withstand adverse weather conditions.

A gamma match (Fig. 4-27) can be fed from an unbalanced coax line. The shield of the coax connects to the shorted center connector of the dipole. The center conductor taps into one side of the solid rod. Moving the tap away from the center increases the input resistance. The inductive reactance is series-tuned with a capacitor. Both of these connections reduce the bandwidth of the antenna as the input impedance is raised. The combination of the series capacitor and the shunt inductive stub increases the stored energy and Q of the antenna.

4-13 Waveguide-Fed Slots [17, 18]

Waveguide is an ideal transmission line for feeding slots. Although its impedance cannot be uniquely defined, all possible candidates—voltage and current, power and current, or power and voltage—yield high values that match the high values of impedance of half-wavelength slots. Waveguide provides a rigid structure with shielded fields. The slots couple to the internal fields and allow the easy construction of linear arrays fed from traveling waves or standing waves in the waveguide. By controlling the position of the slots in the walls, the amplitude of the slot excitation can be controlled.

The waveguide fields excite a slot when the slot interrupts the waveguide wall currents. When excited, the slot loads the waveguide transmission line. We make the following assumptions about the wall slots.

1. The slot width is narrow. When slot grows in width, we must either consider it to be an aperture in the wall or assume it is excited by interrupting currents in two coordinate directions.

2. The slot is a resonant length; that is, its length is near $\lambda/2$. The waveguide environment, the wall thickness, and the position in the wall all

affect the resonant length. In most cases, experiments must determine the resonant length.

3. The electric field is directed across the narrow width of the slot and varies sinusoidally along the length independently of the excitation fields. This reiterates assumptions 1 and 2. An aperture radiates the polarization of the incident fields, but resonant-length slots can be excited only with a sinusoidal voltage standing wave. The slot direction determines polarization.

4. The waveguide walls are perfectly conducting and infinitely thin. Even though the walls have thickness, the difference has a small effect on the general form of the slot excitation formulas. As in the case of the resonant length, experiments determine a few values from which the rest must be interpolated or the values provide the constants for more elaborate models.

Waveguide wall currents flow either in the direction of propagation (z axis) or around the guide. The z-axis currents are traveling waves associated with power transfer. Slots which cut these currents are series loads to the waveguide. Only standing waves can flow around the walls, since the waveguide is shorted on both ends. The fields in waveguide divide into two plane waves reflecting off the walls as the wave propagates. The mode and size of the waveguide determine the angle of the reflections on the walls. In the transverse plane, the reflecting waves establish standing waves and shunt currents. Slots which interrupt the shunt standing wave currents are shunt loads to the waveguide. Whether the slot series or shunt loads the waveguide, its direction determines its polarization. The phases of waveguide currents decide the relative phases between slots.

Waves either travel along the guide into a terminating load or reflect from a short and set up standing waves along the z axis. Traveling wave currents excite the slots as they pass, and slots may be placed anywhere relative to the load. The distance between slots and the propagation constant determine the relative phases. Standing waves set up a fixed sinusoidal current pattern along the waveguide at a given frequency. The standing wave phase is either 0° or 180°. Slots placed in the current nulls of standing waves interrupt no currents and fail to be excited by the waveguide. We can vary the amplitude by the z-axis placement of the slots. We divide arrays of slots into two groups: nonresonant, excited by traveling waves, and resonant, excited by standing waves. The termination determines the array type. Do not confuse transverse standing waves that produce shunt currents and z-axis standing waves caused by a short-circuit termination. Both traveling and standing waves on the z axis have shunt currents.

Standing waves (resonant array) produce beams normal to the array axis. A resonant array maintains its beam direction when frequency changes, but the standing wave pattern shifts and changes the excitation of the slots. The amplitudes of the slots farthest from the short circuit change the most, since the standing waves have shifted farther. The length of the resonant array determines the array's bandwidth. The pattern shape changes because distribution and input impedance change as the loads change when the standing wave currents shift.

Nonresonant array (traveling wave) beam directions are functions of the propagation constant of the wave exciting the slots. When frequency changes, the beam direction changes. If the load on the end reflects a wave, then another beam forms from the reflected traveling wave. The second beam appears at the same angle to the axis of the waveguide as the first but measured from the -z axis. The load return loss determines the level of this second beam relative to the first.

4-14 Rectangular-Waveguide Wall Slots

The lowest-order mode (TE_{10}) in rectangular waveguide has the following fields [19]:

$$E_y = E_0 \sin(k_c x)\, e^{-jk_g z}$$

$$H_x = -\frac{k_g E_0}{\omega\mu} \sin(k_c x)\, e^{-jk_g z}$$

$$H_y = \frac{k_c E_0}{-j\omega\mu} \cos(k_c x)\, e^{-jk_g z}$$

where $k_c = \pi/a$, $k_g^2 = k_c^2 - k^2$, and a is the guide width. The wall currents $\mathbf{J}$ are determined by

$$\mathbf{J} = \mathbf{n} \times \mathbf{H} \tag{4-10}$$

where $\mathbf{n}$ is the unit normal to the wall. When we apply this boundary condition to the walls, we obtain the following wall currents.

Sidewalls:

$$J_y = -j\frac{E_0 k_c}{\omega\mu} e^{-jk_g z}$$

Bottom wall ($y = 0$):

$$J_s = \frac{E_0}{\omega\mu} e^{-jk_g z}[k_g \sin(k_c x)\mathbf{a}_z + jk_c \cos(k_c x)\mathbf{a}_x]$$

Top wall ($y = b$):

$$J_s = \frac{-E_0}{\omega\mu} e^{-jk_g z}[k_g \sin(k_c x)\mathbf{a}_z + jk_c \cos(k_c x)\mathbf{a}_x]$$

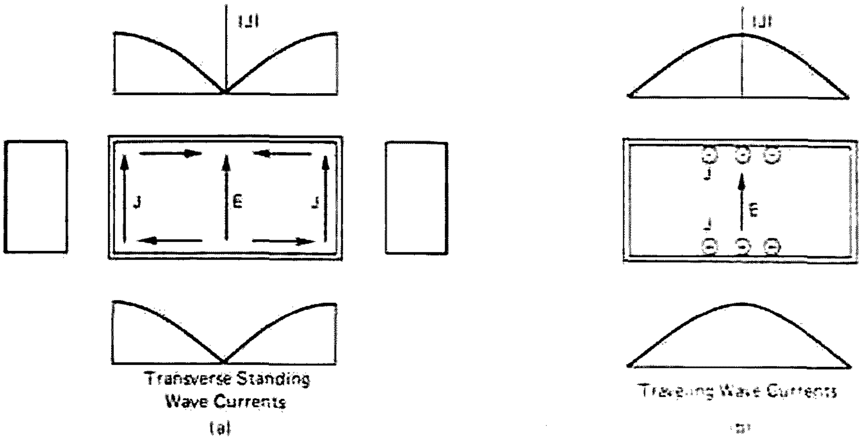

Transverse Standing Wave Currents
(a)

Traveling Wave Currents
(b)

Figure 4-28 TE_{10}-mode rectangular-waveguide wall currents: (*a*) transverse standing wave currents; (*b*) traveling wave currents.

Standing wave currents are 90° out of phase with respect to the electric field E_0. The sidewalls have only standing waves. The top and bottom walls have x-directed standing waves. Figure 4.28*a* shows the direction and amplitude distribution of these transverse standing waves. Slots interrupting these currents are shunt loads to the waveguide. In a traveling wave along the z axis, these transverse standing waves propagate in the z-axis direction. Sidewall slots (Fig. 4-29) interrupt shunt transverse standing waves. Slot *a* fails to cut surface currents and is not excited. By tilting slot *b*, currents are cut. The sidewall slot conductance is given by

$$g = g_0 \sin^2 \theta \tag{4-11}$$

where g_0 is the peak conductance. Note that the sidewall slots must cut into the top and bottom walls to achieve resonant length.

Tilting the slots to interrupt currents introduces cross-polarization components in the array pattern. We can alternate the direction of tilt to cancel the polarization. Two things prevent the total cancellation of cross-polarization. First, the amplitude taper of the array changes the amplitude from element to element and the fields do not cancel. Alternating the tilt of

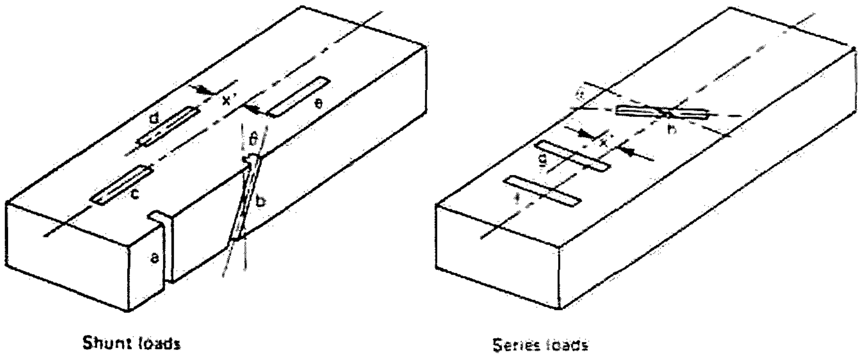

Shunt loads

Series loads

Figure 4-29 TE_{10}-mode rectangular-waveguide wall slots.

the slots symmetrically about the centerline in an array with an even number of elements prevents cross-polarization on boresight. Off boresight, the array effect of the spaced elements introduces a cross-polarization pattern, since cross-polarization is not canceled at each element.

The transverse standing wave currents are 90° out of phase with the traveling wave currents. The current alternates between the two types of current as the wave propagates down the waveguide. In the case of a standing wave along the z axis caused by a short circuit, the traveling wave currents are 90° out of phase with the electric field across the waveguide (Fig. 4-1). The peak amplitude of the transverse standing wave currents occurs at the same point as the electric field in a standing wave along the z axis, since both are 90° out of phase with the traveling wave currents. In a resonant array, the peak values of the transverse standing wave currents occur at odd multiples of a quarter wavelength from the short circuit, and the peak values of the traveling wave, z-axis-directed currents occur at half-wavelength multiples from the short.

Longitudinal top and bottom wall slots cut x-directed transverse shunt currents. The central slot c, located at a current null, fails to be excited. We use this nonradiating slot to insert a traveling probe to measure VSWR. When moved off center, slots d and e cut x-directed currents and are excited. The shunt conductance has the relation

$$g = g_0 \cos^2 \frac{\pi x'}{a} \tag{4-12}$$

where x' is the distance from the guide centerline. Shunt currents on either side of the centerline of the top or bottom wall (Fig. 4-28*a*) have different directions. Besides any traveling wave phase, slots d and e (Fig. 4-29) are 180° out of phase. Top-wall longitudinal slots generate no cross-polarization, since all maintain the same polarization.

Traveling z-directed waves (Fig. 4-28*b*) peak in the center of the broad walls and taper to zero at the edges. They remain zero on the sidewalls. Transverse slots f and g (Fig. 4-29), when centered, interrupt the maximum current. When moved off center, g, their series loading to the waveguide drops

$$R = R_0 \cos \frac{\pi x'}{a} \tag{4-13}$$

Rotating the broadwall transverse slot, h, reduces the series current interrupted. When the slot is centered, equal and opposite shunt currents are cut by the slot and the slot fails to present a load to shunt currents.

$$R = R_0 \cos^2 \theta \tag{4-14}$$

We can excite slots a and c by probe-coupling into the waveguide. A probe placed next to the slot and extending into the guide feeds the slot. The longer the probe, the more it disturbs the waveguide fields to excite the slot. Probes placed on opposite sides of the slots induce fields 180° out of phase with respect to each other.

4-15 Circular-Waveguide Slots

Figure 4-30 shows the transverse standing wave and traveling wave currents of the circular waveguide TE_{11} dominant mode. Slots may be successfully placed only at the current maximums without affecting the polarization of the internal wave. A longitudinal slot placed halfway between the current maximums, 45°, interrupts only shunt transverse standing waves. Since any polarization is possible in the circular waveguide, divide the incident wave into two waves. One is polarized in the direction of the slot; the other is polarized perpendicular to the slot axis. The wave polarized perpendicular to the slot location places its current maximum at the slot. The slot removes energy from the wave. The other wave places a current null on the slot. Adding the fields after the slot, the unloaded wave dominates and rotates polarization toward the slot when the waves combine. Circumferential slots interrupting traveling wave currents have the same polarization rotation of the wave when not centered 90° from the electric field direction.

Slots placed at the maximum of transverse shunt currents can cut currents by rotating about the axis of the waveguide. Like rectangular-waveguide sidewall slots, the slots orientated perpendicular to the guide axis, circumferential, do not load the waveguide. Rotating the slot shunt-loads the waveguide.

Slots placed at the maximum of the traveling wave cut z-directed currents. Field probes can monitor the internal fields of the waveguide through a longitudinal slot without radiation from the slot. When the slot is rotated away from the axis direction, it interrupts series traveling wave currents, loads the waveguide, and radiates.

Coaxial TEM-mode transmission line and TM_{11}-mode circular waveguide have the same outer wall currents (Fig. 4-31). Slots can be excited and load

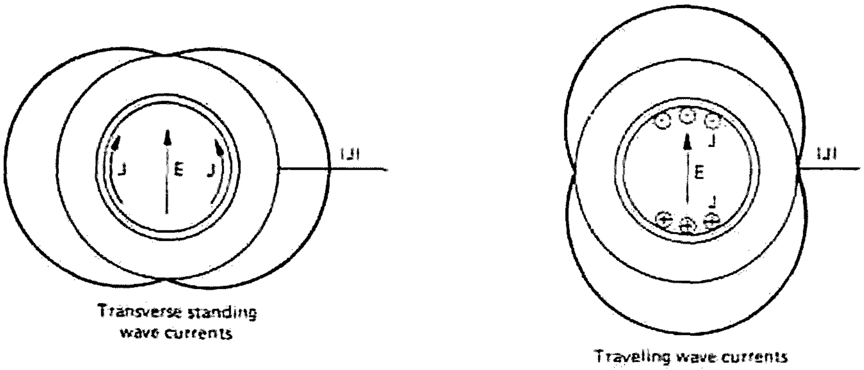

Transverse standing wave currents

Traveling wave currents

Figure 4-30 TE_{11}-mode circular-waveguide wall currents.

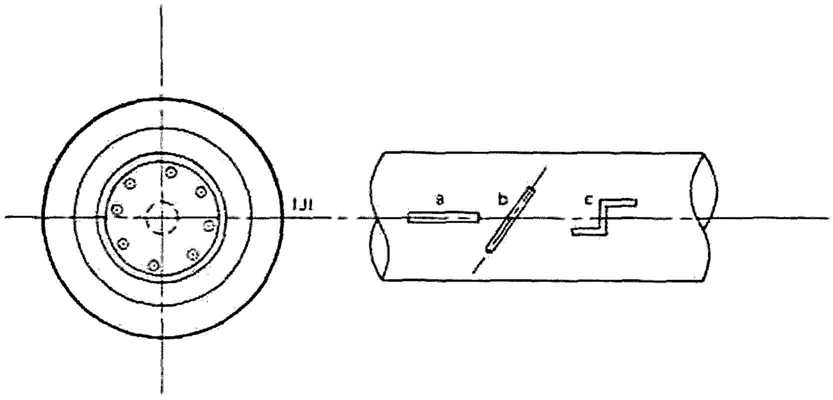

Traveling wave currents

Wall slots

Figure 4-31 Coax or TM_{11}-mode circular-waveguide wall currents and slots.

the waveguide only by interrupting these traveling wave currents. In Fig. 4-31, slot *a* fails to cut currents and is not excited. VSWR measuring probes use this slot. Slots *b* and *c* interrupt the currents and series-load the guide. Slot *c*, whose total length is resonant, is excited by the small portion in the center cutting z-directed currents.

4-16 Waveguide Slot Arrays [20]

Waveguide slot arrays can produce the lowest sidelobe antennas for pencil beams with good aperture efficiency. The array requires close tolerances to achieve the required amplitude distribution. Random errors in manufacture produce unwanted sidelobes. Producing these arrays is an art requiring careful analysis of all slot interactions, slot dimensioning determined from models and measurements, and precision machining and assembly.

The array consists of a set of waveguides loaded with slots and joined with a corporate feed into the total array. The corporate feed can also be a slotted array feeding the individual waveguides which contain the radiating slots. Aperture size and distribution determine the beamwidths in the various planes.

REFERENCES

1. R. F. Harrington, *Time-Harmonic Electromagnetic Fields*, McGraw-Hill, New York, 1961, p. 82.
2. C. A. Balanis, *Antenna Theory, Analysis and Design*, Harper & Row, New York, 1982, p. 120.
3. H. G. Booker, "Slot Aerials and Their Relation to Complementary Wire Aerials," *J. Inst. Elec. Engr.*, pt. IIIA, 1946, pp. 620–626.
4. R. S. Elliott, *Antenna Theory and Design*, Prentice-Hall, Englewood Cliffs, N.J., 1981, p. 337.
5. V. H. Rumsey, *Frequency Independent Antennas*, Academic Press, New York, 1966, p. 28.

6. N. Marchand, "Transmission-Line Conversion Transformers," *Electronics*, December 1941, pp. 142–145.
7. W. L. Weeks, *Antenna Engineering*, McGraw-Hill, New York, 1968, pp. 167–180.
8. S. Silver (ed.), *Microwave Antenna Theory and Design*, McGraw-Hill, New York, 1949, p. 245.
9. J. W. Duncan and V. P. Minerva, "100:1 Bandwidth Balun Transformer," *Proc. IRE*, vol. 48, February 1960, pp. 156–164.
10. E. L. Bock, J. A. Nelson, and A. Dorne, *Very High Frequency Techniques*, McGraw-Hill, New York, 1947, chap. 5.
11. J. D. Kraus, *Antennas*, McGraw-Hill, New York, 1950, p. 422.
12. A. J. Poggio and P. E. Mayes, "Pattern Bandwidth Optimization of the Sleeve Monopole Antenna," *IEEE Trans. Antennas Propagat.*, vol. AP-14, September 1966, pp. 623–645.
13. W. L. Stutzman and G. A. Thiele, *Antenna Theory and Design*, Wiley, New York, 1981, p. 278.
14. *The ARRL Antenna Book*, American Radio Relay League, Inc., Newington, Conn., 1974, p. 158.
15. T. Tsukiji and S. Tou, "On Polygonal Loop Antennas," *IEEE Trans. Antennas Propagat.*, vol. AP-28, no. 4, July 1980, p. 571.
16. *The ARRL Antenna Book*, American Radio Relay League, Inc., Newington, Conn., 1974, p. 118.
17. S. Silver (ed.), *Microwave Antenna Theory and Design*, McGraw-Hill, New York, 1949, p. 291.
18. R. C. Hansen (ed.), *Microwave Scanning Antennas*, Vol. II, Academic Press, New York, 1966, p. 95.
19. R. F. Harrington, *Time-Harmonic Electromagnetic Fields*, McGraw-Hill, New York, 1961, p. 69.
20. R. S. Elliott, *Antenna Theory and Design*, Prentice-Hall, Englewood Cliffs, N.J. 1981, p. 402.

CHAPTER

5

CONFORMAL ANTENNAS

Conformal antennas follow the shape of the surface on which they are mounted and generally exhibit a very low profile. Because of their low profile, they reduce turbulence effects in flight when mounted on aircraft, missiles, and instrumented artillery shells. Many different types of antennas can be mounted in cavities and made conformal, but we will mainly discuss stripline and microstrip antennas. Printed circuit techniques are used to etch the antennas on soft substrates; they provide low-cost and repeatable antennas in a low profile. The antennas made on soft substrates withstand tremendous shock and vibration environments.

As electronic devices continue to shrink in size, the antenna designer is pushed to reduce the antenna size as well. Cavity antennas use valuable internal volume, but restricting the volume limits the antenna impedance bandwidth. The antenna bandwidths will widen with increased circuit losses (material losses) or by the efficient use of the restricted volume. Applications with good link budget margins can use lossy antennas such as the ferrite core multiturn loops used around 1 MHz.

Bounds on bandwidth can be found by enclosing the antenna in a sphere and expanding the fields into TE and TM spherical modes [1, 2]. Each mode radiates, but it requires more and more stored energy as the mode number increases. Decreasing the volume increases the Q of each mode. A sum, weighted by the energy in each mode, determines the overall Q. Antennas which use the spherical volume efficiently and reduce power in the higher-order modes have the greatest bandwidths. A single mode puts an upper bound on bandwidth, given the size of the enclosing sphere. Greater volumes have potential for greater bandwidth provided the energy in higher-order spherical modes is restricted. Increasing material losses increases bandwidth beyond the single mode bound [2].

We find that increasing the volume of flush antennas will increase the impedance bandwidth provided the radiation mode on the structure can be maintained. Thicker substrates develop greater bandwidths, but they increase the possibility of higher-order-mode excitation. Losses limit the lower bound of bandwidth as we reduce the thickness, and efficiency degrades while the bandwidth remains constant.

5-1 Stripline Series Slots

Stripline consists of a center strip equally spaced between two flat ground planes. It supports a coaxial-type TEM mode wave between the central strip and the two ground planes. The ground plane currents match the currents flowing in the central strip. Without any waves reflected transversely, as in a waveguide, no shunt currents exist. Any slots cut in the ground plane can only interrupt traveling wave currents and present series loads to the transmission line. The load that a slot presents to the transmission line is a parallel combination of a radiation conductance and an energy storage susceptance. Low values of inductive reactance shunt power around the high resistance of short slots. The inductance increases with increasing electrical length and supports higher voltages across the slot radiation resistance. This increases the radiated power. The inductance increases to an antiresonance near $\lambda/2$, where further increases in electrical length decrease the capacitive reactance.

Oliner [3] gives an expression for slot conductance normalized to the stripline characteristic impedance. When unnormalized, it becomes

$$G = \frac{8\sqrt{\epsilon_r}}{45\pi^2}\left(\frac{a'}{\lambda}\right)^2\left[1 - 0.374\left(\frac{a'}{\lambda}\right)^2 + 0.130\left(\frac{a'}{\lambda}\right)^4\right] \tag{5-1}$$

where a' is the length of the slot and ϵ_r is the dielectric constant of the stripline boards. More complete expressions for full series admittance are available [4], but near resonance Eq. (5-1) suffices.

Most striplines are etched on dielectric substrates. The dielectric fills the slot and reduces the resonant length. The effective dielectric constant in the slot is [5]

$$\epsilon_r' = \frac{2\epsilon_r}{1 + \epsilon_r} \tag{5-2}$$

Slot length determines the radiation conductance. Decreasing the resonant length increases radiation resistance at resonance.

Example A set of woven teflon fiberglass ($\epsilon_r = 2.55$) dielectric boards supports a resonant-length slot in a stripline circuit. Find the resonant length and center-fed radiation conductance for a slot which resonates when $a' = 0.48\lambda$ in air.
The effective dielectric constant from Eq. (5.2) is 1.44. The effective dielectric constant reduces the resonant length.

$$\frac{a'}{\lambda} = \frac{0.48}{\sqrt{1.44}} = 0.40$$

Equation (5-1) finds the resonant conductance as 3.27 mS or 306 Ω resistance. The high impedance requires an offset feed to match the slot to a stripline. Section 4-8 gives the feed location measured from the slot center.

$$\xi = \frac{a'}{2} - \frac{\lambda}{2\pi\sqrt{\epsilon_r'}} \sin^{-1} \sqrt{\frac{Z_{in}}{Z_c}} \tag{5-3}$$

We can find the 50- and 100-Ω feed points of the slot.

$$50\ \Omega \qquad \xi = \frac{0.40\lambda}{2} - \frac{\lambda}{2\pi\sqrt{1.44}} \sin^{-1} \sqrt{\frac{50}{307}} = 0.145\lambda$$

$$100\ \Omega \qquad \xi = \frac{0.40\lambda}{2} - \frac{\lambda}{2\pi\sqrt{1.44}} \sin^{-1} \sqrt{\frac{100}{307}} = 0.119\lambda$$

At 2 GHz, the dimensions of the slot and the feed locations become

$a' = 6$ cm	$\xi = 2.17$ cm (50 Ω)	0.83 cm from edge
	$\xi = 1.79$ cm (100 Ω)	1.21 cm from edge

Increasing the slot width decreases the impedance below that of the thin width slot result given above and will require experimental work to find the exact feed point. Measuring the center-fed impedance allows the use of Eq. (5.3) to find the approximate offset feed point.

Figure 5-1 illustrates a typical stripline-fed slot. Shorting the center strip to ground at the location of the slot creates a current maximum at the slot for feeding. An open circuit a quarter wavelength beyond the slot creates the same standing wave current maximum at the slot. Convenience determines the feeding method.

The slot interrupts currents only in the top ground plane. Unequal current flow on the two ground planes unbalances the stripline and excites a parallel-plate mode between the ground planes. Waveguide wall slots also excite higher-order modes, but these cannot propagate because they are below their cutoff frequencies. The parallel-plate mode is another TEM mode without a low-frequency cutoff. Power in this mode propagates away from the slot.

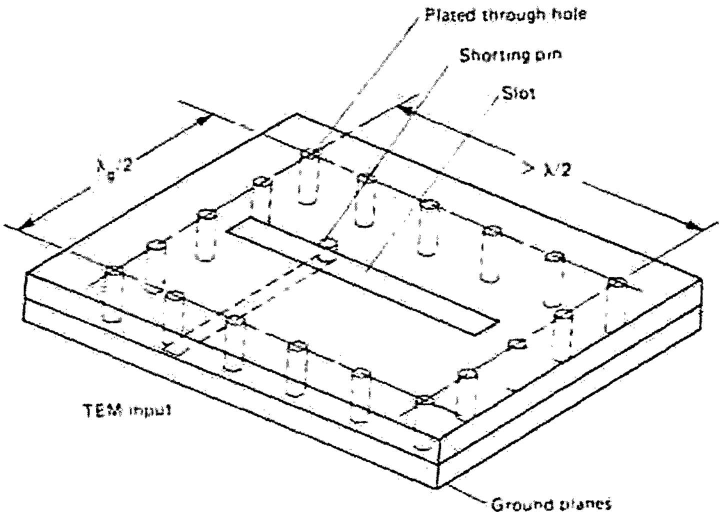

Figure 5-1 Stripline series slot.

Shorting pins between the two ground planes contain the parallel-plate mode around the slot. By placing the rows of pins parallel with the axis of the slot and a quarter wavelength away from the slot, the rows of pins reflect an open circuit at the slot. The side rows of pins complete the box and convert the parallel-plate mode into a waveguide TE_{10} mode. The box formed by the rows of shorting pins and the two ground planes form a resonant cavity in shunt with the slot admittance. The resonant cavity places a standing wave current null on a centered slot and does not excite the slot. Only the normal stripline currents feed the slot.

From an impedance point of view, the cavity is a second parallel resonant circuit increasing the stored energy of the antenna. Q increases and bandwidth decreases. Because only a portion of the available power would be converted to the parallel-plate mode by the slot discontinuity, we analyze the cavity as a circuit coupled through a transformer to the input. The transformer increases the impedance of the resonant cavity at the input and controls the division of power between the slot and the cavity. The cavity reactance slope limits the bandwidth of the stripline-fed slot to a few percent. Increasing the impedance of the waveguide cavity transmission line reduces the reactance slope contributed by the cavity. We increase the bandwidth by using greater distances between the ground planes and thereby increase the waveguide transmission line impedance. Greater volumes make impedance bandwidths greater.

Rotating the slot relative to the stripline feeding line reduces its load on the transmission line. The waveguide top wall series slot relation [Eq. (4-14)] applies in this case. The slot maintains its polarization while the nonradiating stripline center conductor approaches the slot at an angle. Rotated slots in waveguide must be paired symmetrically to reduce cross-polarization. A longitudinal array [6] can be made by placing all the slots on the centerline of a boxed stripline. Either edge plating or a series of plated-through holes forms a waveguide structure that supports only the TE_{10} mode. Slots placed on the centerline (as in Fig. 4-29, slot *c*) fail to interrupt the waveguide mode currents. The stripline meanders below and varies the excitation by changing the angle between the slot and the stripline center conductor. The slight loading of each slot excites very little of the parallel-plate mode that causes unwanted slot coupling. Both traveling wave and resonant linear arrays are possible.

5-2 Microstrip Patch Antennas

Microstrip consists of a metal strip on a dielectric substrate covered by a ground plane on the other side. Unlike stripline, the single ground plane shields the circuit on only one side. Normal packaged microstrip—within a receiver, for example—has a second shielding ground plane to reduce circuit interactions. The dielectric substrate retains most of the power because the shielding ground plane is spaced a few substrate thicknesses away. Removing the shield in antenna applications allows radiation from resonant cavities. The feeding circuits etched on the substrate radiate to some extent, but the radiations are comparatively small.

Arrays of antennas are photoetched on the substrate, as are the feeding networks. Microstrip provides easy connections to active devices and allows placement of preamps or distributed transmitters next to the antenna elements. Diode phase shifter circuits etched in the microstrip form single-board phased arrays. Microstrip circuits make a wide variety of antennas possible through the use of simple photoetching techniques.

Microstrip patch antennas consist of metal patches that are large with respect to normal transmission line widths. A patch radiates from fringing fields around its edges. Impedance match occurs when a patch resonates as a resonant cavity. When matched, the antenna achieves peak efficiency. Normal transmission line radiates little power because the fringing fields are matched by nearby counteracting fields. Power radiates from open circuits and from discontinuities, such as corners, but the amount depends on the radiation conductance load to the line relative to the patches. Without proper matching, little power radiates.

The edges of a patch appear as slots whose excitations depend on the internal fields of the cavity. A general analysis of an arbitrarily shaped patch considers the patch to be a resonant cavity with metal (electric) walls of the patch and the ground plane and magnetic or impedance walls around the edges. The radiating edges and fringing fields present a load at the point of the edge. In one analysis [7] the patch effective size is increased to account for the capacitive susceptance of fringing fields and the radiation admittance is ignored to find the resonant frequency. The far field is integrated to find the radiated power and the radiation conductance. The second method [8] is to retain the patch size but satisfy boundary conditions into a loaded wall whose load is determined by radiation and fringing fields. Assuming a constant electric field from the ground plane to the substrate allows solutions in terms of modes TM to the substrate thickness. Boundary conditions determine possible modes and correspond to the dual TE modes of waveguides having electric walls. Patches in the shape of standard coordinate system axes, such as rectangular and circular, give solutions in terms of tabulated functions. Numerical techniques used for arbitrarily shaped waveguides can be applied to patches with nonstandard shapes. We will consider only rectangular and circular patches.

5-3 Rectangular Microstrip Patch Antenna

Rectangular patch antenna design problems can be solved by using a transmission line model [9] suitable for moderate bandwidth antennas. Patches with bandwidths less than 1 percent or greater than 4 percent require a cavity analysis for accurate results, but the transmission line model covers most designs. The lowest-order mode, TM_{10}, resonates when the effective length across the patch is a half wavelength. Figure 5-2 demonstrates the patch fed below from a coax along the resonant length. Radiation occurs from the fringing fields. These fields extend the effective open circuit (magnetic wall) beyond the edge. The extension is given by [10]

$$\frac{\Delta}{H} = 0.412\frac{\epsilon_{\text{eff}} + 0.300}{\epsilon_{\text{eff}} - 0.258}\,\frac{W/H\ + 0.262}{W/H\ + 0.813} \tag{5-4}$$

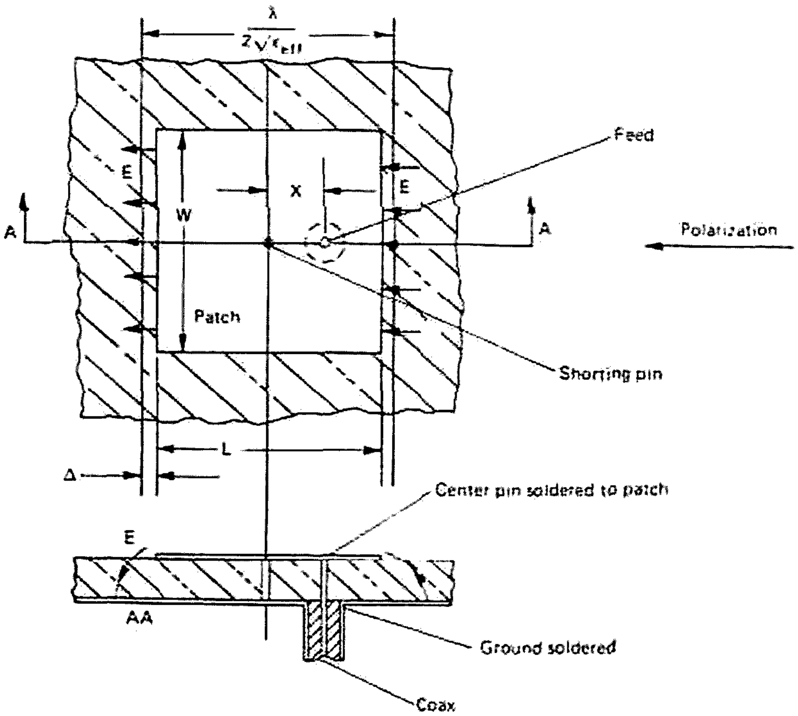
$\frac{\lambda}{2\sqrt{\epsilon_{\text{eff}}}}$
Feed
E
X
E
W
A
A
Polarization
Patch
Shorting pin
L
Δ
Center pin soldered to patch
E
AA
Ground soldered
Coax

Figure 5-2 Coax-fed microstrip patch antenna.

where H is the substrate thickness, W is the patch nonresonant width, and ϵ_{eff} is the effective dielectric constant of a microstrip transmission line the same width as the patch.

A suitable approximation for ϵ_{eff} is given by [11]

$$\epsilon_{\text{eff}} = \frac{\epsilon_r + 1}{2} + \frac{\epsilon_r - 1}{2}\left(1 + \frac{10H}{W}\right)^{-1/2} \tag{5-5}$$

where ϵ_r is the substrate dielectric constant. The transmission line model represents the patch as a low-impedance microstrip line whose width determines the impedance and effective dielectric constant. A combination of parallel-plate radiation conductance and capacitive susceptance loads both radiating edges of the patch.

Harrington [12] gives the radiation conductance for a parallel plate radiator as

$$G = \frac{\pi W}{\eta \lambda_0}\left[1 - \frac{(kH)^2}{24}\right] \tag{5-6}$$

where λ_0 is the free-space wavelength. The capacitive susceptance relates to the effective strip extension

$$B = 0.01668\frac{\Delta}{H}\left(\frac{W}{\lambda_0}\right)\epsilon_{\text{eff}} \tag{5-7}$$

Example Design a square microstrip patch antenna at 3 GHz on a 1.6-mm substrate with a dielectric constant of 2.55 (woven teflon fiberglass).

The patch will be approximately a half wavelength long in the dielectric. Assume at first that the width is $\lambda/2$.

$$W = \frac{c}{2f\sqrt{\epsilon_r}} = 31.3 \text{ mm}$$

By Eq. (5-5), $\epsilon_{\text{eff}} = 2.405$. On substituting that value into Eq. (5-4), we obtain the effective cutback on each edge: $\Delta = 0.81$ mm. The resonant length is

$$L = \frac{c}{2f\sqrt{\epsilon_{\text{eff}}}} - 2\Delta = 30.62 \text{ mm}$$

When we use this length as the width (square patch) to calculate the effective dielectric constant, we obtain 2.403, which is very close to the initial value. We can iterate it once more and obtain 30.64 mm for the resonant length.

The input conductance of the patch fed on the edge will be twice the conductance of one of the edge slots [Eq. (5-6)].

$$G = \frac{30.64 \text{ mm}}{120(100 \text{ mm})}\left\{1 + \frac{[2\pi(1.6)/100]^2}{24}\right\} = 2.55 \text{ mS}$$

$$R = \frac{1}{2G} = 196\ \Omega$$

A microstrip feeding line attaches to the center of one of the radiating edges. 50-Ω transmission lines become inconveniently wide on low-dielectric-constant substrates. More convenient 100-Ω narrower lines have about the same low loss and are generally used in feed networks. To transform the 196-Ω input resistance of the above example to 100 Ω, we use a 140-Ω quarter-wavelength transformer. The bandwidth of the transformer far exceeds that of the antenna.

In the above example, we have a square patch. Why doesn't the antenna radiate from the other two edges? We can equally well say that the patch is a transmission line in the other direction. The equal distances from the feed point to the nonradiating edges produce equal fields from the patch to ground. Equal fields on the edges set up a magnetic wall (virtual open circuit) through the centered feed line.

We expand the radiating edge fields in an odd mode, since the power traveling across the patch loses 180° of phase. The odd mode places a virtual short circuit halfway through the patch. A shorting pin through the center (Fig. 5-2) has no effect on radiation or impedance, but it allows a low-frequency grounding of the antenna.

The patch can be fed by a coax line from underneath (Fig. 5-2). The impedance varies from zero in the center to the edge resistance approximately as

$$R_i = R_e \sin^2 \frac{\pi x}{L} \qquad 0 \le x \le \frac{L}{2} \tag{5-8}$$

where R_i is the input resistance, R_e is the input resistance at the edge, and x is the distance from the patch center. The feed location does not affect the resonant frequency. By using Eq. (5-8), we find the feed point for a given input impedance:

$$x = \frac{L}{\pi} \sin^{-1} \sqrt{\frac{R_i}{R_e}} \tag{5-9}$$

Find the 50-Ω feed point in the above example.

$$x = \frac{30.64}{\pi} \sin^{-1} \left(\frac{50}{196} \right)^{1/2} = 5.16 \text{ mm}$$

The round rod across the gap of the microstrip patch is a series inductor at the input. Higher-order modes excited in the patch by the feeding method add to the inductive component of the antenna. Below resonance, the antenna is inductive and has near-zero resistance. As frequency increases, the inductance and resistance grow as the parallel resonance is approached. Above the resonant frequency, the antenna is capacitive as the impedance sweeps clockwise around the Smith chart back to a slight inductive component near a short circuit. Increasing the input resistance causes the resonant frequency response circle to grow on the Smith chart and cross the resistance line at a higher level. This general impedance response holds for circular patches also.

The transmission line model consists of a parallel combination of radiation conductance and shunt capacitance on each slot separated by a low-frequency microstrip transmission line. It can be used to find the frequency response of the rectangular patch. It fails to give us an accurate prediction of the bandwidth for very thin and thick substrates. A cavity model [13] accounting for radiation from all edges predicts the bandwidths given in Table 5-1. Dielectric constants of various common substrates were used. Besides the dielectric constant, thickness in wavelengths determines the bandwidth. Average values over the 1- to 10-GHz range are used. Thin substrates have poor efficiency that increases with frequency. We use Table 5-1 to determine bandwidth and specify thickness.

Example Find the substrate thickness needed to cover the band from 2.2 to 2.3 GHz with less than 2:1 VSWR by using a square patch with $\epsilon_r = 2.21$.

$$\text{Bandwidth } (\%) = \frac{(2.3 - 2.2)(100)}{\sqrt{2.3(2.2)}} = 4.44\%$$

TABLE 5-1 2:1 VSWR Bandwidth, %, of Square Microstrip Patch Antennas

Substrate thickness/λ_0*	Bandwidths, %, when substrate dielectric constants are as follows:				
	1.00	2.21	2.55	4.70	10.2
0.005	1.16	0.81	0.85	0.76	0.58
0.010	1.87	1.12	1.13	0.88	0.56
0.015	2.70	1.58	1.52	1.12	0.66
0.020	3.55	2.06	1.96	1.38	0.79
0.025	4.43	2.57	2.41	1.67	0.95
0.030	5.32	3.08	2.88	1.98	1.11
0.035	6.23	3.61	3.36	2.30	1.29
0.040	7.14	4.15	3.84	2.62	1.47
0.045	8.06	4.69	4.34	2.95	1.66
0.050	8.90	5.24	4.84	3.28	1.86
0.055	9.92	5.79	5.34	3.63	2.06
0.060	10.85	6.35	5.86	3.93	2.27
0.065	11.79	6.91	6.37	4.34	2.49
0.070	12.72	7.48	6.90	4.70	2.72
0.075	13.67	8.06	7.42	5.07	2.95
0.080	14.61	8.64	7.96	5.45	3.18
0.085	15.56	9.22	8.50	5.83	3.42
0.090	16.51	9.81	9.04	6.22	3.67
0.095	17.46	10.40	9.60	6.62	3.92
0.100	18.42	11.00	10.15	7.02	4.17

* λ_0 is the free-space wavelength.

We interpolate the chart to find the required thickness in wavelengths: 0.043. Thickness equals 5.70 mm. We could use a standard 6.35-mm (0.25-in) substrate.

Bandwidth increases when the feed point resonant resistance increases to about 65 Ω. We trade off perfect impedance match at a single frequency for an increased 2:1 VSWR bandwidth. The bandwidth also increases for increased patch widths, but the effect is slight.

Table 5-1 shows us that increasing the dielectric constant decreases the frequency bandwidth. Substrates with higher dielectric constants decrease the resonant size of the antenna and lead to narrower bandwidths. Resonant cavities on substrates with low dielectric constants radiate more easily than those with high dielectric constants because the fields have looser bonds to the substrate.

Circuit board losses become significant when substrates are thin. Table 5-2 lists the losses versus frequency for various thicknesses in wavelengths. The substrate thickness shrinks and the loss increases as frequency increases for a given thickness in wavelengths. Table 5-2 also shows that bandwidth increases as the increased loss reduces return loss. We must account for frequency to find the bandwidth of thin substrates and decide on the allowable loss in efficiency.

We can find the pattern by assuming a slot is located on each radiating edge. The fields along a radiating edge are approximately uniform with some tapering near the edge. Near-field probing reveals a slight increase in the fields on the edge nearest the feed. The fields do not stop abruptly at the end of a radiating edge but instead taper off in a fringing field. The fields on the so-called nonradiating edges form a difference distribution with matching amplitude fields and a 180° phase difference about a central null. These fields

TABLE 5-2 The Effects of Material Losses on the Bandwidth and Efficiency of a Square Microstrip Patch Antenna on Thin Glass-Cloth PTFE Laminate Substrates, $\epsilon_r = 2.55$

	$0.005\lambda_0$*		$0.010\lambda_0$		$0.015\lambda_0$	
Frequency, GHz	Bandwidth, %	Efficiency, dB	Bandwidth, %	Efficiency, dB	Bandwidth, %	Efficiency, dB
0.5	0.65	−1.92	1.03	−0.81	1.45	−0.49
1.0	0.69	−2.20	1.05	−0.90	1.47	−0.53
2.0	0.75	−2.57	1.08	−1.03	1.49	−0.59
4.0	0.84	−3.05	1.12	−1.20	1.52	−0.67
8.0	0.96	−3.64	1.18	−1.42	1.56	−0.78
16.0	1.14	−4.37	1.27	−1.73	1.61	−0.93
32.0	1.38	−5.22	1.39	−2.12	1.69	−1.14

* λ_0 is the free-space wavelength.

radiate a cross-polarized pattern off boresight. We replace the slot fields with magnetic currents in the direction of the edges for calculating the pattern. The linear magnetic currents produce a null in the pattern in the H plane at 90° from boresight. The two-slot array model of the microstrip antenna gives a broad pattern. Its gain is about 7 to 8 dB depending on the ground plane size. When the ground plane shrinks to the same size as the patch, the antenna radiates identical patterns on both sides. That reduces gain, and the antenna can no longer be made conformal.

Bandwidth to a 50-Ω system increases slightly with an increase in nonresonant patch width. We mostly discuss the square patch because, when fed from opposite edges, it radiates two linear polarizations or a circular polarization. For example, an antenna designed at 3 GHz has a 2.5 percent bandwidth when square that increases to 2.8 percent when the width is 3 times the resonant length. Decreasing the width to one-half the resonant length decreases the bandwidth to 2.3 percent. We change the width to control input impedance and only slightly affect the bandwidth. We achieve a 50-Ω input impedance on the edge with $W/L = 3.6$ and 100 Ω when $W/L = 1.9$. Increasing the width will also decrease the H-plane beamwidth and increase gain, but the effect is small.

5-4 Circular Microstrip Patch

In some applications, a circular patch fits in the available space better than a rectangular one. In a triangularly spaced array, they maintain a more uniform element environment. No suitable transmission line model presents itself, and the cavity model must determine the resonant frequency and bandwidth. The cutoff frequencies of TE modes of circular waveguides give the resonant frequencies of circular patch antennas. The patch with its magnetic walls and TM modes is the dual of the waveguide.

The resonant frequencies are given by

$$f_{np} = \frac{X'_{np}c}{2\pi a_{\text{eff}}\sqrt{\epsilon_r}} \tag{5-10}$$

where X'_{np} are the zeros of the derivative of the Bessel function $J_n(x)$ of order n, as is true of TE-mode circular waveguides. The term a_{eff} is an effective radius of the patch [14].

$$a_{\text{eff}} = a\left\{1 + \frac{2H}{\pi a\epsilon_r}\left[\ln\left(\frac{\pi a}{2H}\right) + 1.7726\right]\right\}^{1/2} \tag{5-11}$$

where a is the physical radius and H is the substrate thickness. Using the effective radius gives the resonant frequency within 2.5 percent.

We combine Eqs. (5-10) and (5-11) to find the radius to give a particular resonant frequency.

$$a_{\text{eff}} = \frac{X'_{np}c}{2\pi f_{np}\sqrt{\epsilon_r}} \tag{5-12}$$

Since a and a_{eff} are nearly the same, we can iterate Eq. (5-11) to find a, the physical radius [15].

$$a = \frac{a_{\text{eff}}}{\left\{1 + \frac{2H}{\pi a \epsilon_r}\left[\ln\left(\frac{\pi a}{2H}\right) + 1.7726\right]\right\}^{1/2}} \tag{5-13}$$

We start by using a_{eff} for a in Eq. (5-13), which converges rapidly.

The lowest order mode, TM_{11}, uses X'_{11} (1.84118) and produces a linearly polarized field similar to a square patch. The TM_{01} mode ($X'_{01} = 3.83171$) produces a monopole-type pattern from a uniform edge fringing field.

Example Design a circular microstrip patch antenna (TM_{11} mode) at 3 GHz on a 1.6-mm substrate that has a dielectric constant of 2.55 (woven Teflon fiberglass). We find the effective radius from Eq. (5-12).

$$a_{\text{eff}} = \frac{1.84118(300) \times 10^9 \text{ mm/s}}{2\pi(3) \times 10^9 \text{ Hz}\sqrt{2.55}} = 18.35 \text{ mm}$$

The physical radius will be slightly less. By using a_{eff} in the denominator of Eq. (5-13), we obtain a physical radius: $a = 17.48$ mm. We can then substitute this back into Eq. (5-13) and obtain $a = 17.45$ mm. Equation (5-13) converges in two iterations to a reasonable tolerance, since another iteration gives the same value. Actually, a single iteration gives the value within 0.2 percent on a formula accurate to only 2.5 percent.

A cavity model [16] predicts the 2:1 VSWR bandwidths given in Table 5-3. For a given stored energy, three loss conductances—(1) radiation, (2) conduction losses, and (3) dielectric losses—are found referenced to the edge voltage. By using them, the circuit Q and bandwidth are found. Average values over the 1- to 10-GHz range are used. Like rectangular patches, thin substrates have poor efficiency that degrades with decreasing frequency. The differences between the bandwidths at 1 GHz and 10 GHz are very small except for thin substrates when thickness is specified in wavelengths. On comparing Tables 5-1 and 5-3, we see that circular patches have less bandwidth than square patches for a substrate of the same thickness.

The fields of the TM_{11} mode produce a virtual short circuit at the center of the patch. We can reinforce the short circuit with a pin soldered between the patch and ground. The radial line along which the feed is placed establishes the radiation polarization. The nonuniform radiation along the edge gives a higher edge impedance than the square patch has. Experience shows that the 50-Ω feed point is located at about one-third the radius. Experiments will be required to find the proper point. Use a network analyzer with a Smith chart display to measure the input impedance. If the resonance circle swings around the origin, the impedance is too high. Move the feed

TABLE 5-3 2:1 VSWR Bandwidth, %, of Circular Microstrip Patch Antennas

Substrate thickness/λ_0*	Bandwidths, %, when substrate dielectric constants are as follows:				
	1.00	2.21	2.55	4.70	10.2
0.005	0.93	0.86	0.92	0.84	0.63
0.010	1.36	1.20	1.22	1.02	0.65
0.015	1.85	1.61	1.61	1.28	0.78
0.020	2.35	2.04	2.02	1.57	0.93
0.025	2.84	2.47	2.43	1.87	1.08
0.030	3.32	2.88	2.83	2.16	1.25
0.035	3.79	3.30	3.22	2.46	1.41
0.040	4.25	3.70	3.61	2.77	1.58
0.045	4.70	4.08	3.99	3.05	1.74
0.050	5.15	4.47	4.36	3.34	1.90
0.055	5.59	4.84	4.73	3.62	2.07
0.060	6.03	5.21	5.09	3.91	2.23
0.065	6.48	5.57	5.44	4.19	2.40
0.070	6.91	5.92	5.79	4.47	2.56
0.075	7.35	6.27	6.13	4.75	2.72
0.080	7.79	6.61	6.47	5.02	2.88
0.085	8.23	6.94	6.80	5.30	3.05
0.090	8.67	7.27	7.13	5.57	3.21
0.095	9.12	7.59	7.45	5.84	3.37
0.100	9.57	7.90	7.77	6.10	3.53

* λ_0 is the free-space wavelength.

toward the center. A scalar return loss display cannot give you the direction of movement required. Like the rectangular patch, mismatching the impedance at center frequency to about 65 Ω increases the bandwidth slightly. Dernery d [16] gives an approximate expression for the radial impedance variation.

$$R_{in} = R_r \frac{J_1^2(k_\epsilon \rho)}{J_1^2(k_\epsilon a)} \tag{5-14}$$

where R_r is the edge resistance, ρ is the radial distance, and J_1 is the Bessel function of the first kind. k_ϵ is the propagation constant in the substrate dielectric constant.

$$k_\epsilon = k\sqrt{\epsilon_r}$$

5-5 Patch Antenna Feed Networks

Patch antenna arrays may be fed from below (Fig. 5-2) by using a stripline distribution network. The required connections between the boards greatly complicate the assembly. Connections made vertically from the center strip of a stripline unbalances the stripline and induces parallel-plate modes. Shorting pins between the ground planes suppress this mode. It is far easier to etch the feed network on the microstrip. Feed networks radiate very little in comparison with the patches when etched on the same substrate. Fringing fields on the two sides of the microstrip lines cancel each other except at discontinuities (corners and steps).

Consider the equally fed array (Fig. 5-3). Equal feeding establishes magnetic walls between the patches as shown. We can join the edges between the patches without effect, since the midpoint remains a virtual open circuit. The separate patches join into a continuous strip. The feeds must be spaced to prevent grating lobes and to provide uniform illumination along the edges. These antennas can be wrapped around missiles to provide omnidirectional coverage about the roll axis. To prevent pattern ripple, feeds must be spaced about every 0.75λ in a circular array. The resistance at each feed at resonance will be the combination of the radiation conductances from the portions of the edges between the magnetic walls.

Figure 5-3 illustrates an equally fed four-element array. Starting from the patch, a quarter-wavelength transformer reduces the roughly 200-Ω impedance to 100 Ω. Two 100-Ω lines join in shunt to 50 Ω at their juncture. A 70.7-Ω quarter-wavelength line transforms the 50 Ω back to 100 Ω. We could continue this for any 2^N array. Equal path lengths from the input maintain equal phases on the patches. Arrays with the number of elements different from 2^N are possible, but they require more difficult feed networks. A 100-Ω system was picked because 50-Ω lines on low dielectric-constant substrates are quite wide.

The reactive power divider (Fig. 5-3) provides more than sufficient bandwidth. It is matched at the input, but not at its outputs. The network can be analyzed by using even and odd modes. The output return loss is 6 dB, and

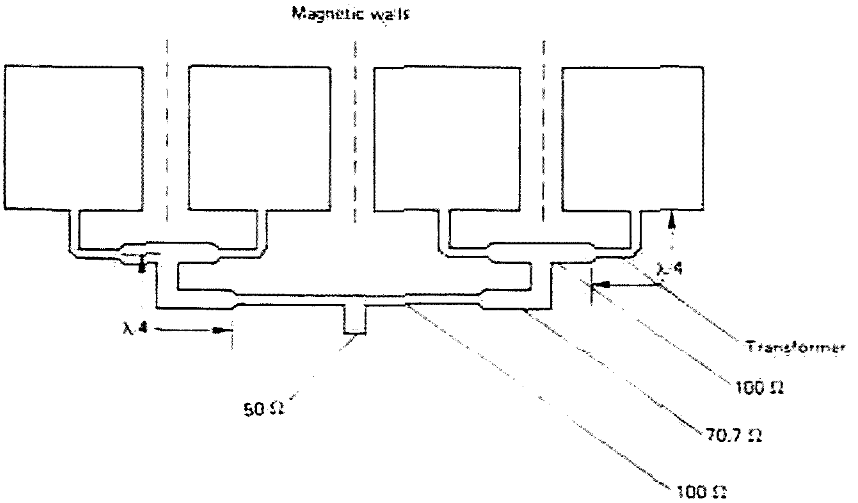

Figure 5-3 Equally fed microstrip patch array.

it provides only 6 dB of isolation between outputs. The power from a damaged antenna distributes to the other elements of the array and produces an effect greater than that of just a missing element. Making power dividers with isolation resistors solves this problem. We cannot justify the added difficulty of the resistors when both good etchings and low probability of damage make the resistors unnecessary.

We must be wary of coupling between different parts of the feed network. We want to pack the feed network into the smallest area, but coupled signals produce unexpected pattern anomalies. Distinguishing direct radiation from the feed and coupling is difficult. Although couplings are predictable, they appear as random errors when we cannot perform a full analysis. Unfortunately, the coupling between microstrip lines falls off quite slowly. Table 5-4 lists the coupling and peak errors for 100-Ω lines; those of 50-Ω lines are very similar.

5-6 Microstrip Transmission Line

Schneider [11] provides us with convenient expressions for microstrip lines. The effective dielectric constant changes with the ratio of stripwidth W to thickness H [Eq. (5-5)]:

$$\epsilon_{\text{eff}} = \frac{\epsilon_r + 1}{2} + \frac{\epsilon_r - 1}{2\sqrt{1 + 10H/W}} \tag{5-5}$$

We define an impedance Z_0

$$Z_0 = Z\sqrt{\epsilon_{\text{eff}}}$$

where Z is the strip impedance. The formulas separate at $W/H = 1$.

$$Z_0 = 60 \ln \left(\frac{8H}{W} + \frac{W}{4H}\right) \quad \frac{W}{H} \leq 1 \tag{5-15}$$

TABLE 5-4 Peak Feed Errors Due to Microstrip Coupling for 100-Ω Lines ($\epsilon_r = 2.4$)

Spacing/substrate thickness	Coupling, dB	Peak errors Amplitude, dB	Peak errors Phase, °
1.0	16	1.5	9.0
2.0	23	0.7	4.0
3.0	28	0.4	2.3
4.0	32	0.22	1.5
5.0	35	0.12	1.0

$$Z_0 = \frac{120\pi}{W/H + 2.42 - 0.44H/W + (1 - H/W)^6} \qquad W/H \geq 1 \tag{5-16}$$

We can find the impedance when W/H is known, but most design problems require the opposite: given Z, find W/H.

We use Eq. (5-5) and Eq. (5-15) or (5-16) in an iterative process to find W/H when we know Z. The formulas separate when $W/H = 1$. Find Z_0 at $W/H = 1$.

$$\epsilon_{\text{eff}}(1) = \frac{\epsilon_r + 1}{2} + \frac{\epsilon_r - 1}{6.63} \qquad W/H = 1 \tag{5-17}$$

Calculate $Z_0 = Z\sqrt{\epsilon_{\text{eff}}(1)}$. $Z_0(1) = 126.6$ ($W/H = 1$). If Z_0 is greater than $Z_0(1)$, then W/H is less than or equal to 1.

Case 1. $W/H \leq 1$. We solve for W/H in Eq. (5-15).

$$\frac{W}{H} = 2\left\{\exp\left(\frac{Z_0}{60}\right) - \sqrt{\left[\exp\left(\frac{Z_0}{60}\right)\right]^2 - 8}\right\} \tag{5-18}$$

Start with $\epsilon_{\text{eff}}(1)$ and solve for W/H. Use that value to find $\epsilon_{\text{eff}}(W/H)$, Eq. (5-5), and substitute back into Eq. (5-18) to find a new value of W/H. The loop between Eq. (5-18) and Eq. (5-5) converges rapidly.

Case 2. $W/H > 1$. We use Newton's method of finding function zeros to form an iteration equation. Let $X = (W/H)_{\text{old}}$.

$$\left(\frac{W}{H}\right)_{\text{new}} = X\left(1 - \frac{X^2 + X[2.42 + (1 - 1/X)^6 - 120\pi/Z_0] - 0.44}{X^2 + 0.44 + 6(1 - 1/X)^5}\right) \tag{5-19}$$

Use this new W/H to find $\epsilon_{\text{eff}}(W/H)$ and a new Z_0. A good starting value for the iterations is found from

$$\frac{W}{H} = \frac{120\pi}{Z_0} - 1.98$$

Iterations between Eqs. (5-19) and (5-5) converge in a few cycles.

Example Find the width-to-thickness ratio of a 139-Ω microstrip line on a thin glass-cloth PTFE laminate substrate ($\epsilon_r = 2.55$).

Use Eq. (5-17) to find $\epsilon_{\text{eff}}(1) = 2.01$. From this, we find Z_0

$$Z_0 = 139\sqrt{2.01} = 197$$

We compare Z_0 to 126.6 and discover that $W/H < 1$, which leads us to Eq. (5-18) for iterations. From the first iteration of Eq. (5-18), $W/H = 0.30$. Substitute this into Eq. (5-5) to find $\epsilon_{\text{eff}}(0.3) = 1.91$ and Z_0 (192). By using Eq. (5-18), we find the second $W/H = 0.33$. Another iteration gives the same values. For a 1.6-mm substrate, we have a stripwidth of 0.52 mm. At 3 GHz the quarter wavelength of a transformer is found by using ϵ_{eff}

$$\frac{\lambda}{4} = \frac{c}{4f\sqrt{\epsilon_{\text{eff}}}} = \frac{300}{4 \cdot 3\sqrt{1.91}} = 18.09 \text{ mm}$$

Table 5-5 lists the width-to-thickness ratios of 50-, 70.7-, and 100-Ω lines for various common substrate dielectric constants.

5-7 Circularly Polarized Patch Antennas

Figure 5-4 shows methods of achieving circular polarization with square patches fed with two inputs. The patches are fed by equal signals 90° out of phase.

The branch-line hybrid (Fig. 5-4*a*) consists of four transmission lines connected in a square. The hybrid shown (100-Ω system) produces equal outputs that are 90° out of phase at center frequency. The two inputs give opposite senses of circular polarization. Both the VSWR and axial ratio bandwidths far exceed the singly fed patch bandwidth. Reflections due to the patch mismatch appear at the opposite input. Patch input reflections, undetected at the input, reduce the efficiency of the antenna by the same amount as the singly fed patch mismatches do. The antenna can be fed from below in two places by using a coupled line hybrid, but it suffers from the same efficiency problem.

The cross-fed antenna (Fig. 5-4*b*) splits the signal to feed both edges. A quarter wavelength longer line provides the extra 90° phase shift to give

TABLE 5-5 Microstrip *W/H* and ϵ_{eff} at Selected Characteristic Impedances for Various Substrates

Dielectric constant	50-Ω line		70.7-Ω line		100-Ω line	
	W/H	ϵ_{eff}	W/H	ϵ_{eff}	W/H	ϵ_{eff}
1.00	4.95	1.00	2.97	1.00	1.62	1.00
2.08	3.22	1.81	1.84	1.75	0.94	1.70
2.17	3.13	1.87	1.78	1.81	0.90	1.75
2.21	3.09	1.90	1.75	1.84	0.89	1.78
2.33	2.99	1.98	1.68	1.92	0.85	1.85
2.55	2.82	2.14	1.57	2.06	0.78	1.98
4.70	1.80	3.57	0.94	3.39	0.40	3.22
5.30	1.63	3.96	0.84	3.75	0.35	3.54
9.00	1.03	6.22	0.47	5.84	0.16	5.50
9.60	0.97	6.58	0.43	6.17	0.14	5.81
10.20	0.92	6.93	0.40	6.50	0.13	6.12

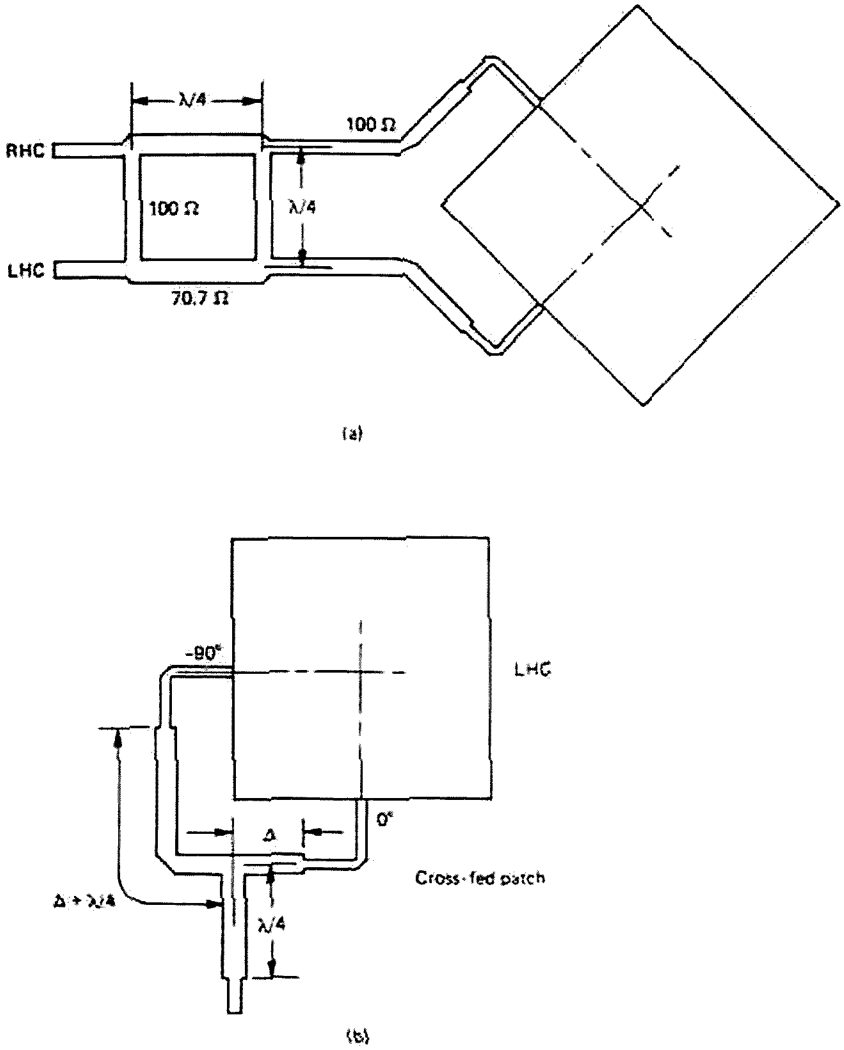

Figure 5-4 Dual fed circularly polarized patch antennas: (*a*) branchline hybrid feed; (*b*) cross-fed patch.

circular polarization. Shifting the impedance from one input through a quarter-wavelength line before adding the two in shunt tends to cancel the reflection from the second line and increase the impedance bandwidth. The impedance bandwidth approximately doubles from the bandwidth of the singly fed patch on the same substrate. The 6-dB axial ratio bandwidth roughly equals the singly fed square patch bandwidth. The polarization loss (0.5 dB) of a 6-dB axial ratio equals the 2:1 VSWR mismatch loss.

The antennas in Fig. 5-5 use asymmetries to perturb the resonances to two possible modes and achieve circular polarization. We can understand the operation of the corner-fed patch (Fig. 5-5*a*) from that of the turnstile dipole antenna (Fig. 5-6). The orthogonal dipoles could be equal length and could be fed from a 90° hybrid to achieve circular polarization (like the patch in Fig. 5-4*a*). Instead, the lengths are changed to shift the phase of each dipole by 45° at resonance. If we lengthen the dipole beyond resonance, the input impedance becomes inductive. The current becomes

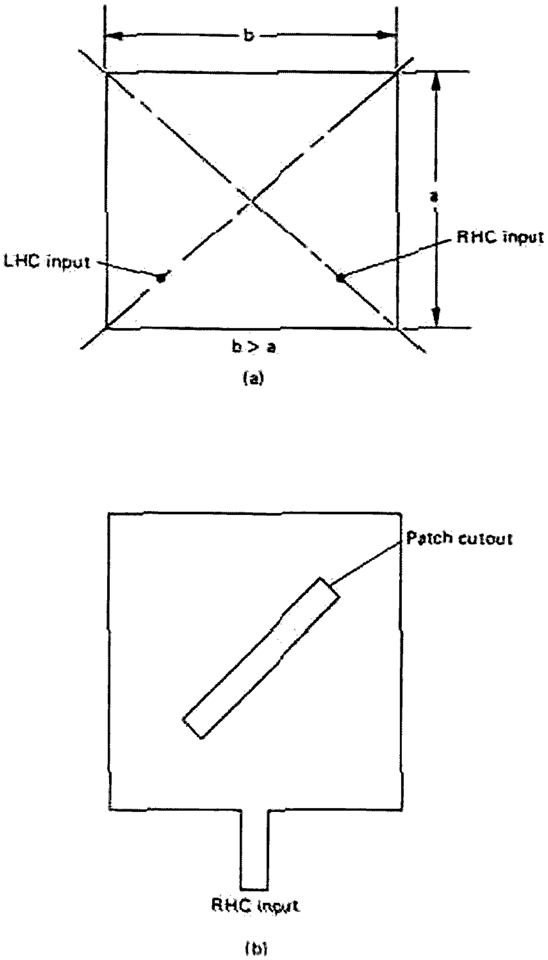

Figure 5-5 Circularly polarized patch antennas using asymmetry.

$$I = \frac{V}{R_2 + jX_2} = \frac{V(R_2 - jX_2)}{R_2^2 + X_2^2}$$

The far field is proportional to the magnetic vector potential found from the current. The radiated field phase decreases relative to the resonant-length dipole. Shortening the dipole from resonance increases the far-field phase.

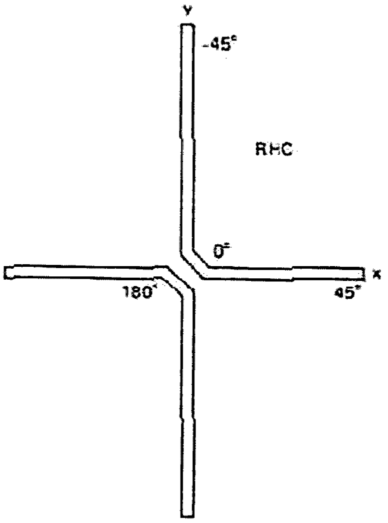

Figure 5-6 Turnstile dipole antenna.

We adjust the lengths until the phase difference of the radiated fields is 90° and the susceptances from the two dipoles cancel at center frequency.

We achieve the same effect with a patch by perturbing the lengths of a square patch and feeding both polarizations. An input along the diagonal feeds all edges in two separate resonances. The ratio of the edge lengths is found in terms of Q by a perturbation technique [7].

$$\frac{b}{a} = 1 + \frac{1}{Q} \tag{5-20}$$

We find the resonant frequencies for the two lengths from Eq. (5-20):

$$f_1 = \frac{f_0}{\sqrt{1 + 1/Q}} \qquad f_2 = f_0\sqrt{1 + 1/Q} \tag{5-21}$$

Q is related to the VSWR bandwidth by

$$\text{BW} = \frac{\text{VSWR} - 1}{Q\sqrt{\text{VSWR}}} \qquad Q = \frac{\text{VSWR} - 1}{\text{BW}\sqrt{\text{VSWR}}} \tag{5-22}$$

For a 2:1 VSWR bandwidth, Eq. (5-22) becomes

$$Q = \frac{1}{\sqrt{2}\,\text{BW}} \tag{5-23}$$

We use Table 5-1 bandwidths to find Q and the resonant lengths.

Example Find the resonant lengths for a corner-fed patch on a 1.6-mm substrate with $\epsilon_r = 2.55$ at 3 GHz.

We have $\lambda = 100$ mm and thickness/$\lambda = 0.016$. From Table 5-1, we interpolate the 2:1 VSWR bandwidth: 1.61 percent. From Eq. (5-23) we find the Q:

$$Q = \frac{1}{\sqrt{2}\,(0.0161)} = 43.9$$

Use Eq. (5-21) to find the resonant frequencies

$$f_1 = \frac{3}{(1 + 1/43.9)^{1/2}} = 2.966 \text{ GHz}$$

$$f_2 = 3(1 + 1/43.9)^{1/2} = 3.034 \text{ GHz}$$

By using the techniques of Sec. 5-3, we calculate the resonant lengths:

$$a = 30.27 \text{ mm} \qquad b = 31.01 \text{ mm}$$

A circular patch perturbed into an elliptical patch radiates circular polarization when fed on a 45° diagonal from the major or minor axis. The ratio of the major to minor axes relates to the Q [7]:

$$\frac{b}{a} = 1 + \frac{1.0887}{Q} \tag{5-24}$$

with resonant frequencies

$$f_1 = \frac{f_0}{(1 + 1.0887/Q)^{1/2}} \qquad f_2 = f_0(1 + 1.0887/Q)^{1/2} \tag{5-25}$$

The Q is found by using Eq. (5-23) and the bandwidths in Table 5-3 for circular patches. Use the techniques of Sec. 5-4 to calculate the physical radius of the major and minor axes from the frequencies [Eq. (5-25)].

The 2:1 VSWR bandwidth is unchanged from the square or circular patch fed for linear polarization. The 6-dB axial ratio bandwidth equals the 2:1 VSWR bandwidth.

Kerr [17] achieves circular polarization by orientating a rectangular cutout on a square patch (Fig. 5-5*b*). The size of the cutout is determined experimentally. Like other perturbation techniques, we can expect unchanged bandwidths from the linearly polarized antennas.

Equation (5-22) gives us a relation between bandwidths at different VSWR levels. Antenna Q remains constant.

$$\frac{\mathrm{BW}_2}{\mathrm{BW}_1} = \frac{(\mathrm{VSWR}_2 - 1)\sqrt{\mathrm{VSWR}_1}}{(\mathrm{VSWR}_1 - 1)\sqrt{\mathrm{VSWR}_2}} \tag{5-26}$$

For example, if $\mathrm{VSWR}_1 = 2$ and $\mathrm{VSWR}_2 = 3$, then $\mathrm{BW}_3/\mathrm{BW}_2 = 1.633$.

Example Find the thickness of a circular patch antenna to give a 4 percent 3:1 VSWR bandwidth ($\epsilon_r = 2.21$).

The 2:1 VSWR bandwidth is 4/1.633 = 2.45 percent. By using Table 5-3, we interpolate the thickness: 0.025λ.

5-8 Series-Fed Array

If we reduce the width of the patch, the radiation conductance is insufficient to match the input. We can use the microstrip patch as a transmission line and connect a line opposite the feed to lead to other patches (Fig. 5-7*a*). If we space the patches by half-wavelengths, the impedances of the patches will add in phase at the input. The impedance level of the connecting lines has no effect at center frequency. The junction of the transmission line feeder and the patch introduces excess phase shift. In arrays of a few elements the extra phase shift can be ignored, but arrays with a large number of elements or a critical amplitude taper must account for δ. Of course, traveling wave or resonant arrays can be designed. The frequency dispersion of the traveling wave array can be used to frequency-scan the beam.

Various experimental methods have been devised to measure the parameters of the series array. Metzler [18] performed experiments on uniform-

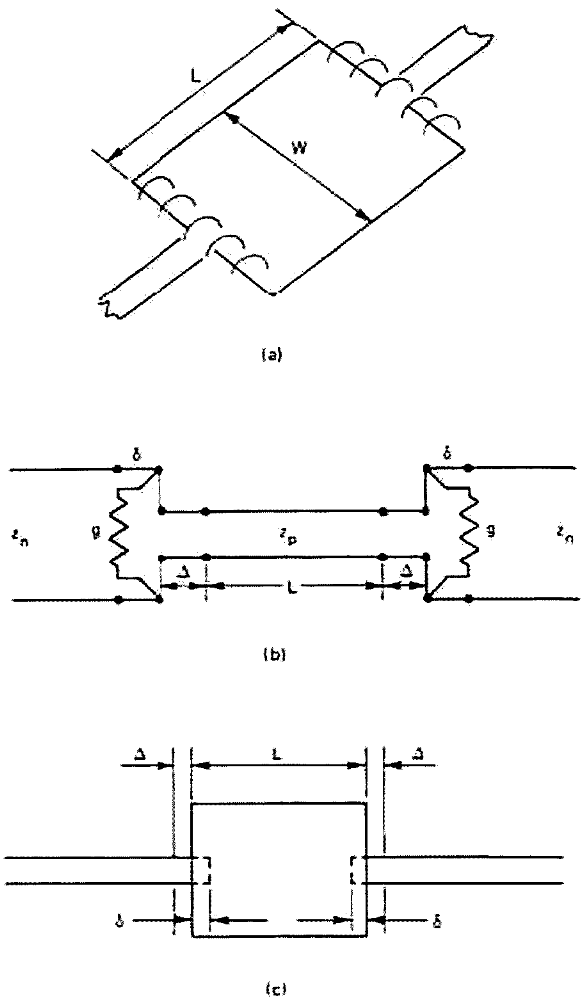

Figure 5-7 Series-fed patch and its equivalent circuit. (Source: Jones et al., "The Synthesis of Shaped Patterns with Series Fed Microstrip Patch Arrays," *IEEE Trans. Antennas Propagat.*, vol. AP-30, no. 6, November 1982, p. 1207. © 1982 IEEE.)

width element arrays to determine the radiation conductance and excess phase shift. Measuring the transmission loss through the array as a network with input and output connectors determines the radiation conductance of the patches. An empirical equation was obtained

$$G = 0.0162\left(\frac{W}{\lambda_0}\right)^{1.757} \qquad 0.033 \leq \frac{W}{\lambda} \leq 0.254 \tag{5-27}$$

where G is the total radiation conductance of each patch; half at each edge. Measurement of the beam direction of the uniform traveling wave array determines the excess phase shift in each patch.

Jones et al. [19] model the patch (Fig. 5-7) with extensions Δ that are due to the fringing fields as a transmission line: $L + 2\Delta$ long. The other excess phase shift, due to the step, is modeled as extensions to the input lines (δ). Jones et al. perform measurements on single elements to establish these lengths. Δ is found from the resonant frequency of the patch

$$L + 2\Delta = \frac{\lambda}{2\sqrt{\epsilon_{\text{eff}}}}$$

where ϵ_{eff} is given by Eq. (5-5). When the transmission line phase is measured through the patch at resonance, the excess phase beyond π is equated to a phase shift length in the narrow feeder lines

$$2\delta = \frac{\lambda_N}{2\pi}\phi_{\text{excess}}$$

where λ_N is the wavelength in the narrow line.

When designing the array, we vary the widths of the patches to achieve the desired amplitude taper. The voltage distribution at each patch is given by $V\sqrt{g}$, where g is the patch conductance. Standing wave (resonant) arrays require that the sum of the conductances be equal to the desired input conductance. We have some latitude when we feed the array through a quarter-wavelength transformer. The nonresonant array requires a matched load on the end to prevent standing waves. We must pick the ratio of the power dissipated to the radiated power. This gives us an extra parameter to optimize the design. We control the beam direction by spacing the elements to achieve the required phase shift.

5-9 Half-Patch Antenna

When operation is in the lowest mode of a patch, a virtual short circuit forms through a plane centered between the two radiating edges. We can make an antenna by using half the patch and supplying the short circuit (Fig. 5-8). The E-plane pattern broadens to that of a single slot. The resonant length is about a quarter wavelength in the dielectric of the substrate.

$$\frac{L}{2} = \frac{\lambda}{4\sqrt{\epsilon_{\text{eff}}}} - \Delta \tag{5-28}$$

We have only the conductance and susceptance of a single edge. This doubles the resonant resistance at the edge as compared with the full patch.

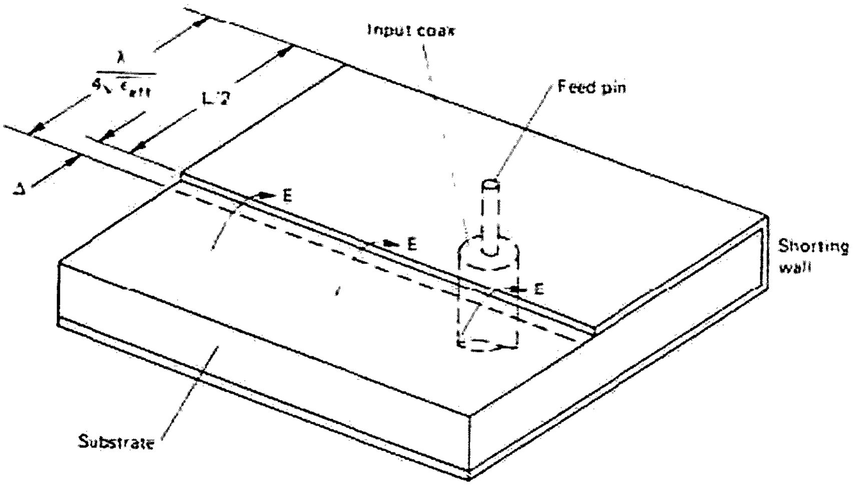

Figure 5-8 Half-patch antenna.

It becomes difficult to feed the antenna from microstrip because the required quarter-wavelength transformer has a higher impedance with narrower lines. We can increase the edge width to reduce the edge input resistance, but the antenna is usually fed from underneath. Equation (5-9) gives the approximate feed location measured from the short circuit. The resonant frequency shifts slightly as the feed point moves. While an impedance match is tuned for, the length of the cavity will have to be adjusted to maintain the desired resonant frequency.

The half- and full-patch antennas have the same Q. The half-patch antenna has half the radiation conductance but only half the stored energy of the full-patch antenna. We can use Tables 5-1, 5-2, and 5-3 for the bandwidths.

Example Design a half-patch antenna at 5 GHz on a 0.8-mm-thick substrate ($\epsilon_r = 2.21$) with a radiating width of 0.75λ.

The edge width is 0.75(300 mm)/5 = 45 mm. By using Eq. (5-5), we find the effective dielectric constant in the cavity: $\epsilon_{\text{eff}} = 2.16$. Equation (5-4) gives us the cutback for fringing fields: $\Delta = 0.42$ mm. The resonant length becomes

$$\frac{L}{2} = \frac{\lambda}{4\sqrt{\epsilon_{\text{eff}}}} - \Delta = 10.20 - 0.42 = 9.78 \text{ mm}$$

The radiation conductance from the single edge is [Eq. (5-6)]

$$G = \frac{45}{120(60)} = 6.25 \text{ mS} \qquad \text{or} \qquad R = 160\ \Omega$$

The 50-Ω feed point is found from Eq. (5-9):

$$x = \frac{19.56}{\pi} \sin^{-1}\left(\frac{50}{160}\right)^{1/2} = 3.69 \text{ mm}$$

where x is the distance from the short.

The short circuit of the antenna is quite critical. The low impedance of the microstrip cavity raises the currents in the short circuit. Without a good low-impedance short, the antenna will detune and have spurious radiation. If the antenna is made from a machined cavity, careful attention must be paid to the junction between the top plate and the cavity to assure good electrical contact.

If we close off the nonradiating edges with metal walls, the walls convert the parallel-plate line into a waveguide. We use the waveguide propagation constant to calculate the quarter-wavelength cavity depth. The slot fields vanish on the ends and establish a sinusoidal slot distribution. We can offset the feed both toward the back wall and the sidewall to reduce the input impedance. The peak voltage (minimum current and peak resistance) occurs at the slot center.

The spiral-slot antenna [20, 21] is an interesting variation of the half-patch antenna. The antenna (Fig. 5-9) is a half-patch one wrapped in a spiral about

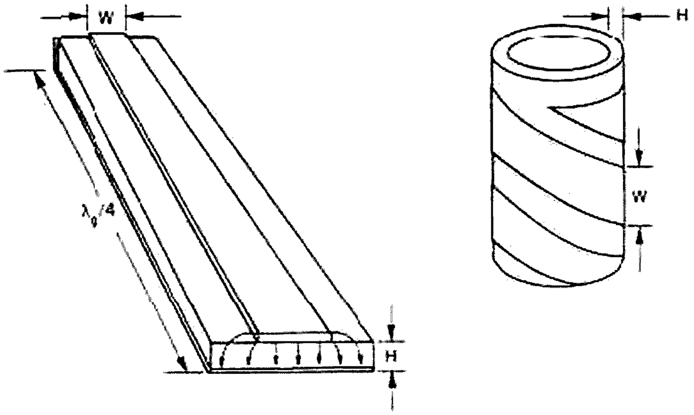

(a) (b)

Figure 5-9 Spiral-slot antenna. (Source: A. D. Krall et al., "The Omni Microstrip Antenna," *IEEE Trans. Antennas Propagat.*, vol. AP-27, no. 6, November 1979, p. 850.)

a small-diameter missile. We find its resonant frequency from the straight conductor. A shunt feed, like the half patch, excites the strip from underneath at the desired feed impedance level. Wrapped around the missile, the antenna gives a good omnidirectional pattern.

5-10 Microstrip Dipole [22]

As the width W of a patch narrows, the input impedance increases. When the width approaches that of a microstrip feed line, either the patch fails to be a resonator or the feed line becomes very narrow in trying to transform the impedance. The microstrip dipole solves these problems by having a coupled line feeder. The dipole is a half-wavelength strip whose width equals that of a microstrip feed line.

A line etched on a substrate below the dipole couples energy into the strip (Fig. 5-10*a*). The equivalent circuit (Fig. 5-10*b*) transforms the high impedance of the dipole through the unequal coupled lines. By varying the coupling, we can change the input impedance at resonance. Best results occur for quarter-wavelength overlap where the equivalent stubs (Fig. 5-10*b*) do not contribute reactance. We vary the coupling by changing the thickness of the substrate between the strips or by offsetting the lower strip.

The dipole radiates as a narrow patch and not as a dipole. No pattern nulls appear along the axis of the strip, but they occur more strongly in the direction of the equivalent magnetic currents of the edges. The H-plane pattern becomes quite broad for the narrow strip width.

The feed distribution circuit is etched on the substrate below the dipoles. With the feed circuit on a separate level, we have greater freedom in the feed network design to excite desired distributions. Also , because the dipoles are

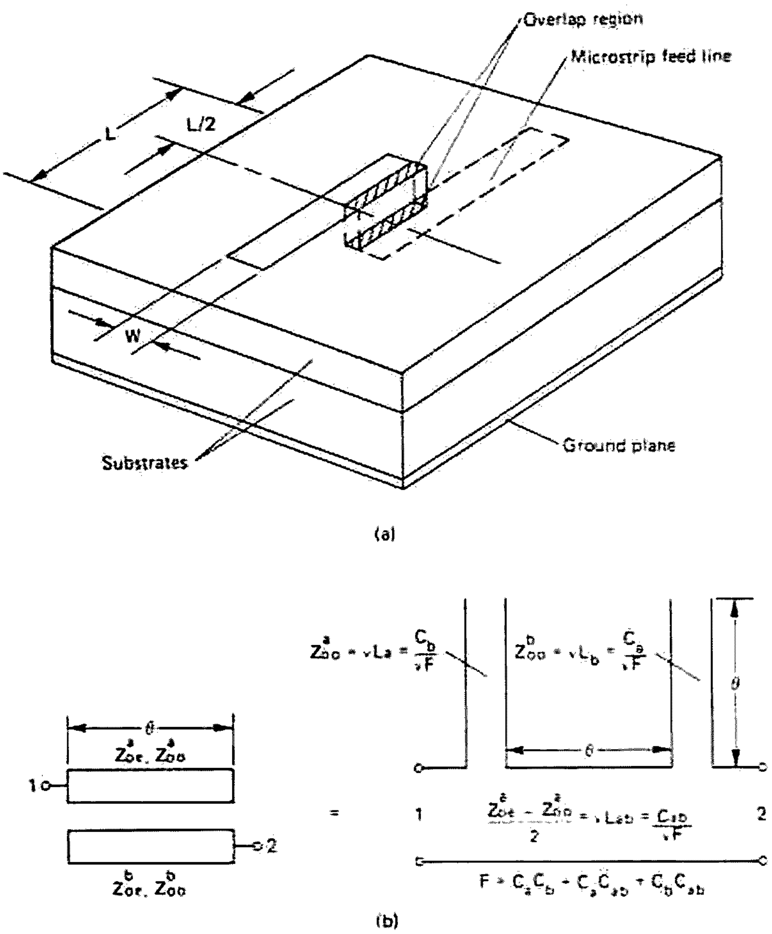
Overlap region
Microstrip feed line
L
L/2
W
Substrates
Ground plane
(a)
$Z_{0o}^{a} = vL_a = \frac{C_b}{vF}$
$Z_{0o}^{b} = vL_b = \frac{C_a}{vF}$
θ
θ
θ
Z_{0e}^{a}, Z_{0o}^{a}
1
2
Z_{0e}^{b}, Z_{0o}^{b}
=
1
$\frac{Z_{0e}^{a} - Z_{0o}^{a}}{2} = vL_{ab} = \frac{C_{ab}}{vF}$
2
$F = C_aC_b + C_aC_{ab} + C_bC_{ab}$
(b)

Figure 5-10 Microstrip dipole and equivalent circuit of coupling. (Source, (*b*): G. L. Matthaei et al., *Microwave Filters, Impedance Matching Networks, and Coupling Structures*, Artech House, Dedham, Mass., 1980, p. 226. Used by permission.)

small, we can use density tapering of the dipoles to that end. Proper design requires sets of measurements [23] to obtain the desired effect, since mutual coupling will change the distribution by changing the active impedance of each dipole. The feed network must compensate for the coupling.

5-11 Microstrip Franklin Array [24]

An electrically long line with a standing wave on it fails to radiate on broadside because the many cycles cancel each other. We obtain a pattern with many nulls and lobes. By folding the lines with out-of-phase standing wave currents close together, we can prevent their radiation. The other portions are free to radiate (Fig. 5-11*a*). The Franklin array consists of straight sections $\lambda/2$ long connected by $\lambda/4$ shorted stubs. The standing wave currents on the straight portions add in phase.

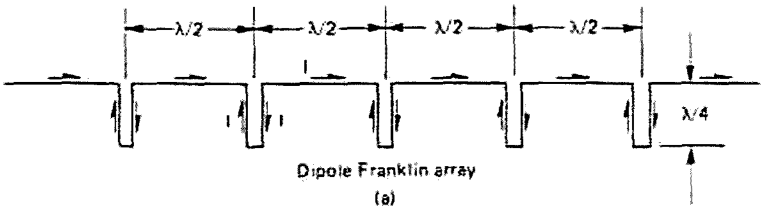

Dipole Franklin array
(a)

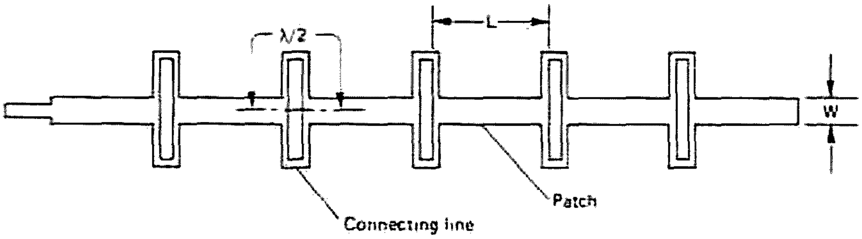

(b)

Figure 5-11 (*a*) Dipole and (*b*) microstrip Franklin arrays.

We can construct a microstrip version (Fig. 5-11*b*). Half-wavelength lines act as radiators (patches). We connect them with half-wavelength lines folded into stubs so the counteracting standing wave currents do not radiate. The straight lines are narrow patches. The total radiation conductance of each strip is

$$G = \frac{1}{45}\left(\frac{W}{\lambda}\right)^2 \tag{5-29}$$

for narrow stripwidths W, where λ is the free-space wavelength.

Using lines for the stubs whose impedance is twice the radiating strip impedance reduces unwanted internal reflections. The two stubs add in shunt. Since the antenna is quite narrow-band and the length of the lines between patches is a half wavelength long, the impedance of these connecting arms has a secondary effect.

Example Design an eight-wavelength array at 10 GHz. There are 16 patches in the array. The radiation conductances add for elements spaced at $\lambda/2$ intervals. For a 100-Ω input, each patch supplies a conductance 0.01/16.

We solve Eq. (5-29) for the width:

$$W = \left[\frac{.01(45)}{16}\right]^{1/2}\lambda = 0.168\lambda$$

If we use Eq. (5-27) from the series patch, we obtain $W = 0.157\lambda$, which is within the range of the empirical formula. For 10 GHz, $W = 4.71$ mm. On an 0.8-mm substrate ($\epsilon_r = 2.21$), $W/H = 5.89$. We use Eq. (5-16) to find the impedance of the strip radiator: $Z_0 = 44.01\ \Omega$. We need to find the effective dielectric constant of the strip to find the length of the patch and the impedance. From Eq. (5-5), $\epsilon_{\text{eff}} = 1.97$.

We calculate the cutback from each end by using Eq. (5-4): $\Delta = 0.40$ mm. Each radiating strip is

$$L = \frac{300 \times 10^9}{10^{10}(2)(1.97)^{1/2}} - 2(0.40) = 9.88 \text{ mm}$$

The radiating strip impedance is $Z_0/\epsilon_{\text{eff}}^{1/2} = 31.3\ \Omega$. We need 62.6-Ω connecting lines in the stubs to achieve the broadest bandwidth. With so few radiators, we could use 100-Ω connecting arms with little change in bandwidth and have more reasonable connecting arm widths: 0.71 mm (Table 5-5).

The example shows that the microstrip Franklin array works best for high frequencies or long arrays. The elements are narrow, and the interconnecting arms are thin.

5-12 Microstrip Antenna Mechanical Properties

The microstrip patch antenna has very desirable mechanical properties. It can withstand tremendous shock and vibration. Because the antenna is on a solid substrate, the patch cannot flex and small changes in the substrate thickness have only a minor effect on the resonant frequency. The commonly used soft substrate (Teflon and fiberglass) has a good damped resilience. Microstrip patch antennas have been used to telemeter data from artillery shells and high-velocity rockets which have high shock and vibration levels. The repeatability of the dimensions of the patches depends only on the etcher's art. Complicated shapes and feed networks are produced as cheaply as simple ones.

The antennas can withstand exposure to high temperatures when covered by a radome made of the same soft dielectric as the substrate. The cover protects the metal patches, but has only a minor effect on the resonant frequency [25]. High temperatures on the surface of the radome or ablation fail to change the resonance by any significant amount because the radome itself has only a minor effect.

The variation of the dielectric constant of the substrate from lot to lot causes problems with repeatability. The narrowband antennas require measurement of the dielectric constant of each lot, and sometimes of each sheet, to get the desired center frequency. A series of etching masks can be made to cover the expected range. The antennas can be tuned with inductive shorting pins or capacitive screws, but tuning is prohibitive when the number of elements in an array is large. Careful quality control of the dielectric constant is the answer. Close monitoring of the etching process also may be needed to prevent excessive undercutting.

Temperature variations can be a problem with thin substrates when the bandwidth is narrow. The patch and substrate size grow when the temperature rises, but they are overshadowed by the change in dielectric constant of soft substrates. Instead of decreasing the resonant frequency because of the increased patch size, a lowered dielectric constant raises the center frequency.

Whenever we need more bandwidth than a microstrip patch can provide, we must turn to cavity antennas. We increase the antenna volume by penetrating the vehicle for the cavity, but we gain a new freedom of design.

5-13 Shallow-Cavity Crossed-Slot Antenna

We can feed the slot in Fig. 5-1 by exciting the cavity in an odd mode from two points on opposite sides of the slot. To be able to excite both polarizations, we divide the slot in two and rotate the two parts in opposite directions by 45° to form a cross. We square the cavity to maintain symmetry, and we can replace the shorting pins with solid walls (Fig. 5-12*c*). Since we feed across the diagonal between the crossed slots, we excite both slots. The sum of the fields radiated from the two slots is polarized in the direction of the diagonal. We increase the radiation conduction by lengthening the crossed slots to the maximum which lowers the Q (increased bandwidth). The cavity compensates for the slot susceptance to obtain resonance.

A crossed-slot antenna was built [26] with the following dimensions:

Cavity edge	0.65λ
Cavity thickness	0.08λ
Slot length	0.915λ

The measured 2:1 VSWR bandwidth was 20.8 percent. The bandwidth exceeded that of a microstrip patch of the same thickness by about $\sqrt{2}$. Lindberg [27] found that the resonant length of the slot depends on the cavity thickness and requires some experimental adjustment.

King and Wong [26] added ridges (Fig. 5-12*b*) to increase the bandwidth. Antennas with ridges need a larger cavity width and a longer slot than the unridged design. The ridges can be stepped as shown to increase the bandwidth. Adding ridges gives us extra parameters to adjust for best input match performance. The following design with uniform ridges gives us a 58.7 percent 2.5:1 VSWR bandwidth with a double resonance curve.

Cavity edge	0.924λ	Slot width, W_2	0.058λ
Slot length	1.3λ	Ridge height	0.076λ
Ridge width	0.087λ	Feed width, W_1	0.144λ
Cavity thickness	0.115λ		

Both the ridge and slot shapes can be varied to improve the performance. As fed in Fig. 5-12*c*, the antenna radiates circular polarization on boresight. Near the horizon (90° from boresight), the polarization reduces to linear as we enter the null of one of the slots.

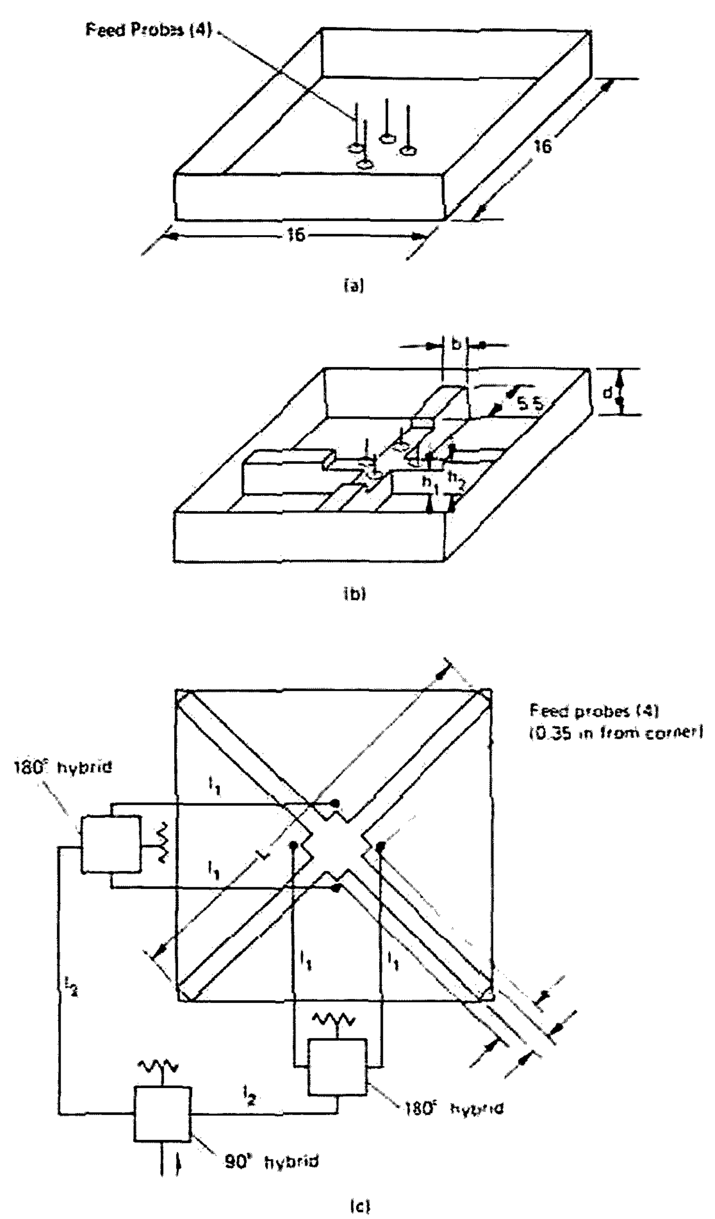

Figure 5-12 Shallow-cavity crossed-slot antenna: (*a*) cavity without ridge; (*b*) cavity with ridge; (*c*) typical slot configuration. All dimensions are in inches. (Source: H. E. King and J. L. Wong, "A Shallow Ridged-Cavity Crossed-Slot Antenna for the 240- to 400-MHz Frequency Range," *IEEE Trans. Antennas Propagat.*, vol. AP-23, no. 5, September 1975, p. 688. © 1975 IEEE.)

5-14 T-Bar-Fed Slot Antenna

The T-bar antenna (Fig. 5-13) looks more like an open-circuited waveguide to coax transition than a slot. Its pattern, like a slot, is very broad. The antenna has been designed experimentally [28] and still provides a good starting point. The following table lists two designs [28] referred to Fig. 5-13.

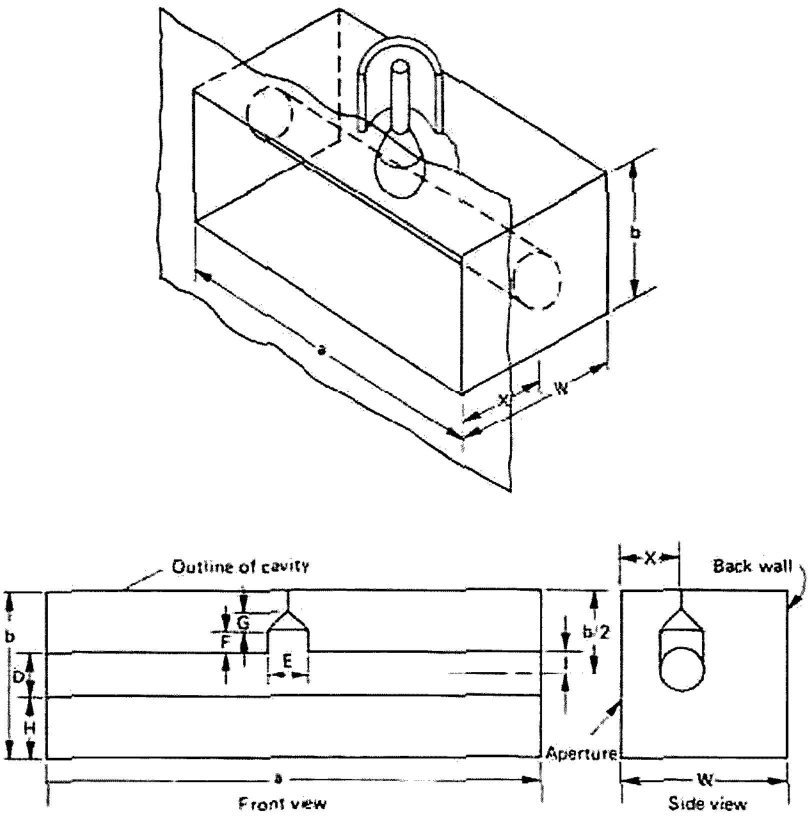

Figure 5-13 T-bar-fed cavity-slot antenna. (Source: E. H. Newman and G. A. Thiele, "Some Important Parameters in the Design of T-Bar-Fed Slot Antennas," *IEEE Trans. Antennas Propagat.*, vol. AP-23, no. 1, January 1975, p. 97. © 1975 IEEE.)

Dimensions	*Antenna* 1	*Antenna* 2
b/a	0.323	0.226
W/a	0.323	0.295
x/a	0.118	0.113
D/a	0.118	0.090
I/a	0.059	0.045
E/a	0.118	0.090
F/a	0.057	0.045

The aperture admittance is a combination of the radiation admittance and a capacitive susceptance. Behind the feed point, the length of short circuited waveguide adds an inductive susceptance that grows as frequency decreases. The horizontal bar produces a capacitive susceptance at the input to counteract the back-wall susceptance. These susceptances track with frequency changes; each one decreases to maintain the sum near resonance.

More recent experimental work [29] has revealed further properties of the antenna. Measurements on antenna 1 show that the lower-end 2:1 VSWR banded edge occurs when $a = 0.57\lambda$ and the upper end when

$a = 0.9\lambda$. The bandwidth is about 1.6:1. Antenna 2 was reported [28] as having less bandwidth than antenna 1. When the round rod was replaced with a flat strip, whose width across the guide was the same as the diameter of the rod, almost identical results were obtained. We have a choice. The flat strip is an easier construction, but the round rod gives better mechanical support in all axes to withstand shock and vibration.

The flat strip adds to the freedom of design. The bandwidth potential increases when H is decreased while I is held constant. Newman and Thiele [29] found that, when H was decreased, the nominal impedance level was raised. When the input impedance is plotted on the Smith chart, the locus is centered about a higher resistance. By adding a broadband impedance transformer on the input, we can achieve the higher bandwidth potential. Newman and Thiele achieved a nearly 2:1 VSWR bandwidth from $a = 0.52\lambda$ to $a = 1.12\lambda$, or 2.3:1 bandwidth.

5-15 Cavity-Mounted Dipole Antenna

A dipole can be placed in a cup, and the assembly can be flush-mounted in a ground plane. The antenna shown in Fig. 5-14 has disks above and below to stretch the bandwidth over a 1.8:1 range [30] by making the turnstile a sleeve antenna. The following are the dimensions referred to the dipole length.

$$\frac{D}{L} = 2.57 \qquad \frac{H}{L} = 0.070$$

$$\frac{T}{L} = 0.68 \qquad \frac{G}{L} = 0.40$$

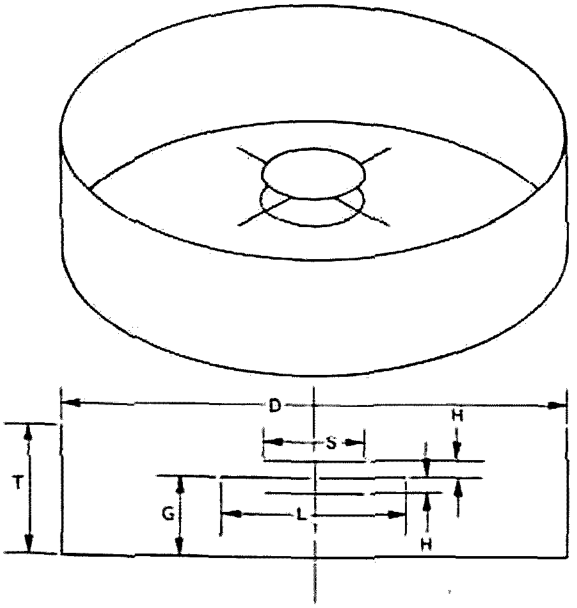

Figure 5-14 Cavity-mounted sleeve dipole antenna.

$$\frac{S}{L} = 0.505$$

The operating range is $0.416\lambda \leq L \leq 0.74\lambda$.

The antenna cavity ranges from 0.28λ to 0.50λ deep and can no longer be considered thin. The cup antenna has a nearly constant gain (±0.5 dB) of 10.5 dB over the band. Mounting the antenna in a cavity opens up new possibilities, because extra parameters are added to the design.

REFERENCES

1. R. F. Harrington, "Effects of Antenna Size on Gain, Bandwidth, and Efficiency," *J. Res. NBS, D, Radio Propagation*, vol. 64D, January–February 1960, pp. 1–12.
2. R. C. Hansen, "Fundamental Limitations in Antennas," *Proc. IEEE*, vol. 69, no. 2, February 1981, pp. 169–173.
3. A. A. Oliner, "Equivalent Circuits for Discontinuities in Balanced Strip Transmission Line," *IRE Trans. Microwave Theory and Tech.*, vol. MTT-3, March 1955, pp. 134–143.
4. J. S. Rao and B. N. Ras, "Impedance of Off-centered Stripline Fed Series Slot," *IEEE Trans. Antennas Propagat.*, vol. AP-26, no. 6, November 1978, pp. 893,894.
5. J. Van Bladel, "Small Hole in Waveguide Wall," *Proc. IEE*, vol. 118, January 1971, pp. 43–50.
6. Pyong K. Park and R. S. Elliott, "Design of Collinear Longitudinal Slot Arrays Fed by Boxed Stripline," *IEEE Trans. Antennas Propagat.*, vol. AP-29, no. 1, January 1981, pp. 135–140.
7. Y. T. Lo et al., "Study of Microstrip Antenna Elements, Arrays, Feeds, Losses, and Applications," *Final Rep.*, RADC-TR-81-98, Rome Air Development Center, June 1981.
8. K. R. Carver and E. L. Coffey, "Theoretical Investigation of the Microstrip Antenna," *Tech. Rep. PT-00929*, Physical Science Lab., New Mexico State University, January, 1979.
9. R. E. Munson, "Conformal Microstrip Antennas and Microstrip Phased Arrays," *IEEE Trans. Antennas Propagat.*, vol. AP-22, January 1974, pp. 74–78.
10. E. O. Hammerstad, "Equations for Microstrip Circuit Design," *Proc. 5th European Microstrip Conf.*, Hamburg, September 1975, pp. 268–272.
11. M. V. Schneider, "Microstrip Lines for Microwave Integrated Circuits," *Bell System Tech. J.*, vol. 48, May–June 1969, pp. 1421–1444.
12. R. F. Harrington, *Time-Harmonic Electromagnetic Fields*, McGraw-Hill, New York, 1961, p. 183.
13. A. G. Derneryd and A. G. Lind, "Extended Analysis of Rectangular Microstrip Resonator Antennas," *IEEE Trans. Antennas Propagat.*, vol. AP-27, no. 6, November 1979, pp. 846–849.
14. L. C. Shen et al., "Resonant Frequency of a Circular Disk, Printed Circuit Antenna," *IEEE Trans. Antennas Propagat.*, vol. AP-25, no. 4, July 1977, pp. 595, 596.
15. I. J. Bahl and P. Bhartia, *Microstrip Antennas*, Artech House, Dedham, Mass., 1980, p. 119.
16. A. G. Derneryd, "Analysis of the Microstrip Disk Antenna Element," *IEEE Trans. Antennas Propagat.*, vol. AP-27, no. 5, September 1979, pp. 660–664.
17. J. L. Kerr, "Microstrip Antenna Developments," *Proc. Workshop on Printed Circuit Antennas*, New Mexico State University, October 1979, pp. 3.1–3.20.
18. T. Metzler, "Microstrip Series Arrays," *Proc. Workshop on Printed Circuit Antennas*, New Mexico State University, October 1979, pp. 20.1–20.16.
19. B. B. Jones, F. V. M. Chow, and A. W. Seeto, "The Synthesis of Shaped Patterns with Series-Fed Microstrip Patch Arrays," *IEEE Trans. Antennas Propagat.*, vol. AP-30, no. 6, November 1982, pp. 1206–1212.

20. D. H. Schaubert and F. G. Farrar, "Some Conformal, Printed Circuit Antenna Designs," *Proc. Workshop on Printed Circuit Antennas*, New Mexico State University, October 1979, pp. 5.1–5.21.
21. A. D. Krall et al., "The Omni Microstrip Antenna: A New Small Antenna," *IEEE Trans. Antennas Propagat.*, vol. AP-27, no. 6, November 1979, pp. 850–853.
22. D. A. Hueber, "An Electrically Small Dipole Planar Array," *Proc. Workshop on Printed Circuit Antennas*, New Mexico State University, October 1979, pp. 17.1–17.16.
23. R. S. Elliott and G. J. Stern, "The Design of Microstrip Dipole Arrays Including Mutual Coupling," Parts I and II, *IEEE Trans. Antennas Propagat.*, vol. AP-29, no. 5, September 1981, pp. 757–765.
24. K. Solbach, "Microstrip-Franklin Antenna," *IEEE Trans. Antennas Propagat.*, vol. AP-30, no. 4, July 1982, pp. 773–775.
25. I. J. Bahl et al., "Design of Microstrip Antennas Covered with a Dielectric Layer," *IEEE Trans. Antennas Propagat.*, vol. AP-30, no. 2, March 1982, pp. 314–318.
26. H. E. King and J. L. Wong, "A Shallow Ridged-Cavity Cross-Slot Antenna for the 240- to 400-MHz Frequency Range," *IEEE Trans. Antennas Propagat.*, vol. AP-23, no. 5, September 1975, pp. 687–689.
27. C. A. Lindberg, "A Shallow-Cavity UHF Crossed-Slot Antenna," *IEEE Trans. Antennas Propagat.*, vol. AP-17, September 1969, pp. 558–563.
28. A. Dorne and D. Lazarno, Radio Research Laboratory Staff, *Very High Frequency Techniques*, McGraw-Hill, New York, 1947, pp. 184–190.
29. E. H. Newman and G. A. Thiele, "Some Important Parameters in the Design of T-Bar Fed Slot Antennas," *IEEE Trans. Antennas Propagat.*, vol. AP-23, no. 1, January 1975, pp. 97–100.
30. J. L. Wong and H. E. King, "A Cavity-Backed Dipole Antenna with Wide Bandwidth Characteristics," *IEEE Trans. Antennas Propagat.*, vol. AP-21, no. 5, September 1973, pp. 725–727.

CHAPTER

6

RADIATION FROM APERTURES

Many antennas that are large in wavelengths can be analyzed with a common-aperture theory. The method gives only approximate answers or results that are valid over only part of the pattern, but simplicity is its greatest virtue. We will analyze a variety of antennas, such as horns and reflectors, with the method. Usually, we can separate out polarization effects and reduce the work to a scalar problem.

6-1 Fourier Transform in *k* Space

We can find the far-field radiation pattern for various distributions by a Fourier transform relation. A planar aperture requires a two-dimensional transform that separates into one-dimensional transforms when the distribution involves a product each factor of which is a function of only one coordinate.

We draw on our familiarity with signal processing to help us visualize the relations between aperture distributions and patterns. Large apertures give small beamwidths, just as long time pulses relate to low frequencies in normal time-frequency transforms. The sidelobes of the pattern correspond to the frequency harmonics of an equivalent time waveform under the Fourier transform. Rapid transitions in the time response lead to high levels of harmonics in the frequency domain. Rapid amplitude transitions in the aperture plane give high sidelobes (harmonics) in the far-field response (Fourier transform).

Given the fields in an aperture, we can equate them to magnetic and electric currents

$$\mathbf{M}_s = \mathbf{E}_a \times \mathbf{n} \qquad \mathbf{J}_s = \mathbf{n} \times \mathbf{H}_a \tag{6-1}$$

where $\mathbf{E}_a$ and $\mathbf{H}_a$ are the aperture fields and n is the outward normal. The equivalence theorem [1] results in exact solutions, and the induction theorem results in approximate solutions. By using the equivalence theorem, we replace the total fields present with equivalent currents. The induction theorem equates currents only to the fields incident on the aperture.

We find the radiated fields from each distribution of currents by using vector potentials:

$$\mathbf{F} = \iint_s \frac{\mathbf{M}_s e^{-jk|\mathbf{r}-\mathbf{r}'|}}{4\pi|\mathbf{r} - \mathbf{r}'|}\, ds' \qquad \mathbf{A} = \iint_s \frac{\mathbf{J}_s e^{-jk|\mathbf{r}-\mathbf{r}'|}}{4\pi|\mathbf{r} - \mathbf{r}'|}\, ds' \tag{6-2}$$

where r is the field point and r′ is the source point in the aperture. These expressions are valid in the near and far fields. By integrating over only a finite aperture, we assume that the fields are zero outside. Rigorous expressions require integrals over closed boundaries. A planar aperture must extend to infinity, but the fields outside the aperture are nearly zero and contribute little.

Fresnel and Fraunhofer Regions The Fresnel and Fraunhofer regions are characterized by the approximations made to the integrals [Eq. (6-2)]. The Fresnel region lies between the near field, with no approximations, and the far-field, Fraunhofer region. In both approximations the field (observation) distance r is substituted for $|\mathbf{r} - \mathbf{r}'|$ in the amplitude term. The vector potentials reduce to

$$\mathbf{F} = \frac{1}{4\pi r} \iint_s \mathbf{M}_s e^{-jk|\mathbf{r}-\mathbf{r}'|}\, ds' \qquad \mathbf{A} = \frac{1}{4\pi r} \iint_s \mathbf{J}_s e^{-jk|\mathbf{r}-\mathbf{r}'|}\, ds' \tag{6-3}$$

We handle the phase term differently in the two regions. Expand the phase term in a Taylor series

$$|\mathbf{r} - \mathbf{r}'| = (r^2 + r'^2 - 2\mathbf{r} \cdot \mathbf{r}')^{1/2}$$

$$= r - \mathbf{a}_r \cdot \mathbf{r}' + \frac{1}{2r}[r'^2 - (\mathbf{a}_r \cdot \mathbf{r}')^2] + \cdots$$

where $\mathbf{a}_r$ is the unit vector in the field point direction. We retain the first two terms for the Fraunhofer, far-field, approximation. The vector potentials become

$$\mathbf{F} = \frac{e^{-jkr}}{4\pi r} \iint_s \mathbf{M}_s e^{j\mathbf{k}\cdot\mathbf{r}'}\, ds', \qquad \text{etc.} \tag{6-4}$$

where we have combined k, the propagation constant, with the unit vector $\mathbf{a}_r$.

$$\mathbf{k} = k\mathbf{a}_r = k(\sin\theta\cos\phi\,\mathbf{a}_x + \sin\theta\sin\phi\,\mathbf{a}_y + \cos\theta\,\mathbf{a}_z)$$

The magnetic vector potential integral parallels Eq. (6-4) as in Eq. (6-3).

In the Fresnel zone approximation the terms in r'^2 are retained and the following integral for the electric vector potential is obtained:

$$\mathbf{F} = \frac{e^{-jkr}}{4\pi r} \iint_s \mathbf{M}_s \exp\left[j\left(\mathbf{k}\cdot\mathbf{r}' + \frac{(\mathbf{k}\cdot\mathbf{r}')^2}{2rk} - \frac{kr'^2}{2r}\right)\right] ds' \tag{6-5}$$

No clear boundary between the three regions exists. Common boundaries are

$$\frac{r}{L'} < 1 \qquad \text{near field}$$

$$1 < \frac{r}{L'} < \frac{L'}{\lambda} \qquad \text{Fresnel}$$

$$\frac{r}{L'} > \frac{L'}{\lambda} \quad \text{or} \quad \frac{2L'}{\lambda} \qquad \text{Fraunhofer}$$

where L' is the maximum dimension on the aperture.

Example Find the maximum difference between the Fresnel and Fraunhofer approximations at a point normal to the maximum aperture dimension and at $r = L^2/\lambda$ and $r = 2L^2/\lambda$.

Normal to the maximum dimension, $\mathbf{a}_r \cdot \mathbf{r}' = 0$. The phase difference is

$$\frac{kr'^2_{\max}}{2r} \qquad \text{where } r'_{\max} = \frac{L}{2}$$

$$\text{Phase difference } \phi = \frac{2\pi L^2}{8\lambda r}$$

$$\phi = \pi/4 \quad \text{at} \quad r = L^2/\lambda, \quad \text{and} \quad \phi = \pi/8 \quad \text{at} \quad r = 2L^2/\lambda$$

The usual minimum distance used for antenna patterns is $2L^2/\lambda$, where L is the maximum dimension of the antenna. At that distance, the phase error across the aperture from a point source antenna is $\pi/8$. The distance is not sufficient for low-sidelobe antennas [2] because the quadratic phase error raises the measured sidelobes.

We can use vector potentials in the aperture after finding equivalent currents, but we will find it more convenient to use the fields directly. Define the following integrals

$$\mathbf{f} = \iint_s \mathbf{E}_a e^{j\mathbf{k}\cdot\mathbf{r}'}\,ds' \qquad \mathbf{g} = \iint_s \mathbf{H}_a e^{j\mathbf{k}\cdot\mathbf{r}'}\,ds' \tag{6-6}$$

by using the Fraunhofer approximation. Fresnel or near-field integrals require additional phase terms. Given an aperture, we find the vector potentials in terms of $\mathbf{E}_a$ and $\mathbf{H}_a$ through the currents by using either the equivalence or inductance theorems, and we use the integrals of Eq. (6-6) in the vector potentials. We combine the fields in the far field due to each partial source

$$\mathbf{E} = -j\omega\mu\mathbf{A} - j\eta\omega\varepsilon\mathbf{F} \times \mathbf{a}_r$$

For an aperture in the xy plane, we can carry out these steps by using the inductance theorem and obtain the following far fields from the incident aperture fields

$$E_\theta = \frac{jke^{-jkr}}{4\pi r}[f_x \cos\phi + f_y \sin\phi + \eta\cos\theta\,(-g_x \sin\phi + g_y \cos\phi)]$$

$$\begin{aligned} E_\phi = \frac{-jke^{-jkr}}{4\pi r}&[(f_x \sin\phi - f_y \cos\phi)\cos\theta \\ &+ \eta\,(g_x \cos\phi + g_y \sin\phi)] \end{aligned} \tag{6-7}$$

where $\mathbf{f}$ and $\mathbf{g}$ have been expanded in terms of their x and y components and η is the impedance of free space.

Huygens Source The Huygens source approximation is based on the assumption that the magnetic and electric fields are related as in a plane wave in the aperture. That is,

$$\eta g_y = f_x \qquad \text{and} \qquad -\eta g_x = f_y$$

since

$$\eta H_y = E_x \qquad \text{and} \qquad -\eta H_x = E_y \quad \text{in the aperture.}$$

With this approximation, the far field [Eq. (6-7)] becomes

$$\begin{aligned} E_\theta &= \frac{jke^{-jkr}}{4\pi r}(1 + \cos\theta)(f_x \cos\phi + f_y \sin\phi) \\ E_\phi &= \frac{-jke^{-jkr}}{4\pi r}(1 + \cos\theta)(f_x \sin\phi - f_y \cos\phi) \end{aligned} \tag{6-8}$$

The two-dimensional vector Fourier transform $\mathbf{f} = (f_x, f_y)$ of the aperture electric field in the xy plane determines the far-field components. We find the radiated components by projecting (vector scalar product) this field onto the vectors $\mathbf{a}_\theta/\cos\theta$ and $\mathbf{a}_\phi$. The transform $\mathbf{f}$ expands the field in $\mathbf{k}$ space [usually (k_x, k_y)]. This normalizes the pattern and removes the direct dependence on the aperture length.

We will separate out all but $\mathbf{f}$ when we consider aperture distributions. We drop the terms for the radiation from a point source and the pattern of a Huygens point source [Eq. (2-8)]. We will limit our discussions to Huygens sources and far fields. General aperture fields require Eq. (6-7). For any region other than the far field, additional phase terms are needed in the transforms [Eq. 6-6)].

Scanned Aperture We can consider an aperture as a continuous array. To scan in a given direction, we add phase shift depending on the element location

$$e^{-j\mathbf{k}_0\cdot\mathbf{r}'} \tag{3-9}$$

where

$$\mathbf{k}_0 = \frac{2\pi}{\lambda}(\sin\theta_0\cos\phi_0\,\mathbf{a}_x + \sin\theta_0\sin\phi_0\,\mathbf{a}_y + \cos\theta_0\,\mathbf{a}_z)$$

is the vector propagation constant in the direction of the beam (θ_0, ϕ_0) and $\mathbf{r}'$ is the position vector in the aperture. Equation (3-9) reduces to a linear phase distribution for a given direction and multiplies the integrals of Eq. (6-6).

Scanning the beam reduces the effective area of the aperture. The beamwidth of the scanned aperture broadens as the linear dimension in the plane of scan reduces by $\cos\theta_0$ for an aperture in the xy plane. Suppose we have a linear aperture along the x axis scanned to θ_0; then Eq. (6-6) becomes

$$\mathbf{f}(k_x) = \int \mathbf{E}_a(x)e^{jkx(\sin\theta-\sin\theta_0)}\,dx \tag{6-9}$$

Equation 6-9 shows that we replace $e^{j\mathbf{k}\cdot\mathbf{r}'}$ in Eq. (6-6) with $e^{j(\mathbf{k}-\mathbf{k}_0)\cdot\mathbf{r}'}$ to analyze the general scanned aperture pattern.

Example Find the position phase function to scan an aperture in the xy plane to $(\theta = 30°, \phi = 60°)$, where $\phi = 0$ corresponds to the x axis.

$$\mathbf{k}_0 = \frac{2\pi}{\lambda}(\sin 30°\cos 60°\,\mathbf{a}_x + \sin 30°\sin 60°\,\mathbf{a}_y)$$

$$= \frac{360°}{\lambda}\left(\frac{\mathbf{a}_x}{4} + \frac{\sqrt{3}\mathbf{a}_y}{4}\right)$$

The phase shift at point (x_0, y_0) is $-\mathbf{k}_0\cdot\mathbf{r}'$, or

$$\frac{-90°}{\lambda}(\mathbf{a}_x + \sqrt{3}\,\mathbf{a}_y)\cdot(x_0\mathbf{a}_x + y_0\mathbf{a}_y) = \frac{-90°}{\lambda}(x_0 + \sqrt{3}\,y_0)$$

6-2 Amplitude Taper and Phase Error Efficiencies

When we use the Huygens source approximation, we can find the power radiated by summing (integrating) the magnitude squared of the electric field in the aperture and dividing by the impedance of free space. The average radiation intensity is the radiated power divided by the area of a unit sphere, 4π. We find the maximum radiation intensity by dividing the maximum of the magnitude squared of Eq. (6-8) by the impedance of free space. Directivity ($U_{\max}/U_{\text{avg}}$) becomes

$$\frac{\pi(1+\cos\theta)^2}{\lambda^2}\,\frac{\left|\iint_s Ee^{jk\cdot r'}\,ds'\right|^2_{\max}}{\iint_s |E|^2\,ds'} \tag{2-12}$$

Equation (2-12) is the directivity for a point other than the maximum of the numerator integral as well.

An aperture with a uniform amplitude and phase distribution has a directivity $4\pi A/\lambda^2$, where A is the area. We would like to separate the loss in directivity due to aperture field amplitude and phase variations. We express the general aperture directivity as

$$\text{Directivity} = \frac{4\pi A}{\lambda^2}\,\text{ATL PEL}$$

where ATL is the amplitude taper efficiency (loss) and PEL is the phase error efficiency (loss). Only amplitude variations contribute to ATL, and only phase variations cause PEL.

Assume a uniform phase distribution in the aperture. The beam peak occurs normal to the aperture ($\theta = 0°$), and PEL = 1. We obtain uniform phase fields by using only $|E|$ in Eq. (2-12)

$$\text{Directivity} = \frac{4\pi}{\lambda^2}\,\frac{\left(\iint_s |E|\,ds\right)^2}{\iint_s |E|^2\,ds} = \frac{4\pi A}{\lambda^2}\,\text{ATL}$$

where $k_x = k_y = 0$ on boresight ($\theta = 0°$). On solving for ATL, we find

$$\text{ATL} = \frac{\left(\iint_s |E|\,ds\right)^2}{A\iint_s |E|^2\,ds} \tag{6-10}$$

We have forced the phase to zero everywhere in the aperture to separate out the amplitude taper effects. We account for nonuniform phase with PEL.

The phase error efficiency can be found from

$$\mathrm{PEL}(\theta,\phi)=\frac{\mathrm{directivity}(\theta,\phi)}{(4\pi A/\lambda^2)\ \mathrm{ATL}}$$

where we use directivity (θ, ϕ) and $\mathrm{PEL}(\theta, \phi)$ depends on the pattern point (θ, ϕ).

$$\mathrm{PEL}(\theta,\phi)=\frac{(1+\cos\theta)^2}{4}\,\frac{\left|\iint_s Ee^{j\mathbf{k}\cdot\mathbf{r}'}\,ds\right|^2}{\left(\iint_s |E|\,ds\right)^2} \tag{6-11}$$

$$\mathbf{k}=k(\sin\theta\cos\phi\,\mathbf{a}_x+\sin\theta\sin\phi\,\mathbf{a}_y+\cos\theta\,\mathbf{a}_z)$$

For an aperture in the xy plane

$$\mathbf{k}\cdot\mathbf{r}'=k(x'\sin\theta\cos\phi+y'\sin\theta\sin\phi)$$

We can find the maximum PEL to relate it and ATL to directivity. Traditionally, we use the boresight value ($\theta = 0°$) and Eq. (6-11) reduces to

$$\mathrm{PEL}=\frac{\left|\iint_s E\,ds\right|^2}{\left(\iint_s |E|\,ds\right)^2} \tag{6-12}$$

Unless specified, PEL will be Eq. (6-12). We use Eq. (6-11) when we consider scanned apertures.

Equations (6-10) and (6-12) separate the effects of amplitude and phase variations in the aperture on the directivity at boresight. If these efficiencies are expressed in dB, the directivity becomes

$$\text{Directivity (dB)}=10\log\left(\frac{4\pi A}{\lambda^2}\right)+\mathrm{ATL}_{\mathrm{dB}}+\mathrm{PEL}_{\mathrm{dB}}$$

Expressed in dB, the efficiencies are called losses: amplitude taper loss (ATL) and phase error loss (PEL). It is important to remember that these are the losses at boresight. A linear phase taper across the aperture scans the beam, but Eq. (6-12) predicts the boresight loss, which could be a null of the pattern. ATL is independent of phase variations that cause squinting of the beam.

Separable Rectangular Aperture Distributions If the distribution in a rectangular aperture is separable, that is,

$$E(x, y) = E_1(x)E_2(y)$$

then the efficiencies also are separable.

$$\text{ATL} = \text{ATL}_x\,\text{ATL}_y \qquad \text{and} \qquad \text{PEL} = \text{PEL}_x\,\text{PEL}_y \tag{6-13}$$

Given a rectangular aperture with an x dimension excursion of $\pm a/2$

$$\text{ATL}_x = \frac{\left(\int_{-a/2}^{a/2} |E_1(x)|\,dx\right)^2}{a\int_{-a/2}^{a/2} |E_1(x)|^2\,dx} \tag{6-14}$$

$$\text{PEL}_x = \frac{\left|\int_{-a/2}^{a/2} E_1(x)\,dx\right|^2}{\left(\int_{-a/2}^{a/2} |E_1(x)|\,dx\right)^2} \tag{6-15}$$

The formulas for the y axis are the same except for the y dimensions.

Circularly Symmetrical Distributions If a circular aperture has a circularly symmetrical distribution, we can easily reduce Eqs. (6-10) and (6-12) to

$$\text{ATL} = \frac{2\left[\int_0^a |E(r)|r\,dr\right]^2}{a^2\int_0^a |E(r)|^2 r\,dr} \tag{6-16}$$

$$\text{PEL} = \frac{\left|\int_0^a E(r)r\,dr\right|^2}{\left(\int_0^a |E(r)|r\,dr\right)^2} \tag{6-17}$$

where a is the radius.

We need a short word on formulas using integrals. They look formidable and seem to have little immediate practical use. In the catalog of distributions to follow, results will be given. A general distribution must be solved by numerical integration techniques. One of the Newton-Cotes methods, such as Simpson's rule, or the Rhomberg integration can be used when evenly spaced values are known. With a known function for the distribution, we can use the Gauss-Legendre technique whereby the needed function values are picked. It is sometimes easier to calculate the integrals numerically instead of writing routines for special functions. Exact expressions are ideal; but unless a distribution is forced by a mode on the structure, it is difficult to achieve the exact distribution. We need only find approximations to the level of practical interest.

LINEAR DISTRIBUTIONS

We will assume that rectangular apertures have separable distributions so that we can deal with one coordinate at a time. Pattern cuts are in the plane containing the line. By drawing the pattern in k_x (or k_y) space, we can find patterns that are independent of the aperture size in a way similar to that used for arrays in Chap. 3.

6-3 Uniform Distribution

In Chap. 2 we derived the k_x-space pattern for a uniform distribution

$$\frac{a \sin (k_x a/2)}{k_x a/2} \tag{6-18}$$

where a is the aperture width and $k_x = k \sin \theta \cos \phi$. We will suppress $\cos \phi$ and consider only patterns in the $\phi = 0°$ plane. Figure 6-1 shows the $k \sin \theta$ space pattern. The pattern does not repeat at 2π intervals (radians) as the array does, but the sidelobes continue to decrease at a $1/x$ rate. The first sidelobe is 13.2 dB below the peak. The aperture size a, along with the scanning variable $\sin \theta_0$, determines the visible region in Fig. 6-1. It ranges between $\pm ka/2$ centered on $ka/2 \sin \theta_0$, since the maximum value of $\sin \theta = 1$.

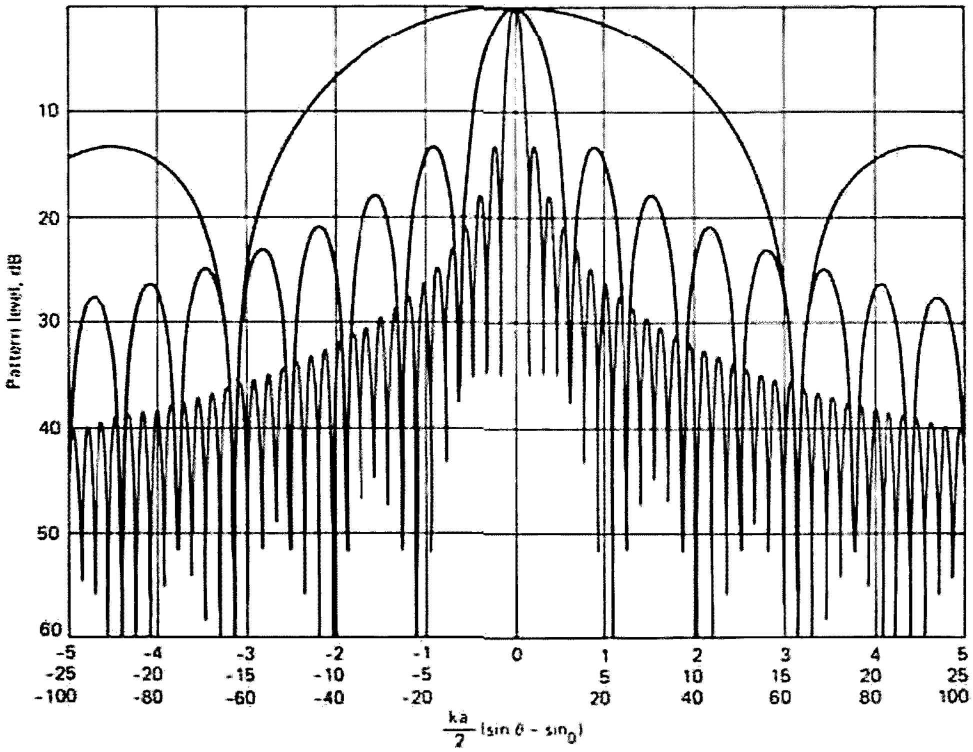

Figure 6-1 k_x-space pattern of uniform line source distribution.

Example An aperture is four wavelengths long. Find the number of sidelobes between $\theta = \pm 90°$ when $\sin\theta_0 = 0$ (boresight).

The maximum value in $k \sin\theta$ space is

$$\frac{2\pi}{\lambda}\frac{4\lambda}{2} = 4\pi, \text{ or } 12.57$$

There are three sidelobes on each side of the main beam (Fig. 6-1) in the visible region. The first sidelobe occurs when $ka/2 \sin\theta_1 = 4.5$ or

$$\theta_1 = \sin^{-1}\frac{4.5\lambda}{a\pi} = 21°$$

We found the half-power beamwidth in Chap. 2:

$$\text{HPBW} = 2\sin^{-1}\frac{0.4429\lambda}{a} \tag{6-19}$$

which is valid when we ignore the obliquity factor, $(1 + \cos\theta)/2$. When we approximate $x = \sin x$ (radians) for small angles, we obtain

$$\text{HPBW} = 50.76°\frac{\lambda}{a} \tag{6-20}$$

We will use this as a standard and describe other HPBW by their beamwidth factors. The beamwidth factor of the uniform distribution is 1.00. We also consider the null beamwidth of the distribution. The first null occurs at $\pm\pi$ in the $k \sin\theta$ pattern.

$$\text{BW}_{\text{null}} = 2\sin^{-1}\frac{\lambda}{a} \approx 114.59°\frac{\lambda}{a}$$

We can also establish a beamwidth factor for the null beamwidth.

When we scan the beam to a direction θ_0, the visible region centers on $\pi a/\lambda \sin\theta_0$ in $k \sin\theta$ space.

Example Find the beam edges when $\theta_0 = 30°$ and $a = 6\lambda$ for a uniform distribution.

$$\frac{a}{\lambda}(\sin\theta_{1,2} - \sin\theta_0) = \pm 0.4429$$

$$\sin\theta_{1,2} = \frac{\pm 0.4429}{6} + 0.5$$

$$\theta_1 = 35.02° \qquad \theta_2 = 25.23°$$

The beamwidth is the difference, 9.79°. If we take the beam center as the average between the 3-dB beam edges, we get 30.12° for the beam center. By using the cosine of the beam center times the aperture size, we get 5.19λ, the projected aperture dimension. On substituting this in Eq. (6.19), we calculate the

HPBW = 9.79°. The actual beam peak is at $\theta = 30°$, but the pattern is asymmetric about θ_0.

6-4 Other Simple Geometrical Distributions

Other simple geometrical distributions on a linear aperture follow the same Fourier transform relation as the uniform distributions with differing transforms in $k \sin \theta$ space. The properties of some common distributions are listed in Table 6-1.

Example Find the beamwidth of a 7λ aperture with a cosine distribution. From Table 6-1: beamwidth factor = 1.342. The taper increases the beamwidth over that of a uniform distribution.

$$\text{HPBW} = 1.342 \frac{50.76\lambda}{a} = 9.73°$$

or

$$\text{HPBW} = 2 \sin^{-1} 1.342 \frac{0.4429\lambda}{a} = 9.74°$$

We can add distributions and find the pattern from the sum of the transforms. Adding a pedestal (uniform distribution) to the cosine-squared distribution decreases the beamwidth and the sidelobes of the cosine-squared distribution. The aperture distribution is given by

$$E(x) = \text{PD} + (1 - \text{PD}) \cos^2 \frac{\pi x}{a} \qquad |x| \le \frac{a}{2}$$

where PD is the voltage pedestal level. The first sidelobe of the uniform distribution lies within the null beamwidth of the cosine-squared distribu-

TABLE 6-1 Common Linear Distribution Characteristics

Distribution	f_x	First sidelobe, dB	HPBW factor	BW_null factor	ATL, dB
Uniform	$\dfrac{\sin(k_x a/2)}{k_x a/2}$	13.2	1.00	1.00	0
Triangular	$\left[\dfrac{\sin(k_x a/4)}{k_x a/4}\right]^2$	26.5	1.439	2.00	1.25
Cosine	$\dfrac{\cos(k_x a/2)}{1 - (a/\lambda)^2}$	23.0	1.342	1.5	0.91
Cosine^2	$\dfrac{\sin(k_x a/2)}{(k_x a/2)[1 - (a/2\lambda)]^2}$	31.5	1.625	2.00	1.76

tion. The phase of sidelobes with respect to the main beam alternates between 180° and 0°. The sidelobe of the pedestal subtracts from the main lobe. The second sidelobe of the pedestal occurs in almost exactly the same place as the first sidelobe of the cosine-squared distribution. These lobes cancel each other to some extent. Table 6-2 gives the required pedestal for a given maximum sidelobe level where it is measured relative to the peak of the distribution. The minimum sidelobes (43.2 dB) occur for a pedestal level of −22.3 dB. At lower pedestal levels, the sidelobes rise and the beamwidth factor increases at a constant rate as the pedestal level decreases.

The amplitude taper efficiency of the cosine squared on a pedestal is

$$\text{ATL} = \frac{2(1 + \text{PD})^2}{3 + 2\,\text{PD} + 3\,\text{PD}^2} \quad \text{ratio} \tag{6-21}$$

Amplitude distributions based on simple functions have limited use. The uniform and cosine distributions or close approximations occur naturally, but the others must be forced on an aperture. An array can sample a distribution to achieve results similar to those for an aperture. A sampled cosine squared on a pedestal is handy for quick tolerance studies of array feed networks, but is far from optimum. We will consider distributions that allow close control of sidelobes and achieve minimum beamwidths.

The rate of decrease of the far-out sidelobe depends on the functional relation of the distribution at the edges [3]. If α is the exponent of the distribution approximation x_e^{α}, where x_e is the distance from the edge, then the sidelobes decay as

$$U^{-(1+\alpha)}$$

where U is a linear function of the k-space variable. Both the triangular and cosine distributions have $\alpha = 1$, and the far-out sidelobes decay as $1/U^2$.

TABLE 6-2 Pedestal Level to Achieve a Given Maximum Sidelobe Level for a Cosine Squared on a Pedestal Distribution

Sidelobe, dB	Pedestal, dB	Beamwidth factor	ATL, dB
30	−12.9	1.295	0.79
32	−14.2	1.325	0.89
34	−15.7	1.357	0.99
36	−17.3	1.390	1.10
38	−18.7	1.416	1.18
40	−20.0	1.439	1.25
42	−21.4	1.463	1.32
42.7*	−21.9	1.471	1.34
43.2†	−22.3	1.476	1.36

*Hamming distribution
†*Maximum sidelobe level*

(See Table 6-1.) The cosine-squared distribution sidelobes decay as $1/U^3$, since $\alpha = 2$. In the case of a cosine squared on a pedestal, the edge functional relation is a step (pedestal, $\alpha = 0$) and the far-out sidelobes decay as $1/U$. That is, the sidelobes of the pedestal eventually overtake the cosine-squared distribution sidelobes decreasing as $1/U^3$. To achieve uniform sidelobes, α must be -1. $\alpha = -1$ occurs only when the distribution edges are Dirac delta functions requiring infinite energy in the aperture or reduction to discrete sources (an array).

We must accept a trade-off between radiated power in the main beam and in the sidelobes. When we narrow the main beam, more power radiates in the sidelobes. We achieve minimum beamwidth in the main beam when all the sidelobes radiate the same power (maximum radiated power in the sidelobes for a given level). That is, all sidelobes are the same level. This case leads to the Dolph-Chebyshev array [4], which is impossible to duplicate in a continuous aperture.

6-5 Taylor Line Distribution [3]

The Taylor line source distribution modifies the location of the inner pattern zeros (nulls) of a uniform distribution to approximate the Dolph-Chebyshev distribution. The distribution remains on a pedestal $\alpha = 0$ and retains the $1/U$ fall-off for the far-out sidelobes. We can modify any number of inner zeros of the pattern to approximate the uniform sidelobe level distribution, but we force the aperture voltage to peak at the ends in approximating the Dirac delta functions. We will limit the number of changed zeros to keep the distribution practical. After a point, adding more zeros improves beamwidth negligibly.

We manipulate the location of pattern zeros to obtain desired patterns. Both aperture and array syntheses depend on zero locations. The number of array elements determines the number of independent zeros ($n - 1$), but a continuous aperture has an infinite number of independent zeros. Practical considerations of the distribution edge limits the number, but we are free to move zeros. For a given aperture size, we can move zeros out of the invisible region into the visible region and narrow the main beam as much as we want while maintaining low sidelobes. The invisible region represents stored energy in the aperture. When a zero moves out of the invisible region, the amount of stored energy and the Q of the antenna increase. The overall efficiency of the antenna decreases while the antenna becomes more and more narrowband. The antenna becomes superdirective; it exceeds that of a uniform distribution. The Taylor line source distribution retains the zeros in the invisible region and prevents superdirectivity. There is no limit to the directivity achievable on paper for a given aperture, but the theoretical distributions are unrealizable except for very small levels of superdirectivity. The costs are decreased bandwidth and efficiency.

The uniform distribution has k-space zeros at (Fig. 6-1)

$$\pm n\pi \qquad n = 1, 2, 3, \ldots$$

Taylor defines a new variable U to replace $k \sin \theta$

$$\frac{\sin \pi U}{\pi U} \tag{6-22}$$

where $U = (a/\lambda)(\sin \theta - \sin \theta_0)$ and a is the aperture width. The nulls (zeros) are then located at integer values of U. We will modify the location of the first $\bar{n} - 1$ pairs of inner nulls to lower the sidelobes. Picking the zeros symmetrically about the origin of U space gives us a constant phase distribution. We remove the inner zeros by dividing them out of the uniform distribution U-space pattern.

$$\frac{\sin \pi U}{\pi U \prod_{N=1}^{\bar{n}-1} \left(1 - \frac{U^2}{N^2}\right)}$$

We can then add new nulls U_n without becoming superdirective.

$$F(U) = \frac{\sin \pi U \prod_{N=1}^{\bar{n}-1} \left(1 - \frac{U^2}{U_N^2}\right)}{\pi U \prod_{N=1}^{\bar{n}-1} \left(1 - \frac{U^2}{N^2}\right)} \tag{6-23}$$

Because we want to approximate the Dolph-Chebyshev response, we pick the inner zeros from the array.

$$U_N = \bar{n}\frac{\sqrt{A^2 + (N - \frac{1}{2})^2}}{\sqrt{A^2 + (\bar{n} - \frac{1}{2})^2}} \qquad N = 1, 2, \ldots, \bar{n} - 1 \tag{6-24}$$

where A relates to the maximum sidelobe level

$$\cosh \pi A = b \tag{6-25}$$

in which $20 \log b$ = sidelobe level.

Equation (6-23) gives us the U-space (k-space) pattern of the distribution with modified zeros. We find the aperture distribution by expanding it in a Fourier cosine series

$$E(x) = \sum_{m=0}^{\infty} B_m \cos 2m\pi x \qquad |x| \le 0.5 \tag{6-26}$$

where the aperture size has been normalized. The pattern of the distribution is found from the Fourier transform.

$$f(k_x) = \int_{-1/2}^{1/2} E(x)e^{jk_x x}\,dx \qquad \text{or} \qquad f(U) = \int_{-1/2}^{1/2} E(x)e^{j2\pi Ux}\,dx$$

We substitute Eq. (6-26) for $E(x)$ and reverse the order of summation and integration.

$$f(U) = \sum_{m=0}^{\infty} B_m \int_{-1/2}^{1/2} \cos 2m\pi x \cos 2\pi U x \, dx \tag{6-27}$$

Since the aperture function is an even function, the odd function part of the integral is zero as reflected in Eq. (6-27). We find the coefficients B_m by matching the patterns at integer values of U. The integral [Eq. (6-27)] is zero unless $U = m$.

$$B_0 = f(0) \qquad \frac{B_m}{2} = f(m) \qquad m = 1, 2, \ldots, \bar{n} - 1$$

Since we have only modified the location of the first $\bar{n} - 1$ zeros of the U-space pattern, $f(m) = 0$ for $m \geq \bar{n}$ and the Fourier cosine series has only $\bar{n}$ components.

$$E(x) = f(0) + 2 \sum_{m=1}^{\bar{n}-1} f(m) \cos 2m\pi x \tag{6-28}$$

The coefficients are given by

$$f(0) = 1$$

$$f(m) = \frac{(-1)^m \prod_{N=1}^{\bar{n}-1} \left(1 - \frac{m^2}{U_N^2}\right)}{-2 \prod_{\substack{N=1 \\ N \neq m}}^{\bar{n}-1} \left(1 - \frac{m^2}{N^2}\right)} \qquad m = 1, 2, \ldots, \bar{n} - 1 \tag{6-29}$$

Example Find the Taylor line source distribution with 30-dB maximum sidelobes and $\bar{n} = 6$.

We use Eq. (6-25) to find the constant A

$$b = 10^{30/20} = 31.6228$$

$$A = \frac{\cosh^{-1} b}{\pi} = 1.3200$$

We substitute this constant into Eq. (6-24) to find the five $(\bar{n} - 1)$ nulls.

No.	*Null* U_N
1	1.4973
2	2.1195
3	2.9989
4	3.9680
5	4.9747

The first null value gives us the $\mathrm{BW}_{\text{null}}$ factor (1.4973). The null beamwidth has been increased almost 50 percent from the uniform distribution null beamwidth.

The coefficients of the Fourier cosine aperture distribution are found from Eqs. (6-28) and (6-29).

No.	B_m	B_m *normalized*	*Function*
0	1.0000	0.64672	1
1	0.5733	0.37074	$\cos 2\pi x$
2	−0.0284	−0.01835	$\cos 4\pi x$
3	−0.000213	−0.0001377	$\cos 6\pi x$
4	0.005561	0.003597	$\cos 8\pi x$
5	−0.003929	−0.002541	$\cos 10\pi x$

Coefficients of the series are normalized so that the distribution is 1 at $x = 0$, and the amplitude distribution is found by plotting the Fourier cosine series. We find the U-space pattern by substituting the zeros into Eq. (6-23). The half-power point can be found and compared with the uniform distribution to find the HPBW beamwidth factor, 1.2611. By using Eq. (6-14), we calculate ATL = 0.66 dB from the distribution.

The k-space plot (Fig. 6-2) of the above example shows the 30-dB sidelobe level. The first sidelobe is at 30 dB, and lobes after that fall away from 30 dB. With a higher value of $\bar{n}$, the first unchanged zero, more sidelobes would be nearer 30 dB. The second plot is a Bayliss difference pattern also designed to give 30-dB sidelobes when combined with the Taylor distribution.

The amplitude taper efficiency was calculated for a number of designs; it is given in Table 6-3. The corresponding beamwidth factors are listed in

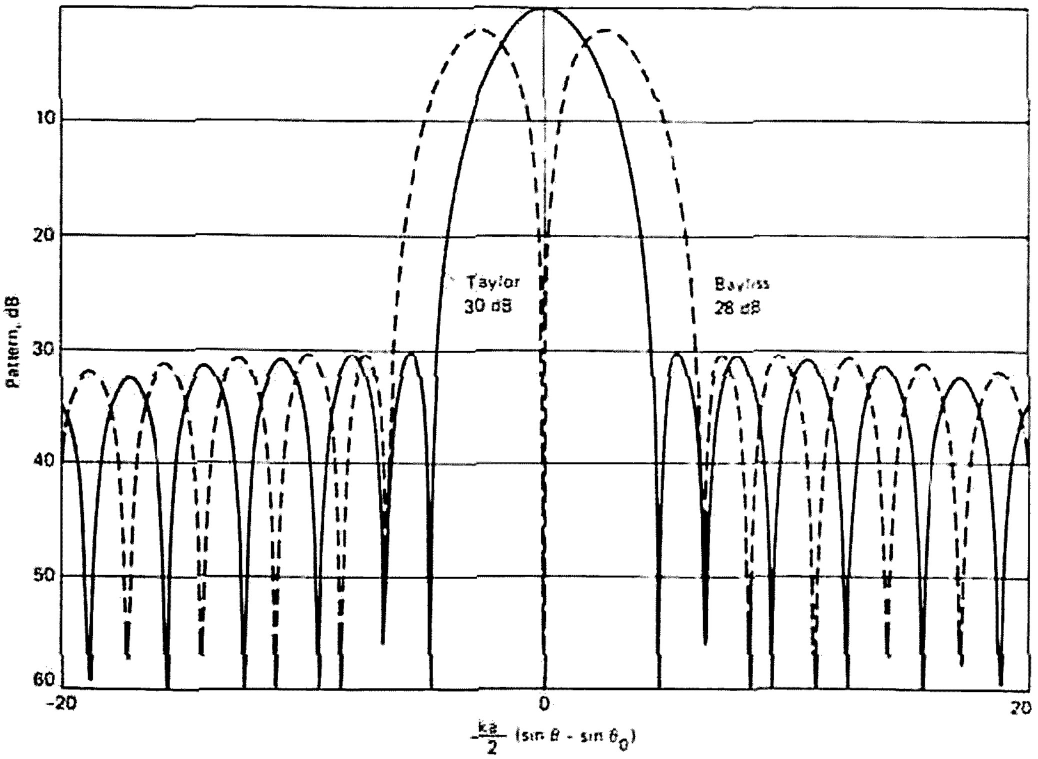

Figure 6-2 Taylor and Bayliss line distributions to give 30-dB sidelobes ($\bar{n} = 6$).

TABLE 6-3 Amplitude Taper Losses of Taylor Line Source Distributions

	ATL, dB, when sidelobe levels, dB, are as follows:						
$\bar{n}$	20	25	30	35	40	45	50
4	0.17	0.43	0.69	0.91			
5	0.15	0.41	0.68	0.93	1.14		
6	0.15	0.39	0.66	0.92	1.15	1.35	
7	0.15	0.37	0.65	0.91	1.15	1.36	1.54
8	0.16	0.36	0.63	0.90	1.14	1.36	1.55
10	0.19	0.34	0.61	0.88	1.13	1.35	1.55
12	0.24	0.34	0.59	0.86	1.11	1.34	1.54
16	0.35	0.35	0.57	0.84	1.09	1.32	1.53
20	0.46	0.37	0.56	0.82	1.07	1.30	1.51

Table 6-4, along with the null beamwidth factors (location of first zero in U space) in Table 6-5. ATL depends on the sidelobe level (Table 6-3) more than the number of modified zeros. Both the 20- and 25-dB sidelobe levels show that there is an optimum number of zeros. The edge of the distribution peaks toward the Dirac delta function and reduces the amplitude taper efficiency. More than three modified zeros are needed to reduce the sidelobes below 40 dB; hence, the blanks represent unrealizable designs. The beamwidth factor (Table 6-4) reduces with increasing $\bar{n}$, but it depends mainly on the sidelobe level.

Example Find the beamwidths and ATL of an 8λ-wide aperture with $\bar{n} = 8$, 40-dB sidelobes, and a Taylor line source distribution design.

From Table 6-4 $\text{HPBW} = \dfrac{1.4066(50.76°)}{8} = 8.92°$

TABLE 6-4 Beamwidth Factor of Taylor Line Source Distributions

	Beamwidth factors when sidelobe levels, dB, are as follows:						
$\bar{n}$	20	25	30	35	40	45	50
4	1.1043	1.1925	1.2696	1.3367			
5	1.0908	1.1837	1.2665	1.3404	1.4065		
6	1.0800	1.1752	1.2611	1.3388	1.4092	1.4733	
7	1.0715	1.1679	1.2555	1.3355	1.4086	1.4758	1.5377
8	1.0646	1.1617	1.2504	1.3317	1.4066	1.4758	1.5400
10	1.0545	1.1521	1.2419	1.3247	1.4015	1.4731	1.5401
12	1.0474	1.1452	1.2353	1.3189	1.3967	1.4695	1.5379
16	1.0381	1.1358	1.2262	1.3103	1.3889	1.4628	1.5326
20	1.0324	1.1299	1.2203	1.3044	1.3833	1.4576	1.5280

TABLE 6-5 Null Beamwidth Factor of Taylor Line Source Distributions

	Null beamwidth factors when sidelobe levels, dB, are as follows:						
$\bar{n}$	20	25	30	35	40	45	50
4	1.1865	1.3497	1.5094	1.6636			
5	1.1696	1.3376	1.5049	1.6696	1.8302		
6	1.1566	1.3265	1.4973	1.6671	1.8347	1.9990	
7	1.1465	1.3172	1.4897	1.6622	1.8337	2.0031	2.1699
8	1.1386	1.3095	1.4828	1.6569	1.8306	2.0032	2.1739
10	1.1270	1.2978	1.4716	1.6471	1.8231	1.9990	2.1740
12	1.1189	1.2894	1.4632	1.6392	1.8161	1.9934	2.1705
16	1.1086	1.2783	1.4518	1.6277	1.8051	1.9835	2.1623
20	1.1023	1.2714	1.4444	1.6200	1.7975	1.9760	2.1553

From Table 6-5 $\mathrm{BW}_{\mathrm{null}} = \dfrac{1.8306(114.59°)}{8} = 26.22°$

From Table 6-3 $\mathrm{ATL} = 1.14\ \mathrm{dB}$

A square aperture with the same distribution in both directions has a directivity

$$\text{Directivity} = 10 \log \frac{4\pi A}{\lambda^2} - 2\ \mathrm{ATL} = 26.77\ \mathrm{dB}$$

6-6 Taylor Line Distribution with Edge Nulls

Rhodes [5] has shown that it is impossible to have a step discontinuity of the fields at the edge of a physical aperture. Given the radius of curvature of the edge, ρ, the field varies as

$$E_d \sim \frac{C_2}{\rho} d \qquad \text{polarized perpendicular to the aperture edge}$$

$$E_s \sim \frac{C_1}{\rho} d^2 \qquad \text{polarized parallel to the aperture edge}$$

where C_1 and C_2 are constants and d is the distance from the edge. Without the possibility of an edge pedestal, a traditional Taylor line source cannot be realized with a physical aperture. We can sample the distribution with an array or closely approximate it, but we cannot achieve the exact distribution. A Taylor distribution with a null at the edge satisfies the physical realizability criterion.

Rhodes [6] extended the Taylor line source by modifying the U-space pattern zeros of the cosine distribution. Since $\alpha = 1$, the far-out sidelobes drop off as $1/U^2$ and the distribution is zero on the edges.

The zeros of the cosine distribution occur at

$$(N+\tfrac{1}{2})\pi \qquad N = 1, 2, 3, \ldots \qquad k \text{ space}$$

When the Taylor U-space variable is used, the modified U-space pattern becomes

$$f(U) = \frac{\cos \pi U \prod_{N=1}^{\bar{n}-1}\left(1 - \dfrac{U^2}{U_N^2}\right)}{[1-(2U)^2]\prod_{N=1}^{\bar{n}-1}\left[1 - \dfrac{U^2}{(N+\frac{1}{2})^2}\right]} \tag{6-30}$$

We remove the inner $\bar{n}-1$ zeros at $N+\frac{1}{2}$ and substitute new ones given by

$$U_N = \pm(\bar{n}+\tfrac{1}{2})\frac{\sqrt{A^2+(N-\frac{1}{2})^2}}{\sqrt{A^2+(\bar{n}-\frac{1}{2})^2}} \qquad N = 1, 2, \ldots, \bar{n}-1 \tag{6-31}$$

On comparing Eqs. (6-31) and (6-24), we see that the nulls are shifted by

$$\frac{\bar{n}+\frac{1}{2}}{\bar{n}}$$

between the two Taylor distributions. When $\bar{n}$ is large, the nulls are close to the same for the two distributions.

To find the amplitude distribution in the aperture, we expand the aperture fields in a Fourier cosine series

$$E(x) = \sum_{m=0}^{\infty} B_m \cos(2m+1)\pi x \qquad |x| \le 0.5 \tag{6-32}$$

Like the Taylor line source, there are only $\bar{n}$ terms in the series whose coefficients are found by equating the pattern from the Fourier transform of Eq. (6-32) to Eq. (6-30). The coefficients are given by

$$B_0 = \frac{2\prod_{N=1}^{\bar{n}-1}\left(1 - \dfrac{\frac{1}{4}}{U_N^2}\right)}{\prod_{N=1}^{\bar{n}-1}\left[1 - \dfrac{\frac{1}{4}}{(N+\frac{1}{2})^2}\right]}$$

$$B_m = \frac{(-1)^m(m+\frac{1}{2})\prod_{N=1}^{\bar{n}-1}\left[1 - \dfrac{(m+\frac{1}{2})^2}{U_N^2}\right]}{[1-(2m+1)^2]\prod_{\substack{N=1\\N\ne m}}^{\bar{n}-1}\left[1 - \dfrac{(m+\frac{1}{2})^2}{(N+\frac{1}{2})^2}\right]} \qquad m = 1, 2, \ldots, \bar{n}-1 \tag{6-33}$$

Example Find the Taylor line source distribution with edge nulls for 30-dB maximum sidelobes and $\bar{n} = 6$.

We use Eq. (6-25) to find the constant A

$$b = 10^{30/20} = 31.6228$$

$$A = \frac{\cosh^{-1} b}{\pi} = 1.32$$

the same as the pedestal edge Taylor line source distribution. We substitute this constant into Eq. (6-31) to find the five modified nulls.

No.	*Null* U_N
1	1.6221
2	2.2962
3	3.2488
4	4.2987
5	5.3892

The null locations have increased by $(\bar{n} + \frac{1}{2})/\bar{n} = 6.5/6 = 1.0833$ from the pedestal Taylor line source design. The null beamwidth factor has also increased by this factor. The coefficients of the Fourier cosine aperture distribution are found from Eq. (6-33).

No.	B_m	B_m *normalized*	*Function*
0	0.50265	0.94725	$\cos \pi x$
1	0.023087	0.04351	$\cos 3\pi x$
2	0.017828	0.02220	$\cos 5\pi x$
3	−0.010101	−0.02075	$\cos 7\pi x$
4	0.007374	0.01390	$\cos 9\pi x$
5	−0.003245	−0.006116	$\cos 11\pi x$

The normalized coefficients sum to 1 at $x = 0$. Equation (6-30) determines the U-space pattern given the nulls. On finding the half-power point and comparing it with the uniform distribution half-power point, we find the beamwidth factor: 1.3581.

Tables 6-6, 6-7, and 6-8 give results for this Taylor line source. As $\bar{n}$ increases, the results approach the result of the pedestal Taylor line source. Since the maximum sidelobe of the cosine distribution is 23 dB, a distribution must have peaking toward the edges to raise the sidelobes above that level. In all distributions the voltage approaches zero linearly at the edges.

6-7 Bayliss Line Source Distribution [7]

The Bayliss distribution produces a pattern null on boresight while controlling the height of the sidelobes. As in the Taylor distribution, the first few

TABLE 6-6 Amplitude Taper Losses of Taylor Line Source with Edge Null Distribution

$\bar{n}$	ATL, dB, when sidelobe levels, dB, are as follows:					
	25	30	35	40	45	50
4	0.86	1.13	1.36	1.55	1.71	1.84
6	0.67	0.97	1.24	1.47	1.66	1.84
8	0.56	0.87	1.14	1.39	1.60	1.79
12	0.45	0.74	1.02	1.28	1.51	1.71
16	0.41	0.68	0.96	1.22	1.45	1.66
20	0.39	0.64	0.92	1.17	1.41	1.62

TABLE 6-7 Beamwidth Factor of Taylor Line Source with Edge Null Distribution

$\bar{n}$	Beamwidth factors when sidelobe levels, dB, are as follows:					
	25	30	35	40	45	50
4	1.3559	1.4092	1.4815	1.5443	1.5991	1.6470
6	1.2666	1.3581	1.4407	1.5153	1.5831	1.6448
8	1.2308	1.3242	1.4097	1.4882	1.5608	1.6280
12	1.1914	1.2850	1.3716	1.4522	1.5276	1.5984
16	1.1705	1.2635	1.3500	1.4308	1.5068	1.5785
20	1.1576	1.2502	1.3363	1.4170	1.4930	1.5649

TABLE 6-8 Null Beamwidth Factor of Taylor Line Source with Edge Null Distribution

$\bar{n}$	Null beamwidth factors when sidelobe levels, dB, are as follows:					
	25	30	35	40	45	50
4	1.5184	1.6980	1.8715	2.0374	2.1949	2.3433
6	1.4371	1.6221	1.8060	1.9875	2.1656	2.3395
8	1.3913	1.5755	1.7604	1.9450	2.1284	2.3097
12	1.3431	1.5242	1.7075	1.8918	2.0765	2.2610
16	1.3182	1.4971	1.6786	1.8616	2.0455	2.2298
20	1.3031	1.4805	1.6605	1.8424	2.0254	2.2091

sidelobes are nearly the same height to minimize the beamwidth of the two beams split about boresight.

A monopulse tracking system uses an auxiliary pattern with a boresight null coincident with the beam peak of the main pattern. The tracking system drives the antenna positioner until the signal in this difference channel nulls so that the main channel (sum) points at the emitter or radar target. The accuracy of the pointing angle is improved, since a null is a more exact position than the broad sum pattern peak. Noise and receiver sensitivity, along with the slope of the difference pattern, limit the tracking accuracy. Stronger signals can be tracked further into the null. Because the phase of a pattern shifts by 180° when passing through a null, phase relative to the sum pattern (a reference signal) can be used to give direction. Without monopulse or some other sequential lobing technique, such as conical scan, a radar cannot track effectively.

Any odd function distribution produces a null on boresight. A uniform distribution that switches phase by 180° in the center has the best amplitude taper efficiency, but high sidelobes (10 dB). These high sidelobes allow interfering or noise signals to enter the receiver. The Bayliss distribution adjusts the inner nulls of the U-space pattern to lower the sidelobes. Adjusting the zeros to correspond to the Dolph-Chebyshev array does not lower the sidelobes to the same level as it did in the Taylor distribution. Further adjustments of the four inner zeros are required. Bayliss found the proper location through a computer search. We locate the zeros by

$$U_N = \begin{cases} (\bar{n} + \frac{1}{2})\left(\dfrac{\xi_N^2}{A^2 + \bar{n}^2}\right)^{1/2} & N = 1, 2, 3, 4 \\ (\bar{n} + \frac{1}{2})\left(\dfrac{A^2 + N^2}{A^2 + \bar{n}^2}\right)^{1/2} & N = 5, 6, \dots, \bar{n} - 1 \end{cases} \tag{6-34}$$

By using the U-space pattern, we have

$$f(U) = U \cos \pi U \frac{\prod_{N=1}^{\bar{n}-1} \left(1 - \dfrac{U^2}{U_N^2}\right)}{\prod_{N=0}^{\bar{n}-1} \left[1 - \dfrac{U^2}{(N + \frac{1}{2})^2}\right]} \tag{6-35}$$

The coefficients were fitted to polynomials depending on the sidelobe level. Given $S = |\text{sidelobe level (dB)}|$

$$A = 0.3038753 + S\llbracket 0.05042922 + S\{-0.00027989 + S[0.343 \times 10^{-5} - S(0.2 \times 10^{-7})]\}\rrbracket \tag{6-36a}$$

$$\xi_1 = 0.9858302 + S\llbracket 0.0333885 + S\{0.00014064 + S[-0.19 \times 10^{-5} + S(0.1 \times 10^{-7})]\}\rrbracket \tag{6-36b}$$

$$\xi_2 = 2.00337487 + S\llbracket 0.01141548 + S\{0.0004159 + S[-0.373 \times 10^{-5} + S(0.1 \times 10^{-7})]\}\rrbracket \tag{6-36c}$$

$$\xi_3 = 3.00636321 + S\{0.00683394 + S[0.00029281 + S(-0.161 \times 10^{-5})]\} \tag{6-36d}$$

$$\xi_4 = 4.00518423 + S\{0.00501795 + S[0.00021735 + S(-0.88 \times 10^{-6})]\} \tag{6-36e}$$

The location of the pattern peak was also fitted to a polynomial

$$U_{\max} = 0.4797212 + S[\![0.01456692 + S\{-0.00018739 + S[0.218 \times 10^{-5} + S(-0.1 \times 10^{-7})]\}]\!] \tag{6-37}$$

We obtain the aperture distribution by a Fourier sine series having only $\bar{n}$ terms

$$E(x) = \sum_{m=0}^{\bar{n}-1} B_m \sin\,(m + \tfrac{1}{2})2\pi x \qquad |x| \le 0.5 \tag{6-38}$$

where

$$B_m = \frac{(-1)^m(m + \frac{1}{2})^2}{2j} \frac{\prod_{N=1}^{\bar{n}-1}\left[1 - \frac{(m + \frac{1}{2})^2}{U_N^2}\right]}{\prod_{\substack{N=0 \\ m \ne N}}^{\bar{n}-1}\left[1 - \frac{(m + \frac{1}{2})^2}{(N + \frac{1}{2})^2}\right]} \tag{6-39}$$

The phase constant $(-j)$ has little effect on the coefficient B_m except to balance the phase ±90° about the null.

Example Design a Bayliss distribution with 30-dB sidelobes and $\bar{n} = 6$. Use Eqs. (6-36) to find the coefficients.

$A = 1.64126 \qquad \xi_1 = 2.07086 \qquad \xi_2 = 2.62754 \qquad \xi_3 = 3.43144$

$\xi_4 = 4.32758$

We substitute these constants into Eq. (6-34) to find the five $(\bar{n} - 1)$ nulls.

No.	*Null* U_N
1	2.1639
2	2.7456
3	3.5857
4	4.5221
5	5.4990

Equation (6-37) finds the beam peak of the split beam pattern in U space.

$U_{\max} = 0.7988 \qquad (ka/2) \sin \theta_{\max} = \pi U_{\max} = 2.5096$

where a is the aperture width.

We substitute these zeros into Eq. (6-39) to find the coefficients of the Fourier sine series of the aperture distribution. By evaluation of the series across the aperture, the coefficients can be normalized to give a maximum aperture voltage of 1.

No.	B_m	B_m *normalized*	*Function*
0	0.13421	0.85753	$\sin \pi x$
1	0.081025	0.51769	$\sin 3\pi x$
2	−0.0044151	−0.028209	$\sin 5\pi x$
3	0.001447	0.0092453	$\sin 7\pi x$
4	−0.0003393	−0.0021679	$\sin 9\pi x$
5	−0.000014077	−0.00008994	$\sin 11\pi x$

We use Eq. (6-35), after substituting the zeros, to evaluate the pattern. The 3-dB pattern points can be found by searching the pattern

$$(ka/2)\sin\theta_1 = 1.27232 \qquad (ka/2)\sin\theta_2 = 4.10145$$

Figure 6-2 contains a plot of a Bayliss distribution ($\bar{n} = 6$) designed to have sidelobes 30 dB below the Taylor distribution with 30-dB sidelobes. The losses to the difference pattern are about 2 dB higher than the sum pattern. We can design the Bayliss distribution to have 28-dB sidelobes. If designed for 30-dB sidelobes as in the above example, then relative to the sum Taylor distribution, the sidelobes would be 32 dB down from the sum pattern peak. The last nulls show that the unmodified zeros of the Taylor distribution occur at $\pm n\pi$, whereas the unmodified zeros of the Bayliss distribution occur at $\pm(n + \frac{1}{2})\pi$.

By using Eq. (6-14), we find the amplitude taper efficiency of the pattern at the beam peak. When we evaluate the phase error efficiency by using Eq. (6-15), the result is zero because of the boresight null. We can use Eq. (6-11) to evaluate the phase error efficiency at the beam peak.

$$\text{PEL} = \frac{\left|\displaystyle\int_{-a/2}^{a/2} E(x)e^{jk\sin\theta_{\max}x}\,dx\right|^2}{\left(\displaystyle\int_{-a/2}^{a/2} |E(x)|\,dx\right)^2} \qquad \text{(6-40)}$$

Table 6-9 lists results of calculations on Bayliss distributions with $\bar{n} = 10$ for various sidelobe levels. Lower sidelobe levels produce higher distribution losses and push the beam peak out. The position of the beam peak is independent of $\bar{n}$, since the first four zeros are fixed by Eqs. (6-36). Like the Taylor distribution, sidelobe level determines most of the parameters of the Bayliss distribution. Changing $\bar{n}$ has less effect than it has for the Taylor distribution. The values of parameters for distribution with $\bar{n} \neq 10$ will differ little from those in Table 6-9.

Example Find the beam peak and beam edges for an 8λ-wide aperture excited in a Bayliss distribution with $\bar{n} = 10$ and 30-dB sidelobes.

$$\frac{2\pi}{\lambda}\sin\theta_{\max}\frac{8\lambda}{2} = 2.5096$$

TABLE 6-9 Characteristics of a Bayliss Line Source Distribution with $\bar{n} = 10$ Parameters

	Beam peak	3-dB beam edges			
Sidelobe level, dB	$\frac{ka}{2}\sin\theta_{\max}$	$\frac{ka}{2}\sin\theta_1$	$\frac{ka}{2}\sin\theta_2$	ATL, dB	PEL, dB
20	2.2366	1.140	3.620	0.50	1.81
25	2.3780	1.204	3.855	0.54	1.90
30	2.5096	1.263	4.071	0.69	1.96
35	2.6341	1.318	4.270	0.85	2.01
40	2.7536	1.369	4.455	1.00	2.04

$$\sin\theta_{\max} = \frac{2.5096}{8\pi}$$

$$\sin\theta_1 = \frac{1.263}{8\pi} \qquad \sin\theta_2 = \frac{4.071}{8\pi}$$

$$\theta_{\max} = 5.73^\circ \qquad \theta_1 = 2.88^\circ \qquad \theta_2 = 9.32^\circ$$

6-8 Line Sources with Arbitrary Sidelobe Levels

Antennas for certain special applications require beams with controlled sidelobe levels. If there is a particularly strong interfering signal always in the direction of particular sidelobes, those sidelobes can be reduced without reducing all sidelobes. To obtain the minimum beamwidth, we must radiate power in the sidelobes. When all sidelobes are reduced, the beamwidth widens more than necessary. We achieve a true optimum by designing for only the needed low sidelobes.

All methods use some form of pattern zero manipulation to control the sidelobes. Moving two zeros closer together reduces the lobe between them. Another lobe will increase, or the distribution becomes superdirective as zeros move in from invisible space. That is, lobes in invisible space increase and represent stored energy in the aperture. If the sidelobes are symmetrical about boresight, the pattern phase remains uniform or has a simple 180° shift through the center for difference patterns.

Elliott [8] gives an excellent discussion of various methods for obtaining distributions with arbitrary sidelobes. Various techniques are discussed in the literature; see Hyneman [9] or Elliott [10, 11]. Elliott also extends the arbitrary sidelobe level technique to Bayliss difference distributions [12]. With these techniques an iterative process is required to converge to a design. Tseng [13] discusses a technique of adding a broad, deep null to a Taylor distribution. With an adaptive array this technique can be used to eliminate a single interference signal. If known beforehand, the required null is designed into the line source instead of the dynamic design of the adaptive array.

6-9 Woodward Line Source Synthesis [14]

In the preceding sections methods to find distributions that give the minimum beamwidth for specified sidelobe levels are discussed. Some applications require shaped beams extending over a range of angles. The Woodward synthesis samples the desired k-space pattern at even intervals to find the aperture distribution. No integrals are required to find the coefficients.

The technique is based on the scanned pattern of a uniform amplitude distribution. Express the pattern in terms of U space so that, when scanned to U_0, it becomes

$$\frac{\sin \pi(U - U_0)}{\pi(U - U_0)}$$

with the nulls of the pattern occurring at integer values of $U - U_0$.

$$U = \frac{a}{\lambda} \sin \theta \qquad U_0 = \frac{a}{\lambda} \sin \theta_0$$

The visible region extends between $+a$ and $-a$ centered about U_0.

Figure 6-3 shows two patterns scanned to $U_0 = 1$ and $U_0 = 2$. The peak of the curve scanned $U_0 = 2$ occurs at one of the nulls of the pattern scanned

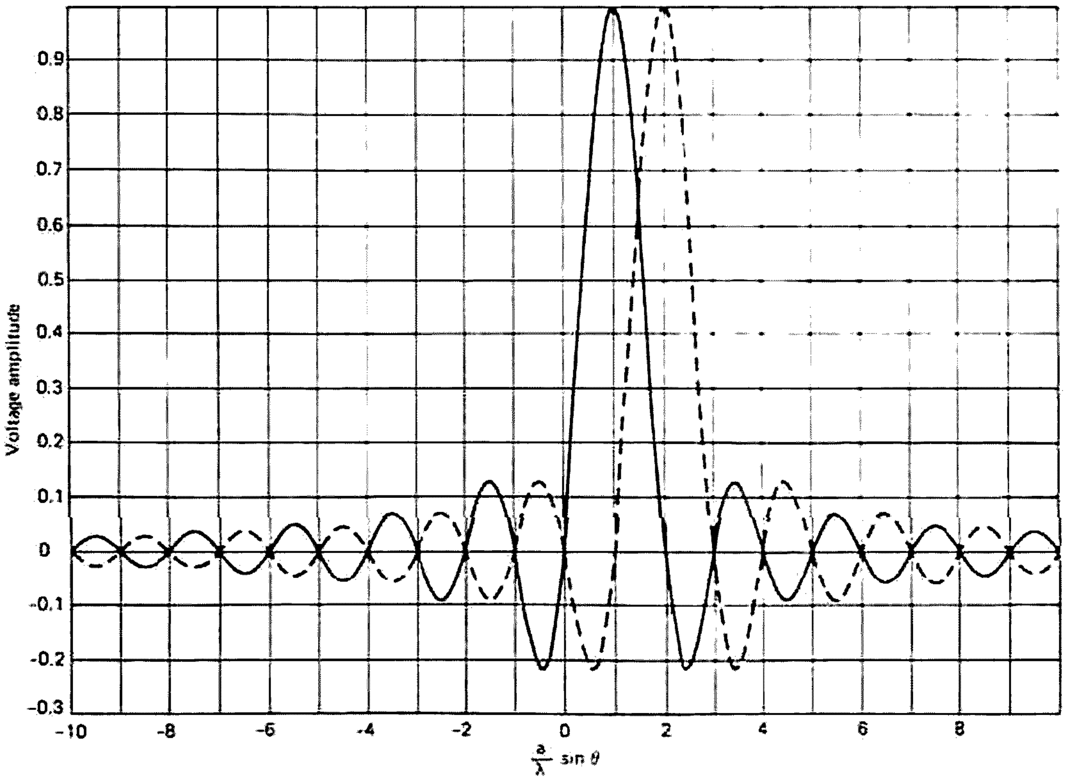

Figure 6-3 Scanned uniform distributions: $U_0 = 1$ and $U_0 = 2$.

to $U_0 = 1$. If we allow only integer values of U_0, then the pattern scanned to U_0 solely determines the pattern at the point U_0 in U space. The two curves (Fig. 6-3) in the regions below $U = 0$ and above $U = 3$ cancel each other to some extent when the distributions are added. We form the aperture distribution from a sum of $2a/\lambda + 1$ independent sample points of scanned apertures.

$$E(x) = \sum_{i=-N}^{N} E_i e^{-j(i/a)x} \tag{6-41}$$

where N = integer part (a/λ). Each term is a uniform amplitude distribution scanned to an integer value of U. The amplitudes E_i are determined by the sample values of the U-space pattern at those points.

Example Design a 10λ aperture with a constant beam between $\theta = 0°$ and $\theta = 30°$. The nonzero portion of the U-space pattern extends from

$$U_1 = 10 \sin 0° = 0 \qquad \text{to} \qquad U_2 = 10 \sin 30° = 5$$

When we sample the U-space pattern, we find 6 nonzero terms.

i	0	1	2	3	4	5
E_i	0.5	1.0	1.0	1.0	1.0	0.5

At $U_1 = 0$ and $U_2 = 5$, we use the average value. The aperture distribution is

$$0.5 + e^{-jx/a} + e^{-j2x/a} + e^{-j3x/a} + e^{-j4x/a} + 0.5e^{-j5x/a}$$

The U-space pattern of this distribution (Fig. 6-4) shows some ripple in the beam and reduction to 6 dB at the beam edges. If we increased the sample level at the edges, $U = 0$ and $U = 5$, the pattern would increase to that level.

A cosecant-squared power pattern can be designed by the method of the preceding example. When an antenna with this pattern on the ground points its maximum toward the horizon, it delivers a constant signal to an aircraft that maintains its altitude. The pattern fall-off matches the range decrease as the aircraft flies toward the antenna. The voltage pattern is given by

$$E = \frac{E_0 \sin \theta_m}{\sin \theta}$$

where θ_m is the angle of the pattern maximum. In U space this becomes

$$E(U) = \frac{E_0 U_m}{U}$$

The amplitudes of the scanned apertures decrease as $1/U$.

Example Design a 10λ aperture with a cosecant-squared pattern from $\theta = 5°$ to $\theta = 70°$ with the maximum at 5°.

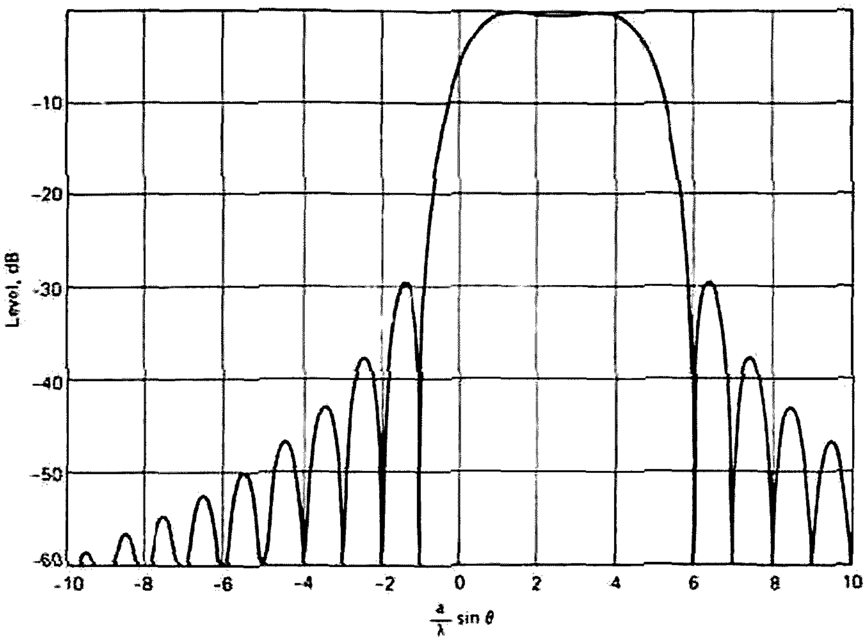

Figure 6-4 *U*-space pattern of Woodward-Lawson sampling for constant beam from 0° to 30° (10λ aperture).

There are $2a/\lambda + 1$ possible sample points (21). The nonzero portion of the *U*-space pattern extends from

$$U_{\min} = 10 \sin 5° = 0.87 \qquad \text{to} \qquad U_{\max} = 10 \sin 70° = 9.4$$

We sample only at integer values of *U*, which gives us nine nonzero terms.

$$U_m = 0.8716$$

The coefficients are

i	E_i	i	E_i	i	E_i
1	0.8716	4	0.2179	7	0.1245
2	0.4358	5	0.1743	8	0.1089
3	0.2905	6	0.1453	9	0.0968

The sum [Eq. (6-41)] for this distribution contains nine terms.

$$E(x) = \sum_{i=1}^{9} E_i e^{-j(i/a)x}$$

Figure 6-5 shows the amplitude and phase of this aperture distribution. The pattern obtained by summing the scanned aperture distributions (Fig. 6-6) shows ripple about the desired pattern. Increasing the aperture size increases the number but not the size of ripples. The aperture listribution (Fig. 6-5) has a negative phase slope to scan the beam off broadside.

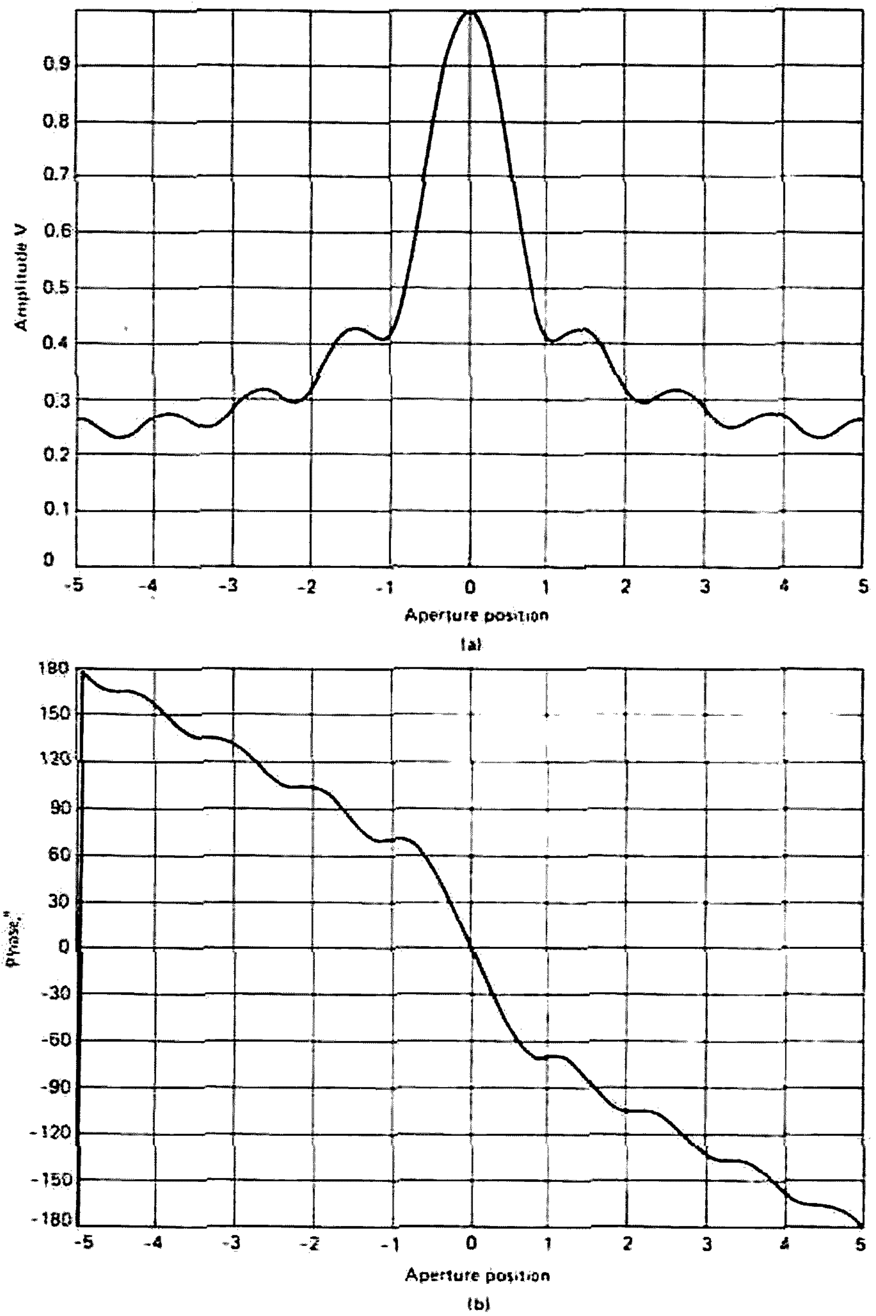

Figure 6-5 Aperture distribution of Woodward-Lawson sampling for cosecant-squared pattern (10λ aperture). (*a*) Aperture amplitude distribution, (*b*) aperture phase distribution.

CIRCULAR APERTURES

Many common apertures conform to circles. The two-dimensional Fourier transform relation for the pattern holds for any aperture rim shape and becomes for the circle

$$f(\theta, \phi) = \int_0^{2\pi} \int_0^a E(r', \phi') e^{jkr' \sin\theta \cos(\phi - \phi')} r'\, dr'\, d\phi \tag{6-42}$$

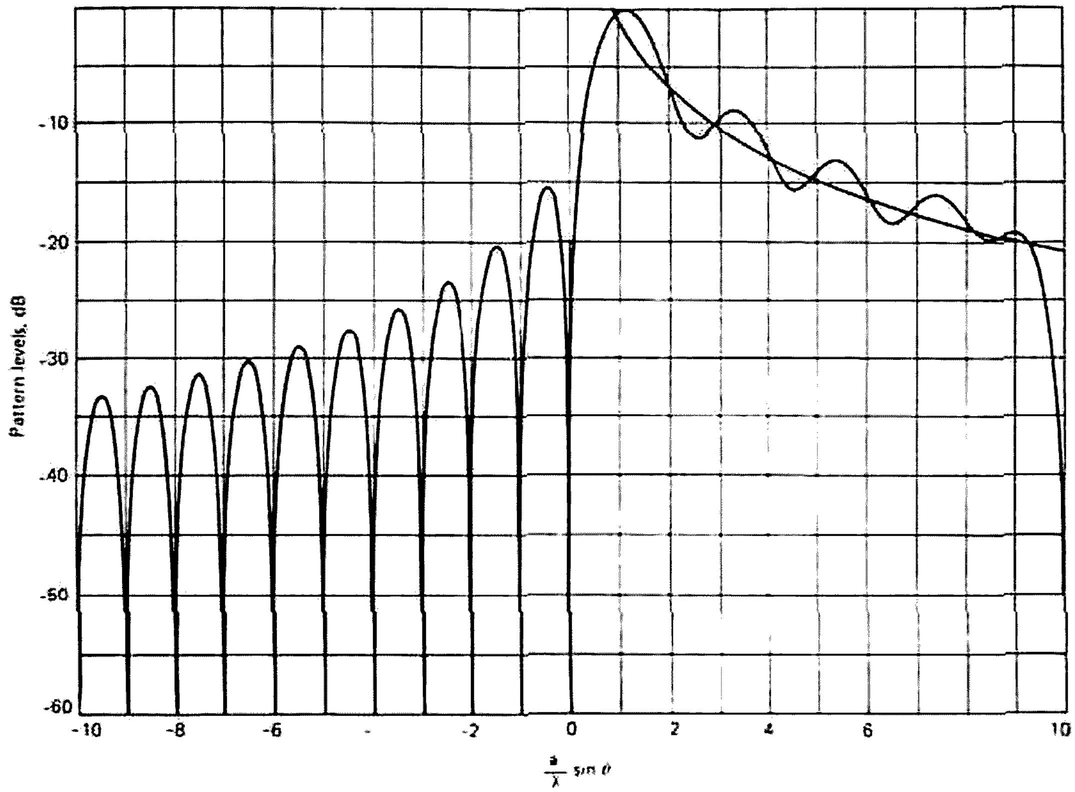

Figure 6-6 U-space pattern of 10λ aperture Woodward-Lawson sampling for a cosecant-squared pattern.

where a is the radius, r' is the radial coordinate, and ϕ' is the angle coordinate of the aperture point. The integral leads to a k_r space.

When the distribution has circular symmetry, the ϕ' integral can be evaluated easily which reduces Eq. (6-42) to

$$f(k_r) = 2\pi \int_0^a E(r')J_0(kr' \sin\theta)r'\,dr' \tag{6-43}$$

where $J_0(x)$ is the zeroth-order Bessel function of the first kind. All great-circle patterns (constant ϕ) are identical.

6-10 Parabolic^N Circular-Aperture Distribution [15]

A parabolic distribution to a power N approximates many distributions.

$$E(r) = \left[1 - \left(\frac{r}{a}\right)^2\right]^N \tag{6-44}$$

If we include $N = 0$, we also cover the uniform distribution. The distribution is zero on the edges ($N > 0$). We find the pattern from its closed-form Fourier transform

$$f(k_r) = \frac{2^{N+1}(N+1)!\,J_{N+1}(ka \sin\theta)}{(ka \sin\theta)^{N+1}} \tag{6-45}$$

found from Eq. (6-43) for circularly symmetrical distributions.

When $N = 0$ (uniform distribution)

$$f(k_r) = \frac{2J_1(ka \sin\theta)}{ka \sin\theta}$$

plotted in Fig. 6-7. The zeros occur at the zeros of $J_1(x)$. The 3-dB pattern point of the uniform distribution is

$$ka \sin\theta_1 = 1.6162 \qquad \sin\theta_1 = 0.5145\frac{\lambda}{D}$$

$$\text{HPBW} = 2\sin^{-1}\frac{0.5145\lambda}{D} \tag{6-46}$$

where D is the diameter. For large apertures, we can approximate $\sin\theta$ by θ (radians). Converted to degrees, the half-power beamwidth becomes

$$\text{HPBW} = 58.95^\circ\frac{\lambda}{D} \tag{6-47}$$

All other circular distributions relate to Eq. (6-46) or (6-47) through a beamwidth factor. The uniform distribution has a unity beamwidth factor.

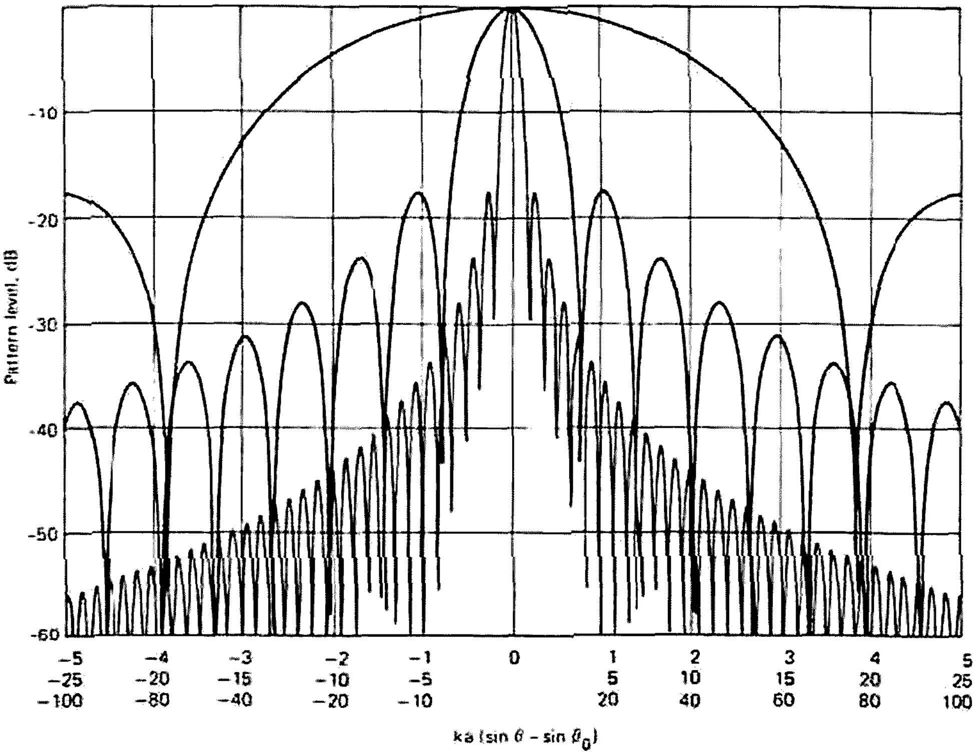

Figure 6-7 k_r-space pattern of uniform circular aperture distribution.

Example Find the beamwidth of a uniform distribution circular aperture 10.5λ in diameter.

The beamwidths are found by Eqs. (6-46) and (6-47):

$$\text{HPBW} = 2\sin^{-1}\frac{0.5145}{10.5} = 5.62^\circ$$

$$\text{HPBW} = \frac{58.95^\circ}{10.5} = 5.61^\circ$$

The first zero of $J_1(x)$ gives the k-space pattern null point.

$$ka\sin\theta_{\text{null}} = 3.8317$$

$$\text{BW}_{\text{null}} = 2\sin^{-1}\frac{1.2197\lambda}{D} \simeq 139.76^\circ\frac{\lambda}{D} \tag{6-48}$$

We can also define a null beamwidth factor and relate the beams of other distributions to the uniform circular distribution beamwidth [Eq. (6-48)].

We use Eq. (6-16) with the parabolic^N distribution to find the amplitude taper efficiency.

$$\text{ATL} = \frac{2N+1}{(N+1)^2} \qquad \text{(ratio)} \tag{6-49}$$

The characteristics of the first few parabolic^N distributions are listed in Table 6-10.

Example Find the half-power beamwidth of a 30λ-diameter aperture when $N = 1$ or 2.

$$N = 1 \qquad \text{HPBW} = 58.95^\circ\frac{1.2337}{30} = 2.42^\circ$$

$$N = 2 \qquad \text{HPBW} = 58.95^\circ\frac{1.4311}{30} = 2.81^\circ$$

We combine the beamwidth factor (Table 6-10) with Eq. (6-47) for the uniform distribution to find the half-power beamwidths.

TABLE 6-10 Parameters of Parabolic^N Circular-Aperture Distribution $E(r) = \left[1 - \left(\frac{r}{a}\right)^2\right]^N$

N	First side-lobe, dB	HPBW factor	BW_{null} factor	ATL, dB
0	17.6	1.0000	1.0000	0
1	24.7	1.2337	1.3403	1.25
2	30.6	1.4311	1.6651	2.55
3	36.0	1.6104	1.9804	3.59

Placing a cosine-squared line source distribution on a pedestal reduced the beamwidth and the sidelobes through sidelobe cancellation between the two distributions. Likewise, placing a circular parabolic distribution (PD) on a pedestal reduces the sidelobes and the beamwidth for $N = 2$ and $N = 3$.

$$E(r) = \mathrm{PD} + (1 - \mathrm{PD})\left[1 - \left(\frac{r}{a}\right)^2\right]^N$$

where PD is the voltage pedestal. The pattern is the sum of the individual transforms.

Integrating Eq. (6-16) with the distribution gives the amplitude taper efficiency

$$\mathrm{ATL} = \frac{[\mathrm{PD} + (1 - \mathrm{PD})/(N + 1)]^2}{\mathrm{PD}^2 + \dfrac{2\,\mathrm{PD}\,(1 - \mathrm{PD})}{N + 1} + \dfrac{(1 - \mathrm{PD})^2}{2N + 1}} \tag{6-50}$$

Table 6-11 lists the pedestal level for a given sidelobe ($N = 3$) along with various pattern parameters.

6-11 Circular Gaussian Distribution [16]

A truncated gaussian distribution has a simple functional relation:

$$E(r) = e^{-\rho r^2} \qquad |r| \le 1 \tag{6-51}$$

We can easily calculate the edge taper through the conversion between logarithms.

$$\text{Edge taper (dB)} = 8.686\rho \tag{6-52}$$

We find the amplitude taper efficiency by substituting Eq. (6-51) into

TABLE 6-11 Pedestal Level to Achieve a Given Maximum Sidelobe for a Parabolic^3 on a Pedestal Circular-Aperture Distribution

Sidelobe level, dB	*Pedestal,* dB	*Beamwidth* factor	ATL, dB
30	−11.7	1.1673	0.87
32	−14.0	1.2121	1.21
34	−15.9	1.2504	1.50
35	−16.8	1.2686	1.64
36	−17.7	1.2868	1.77
38	−18.5	1.3029	1.88
40	−20.8	1.3477	2.19
42	−23.0	1.3877	2.44
44	−25.4	1.4273	2.68
44.7	−27.0	1.4508	2.82

TABLE 6-12 Circular-Aperture Gaussian Distribution $e^{-\rho r^2}$ $|r| \le 1$

Sidelobe level, dB	Edge taper, dB	ATL, dB	Beamwidth factor
20	4.30	0.09	1.0466
22	7.18	0.24	1.0800
24	9.60	0.41	1.1109
25	10.67	0.50	1.1247
26	11.67	0.59	1.1385
28	13.42	0.76	1.1626
30	14.93	0.92	1.1839
32	16.23	1.06	1.2028
34	17.32	1.18	1.2188
35	17.81	1.23	1.2263
36	18.75	1.34	1.2405
38	21.43	1.65	1.2820
40	24.42	2.00	1.3296

Eq. (6-16) and carrying out the integrations:

$$\text{ATL} = \frac{2(1 - e^{-\rho})^2}{\rho(1 - e^{-2\rho})} \tag{6-53}$$

Table 6-12 lists designs for various sidelobe levels in terms of the single parameter: edge taper. Equation (6-52) relates the parameter ρ to the edge taper.

Example Estimate the beamwidth of the pattern radiated from a circular distribution with a 13-dB edge taper and radius of three wavelengths.

We can use linear interpolation in Table 6-12 to find the beamwidth factor.

$$\text{From Eq. (6-46) HPBW} = 2\sin^{-1}\frac{1.1568(0.5145)}{6} = 11.38^\circ$$

$$\text{From Eq. (6-47) HPBW} = 58.95^\circ\frac{1.1568}{6} = 11.36^\circ$$

The amplitude taper efficiency is calculated from Eq. (6-53):

$$\rho = \frac{13}{8.686} = 1.497$$

$$\text{ATL} = \frac{2(1 - e^{-1.497})^2}{1.497(1 - e^{-2.993})} = 0.847 \quad (-0.72\text{ dB})$$

We obtain the same value by interpolating in Table 6-12.

Sidelobes below 40 dB are difficult to obtain with this distribution. The inner sidelobes continue to decrease with a decreasing edge level, but the outer lobes fail to reduce and dominate over the first few sidelobes.

Table 6-12 results from a search because no direct method exists for finding the edge taper for a specified sidelobe level.

6-12 Hansen Single-Parameter Circular Distribution [17, 18]

This distribution leads directly from sidelobe level to a single parameter H that relates through closed-form expressions to all other distribution parameters. The pattern of a uniform distribution is modified close in to the main beam. By using the U-space variable of Taylor, we have

$$U = \frac{2a}{\lambda} \sin \theta$$

where a is the radius. The pattern has different expressions in two regions

$$f(U) = \frac{2I_1(\pi\sqrt{H^2 - U^2})}{\pi\sqrt{H^2 - U^2}} \qquad |U| \leq H \tag{6-54a}$$

$$f(U) = \frac{2J_1(\pi\sqrt{U^2 - H^2})}{\pi\sqrt{U^2 - H^2}} \qquad |U| \geq H \tag{6-54b}$$

$I_1(x)$ is the first-order modified Bessel function of the first kind.

The high function value of Eq. (6-54a) at boresight reduces the sidelobes of the uniform distribution [Eq. (6-54b)], 17.57 dB, below the level at $U = H$. The sidelobe level is

$$\text{SLR} = 17.57 + 20 \log \frac{2I_1(\pi H)}{\pi H} \tag{6-55}$$

Given the sidelobe level [positive (dB)], we use Eq. (6-55) in an iteration scheme to find H.

The aperture distribution is given by

$$E(r) = I_0(\pi H\sqrt{1 - r^2}) \qquad |r| \leq 1 \tag{6-56}$$

where I_0 is the zeroth-order modified Bessel function of the first kind.

Equation (6-16) can be integrated for this circularly symmetrical distribution [Eq. (6-56)] to find the amplitude taper efficiency.

$$\text{ATL} = \frac{4I_1^2(\pi H)}{\pi^2 H^2[I_0^2(\pi H) - I_1^2(\pi H)]} \tag{6-57}$$

Table 6-13 lists the parameters of the Hansen distribution for various sidelobe levels. At the top, Tables 6-12 and 6-13 are very similar. Any sidelobe level can be achieved with this distribution subject to tolerance problems generated by any low-sidelobe design. The distribution is not optimum, but it is convenient.

TABLE 6-13 Hansen Single-Parameter Circular-Aperture Distribution

Sidelobe level, dB	H	Edge taper, dB	ATL, dB	Beamwidth factor
20	0.48717	4.49	0.09	1.0484
22	0.66971	7.79	0.27	1.0865
24	0.82091	10.87	0.48	1.1231
25	0.88989	12.35	0.60	1.1409
26	0.95573	13.79	0.72	1.1584
28	1.08027	16.59	0.96	1.1924
30	1.19770	19.29	1.19	1.2252
32	1.30988	21.93	1.42	1.2570
34	1.41802	24.51	1.64	1.2876
35	1.47084	25.78	1.75	1.3026
36	1.52295	27.04	1.85	1.3174
38	1.62525	29.53	2.05	1.3462
40	1.72536	31.98	2.24	1.3742
45	1.96809	38.00	2.68	1.4410
50	2.20262	43.89	3.08	1.5039

6-13 Taylor Circular-Aperture Distribution [19]

Like the line source, the Taylor circular-aperture distribution modifies inner zeros of the uniform amplitude and phase circular-aperture k-space pattern to approximate the Dolph-Chebyshev distribution. By use of the variable

$$\pi U = ka \sin \theta$$

the uniform distribution pattern is found to be

$$\frac{J_1(\pi U)}{\pi U}$$

We remove $\bar{n} - 1$ inner zeros and add those of the Dolph-Chebyshev distribution.

$$f(U) = \frac{J_1(\pi U)\prod_{N=1}^{\bar{n}-1}\left(1 - \frac{U^2}{U_N^2}\right)}{\pi U \prod_{N=1}^{\bar{n}-1}\left(1 - \frac{U^2}{S_N^2}\right)} \tag{6-58}$$

Given a zero of $J_1(x)$, $J_1(x_{1N}) = 0$, let $x_{1N} = \pi S_N$. By retaining approximately the same number of zeros in the visible region as the uniform distribution, we avoid superdirectivity. The new zeros U_N are modified zeros of the uniform distribution

$$U_N = S_{\bar{n}} \frac{\sqrt{A^2 + (N - \frac{1}{2})^2}}{\sqrt{A^2 + (\bar{n} - \frac{1}{2})^2}} \tag{6-59}$$

where A relates to the maximum sidelobe level

$$\cosh \pi A = b$$

and $20 \log b =$ sidelobe level (dB). Equation (6-59) is the same as Eq. (6-24) except for the scaling constant $S_{\bar{n}}$, the $\bar{n}$th zero of $J_1(x)$ divided by π.

Equation (6-58) gives the U-space pattern of the new distribution. We expand the aperture distribution in a Fourier-Bessel series.

$$E(r) = \sum_{m=0}^{\bar{n}-1} B_m J_0(\pi S_m r) \qquad r \le 1 \tag{6-60}$$

We find the coefficients B_m by transforming the Fourier-Bessel series, Eq. (6-60), into U space and comparing the far-field pattern with Eq. (6-58). As indicated in Eq. (6-60), the series contains only $\bar{n}$ nonzero terms.

$$B_0 = 1$$

$$B_m = \frac{-\prod_{N=1}^{\bar{n}-1}\left(1 - \dfrac{S_m^2}{U_N^2}\right)}{J_0(\pi S_m)\prod_{\substack{N=1 \\ N \ne m}}^{\bar{n}-1}\left(1 - \dfrac{S_m^2}{S_N^2}\right)} \qquad m = 1, 2, \ldots, \bar{n} - 1 \tag{6-61}$$

Example Design a Taylor circular-aperture distribution with 30-dB maximum sidelobes and $\bar{n} = 6$.

We use Eq. (6-25) to find the constant A:

$$b = 10^{30/20} = 31.6228$$

$$A = \frac{\cosh^{-1} b}{\pi} = 1.32$$

We substitute this value into Eq. (6-59) to find the five nulls.

No.	*Null* U_N
1	1.5582
2	2.2057
3	3.1208
4	4.1293
5	5.1769

The first null of the uniform distribution occurs at

$$x_{11} = 3.83171 \qquad S_1 = \frac{x_{11}}{\pi} = 1.2197$$

We use this with the location of the first zero to find the null beamwidth factor

$$\mathrm{BW}_{\text{null}} = \frac{U_1}{S_1} = \frac{1.5582}{1.2197} = 1.2775$$

The coefficients of the Fourier series [Eq. (6-61)] are given below.

No.	B_m	B_m *normalized*	*Function*
0	1.0000	0.53405	1
1	0.93326	0.49841	$J_0(x_{11}r)$
2	0.038467	0.01808	$J_0(x_{12}r)$
3	−0.16048	−0.08570	$J_0(x_{13}r)$
4	0.16917	0.09035	$J_0(x_{14}r)$
5	−0.10331	−0.05517	$J_0(x_{15}r)$

Figure 6-8 contains the k-space pattern.

Tables 6-14, 6-15, and 6-16 list parameters for some designs of the circular Taylor distribution. Table 6-14, amplitude taper loss, shows that for each sidelobe level there is an optimum $\bar{n}$. As the sidelobes are lowered, the optimum value of $\bar{n}$ increases. The blanks are unsuitable designs. The beamwidth factor (Table 6-15) and the null beamwidth factor (Table 6-16) continue to decrease as $\bar{n}$ increases at a given sidelobe level. In all three tables the values depend primarily on the sidelobe level.

6-14 Bayliss Circular-Aperture Distribution [7]

We can also design a Bayliss distribution (difference pattern) for circular apertures. This gives us the pattern necessary for monopulse tracking along

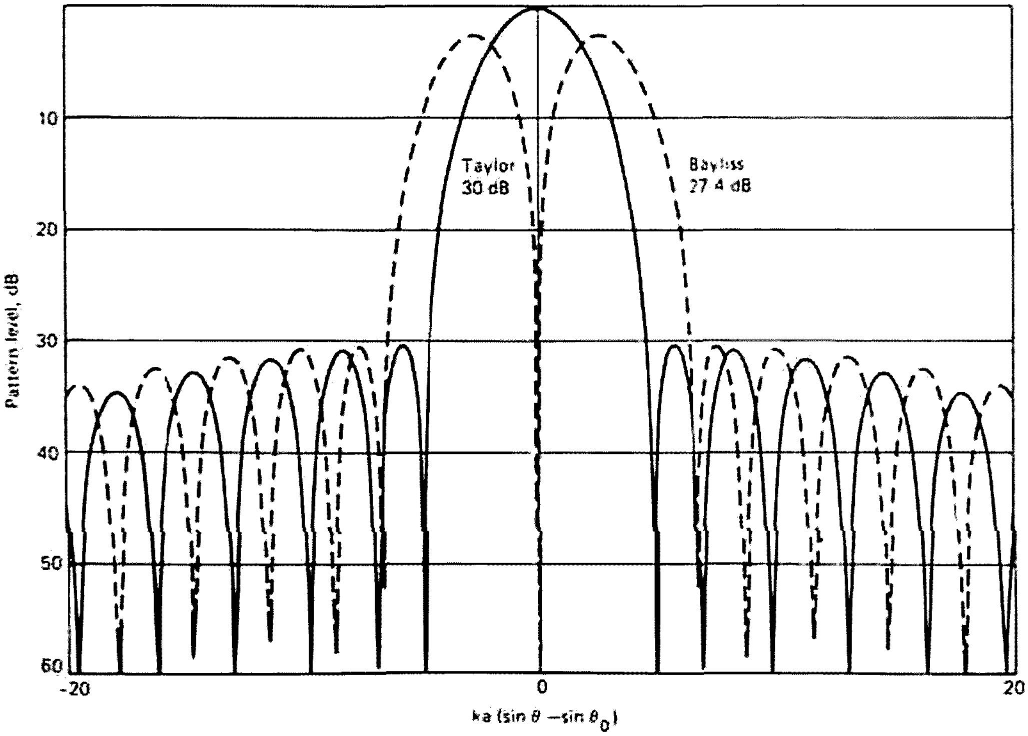

Figure 6-8 Taylor and Bayliss circular-aperture distributions to give 30-dB sidelobes ($\bar{n}$ = 6).

TABLE 6-14 Amplitude Taper Losses of Taylor Circular-Aperture Distribution

	ATL, dB, when sidelobe levels, dB, are as follows:					
$\bar{n}$	25	30	35	40	45	50
4	0.30	0.71	1.14	1.51	1.84	
6	0.28	0.59	1.03	1.48	1.88	2.23
8	0.43	0.54	0.94	1.40	1.82	2.21
12	1.03	0.62	0.86	1.28	1.71	2.12
16	1.85	0.86	0.87	1.22	1.64	2.05
20	—	1.20	0.94	1.20	1.60	2.01

TABLE 6-15 Beamwidth Factor of Taylor Circular-Aperture Distribution

	Beamwidth factors when sidelobe levels, dB, are as follows:					
$\bar{n}$	25	30	35	40	45	50
4	1.0825	1.1515	1.2115	1.2638	1.3095	
6	1.0504	1.1267	1.1957	1.2581	1.3149	1.3666
8	1.0295	1.1079	1.1796	1.2457	1.3067	1.3632
12	1.0057	1.0847	1.1580	1.2262	1.2899	1.3499
16	0.9927	1.0717	1.1451	1.2137	1.2782	1.3391
20	—	1.0634	1.1367	1.2054	1.2701	1.3314

TABLE 6-16 Null Beamwidth Factor of Taylor Circular-Aperture Distribution

	Null beamwidth factors when sidelobe levels, dB, are as follows:					
$\bar{n}$	25	30	35	40	45	50
4	1.1733	1.3121	1.4462	1.5744	1.6960	
6	1.1318	1.2775	1.4224	1.5654	1.7056	1.8426
8	1.1066	1.2530	1.4001	1.5470	1.6928	1.8370
12	1.0789	1.2244	1.3716	1.5197	1.6680	1.8162
16	1.0643	1.2087	1.3552	1.5029	1.6514	1.8003
20	—	1.1989	1.3442	1.4920	1.6402	1.7890

one axis. The U-space pattern has modified zeros to produce nearly equal sidelobes close in to the main lobes

$$f(U,\phi) = \cos\phi\; \pi U J_1'(\pi U) \frac{\prod_{N=1}^{\bar{n}-1}\left(1 - \frac{U^2}{U_N^2}\right)}{\prod_{N=0}^{\bar{n}-1}\left(1 - \frac{U^2}{\mu_N^2}\right)} \tag{6-62}$$

TABLE 6-17 Bessel Function Zeros, $J_1'(\pi\mu_N)$

N	μ_N	N	μ_N	N	μ_N	N	μ_N
0	0.5860670	5	5.7345205	10	10.7417435	15	15.7443679
1	1.6970509	6	6.7368281	11	11.7424475	16	16.7447044
2	2.7171939	7	7.7385356	12	12.7430408	17	17.7450030
3	3.7261370	8	8.7398505	13	13.7435477	18	18.7452697
4	4.7312271	9	9.7408945	14	14.7439856	19	19.7455093

where U_N are the new zeros and $\pi\mu_N$ are zeros of $J_1'(\pi U)$. Bayliss lists those zeros μ_N; see Table 6-17. The inner zeros have been removed and replaced by new ones, U_N. We find the zeros in a manner similar to that used for a linear distribution (Sec. 6-7).

$$U_N = \begin{cases} \mu_{\bar{n}}\left(\dfrac{\xi_N^2}{A^2 + \bar{n}^2}\right)^{1/2} & N = 1, 2, 3, 4 \\[2ex] \mu_{\bar{n}}\left(\dfrac{A^2 + N^2}{A^2 + \bar{n}^2}\right)^{1/2} & N = 5, 6, \ldots, \bar{n} - 1 \end{cases} \tag{6-63}$$

The four inner zeros had to be adjusted to achieve the desired sidelobe level. Bayliss found them through a computer search. The values for ξ_N and A can be found through the polynomial approximations [Eq. (6-36)].

The aperture distribution, like the Taylor circular aperture distribution, is expanded in a finite-length Fourier-Bessel series

$$E(r, \phi) = \cos\phi' \sum_{m=0}^{\bar{n}-1} B_m J_1(\pi\mu_m r) \qquad r \le 1 \tag{6-64}$$

where the coefficients are found by transforming Eq. (6-64) and comparing it with a U-space pattern [Eq. (6-62)]. The coefficients are given by

$$B_m = \frac{\mu_m^2}{jJ_1(\pi\mu_m)} \frac{\prod_{N=1}^{\bar{n}-1}\left(1 - \dfrac{\mu_m^2}{U_N^2}\right)}{\prod_{\substack{N=0 \\ N \ne m}}^{\bar{n}-1}\left(\dfrac{1 - \mu_m^2}{\mu_N^2}\right)} \tag{6-65}$$

Example Design a Bayliss circular-aperture distribution with 30-dB sidelobes and $\bar{n} = 6$.

We start with Eqs. (6-36) to find the coefficients A and ξ_N: $A = 1.64126$, $\xi_1 = 2.07086$, $\xi_2 = 2.62754$, $\xi_3 = 3.43144$, and $\xi_4 = 4.32758$. We substitute those constants into Eq. (6-63) along with the zeros from Table 6-17 to find the modified zeros.

N	1	2	3	4	5
U_N	2.2428	2.8457	3.7163	4.6868	5.6994

We use the zeros in Eq. (6-62) to find the pattern. The U-space pattern peak can be found by using Eq. (6-37)

$$U_{\max} = 0.7988 \qquad ka \sin\theta_{\max} = \pi U_{\max} = 2.5096$$

where a is the aperture radius.

The coefficients of the Fourier-Bessel series are found from Eq. (6-65).

No.	B_m	B_m *normalized*	*Function*
0	0.62680	1.2580	$J_1(\pi\mu_0 r)$
1	0.50605	1.0157	$J_1(\pi\mu_1 r)$
2	−0.06854	−0.03415	$J_1(\pi\mu_2 r)$
3	−0.0028703	−0.005761	$J_1(\pi\mu_3 r)$
4	0.014004	0.028106	$J_1(\pi\mu_4 r)$
5	−0.011509	−0.02310	$J_1(\pi\mu_5 r)$

The normalized coefficients give an aperture distribution peak of 1. The 3-dB pattern points can be found by searching the pattern.

$$ka \sin\theta_1 = 1.3138 \qquad ka \sin\theta_2 = 4.2384$$

Figure 6-8 contains a plot of a Bayliss circular-aperture distribution ($\bar{n} = 6$) designed to have sidelobes 30 dB below those of the Taylor distribution with 30-dB sidelobes. The losses to the difference pattern are about 2.6 dB higher than the sum pattern. The amplitude taper efficiency is calculated from

$$\mathrm{ATR} = \frac{\left(\int_0^1 4\left|\sum_{m=0}^{\bar{n}-1} B_m J_1(\pi\mu_m r)\right| r\,dr\right)^2}{\pi^2 \int_0^1 \left|\sum_{m=0}^{\bar{n}-1} B_m J_1(\pi\mu_m r)\right|^2 r\,dr} \tag{6-66}$$

where the integrals over ϕ' have been separated and evaluated. Likewise, an integral expression for the phase error efficiency can be found by evaluating the separable $\cos\phi'$ integrals along the coordinate $\phi = 0$, the peak.

$$\mathrm{PEL}(U) = \frac{\left|2\pi \int_0^1 \sum_{m=0}^{\bar{n}-1} B_m J_1(\pi\mu_m r) J_1(\pi U r)\, r\,dr\right|^2}{\left(4\int_0^1 \left|\sum_{m=0}^{\bar{n}-1} B_m J_1(\pi\mu_m r)\right| r\,dr\right)^2} \tag{6-67}$$

Table 6-18 lists the parameters of Bayliss circular-aperture distributions with $\bar{n} = 10$ and various sidelobe levels. The optimum design for $\bar{n} = 10$ occurs for 25-dB sidelobes.

6-15 Aperture Blockage

Blocking an aperture reduces the gain and raises the sidelobes. The blockage either scatters the aperture power in unwanted directions in a broad pattern

TABLE 6-18 Characteristics of a Bayliss Circular-Aperture Distribution with $\bar{n}$ = 10

	Beam peak	3-dB beam edges			
Sidelobe level, dB	$\frac{ka}{2}\sin\theta_{\max}$	$\frac{ka}{2}\sin\theta_1$	$\frac{ka}{2}\sin\theta_2$	ATL, dB	PEL, dB
20	2.2366	1.165	3.700	1.47	1.80
25	2.3780	1.230	3.940	1.15	1.89
30	2.5096	1.290	4.160	1.32	1.96
35	2.6341	1.346	4.363	1.62	2.01
40	2.7536	1.399	4.551	1.95	2.05

or is just an area without fields. Scattering blockage causes higher sidelobes and greater loss than the nonexcitation blockage.

Scattered blockage has the same power input as the unblocked aperture, but fields scattered off the blockage do not contribute significantly to the maximum field. Compared to the unblocked aperture, the blockage efficiency becomes

$$\text{Blockage efficiency} = \frac{\left|\iint_{\text{blocked}} Ee^{jk\cdot r'}\,ds'\right|^2_{\max}}{\left|\iint_{\text{unblocked}} Ee^{jk\cdot r'}\,ds'\right|^2_{\max}} \qquad \text{scattered} \qquad (6\text{-}68)$$

We use Eq. (2-12) to find the directivity of each distribution by the total power radiated from the unblocked aperture [denominator of Eq. (2-12)] for the blocked aperture. A centrally blocked circular aperture with a uniform distribution has the following blockage efficiency

$$(1 - b^2)^2 \qquad \text{scattered}$$

where b is the normalized blockage radius.

The second type of blockage is an area without fields. The blockage does not waste power in the aperture. When we take the ratio of the two directivities, we must account for the power in each aperture

$$\text{Blockage efficiency} = \frac{\left|\iint_{\text{blocked}} Ee^{jk\cdot r'}\,ds'\right|^2_{\max} \iint_{\text{unblocked}} |E|^2\,ds'}{\left|\iint_{\text{unblocked}} Ee^{jk\cdot r'}\,ds'\right|^2_{\max} \iint_{\text{blocked}} |E|^2\,ds'} \qquad \text{nonexcitation} \qquad (6\text{-}69)$$

The blockage of a uniformly excited centrally blocked circular aperture where the center is not excited reduces the directivity only by the area lost from the aperture

$1 - b^2$ nonexcitation

In a sense, nonexcitation blockage is not a true loss; it is a loss of potential radiation aperture.

Table 6-19 lists the blockage losses of centrally blocked circular apertures calculated by Eq. (6-68), the more severe case. The uniformly excited aperture is affected least by blockage. All points are equally important. The tapered distributions suffer more loss with increased taper toward the edge. The lists for different tapered distributions track each other fairly closely, and any one of them gives a good estimate of the blockage loss.

Blockage causes sidelobes. In the case of scattered blockage the exact sidelobes cannot be found without an analysis of the scatterer. A Cassegrain reflector would need a geometric theory of diffraction (GTD) analysis to locate the directions of scattering from the subreflector. We can handle the nonexcitation blockage in a general fashion. Consider the aperture to be broken into two radiating apertures. The first is the unblocked aperture; the

TABLE 6-19 Blockage Losses, dB, of Circular-Aperture Distributions

	Distribution					
			Taylor, $\bar{n} = 6$		Hansen single-parameter	
	Uniform	Parabolic	30 dB	40 dB	30 dB	40 dB
Central blockage, %	Blockage losses, dB					
5	0.02	0.04	0.04	0.05	0.05	0.07
6	0.03	0.06	0.06	0.08	0.07	0.09
7	0.04	0.08	0.08	0.11	0.09	0.13
8	0.06	0.11	0.10	0.14	0.12	0.17
9	0.07	0.14	0.13	0.18	0.16	0.21
10	0.09	0.18	0.16	0.22	0.19	0.26
11	0.11	0.21	0.20	0.26	0.23	0.32
12	0.13	0.25	0.24	0.31	0.28	0.38
13	0.15	0.30	0.28	0.37	0.33	0.44
14	0.17	0.34	0.32	0.43	0.38	0.51
15	0.20	0.40	0.37	0.49	0.43	0.59
16	0.22	0.45	0.42	0.56	0.49	0.67
17	0.26	0.51	0.48	0.63	0.56	0.76
18	0.29	0.57	0.54	0.71	0.63	0.85
19	0.32	0.64	0.60	0.79	0.70	0.95
20	0.36	0.71	0.67	0.88	0.77	1.06
21	0.39	0.78	0.74	0.97	0.86	1.17
22	0.43	0.86	0.81	1.07	0.94	1.28
23	0.47	0.94	0.88	1.17	1.03	1.40
24	0.52	1.03	0.96	1.27	1.12	1.53
25	0.56	1.12	1.05	1.38	1.22	1.66

second is the blockage. If we take the blockage aperture to be 180° out of phase with respect to the unblocked aperture distribution, the sum gives us the blocked distribution. We use this analysis as an approximation to scattered blockage with the realization that scattering may produce unpredicted lobes.

We can find an upper bound on the sidelobes easily. Assume that the blockage distribution is uniform and produces a broad flat beam in comparison to the main aperture. Since the blockage aperture fields are 180° out of phase from the unblocked aperture fields, their radiation subtracts from the main beam and adds sidelobes that are 180° out of phase with respect to the main lobe. The sidelobe due to the blockage is proportional to the area.

$$\text{Sidelobe level} = 20 \log b$$

This formula gives values much higher than are realized. Table 6-20 lists the sidelobes of a centrally blocked Taylor circular aperture distribution with 40-dB design sidelobes. They are far less than predicted by the upper bound.

Ludwig [20] has found distributions to reduce the sidelobes of blocked apertures. The first sidelobe can be reduced only a little, but the outer sidelobe levels can be controlled. In many applications one high sidelobe next to the main beam is acceptable. A Taylor distribution for circular apertures with a zero edges value, like Sec. 6-6 for linear apertures, reduces the far-out sidelobes. A second aperture function with a doughnut distribution also reduces all but the first sidelobe. Reducing the edge taper of the blockage distribution lowers the blockage caused sidelobes.

Sachidananda and Ramakrishna [21] use a numerical optimization technique to reduce the sidelobes of a blocked aperture for both the sum and difference patterns of a monopulse excitation. They start with the Taylor and Bayliss circular-aperture distribution functions [Eqs. (6-60) and (6-64)]. The coefficients B_m are determined through the numerical optimization which restrains the sidelobes while optimizing the monopulse tracking coefficients and sum pattern gain.

TABLE 6-20 Sidelobe Level Due to Central Blockage of a Circular Aperture with Taylor Distribution (40 dB, $\bar{n}$ = 6)

Blockage, % of diam.	Sidelobe level, dB	Blockage, % of diam.	Sidelobe level, dB	Blockage, % of diam.	Sidelobe level, dB
7	34.5	13	26.1	19	21.1
8	32.8	14	25.6	20	20.4
9	31.3	15	24.2	21	19.7
10	29.8	16	23.3	22	19.1
11	28.5	17	22.5	23	18.5
12	27.3	18	21.7	24	18.0

6-16 Quadratic Phase Error

A linear phase error function scans the aperture beam with some loss of gain because of the shrinking of the projected aperture in the direction of the main beam. Quadratic phase error (order 2) does not scan the beam but causes loss and a change in the sidelobe levels and the depth of the nulls between them. This phase error arises mainly from defocusing when the source of radiation appears as a point source. A feed axially displaced from the focus of a parabolic reflector produces quadratic phase error in the aperture. The flare angle of a horn changes the distance from the assumed point source in the throat to different points in the aperture at the end of the flare. We can approximate the phase distribution as quadratic.

We express the quadratic phase error in a line source aperture as

$$\text{Linear} \qquad e^{-j2\pi S(2x/a)^2} \qquad |x/a| \le 0.5 \tag{6-70a}$$

where S is a dimensionless constant, cycles, and a is the aperture width. Likewise, the circular-aperture phase is

$$\text{Circular} \qquad e^{-j2\pi Sr^2} \qquad r \le 1 \tag{6-70b}$$

where r is the normalized radius. We use Eq. (6-15) with the linear source aperture phase error [Eq. (6-70a)] and use Eq. (6-17) with the quadratic phase error [Eq. (6-70b)] in a circularly symmetrical aperture distribution to find the phase error loss.

$$\text{PEL}_x = \frac{\left|\int_{-a/2}^{a/2} E(x)e^{-j2\pi S(2x/a)^2}\,dx\right|^2}{\left(\int_{-a/2}^{a/a} |E(x)|\,dx\right)^2} \qquad \text{linear} \tag{6-71}$$

$$\text{PEL} = \frac{\left|\int_0^1 E(r)e^{-j2\pi Sr^2}r\,dr\right|^2}{\left(\int_0^1 |E(r)|r\,dr\right)^2} \qquad \text{circular} \tag{6-72}$$

A few distributions have simple formulas for the phase error efficiency when excited with quadratic phase error [22].

$$\text{Uniform linear} \qquad \text{PEL}_x = \frac{1}{4S}[C^2(2\sqrt{S}\,) + S^2(2\sqrt{S}\,)] \tag{6-73}$$

where $C(t)$ and $S(t)$ are the Fresnel integrals, which are tabulated functions.

$$\text{Uniform circular} \qquad \text{PEL} = \left(\frac{\sin \pi S}{\pi S}\right)^2 \tag{6-74}$$

Circular gaussian $(e^{-\rho r^2})$

$$\text{PEL} = \frac{\rho^2[1 - 2e^{-\rho}\cos(2\pi S) + e^{-2\rho}]}{[\rho^2 + (2\pi S)^2](1 - e^{-\rho})^2} \tag{6-75}$$

We use numerical integration for the general distribution.

Table 6-21 lists quadratic phase error losses for various linear-aperture distributions. We will use the lists for uniform and cosine distributions to evaluate the gains of rectangular horns. The effect of quadratic phase error decreases as the distribution taper increases. Table 6-22 lists results for a few circularly symmetrical aperture distributions.

Quadratic phase error raises the sidelobes of low-sidelobe antennas. Figure 6-9 shows the effects on a circular Taylor distribution with 35-dB design sidelobes. The first lobe increases, and the null between the main lobe and the first sidelobe disappears as the quadratic phase error increases. A source antenna spaced a finite distance, as on an antenna measurement range, feeds the aperture with a quadratic phase error. The source would have to be spaced $8D^2/\lambda$ to measure the sidelobe level within 0.5 dB.

TABLE 6-21 Quadratic Phase Error Loss, dB, of Linear-Aperture Distributions

Cycles S	Distribution			
	Uniform	cos	$\cos^2$	$\cos^2$ + pedestal (−19.9 dB)
	Quadratic phase error loss, dB			
0.05	0.04	0.02	0.01	0.02
0.10	0.15	0.07	0.04	0.07
0.15	0.34	0.16	0.09	0.16
0.20	0.62	0.29	0.16	0.28
0.25	0.97	0.45	0.25	0.44
0.30	1.40	0.65	0.36	0.63
0.35	1.92	0.88	0.49	0.84
0.40	2.54	1.14	0.64	1.08
0.45	3.24	1.43	0.80	1.34
0.50	4.04	1.75	0.97	1.62
0.55	4.93	2.09	1.16	1.90
0.60	5.91	2.44	1.36	2.19
0.65	6.96	2.82	1.57	2.48
0.70	8.04	3.20	1.79	2.76
0.75	9.08	3.58	2.01	3.04
0.80	9.98	3.95	2.23	3.29
0.85	10.60	4.31	2.46	3.52
0.90	10.87	4.65	2.69	3.73
0.95	10.80	4.97	2.91	3.92
1.00	10.50	5.25	3.13	4.09

TABLE 6-22 Quadratic Phase Error Loss, dB, of Circular-Aperture Distributions

Cycles S	Distribution					
			Taylor, $\bar{n} = 6$		Hansen single-parameter	
	Uniform	Parabolic	30 dB	40 dB	30 dB	40 dB
	Quadratic phase error loss, dB					
0.05	0.04	0.02	0.04	0.03	0.03	0.02
0.10	0.14	0.10	0.15	0.11	0.11	0.08
0.15	0.32	0.22	0.33	0.26	0.25	0.19
0.20	0.58	0.38	0.59	0.46	0.45	0.34
0.25	0.91	0.60	0.93	0.72	0.70	0.53
0.30	1.33	0.87	1.36	1.03	1.01	0.76
0.35	1.83	1.18	1.86	1.41	1.38	1.03
0.40	2.42	1.55	2.46	1.84	1.81	1.34
0.45	3.12	1.97	3.16	2.33	2.30	1.69
0.50	3.92	2.44	3.95	2.87	2.85	2.08
0.55	4.86	2.97	4.86	3.47	3.46	2.50
0.60	5.94	3.56	5.88	4.11	4.16	2.95
0.65	7.20	4.20	7.01	4.79	4.85	3.43
0.70	8.69	4.89	8.25	5.50	5.63	3.94
0.75	10.46	5.64	9.56	6.21	6.43	4.46
0.80	12.62	6.44	10.87	6.91	7.26	4.98
0.85	15.39	7.29	12.01	7.56	8.09	5.51
0.90	19.23	8.16	12.80	8.14	8.88	6.03
0.95		9.06		8.62	9.60	6.53
1.00		9.94		8.99	10.20	6.99

Low-sidelobe antennas require greater distances than the usual $2D^2/\lambda$ for accurate sidelobe measurement [2].

6-17 Beam Efficiency of Circular Apertures with Axisymmetric Distributions

From Eq. (1-17) we can derive an approximate formula for axisymmetric distributions that depends on the normalized variable k_r (or U). For large apertures we can approximate $\cos\theta \approx 1$ in the main beam, integrate the ϕ integral to obtain 2π, and incorporate the $(ka)^2$ directivity factor into the integral.

$$\text{Beam efficiency} = \frac{\text{ATL PEL} \displaystyle\int_0^{k_{r1}} |f(k_r)|^2 k_r \, dk_r}{2|f(0)|^2} \tag{6-76}$$

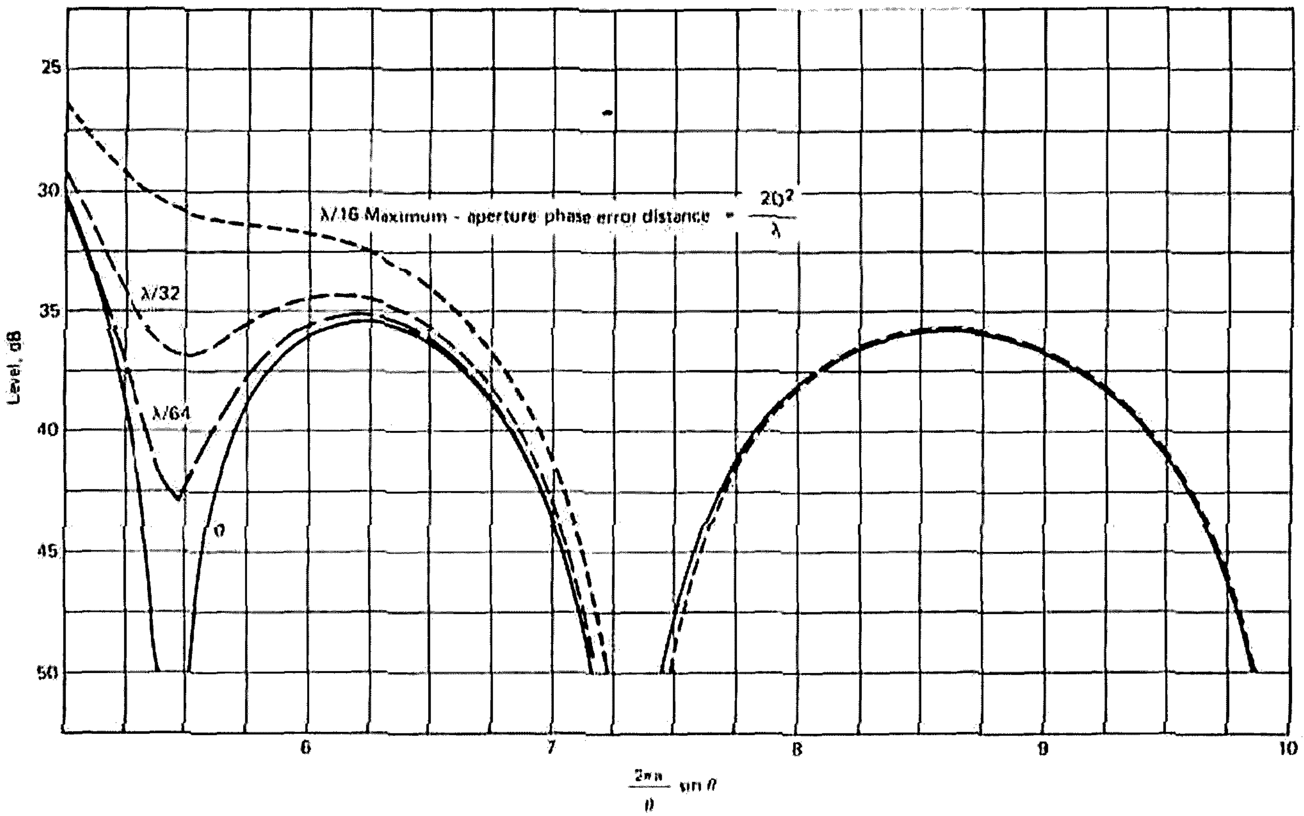

Figure 6-9 Effects of quadratic phase error on 35-dB circular Taylor distribution ($\bar{n}$ = 6).

TABLE 6-23 Beam Efficiencies of Axisymmetric Circular-Aperture Distributions

Distribution	Null k_r	Beam eff. at null, %	Specified beam efficiency 80%	85%	90%	95%
			$k_r = \frac{2\pi a \sin\theta}{\lambda}$			
Uniform	3.83	83.7	2.82	4.71	5.98	
Parabolic	5.14	98.2	2.81	3.03	3.31	3.75
Parabolic + 12-dB pedestal	4.58	96.4	2.60	2.81	3.10	3.64
Taylor; 30 dB, $\bar{n} = 6$	4.90	96.2	2.65	2.88	3.19	3.82
Taylor; 30 dB, $\bar{n} = 10$	4.74	91.4	2.76	3.06	3.65	
Taylor; 40 dB, $\bar{n} = 6$	6.00	99.5	2.90	3.13	3.42	3.85
Hansen, 30 dB	5.37	99.3	2.79	3.01	3.28	3.69
Hansen, 40 dB	6.64	99.9	3.17	3.42	3.73	4.19

$$\text{Beam efficiency} = \frac{\text{ATL PEL} \int_0^{U_1} |f(U)|^2 U \, dU}{2|f(0)|^2} \tag{6-77}$$

where k_r is the factor $(2\pi a \sin\theta)/\lambda$, U (the Taylor distribution factor) is $(2a \sin\theta)/\lambda$, and a is the aperture radius. U_1 and k_{r1} correspond to the beam edge θ_1. The integrals of Eqs. (6-76) and (6-77) cause underestimations of beam efficiency for small apertures when we ignore the cos θ factor which should divide the argument of the integral.

Table 6-23 lists beam edges in k_r space $(2\pi a \sin\theta/\lambda)$ for various distributions along with the beam efficiency at the null beam edge. We can use it to determine the aperture size required for a given beam efficiency beamwidth specification.

Example Find the aperture radius to give a 90 percent beam efficient beamwidth of 5° for the distribution: parabolic on 12-dB pedestal.

From Table 6-23, $k_r\,(90\%) = 3.10 = \dfrac{2\pi a}{\lambda} \sin \dfrac{5°}{2}$

$$\frac{a}{\lambda} = \frac{3.10}{2\pi \sin(5°/2)} = 11.31$$

The beam edge has cos 2.5° = 0.999, which justifies the approximation in Eq. (6-76).

REFERENCES

1. R. F. Harrington, *Time Harmonic Electromagnetic Fields,* McGraw-Hill, New York, 1961, pp. 106–110, 113–115.
2. P. S. Hacker and H. E. Schrank, "Range Requirements for Measuring Low and Ultralow Sidelobe Antenna Patterns," *IEEE Trans. Antennas Propagat.*, vol. AP-30, no. 5, September 1982, pp. 956–966.
3. T. T. Taylor, "Design of Line Source Antennas for Narrow Beamwidth and Low Sidelobes," *IEEE Trans. Antennas Propagat.*, vol. AP-4, no. 1, January 1955, pp. 16–28.
4. C. L. Dolph, "A Current Distribution for Broadside Arrays which Optimizes the Relationship between Beamwidth and Sidelobe Level," *Proc. IRE*, vol. 34, June 1946, pp. 335–348.
5. D. R. Rhodes, "On a New Condition for Physical Realizability of Planar Antennas," *IEEE Trans. Antennas Propagat.*, vol. AP-19, no. 2, March 1971, pp. 162–166.
6. D. R. Rhodes, "On the Taylor Distribution," *IEEE Trans. Antennas Propagat.*, vol. AP-20, no. 2, March 1972, pp. 143–145.
7. E. T. Bayliss, "Design of Monopulse Antenna Difference Patterns with Low Sidelobes," *Bell System Tech. J.*, vol. 47, May–June 1968, pp. 623–650.
8. R. S. Elliott, *Antenna Theory and Design*, Prentice-Hall, Englewood Cliffs, N.J., 1981.
9. R. F. Hyneman, "A Technique for the Synthesis of Line Source Antenna Patterns Having Specified Sidelobe Behavior," *IEEE Trans. Antennas Propagat.*, vol. AP-16, no. 4, July 1968, pp. 430–435.
10. R. S. Elliott, "Design of Line Source Antennas for Narrow Beamwidth and Asymmetric Low Sidelobes," *IEEE Trans. Antennas Propagat.*, vol. AP-23, no. 1, January 1975, pp. 100–107.
11. R. S. Elliott, "Design of Line Source Antennas for Sum Patterns with Sidelobes of Individually Arbitrary Heights," *IEEE Trans. Antennas Propagat.*, vol. AP-24, no. 1, January 1976, pp. 76–83.
12. R. S. Elliott, "Design of Line Source Antennas for Difference Patterns with Sidelobes of Individually Arbitrary Heights," *IEEE Trans. Antennas Propagat.*, vol. AP-24, no. 3, May 1976, pp. 310–316.
13. F. I. Tseng, "Design of Array and Line Source Antennas for Taylor Patterns with a Null," *IEEE Trans. Antennas Propagat.*, vol. AP-27, no. 4, July 1979, pp. 474–479.
14. P. M. Woodward, "A Method of Calculating the Field Over a Plane Aperture Required to Produce a Given Polar Diagram," *Proc. IEE*, vol. 93, pt. IIIA, 1947, pp. 1554–1558.
15. S. Silver (ed.), *Microwave Antenna Theory and Design*, McGraw-Hill, New York, 1949, p. 194.
16. G. Doundoulakis and S. Gethin, "Far Field Patterns of Circular Paraboloidal Reflectors," *IRE Natl. Conv. Record*, pt. 1, 1959, pp. 155–173.
17. R. C. Hansen, "Circular Aperture Distribution with One Parameter," *Electronic Letters*, vol. 11, no. 8, 17th April 1975, p. 184.
18. R. C. Hansen, "A One-Parameter Circular Aperture with Narrow Beamwidth and Low Sidelobes," *IEEE Trans. Antennas Propagat.*, vol. AP-24, no. 4, July 1976, pp. 477–480.
19. T. T. Taylor, "Design of Circular Apertures for Narrow Beamwidth and Low Side Lobes," *IEEE Trans. Antennas Propagat.*, vol. AP-8, no. 1, January 1960, pp. 17–22.
20. A. C. Ludwig, "Low Sidelobe Aperture Distributions for Blocked and Unblocked Circular Apertures," *IEEE Trans. Antennas Propagat.*, vol. AP-30, no. 5, September 1982, pp. 933–946.
21. M. Sachidananda and S. Ramakrishna, "Constrained Optimization of Monopulse Circular Aperture Distribution in the Presence of Blockage," *IEEE Trans. Antennas Propagat.*, vol. AP-31, no. 2, March 1983, pp. 286–293.
22. A. W. Love, "Quadratic Phase Error Loss in Circular Apertures," *Electronics Letters*, vol. 15, no. 10, 10th May 1979, pp. 276, 277.

CHAPTER 7

HORN ANTENNAS

Horn antennas have a long history traced, in part, in the collection of papers by Love [1] along with papers on every other horn topic. Horns have a wide variety of uses from small-aperture antennas to feed reflectors to large-aperture antennas used by themselves as medium-gain antennas. Horns can be excited in any polarization or combinations of polarizations. The purity of polarization possible and the unidirectional pattern make horns good laboratory standards and ideal reflector feeds. Horns also closely follow the characteristics predicted by simple theories.

Horns are analyzed with a variety of techniques. Barrow and Chu [2] analyzed a sectoral horn, flaring in only one plane, by solving the boundary value problem in the wedge. They expanded the fields in terms of Hankel functions in cylindrical coordinates. The fields form an equiphase surface over a cylindrical cap on which the Kirchhoff-Huygens equivalent current method [Eq. (6-7)] can be applied to find the pattern. Similarly, Schorr and Beck [3] use spherical Hankel and Legendre functions to analyze conical horns. The integration surface consists of a spherical cap. Schelkunoff and Friis [4] use the mouth of the horn as the aperture and approximate the phase distribution as quadratic. Both aperture theories have the same valid pattern range. The method accurately predicts patterns in the area in front of the aperture. The error increases as the plane of the aperture is approached. The predicted pattern remains continuous and gives no indication of its increasing error. GTD methods [5] predict the pattern in back of as well as in front of the aperture while providing estimates of the error in the predictions. Most of the details needed for design can be obtained from the aperture theory. Only GTD accurately predicts sidelobes, since no assumption of zero fields outside the horn aperture is made.

Figure 7-1 shows the general horn geometry. The input waveguide can be either rectangular or circular (elliptical). W is the width of a rectangular aperture, and a is the radius of a circular aperture. The distance from the junction of the projected sides to the aperture is the slant radius R. Distance along the centerline from the aperture to the waveguide is the axial length.

We find the aperture field amplitude from the input waveguide mode. The phase distribution is approximately quadratic across the aperture. We assume that the aperture fields radiate in spherical waves from the projected juncture of the sides. The extra distance along the sides compared with the distance to the center of the aperture is given by

$$\begin{aligned}\Delta &= R - \sqrt{R^2 - a^2}\\ &= R\left(1 - \sqrt{1 - \frac{a^2}{R^2}}\right)\\ &\approx R\left[1 - \left(1 - \frac{a^2}{2R^2}\right)\right] = \frac{a^2}{2R} = \frac{W^2}{8R}\end{aligned}$$

On dividing by the wavelength, we obtain the dimensionless constant S of the quadratic phase distribution.

$$S = \frac{\Delta}{\lambda} = \frac{W^2}{8\lambda R} = \frac{a^2}{2\lambda R} \tag{7-1}$$

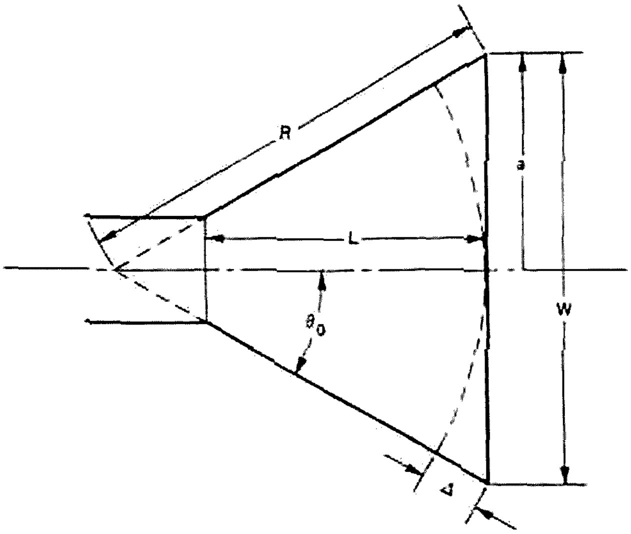

Figure 7-1 General geometry of a horn.

Since the semiflare angle θ_0 of most practical horns is small, we will use the quadratic phase error approximation.

7-1 Rectangular Horn (Pyramidal)

The rectangular horn flares out of a rectangular or square waveguide with flat metal walls. Figure 7-2 shows the horn geometry. The slant radii along the sides will be unequal, in general. The input waveguide dimensions are a width and b height. The aperture has width W in the H plane and height H in the E plane. Each aperture coordinate has its own quadratic phase distribution constant

$$S_e = \frac{H^2}{8\lambda R_e} \qquad S_h = \frac{W^2}{8\lambda R_h} \tag{7-2}$$

The TE_{10} mode of the lowest-order waveguide mode has the field distribution

$$E_y = E_0 \cos\left(\frac{\pi x}{a}\right) ,$$

In the aperture the electric field is approximated by

$$E_y = E_0 \cos\left(\frac{\pi x}{W}\right) \exp\left\{-j2\pi\left[S_e\left(\frac{2y}{H}\right)^2 + S_h\left(\frac{2x}{W}\right)^2\right]\right\} \tag{7-3}$$

The ratio of the electric and magnetic fields approaches the impedance of free space for large apertures. In this case, we use the Huygens source approximation and need only the electric field with Eq. (6-8) to find the pattern. Small-aperture horns require Eq. (6-7) with an arbitrary ratio of the magnetic and electric fields.

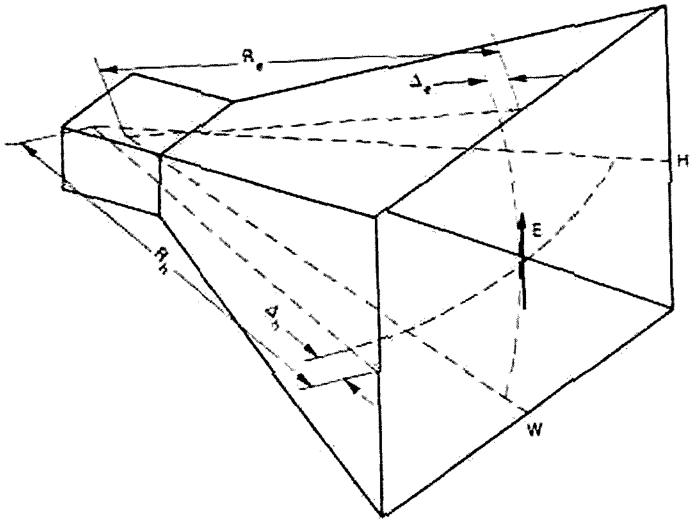

Figure 7-2 Rectangular-horn geometry.

The E-plane pattern comes from a uniform aperture distribution, and the H-plane aperture has a cosine distribution. Both have a quadratic phase error. In Figs. 7-3 and 7-4 the E- and H-plane patterns in U space of the Taylor distribution with S as a parameter are plotted. We can use them to find the pattern of a general rectangular horn.

Example Find the pattern level at $\theta = 15°$ in the E and H planes of a horn with the following measured dimensions:
Aperture: W (H plane) = 28.9 cm H (E plane) = 21.3 cm
Input waveguide: Width a = 3.50 cm height b = 1.75 cm
The slant distance from the aperture to the waveguide along the center of each plate of the flare was measured.

$$D_h = 44.8 \text{ cm} \qquad D_e = 44.1 \text{ cm}$$

We find the slant radius from similar triangles

$$\frac{R_h}{D_h} = \frac{W}{W - a} \qquad \frac{R_e}{D_e} = \frac{H}{H - b} \tag{7-4}$$

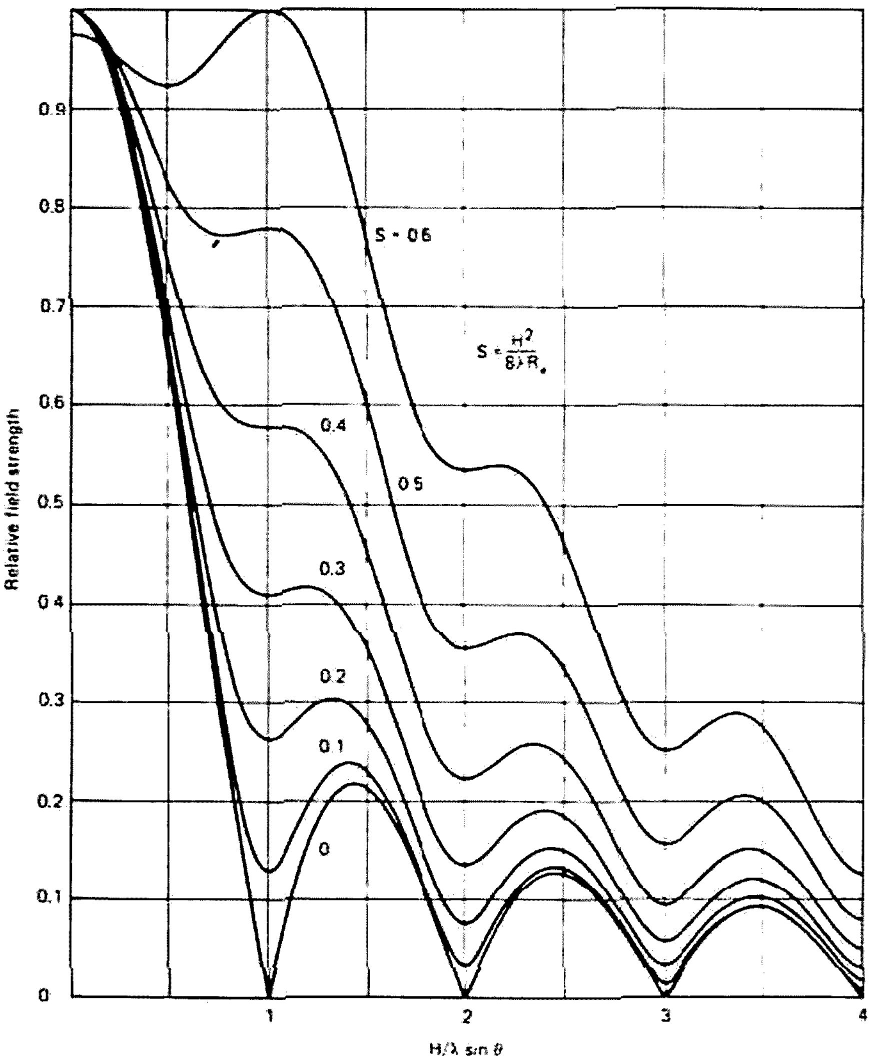

Figure 7-3 E-plane universal pattern of a rectangular horn, TE_{10} mode.

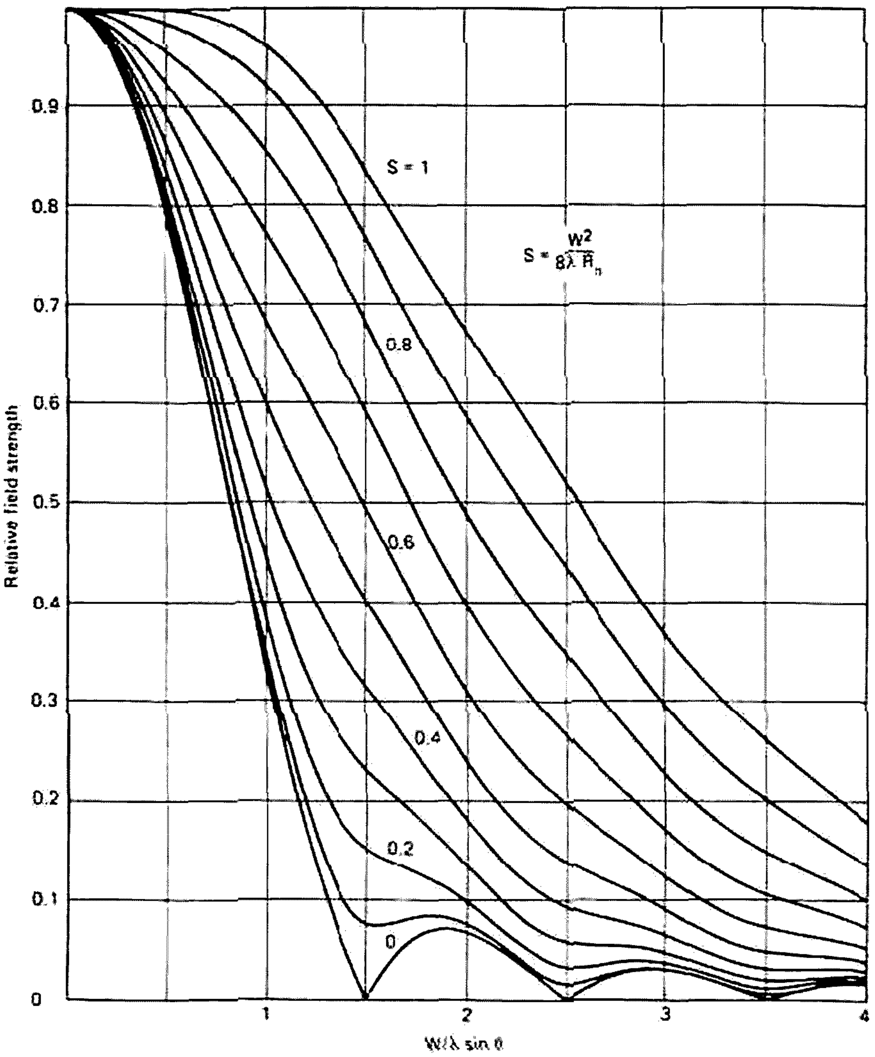

Figure 7-4 *H*-plane universal pattern of a rectangular horn, TE_{10} mode.

Slant radius: $R_h = 50.97$ cm $R_e = 48.05$ cm
The frequency is 8 GHz ($\lambda = 3.75$ cm). From Eqs. (7-2) we find $S_h = 0.55$ and $S_e = 0.31$. We use Figs. 7-3 and 7-4 to find the universal pattern field intensity (voltage)

$$\frac{W}{\lambda}\sin\theta = 2.0 \qquad \frac{H}{\lambda}\sin\theta = 1.47$$

The fields from the figures are 0.27 (*H* plane) and 0.36 (*E* plane). We must include the obliquity factor of the Huygens source element pattern: $(1 + \cos\theta)/2$ to obtain the proper pattern level. At $\theta = 15°$, the obliquity factor is 0.983. We find the pattern level in dB from 20 times the logarithm of the product of the field intensity from the figures and the obliquity factor.

H plane: −11.5 dB *E* plane: −9 dB

We can find the gain of this horn by using aperture efficiencies.

ATL	*H* plane (cosine) (Table 6-1):	0.91 dB
	E plane (uniform):	0 dB

These values hold for all rectangular horns excited by the TE_{10} mode. The quadratic phase distributions give us the phase error loss. From Table 6-21, we find these losses

$S_h = 0.55$ cosine distribution $\quad PEL_h = 2.09$ dB

$S_e = 0.31$ uniform distribution $\quad PEL_e = 1.50$ dB

The directivity is given by

$$\text{Directivity} = 10\log\left(\frac{4\pi WH}{\lambda^2}\right) - ATL_h - ATL_e - PEL_h - PEL_e$$
$$= 22.9 \text{ dB} \tag{7-5}$$

The aperture efficiency is 35.5 percent, since $ATL_h + PEL_h + PEL_e = 4.5$ dB

We usually equate gain to directivity, since the wall losses are very small. Of course, for millimeter wave horns we must include wall losses. We can use Table 6-21 along with the fixed amplitude taper loss of 0.91 dB to find the aperture efficiency of a rectangular horn. Schelkunoff and Friis [4] give the following closed-form equation for the directivity

$$\text{Directivity} = \frac{8R_hR_e}{WH}\{[C(u) - C(v)]^2 + [S(u) - S(v)]^2\}[C^2(z) + S^2(z)] \tag{7-6}$$

where $\quad u = \frac{1}{\sqrt{2}}\left(\frac{\sqrt{\lambda R_h}}{W} + \frac{W}{\sqrt{\lambda R_h}}\right) \qquad v = \frac{1}{\sqrt{2}}\left(\frac{\sqrt{\lambda R_h}}{W} - \frac{W}{\sqrt{\lambda R_h}}\right)$

$$z = \frac{H}{\sqrt{2\lambda R_e}}$$

and $\quad C(x) = \int_0^x \cos\left(\frac{\pi t^2}{2}\right)dt \qquad S(x) = \int_0^x \sin\left(\frac{\pi t^2}{2}\right)dt$

are the Fresnel integrals. Closed-form expressions for these integrals are available [6].

Beamwidth We can use Figs. 7-3 and 7-4 to find the beamwidths. The 3-dB point corresponds to 0.707 and the 10-dB point to 0.316 on the graphs. Table 7-1 lists the 3- and 10-dB points (values of U) for different quadratic phase constants S in the H plane. Likewise, Table 7-2 lists the E-plane points. The tables are more convenient than the graphs. Because we remove the obliquity factor to get a universal pattern, we must modify the beamwidths found by using the tables. We find the beamwidth, but then we must add the obliquity factor to the beamwidth level. The beamwidth is found for a lower pattern level than specified. We could use Fig. 2-1 to obtain the actual beamwidth; but since the beamwidth levels are close, we will use a relation by Kelleher [7] with good results.

TABLE 7-1 Rectangular-Horn H-Plane Beamwidth Points, TE$_{10}$ Mode

	Beamwidth level			Beamwidth level	
	3 dB	10 dB		3 dB	10 dB
S	Location	$(W/\lambda)\sin\theta$	S	Location	$(W/\lambda)\sin\theta$
0	0.5945	1.0194	0.52	0.8070	1.8062
0.04	0.5952	1.0220	0.56	0.8656	1.8947
0.08	0.5976	1.0301	0.60	0.9401	1.9861
0.12	0.6010	1.0442	0.64	1.0317	2.0872
0.16	0.6073	1.0652	0.68	1.1365	2.2047
0.20	0.6150	1.0949	0.72	1.2445	2.3418
0.24	0.6248	1.1358	0.76	1.3473	2.4876
0.28	0.6372	1.1921	0.80	1.4425	2.6246
0.32	0.6526	1.2700	0.84	1.5320	2.7476
0.36	0.6716	1.3742	0.88	1.6191	2.8618
0.40	0.6951	1.4959	0.92	1.7071	2.9744
0.44	0.7243	1.6123	0.96	1.7991	3.0924
0.48	0.7609	1.7143	1.00	1.8970	3.2208

TABLE 7-2 Rectangular-Horn E-Plane Beamwidths: TE$_{10}$ Mode

	Beamwidth level			Beamwidth level	
	3 dB	10 dB		3 dB	10 dB
S	Location	$(H/\lambda)\sin\theta$	S	Location	$(H/\lambda)\sin\theta$
0	0.4430	0.7380	0.24	0.4676	1.4592
0.04	0.4435	0.7405	0.28	0.4793	1.5416
0.08	0.4452	0.7484	0.32	0.4956	1.6034
0.12	0.4482	0.7631	0.36	0.5193	1.6605
0.16	0.4527	0.7879	0.40	0.5565	1.7214
0.20	0.4590	0.8326	0.44	0.6281	1.8004

$$\frac{\mathrm{BW}_1}{\mathrm{BW}_2} = \sqrt{\frac{\mathrm{level}_1\ (\mathrm{dB})}{\mathrm{level}_2\ (\mathrm{dB})}} \tag{7-7}$$

Example Find the 3- and 10-dB beamwidths for the horn in the above example. We have $S_h = 0.55$ and $S_e = 0.31$. From Tables 7-1 and 7-2,

$$\frac{W}{\lambda}\sin\theta_{h3} = 0.851 \qquad \frac{H}{\lambda}\sin\theta_{e3} = 0.4915$$

$$\frac{W}{\lambda}\sin\theta_{h10} = 1.8726 \qquad \frac{H}{\lambda}\sin\theta_{e10} = 1.588$$

$$\frac{W}{\lambda} = \frac{28.9}{3.75} = 7.707 \qquad \frac{H}{\lambda} = \frac{21.3}{3.75} = 5.68$$

$$\theta_{h3} = 6.34 \qquad \theta_{h10} = 14.06 \qquad \theta_{e3} = 4.96 \qquad \theta_{e10} = 16.24$$

We consider the obliquity factor, $(1 + \cos\theta)/2$ at these angles, and apply Eq. (7-7) to reduce the beamwidths found.

$$\mathrm{BW}_{h3} = 12.68^\circ \text{ at } 3.03\text{ dB} \qquad \mathrm{BW}_{h3} = 12.62^\circ \text{ at } 3.01\text{ dB}$$

$$\mathrm{BW}_{e3} = 9.92^\circ \text{ at } 3.02\text{ dB} \qquad \mathrm{BW}_{e3} = 9.89^\circ \text{ at } 3.01\text{ dB}$$

$$\mathrm{BW}_{h10} = 28.12^\circ \text{ at } 10.13\text{ dB} \qquad \mathrm{BW}_{h10} = 27.94^\circ \text{ at } 10\text{ dB}$$

$$\mathrm{BW}_{e10} = 32.48^\circ \text{ at } 10.18\text{ dB} \qquad \mathrm{BW}_{e10} = 32.2^\circ \text{ at } 10\text{ dB}$$

Including the obliquity factor has a very small effect on the results. The effect increases with larger beamwidths (smaller apertures).

Optimum Rectangular Horn A rectangular horn has extra parameters. We can use them to design various optimum horns. Given a required gain, we can design any number of horns with the same gain. Any optimum design depends on the requirements. Without any particular requirements, we will pick an antenna with equal E- and H-plane 3-dB beamwidths [8]. Even this does not totally determine the design.

If we pick a constant slant radius and vary the aperture width, the gain increases with increasing aperture width but the quadratic phase error loss increases faster and produces a maximum point. The maximum occurs in the two planes at approximately constant phase deviations independent of the slant radius.

$$S_h = 0.40 \qquad S_e = 0.26 \tag{7-8}$$

At these points we find the 3-dB points from Tables 7-1 and 7-2

$$\frac{W}{\lambda}\sin\theta = 0.6951 \qquad \frac{\mathrm{H}}{\lambda}\sin\theta = 0.4735$$

On dividing these equations to eliminate the constant $\sin\theta$ in the two planes, we find the ratio of width to height to give a constant 3-dB beamwidth in the two planes for this optimum point.

$$\frac{H}{W} = 0.68 \qquad 3\text{ dB} \tag{7-9}$$

The ratio depends on the beamwidth level. For 10-dB beamwidths

$$\frac{H}{W} = 1.00 \qquad 10\text{ dB} \tag{7-10}$$

The values of S fix the efficiency of the optimum horn. We find the PEL of the quadratic phase distribution from Table 6-21 by using a cosine distribution for the H plane and a uniform distribution for the E plane. The H-plane distribution has an ATL of 0.91 dB.

$$\text{PEL}_h = 1.14 \text{ dB} \qquad \text{PEL}_e = 1.05 \text{ dB} \qquad \text{ATL}_h = 0.91 \text{ dB}$$

or an efficiency of 49 percent.

$$\text{Gain} = \frac{4\pi HW}{\lambda^2} 0.49$$

We can solve for H and W for a given gain, since we know the ratio between them [Eq. (7-9)].

$$\frac{W}{\lambda} = \sqrt{\frac{\text{gain}}{4\pi(0.68)(0.49)}} \qquad \frac{H}{\lambda} = \sqrt{\frac{\text{gain}(0.68)}{4\pi(0.49)}}$$

$$\frac{W}{\lambda} = 0.489\sqrt{\text{gain}} \qquad \frac{H}{\lambda} = 0.332\sqrt{\text{gain}} \tag{7-11}$$

We combine Eqs. (7-8) and (7-11) to find the slant radii

$$\frac{R_h}{\lambda} = 0.0746 \text{ gain} \qquad \frac{R_e}{\lambda} = 0.0531 \text{ gain} \tag{7-12}$$

If, given gain, we use Eqs. (7-11) and (7-12) to design a horn, the dimensions will not be practical with an arbitrary input waveguide. The axial lengths from the waveguide to the aperture must be equal in the E and H planes so the horn will meet the waveguide in a single plane. Given waveguide dimensions a and b, the axial lengths are

$$L_h = \frac{W - a}{W}\sqrt{R_h^2 - \frac{W^2}{4}} \qquad L_e = \frac{H - b}{H}\sqrt{R_e^2 - \frac{H^2}{4}} \tag{7-13}$$

We have a choice between retaining the E-plane or H-plane slant radius given by Eq. (7-12) and forcing the other radius to give the same axial length. The primary factor affecting gain is the aperture dimensions which we retain from Eq. (7-11). The slant radius is secondary. We will retain the H-plane radius calculated from Eq. (7-12) and modify the E-plane radius. Modifying the H-plane radius would give us a second optimum design.

$$R_e = \frac{H}{H - b}\sqrt{L^2 + \frac{(H - b)^2}{4}} \tag{7-14}$$

To obtain the proper gain, we must iterate, since we cannot use both Eqs. (7-12). Design the horn by using Eqs. (7-11), (7-12*a*), (7-13*a*), and (7-14). Calculate the gain from the dimensions and obtain a new design gain from

$$G_{d,\text{new}} = \frac{G_{\text{req}} G_{d,\text{old}}}{G_{\text{actual}}} \tag{7-15}$$

where G_{req} is the required gain, G_{actual} is the actual gain, and $G_{d,old}$ is the old design gain.

Example Design a horn fed from WR-90 waveguide to have 22 dB gain at 10 GHz.
The waveguide dimensions are 2.286 cm × 1.016 cm (0.9 in × 0.4 in)

$$\text{Gain}_{req} = G_d = 10^{22/10} = 158.5$$

On substituting in Eq. (7-11), we find the aperture dimensions:

$$W = 18.47 \text{ cm} \qquad H = 12.54 \text{ cm}$$

From Eqs. (7-12*a*) and (7-13*a*), $R_h = 35.47$ cm and $L = 30.01$ cm. To get the same axial length in the *E* plane [Eq. (7-14)], $R_e = 33.25$ cm.
We now calculate gain and compare it with the required gain. The amplitude taper loss and phase error loss in the *H* plane remain constant, since S_h is fixed.

$$\text{ATL} = 0.91 \text{ dB} \qquad \text{PEL}_h = 1.14 \text{ dB} \qquad \text{at} \qquad S_h = 0.40$$

Calculate S_e

$$S_e = \frac{H^2}{8\lambda R_e} = 0.197 \qquad \text{PEL}_e = 0.60 \text{ dB} \qquad \text{Table 6-21}$$

$$G_{actual}(\text{dB}) = 10 \log \left(\frac{4\pi HW}{\lambda^2}\right) - \text{ATL} - \text{PEL}_h - \text{PEL}_e = 22.45 \text{ dB}$$

$$G_{actual} = 175.8$$

We must pick a new design gain [Eq. (7-15)]

$$G_d = \frac{158.5(158.5)}{175.8} = 142.9$$

A second iteration with this gain gives the following dimensions

$$W = 17.54 \text{ cm} \qquad H = 11.91 \text{ cm} \qquad R_h = 31.98 \text{ cm}$$

$$L = 26.75 \text{ cm}$$

$$R_e = 29.84 \text{ cm} \qquad S_e = 0.198 \qquad \text{PEL}_e = 0.60$$

$$\text{Gain} = 10 \log \left(\frac{4\pi HW}{\lambda^2}\right) - 0.91 - 1.14 - 0.60 = 22.00 \text{ dB}$$

We obtain the required gain, but the 3-dB beamwidths are only close to equality:

H plane: 13.66° *E* plane: 13.28°

Designing to Given Beamwidths The beamwidths in the two planes of a rectangular horn can be designed independently. The axial lengths in the two planes must be equal if the design is to be realizable, but the aperture width and height can be adjusted to give the desired beamwidths. We will pick *S* in one plane and then must vary *S* in the other plane to produce the required beamwidth and the same axial length as in the first plane. Since the first S is arbitrary, the design is not unique. In only a limited range of S will designs be realizable.

Example Design a rectangular horn for the following 10-dB beamwidths: 30° H plane and 70° E plane at 7 GHz using a 3.5- by 1.75-cm waveguide. Since the H plane has the narrower beamwidth and therefore the wider aperture, we design for it to establish the horn length.
Pick $S_h = 0.20$ (an arbitrary choice). The obliquity factor at 15° is 0.15 dB. When using Table 7-1, we must design for wider than a 30° beamwidth to compensate for the obliquity factor.

$$\mathrm{BW}_d = \sqrt{\frac{10.15}{10}}\,30^\circ = 30.22^\circ$$

The horn width to provide that beamwidth is

$$\frac{W}{\lambda} = \frac{1.0949}{\sin(\mathrm{BW}_d/2)} = 4.200$$

$$W = 18.00 \text{ cm at 7 GHz} \qquad R_h = 47.25 \qquad [\text{Eq.}(7.2)]$$

Use Eq. (7-13a) to find the axial length: $L_h = L = 37.36$ cm
Because the E-plane beamwidth is wider than the H-plane beamwidth, the E-plane aperture will be smaller. We try a smaller value of S_e than S_h for our initial guess: $S_e = 0.04$. The obliquity factor at 35° adds 0.82 dB to the pattern loss and requires a larger design beamwidth.

$$BW_d = \sqrt{\frac{10.82}{10}}\,70^\circ = 72.82$$

$$\frac{H}{\lambda} = \frac{0.7405}{\sin(\mathrm{BW}_d/2)} = 1.248 \quad (\text{Table 7-2}) \qquad H = 5.346 \text{ cm}$$

We use Eqs. (7-2) and (7-13b) to find the slant radius and axial length:

$$R_e = 20.84 \text{ cm} \qquad L_e = 13.90 \text{ cm}$$

$$\text{At } S_e = 0.02, \quad H = 5.337 \text{ cm} \qquad R_e = 41.54 \text{ cm} \qquad \text{and} \qquad L_e = 27.86 \text{ cm}$$

L_e has doubled when S_e changes from 0.04 to 0.02, but H changes by only 0.01 cm. We will pick $H = 5.33$ cm and force R_e to give the same axial length as the H plane.

$$R_e = 55.69 \text{ cm [from Eq. (7-14)]} \qquad \text{or} \qquad S_e = 0.0149$$

Phase Center We define the phase center as the point from which it appears that an antenna radiates spherical waves. Measurements show that the phase center is seldom a unique point in a plane; it depends on the pattern angle. The E- and H-plane phase centers will also be unequal in general. Usually, they are extremes and the axial length varies elliptically between the planes. Even with the phase center location fuzzy, it is a useful

TABLE 7-3 Phase Center Axial Location of a Rectangular Horn (TE_{10} Mode) behind the Aperture as a Ratio of the Slant Radius

S	H-plane L_{ph}/R_h	E-plane L_{pe}/R_e	S	H-plane L_{ph}/R_h	E-plane L_{pe}/R_e
0	0	0	0.28	0.258	0.572
0.04	0.0054	0.011	0.32	0.334	0.755
0.08	0.022	0.045	0.36	0.418	
0.12	0.048	0.102	0.40	0.508	
0.16	0.086	0.182	0.44	0.605	
0.20	0.134	0.286	0.48	0.705	
0.24	0.191	0.416	0.52	0.808	

point. We place the phase center of a feed at the focus of a parabolic reflector to minimize the reflector aperture phase error loss.

An aperture with a quadratic phase distribution appears to be radiating from a point behind the aperture. Without quadratic phase error ($S = 0$), the phase center is on the aperture plane. Increasing S moves the phase center toward the apex of the horn. Muehldorf [9] has calculated the phase center location as a function of S. Table 7-3 summarizes his results. The phase center location behind the aperture is given as a ratio of the slant length.

Example Find the phase center location for the above beamwidth design example.

$$S_h = 0.20 \qquad R_h = 47.25 \text{ cm}$$

$$S_e = 0.015 \qquad R_e = 55.69 \text{ cm}$$

From Table 7-3, we find (or interpolate)

$$H\text{-plane phase center} = 0.134(47.25 \text{ cm}) = 6.33 \text{ cm}$$

$$E\text{-plane phase center} = 0.004(55.69 \text{ cm}) = 0.22 \text{ cm}$$

The difference in the phase center location in the two planes is 1.43λ.

As in the example, antennas with widely differing beamwidths will have widely separated phase centers.

7-2 Circular-Aperture Horn

When we use a circular-aperture horn, we lose the independent control of the beamwidths in the E and H planes. The circular waveguide can support any orientation of the electric field and thereby allow any polarization in the horn.

We use the same aperture field method as with the rectangular horn. The waveguide mode determines the aperture amplitude. The cone of the horn projects to a point in the feed waveguide where we assume a point source radiating to the aperture. The aperture phase is approximately quadratic. The waveguide fields are given by

$$E_\rho = \frac{E_0}{\rho} J_1\left(\frac{x'_{11}\rho}{a}\right) \cos \phi_c$$

$$E_{\phi c} = -\frac{E_0 x'_{11}}{a} J'_1\left(\frac{x'_{11}\rho}{a}\right) \sin \phi_c \tag{7-16}$$

where J_1 is the Bessel function, ρ is the radial component in the waveguide, a is the radius, and ϕ_c is the cylindrical coordinate. x'_{11} (1.841) is the first zero of $J'_1(x)$. Equation (7-16) has a maximum electric field directed along the $\phi_c = 0$ plane.

We add the quadratic phase factor to Eq. (7-16) and calculate the Fourier transform on the circular aperture to find the far field. The direction of the electric field changes from point to point in the aperture. For a given direction (θ, ϕ) we must project the fields in the aperture onto the $\mathbf{a}_\theta$ and $\mathbf{a}_\phi$ directions before integrating over the aperture.

$$E_\theta = E_0 \int_0^{2\pi} \int_0^a \left[\frac{J_1(x'_{11}\rho/a)}{\rho} \cos \phi_c \frac{\mathbf{a}_\theta \cdot \mathbf{a}_\rho}{\cos \theta} - \frac{x'_{11}}{a} J'_1\left(\frac{x'_{11}\rho}{a}\right) \sin \phi_c \frac{\mathbf{a}_\theta \cdot \mathbf{a}_{\phi_c}}{\cos \theta} \right]$$

$$\times\ \rho \exp\left\{ j\left[k\rho \sin \theta \cos (\phi - \phi_c) - 2\pi S\left(\frac{\rho}{a}\right)^2 \right] \right\} d\rho\, d\phi_c \tag{7-17}$$

$$E_\phi = E_0 \int_0^{2\pi} \int_0^a \left[\frac{J_1(x'_{11}\rho/a)}{\rho} \cos \phi_c\, \mathbf{a}_\phi \cdot \mathbf{a}_\rho - \frac{x'_{11}}{a} J'_1\left(\frac{x'_{11}\rho}{a}\right) \sin \phi_c\, \mathbf{a}_\phi \cdot \mathbf{a}_{\phi_c} \right]$$

$$\times\ \rho \exp\left\{ j\left[k\rho \sin \theta \cos (\phi - \phi_c) - 2\pi S\left(\frac{\rho}{a}\right)^2 \right] \right\} d\rho\, d\phi_c \tag{7-18}$$

$$\mathbf{a}_\theta \cdot \mathbf{a}_\rho = \cos \theta (\cos \phi \cos \phi_c + \sin \phi \sin \phi_c)$$

$$\mathbf{a}_\theta \cdot \mathbf{a}_{\phi_c} = \cos \theta (\sin \phi \cos \phi_c - \cos \phi \sin \phi_c)$$

$$\mathbf{a}_\phi \cdot \mathbf{a}_\rho = \cos \phi \sin \phi_c - \sin \phi \cos \phi_c$$

$$\mathbf{a}_\phi \cdot \mathbf{a}_{\phi_c} = \cos \phi \cos \phi_c + \sin \phi \sin \phi_c$$

By a suitable change of variables in the integrals, universal radiation patterns can be generated for the E and H planes (Figs. 7-5 and 7-6). The equality of S in the two planes ties the curves together. The axis is the k-space variable. *We can find a few pattern points for a given horn with those* curves if we remember to add the obliquity factor to the values taken from the curves.

Example A horn has an aperture radius of 12 cm and a slant radius of 50 cm. Find the pattern level at $\theta = 20°$ at 5 GHz.

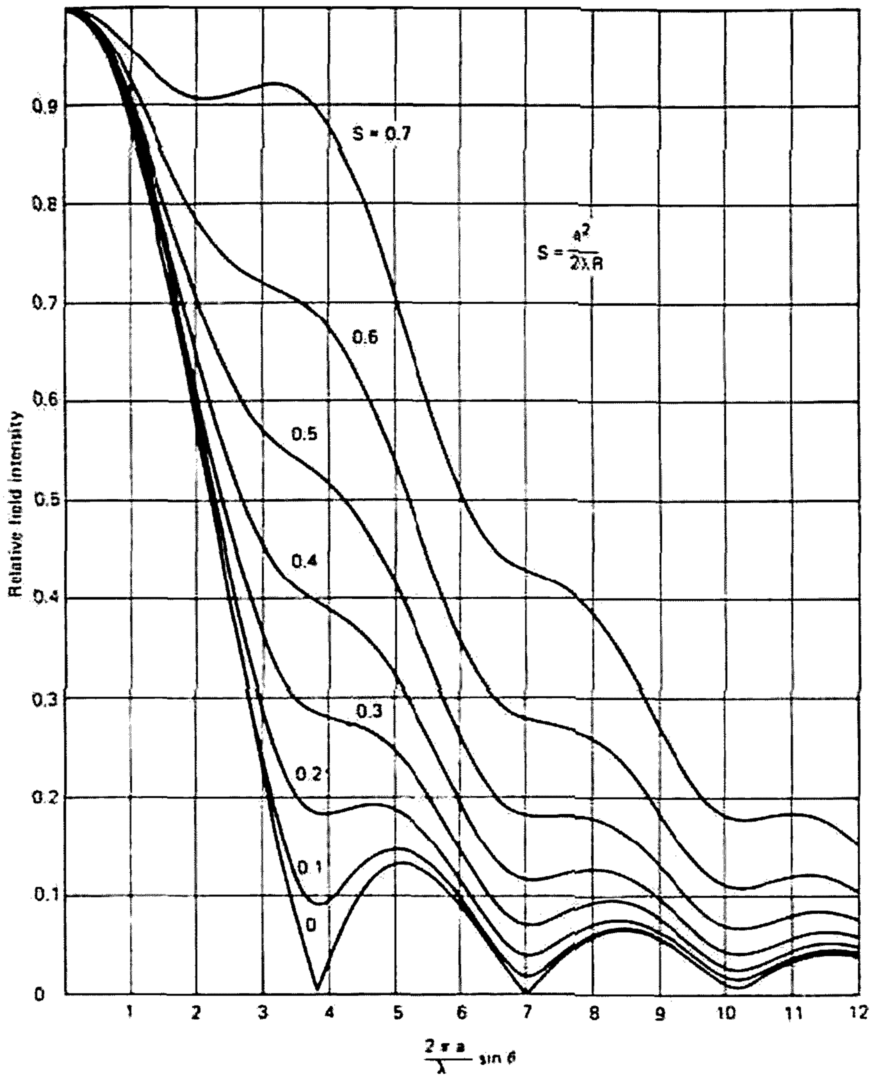

Figure 7-5 *E*-plane universal pattern of a circular horn, TE_{11} mode. (Source: T. Milligan, "Universal Patterns Ease Circular Horn Design," *Microwaves*, vol. 20, no. 3, March 1981, p. 84.)

$$S = \frac{a^2}{2\lambda R} = \frac{12^2}{2(6)(50)} = 0.24$$

$$\frac{2\pi a}{\lambda}\sin\theta = 4.3$$

From Figs. 7-5 and 7-6 we find the pattern voltage level:

H-plane level = 0.18 (−14.7 dB) *E*-plane level = 0.22 (−13.1 dB)

The obliquity factor is 20 log [(1 + cos 20°)/2] = −0.3 dB
The plane level at 20° becomes

H-plane level = −15 dB *E*-plane level = −13.4 dB

Beamwidth Table 7-4 lists the 3- and 10-dB points from Figs. 7-5 and 7-6. We can use them to find the beamwidths from dimensions.

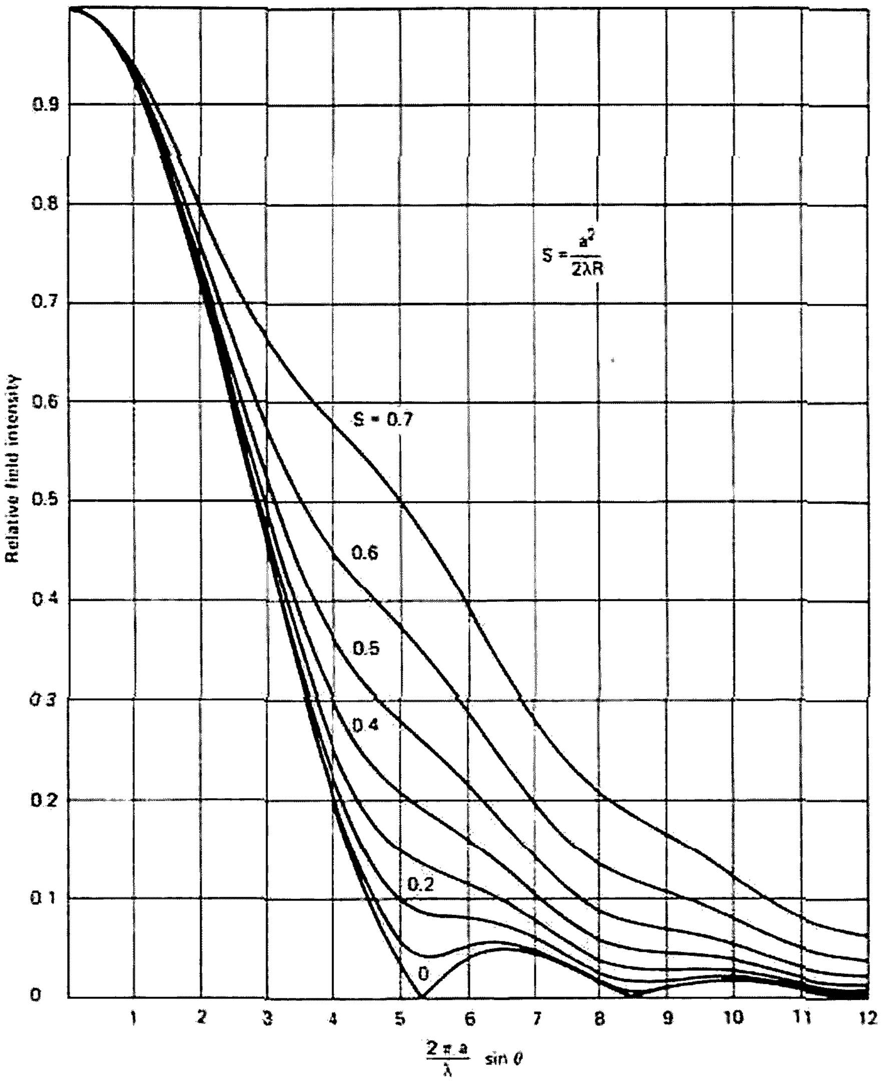

Figure 7-6 *H*-plane universal pattern of a circular horn, TE_{11} mode. (Source: T. Milligan, "Universal Patterns Ease Circular Horn Design," *Microwaves*, vol. 20, no. 3, March 1981, p. 84.)

Example Find the 10-dB beamwidths of the horn in the above example.

$S = 0.24 \qquad a = 12\text{ cm} \qquad \lambda = 6\text{ cm}$

From Table 7-4 we find the *k*-space values at 10 dB.

$$H\text{-plane } k \text{ space} = \frac{2\pi a}{\lambda}\sin\theta_h = 3.6115$$

$$E\text{-plane } k \text{ space} = \frac{2\pi a}{\lambda}\sin\theta_e = 3.0024$$

$$\text{BW} = 2\sin^{-1}\frac{3.6115}{4\pi} \qquad \text{BW} = 2\sin^{-1}\frac{3.0024}{4\pi}$$

$$= 33.40^\circ \qquad\qquad = 27.65^\circ$$

TABLE 7-4 Circular-Horn Beamwidths, TE_{11} Mode

	Beamwidth level				
	3 dB		10 dB		
	E plane	*H* plane	*E* plane	*H* plane	
S	Location	$\frac{2\pi a}{\lambda}\sin\theta$	Location	$\frac{2\pi a}{\lambda}\sin\theta$	ATL + PEL, dB
0	1.6163	2.0376	2.7314	3.5189	0.77
0.04	1.6175	2.0380	2.7368	3.5211	0.80
0.08	1.6212	2.0391	2.7536	3.5278	0.86
0.12	1.6273	2.0410	2.7835	3.5393	0.96
0.16	1.6364	2.0438	2.8296	3.5563	1.11
0.20	1.6486	2.0477	2.8982	3.5799	1.30
0.24	1.6647	2.0527	3.0024	3.6115	1.54
0.28	1.6855	2.0592	3.1757	3.6536	1.82
0.32	1.7123	2.0676	3.5720	3.7099	2.15
0.36	1.7471	2.0783	4.6423	3.7863	2.53
0.40	1.7930	2.0920	5.0492	3.8933	2.96
0.44	1.8552	2.1100	5.3139	4.0504	3.45
0.48	1.9441	2.1335	5.5375	4.2967	3.99
0.52	2.0823	2.1652	5.7558	4.6962	4.59
0.56	2.3435	2.2089	6.0012	5.2173	5.28
0.60	3.4329	2.2712	6.3500	5.6872	5.98
0.64	4.3656	2.3652	7.6968	6.0863	6.79
0.68	4.8119	2.5195	8.4389	6.4622	7.66
0.72	5.1826	2.8181	8.8519	6.8672	8.62

We must add the obliquity factor to the 10-dB universal pattern level:

$$\frac{1+\cos 16.7^\circ}{2}: \quad 0.18\text{ dB} \quad H\text{ plane}$$

$$\frac{1+\cos 13.8^\circ}{2}: \quad 0.13\text{ dB} \quad E\text{ plane}$$

$$BW_{h10} = \sqrt{\frac{10}{10.18}}\,33.40^\circ = 33.10^\circ \qquad BW_{e10} = \sqrt{\frac{10}{10.13}}\,27.65^\circ = 27.48^\circ$$

We can also use Table 7-4 to design a horn to a given beamwidth, but we can design to only one of the planes. Any number of horns can be designed to a given beamwidth, since *S* is an independent parameter.

Gain Table 7-4 lists the combined amplitude taper loss and phase error loss as a function of *S* for the circular horn. With this table we can easily find the gain of a given horn or design horns to a given gain.

Example Find the gain of a horn with a 12-cm aperture radius and 50-cm slant radius at 5 GHz.
From the above examples we find $S = 0.24$ and $\lambda = 6$ cm

$$\text{Gain} = 20 \log \left(\frac{\pi D}{\lambda}\right) - \text{GF} \qquad \text{where GF} = \text{ATL} + \text{PEL (dB)} \tag{7-19}$$

$$\text{Gain} = 20 \log \left(\frac{\pi 24}{6}\right) - 1.54 = 20.4 \text{ dB}$$

Example Design a circular horn at 8 GHz with a gain of 22 dB. The quadratic phase distribution constant S is arbitrary. Pick $S = 0.20$. Rearrange Eq. (7-19) to find the diameter.

$$D = \frac{\lambda}{\pi} 10^{(\text{gain}+\text{GF})/20} \tag{7-20}$$

$$D = \frac{3.75}{\pi} 10^{(22+1.30)/20} = 17.45 \text{ cm} \qquad R = \frac{D^2}{8\lambda S} = 50.77 \text{ cm}$$

We can find an optimum circular horn in the sense of minimizing the slant radius at a given gain. When we plot gain as a function of aperture radius for a fixed slant radius, we discover a broad region in which the gain peaks. By plotting a series of these lines with a voltage gain ordinate, we see that a single line corresponding to $S = 0.39$ can be drawn through the peaks. This is our optimum with GF = 2.85 dB (ATL + PEL).

Example Design an optimum horn at 8 GHz with gain of 22 dB.

From Eq. (7-20) $$D = \frac{3.75}{\pi} 10^{(22+2.85)/20} = 20.86 \text{ cm}$$

$$R = \frac{D^2}{8\lambda S} = \frac{20.86^2}{8(3.75)(0.39)} = 37.2 \text{ cm}$$

The optimum is quite broad. A horn designed with $S = 0.38$ has a 0.07-cm longer slant radius and a 0.25-cm smaller aperture diameter.

Phase Center The phase center location behind the aperture plane is a function of S. Table 7-5 lists the phase center location as a ratio of the slant radius. As S increases, the phase center migrates toward the horn apex and the difference between the phase center locations in the E and H planes increases.

Example Use Table 7-5 to find the phase center locations in the E and H planes for the circular horns of the preceding two examples.

$R = 50.77$ cm $\qquad S = 0.20$

H-plane phase center = 0.117(50.77) = 5.94 cm

E-plane phase center = 0.305(50.77) = 15.48 cm

TABLE 7-5 Phase Center Axial Location of a Circular-Waveguide Horn (TE_{11} Mode) behind the Aperture as a Ratio of the Slant Radius

S	H-plane L_{ph}/R	E-plane L_{pe}/R	S	H-plane L_{ph}/R	E-plane L_{pe}/R
0	0	0	0.28	0.235	0.603
0.04	0.0046	0.012	0.32	0.310	0.782
0.08	0.018	0.048	0.36	0.397	0.801
0.12	0.042	0.109	0.40	0.496	0.809
0.16	0.075	0.194	0.44	0.604	0.836
0.20	0.117	0.305	0.48	0.715	0.872
0.24	0.171	0.441			

The phase centers differ by 2.5 wavelengths at 8 GHz. The optimum horn has the dimensions

$$R = 37.2 \text{ cm} \qquad S = 0.39$$

$$H\text{-plane phase center} = 0.471(37.2) = 17.5 \text{ cm}$$

$$E\text{-plane phase center} = 0.807(37.2) = 30.0 \text{ cm}$$

The phase centers of the optimum horn differ by 3.3 wavelengths. The difference increases with increasing S.

7-3 Overmoded Circular-Aperture Horns

TM_{01} and TE_{01} circular-waveguide modes feeding an aperture produce useful horns. The modes produce patterns with a null on the horn axis. Each radiates a single polarization that is independent of rotation of the horn about its axis. Circular apertures with axisymmetric distributions have identical patterns in all planes that contain the axis.

The TM_{01} circular-waveguide mode has the aperture field

$$E_\rho = -E_0 J_0'\left(\frac{x_{01}\rho}{a}\right)$$

By use of the Bessel function properties, this becomes

$$E_\rho = E_0 J_1\left(\frac{x_{01}\rho}{a}\right) \qquad TM_{01} \tag{7-21}$$

where $x_{01} = 2.405$ is the first zero of J_0 and a is the aperture radius. The TM_{01}-mode horn radiates E_θ only when the horn axis is on the z axis.

The aperture field of the TE_{01} mode is

$$E_\phi = -E_0 J_0'\left(\frac{x_{01}'\rho}{a}\right)$$

where $x_{01}' = 3.832$ is the first zero of $J_0'(x)$. The tangential field E_ϕ vanishes on the waveguide walls. We find the radiated pattern shape of the TE_{01} mode to be similar to the TM_{01}-mode radiated field.

$$E_\phi = E_0 J_1\left(\frac{x'_{01}\rho}{a}\right) \qquad \mathrm{TE}_{01} \tag{7-22}$$

This radiates only E_ϕ when pointed along the z axis.

The two horns radiate complementary polarizations; but because the constants x_{01} and x'_{01} are different, the patterns differ. If mounted on a satellite and pointed toward the earth, each horn radiates a constant polarization to the ground. The TM_{01}-mode horn produces vertical polarization everywhere in the view area. The TE_{01}-mode horn radiates horizontal polarization to the ground.

The Fourier transform of the TM_{01}-mode aperture fields is

$$\int_0^{2\pi}\int_0^a J_1\left(\frac{x_{01}\rho}{a}\right) \exp\left\{j\left[k\rho \sin\theta \cos\phi_c - 2\pi S\left(\frac{\rho}{a}\right)^2\right]\right\}\frac{\mathbf{a}_\rho \cdot \mathbf{a}_\theta}{\cos\theta}\rho\, d\rho\, d\phi_c$$

where we pick the pattern plane $\phi = 0$ because all patterns for varying ϕ are the same. We account for the aperture polarization rotation through the scalar product of the far-field unit vector and the aperture field unit vector.

$$\mathbf{a}_\rho \cdot \mathbf{a}_\theta = \cos\theta\cos\phi_c \qquad \text{at} \qquad \phi = 0$$

The pattern integral becomes

$$E_\theta = E_0 \int_0^{2\pi}\int_0^a J_1\left(\frac{x_{01}\rho}{a}\right)\cos\phi_c \cdot \exp\left\{j\left[k\rho\sin\theta - 2\pi S\left(\frac{\rho}{a}\right)^2\right]\right\}\rho\, d\rho\, d\phi_c$$

The integral over ϕ_c can be found in closed form.

$$\int_0^{2\pi}\cos\phi_c e^{jU\cos\phi_c}\, d\phi_c = j2\pi J_1(U)$$

The pattern function reduces to

$$E_\theta = j2\pi E_0 \int_0^a J_1(k\rho\sin\theta) J_1\left(\frac{x_{01}\rho}{a}\right)\exp\left[-j2\pi S\left(\frac{\rho}{a}\right)^2\right]\rho\, d\rho \tag{7-23}$$

Figure 7-7 is a plot of a universal pattern for the TM_{01}-mode horn ignoring $(1 + \cos\theta)/2$. The beam peak occurs at 2.43 on the pattern for practical values of S.

$$\frac{2\pi a}{\lambda}\sin\theta_{\max} = 2.4$$

$$\theta_{\max} = \sin^{-1}\frac{0.382\lambda}{a} \qquad \mathrm{TM}_{01} \tag{7-24}$$

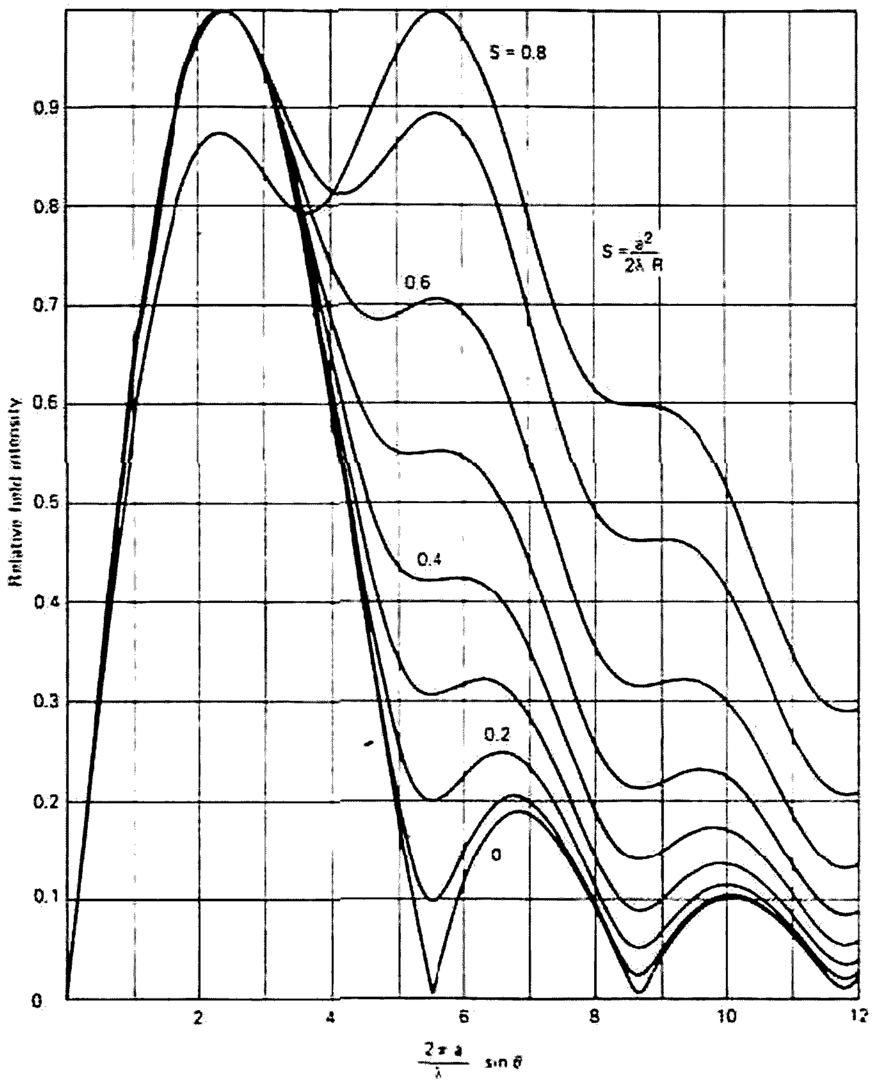

Figure 7-7 Universal pattern of a circular horn, TM_{01} mode. (Source: T. Milligan, "Universal Patterns Ease Circular Horn Design," *Microwaves*, vol. 20, no. 3, March 1981, p. 84.)

Equation (7-24) gives the approximate beam peak modified by the obliquity factor.

The TE_{01}-mode pattern analysis is parallel the TM_{01}-mode pattern analysis. The polarization in the far field is related to the aperture fields by

$$\mathbf{a}_\phi \cdot \mathbf{a}_{\phi_c} = \cos\phi_c \qquad \text{at} \qquad \phi = 0$$

The pattern integral becomes

$$E_\phi = j2\pi E_0 \int_0^a J_1(k\rho \sin\theta) J_1\left(\frac{x'_{01}\rho}{a}\right) \exp\left[-j2\pi S\left(\frac{\rho}{a}\right)^2\right] \rho\, d\rho \qquad (7\text{-}25)$$

Equations (7-23) and (7-25) differ by the constant of the Bessel function: x_{01} or x'_{01}.

A plot of the universal pattern (Fig. 7-8) ignores the obliquity factor. As is true of the TM_{01}-mode horn, there is a null on the axis. The maximum

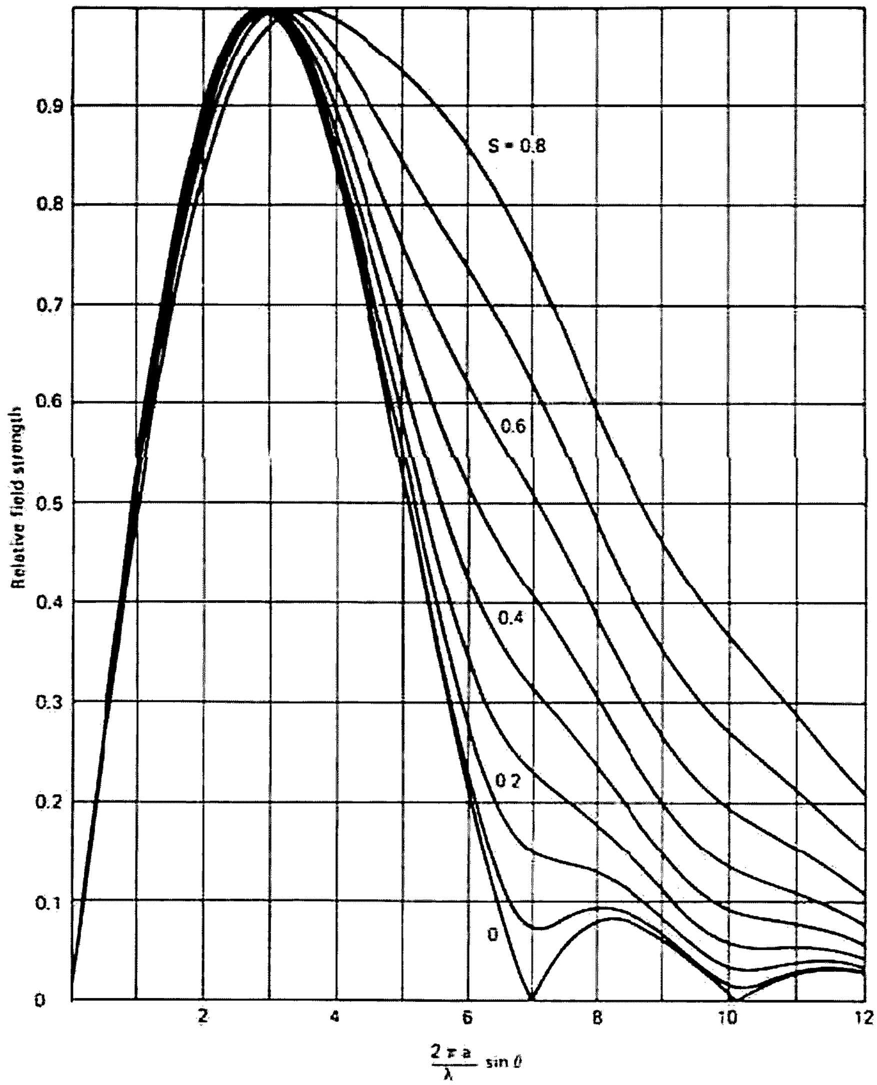

Figure 7-8 Universal pattern of a circular horn, TE_{01} mode. (Source: T. Milligan, "Universal Patterns Ease Circular Horn Design," *Microwaves*, vol. 20, no. 3, March 1981, p. 84.)

occurs at approximately the same point on the universal pattern, giving us

$$\theta_{\max} = \sin^{-1}\frac{0.462\lambda}{a} \qquad TE_{01} \tag{7-26}$$

When we calculate the amplitude taper loss from the aperture distribution, we must include the polarization factor, $\cos\phi_c$. We cannot use Eq. (6-16) for circularly symmetrical distributions; instead we must use Eq. (6-10), the general expression.

TM_{01} mode: ATL = 1.09 dB

TE_{01} mode: ATL = 1.91 dB

Equation (6-12) gives us a zero phase error efficiency, since the pattern has a boresight null. We use Eq. (6-11) at the beam peak to find phase error loss.

TABLE 7-6 Phase Error Losses at Beam Peak of a Circular Horn in the TM_{01} and TE_{01} Modes

	Mode			Mode	
	TM_{01}	TE_{01}		TM_{01}	TE_{01}
S	Phase error loss, dB		S	Phase error loss, dB	
0	1.59	1.84	0.40	3.38	3.08
0.05	1.62	1.86	0.45	3.88	3.41
0.10	1.70	1.92	0.50	4.45	3.78
0.15	1.84	2.02	0.55	5.10	4.20
0.20	2.03	2.15	0.60	5.82	4.65
0.25	2.28	2.32	0.65	6.64	5.14
0.30	2.58	2.54	0.70	7.57	5.66
0.35	2.95	2.79			

Table 7-6 lists the beam peak PEL at various S for the two modes. The obliquity factor has been removed.

Example Find the beam peaks and gains of a horn with an aperture radius of 1.5λ and $S = 0.20$ fed in the TM_{01} and TE_{01} modes. The beam peaks are as follows.

$$TM_{01},\ \text{Eq. (7-24)} \qquad \theta_{\max} = \sin^{-1}\frac{0.382}{1.5} = 14.8^\circ$$

$$TE_{01},\ \text{Eq. (7-26)} \qquad \theta_{\max} = \sin^{-1}\frac{0.462}{1.5} = 17.9^\circ$$

The gain is found from the aperture area and the distribution losses

$$\text{Gain} = 20\log\left(\frac{\pi D}{\lambda}\right) - \text{ATL} - \text{PEL} + 20\log\left(\frac{1+\cos\theta_{\max}}{2}\right) \qquad TE_{01}$$

From Table 7-6: $\text{PEL}_{\text{TM}} = 2.03$ dB $\qquad \text{PEL}_{\text{TE}} = 2.15$ dB

$$\text{Gain}_{\text{TM}} = 19.48 - 1.09 - 2.03 - 0.14 = 16.2 \text{ dB}$$

$$\text{Gain}_{\text{TE}} = 19.48 - 1.91 - 2.15 - 0.21 = 15.2 \text{ dB}$$

The TM_{01} mode can be excited directly from coax by flaring the outer shield of the coax until the diameter is sufficient to support the mode. At that point the conductor can be tapered away. A second method is to use a finite step in the outer shield of the coax feeder. Good symmetry prevents excitation of the TE_{11} mode. We adjust the length of the center conductor in the waveguide to give a good match.

The TE_{01} mode is difficult to excite cleanly. It is the fourth possible mode, and the lower-order modes are excited easily. We can excite the mode by feeding the circular waveguide with four rectangular guides with the inputs phased to provide a circulating electric field in the ϕ_c direction. By providing a smooth transition and good feed symmetry or by using mode suppressors, we prevent the excitation of lower-order modes in the circular guide. A series of flat plates placed along radial planes suppress the four lower-order modes.

7-4 Circular (Conical) Corrugated Horn

Normal smooth-wall horns present problems that can be eliminated by corrugating the walls. Many applications require dual linear or circular polarizations. The horn aperture must be square or circular. We have seen that the beamwidths in the two planes are unequal. When the smooth wall horn feeds a reflector, we have astigmatism (unequal phase centers in orthogonal planes). A horn has higher sidelobes in the E plane than the H plane without means of reducing them. Finally, the diffraction off E-plane walls causes backlobes. The aperture theory fails to predict them, but measurement or a GTD analysis shows them. Corrugating the walls can prevent all these problems.

Figure 7-9 shows the cross sections of two types of corrugated horns. The small-flare horn (a) is nominally the corrugated horn, and the wide-flare horn (b) is the scalar horn of Simmons and Kay [10]. Many papers appear in

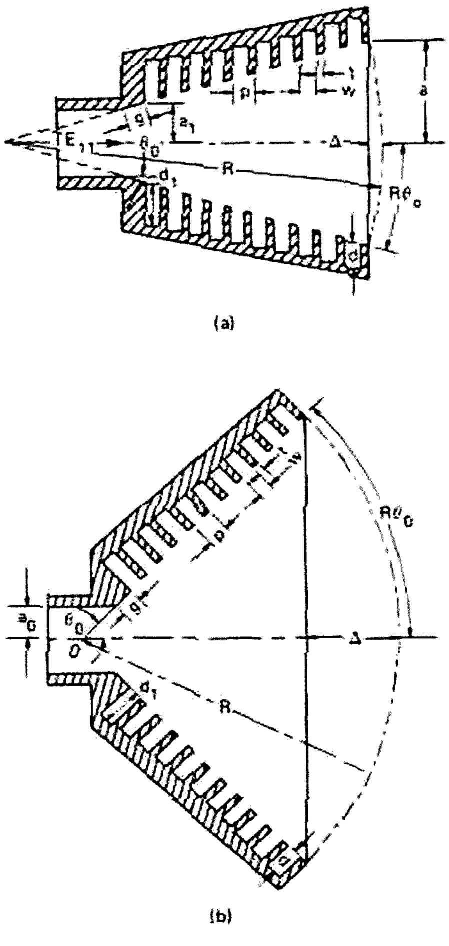

Figure 7-9 (a) Corrugated horn; (b) scalar horn. (Source: B. MacA. Thomas, "Design of Corrugated Conical Horns," *IEEE Trans. Antennas Propagat.*, vol. AP-26, no. 2, March 1978, p. 367. © 1978 IEEE.)

Section VI of Love's [1] collection of papers. Thomas [11] provides a good design summary in a topic with many papers. The corrugations that extend circumferentially should be cut normal to the slant radius as in (*b*), but they may be cut normal to the axis (*a*) for small flare angles.

The corrugated wall presents equal boundary conditions to the electric and magnetic fields when it is capacitive (slots $\lambda/4$ to $\lambda/2$ deep). The TE_{11} and TM_{11} modes, when excited in the transition between the smooth-wall waveguide and the corrugated-wall cone, have equal phase velocities. The combination of these modes forms the hybrid mode HE_{11} when the mode phases are equal. *When the modes are out of phase by 180°, the hybrid mode is* denoted EH_{11}. The ratio of the modes is called γ and $\gamma = 1$ for the balanced HE_{11} mode. $\gamma = 0$ corresponds to having only the TM_{11} mode and $\gamma = \infty$ to having only the TE_{11} mode. $\gamma = 1$ occurs when the corrugation depth is $\lambda/4$, but the horn parameters vary slowly with changing γ [12]. We will consider only $\gamma = 1$. Changing γ has its biggest effect on the cross-polarization [11, 13].

When $\gamma = 1$, the amplitude of the aperture fields is given by [14]

$$E_\rho = J_0\left(\frac{x_{01}\rho}{a}\right) \cos \phi_c \tag{7-27}$$

$$E_\phi = -J_0\left(\frac{x_{01}\rho}{a}\right) \sin \phi_c$$

where $x_{01} = 2.405$ is the first zero of $J_0(x)$, the Bessel function. The fields vanish at the walls and prevent edge diffractions that produce sidelobes and back scatter. The lower-order slope diffractions produce small sidelobes and backlobes, but we get *H*-plane-type lobes in all planes. In amplitude the aperture fields are symmetrical about the axis. All patterns through the cone axis are identical.

A Huygens source analysis of the aperture fields with a quadratic phase distribution produces Fig. 7-10, which is valid when the 10-dB beamwidth is less than 74° [11]. For greater beamwidths the flange changes the beamwidths of the small-aperture horn in the two planes and we should use the scalar horn. Table 7-7 lists the 3-, 10-, and 20-dB points from Fig. 7-10. We can use the table to find beamwidths of given horns or design to given beamwidths. Table 7-7 also lists the sum of ATL and PEL (GF) for various S. We can find gain or design to a given gain with this listing.

Example Find the 10-dB beamwidths and gain of a corrugated conical horn with an aperture radius of 12 cm and a slant radius of 50 cm at 5 GHz.

$$S = \frac{a^2}{2\lambda R} = \frac{12^2}{2(6)(50)} = 0.24$$

From Table 7-7 we find the k-space value at 10 dB for $S = 0.24$.

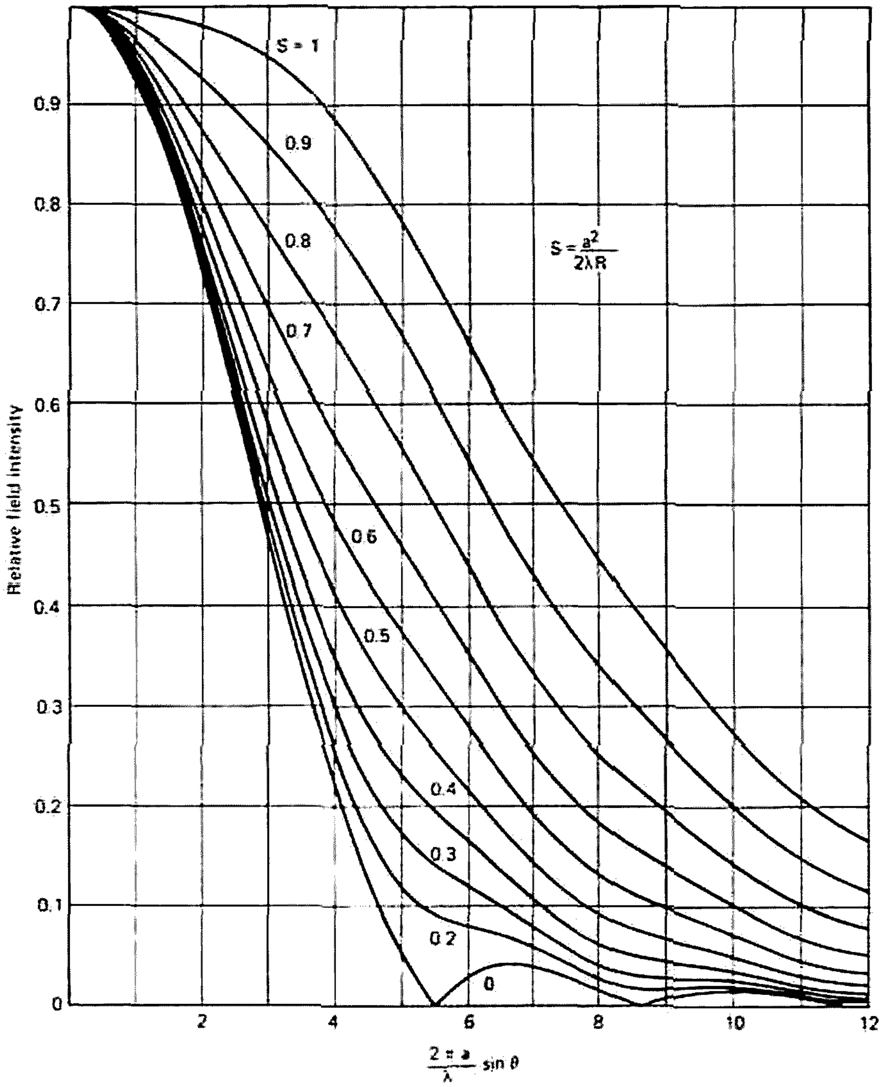

Figure 7-10 Universal pattern of a circular corrugated horn: HE_{11} mode.

$$\frac{2\pi a}{\lambda} \sin\theta = 3.7699 \qquad \text{or} \qquad \theta = 17.46^\circ$$

We include the obliquity factor, since the pattern loss will be greater than 10 dB at $\theta = 17.46^\circ$; $(1 + \cos 17.46^\circ)/2$: -0.20 dB.

$$BW_{10} = \sqrt{\frac{10}{10.20}}\,34.92^\circ = 34.57^\circ$$

A smooth-wall horn with the same dimensions has a similar H-plane beamwidth (33.4°).

We find the gain from the distribution losses and aperture area.

$$GF = ATL + PEL = 2.12 \text{ dB}$$

$$\text{Gain} = 20 \log\left(\frac{\pi D}{\lambda}\right) - GF = 19.86 \text{ dB}$$

The smooth-wall horn has about 0.5 dB more gain (20.4 dB).

TABLE 7-7 Resonant Circular Corrugated Horn Beamwidth Points, HE_{11} Mode

	Beamwidth level					Beamwidth level			
	3 dB	10 dB	20 dB	ATL + PEL, dB		3 dB	10 dB	20 dB	ATL + PEL, dB
S	Location $(2\pi a/\lambda)\sin\theta$				S	Location $(2\pi a/\lambda)\sin\theta$			
0	2.0779	3.5978	4.6711	1.60	0.52	2.3688	4.9532	7.9936	4.04
0.04	2.0791	3.6020	4.6878	1.62	0.56	2.4411	5.2720	8.4261	4.44
0.08	2.0827	3.6150	4.7405	1.66	0.60	2.5317	5.5878	8.9472	4.86
0.12	2.0887	3.6371	4.8387	1.73	0.64	2.6469	5.8913	9.4352	5.31
0.16	2.0974	3.6692	5.0061	1.83	0.68	2.7966	6.1877	9.8514	5.79
0.20	2.1088	3.7129	5.3052	1.96	0.72	2.9946	6.4896	10.2337	6.30
0.24	2.1234	3.7699	5.8451	2.12	0.76	3.2597	6.8134	10.6250	6.83
0.28	2.1415	3.8433	6.3379	2.30	0.80	3.6061	7.1788	11.0735	7.39
0.32	2.1637	3.9372	6.6613	2.52	0.84	4.0189	7.6042	11.6356	7.96
0.36	2.1906	4.0572	6.9179	2.76	0.88	4.4475	8.0852	12.2658	8.54
0.40	2.2231	4.2112	7.1534	3.04	0.92	4.8536	8.5773	12.8236	9.13
0.44	2.2624	4.4090	7.3939	3.34	0.96	5.2331	9.0395	13.3059	9.72
0.48	2.3103	4.6578	7.6633	3.68	1.00	5.5984	9.4701	13.7706	10.29

Example Design a circular corrugated-wall horn at 8 GHz with a gain of 22 dB. We use Eq. (7-20) with the GF from Table 7-7. Pick $S = 0.20$ (arbitrary).

$$D = \frac{3.75\text{ cm}}{\pi}10^{(22-1.96)/20} = 18.83\text{ cm}$$

$$R = \frac{D^2}{8\lambda S} = 59.10\text{ cm}$$

The phase center, like that of other horns, starts at the aperture for $S = 0$ ($R = \infty$) and moves toward the apex as S increases. Table 7-8 lists the phase center location as a ratio of the slant radius. Because the aperture distribution is the same along all radial lines of the aperture, the phase center is the same in all planes. We measure some variation, since the balance between modes will not be perfect and some higher-order modes will be generated. The phase center moves least over a frequency band for long horns (small S). A wide-flare-angle horn has its phase center at the apex and is better described as a scalar horn.

Scalar Horn The scalar horn has a wide half flare angle, θ_0. Its beamwidth depends on the half flare angle. Since the phase distribution in the aperture is large, there is an optimum diameter for a given flare angle. Table 7-9 lists the optimum diameter versus the flare angle [15]. The beamwidth is approximately a linear function of the half flare angle, θ_0, for the optimum horn.

TABLE 7-8 Phase Center Axial Location of a Circular Corrugated Horn (HE_{11} Mode) behind the Aperture as a Ratio of the Slant Length

S	L_p/R	S	L_p/R
0	0	0.36	0.386
0.04	0.005	0.40	0.464
0.08	0.020	0.44	0.542
0.12	0.045	0.48	0.614
0.16	0.080	0.52	0.673
0.20	0.124	0.56	0.718
0.24	0.178	0.60	0.753
0.28	0.240	0.64	0.783
0.32	0.310	0.68	0.811

TABLE 7-9 Optimum Diameter of Scalar Horn

Half flare angle θ_0,°	Aperture diameter, λ	Half flare angle θ_0,°	Aperture diameter, λ
15	10.5	45	3.5
20	8.0	50	3.0
25	6.4	55	2.8
30	5.2	60	2.6
35	4.5	65	2.4
40	3.9	70	2.3

Source: A. W. Rudge et al. (eds.), *The Handbook of Antenna Design*, Vol. I, Peregrinus, London, 1982, p. 429.

$$\begin{aligned} BW_3\ \mathrm{dB} &= 0.74\theta_0 \\ BW_{10}\ \mathrm{dB} &= 1.51\theta_0 \qquad (7\text{-}28) \\ BW_{20}\ \mathrm{dB} &= 2.32\theta_0 \end{aligned}$$

The scalar horn has a greater bandwidth as a reflector feed than the small-flare-angle corrugated horn, since the phase center is fixed at the horn apex.

Corrugation Design The corrugations present a capacitive reactance to the passing wave. When a corrugated surface is inductive, it will support surface waves. The depth of corrugations must be between $\lambda/4$ and $\lambda/2$. Less than $\lambda/4$ or greater than $\lambda/2$, it is inductive. Between $3\lambda/3$ and λ it will be capacitive again, but this second passband is seldom used.

A quarter-wavelength slot depth balances the two modes and gives the best results. The corrugations need be only $\lambda/4$ at the aperture. Before the aperture we find it better to deepen the slots. Quarter-wavelength deep corrugations mismatch the horn in the transition region, where the TM_{11} mode is generated from the TE_{11} mode. Corrugation depths approaching $\lambda/2$ affect the match less than $\lambda/4$ depths do.

To design for a particular band, limited to about 1.5:1 for a good match, we design with tapered corrugation depths. We make the corrugations $\lambda/4$ deep at the aperture at the low-frequency end. The high-frequency band edge determines the corrugation depth at just short of $\lambda/2$ in the throat. The horn needs at least four corrugations per wavelength along the slant radius. The high-frequency end determines the corrugation spacing. The first few corrugations can be used to match the horn to the waveguide, and we can improve the match by shaping the corrugation widths [13]. The slots should be as wide as practical spacers will allow. Mechanical considerations, such as shock and vibration, will determine the limits on the spacers.

The circular geometry of the horn changes the corrugation depth necessary for the balanced HE_{11} mode from $\lambda/4$. An empirical formula for the depth is given by [16]

$$d = \frac{\lambda}{4} \exp \frac{1}{2.5ka} \qquad ka > 2 \tag{7-29}$$

We increase the depth slightly at the horn aperture.

Choke Horns (Fig. 7-11) We can place corrugations in the flanges of small-aperture horns and design wide-beamwidth antennas with good pattern symmetry and low cross-polarization. The choke horn is the limit of a scalar horn opened to $\theta_0 = 90°$. The corrugations consist of concentric rings about the aperture and are generally a quarter wavelength deep. The best location for the corrugated rings may not be in the same plane as the aperture but instead somewhat behind as reported for a feed for a $F/D = 0.3$ reflector [17].

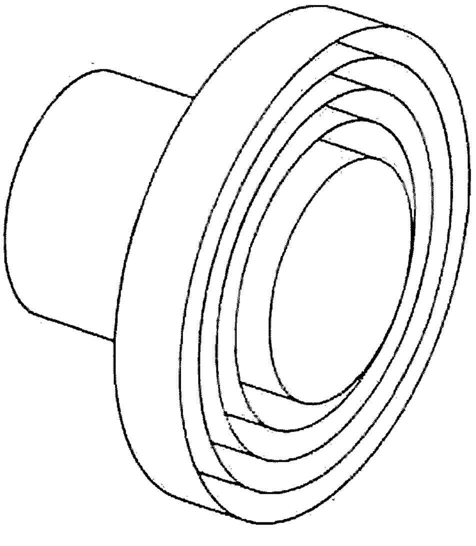

Figure 7-11 Choke horn.

The design for the reflector feed [17] used four corrugations. James [18] and Kumer [19] show that using only one corrugation is quite effective. More corrugations improve the design but only add marginally. Small apertures need the corrugations to reduce the cross-polarization peaking in the diagonal planes between the E and H planes.

We usually assume a Huygens source in the aperture plane of the horn. The approximation collapses as we shrink the aperture to achieve wide beamwidths. In the limit we have only a slot analyzed from magnetic currents replacing the electric field in the aperture. The magnetic field is ignored in the slot. A Huygens source assumption is that the ratio of the electric to magnetic field is the same as the impedance of free space. Waveguides have high wave impedances, which implies small magnetic fields. To calculate the far field, Eq. (6-7) must be used with the actual ratio of fields in the aperture instead of Eq. (6-8) with its Huygens source approximation. Restricting the aperture dimensions to achieve wide beamwidths will limit the bandwidth, as well as the cross-polarization isolation, because reducing the volume of the antenna raises the Q.

Rectangular Corrugated Horns We can design rectangular horns with corrugated walls. We only need to cut corrugations in the E-plane walls to establish a cosine distribution in the E plane. Only when dual polarization is radiated are corrugations needed on the H-plane walls. We analyze the horn as having an H-plane distribution (cosine) in both planes and use the results of Sec. 7-1. The rectangular horn can provide a cheaper substitute for the circular corrugated horn in many applications. The larger aperture dimension in the diagonal plane decreases the beamwidth slightly, but the rectangular horn still provides an acceptable design.

Both planes have a linear amplitude taper loss of 0.91 dB. We use the cosine column of Table 6-21 for the quadratic phase error loss. We design to beamwidths by using Table 7-1. Equalizing distributions in both planes of square horns results in equal phase centers given by Table 7-3 (H plane).

Example Find the gain of a square corrugated horn with an aperture width of 24 cm and a slant radius of 50 cm at 5 GHz.
From Eq. (7-1)

$$S = \frac{W^2}{8\lambda R} = \frac{24^2}{8(6)(50)} = 0.24$$

We use the cosine column of Table 6-21 for the phase error loss: $\text{PEL}_x = \text{PEL}_y = 0.42$ (cosine).
The amplitude taper loss is the same in both planes: 0.91 dB.

$$\text{Gain} = 10 \log \frac{4\pi W^2}{\lambda^2} - \text{ATL}_x - \text{ATL}_y - \text{PEL}_x - \text{PEL}_y$$

$$\text{Gain} = 23.03 \text{ dB} - 0.91 - 0.91 - 0.42 - 0.42 = 20.4 \text{ dB}$$

A circular corrugated horn with a diameter equal to the width and having the same slant radius has a gain of 19.9 dB or 0.5 dB less. The larger aperture area increased the gain over the circular horn.

7-5 Box Horn [20]

With the box horn (Fig. 7-12) multiple waveguide modes are used to decrease the *H*-plane amplitude taper loss and axial length of the horn. We add the TE_{30} mode to the TE_{10} mode to reduce the cosine distribution taper of the *H* plane. By phasing the modes 180° out of phase in the center of the aperture, the cos $3\pi x$ distribution subtracts from the TE_{10}-mode distribution in the center and adds in the region near the edges.

A step in the width of a waveguide generates TE_{N0} modes when fed by the TE_{10} mode. Any modes not cut off will propagate to the aperture. If we maintain symmetry about the axis of the waveguide, then only odd-order modes, TE_{30}, TE_{50}, etc., will be generated. The width *W* of the waveguide (Fig. 7-12) beyond the step determines the possible propagating modes

$$\lambda_c = \frac{2W}{N}$$

where *N* is the mode number. If we limit the modes to only the TE_{10} and TE_{30} modes in the aperture, then the cutoff wavelength of the TE_{50} mode determines the maximum width

$$W_{\max} = 2.5\lambda$$

The TE_{30} mode cutoff wavelength establishes the minimum width.

$$W_{\min} = 1.5\lambda$$

Within this range short horns with good aperture efficiency can be designed.

We can flare the *E* plane to increase its aperture (Fig. 7-12), but the limited axial length of the horn bounds the possible flare without an excessive

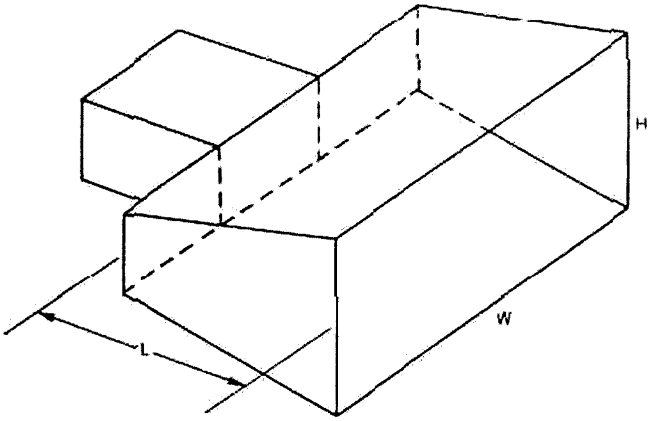

Figure 7-12 Box horn.

phase error loss. The H plane also can be flared, but flaring it complicates the design for the proper length L. The step generates smaller amplitudes of higher-order modes with each increase in N. Small amounts of higher-order modes—TE_{50}, TE_{70}, etc.—will decrease the efficiency only marginally, since the mode amplitudes are small.

The step generates modes in phase with the input TE_{10} mode, since the higher-order modes must peak in the center and subtract from the TE_{10} fields on the back wall of the larger waveguide section. The aperture distribution is a sum of TE_{10} and TE_{30} modes:

$$\begin{aligned} E_y(x) &= a_1 \cos\left(\frac{\pi x}{W}\right) \exp(-jk_{10}L) \\ &\quad + a_3 \cos\left(\frac{3\pi x}{W}\right) \exp(-jk_{30}L) \end{aligned} \tag{7-30}$$

where k_{10} and k_{30} are the propagation constants of the two modes. The amplitude distribution in the H plane will be more nearly uniform if the phase between the modes is 180°. The modes travel from the step with different phase velocities depending on their cutoff frequencies. We adjust the length L to give a 180° phase difference between the modes:

$$(k_{10} - k_{30})L = \pi$$

where $k_{10} = k\sqrt{1 - \left(\dfrac{\lambda}{2W}\right)^2}$ and $k_{30} = k\sqrt{1 - \left(\dfrac{3\lambda}{2W}\right)^2}$

We solve for the length

$$L = \frac{\lambda/2}{\sqrt{1 - (\lambda/2W)^2} - \sqrt{1 - (3\lambda/2W)^2}} \tag{7-31}$$

The ratio of the modes generated by the step can be found from mode matching on the input waveguide aperture of width a:

$$\frac{a_N}{a_1} = \frac{\displaystyle\int_{-a/2}^{a/2} \cos(\pi x/a)\cos(N\pi x/W)\,dx}{\displaystyle\int_{-a/2}^{a/2} \cos(\pi x/a)\cos(\pi x/W)\,dx} \tag{7-32}$$

where a_N is the TE_{N0} mode amplitude. Table 7-10 lists the step dimensions needed to design to a given ratio of modes. The amplitude taper loss is a minimum at $a_3/a_1 = 0.32$. The possible 3-dB beamwidths with a single mode, TE_{30}, range from 20° to 44°.

Example Design a box horn with an H-plane 10-dB beamwidth of 50°. We pick $a_3/a_1 = 0.35$. From Table 7-10

$$\frac{W}{\lambda}\sin\theta = 0.824$$

TABLE 7-10 Box Horn Characteristics

Ratio of TE_{30} and TE_{10} modes (voltages)	Ratio of input waveguide to aperture	Linear ATL_W, dB	Pattern level points	
			3 dB	10 dB
			Location	$(W/\lambda)\sin\theta$
0.00	1.000	0.91	0.594	1.019
0.05	0.940	0.78	0.575	0.981
0.10	0.888	0.67	0.558	0.947
0.15	0.841	0.58	0.544	0.917
0.20	0.798	0.52	0.530	0.890
0.25	0.758	0.48	0.518	0.866
0.30	0.719	0.46	0.507	0.844
0.35	0.682	0.46	0.496	0.824
0.40	0.645	0.47	0.487	0.806
0.45	0.609	0.50	0.479	0.790
0.50	0.573	0.54	0.471	0.775
0.55	0.537	0.60	0.463	0.761
0.60	0.500	0.66	0.456	0.749
0.65	0.462	0.74	0.450	0.737
0.70	0.424	0.82	0.444	0.726

The obliquity factor at 25° adds 0.42 dB loss. We must design with a wider 10-dB beamwidth.

$$BW_d = 50^\circ \sqrt{\frac{10.42}{10}} = 51.03^\circ$$

$$\frac{W}{\lambda} = \frac{0.824}{\sin(51.03^\circ/2)} = 1.913$$

This is within the permissible range for only two modes in the aperture. We find the length to phase the modes by 180° from Eq. (7-31); it is $L = 1.451\lambda$. The horn is shorter than the aperture width.

7-6 Multimode Circular Horn [21]

A step in the diameter of a circular waveguide generates the TM_{11} mode to satisfy the boundary conditions. The fields of the TM_{11} mode can be phased to cancel the fields from the TE_{11} mode at the edges of the aperture in the E plane. The tapering of the fields in the aperture reduces the E-plane sidelobes while broadening the beamwidth. Equalizing the field distributions in the two planes helps to bring the E- and H-plane phase centers closer together.

The modes generated by the step are more complicated than for the box horn. Symmetry eliminates the generation of the unwanted modes: TM_{01}, TE_{21}, and TE_{01}. The step transition shifts the phase of the TM_{11} mode relative to the TE_{11} mode [22]. Since the waveguide modes have different phase velocities, they can be phased to produce the desired field at the aperture. Although calculated information [22] is helpful, the designs must be completed empirically. The required phasing to achieve field cancellation limits the bandwidth, but for narrow-band applications the stepped horn is cheaper than a corrugated horn.

Satoh [23] loads the flare of a conical horn with a conical dielectric step to generate the TM_{11} mode. Symmetry prevents the excitation of the unwanted modes. He places the step at a diameter where the TM_{11} mode can propagate. By using two steps, the bandwidth can be increased because the lengths can be adjusted to give perfect mode cancellation at two frequencies. We can replace the dielectric cone by metal steps each of which generates the TM_{11} mode and thereby achieve good results, in theory, at multiple frequencies.

7-7 Biconical Horn [4]

The biconical horn consists of two cones with a common vertex. The angle of the generating lines of the cones is measured from a common axis. The cones of the usual antenna have angles that sum to 180°. Spherical modes describe the fields between the cones, but we can use approximations with good results. The lowest-order mode is TEM between the cones, and it is easily excited by a coax line. The outer conductor connects to one cone, and the second line feeds out of the center conductor. The electric field of the TEM mode is polarized in the direction of the axis. The first higher-order mode has a circulating electric field with the magnetic field in the direction of the axis. It can be excited either from a TE_{01}-mode circular waveguide or by an array of slots on a cylinder. The distance between cones must be at least $\lambda/2$ at the point of excitation of the TE_{01} biconical mode.

We will approximate the distribution of the zeroth-order mode, TEM, as uniform along the axis. The first-order mode, TE_{01}, distribution is approximately cosine along the axis. We find the gain by using aperture distribution losses. We describe the horn with a slant radius along the generating line and a height between the ends of the cones. The expansion in spherical modes requires an integration over a spherical cap at the aperture if a constant phase surface is used. We obtain good results by using a cylindrical aperture and a quadratic phase distribution. The antenna has circular symmetry about the z axis, and its directivity is bounded by Eq. (2-14). We use linear distribution efficiencies to find the directivity (gain)

$$\text{Gain} = 10 \log \left(\frac{2L}{\lambda}\right) - \text{ATL}_x - \text{PEL}_x \qquad (7\text{-}33)$$

The TEM mode has a uniform distribution, so we use the "uniform" column of Table 6-21 to find the phase error loss. The uniform distribution has no amplitude taper loss. The cosine distribution of the first-order mode requires an ATL = 0.91 dB and the use of the cosine distribution quadratic phase error loss of Table 6-21. Given a height between the ends of the cones H and the slant radius R, we find the quadratic phase distribution constant from

$$S = \frac{H^2}{8\lambda R} \tag{7-34}$$

Example Find the gain of a biconical horn with a slant radius of 10λ and cone angles of 75° and 105°.

$$H = 2R \cos 75° = 5.176\lambda \qquad S = 0.33$$

From Table 6-21, we find

$$\text{PEL}_{\text{TEM}} = -1.76 \text{ dB} \qquad \text{PEL}_{\text{TE}_{01}} = -0.79 \text{ dB}$$

Vertical mode, TEM: $\text{Gain} = 10 \log [2(5.176)] + \text{PEL}_{\text{TEM}}$

$$10.15 \text{ dB} - 1.76 \text{ dB} = 8.4 \text{ dB}$$

Horizontal mode, TE_{01}: $\text{Gain} = 10 \log [2(5.176)] - \text{PEL}_{\text{TE}_{01}} + \text{ATL}_{\text{cosine}}$

$$10.15 \text{ dB} - 0.79 \text{ dB} - 0.91 \text{ dB} = 8.45 \text{ dB}$$

We can find the beamwidths by using the results of the rectangular horn. We measure the angles from $\theta = 90°$ for the complementary angled biconical horn.

Example Find the 3-dB beamwidths of the above horn.

$$S = 0.33 \qquad H = 5.176\lambda$$

Use Table 7-2 with the TEM mode and α as the angle from $\theta = 90°$.

$$\frac{H}{\lambda} \sin \alpha = 0.5015 \qquad \alpha = 5.56°$$

The obliquity factor is insignificant.

$$\text{HPBW} = 11.1° \qquad \text{TEM mode}$$

Use Table 7-1 with the TE_{01} mode.

$$\frac{H}{\lambda} \sin \alpha = 0.6574 \qquad \text{HPBW} = 14.6° \qquad \text{TE}_{01} \text{ mode}$$

The two modes have about the same gain, but the TE_{01} mode has a greater beamwidth. When we refer to Figs. 7-3 and 7-4, we see that the TEM-mode horn has about 7-dB sidelobes and the TE_{01}-mode horn has practically no sidelobes. The sidelobes reduce the gain of the TEM mode with its narrower beamwidth.

REFERENCES

1. A. W. Love (ed.), *Electromagnetic Horn Antennas*, IEEE Press, New York, 1976.
2. W. L. Barrow and L. J. Chu, "Theory of Electromagnetic Horn," *Proc. IRE*, vol. 27, January 1939, pp. 51–64.
3. M. G. Schorr and F. J. Beck, "Electromagnetic Field of the Conical Horn," *J. Appl. Phys.*, vol. 21, August 1950, pp. 795–801.
4. S. A. Schelkunoff and H. Friis, *Antenna Theory and Practice*, Wiley, New York, 1952.
5. P. M. Russo et al., "A Method of Computing *E* Plane Patterns of Horn Antennas," *IEEE Trans. Antennas Propagat.*, vol. AP-13, March 1965, pp. 219–224.
6. J. Boersma, "Computation of Fresnel Integrals," *Math. Comp.*, vol. 14, 1960, p. 380.
7. K. S. Kelleher in H. Jasik (ed.), *Antenna Engineering Handbook*, McGraw-Hill, New York, 1961, p.12-5.
8. E. H. Braun, "Gain of Electromagnetic Horns," *Proc. IRE*, vol. 41, January 1953, pp. 109–115.
9. E. I. Muehldorf, "The Phase Center of Horn Antennas," *IEEE Trans. Antennas Propagat.*, vol. AP-18, November 1970, pp. 753–760.
10. A. J. Simmons and A. F. Kay, "The Scalar Feed—A High Performance Feed for Large Paraboloid Reflectors," *Design and Construction of Large Steerable Aerials*, IEE Conf. Publ. 21, 1966, pp. 213–217.
11. B. MacA. Thomas, "Design of Corrugated Conical Horns," *IEEE Trans. Antennas Propagat.*, vol. AP-26, no. 2, March 1978, pp. 367–372.
12. T. S. Chu and W. E. Legg, "Gain of Corrugated Conical Horn," *IEEE Trans. Antennas Propagat.*, vol. AP-30, no. 4, July 1982, pp. 698–703.
13. G. L. James, "TE_{11} to HE_{11} Mode Converters for Small Angle Corrugated Horns," *IEEE Trans. Antennas Propagat.*, vol. AP-30, no. 6, November 1982, pp. 1057–1062.
14. P. J. B. Clarricoats and P. K. Saha, "Propagation and Radiation of Corrugated Feeds," *Proc. IEE*, vol. 118, September 1971, pp. 1167–1176.

15 A. W. Rudge et al. (eds.), *The Handbook of Antenna Design*, Vol. I, Peregrinus, London, 1982, p. 429.

16. G. L. James and B. MacA. Thomas, "TE_{11}-to-HE_{11} Corrugated Cylindrical Waveguide Mode Converters Using Ring-Loaded Slots," *IEEE Trans. Microwave Theory Tech.*, vol. MTT-30, March 1982, pp. 278–285.
17. R. Wohlleben, H. Mattes, and O. Lochner, "Simple Small Primary Feed for Large Opening Angles and High Aperture Efficiency," *Electronics Letters*, vol. 8, 21st September 1972, pp. 474–476.
18. G. L. James, "Radiation Properties of 90° Conical Horns," *Electronics Letters*, vol. 13, no. 10, 12th May 1977, pp. 293–294.
19. A. Kumer, "Reduce Cross-Polarization in Reflector-Type Antennas," *Microwaves*, March 1978, pp. 48–51.
20. S. Silver (ed.) *Microwave Antenna Theory and Design*, McGraw-Hill, New York, 1949, pp. 377–380.
21. P. D. Potter, "A New Horn Antenna with Suppressed Sidelobes and Equal Beamwidths," *Microwave J.*, vol. 6, June 1963, pp. 71–78.
22. W. J. English, "The Circular Waveguide Step-Discontinuity Mode Transducer," *IEEE Trans. Microwave Theory Tech.*, vol. MTT-21, no. 10, October 1973, pp. 633–636.

23 T. Satoh, "Dielectric Loaded Horn Antenna," *IEEE Trans. Antennas Propagat.*, vol. AP-20, no. 2, March 1972, pp. 199–201.

CHAPTER 8

REFLECTOR ANTENNAS

The importance of reflector antennas cannot be overstated. Large-aperture antennas can be built only with reflectors or arrays. Reflectors are far simpler than arrays. The arrays give us more degrees of freedom than are required in many applications. With plenty of room and slow scan rates a reflector becomes a better design than an array. Of course, there can be many valid reasons for using an array in an application, but a reflector should always be considered. An array needs an elaborate feed network, whereas a reflector uses a simple feed and free space as its feed network.

Most reflector designs require extensive calculations along with full characterization of the feed antenna. Many types of analysis have been developed. As with horn antennas, Love [1] has collected significant papers on reflector antennas. Silver [2], in his classic book, provides the foundation for the analysis based on aperture theory and physical optics (induced currents on the reflector). Aperture theory or physical optics reduced to aperture theory is still used for most designs. Rusch and Potter fully develop aperture and physical optics theories for the design and analysis of both the prime focus and dual-reflector (Cassegrain) antennas [3]. Other methods have been developed to either increase the range of valid patterns or decrease the pattern calculation time so that optimization techniques can be applied. Wood [4] collects the ideas for designing by using the spherical wave expansion method that allow for an overall system optimization with a few terms of an expansion. GTD methods [5, 6] find increasing applications as an analysis technique suitable for a full pattern analysis except at boresight. Improved methods of calculating the secondary pattern have been developed using the aperture fields, such as FFT methods [7] and Jacobi-Bessel series [8]. Many of these techniques and recent hardware implementations of reflectors are summarized in a recent handbook [9]. Although all these methods are available, aperture theory and projected physical optics theory remain the main techniques of reflector design.

8-1 Geometric Optics

Geometric optics (GO) uses ray methods to approximate electromagnetics. It is exact only in the limit of zero wavelength (infinite frequency), but we gain useful insight from it at any frequency. It will not give good results close to physical boundaries; but when we include the geometric theory of diffractions (GTD), the results are accurate to one-wavelength sizes and are useful to $\lambda/4$ sizes. GO gives us the needed physical insight when we deal with reflectors. We must consider three aspects to fully use GO: (1) ray reflections, (2) polarization, and (3) amplitude variations along the ray path and through reflections.

Fermat's Principle and Snell's Laws Rays travel through a medium at the speed of light determined by the index of refraction:

$$n = \sqrt{\epsilon_r \mu_r}$$

We define the optical path length as

$$\int_C n\, dl \qquad (8\text{-}1)$$

where C is a prescribed path in space.

Fermat's principle determines the paths of rays between two points. It states that the optical path length is stationary along a valid ray path. An expression is stationary when its first derivatives are zero; that is, the optical path is a minimum (or maximum). We use Fermat's principle to trace ray paths through reflections or refractions by searching for the minimum optical path lengths. We can find more than one possible ray between points because Fermat's principle requires only a local minimum. When we exclude the boundaries of lenses, that is, regions of homogeneous medium, rays travel in straight lines.

We can derive Snell's laws of reflection and refraction from Fermat's principle.The two laws of reflection are given as:

1. The incident ray, the reflected ray, and the normal of the reflecting surface at the point of reflection lie in the same plane.

2. The incident and reflected rays make equal angles with the surface normal.

Implicit in Snell's laws is the idea that locally the wavefront behaves like a plane wave and that the reflector can be treated as a plane.

Given the direction of the incident ray $\mathbf{S}_1$, reflected ray $\mathbf{S}_2$, and the reflector normal $\mathbf{n}$, Snell's laws of reflection can be expressed vectorially [10].

$$\mathbf{n} \times (\mathbf{S}_2 - \mathbf{S}_1) = 0 \qquad \mathbf{n} \cdot (\mathbf{S}_2 + \mathbf{S}_1) = 0 \tag{8-2}$$

We combine Eqs. (8-2) to determine the ray directions before or after reflection.

$$\mathbf{S}_1 = \mathbf{S}_2 - 2(\mathbf{S}_2 \cdot \mathbf{n})\mathbf{n} \qquad \mathbf{S}_2 = \mathbf{S}_1 - 2(\mathbf{S}_1 \cdot \mathbf{n})\mathbf{n} \tag{8-3}$$

Snell's law of refraction can also be expressed vectorially as

$$\mathbf{n} \times (n_2\mathbf{S}_2 - n_1\mathbf{S}_1) = 0 \tag{8-4}$$

where n_1 and n_2 are the index of refractions in the two mediums.

Polarization Effects The electric field is orthogonal to the ray direction (a free-space wave) and is described by a two-dimensional polarization space (Sec. 1-8). We can describe polarization in any conveniently rotated basis about the ray. We will pick a ray-fixed coordinate system that changes direction after a reflection.

$$\mathbf{E}_i = \mathbf{a}^i_{\parallel} E_{i\parallel} + \mathbf{a}^i_{\perp} E_{i\perp} \tag{8-5}$$

where $\mathbf{a}^i_{\parallel}$ is a unit vector in the plane of incidence, $\mathbf{a}^i_{\perp}$ is perpendicular to the plane of incidence, and

$$\mathbf{a}^i_{\perp} \times \mathbf{S}_i = \mathbf{a}^i_{\parallel} \tag{8-6}$$

$E_{i\parallel}$ is the incident electric field in the direction of $\mathbf{a}^i_{\parallel}$, and $E_{i\perp}$ is that in the direction of $\mathbf{a}^i_{\perp}$. The electric field parallel with the reflector surface must vanish on the conductor surface; that is

$$E_{r\perp} = -E_{i\perp} \tag{8-7}$$

where $E_{r\perp}$ is the reflected field along $\mathbf{a}^r_{\perp}$. We find the reflection properties of $E_{\parallel}$ from the corresponding magnetic fields that are parallel with the surface.

$$H_{r\parallel} = H_{i\parallel} \tag{8-8}$$

By combining Eqs. (8-7) and (8-8), we obtain the dyadic relation for the ray-fixed coordinate system.

$$\begin{bmatrix} E_{r\parallel} \\ E_{r\perp} \end{bmatrix} = \begin{bmatrix} 1 & 0 \\ 0 & -1 \end{bmatrix} \begin{bmatrix} E_{i\parallel} \\ E_{i\perp} \end{bmatrix} \tag{8-9}$$

where $E_{r\parallel}$ and $E_{r\perp}$ are the reflected field components. At each reflection we rotate the polarizations to align $\mathbf{a}_{i\perp}$ with the normal to the plane of incidence. Of course, the alternative method is to describe polarizations in a fixed three-dimensional coordinate system, but it requires a 3 by 3 reflection matrix.

Amplitude Variations along a Ray The power decreases in a general ray as the distance from the source increases. If we expand the constant-phase surface (eikonal) about the ray in a Taylor series, we obtain a surface described by its radii of curvature [11]. The maximum and minimum radii of curvature lie in the orthogonal principal planes. These radii of curvature determine the amplitude spread of the wave from point to point on the ray. We find the ratio of differential areas about the ray at two locations as

$$\frac{dA_2}{dA_1} = \frac{\rho_1\rho_2}{(\rho_1 + d)(\rho_2 + d)} \tag{8-10}$$

where ρ_1 and ρ_2 are the principal radii of curvature and d is the distance between two points on the ray (Fig. 8-1). The electric field variation along the ray becomes

$$E_0 e^{-jkd}\sqrt{\frac{\rho_1\rho_2}{(\rho_1 + d)(\rho_2 + d)}} \tag{8-11}$$

for the astigmatic ray spreading from unequal radii of curvature. When $d = -\rho_1$ or $d = -\rho_2$, GO fails because it predicts an infinite power density. We call these points caustics. Remember that the ray always has differential area and never has any real area as implied by Fig. 8-1.

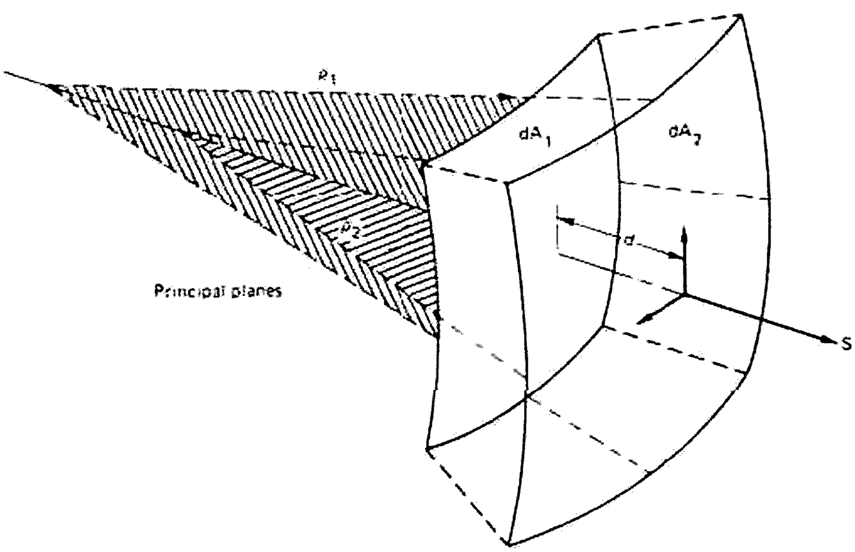

Figure 8-1 Astigmatic ray.

We have three special cases of the astigmatic ray:

1. Spherical wave, $\rho_1 = \rho_2$ $$E_0 e^{-jkd} \frac{\rho}{\rho + d} \qquad (8\text{-}12)$$
2. Cylindrical wave, $\rho_1 = \infty$ $$E_0 e^{-jkd} \sqrt{\frac{\rho}{\rho + d}} \qquad (8\text{-}13)$$
3. Plane wave, $\rho_1 = \rho_2 = \infty$ $$E_0 e^{-jkd} \qquad (8\text{-}14)$$

The plane wave does not spread but has a constant amplitude with distance. Both the cylindrical and the plane waves require infinite power, and they are therefore nonphysical but convenient mathematically.

When a wave reflects from a curved surface, its radii of curvature and principal planes change. The field along the reflected ray is given by

$$\mathbf{E}_r(s) = \mathbf{E}_{io} \cdot \overline{\overline{R}} \sqrt{\frac{\rho_1^r \rho_2^r}{(\rho_1^r + S)(\rho_2^r + S)}} e^{-jkS} \qquad (8\text{-}15)$$

where S is the distance along the ray from the reflection, ρ_1^r and ρ_2^r are the reflected ray radii of curvature, and $\overline{\overline{R}}$ is the reflection dyadic. $\mathbf{E}_{\omega}$ is the incident ray electric field. For a flat surface we use images of the incident ray caustics for ρ_1^r and ρ_2^r, but, in general, ρ_1^r and ρ_2^r become

$$\frac{1}{\rho_1^r} = \frac{1}{2}\left(\frac{1}{\rho_1^i} + \frac{1}{\rho_2^i}\right) + \frac{1}{f_1} \qquad \frac{1}{\rho_2^r} = \frac{1}{2}\left(\frac{1}{\rho_1^i} + \frac{1}{\rho_2^i}\right) + \frac{1}{f_2} \qquad (8\text{-}16)$$

where f_1 and f_2 are generalized focal lengths of the surface.

Kouyoumjian and Pathak [12] have derived formulas for the focal lengths of a surface. Given a surface with principal radii of curvature R_1 and R_2 with directions $\mathbf{u}_1$ and $\mathbf{u}_2$ at the point of reflection. For an incident ray with principal axes defined by unit vectors $\mathbf{x}_1^i$ and $\mathbf{x}_2^i$, we define a matrix relation between the incident ray and surface principal curvature directions:

$$\theta = \begin{bmatrix} \mathbf{x}_1^i \cdot \mathbf{u}_1 & \mathbf{x}_1^i \cdot \mathbf{u}_2 \\ \mathbf{x}_2^i \cdot \mathbf{u}_1 & \mathbf{x}_2^i \cdot \mathbf{u}_2 \end{bmatrix} \qquad (8\text{-}17)$$

where the determinant is $|\theta| = (\mathbf{x}_1^i \cdot \mathbf{u}_1)(\mathbf{x}_2^i \cdot \mathbf{u}_2) - (\mathbf{x}_2^i \cdot \mathbf{u}_1)(\mathbf{x}_1^i \cdot \mathbf{u}_2)$. Given the angle of incidence θ', the following are the focal lengths:

$$\begin{aligned} \frac{1}{f_{\substack{1\\2}}} = {} & \frac{\cos\theta'}{|\theta|^2}\left(\frac{\theta_{22}^2 + \theta_{12}^2}{R_1} + \frac{\theta_{21}^2 + \theta_{11}^2}{R_2}\right) \\ & \pm \frac{1}{2}\left\{\left(\frac{1}{\rho_1^i} - \frac{1}{\rho_2^i}\right)^2 + \left(\frac{1}{\rho_1^i} - \frac{1}{\rho_2^i}\right)\frac{4\cos\theta'}{|\theta|^2}\right. \\ & \cdot \left(\frac{\theta_{22}^2 - \theta_{12}^2}{R_1} + \frac{\theta_{21}^2 - \theta_{11}^2}{R_2}\right) \\ & \left. + \frac{4\cos^2\theta'}{|\theta|^4}\left[\left(\frac{\theta_{22}^2 + \theta_{12}^2}{R_1} + \frac{\theta_{21}^2 + \theta_{11}^2}{R_2}\right)^2 - \frac{4|\theta|^2}{R_1 R_2}\right]\right\}^{1/2} \end{aligned} \qquad (8\text{-}18)$$

With a single reflection, we need not find the direction of the principal axes. We need only the focal lengths. Multiple reflections require a knowledge of the reflected-ray principal plane directions. Define the following matrices to determine the directions of the principal axes after reflection.

$$Q_0^i = \begin{bmatrix} \dfrac{1}{\rho_1^i} & 0 \\ 0 & \dfrac{1}{\rho_2^i} \end{bmatrix} \qquad C_0 = \begin{bmatrix} \dfrac{1}{R_1} & 0 \\ 0 & \dfrac{1}{R_2} \end{bmatrix}$$

$$Q^r = Q_0^i + 2(\theta^{-1})^T C_0 \theta^{-1} \cos\theta_i$$

$$\mathbf{b}_1^r = \mathbf{x}_1^i - 2(\mathbf{n} \cdot \mathbf{x}_1^i)\mathbf{n} \qquad \mathbf{b}_2^r = \mathbf{x}_2^i - 2(\mathbf{n} \cdot \mathbf{x}_2^i)\mathbf{n}$$

where n is the surface normal at the reflection point. One principal-axis direction is

$$\mathbf{x}_1^r = \frac{\left(Q_{22}^r - \dfrac{1}{\rho_1^r}\right) b_1^r - Q_{12}^r \mathbf{b}_2^r}{\sqrt{\left(Q_{22}^r - \dfrac{1}{\rho_1^r}\right)^2 + (Q_{12}^r)^2}} \tag{8-19}$$

We find the other from the cross product of Eq. (8-19) and the reflected ray unit vector.

$$\mathbf{x}_2^r = -\mathbf{S}_r \times \mathbf{x}_1^r \tag{8-20}$$

We must reapply Eqs. (8-16) through (8-20) for every reflection.

We use Eqs. (8-16) through (8-20) for analysis, but except for computer optimizations, they cannot be directly applied to synthesis. If we limit the reflectors to figures of rotation, the radii of curvature are given by the meridians and parallels. The problems reduce to two dimensions. Similarly, a cylindrical reflector fed with a cylindrical wave [Eq. (8-13)] reduces the problem to two dimensions. The incident and reflected waves remain in the single plane picked for the reflector analysis.

Ray Tracing Tracing rays through a reflector system is conceptually straightforward. Where a ray strikes a reflector, we find the normal to the surface. By using Eq. (8-3), we solve for the reflected-ray direction. Equation (8-9) determines the polarization effects when we express the incident and reflected rays in the ray-fixed coordinates. We will use geometric arguments to determine the amplitude variation along the ray through the reflection instead of the general expressions given above. We experience difficulty when we try to find the reflection points for given field and source points. No analytical expressions exist for finding the reflection point of a general surface. The usual computer routines search for the minimum optical path length (Fermat's principle) without using Eq. (8-3), since a local minimum will satisfy this equation.

8-2 Parabolic Reflector Geometry

Figure 8-2 shows the geometry of the parabolic reflector. We form the reflector by rotating the figure about its axis or by moving the figure along an axis out of the paper to form a cylindrical reflector. Because the cylindrical reflector requires a line source, it is less important than the circularly symmetrical reflector fed from a single point source.

A paraboloidal reflector transforms a spherical wave radiated from an antenna at its focus into a plane wave. The wave spreads from the focus, and its amplitude decreases with the spreading. Geometric optics predicts a plane wave reflection off the surface that remains constant after reflection. The reflected wave spreads because the fields must be continuous across the reflection boundary of the plane wave column reflected from the surface. Fields can be discontinuous only across physical boundaries. We will use the

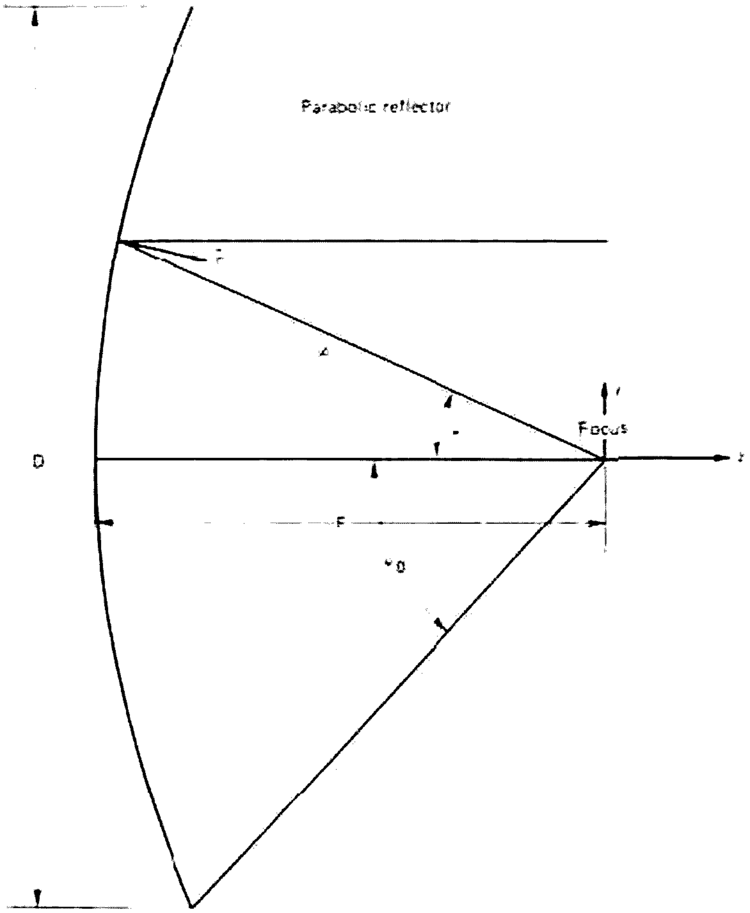

Figure 8-2 Geometry of the parabolic reflector.

aperture theory to predict its performance. Since the reflected rays are parallel, we can place the aperture anywhere close in front of the reflector.

The equations for the reflector surface are

$$r^2 = 4F(F - z) \qquad \rho = \frac{F}{\cos^2(\psi/2)} \tag{8-21}$$

Rectangular coordinates   Polar coordinates

where F is the focal length, D is the diameter, ρ is the distance from the focus to the reflector, and ψ is the angle from the negative z axis.

We will eliminate the dimensions of the reflector by using the ratio F/D. The half subtended angle of the reflector, ψ_0, relates to F/D by

$$\psi_0 = 2\tan^{-1}\frac{1}{4F/D} \tag{8-22}$$

When we place the aperture plane at the focus, the ray path distance becomes

$$\rho + \rho\cos\psi = 2\rho\cos^2\frac{\psi}{2} = 2F$$

That is, all ray paths are equal and the aperture plane is a constant-phase surface (eikonal).

The spherical wave spreads from the focus as $1/\rho$. At the surface of the reflector the wave curvature changes to a plane wave and propagates to the aperture plane at a constant amplitude. The spherical wave spreading multiplies the feed distribution by [Eq. (8-21)] $\cos^2(\psi/2)$ in the aperture. Then

$$\text{Added edge taper} = \cos^2\left(\frac{\psi_0}{2}\right) \qquad \text{(voltage)} \tag{8-23}$$

Deeper reflectors (smaller F/D) have greater edge tapers than shallow reflectors (larger F/D).

Example Find the edge taper of a paraboloidal reflector for $F/D = 0.5$ and an isotropic feed. From Eq. (8-22)

$$\psi_0 = 2\tan^{-1}\tfrac{1}{2} = 53.13°$$

The edge taper is [Eq. (8-23)]

$$\text{Edge taper} = 20\log\cos^2\frac{53.13°}{2} = -1.94\text{ dB}$$

If the feed has its 10-dB pattern point directed toward the reflector edge, the aperture edge taper is 11.9 dB.

8-3 Paraboloidal Reflector Aperture Distribution Losses

We will manipulate Eq. (6-10) for ATL to eliminate the dimensions and relate the integrals to the feed pattern.

$$\mathrm{ATL} = \frac{\left[\int_0^{2\pi}\int_b^a |E_a(r',\phi')|r'\,dr'\,d\phi'\right]^2}{\pi a^2\int_0^{2\pi}\int_b^a |E_a(r',\phi')|^2 r'\,dr'\,d\phi'} \tag{8-24}$$

where a is the aperture radius, b is the central blockage radius, and $E_a(r',\phi')$ *is the aperture field. We make the following substitutions into* Eq. (8-24):

$$r' = \rho\sin\psi = 2\sin\frac{\psi}{2}\cos\frac{\psi}{2}\frac{F}{\cos^2(\psi/2)} = 2F\tan\frac{\psi}{2}$$

$$dr' = F\sec^2\frac{\psi}{2} = \rho\,d\psi \tag{8-25}$$

The aperture field is related to the feed pattern by

$$E_a(r',\phi') = \frac{E(\psi',\phi')}{\rho}$$

These substitutions eliminate dimensions in Eq. (8-24).

$$\mathrm{ATL} = \frac{\left(\int_0^{2\pi}\int_{\psi_b}^{\psi_0} |E(\psi,\phi)|\tan(\psi/2)\,d\psi\,d\phi\right)^2}{\pi[\tan^2(\psi_0/2) - \tan^2(\psi_b/2)]\int_0^{2\pi}\int_{\psi_b}^{\psi_0} |E(\psi,\phi)|^2\sin\psi\,d\psi\,d\phi} \tag{8-26}$$

where $\psi_b = 2\tan^{-1}(b/2F)$

When we substitute the relations in Eq. (8-25) into Eq. (6-12) to eliminate dimensions in the integrals, we obtain an expression with only the feed pattern.

$$\mathrm{PEL} = \frac{\left|\int_0^{2\pi}\int_{\psi_b}^{\psi_0} E(\psi,\phi)\tan(\psi/2)\,d\psi\,d\phi\right|^2}{\left(\int_0^{2\pi}\int_{\psi_b}^{\psi_0} |E(\psi,\phi)|\tan(\psi/2)\,d\psi\,d\phi\right)^2} \tag{8-27}$$

PEL is the efficiency at boresight. We will modify Eq. (8-27) when we scan the beam to give off-boresight values as in Eq. (6-11).

The amplitude taper efficiency (ATL) of Eq. (8-26) and the phase error efficiency (PEL) of Eq. (8-27) do not account for the total directivity loss of the aperture. The reflector does not intercept all the power radiated by the source; some power spills over the edge. This power adds little to the pattern except as sidelobes, since usual feeds have small backlobes. We consider this spilled-over power as a loss.

$$\text{Spillover} = \text{SPL} = \frac{\int_0^{2\pi} \int_{\psi_b}^{\psi_0} |E(\psi, \phi)|^2 \sin \psi \, d\psi \, d\phi}{\int_0^{2\pi} \int_0^{\pi} |E(\psi, \phi)|^2 \sin \psi \, d\psi \, d\phi} \qquad (8\text{-}28)$$

This expression for spillover includes the scattered portion of the central blockage efficiency, but not the loss of potential aperture. We include the remainder in the directivity calculation.

We have ignored the cross-polarized power radiated by the source. We will define a cross-polarization efficiency

$$\text{XOL} = \frac{\int_0^{2\pi} \int_0^{\pi} |E_c(\psi, \phi)|^2 \sin \psi \, d\psi \, d\phi}{\int_0^{2\pi} \int_0^{\pi} (|E_c(\psi, \phi)|^2 + |E_x(\psi, \phi)|^2) \sin \psi \, d\psi \, d\phi} \qquad (8\text{-}29)$$

where E_c is the copolarized field and E_x is the cross-polarized field. These polarizations correspond to Ludwig's [13] third definition of cross-polarization. We naturally measure this on a model tower positioner that splits the power into orthogonal Huygens sources. A Huygens source produces straight reflector currents when projected to the aperture plane. Including the cross-polarization efficiency gives us the true average radiation intensity as in Eq. (1-10).

If we express the efficiencies as ratios, the directivity will be found from

$$\text{Directivity} = \left(\frac{\pi}{\lambda}\right)^2 (D_r^2 - D_b^2) \text{ SPL ATL PEL XOL} \qquad \text{ratio} \quad (8\text{-}30)$$

where D_r is the reflector diameter and D_b is the diameter of the central blockage. Equation (8-30) includes the nonscattered blockage loss; that is, the loss of potential aperture. Equation (8-30) can be expressed in terms of dB ratios.

$$\text{Directivity} = 10 \log\left[\left(\frac{\pi}{\lambda}\right)^2 (D_r^2 - D_b^2)\right] + \text{SPL (dB)} + \text{ATL (dB)}$$
$$+ \text{PEL (dB)} + \text{XOL (dB)} \qquad (8\text{-}31)$$

Of course, all the dB ratios of the efficiencies will be negative and subtract from the directivity calculated from the area.

When measuring an actual feed, we can ignore the cross-polarized power. We must measure the efficiency as the difference between directivity and gain. Actual directivity includes the copolarizations and cross-polarizations in the average radiation intensity. If we ignore the cross-polarization, the measured efficiency decreases by the cross-polarization loss because the measured and true directivity differ by that loss. We must measure the cross-polarization pattern distribution of the feed if we want to calculate the cross-polarized secondary pattern (reflector pattern). When the cross-polarization pattern is not required, we save time without loss of accuracy by measuring only the copolarized feed pattern.

Equations (8-28) and (8-29) are by no means unique. We could include the cross-polarized power in the spillover calculation [Eq. (8-28)] and limit the integration limits in Eq. (8-29) to the reflector. A set of efficiency relations is correct when the equations account for all the power radiated by the feed. When we use calculated feed patterns, we must find the cross-polarization efficiency, since we can only estimate the efficiency due to material losses. The cross-polarization efficiency cannot be included as it is in measurements. The division of cross-polarized power between Eqs. (8-28) and (8-29) becomes arbitrary.

8-4 Approximate Spillover and Amplitude Taper Trade-offs

We will use the approximate pattern $\cos^{2N}(\theta/2)$ for a feed pattern to establish trends. Of course, if the actual feed pattern distribution is available, we should use Eqs. (8-26) through (8-29). We obtain closed-form expressions when we substitute this pattern into Eqs. (8-26) and (8-28). Ignoring any central blockage, we get

$$\text{Spillover efficiency} = 1 - u^{2(N+1)} \tag{8-32}$$

$$\text{Amplitude taper efficiency} = \frac{4(N+1)(1-u^N)^2}{N^2[1-u^{2(N+1)}]}\cot^2\frac{\psi_0}{2} \tag{8-33}$$

where $u = \cos(\psi_0/2)$.

We combine Eqs. (8-32) and (8-33) and plot their combination to find the beamwidth for minimum loss. In Fig. 8-3 the loss versus the 10-dB beamwidth for various *F/D* is plotted. At narrow beamwidths little feed power spills over the reflector edge, but the reflector is underilluminated. Increasing the beamwidth improves the illumination but increases the spillover. The efficiency peaks when the feed 10-dB beamwidth is approximately the subtended angle of the reflector. Figure 8-3 shows a broad peak for any given *F/D*. Small changes in the beamwidth near the peak have no practical effect on the reflector's gain.

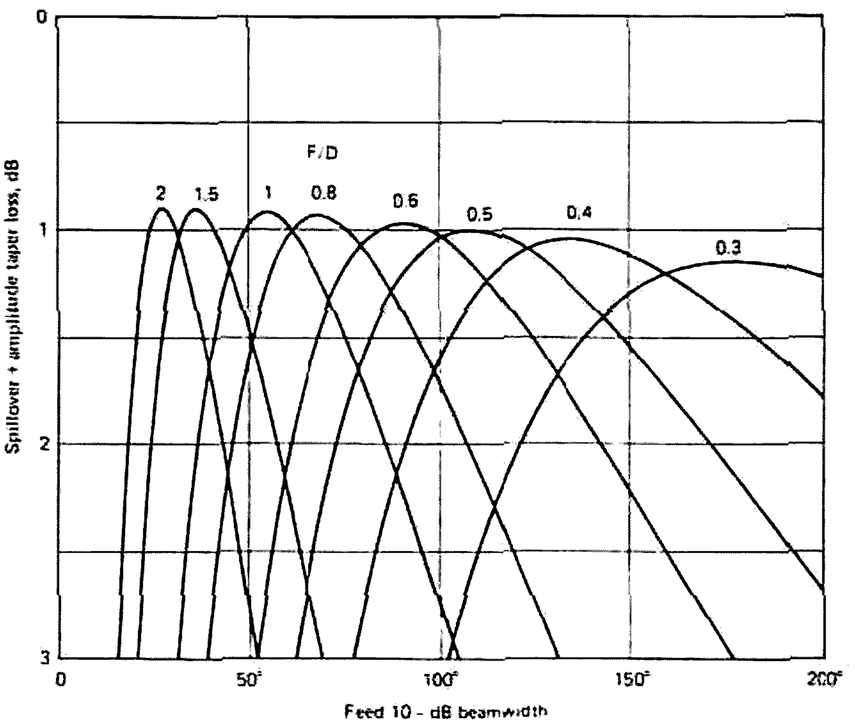

Figure 8-3 Sum of spillover and amplitude taper losses versus feed 10-dB beamwidth.

Example Estimate the amplitude taper loss for a reflector with $F/D = 0.5$ whose feed has a 10-dB edge taper. Compare the loss with that of the circular gaussian and the Hansen single-parameter distributions.

$$\psi_0 = 2\tan^{-1}\tfrac{1}{2} = 53.13^\circ$$

The 10-dB beamwidth of the feed is then 106.26°. We modify Eq. (1-13) to find the exponent N of the $\cos^{2N}(\theta/2)$ feed pattern approximation.

$$N = \frac{\log 0.1}{2\log\cos(106.26^\circ/4)} = 10.32$$

From Eq. (8-33) $u = \cos(53.13/2) = 0.894$

$$\text{ATL} = \frac{4(1-0.894^{10.32})^2(11.32)}{10.32^2(1-0.894^{22.64})}\cot^2\frac{53.13^\circ}{2} = 0.864$$

$$\text{ATL (dB)} = 10\log 0.864 = -0.63\text{ dB}$$

The extra distance from the feed to the reflector edge compared with the center distance adds 1.94 dB and increases the aperture amplitude taper to 11.94 dB. We interpolate Table 6-12 for the circular gaussian distribution and Table 6-13 for the Hansen single-parameter distribution to find the following data:

Gaussian	Hansen
ATL (dB) = −0.62 dB	ATL (dB) = −0.57 dB
Sidelobe level = 26.3 dB	Sidelobe level = 24.7 dB
Beamwidth factor = 1.1422	Beamwidth factor = 1.136

We multiply Eq. (6-47) by the beamwidth factor to estimate the reflector beamwidth.

$$\mathrm{HPBW} = 67.3^\circ \frac{\lambda}{D} \qquad \mathrm{HPBW} = 67^\circ \frac{\lambda}{D}$$

These compare well with the approximation of Chap. 1:

$$\mathrm{HPBW} = 70^\circ \frac{\lambda}{D}$$

for a parabolic reflector. An integration of the aperture distribution for the far-field pattern gives the following results:

$$\mathrm{HPBW} = 67.46^\circ \frac{\lambda}{D} \quad \text{Sidelobe level} = 27\text{ dB}$$

Both aperture approximations give similar results.

8-5 Phase Error Losses and Axial Defocusing

All rays starting at the reflector focus travel the same distance through reflection to the aperture plane. The aperture plane is any convenient plane in front of the dish whose normal is the axis of the reflector. If we could build a feed with a unique phase center and place it at the focus of a perfect paraboloidal reflector, we would eliminate phase error loss in the aperture plane. The aperture plane would be a constant-phase plane. The feed, the positioning of the feed, and the reflector surface all contribute to the phase error loss.

We discussed techniques for obtaining unique phase centers in the various planes for horns. Corrugated horns, unlike smooth-wall horns, can have equal phase centers in all planes through the axis, but even they will wander with changes in frequency. We must measure the feed pattern distribution (amplitude and phase) to predict the contribution of the feed to the overall efficiency. From those measurements we can define a practical phase center as the point on the feed leading to the minimum phase error loss when it is placed at the focus of a perfect reflector. The random and systematic phase error contributions can be measured directly on the feed and calculated numerically by using Eq. (8-27).

The feed phase center cannot always be placed at the focus. The phase center location wanders with changes in frequency, and in any wideband application axial defocusing can be expected. For example, the location of the phase center of a log-periodic antenna moves toward the apex as frequency increases. Figure 8-4 is a plot of the phase error loss due to axial defocusing. Each feed has its 10-dB beamwidth equal to the reflector subtended angle. Axial defocusing affects deep dishes (lower F/D) more than shallow dishes.

We can estimate the axial defocusing phase error loss by approximating the distribution with a quadratic aperture phase distribution. Given z as the

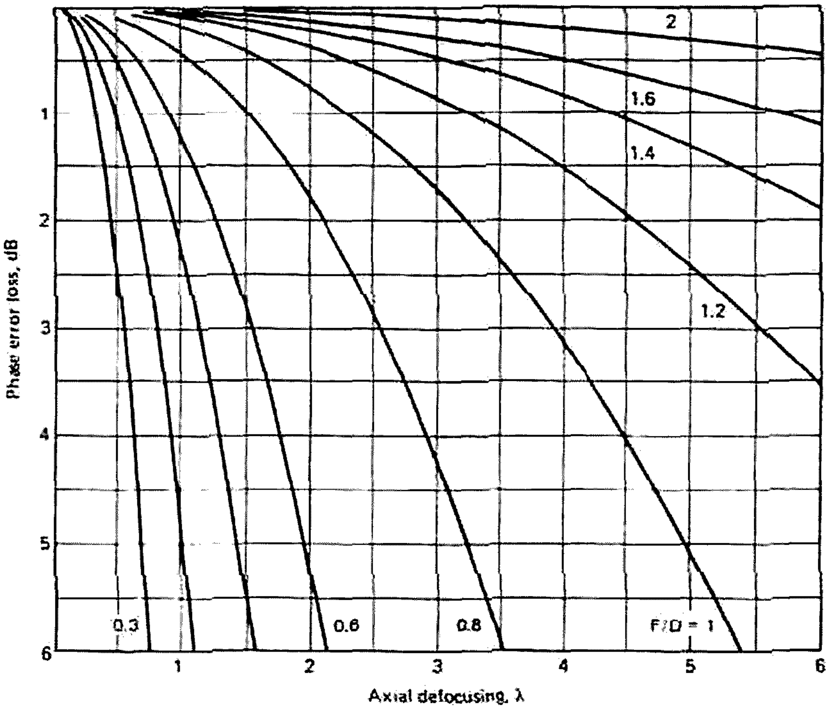

Figure 8-4 Parabolic reflector phase error loss due to axial defocusing of the feed.

axial defocusing, the maximum phase deviation in cycles is

$$S = \frac{z}{\lambda}\left[1 - \cos\left(2 \tan^{-1}\frac{1}{4F/D}\right)\right] \tag{8-34}$$

We will combine this with the quadratic phase error loss of the circular gaussian distribution to estimate the loss. With $z = \lambda$ we obtain a scaling factor

F/D	0.3	0.4	0.5	0.6	0.8	1.0
S	0.82	0.56	0.40	0.30	0.18	0.12

The scaling factor decreases with increasing F/D.

Example Estimate the phase error loss for $z = 2\lambda$ when $F/D = 0.6$ and the feed 10-dB beamwidth equals the reflector subtended angle.
From the list above, $S = 0.30(2) = 0.60$. We use Eq. (8-23) to find the edge taper.

$$\psi_0 = 2 \tan^{-1}\frac{1}{2.4} = 45.2^\circ$$

$$\text{Edge taper} = 20 \log \cos^2\frac{\psi_0}{2} = -1.4 \text{ dB}$$

An equivalent truncated gaussian aperture distribution tapers to

$$10\text{ dB} + 1.4\text{ dB} = 11.4\text{ dB} \qquad \rho = \frac{11.4}{8.69} = 1.31$$

We use Eq. (6-75) to find the phase error efficiency of the truncated gaussian distribution: PEL = 0.305 or PEL (dB) = −5.2 dB
This matches the value from Fig. 8-4 found by integration of the actual distribution.

We detect axial defocusing through the patterns of the reflector. Axial defocusing removes the nulls between the sidelobes. We adjust the feed location to maximize the null depth. Antenna range errors and receiver sensitivity limit our ability to eliminate this defocusing.

8-6 Astigmatism [14]

Both the feed and reflector can have astigmatism. We measure the feed by itself to discover its astigmatism. When the feed is mounted in the reflector, we detect astigmatism by the depth of nulls in the various pattern planes. A series of measurements will separate the feed and reflector astigmatism, but the feed must move along the reflector axis and rotate by 90° during the measurements. Move the feed along the axis to find the locations that give maximum nulls. The maximum locations of the reflector focii may not occur in the *E* and *H* planes and will require a search in the other planes. At this point we cannot separate the feed astigmatism from the reflector astigmatism. We rotate the feed and repeat the measurements. The feed phase center locations shift, and the reflector focii remain fixed. Simple manipulations of the data from the two measurements separate the two sources of astigmatism. The reflector can be shimmed to remove its astigmatism, or the feed phase centers can be matched to the reflector focii.

Figure 8-5 shows the magnitude of phase error losses due to feed astigmatism. Astigmatism is not as severe as axial defocusing because in two planes the feed phase center is at the reflector focus. As is true of axial defocusing, deep dishes are affected more than shallow reflectors.

8-7 Feed Scanning

Moving the phase center of the feed off axis laterally scans the reflector beam to a limited extent without severe pattern problems. Figure 8-6 shows the *k*-space pattern effects of feed scanning. The sidelobes show the effects of coma (cubic phase errors). The sidelobes on the boresight side grow and the sidelobes on the other side decrease. We call these coma lobes, although no new lobes are generated. In fact, we see one lobe becoming a vestigial lobe with increased scan (Fig. 8-6).

Suppose the feed is offset from the axis by a distance *d*. We will measure the offset angle ψ_s from the axis to a line from the feed to the reflector vertex.

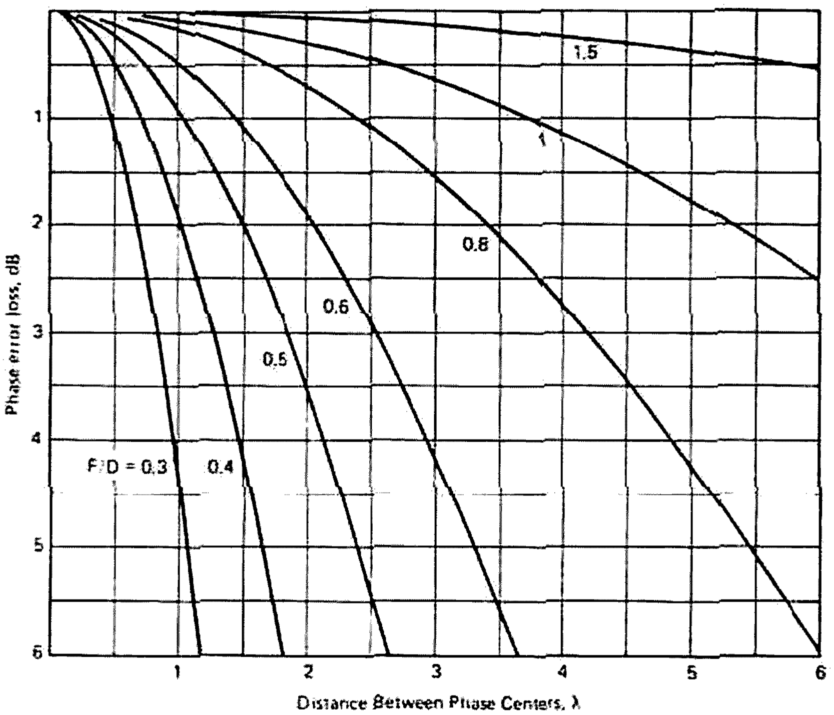

Figure 8-5 Parabolic reflector phase error loss due to astigmatism.

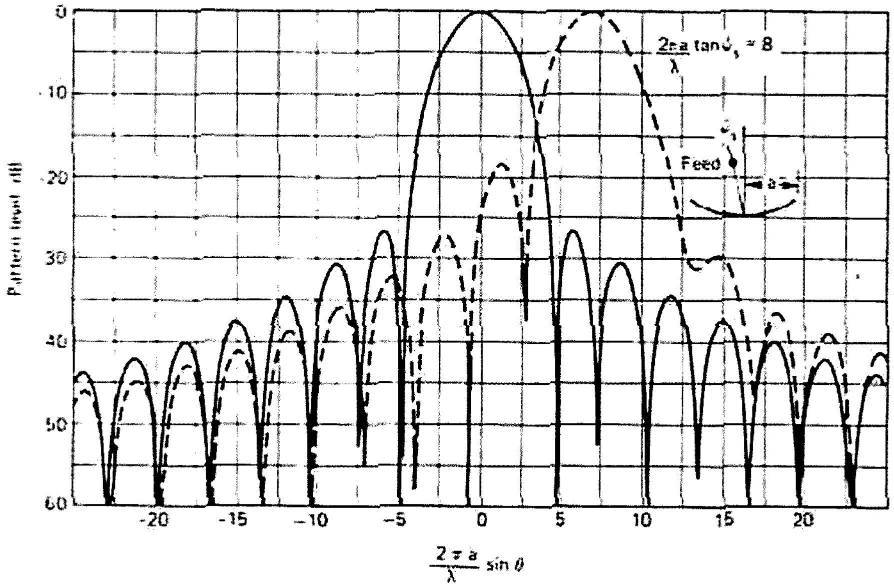

Figure 8-6 Feed-scanned parabolic reflector. $F/D = 0.5$; HPBW = 60°.

$$d = F \tan \psi_s$$

The slight amplitude distribution change due to the small lateral offset will be ignored. Referenced to the focus, the movement produces a phase factor in the feed pattern

$$-kd \sin \psi \cos \phi_c$$

where the feed was moved along the negative x axis.

Equation (8-27) predicts only the boresight phase error loss. Like Eq. (6-11), we must calculate the phase error efficiency at any angle.

$$\mathrm{PEL}\,(\theta,\phi)=\frac{\left|\int_0^{2\pi}\int_0^{\psi_0} E(\psi,\phi_c)\tan(\psi/2)\,e^{jkF\tan(\psi/2)\sin\theta\cos(\phi-\phi_c)}\,d\psi\,d\phi_c\right|^2}{\left[\int_0^{2\pi}\int_0^{\psi_0} |E(\psi,\phi_c)|\tan(\psi/2)\,d\psi\,d\phi_c\right]^2} \tag{8-35}$$

When we include the offset along $\phi = 0$, the phase factor becomes

$$\exp\left\{jkF\cos\phi_c\left[2\tan\frac{\psi}{2}\sin\theta-\tan\psi_s\sin\psi\right]\right\}$$

For large reflectors we make the approximations

$$\psi_s = \tan\psi_s \qquad \text{and} \qquad \theta = \sin\theta$$

The pattern scale and the offset phase factor become

$$ka\theta \qquad \text{and} \qquad ka\psi_s$$

A flat plate would reflect the ray at an equal angle on the other side of the axis, but a curved reflector would modify that slightly. The offset factor in Fig. 8-6 is 8, and the beam peak is at 7. We call the ratio of the beam maximum to offset angle the beam deviation factor (BDF) [15].

$$\mathrm{BDF}=\frac{\theta_m}{\psi_s}=\frac{7}{8} \qquad \theta_m=\mathrm{BDF}\,\psi_s \tag{8-36}$$

The BDF varies from less than 1 for a concave reflector to greater than 1 for a convex reflector. BDF equals 1 for a flat reflector. Table 8-1 lists the BDF for various F/D. The BDF approaches 1 as F/D approaches infinity (flat plate).

TABLE 8-1 Feed-Scanned Parabolic Reflector Beam Deviation Factor

F/D	BDF	F/D	BDF
0.30	0.724	0.80	0.945
0.35	0.778	0.85	0.951
0.40	0.818	0.90	0.957
0.45	0.850	1.00	0.965
0.50	0.874	1.10	0.970
0.55	0.893	1.20	0.975
0.60	0.908	1.40	0.981
0.65	0.921	1.60	0.986
0.70	0.930	1.80	0.989
0.75	0.938	2.00	0.991

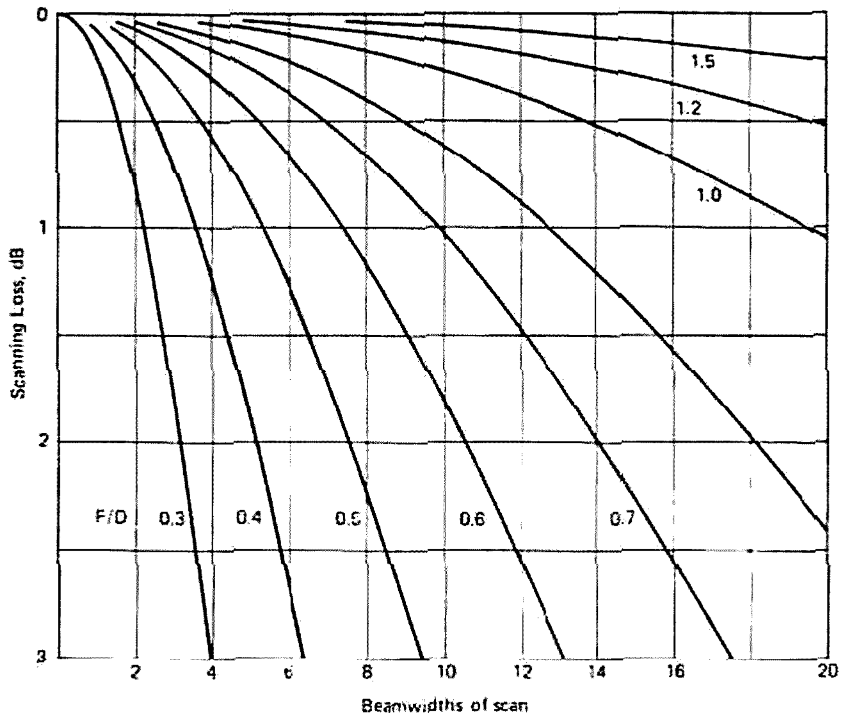

Figure 8-7 Feed-scanning loss of parabolic reflector.

Feed scanning increases the phase error loss. When normalized to beamwidths of scan, a single loss curve can be drawn for each F/D (Fig. 8-7). Scanning also raises the sidelobes. Table 8-2 gives the approximate level of the peak coma lobe for a given scan loss. It is almost independent of F/D.

Example A reflector with a 50λ diameter is feed-scanned to 6°. Find the offset distance and the scanning loss when $F/D = 0.6$.
Use the approximation $\text{HPBW} = 70^\circ \lambda/D = 1.4^\circ$. The reflector is scanned $6/1.4 = 4.3$ beamwidths.

$$\text{Scanning loss (Fig. 8-7)} = 0.4 \text{ dB}$$

$$\text{Sidelobe level (Table 8-2)} = 14.6 \text{ dB}$$

The angle between the axis and the feed point to vertex must be greater than the scan angle, since the reflector is concave.

TABLE 8-2 Sidelobe Level of a Feed-Scanned Parabolic Reflector

Scanning loss, dB	Sidelobe level, dB	Scanning loss, dB	Sidelobe level, dB
0.5	14.1	1.75	10.1
0.75	12.9	2.0	9.7
1.0	11.9	2.5	9.0
1.25	11.2	3.0	8.5
1.5	10.6		

$$\psi_s = \frac{\theta_s}{\text{BDF}} = \frac{6^\circ}{0.908} = 6.61^\circ \qquad \text{(Table 8-1)}$$

The offset distance is $F \tan 6.61^\circ = 0.6\,(50\lambda) \tan 6.61^\circ = 3.48\lambda$.

The scalar analysis of this section gives only approximate results. Large feed scanning produces higher-order aberrations other than coma [16, 17, 18]. The optimum gain point moves off the focal plane but fails to follow the curve predicted from optics for reflectors extremely large in wavelengths [17]. The reflector F/D and illumination taper determine the maximum gain contour for feed-scanning a reflector. Vector analysis improves the match between calculated and measured results [18].

8-8 Random Phase Errors

Reflector anomalies will reduce the gain predicted from the feed analysis. We must specify reasonable manufacturing tolerances for the frequency of operation. It would appear that gain can be increased without bound by increasing the reflector diameter, but the tolerance problems of large reflectors limit the maximum gain. We will consider only surface anomalies so small that the reflector retains its basic shape.

The surface imperfections change the optical path length from the feed to the reflector aperture plane by $\delta(r, \phi)$, which gives us

$$\text{PEL} = \frac{\left| \int_0^{2\pi} \int_0^a E(r, \phi)\, e^{j\delta(r,\phi)} r\, dr\, d\phi \right|^2}{\left(\int_0^{2\pi} \int_0^a |E(r, \phi)|\, r\, dr\, d\phi \right)^2} \tag{8-37}$$

Cheng [19] bounds the phase error loss by using a limit on the integrals. Given a peak phase error of m (radians), the change in gain is bounded.

$$\frac{G}{G_0} \geq \left(1 - \frac{m^2}{2}\right)^2 \tag{8-38}$$

This gain loss estimate is too conservative, but it is useful as an upper bound.

Ruze [20] improved the random surface error loss estimate by using a gaussian distributed error correlated over regions. Dents or segments making up the reflector are in correlation with the errors over a region. The error at a point depends on the location of nearby points in the correlation region. The phase error efficiency becomes an infinite series

$$\text{PEL} = \exp(-\overline{\delta}^2) + \frac{1}{\eta}\left(\frac{2C}{D}\right)^2 \exp(-\overline{\delta}^2) \sum_{n=1}^{\infty} \frac{(\overline{\delta}^2)^n}{n \cdot n!} \tag{8-39}$$

where C is the correlation distance, D is the diameter, and η is the aperture efficiency (ATL). $\overline{\delta}^2$ is the mean square phase deviation given by

$$\overline{\delta}^2 = \frac{\displaystyle\int_0^{2\pi}\int_0^a |E(r,\phi)|\delta^2(r,\phi)r\,dr\,d\phi}{\displaystyle\int_0^{2\pi}\int_0^a |E(r,\phi)|r\,dr\,d\phi} \tag{8-40}$$

If we include the correlation distance, PEL decreases. The infinite series [Eq. (8-39)] converges rapidly. When the correlation distance is small compared with the diameter, the phase error efficiency becomes

$$\text{PEL} = \exp\left(\frac{-4\pi\epsilon_0}{\lambda}\right)^2 = \exp(-\overline{\delta}^2) \tag{8-41}$$

where ϵ_0 is the effective reflector tolerance. We use 4π instead of 2π because the wave travels to and from the reflector and the phase distance is twice the reflector tolerance. From Eq. (8-40) we find the effective rms tolerance.

$$\epsilon_0 = \frac{\displaystyle\int_0^{2\pi}\int_0^a |E(r,\phi)|\epsilon^2(r,\phi)r\,dr\,d\phi}{\displaystyle\int_0^{2\pi}\int_0^a |E(r,\phi)|r\,dr\,d\phi} \tag{8-42}$$

Ruze gives the distance ϵ in terms of the z-axis deviation Δz and the surface normal deviation Δn

$$\epsilon = \frac{\Delta z}{1 + (r/2F)^2} \qquad \epsilon = \frac{\Delta n}{\sqrt{1 + (r/2F)^2}} \tag{8-43}$$

We can evaluate the constants in Eq. (8-41) and convert to a dB ratio.

$$\text{PEL (dB)} = -685.8\left(\frac{\epsilon_0}{\lambda}\right)^2 \text{ dB} \tag{8-44}$$

Example Find the required reflector tolerance at 30 GHz to limit the rms surface tolerance phase error loss to 1 dB.
By using Eq. (8-44), we get

$$\frac{\epsilon_0}{\lambda} = \sqrt{\frac{1}{685.8}} = 0.038$$

at 30 GHz $\lambda = 1$ cm and $\epsilon_0 = 0.38$ mm.
We can also use Eq. (8-38), which gives the upper bound on surface error loss.

$$m = \frac{4\pi\epsilon_0}{\lambda} = \sqrt{2\left(1 - \sqrt{\frac{G}{G_0}}\right)} = 0.466 \text{ at 1 dB}$$

$$\epsilon_0 = 0.037\lambda \qquad \text{or} \qquad \epsilon_0 = 0.37 \text{ mm at 30 GHz}$$

Both methods give about the same answer in this case.

Zarghamee [21] extended tolerance theory to include the effects of the surface error distribution. Some antennas have better support and construction in some areas and are more accurate in those areas. This improves the reflector performance. Zarghamee defined a second variation of surface deviations by

$$\eta_0^4 = \frac{\int_0^{2\pi}\int_0^a |E(r,\phi)|\,[\epsilon^2(r,\phi) - \epsilon_0^2]\,r\,dr\,d\phi}{\int_0^{2\pi}\int_0^a |E(r,\phi)|\,r\,dr\,d\phi}$$

The phase error efficiency becomes

$$\mathrm{PEL} = \exp\left(\frac{-4\pi\epsilon_0}{\lambda}\right)^2 \exp\left(\frac{\pi\eta_0}{\lambda}\right)^4$$

The correlation of random errors increases the probable sidelobe level. The sidelobe level increases with the size of the correlation interval and decreases for larger aperture diameters. Increasing the amplitude taper of the distribution makes the aperture pattern more susceptible to random-error sidelobes, since increasing the taper is somewhat equivalent to decreasing the aperture diameter. Blockage and feed diffraction also limit the achievable sidelobe level in a reflector. A simple feed cannot carefully control the aperture distribution necessary for low sidelobes. Hansen [22] discusses sidelobe limitations caused by random phase error in some detail.

8-9 Physical Optics

In the physical optics method we find the induced currents on the reflector surface and use them to find the pattern response of the reflector. We find the induced surface current density from the incident magnetic field

$$\mathbf{K}_s = \mathbf{n} \times 2\mathbf{H}_i \tag{8-45}$$

where $\mathbf{n}$ is the normal to the reflector surface. Equation (8-45), to be valid, requires large radii of curvature in the reflector. It is the first-order term of an expansion. We use the magnetic vector potential [Eq. (2-4)] to find the pattern. The potential can be used in both the far and near field of the reflector to find not only the pattern but also the reaction of the reflector on the feed and the focal plane fields. By observing the direction of the currents on the reflector, we divide the feed radiation into orthogonal polarizations each of which produces a linearly polarized far field.

Assume the reflector is in the far field of the feed. We use GO to find the field at the reflector surface so that the magnetic field is given by

$$\mathbf{H}_i = \frac{1}{\eta}\mathbf{S}_1 \times \mathbf{E}_i \tag{8-46}$$

where η is the impedance of free space, $\mathbf{S}_i$ is the incident ray unit vector, and $\mathbf{E}_i$ is the incident electric field. The surface current becomes

$$\mathbf{K}_s = \frac{2}{\eta}[\mathbf{n} \times (\mathbf{S}_i \times \mathbf{E}_i)] \tag{8-47}$$

Currents in the direction of the reflector axis produce no fields in the axis direction because that is the null direction of the radiation from those currents. For that reason, Silver [2] projects the reflector surface currents onto the aperture plane, where they have equal phase. He then considers the current directions on the aperture plane for different sources.

Both the incremental dipole and the incremental magnetic dipoles produce curvature in the currents. The curvature increases for deeper dishes. In the E and H planes opposing symmetrical currents in the aperture plane have canceling far-field cross-polarization responses. The diagonal planes between the E and H planes have a difference pattern of cross-polarized signals called Condon lobes [23]. Combining an incremental dipole source with an orthogonal incremental magnetic dipole in the ratio of η, the impedance of free space, eliminates the curvature of the projected currents in the aperture plane. This combination corresponds exactly to the Huygens source.

Since Huygens source feeds produce straight currents in the aperture plane of the paraboloidal reflector, we will separate the feed radiation into orthogonal Huygens sources. To calculate far-field patterns, we can skip the step involving currents and use the Huygens source fields in the aperture plane directly. We transform the measured fields of the feed into orthogonal Huygens sources by

$$\begin{bmatrix} E_c \\ E_x \end{bmatrix} = \begin{bmatrix} \cos\phi & -\sin\phi \\ \sin\phi & \cos\phi \end{bmatrix} \begin{bmatrix} E_{\theta f} \\ E_{\phi f} \end{bmatrix} \tag{8-48}$$

where E_c is the $\phi = 0$ direction of polarization in the feed pattern and E_x is the $\phi = 90°$ polarization. This division corresponds to Ludwig's third definition of cross-polarization. We use Eq. (6-8) with each one of these aperture components to calculate the far field. The following matrix converts the far-field polarizations of the aperture fields to the normal far-field components of spherical coordinates:

$$\begin{bmatrix} E_\theta \\ E_\phi \end{bmatrix} = \begin{bmatrix} \cos\phi & \sin\phi \\ -\sin\phi & \cos\phi \end{bmatrix} \begin{bmatrix} E_c \\ E_x \end{bmatrix} \tag{8-49}$$

In the special case of the paraboloidal reflector, we can reduce physical optics to aperture theory. We cannot do that for the arbitrarily shaped reflector but must find the pattern from the currents.

If we use the orthogonal Huygens source components for the feed, it is unnecessary to find the various efficiencies—ATL, PEL, XOL, and spillover—to find the gain of the reflector pattern. The efficiency or gain of the feed must be known, and we must still account for the reflector rms efficiency; but by keeping track of the magnitudes and phase of the fields, we will find the proper reflector gain.

Consider one Huygens source component. We find its radiated field from the gain and input power.

$$S = \frac{|E|^2}{\eta} = \frac{P_0 g_f(\psi, \phi)}{4\pi R^2}$$

$$E = \sqrt{\frac{\eta P_0 g_f(\psi, \phi)}{4\pi R^2}}\, e^{j\alpha(\psi, \phi)}$$

where $\alpha(\psi, \phi)$ is the feed phase pattern. $g_f(\psi, \phi)$ is the feed gain pattern and P_0 is the input power. The field in the aperture plane is

$$E_a = \sqrt{\frac{\eta P_0 g_f(\psi, \phi)}{4\pi \rho^2}}\, e^{j\alpha(\psi, \phi)} \tag{8-50}$$

where we ignore the phase shift of the optical path from the feed to the aperture plane because all paths are equal. We add 180° to one of the components, E_c or E_x, to account for the polarization shift at reflection. We use the aperture fields with Eq. (6-8) to find the far field:

$$E = \frac{je^{-jkR}}{\lambda R} \iint_S \sqrt{\frac{\eta P_0 g_f(\psi, \phi)}{4\pi \rho^2}}\, e^{j\alpha(\psi, \phi)} e^{jk\cdot r'}\, dS' \tag{8-51}$$

The power spilled over does not appear in the aperture field and is excluded from the reflector field calculation, but it is included in the input power P_0. We apply Eqs. (8-50) and (8-51) to both Huygens source components and remember to add 180° phase shift to one of them.

After finding both components of the Huygens sources in the far field, we convert to the desired polarizations. The gain of each component is found from

$$g = \frac{|E|^2}{\eta} \frac{4\pi R^2}{P_0} \tag{8-52}$$

and the input power P_0 and the impedance of free space η are canceled.

8-10 Focal Plane Fields

We will improve the efficiency and pattern response of the reflector if we match the feed fields to the focal plane fields. GO assumes a point focus, but an actual focus is extended. We determine the reflector and feed efficiency from the field match over the focal plane. When the reflector F/D is large, we use the diffraction pattern of a circular aperture, the Airy function

$$E = \frac{J_1(kr\psi_0)}{kr\psi_0} \tag{8-53}$$

where ψ_0 is the half subtended angle of the reflector (radians), r is the radial coordinate, and k is the propagation constant. J_1 is the Bessel function.

In a more exact method the induced currents on the reflector ($2\mathbf{n} \times \mathbf{H}$) and the magnetic vector potential are used to calculate the focal plane fields. As F/D decreases, the currents on the reflector interact and modify their distribution, but that is a secondary effect [24]. We find the reflector efficiency from the field match of the focal plane fields ($\mathbf{E}_1$, $\mathbf{H}_1$) and the fields of the feed ($\mathbf{E}_2$, $\mathbf{H}_2$) by using Robieux's theorem [4]

$$\eta = \frac{\left| \iint_S (\mathbf{E}_1 \times \mathbf{H}_2 + \mathbf{E}_2 \times \mathbf{H}_1) \cdot d\mathbf{S} \right|^2}{4P_1 P_2} \tag{8-54}$$

where P_1 and P_2 are the input powers to produce the fields and η is the efficiency. The finite size of the feed causes spillover. The extent of amplitude and phase mismatch between the two fields determines the efficiencies. By illuminating the reflector with a cross-polarized wave, we find the cross-polarization radiation level through the field match [Eq. (8-54)].

We maximize the efficiency [Eq. (8-54)] by conjugate-matching the focal plane fields with the feed fields. Corrugated horns can be designed by expanding the focal plane fields in axial hybrid modes of the horn and mode matching [25, 26]. Wood [4] expands the reflector and feed fields in spherical harmonics and matches at a boundary. Both sets of fields can be approximated very well by just a few terms. By this method dual reflector and offset reflector systems, as well as axisymmetric prime focus reflectors, can be handled.

We can feed the reflector with an array to match the focal plane fields [27, 28, 29]. The array samples the focal plane field and conjugate-matches it so that the powers sum in phase. The array can form multiple beams and correct aberrations [27]. By using the multiple feeds of the array, coma can be reduced for scanned beams and the efficiency can be improved. Quantization of the array element locations and excitations, amplitude, and phase, reduces the efficiency and raises the sidelobe level [30].

8-11 Feed Mismatch Due to the Reflector

The feed receives some of its transmitted power reflected from the parabola, and this power appears as a mismatch at the feed terminals. We find the reflected field at the feed by using surface currents and the magnetic vector potential. The only significant contribution comes from areas near where the normal of the reflector points at the feed. Around every other point, the phase of the reflection varies rapidly and cancels. That is, we consider only points of stationary phase. We calculate the reflection from each point of stationary phase from [2]

$$\Gamma = -j\frac{G_f(\rho_0)}{4k\rho_0}\sqrt{\frac{\rho_1\rho_2}{(\rho_1+\rho_0)(\rho_2+\rho_0)}}\,e^{-j(2k\rho_0)} \tag{8-55}$$

where Γ is the reflection coefficient, ρ_0 is the distance to the stationary phase point, $G_f(\rho_0)$ is the feed gain in the direction of ρ_0, and ρ_1 and ρ_2 are the radii of curvature of the reflector at ρ_0.

The vertex is the only point of stationary phase on a paraboloidal reflector.

$$\rho_1 = \rho_2 = -2F \qquad \text{and} \qquad \rho_0 = F$$

Equation (8-55) reduces to

$$\Gamma = -j\frac{G_f(0)}{2kF}e^{-j2kF} \tag{8-56}$$

Example Suppose we have a reflector with $F/D = 0.40$. Find the reflector mismatch for a source with its 10-dB beamwidth equal to the reflector subtended angle.

Half subtended angle [Eq. (8-22)] $\psi_0 = 2\tan(1/1.6) = 64^\circ$

By using the feed approximation $\cos^{2N}(\theta/2)$, we have

$$N = \frac{\log 0.1}{2\log\cos(64^\circ/2)} = 6.98$$

The feed gain at boresight is $N + 1$ [Eq. (1-13)]

$$\text{[Eq. (8-56)]} \qquad |\Gamma| = \frac{8\lambda}{4\pi F} = 1.59\frac{\lambda}{D}$$

As the diameter in wavelengths increases, the reaction of the reflector on the feed decreases. Given a 3-m reflector at 4 GHz, we find the reflector reflection coefficient as 0.04, or VSWR = 1.08.

We can express the reflector reflection of a paraboloidal reflector as

$$|\Gamma| = V\frac{\lambda}{D} \tag{8-57}$$

and calculate the following table of V versus F/D for feeds with 10-dB beamwidths equal the reflector subtended angle:

F/D	0.3	0.4	0.5	0.6	0.7	0.8	1.0	1.2	1.4
V	1.42	1.59	1.80	2.04	2.29	2.56	3.10	3.66	4.23

Higher F/D give higher reflections, since the feed gain increases faster than the reduced area of the reflector seen from the feed.

Narrowband corrections to these reflections can be designed by using a vertex plate (Silver [2]) or by designing sets of concentric ring ridges in the reflector (Wood [4]). The rings can match the feed at more than one frequency. By any of these methods, the free-space mismatch of the feed could be corrected for. Of course, the feed itself can be mismatched to compensate for the reflector reaction.

8-12 Reflections from Conic Sections

We use reflectors made from conic sections other than the parabola as subreflectors. The ellipse and hyperbola rotated about their axes to form solid figures reflect incident spherical waves into spherical waves with different caustics (focal points). Reflectors formed by moving the figure along a line change the caustics of cylindrical waves. We will consider only spherical waves, but we need only convert to cylindrical waves for cylindrical reflectors.

All conic section reflectors convert spherical waves from one focus into spherical waves directed toward the other focus. The ellipse has its two focii located within the figure. As we let one focus approach infinity, the ellipse transforms into a parabola. If the focus is pushed through infinity to the negative axis, the figure becomes a hyperbola located between the two focii. Figure 8-8 shows the ray tracing for axisymmetrical conic section reflectors. A spherical source at one focus is reflected to the second focus by the reflector although it is virtual (not actually reached) in some cases.

We describe all conic sections with the same polar equation

$$r = \frac{eP}{1 - e\cos\theta} \tag{8-58}$$

where P is the distance between the origin, the focus, to a line called the directrix (Fig. 8-9). The eccentricity e is the ratio of the distance from the origin to a point on the curve to the distance from the same point to the directrix.

$$r_1 = er_2$$

In an ellipse, $e < 1$; in a parabola, $e = 1$; and in a hyperbola, $e > 1$. The distance between the focii is

$$2c = \frac{2Pe^2}{1 - e^2} \tag{8-59}$$

8-13 Dual-Reflector Antennas

We derive dual-reflector antennas, Cassegrain and Gregorian, from their optical telescope counterparts. Each increases the effective focal length. In

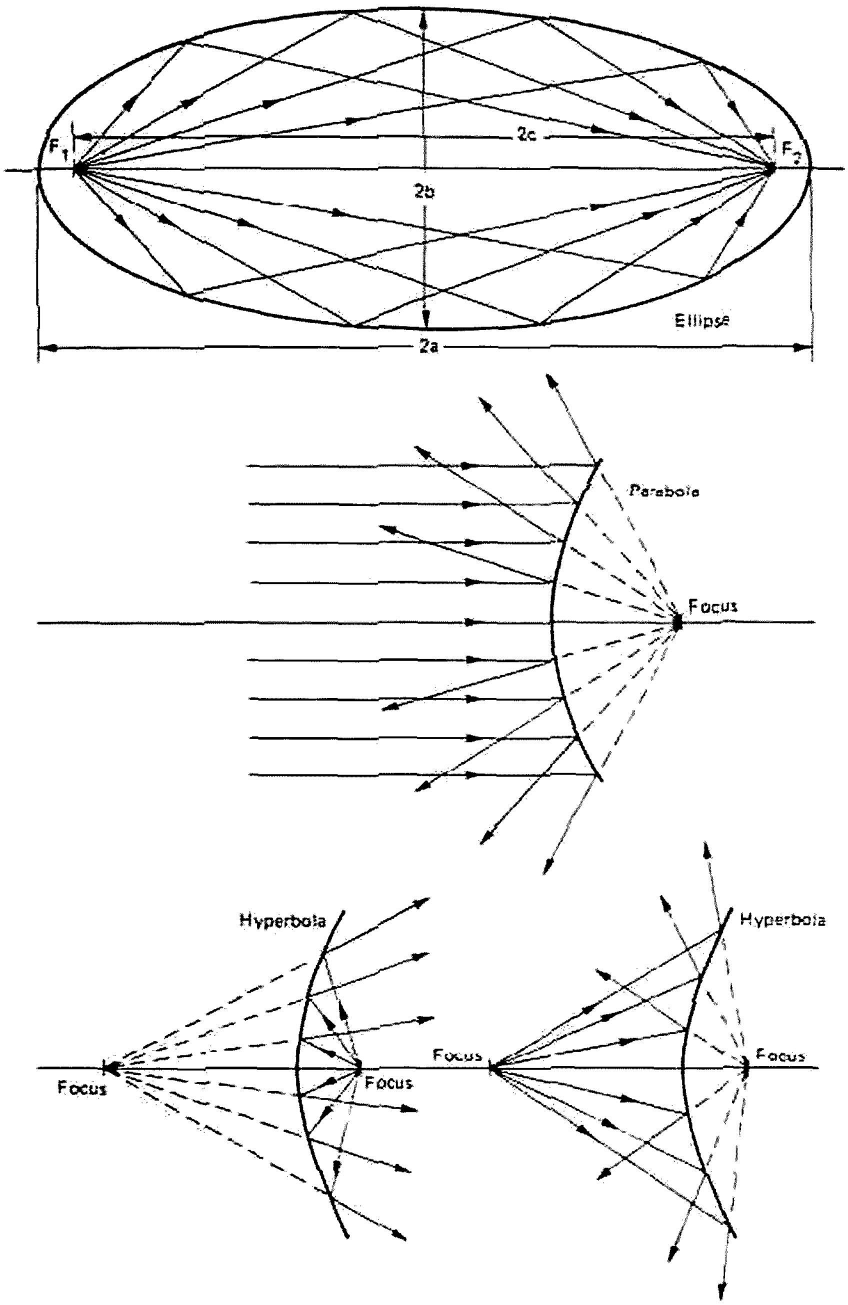

Figure 8-8 Reflections from conic section reflectors.

the Cassegrain dual-reflector antenna a hyperbolic subreflector is used (Fig. 8-10), and in the Gregorian dual-reflector antenna an elliptical subreflector is used (Fig. 8-11). We locate one focus of the subreflector at the focus of the main paraboloidal reflector and place the second focus of the subreflector at the feed antenna phase center. The subreflector changes the curvature of waves coming from one focus into waves with their caustic at the second subreflector focus.

The number of Cassegrain designs exceeds the number of Gregorian dual reflectors. The Gregorian design requires a larger subreflector support because it extends farther from the main reflector vertex. The subreflector

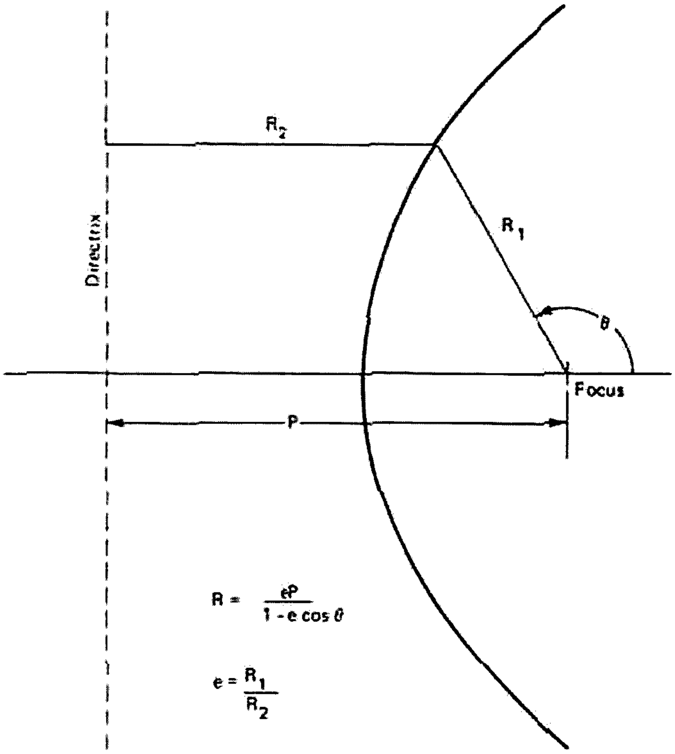

Figure 8-9 Conic section geometry.

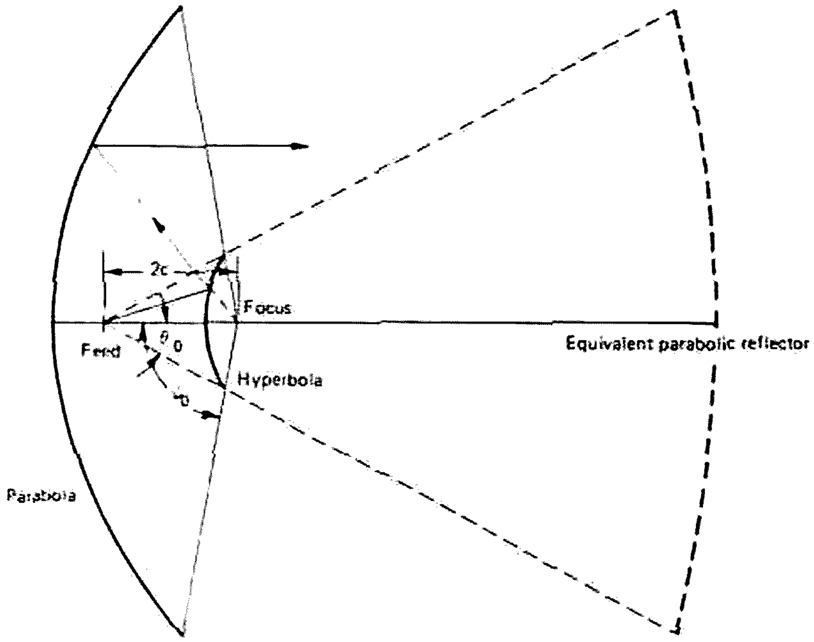

Figure 8-10 Cassegrain reflector antenna.

edge curvature increases the diffraction and reduces the control of the field incident on the main reflector. By shaping the subreflector of the Cassegrain, increased overall efficiency can be obtained. The inversion of the fields in the Gregorian reflector complicates such procedures.

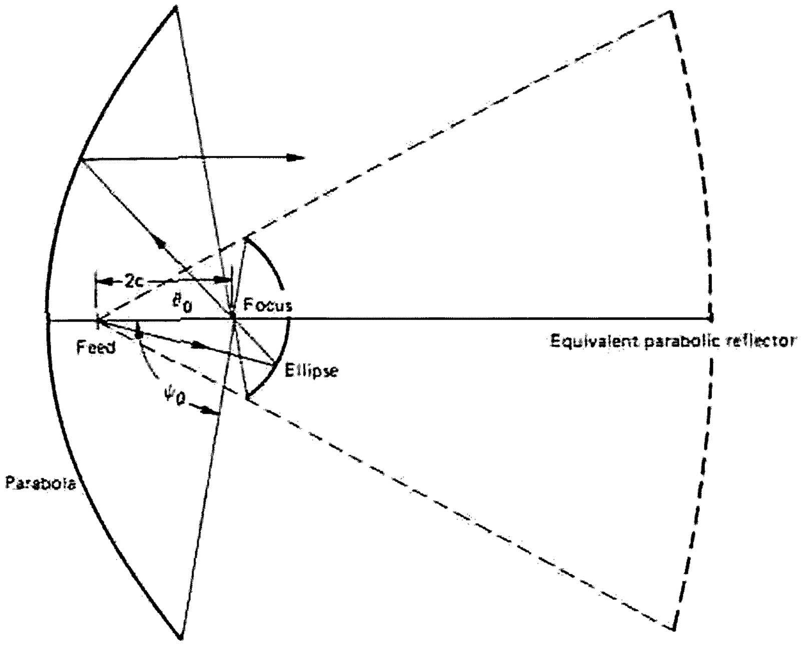

Figure 8-11 Gregorian reflector antenna.

In Figs. 8-10 and 8-11 the subtended angle of the main reflector is $2\psi_0$, but the effective subtended angle at the feed is $2\theta_0$. We can find the subreflector eccentricity from those angles

$$\begin{array}{cc} \text{Cassegrain} & \text{Gregorian} \\ e = \dfrac{\sin \frac{1}{2}(\psi_0 + \theta_0)}{\sin \frac{1}{2}(\psi_0 - \theta_0)} & e = \dfrac{\sin \frac{1}{2}(\psi_0 - \theta_0)}{\sin \frac{1}{2}(\psi_0 + \theta_0)} \end{array} \tag{8-60}$$

We can also analyze the dual-reflector system by using an equivalent parabola (Figs. 8-10 and 8-11) from the subreflector subtended angle $2\theta_0$. Define the magnification factor as the ratio of the effective focal length to the actual focal length of the main reflector

$$M = \frac{F_e}{F}$$

The subreflector eccentricity can be calculated from M

$$\begin{array}{cc} \text{Cassegrain} & \text{Gregorian} \\ e = \dfrac{M + 1}{M - 1} & e = \dfrac{M - 1}{M + 1} \end{array} \tag{8-61}$$

Equation (8-59) gives the distance between the focii of the subreflectors

$$\begin{array}{cc} \text{Cassegrain} & \text{Gregorian} \\ 2c = \dfrac{2Pe^2}{e^2 - 1} & 2c = \dfrac{2Pe^2}{1 - e^2} \end{array} \tag{8-62}$$

We gain the design parameter P and with it some freedom in the placement of the feed. We can easily solve for the length P in terms of the focii distance $2c$

$$\begin{array}{cc} \text{Cassegrain} & \text{Gregorian} \\ P = \dfrac{2c(e^2 - 1)}{2e^2} & P = \dfrac{2c(1 - e^2)}{2e^2} \end{array} \tag{8-63}$$

The subreflector diameter varies with P

$$D_s = \frac{2eP \sin(\pi - \psi_0)}{1 - e \cos(\pi - \psi_0)} \qquad \psi_0 \text{ radians} \tag{8-64}$$

Feed Blockage The increased effective focal length requires feeds with narrow beamwidths. We can no longer consider the feed as a point source. It projects a shadow into the center of the reflector (Fig. 8-12) and causes a central blockage. The subreflector also blocks the center. As we reduce the

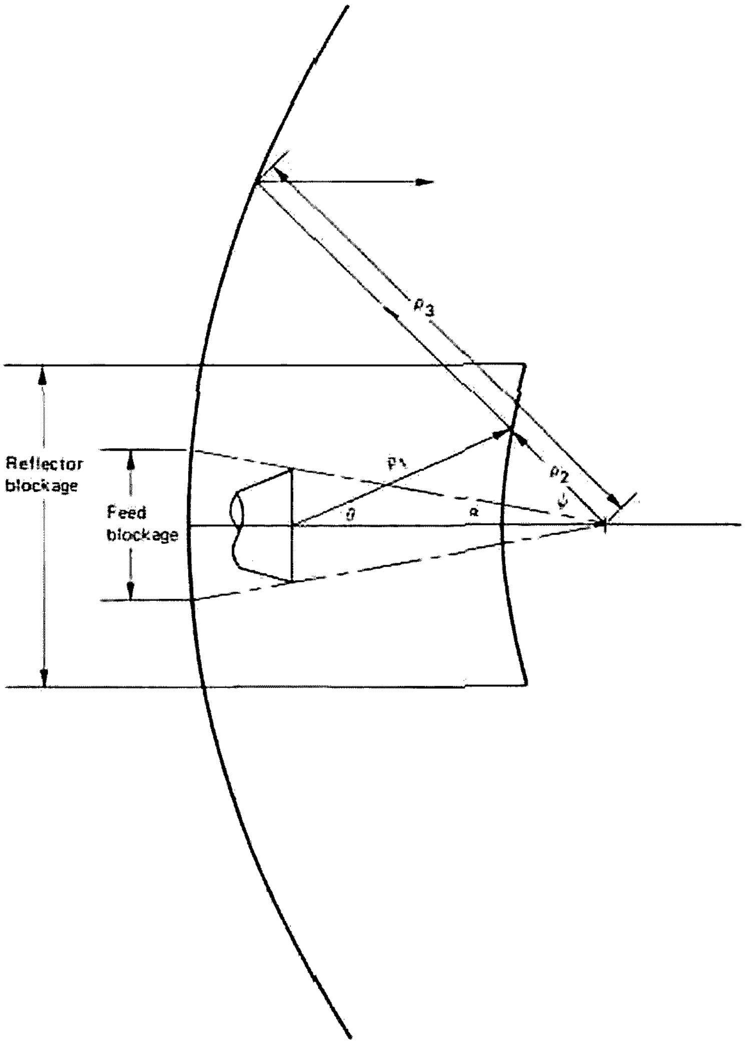

Figure 8-12 Cassegrain central blockage.

subreflector diameter to reduce blockage, the feed antenna moves closer to the subreflector and its projected shadow increases. The optimum occurs when the projected feed blockage diameter equals the subreflector diameter. The feed size depends on the frequency of operation and the effective F/D, whereas the subreflector diameter depends only on geometry. We cannot find the optimum independently of frequency.

Example Design a 10-m-diameter main reflector Cassegrain antenna with $F/D = 0.3$ and an effective $F/D = 1.5$ to operate at 3.9 GHz Minimize the aperture blockage.

$$M = \frac{1.5}{0.3} = 5 \quad \text{Eq. (8-61)} \qquad e = \frac{5+1}{5-1} = 1.5$$

From Eq. (8-22) $$\theta_0 = 2\tan^{-1}\frac{1}{4(1.5)} = 18.9^\circ$$

We feed the reflector with a circular corrugated horn with a 10-dB beamwidth equal to the subtended angle of the subreflector. We use the methods of Sec. 7-4 to design the horn. When we include the thickness of the corrugations, the physical diameter of the horn becomes 0.415 m.
We determine the blockage angle α (Fig. 8-12)

$$\alpha = \tan^{-1}\frac{0.415}{4c}$$

From Eq. (8-62) $\quad 2c = 3.6P$

We use Eq. (8-64) with the parabola P_0 and α to find the projected feed blockage

$$P_0 = 2\frac{F}{D}D = 6\text{ m} \qquad \frac{0.415}{4c} = \frac{0.0577}{P}$$

$$D_{fb} = \frac{2P_0 \sin(\pi - \alpha)}{1 - \cos(\pi - \alpha)} = \frac{12 \sin \tan^{-1}(0.0577/P)}{1 + \cos \tan^{-1}(0.0577/P)}$$

The subreflector blockage is given by Eq. (8-64) also:

$$\psi_0 = 2\tan^{-1}\frac{1}{4(0.3)}$$

$$D_s = \frac{2(1.5)P \sin(\pi - \psi_0)}{1 - 1.5\cos(\pi - \psi_0)} = 2.322P$$

We equate these blockages and solve the transcendental equation for P numerically:

$P = 0.385$ m

$D_s = 0.894$ m subreflector diameter

$2c = 1.386$ m distance between subreflector focii

We find the blockage loss from Table 6-19 by using the parabolic distribution, 0.14 dB. A Gregorian subreflector designed by parallel steps has a diameter about 6 cm larger and has about 0.02 dB more blockage loss.

Diffraction Loss [3, 6, 9, 31] We cannot decrease the subreflector size to reduce the central blockage without penalty. We based the subreflector design on geometric optics (GO), which assumes large reflectors in terms of wavelengths. We size the subreflector to have only subreflector spillover and none from the main reflector based on GO. The finite subreflector size produces diffractions that cause main-reflector spillover, cross-polarized subreflector reflections, phase error losses, and additional amplitude taper losses. We lump these excess losses into a diffraction loss term.

Rusch [3, 31] finds these losses by using vector diffraction theory; he calculates the currents on the subreflector. Similar results can be calculated by using GTD methods [6]. The results of GTD calculations for a circularly polarized feed are listed in Table 8-3. They are similar to the results given for

TABLE 8-3 Diffraction Loss of Cassegrain Antenna

Subreflector diameter, λ	10-dB feed edge amplitude taper Effective F/D					
	0.75	1.0	1.5	2.0	2.5	3.0
	Diffraction loss, dB					
6	0.67	0.81	1.02	1.43	1.85	2.28
8	0.55	0.68	0.78	1.09	1.41	1.75
10	0.48	0.58	0.64	0.89	1.14	1.40
12	0.43	0.51	0.55	0.76	0.97	1.17
14	0.39	0.46	0.48	0.67	0.84	1.01
16	0.36	0.42	0.43	0.60	0.75	0.88
20	0.31	0.37	0.36	0.50	0.62	0.72
30	0.24	0.27	0.25	0.37	0.45	0.49
40	0.20	0.24	0.20	0.30	0.36	0.39
60	0.16	0.20	0.12	0.22	0.27	0.28
100	0.11	0.15	0.09	0.17	0.20	0.22
	15-dB feed edge amplitude taper					
6	0.53	0.66	0.91	1.29	1.72	2.17
8	0.42	0.54	0.68	0.96	1.29	1.64
10	0.36	0.45	0.55	0.77	1.02	1.30
12	0.32	0.39	0.46	0.65	0.85	1.07
16	0.26	0.31	0.36	0.49	0.63	0.78
20	0.22	0.27	0.29	0.40	0.51	0.62
50	0.12	0.15	0.13	0.19	0.22	0.24
100	0.07	0.10	0.11	0.12	0.14	0.14

a TE_{11}-mode circular horn feed [9]. The loss depends on the effective focal length and the diameter of the subreflector. Increasing the feed edge taper level lowers the diffraction loss and produces a broad flat optimum at about a 12-dB edge taper.

Equalizing the feed and subreflector blockage may not lead to the optimum (highest-gain) design. We must trade off diffraction loss and blockage loss.

Example Optimize the 10-m-diameter Cassegrain dual reflector for the sum of diffraction and blockage losses at 3.9 GHz. The subreflector diameter is 0.894 m, or 11.62 λ. We can increase the subreflector diameter without affecting the results of the preceding example; that is, the feed blockage will be less than the subreflector blockage. We generate the following table from Tables 6-19 and 8-3.

Diameter, λ	*Blockage* *dB*	*Diffraction loss,* *dB*	*Sum,* *dB*
11.6	0.14	0.57	0.71
14	0.20	0.48	0.68
16	0.26	0.43	0.69
18	0.33	0.40	0.73

The optimum occurs at about 15λ diameter, or 1.154 m. The table shows a broad optimum with variations of ±1λ having no practical effect. We move the feed back to illumine the larger subreflector

$$2c = 3.6P = 3.6(D_s)/2.322 = 1.789 \text{ m}$$

Kildal [32] has derived a simple formula for the optimum subreflector size to minimize the combination of blockage and diffraction losses

$$\frac{d}{D} = \left[\frac{\cos^4(\theta_0/2)}{(4\pi)^2 \sin\psi_0} E \frac{\lambda}{D}\right]^{1/5}$$

where d is the subreflector diameter, D is the main-reflector diameter, and E is the power illumination at the edge of the subreflector (0.1 for 10 dB). The approximate product of the efficiencies (blockage and diffraction) at the optimum d/D is

$$\eta \approx \left\{1 - C_b\left[1 + 4\sqrt{1 - \frac{d}{D}}\right]\left(\frac{d}{D}\right)^2\right\}^2$$

$$\text{where} \quad C_b = -\ln \frac{\sqrt{E}}{(1 - \sqrt{E})}$$

This analysis gives a good first estimate of the proper subreflector size and associated loss.

Cassegrain Tolerances [9, 33] To calculate the feed movement effects, reduce them by the magnification factor M and use the F/D of the main reflector. The result is the reduction of the tight location tolerances normally required of the deep (small F/D) main reflector. For feed scanning we must multiply the offset required for the main reflector by the magnification factor to find the necessary lateral offset.

Translation of the hyperboloid is nearly equivalent to a movement of the virtual feed; it is reduced by the factor $(M - 1)/M$. Rotating the subreflector laterally offsets the virtual feed by the factor

$$\frac{4c\beta}{M + 1}$$

where $2c$ is the distance from the feed to the virtual feed and β is the rotation (radians). Since all factors are small, we can sum the results.

The surface tolerance of the subreflector adds another phase error loss term in the same form as the main reflector. The tolerance loss factor is less for a hyperbola than for a parabola because the angles of incidence are higher [34]. The ellipsoid of the Gregorian reflector has higher losses. We express the loss at each reflector as

$$\text{PEL} = e^{-A(4\pi\Delta n/\lambda)^2} \tag{8-65}$$

where Δn is the deviation normal to the perfect reflector surface and A is a constant depending on the eccentricity of the reflector and the main reflector F/D. This factor is listed in Table 8-4 [34]. The main reflector has $e = 1$ (parabola). An equation matching Eq. (8-44) is

$$\text{PEL (dB)} = -685.8A\left(\frac{\Delta n}{\lambda}\right)^2 \tag{8-66}$$

TABLE 8-4 Scale Factor for Random Normal Surface Deviations of a Dual Reflector

Eccentricity e	Main reflector F/D					
	0.25	0.30	0.35	0.40	0.45	0.50
	Scale factor					
0.5	0.872	0.898	0.918	0.933	0.944	0.953
0.6	0.834	0.868	0.894	0.914	0.929	0.940
0.7	0.796	0.839	0.871	0.895	0.913	0.928
0.8	0.759	0.811	0.849	0.877	0.899	0.915
0.9	0.725	0.784	0.828	0.860	0.885	0.904
1.0	0.693	0.759	0.808	0.844	0.872	0.893
1.2	0.637	0.715	0.772	0.815	0.847	0.872
1.5	0.569	0.660	0.727	0.778	0.816	0.846
2.0	0.490	0.592	0.671	0.730	0.777	0.812
3.0	0.402	0.512	0.600	0.670	0.725	0.768

8-14 G/T (Gain/Noise Temperature)

A receiving system needs to maximize the signal-to-noise ratio for given resources. System considerations, such as bit error rate, establish the required S/N. We express the noise as an equivalent noise temperature related to the noise power in a given bandwidth

$$N = k_0 B_n T_e \tag{8-67}$$

where k_0 is Boltzmann's constant (1.38×10^{-23} J/K) and B_n is the receiver bandwidth. T_e is the effective noise temperature and really represents noise power. When referring noise temperature to other parts of the network, we increase or decrease it by the gain or loss, since it is a power and not a true temperature. Antenna gain is a measure of the signal level, since we can increase gain somewhat independently of the noise temperature.

An antenna adds to the system noise temperature in two ways. The antenna conductor losses have an equivalent noise temperature

$$T_e = (L - 1)T_0 \tag{8-68}$$

where T_0 is the antenna temperature and L is the loss (a ratio greater than 1). From a systems point of view we include the transmission line to the first amplifier or mixer of the receiver. We do not include the illumination losses (ATL, PEL, SPL, XPL, blockage, etc.) in the losses in Eq. (8-68) because they are a loss of aperture gain and not noise-generating losses (random electrons). An antenna also receives blackbody noise from the environment. The blackbody noise temperature of an antenna depends on the pattern and the direction of the main beam. We average the blackbody noise temperature surrounding the antenna multiplied by the gain pattern distribution over the radiation sphere:

$$T_a = \frac{1}{4\pi}\int_0^{2\pi}\int_0^{\pi} G(\theta,\phi)T_s(\theta,\phi)\sin\theta\, d\theta\, d\phi \tag{8-69}$$

where $G(\theta, \phi)$ is the antenna gain pattern and $T_s(\theta, \phi)$ is the blackbody radiation of the environment. Changing the pointing of the antenna changes the distribution $T_s(\theta, \phi)$.

The ground noise temperature is about 300 K, and the sky noise temperatures are under 50 K. The sky temperature depends on the pointing angle and the frequency of operation. Near zenith the temperature is about 3 K and near the horizon it rises because of the noise from oxygen and water vapor. The exact value must be determined for each application.

Collins [35] has developed a procedure for calculating the noise temperature of Cassegrain antennas pointed near the horizon. First the diffraction pattern of the feed and subreflector combination is calculated. Some of the diffraction is added to the main-reflector spillover. At low elevation angles the antenna points about one-half of the spillover on the ground. It is a major noise temperature contribution

$$\tfrac{1}{2}(1 - \mathrm{SPL})T_G$$

where T_G is the ground temperature and SPL is the spillover efficiency (ratio). The scattered portion of the blockage produces wide-angle sidelobes half of which see the ground. The gain is reduced by the spillover loss, and a uniform distribution for the blockage is assumed (ATL = 1).

$$\frac{1}{2}\frac{S_b}{S_a}\mathrm{SPL}\,T_G$$

where S_b is the blocked area and S_a is the total potential aperture. The main beam points towards the sky and collects noise

$$\mathrm{SPL}\,\eta_b\eta_m T_S$$

where η_b is the blockage efficiency, η_m is the ratio of the power in the main beam and first few sidelobes ($\eta_m \approx 0.99$), and T_S is the sky temperature. We also include a group of minor contributors:

$$\tfrac{1}{2}(1 - \mathrm{SPL})T_S$$

$$\frac{1}{2}\frac{S_b}{S_a}\mathrm{SPL}\,T_S$$

$$\tfrac{1}{2}\mathrm{SPL}\eta_b(1 - \eta_m)(T_G + T_S)$$

Equation (8-69) can be used when the temperature distribution is known, but the procedure of Collins gives good although slightly conservative results. We must calculate the gain noise temperature at the same point in the network. We need to reduce or increase the noise temperature or gain as we move the values to the same point.

8-15 Offset-Fed Reflector

Moving the feed out of the aperture eliminates some of the problems with axisymmetrical reflectors. Blockage losses and diffraction-caused sidelobes and cross-polarization disappear. We can increase the size of the feed structure and include more if not all of the receiver with the feed. For example, the reflector may be deployed from a satellite where we mount the feed on the main satellite body.

Figure 8-13 shows the offset-fed reflector geometry. We form the reflector out of a piece of a larger paraboloid. Every piece of the paraboloid reflector converts spherical waves from the focus into a plane wave moving parallel with the axis. We point the feed toward the center of the reflector

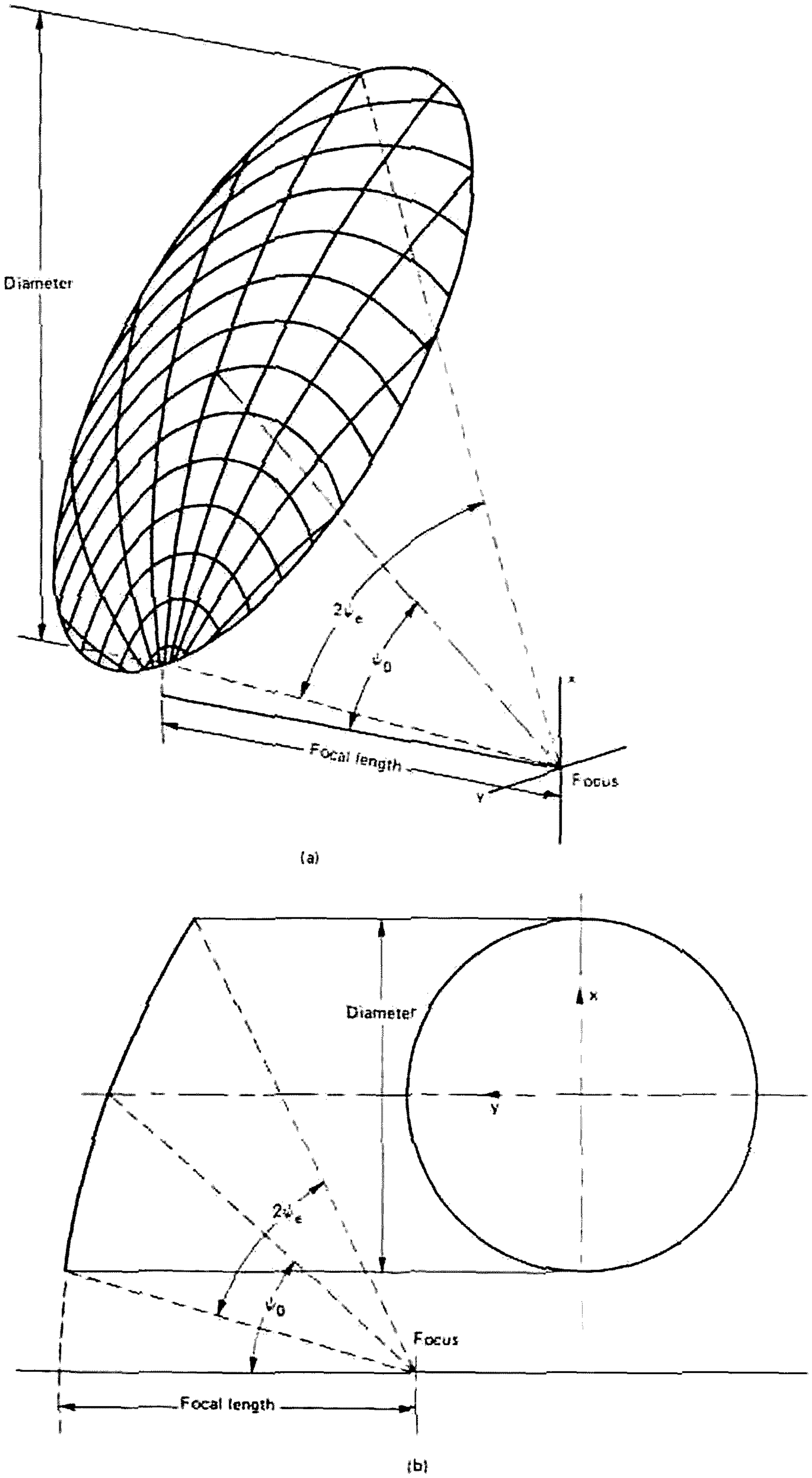

Figure 8-13 Offset-fed reflector geometry: (*a*) perspective; (*b*) orthographic.

to reduce the spillover, but we still locate the feed phase center at the focus of the reflector. The aperture plane projects to a circle, although the rim shape is an ellipse. ψ_0 is the angle from the axis of the parabola to the center of the reflector. The reflector subtends an angle $2\psi_e$ about this centerline.

The offset angle modifies the F/D of the reflector.

$$\frac{F}{D} = \frac{\cos \psi_e + \cos \psi_0}{4 \sin \psi_e} \tag{8-70}$$

We analyze the offset reflector with the same tools as those used with the axisymmetric reflector: aperture field, physical optics, and GTD. The asymmetry of the reflector to feed geometry introduces anomalies. Huygens sources no longer eliminate cross-polarization, because the source must be tilted. Symmetry prevents cross-polarization in the plane containing the x axis (Fig. 8-13), but cross-polarization increases in the plane containing the y axis as F/D decreases. The Condon lobes move off the diagonal planes and into the plane containing the y axis. The asymmetry along the x axis tapers the amplitude distribution from a symmetrical feed, since the spherical wave travels farther to the outer edge of the reflector than to the lower edge. The offset-fed reflector geometry squints circularly polarized signals without generating cross-polarization. An approximate formula for the squint is [9]

$$\psi_s = \sin^{-1} \frac{\lambda \sin \psi_0}{4\pi F} \tag{8-71}$$

where ψ_s is the squint angle. Opposite senses of polarization squint in opposite directions and cause problems with dual circularly polarized feed systems. In all cases increasing the F/D or the effective F/D through a subreflector reduces these problems. The subreflector should be kept out of the aperture of the main reflector.

We can feed-scan the offset-fed reflector by moving the feed laterally along a line that lies perpendicular to the boresight of the feed (the line defined by ψ_0). We must modify the beam deviation factor (BDF).

$$\mathrm{BDF}_{\text{offset fed}} = \mathrm{BDF}_{\text{center fed}} \frac{(F/D)_{\text{offset}}}{(F/D)_{\text{center fed}}} \tag{8-72}$$

Example Given an offset-fed reflector with $\psi_0 = 45°$ and $\psi_e = 40°$, find the beam deviation factor.

From Eq. (8-70),

$$\left(\frac{F}{D}\right)_{\text{center fed}} = \frac{\cos 40° + 1}{4 \sin 40°} = 0.687$$

$$\left(\frac{F}{D}\right)_{\text{offset fed}} = \frac{\cos 40° + \cos 45°}{4 \sin 40°} = 0.573$$

From Table 8-1 we interpolate $\mathrm{BDF}_{\text{center fed}} = 0.928$, and we substitute the values into Eq. (8-72) to find $\mathrm{BDF}_{\text{offset fed}} = 0.774$.

We must laterally offset the feed farther than a center-fed reflector to achieve the same feed scanning.

8-16 Spherical Reflector

When we feed-scan a paraboloidal reflector, the pattern sidelobes develop coma and the beam shape generally degrades. Feed scanning is limited. In a spherical reflector a feed moved in an arc centered on the center of the sphere sees the same reflector geometry if we discount the edge effects. Greater scanning is possible, but the spherical reflector fails to focus an incident plane wave to a point and requires more elaborate feeds.

Many different kinds of feeds can be designed for the spherical reflector. The reflector can be fed from a point source for large F/D by assuming it is a distorted parabola [36, 37]. It can be fed with a line source to follow the axis fields. Corrector subreflectors can be designed to correct the spherical aberrations [10, 39]. Like the parabolic reflector, we can design arrays [27] to compensate for spherical aberrations and give multiple beams.

Figure 8-14 shows the geometry and ray tracing of a spherical reflector illuminated by a plane wave. All rays intersect a radial line of the sphere (the axis) in the direction of the incident wave because the reflector has circular symmetry about all axes. The diagram traces rays hitting the outer portion of the reflector as passing through the axis closer to the vertex than do the rays reflected from areas closer to the axis. The reflector has a line focus. A distorted paraboloidal reflector with a line focus exhibits spherical aberration because the focal length depends on the radial distance from the axis of the reflection point. The spherical reflector has a cusp-like caustic where GO predicts infinite fields. The second side of Fig. 8-14 traces a single ray. We can easily solve the isosceles triangle for the results:

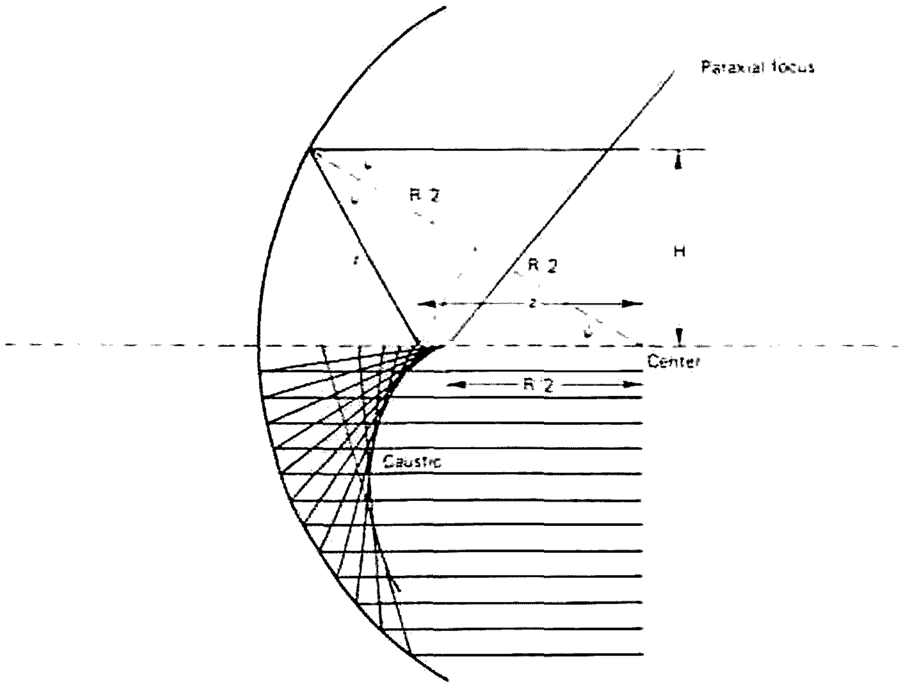

Figure 8-14 Ray tracing in spherical reflector.

$$z = \frac{R/2}{\sqrt{1 - H^2/R^2}} \tag{8-73}$$

$$H^2 = R^2\left(1 - \frac{R^2}{4z^2}\right) \tag{8-74}$$

where z is the location of the focus for a given ray. As H approaches zero, that is, rays near the axis, the reflected ray passes through the paraxial focus ($z = R/2$).

We use Eq. (8-74) to find the power distribution on the axis by using the conservation of power. The power in a differential area of the plane wave reflects into a differential length on the axis.

$$dA = 2\pi H\, dH$$

Differentiate Eq. (8-74) implicitly

$$2H\, dH = \frac{R^2}{2z^3}\, dz$$

The power distribution along the axis is

$$P_z = \frac{P_0 R^3}{8z^3} \tag{8-75}$$

where P_0 is the power at the paraxial focus. The peak power occurs at the paraxial focus and drops by one-eighth (−9 dB) at the vertex.

We determine the required length of the line source feed from the rotation angle ψ of the illuminated portion of the reflector.

$$\text{Feed length} = \frac{R(1/\cos\psi - 1)}{2} \tag{8-76}$$

Example If the half-rotation angle of the illuminated region is 30°, the feed length is $0.0774R$ from Eq. (8-76). The amplitude decreases by

$$[\text{Eq. (8-75)}] \qquad \frac{P_z}{P_0} = \frac{R^3}{8(R/2 + 0.0774R)^3} = 0.65 \quad (-1.9\text{ dB})$$

The rays intersecting the axis are not at constant phase. The path length from the aperture plane through the reflector origin is

$$\text{Path length} = \frac{R^2}{2z} + z \tag{8-77}$$

We can approximate Eq. (8-77) by a linear function if the feed length is short.

Example The feed length is $0.0774R$ long; find the phase change required along the feed.

The feed starts at the paraxial focus ($z = R/2$).

$$\text{Path length} = \frac{R^2}{R} + \frac{R}{2} = 1.5R$$

At $z = R/2 + 0.0774R$, path length $= 1.443R$. The phase change is

$$\frac{2\pi}{\lambda}R(0.0566)$$

If we plot the phase change over the region of the feed, we can approximate the phase change by a linear function very accurately.

The spherical reflector can be fed from a point source when the F/D is large [36]. The center of the reflector approximates a parabola. The optimum focal point is

$$F = \tfrac{1}{4}\left[R + \sqrt{R^2 - \left(\frac{D}{2}\right)^2}\right] \tag{8-78}$$

The maximum phase path length error is [37]

$$\frac{\Delta L}{\lambda} = \frac{1}{2048}\frac{D}{\lambda}\frac{1}{(F/D)^3} \tag{8-79}$$

The approximate gain loss is

$$\frac{\Delta G}{G} = 3.5092\left(\frac{\Delta L}{\lambda}\right)^2$$

or

$$\text{PEL(dB)} = 10 \log\left[1 - 3.5092\left(\frac{\Delta L}{\lambda}\right)^2\right] \tag{8-80}$$

A path length deviation of 0.25λ reduces the gain by 1.08 dB.

Example Find the F/D of a spherical reflector to limit ΔL to $1/16\lambda$ for a reflector diameter of 50λ.

By rearranging Eq. (8-79), we find

$$F/D = \left(\frac{16(50)}{2048}\right)^{1/3} = 0.73$$

8-17 Corrector Subreflector for a Spherical Reflector [10, 39]

We can design a subreflector to correct for spherical aberration of the spherical reflector and focus the rays into a single point. When we find a subreflector surface which gives equal path lengths from the source to the aperture plane, Snell's law of reflection will be automatically satisfied by Fermat's principle. The equal-rays paths are stationary. Figure 8-15 gives the

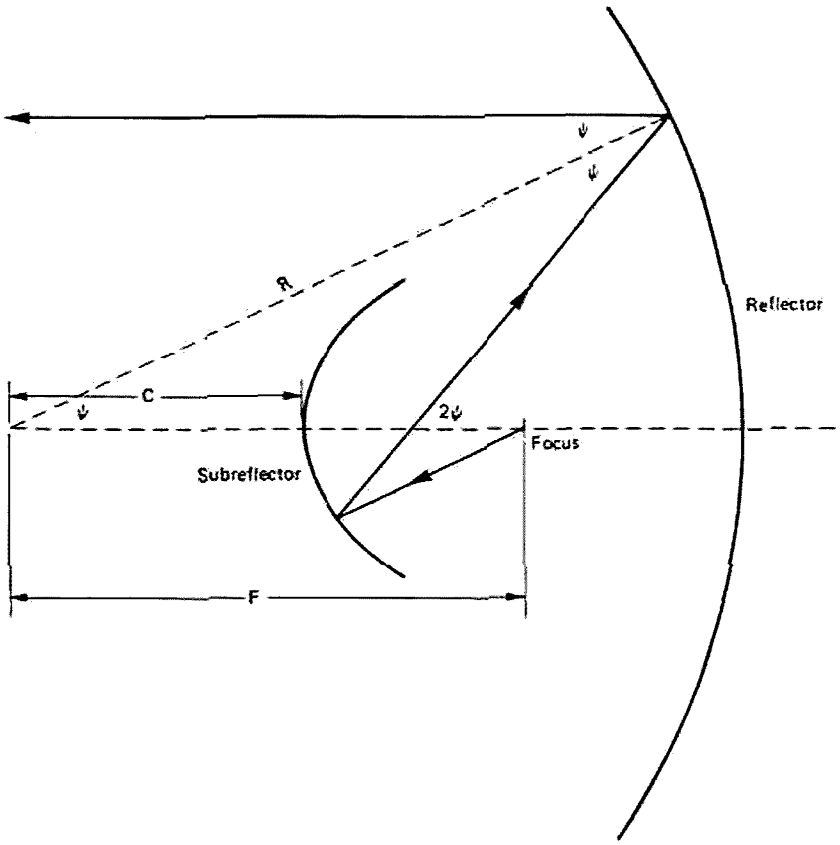

Figure 8-15 Spherical reflector with corrector subreflector.

subreflector geometry. By equating all ray lengths to the central ray length (blocked by the subreflector), we calculate the following equations for r and z of the corrector subreflector.

$$\frac{z}{R} = \cos\psi - \frac{\left\{\cos^2\psi - 4\left(1 - \frac{C}{R}\right)\cos\psi - \left[1 + \left(\frac{F}{R}\right)^2\right] + \left[2 + \frac{F}{R} - 2\left(\frac{C}{R}\right)\right]^2\right\}\cos 2\psi}{4\left(\frac{F}{R}\cos^2\psi - \cos\psi - \frac{C}{F} + 1\right)}$$

$$\frac{r}{R} = \frac{(2Z/R\cos\psi - 1)\sin\psi}{\cos 2\psi} \qquad (8\text{-}81)$$

We have two arbitrary parameters: C/R and F/R. C/R must be less than 0.5 or rays from the central portion of the main reflector will hit the subreflector before crossing the axis. As F/R decreases, the size of the subreflector decreases and the feed blockage area increases because the feed diameter increases to produce the required narrow beam. As is true of the Cassegrain, there are optimum designs.

We relate the feed pattern to the aperture distribution by using conservation of power through differential areas.

$$F(\psi)\sin\psi\,d\psi\,d\phi = A(H)H\,dH\,d\phi$$

where $F(\psi)$ is the feed power pattern, H is the radial distance, and $A(H)$ is the aperture power distribution. The relative aperture field can be found from

$$\frac{E(H)}{E_0} = \sqrt{\frac{F(\psi)\sin\psi}{H}\frac{d\psi}{dH}} \tag{8-82}$$

Example Apply Eq. (8-82) to a parabolic reflector.

$$H = 2F\tan^2\frac{\psi}{2} \qquad dH = F\sec^2\frac{\psi}{2}d\psi = \rho\,d\psi$$

$$E(H) = E_f(\psi)\sqrt{\frac{\sin\psi}{2F\tan^2(\psi/2)}\frac{1}{\rho}}$$

Since $H = 2F\tan^2(\psi/2) = \rho\sin\psi$, $E(H) = E_f(\psi)/\rho$

After we determine the relation between the feed pattern angle and the aperture position H, we can numerically differentiate to find $d\psi/dH$ and substitute into Eq. (8-82) to find the aperture distribution. We then use the techniques of Chap. 6 to calculate the distribution losses and pattern.

8-18 Shaped Reflectors

In the preceding section we looked at a subreflector designed by geometric optics. The reflector transformed through a prescribed second reflector a spherical wave into a plane wave. Shaped reflectors change the wave type in other ways and spread cylindrical or spherical waves into a desired pattern. The method depends on geometric optics. The far-field pattern of the subreflector-corrected spherical reflector is not a plane wave, nor do shaped reflectors radiate patterns exactly as prescribed by GO. In all cases we must apply techniques such as aperture diffraction, induced currents, or geometric theory of diffraction (GTD) to find the actual pattern. We will consider only the first-order GO used to design the reflector. Analysis requires more elaborate techniques.

We use two principles to design shaped reflectors. The first is GO reflection. The second is the conservation of power in ray tubes. We express reflection as a differential equation. Conservation of power can be expressed either in terms of differential areas or integrals over sections of the feed and reflection patterns.

We define two angles for the GO reflection equation. The feed points toward the reflector, and we measure its pattern angle ψ from an axis pointed toward the reflector. The reflector reradiates the incident feed pattern in a far-field pattern whose angle θ is measured from the axis pointing away from the reflector. The edges of the reflector are defined by angles ψ_1 and ψ_2 measured from the feed axis and reflect in directions θ_1 and θ_2. The differential equation of reflection is [2]

$$\tan\frac{\theta+\psi}{2}=\frac{d\rho}{\rho\,d\psi} \tag{8-83}$$

where ρ is the distance of the reflector from the feed. We can integrate this differential equation for a solution:

$$\ln\frac{\rho(\psi)}{\rho_0(\psi_1)}=\int_{\psi_1}^{\psi}\tan\frac{\theta(\psi)+\psi}{2}\,d\psi \tag{8-84}$$

where ψ_1 is some initial angle of the feed and $\rho_0(\psi_1)$ is the initial radius vector locating the reflector at ψ_1.

GO, the zero wavelength approximation, is consistent at any size. All parabolic reflectors collimate spherical waves from the focus regardless of size. Only by considering diffraction or currents induced on the reflector can we find the gain and beamwidth of the antenna.

Example From Eq. (8-84) find the reflector surface to give $\theta(\psi)=0$.

$$\ln\frac{\rho(\psi)}{\rho_0(\psi_1)}=\int_{\psi_1}^{\psi}\tan\frac{\psi}{2}\,d\psi=-2\left(\ln\cos\frac{\psi}{2}-\ln\cos\frac{\psi_1}{2}\right)$$

By the properties of the ln function, this becomes

$$\ln\frac{\rho(\psi)}{\rho_0(\psi_1)}=\ln\frac{\cos^2(\psi_1/2)}{\cos^2(\psi/2)}$$

By taking the exponential of each side, we get the polar equation of the reflector

$$\rho(\psi)=\rho_0(\psi_1)\frac{\cos^2(\psi_1/2)}{\cos^2(\psi/2)}$$

we let $\psi_1=0$ and set $\rho_0(\psi_1)=F$ and we obtain the equation for the parabola [Eq. (8-21)].

The differential equation of reflection tells us only the shape of the reflector locally to produce a reflection in a direction θ for an incident angle ψ. We must still find the power density in various directions. The ratio of differential areas gives us the power densities. Given the pattern of the feed $G_f(\psi,\phi)$ and the pattern of the reflection $P(\theta,\phi)$

$$KP(\theta,\phi)\,dA(\theta,\phi)=G_f(\psi,\phi)\,dA_f(\psi,\phi) \tag{8-85}$$

where $dA(\theta,\phi)$ is the differential area of the reflection pattern, $dA_f(\psi,\phi)$ is the differential area of the feed pattern, and K is a constant found by equating the total incident and reflected powers. Equation (8-85) is based on the assumption that reflections are 1:1 with the feed pattern.

Cylindrical Reflector Synthesis We feed cylindrical reflectors with line sources. The reflector determines the beam shape in one plane and the line source distribution in the other. The problem reduces to designing a single two-dimensional curve moved along an axis to define the reflector.

The power radiated by the feed is given by

$$G_f(\psi)\,d\psi$$

The reflector directs this power at an angle θ whose power density is

$$P(\theta)\,d\theta$$

These are proportional [Eq. (8-85)]

$$KP(\theta)\,d\theta = G_f(\psi)\,d\psi \tag{8-86}$$

At the limits of the reflector, feed angles ψ_1 and ψ_2 reflect to angles θ_1 and θ_2. We calculate the constant K by equating the power in each pattern

$$K = \frac{\displaystyle\int_{\psi_1}^{\psi_2} G_f(\psi)\,d\psi}{\displaystyle\int_{\theta_1}^{\theta_2} P(\theta)\,d\theta} \tag{8-87}$$

We integrate Eq. (8-86) to find a formal solution usually arrived at numerically. By combining Eqs. (8-86) and (8-87), we eliminate K.

$$\frac{\displaystyle\int_{\theta_1}^{\theta} P(\theta)\,d\theta}{\displaystyle\int_{\theta_1}^{\theta_2} P(\theta)\,d\theta} = \frac{\displaystyle\int_{\psi_1}^{\psi} G_f(\psi)\,d\psi}{\displaystyle\int_{\psi_1}^{\psi_2} G_f(\psi)\,d\psi} \tag{8-88}$$

We use Eq. (8-88) with a known feed pattern $G_f(\psi)$ and a desired pattern function $P(\theta)$ to establish the relation $\theta(\psi)$. We insert $\theta(\psi)$ into the differential equation for the reflection [Eq. (8-84)] and find the radial distance as a function of ψ.

$$\rho(\psi) = \rho_0(\psi_1)\exp\left[\int_{\psi_1}^{\psi} \tan\frac{\theta(\psi)+\psi}{2}\,d\psi\right] \tag{8-89}$$

With Eq. (8-89) we can find the reflector coordinates to within a scale factor $\rho_0(\psi_1)$

Circularly Symmetrical Reflector Synthesis The synthesis of circularly symmetrical reflectors is readily reduced to a two-dimensional problem. We must assume that the feed pattern is also axisymmetrical. We describe the feed pattern by $G_f(\psi)$ and the reflector pattern by $P(\theta)$. The differential areas are $\sin\psi\,d\psi$ and $\sin\theta\,d\theta$. Equation (8-85) becomes

$$KP(\theta)\sin\theta\,d\theta = G_f(\psi)\sin\psi\,d\psi \tag{8-90}$$

We integrate Eq. (8-90) to find the function $\theta(\psi)$

$$\frac{\int_{\theta_1}^{\theta} P(\theta)\sin\theta\,d\theta}{\int_{\theta_1}^{\theta_2} P(\theta)\sin\theta\,d\theta} = \frac{\int_{\psi_1}^{\psi} G_f(\psi)\sin\psi\,d\psi}{\int_{\psi_1}^{\psi_2} G_f(\psi)\sin\psi\,d\psi} \tag{8-91}$$

We use Eq. (8-89) from the reflection differential equation with $\theta(\psi)$ to determine the polar equation of the reflector. The design of a shaped reflector can best be explained with an example. The cylindrical reflector synthesis follows parallel steps.

Example Design a reflector to transform the feed pattern of Fig. 8-16*a* into the pattern of Fig. 8-16*b*. The required pattern drops by about 9 dB from 50° to 0°. We will use the feed pattern from 4° to 54° and design a reflector with a ring caustic. The feed pattern at 4° is reflected to 50°, and the feed pattern at 54° is reflected to 0°. The geometric optics rays cross somewhere in front of the reflector. We have the following limits:

Feed: $\psi_1 = 4°$ $\psi_2 = 54°$

Reflection: $\theta_1 = 50°$ $\theta_2 = 0°$

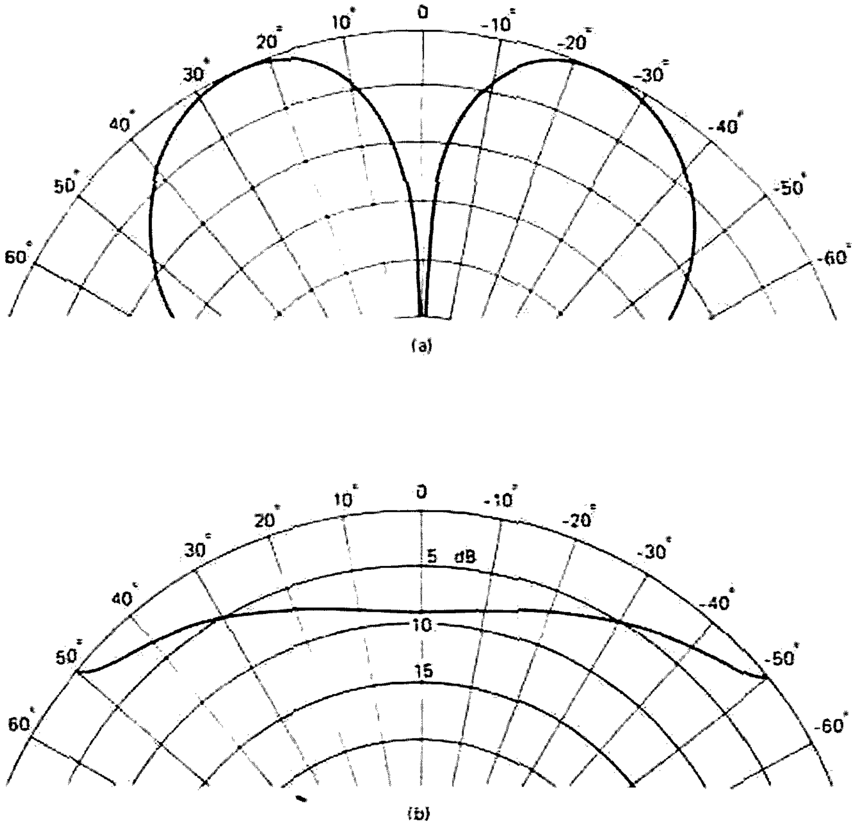

Figure 8-16 Axisymmetric shaped reflector pattern transformation: (*a*) feed pattern; (*b*) reflector pattern.

We insert the patterns of Fig. 8-16 into both sides of Eq. (8-91) and evaluate the ratio of the integrals. Table 8-5 gives the results of these integrals for θ and ψ as normalized in Eq. (8-91). Given ψ, we find θ by equating integrals in the table. For example, follow the line from $\psi = 28°$ (feed) to its integral value, match the values of the integrals, and determine the reflection angle $\theta = 42°$. We trace a number of these through interpolation to generate Table 8-6 of reflection angles $\theta(\psi)$ for given feed angles.

We use Table 8-6 of $\theta(\psi)$ in the integral of Eq. (8-89) to calculate the normalized polar equation of the reflector listed in Table 8-7. Figure 8-17 shows the reflector shape as well as the geometry of axisymmetric shaped reflectors. There is a hole in the center because the procedure fails to specify that region.

Note in Table 8-6 how much of the inner portion of the reflector must reflect rays near 50° to achieve the high required gain of the pattern. We could repeat the example and design without a ring caustic where rays from the feed near 54° reflect to 50° and would find a flatter reflector.

TABLE 8-5 The Use of Normalized Integrals of Feed and Pattern Power to Determine $\theta(\psi)$ in Shaped Reflector Synthesis

Feed angle ψ,°	Feed normalized integral	Reflection normalized integral	Reflection angle θ,°
4	0.0	0.0	50
6	0.002	0.143	48
8	0.006	0.259	46
10	0.016	0.360	44
12	0.031	0.449	42
14	0.054	0.527	40
16	0.086	0.596	38
18	0.128	0.657	36
20	0.178	0.711	34
22	0.237	0.757	32
24	0.302	0.798	30
26	0.373	0.833	28
28	0.445	0.864	26
30	0.518	0.889	24
32	0.590	0.911	22
34	0.658	0.930	20
36	0.720	0.946	18
38	0.777	0.959	16
40	0.827	0.970	14
42	0.869	0.978	12
44	0.905	0.985	10
46	0.934	0.991	8
48	0.958	0.995	6
50	0.976	0.998	4
52	0.999	0.999	2
54	1.000	1.000	0

TABLE 8-6 Shaped Reflector Synthesis Reflection Angles for Given Feed Angles, $\theta(\psi)$

Feed angle ψ,°	Reflection angle θ,°	Feed angle ψ,°	Reflection angle θ,°
4	50.0	30	40.2
6	50.0	32	38.2
8	49.9	34	36.0
10	49.8	36	33.6
12	49.6	38	31.1
14	49.3	40	28.4
16	48.8	42	25.6
18	48.2	44	22.6
20	47.4	46	19.5
22	46.4	48	16.2
24	45.2	50	12.6
26	43.7	52	8.4
28	42.1	54	0.0

Because diffraction effects spread the pattern, we could achieve approximately the pattern of Fig. 8-16b by designing a reflector to point the beam in a cone about the axis. If we take Eq. (8-84) and let $\theta(\psi) = \theta_0$, a constant, we get the surface

$$\rho(\psi) = \rho_0 \frac{\cos^2 [(\psi_0 + \theta_0)/2]}{\cos^2 [(\psi + \theta_0)/2]} \tag{8-92}$$

TABLE 8-7 Shaped Reflector Synthesis Normalized Polar Equation of Reflector, $\rho(\psi)$

Feed angle ψ,°	Normalized radius ρ	Feed angle ψ,°	Normalized radius ρ
4	1.000	30	1.332
6	1.018	32	1.365
8	1.038	34	1.398
10	1.058	36	1.433
12	1.080	38	1.468
14	1.103	40	1.503
16	1.128	42	1.539
18	1.153	44	1.575
20	1.180	46	1.611
22	1.208	48	1.648
24	1.238	50	1.684
26	1.268	52	1.719
28	1.299	54	1.753

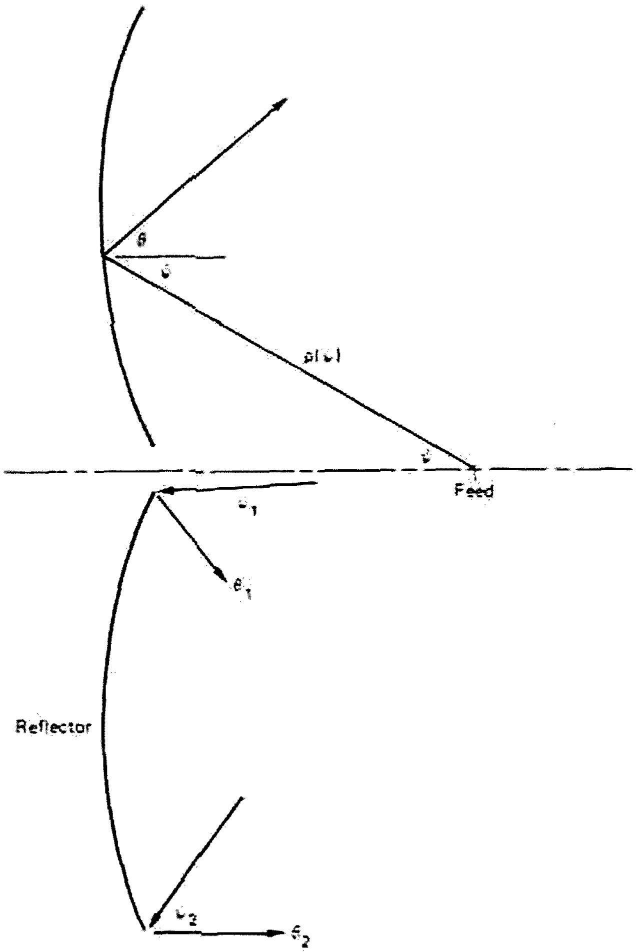

Figure 8-17 Circularly symmetrical shaped reflector designed with caustic reflections.

Example Estimate the directivity of a 40λ-diameter reflector shaped by Eq. (8-92) to scan in a cone to $\theta_0 = 50°$.

Only half of the diameter is used for each side. The effective scanned aperture width becomes

$$\frac{40}{2}\cos 50°\,\lambda = 12.8\lambda$$

If we assume a uniform amplitude aperture distribution, we obtain an upper bound. From Eq. (6-47)

$$\text{HPBW} = \frac{59°}{12.8} = 4.6°$$

We will use Eq. (1-15) to estimate the directivity.

$$\text{Directivity} = \frac{2}{\cos(50° - 2.3°) - \cos(50° + 2.3°)} = 32.5 \quad (15\ \text{dB})$$

The boresight gain of the aperture with a uniform distribution is 42 dB. Spreading the reflection into a cone greatly reduces the gain. The shaped reflector above will have even less directivity because it has an increased edge taper as compared with a parabolic reflector.

Doubly Curved Reflector for Shaped Beams It is a common radar requirement to have a narrow beam in one plane and a shaped beam in the other. Such beams can be obtained from shaped cylindrical reflectors, but it is simpler to replace the line source with a single feed. We will specify only the pattern in the principal planes denoted: θ_V, the shaped pattern coordinate, and θ_H, the pencil beam [2, 40]. Similarly, we will specify the feed antenna pattern in terms of ψ_V and ψ_H. For a given feed angle ψ_V, the reflected wave angle will be θ_V..*The only allowed θ_H is zero. The reflector collimates the* wave in the horizontal plane. This collimation requires a symmetrical reflector made from parabolic curves in the horizontal plane. The problem reduces to the design of the vertical curve through the center of the reflector.

For a given feed angle ψ_V (Fig. 8-18*a*), all incoming rays at an angle θ_V must be reflected into the feed. The incoming rays form the plane *xz'* in Fig. 8-18 and the reflector collimates these to the feed by a parabola in the plane. We call this parabola a rib of the reflector. Figure 8-18*b* shows the

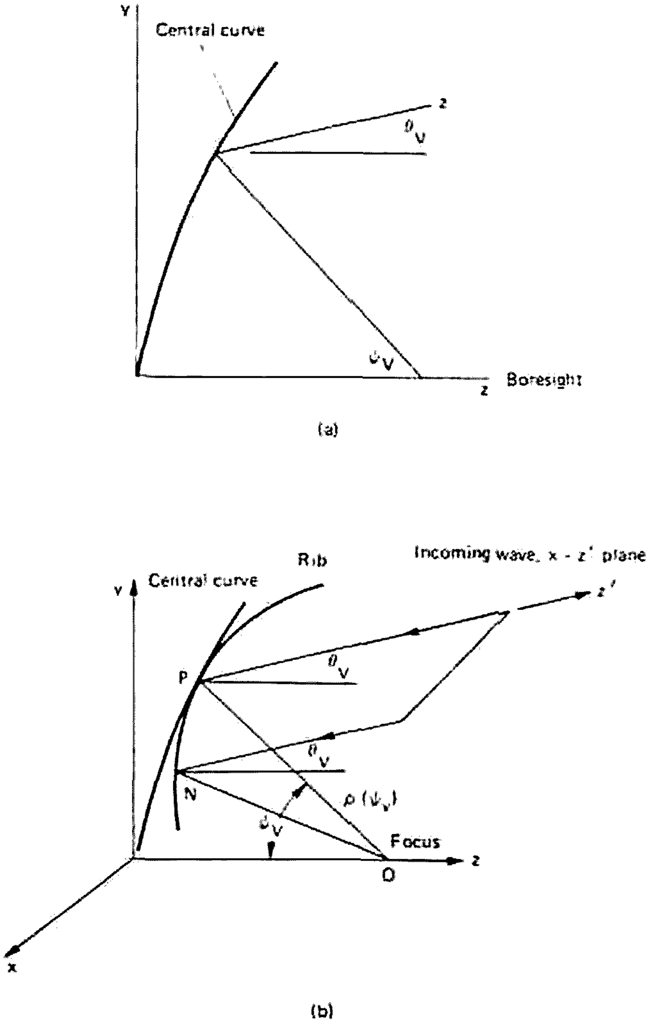

Figure 8-18 Doubly curved shaped reflector geometry.

plane and two rays reflecting into the feed from a wave arriving at an angle θ_V in the xz' plane. For the beam to focus, the optical path lengths must be equal.

$$\overline{BP} + \overline{PO} = \overline{AX} + \overline{XO} \tag{8-93}$$

Equation (8-93) establishes the curve of the rib in the xz' plane as a parabola with focal length

$$F = \rho_c(\psi_V)\cos^2\frac{\theta_V(\psi_V) + \psi_V}{2} \tag{8-94}$$

with the focus located on the z' axis. Using the parabolic ribs reduces the problem to the design of the central curve $\rho_c(\psi_V)$.

The reflected and feed power densities modify Eq. (8-85) to

$$KP(\theta_V)\,d\theta_V\,\rho_c(\psi_V)\,d\psi_H = G_f(\psi_V)\,d\psi_V\,d\psi_H \tag{8-95}$$

We integrate Eq. (8-95) and normalize to the total power.

$$\frac{\displaystyle\int_{\theta_1}^{\theta_V} P(\theta_V)\,d\theta_V}{\displaystyle\int_{\theta_1}^{\theta_2} P(\theta_V)\,d\theta_V} = \frac{\displaystyle\int_{\psi_1}^{\psi_V} \frac{G_f(\psi_V)}{\rho_c(\psi_V)}\,d\psi_V}{\displaystyle\int_{\psi_1}^{\psi_2} \frac{G_f(\psi_V)}{\rho_c(\psi_V)}\,d\psi_V} \tag{8-96}$$

Equation (8-96) is similar to Eqs. (8-88) and (8-91) except that the feed pattern integral depends on the radial distance to the central rib. We must know $\rho_c(\psi_V)$ before we can determine $\theta_V(\psi_V)$, which will be required to find $\rho_c(\psi_V)$ by use of the reflection differential equation [Eq. (8-89)]. The solution can be found only by an iterative process.

We must assume a $\rho_c(\psi_V)$, solve for $\theta_V(\psi_V)$, and use the result to find a new $\rho_c(\psi_V)$. After a few iterations, the values of $\rho_c(\psi_V)$ will converge. We can use the normalized ρ_c with the above ratio of integrals. We start with a parabola

$$\frac{\rho_c(\psi_V)}{\rho_c(\psi_1)} = \frac{\cos^2(\psi_1/2)}{\cos^2(\psi_V/2)}$$

The surface generated by following the method may not be uniquely defined. We pick a constant width for the reflector in the horizontal plane. We define the surface with a continuous series of parabolas each in an xz' plane determined by the reflection angle θ_V, which changes direction along the central rib. We must plot the curve of the vertical coordinate of the edge versus ψ_V to see if it is monotonic. If there are loops in the curve, then the surface defined is not unique.

Given the width x, we calculate the vertical coordinate of the edge by the following development. The location of the rib on the central curve is given by $\rho_c(\psi_V)\sin\psi_V$. The rib is a parabola in the xz' plane with its focus given by Eq. (8-94). The z' coordinate at the edge is

$$z' = \frac{x^2}{4F(\psi_V)}$$

We find the vertical dimension by projecting this point onto the y axis:

$$y = \rho_c(\psi_V)\sin\psi_V + z'\sin\theta_V$$

Elliott [41] points out that by following this method, one does not get the proper slope for reflection at all points, but we will get the desired pattern when we design for only small deviations from a pencil beam. The surface can be designed with or without a caustic depending on the reflection angles at the edges. Reflectors designed with caustic edge reflections have a better chance of being unique [41]. Carberry [42] presents a method of analysis that involves physical optics. When we apply these methods, we must subdivide the reflector into many intervals because the phases of the currents change rapidly with position on the reflector. The analysis must be repeated with finer and finer intervals until the result converges.

Other Beam-Shaping Reflectors We can design a dual-reflector antenna to produce an arbitrary phase and amplitude in the aperture plane by shaping both reflectors. By using both the conservation of power and the differential equations of reflection on the two surfaces, Galindo [43] derived a pair of differential equations in terms of the aperture radius. The Runge-Kutta or any other suitable numerical method can be used to solve the simultaneous differential equations instead of an integration of the power equation. Williams [44] finds a solution to Cassegrain antennas within the restriction of equal amplitude and phase in the aperture plane by integration of the power equation. Collins [45] considers using a parabolic reflector for the main reflector, since the difference between the shaped main reflector and a parabola is small. He accepts a quadratic phase error in the aperture. Existing large reflectors can be retrofitted with a shaped subreflector to improve performance. For the method to work, an axisymmetric feed such as a corrugated horn is required.

Galindo-Israel and Mittra [46] use a pair of reflectors offset from each other to transform a spherical wave from a feed antenna into a second spherical wave with a modified pattern amplitude. This combination of a feed with two reflectors can illuminate either prime focus paraboloidal reflectors or Cassegrain systems without modification of the existing reflector surfaces. For example, a $\sec^4(\theta/2)$ pattern can be realized from an ordinary pattern source to increase the aperture efficiency of the overall reflector system. The reflectors maintain equal GO path lengths for all rays, but they only approximate the desired pattern amplitude from the virtual focus. The procedure can be used to determine the contours of the reflectors along radial lines through numerical solution of differential equations. The equations develop from simplifying assumptions that depend on the extra degree of freedom introduced by the second reflector. In most cases the solution of the equations produces usable designs, although the method is not exact.

Silver [2] discusses using a linear array feed to shape the beam of a paraboloidal reflector. The method is quite empirical and involves the addition of a number of offset beams. A similar technique is used in 3D radar, but the feeds are kept separate so that multiple beams can scan a larger area in a given time. An array feed provides the best solution to beam shaping in many cases. The number of elements in the array limits the number of variables to a finite set to which optimization techniques can be applied.

8-19 Reflectors Made from Flat Plates

We can analyze flat-plate reflectors from three perspectives. The plates restrict the possible radiation directions and thereby increase directivity. Waves polarized parallel with the surface must vanish on the reflector surface and cause a greater restriction of the beam. We see this effect in Fig. 4-7, which shows horizontal dipoles having greater directivities than vertical dipoles for close spacings over a ground plane. By the second method we use aperture theory to analyze the reflector by using an aperture plane and integrate the fields or evaluate illumination losses. If the phase of the fields on the aperture varies rapidly, we must either take fine increments in numerical integration or evaluate only around areas of stationary phase. Third, we can replace the reflector with images and restrict the valid pattern region. In GTD this method is combined with diffractions to smooth the field across shadow and reflection boundaries.

Flat Plate In Sec. 4-6 we analyzed the pattern and gain of a dipole mounted over an infinite ground plane by the method of images. The antenna and its image formed a two-element array, but with real power only into one element. The imaging method gives limited information that can be filled with GTD methods.

Table 8-8 lists the results of a GTD analysis of a half-wavelength horizontal dipole located a quarter wavelength over a limited square ground plane. An infinite ground plane and dipole combination has an infinite front-to-back (F/B) ratio with the fields vanishing in the ground plane direction. By using the methods of Sec. 3-3, we calculate a 120° half-power beamwidth for the two-element half-wavelength spaced array of the dipole and its image. The F/B increases with an increase in size of the reflector (ground plane). We expect zero fields at $\theta = 90°$, and Table 8-8 shows a decrease of the fields with an increase of the ground plane. The half-power beamwidth cycles about 120° as the ground plane increases in size.

TABLE 8-8 Results of a GTD Analysis of a Horizontal Half-Wavelength Dipole a Quarter Wavelength Over a Limited Square Ground Plane (H Plane)

Ground plane size, λ	Front-to-back ratio F/B, dB	Pattern level at 90°, dB	Half-power beamwidth,°	Phase center, λ
0.5	8.4	6.3	108.5	0.18
0.6	10.3	7.6	104.0	0.15
0.7	12.0	8.8	100.9	0.14
0.8	13.5	9.8	97.8	0.12
0.9	14.8	10.6	95.1	0.10
1.0	16.0	11.2	93.2	0.08
1.2	17.8	12.0	93.3	0.04
1.4	19.1	12.3	99.4	0.01
1.6	20.0	12.2	108.4	0.0
1.8	21.1	12.3	112.4	0.0
2.0	22.3	12.4	113.1	0.0
2.5	25.0	12.7	115.8	0.0
3.0	28.3	13.8	111.4	0.0
4.0	32.8	14.8	116.1	0.0
5.0	35.4	16.2	118.0	0.0
10.0	44.0	19.1	121.3	0.0

The phase center of the equivalent two-element array remains fixed on the ground plane. As we decrease the ground plane, the effect of the image decreases and that causes the phase center to move toward the dipole. In the limit of no ground plane the phase center is on the dipole.

Corner Reflector [47] The usual corner reflector (Fig. 8-19) has a dipole located between two flat plates that serve to limit the possible directions of radiation. The angle between the reflectors can be any value, but 90° seems

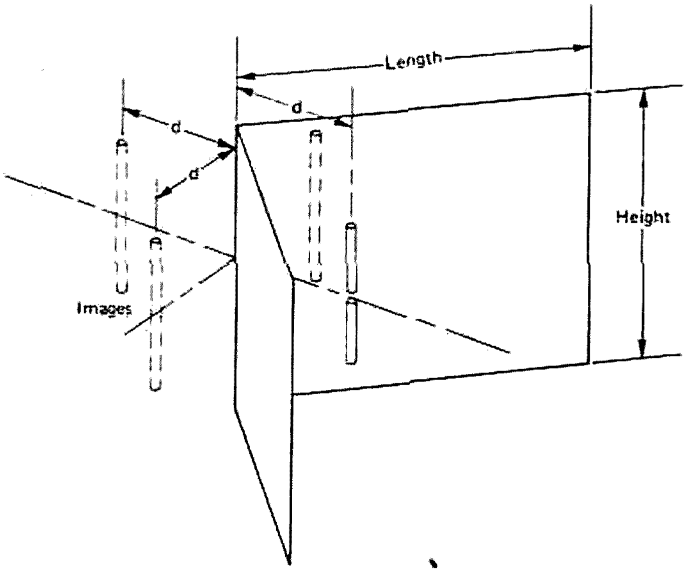

Figure 8-19 90° corner reflector.

to be the most effective one. On paper, decreased angles give better results, but only marginally. We could consider the flat plate as a limiting case. The tangential electric fields must vanish at the surface of the flat plates. We find a greater restriction, since the fields can only decrease gradually in the limited space between the ground planes and the dipole. Most of the power is concentrated in lower-order spherical modes. In the limit of zero vertex distance, the single mode possible restricts the beamwidth to 45° in the H plane.

We analyze the 90° corner reflector by using the three images of the dipole in the ground planes (Fig. 8-19) plus the real dipole. The array factor of the array of dipole and images is

$$\left| e^{jkd\cos\theta} + e^{-jkd\cos\theta} - \left(e^{jkd\sin\theta\sin\phi} + e^{-jkd\sin\theta\sin\phi}\right)\right|^2$$

In the H plane $\phi = 90°$ and we can evaluate terms to get

$$4[\cos(kd\cos\theta) - \cos(kd\sin\theta)]^2$$

where d is the distance from the vertex to the dipole and θ is the H-plane pattern angle from the axis. We must multiply this by the pattern of the dipole to obtain the radiation intensity. We consider only the H plane, where the maximum radiation intensity is found from Eq. (4-9).

$$U = 4[\cos(kd\cos\theta) - \cos(kd\sin\theta)]^2\frac{\eta|I_0|^2}{(2\pi)^2}\left(1 - \cos\frac{kL}{2}\right)^2 \tag{8-97}$$

where η is the impedance of free space, I_0 is the dipole current, and L is the dipole length.

The radiated power of the single dipole is

$$P_{\text{in}} = |I_0|^2[R_{11} + R_{12}(2d) - 2R_{12}(\sqrt{2}d)] \tag{8-98}$$

where R_{11} is the self-resistance of the dipole and $R_{12}(x)$ is the mutual resistance function between the dipole and its images. The directivity is found from

$$\text{Directivity}(\theta) = \frac{4\pi U(\theta)}{P_{\text{in}}} \tag{8-99}$$

We combine Eqs. (8-97) and (8-98) into Eq. (8-99) to find the directivity of the 90° corner reflector with infinite sides

$$\text{Directivity}(\theta) = \frac{4\eta[1 - \cos(kL/2)]^2[\cos(kd\cos\theta) - \cos(kd\sin\theta)]^2}{R_{11} + R_{12}(2d) - 2R_{12}(\sqrt{2}d)} \tag{8-100}$$

TABLE 8-9 Characteristics of the 90° Corner Reflector with Infinite Sides and 0.42λ Dipole

Vertex distance, λ	Directivity, dB	Beamwidth, °	Input impedance, Ω	
0.30	12.0	44.7	29.1	$-j$ 1.1
0.32	12.0	44.6	34.9	j 0.4
0.34	11.9	44.5	40.9	j 1.1
0.36	11.9	44.3	47.0	j 0.8
0.37	11.9	44.2	50.0	j 0.3
0.38	11.8	44.1	53.0	$-j$ 0.5
0.40	11.8	43.9	58.8	$-j$ 2.8
0.42	11.7	43.6	64.1	$-j$ 6.0
0.44	11.7	43.3	68.8	$-j$10.0
0.46	11.6	42.9	72.7	$-j$14.9
0.48	11.5	42.4	75.7	$-j$20.3
0.50	11.4	41.8	77.7	$-j$26.2
0.52	11.4	41.1	78.6	$-j$32.2
0.54	11.3	40.2	78.4	$-j$38.4
0.56	11.2	39.2	77.0	$-j$44.3
0.58	11.1	38.1	74.6	$-j$49.8
0.60	10.9	36.8	71.3	$-j$54.8

Table 8-9 gives the directivity, beamwidth, and impedance of a 90° corner reflector fed from a dipole 0.42λ long and 0.02λ in diameter. We must shorten the dipole further than the free-space dipole to compensate for the mutual coupling between dipoles. The directivity increases as the vertex distance decreases, but the effects of superdirectivity cause the efficiency and gain to fall as the vertex is approached. The antenna has a 50-Ω input impedance for $d = 0.37\lambda$. This point will shift as we increase the dipole's diameter to increase its bandwidth.

Kraus gives the following guidelines for the size of the sides. Each plate should be at least twice the length of the dipole-to-vertex distance, and the plate height (the dipole direction) should be at least 0.6λ. To evaluate those guidelines, a GTD analysis was performed on various combinations (Table 8-10) with $d = 0.37\lambda$. The H-plane beamwidth decreases with an increase in plate length. After about 1.5λ sides, the H-plane beamwidth fluctuates about 45° as the sides increase. Even at 5λ sides the beamwidth is below 45°. The E-plane beamwidth fluctuates with the plate height. The directivity was estimated from the beamwidths by using Fig. 1-2. In one case—1.5λ sides and 1.5λ high—the estimated directivity exceeds the directivity of the infinite-side case. The edge diffractions add to the reflected and direct radiation of the rest of the antenna.

TABLE 8-10 The Results of a GTD Analysis of 90° Corner Reflector with Finite Sides and with Vertex Distance 0.37λ

Side length, λ	Plate height, λ	Half-power beamwidth		F/B, dB	Estimated directivity, dB
		E plane, °	*H* plane, °		
0.75	0.75	70.4	97.4	18.4	7.7
1.0	0.75	73.6	72.4	17.3	8.8
1.5	0.75	72.6	50.8	18.2	10.0
0.75	1.0	60.2	91.6	23.4	8.5
1.0	1.0	61.0	62.8	22.7	10.1
1.5	1.0	58.5	46.0	23.8	11.4
0.75	1.5	53.4	81.6	34.0	9.3
1.0	1.5	51.6	60.0	39.0	11.0
1.5	1.5	48.2	42.6	46.3	12.6
5.0	5.0	68.8	43.4	63.5	10.8

We should not design corner reflectors with large sides, since the gain is limited. The gain of paraboloidal reflectors of the same size soon exceeds that of a corner reflector. A 2λ-diameter paraboloidal reflector at 50 percent efficiency has a gain of 13 dB, and its gain exceeds that of a corner reflector.

Any corner reflector with a vertex angle given by 180°/*N*, where *N* is an integer, can be analyzed by the method of images. Corner reflectors with *N* greater than 2 have only marginally higher gains. Table 8-11 lists results for a 60° vertex angle reflector. We must shorten the half-wavelength dipole to 0.408λ to resonate a 0.02λ-diameter dipole to compensate for the five images. Narrower vertex angle corner reflectors require longer sides than the 90° reflector, and the gain increase is slight. The 90° corner reflector gives the best result for a given amount of material.

TABLE 8-11 Characteristics of a 60° Corner Reflector with Infinite Sides and 0.408λ Dipole

Vertex distance, λ	Directivity, dB	Beamwidth, °	Input impedance, Ω	
0.40	13.0	30	21.2	$-j\ 0.1$
0.42	12.7	30	27.6	$j\ 1.6$
0.46	12.6	30	34.3	$j\ 2.2$
0.48	12.5	30	41.0	$j\ 2.0$
0.49	12.6	30	50.8	$-j\ 0.2$
0.50	12.6	30	53.9	$-j\ 1.4$
0.52	12.7	30	59.8	$-j\ 4.4$
0.54	12.7	30	65.0	$-j\ 8.2$
0.56	12.8	30	69.6	$-j12.7$
0.58	12.9	30.1	73.4	$-j17.8$
0.60	13.0	30.1	76.3	$-j23.2$

Elkamchouchi [48] adds a cylindrical surface between the plates centered on the vertex. This surface adds another set of images within the cylinder. The images increase the gain by about 2 dB and decrease the frequency dependence of the impedance.

REFERENCES

1. A. W. Love, *Reflector Antennas*, IEEE Press, New York, 1978.
2. S. Silver (ed.), *Microwave Antenna Theory and Design*, McGraw-Hill, New York, 1949.
3. W. V. T. Rusch and P. D. Potter, *Analysis of Reflector Antennas*, Academic Press, New York, 1970.
4. P. J. Wood, *Reflector Antenna Analysis and Design*, Peregrinus, London, 1980.
5. C. A. Mentzer and L. Peters, "A GTD Analysis of the Far-out Sidelobes of Cassegrain Antennas," *IEEE Trans. Antennas Propagat.*, vol. AP-23, no. 5, September 1975, pp. 702–709.
6. S. W. Lee et al., "Diffraction by an Arbitrary Subreflector: GTD Solution," *IEEE Trans. Antennas Propagat.*, vol. AP-27, no. 3, May 1979, pp. 305–316.
7. A. D. Craig and P. D. Simms, "Fast Integration Techniques for Reflector Antenna Pattern Analysis," *Electronics Letters*, vol. 18, no. 2, 21st January 1982, pp. 60–62.
8. V. Galindo-Israel and R. Mittra, "A New Series Representation for the Radiation Integral with Application to Reflector Antennas," *IEEE Trans. Antennas Propagat.*, vol. AP-25, no. 5, September 1977, pp. 631–641.
9. A. W. Rudge et al. (eds.), *The Handbook of Antenna Design*, Vol. 1, Peregrinus, London, 1982, chaps. 2 and 3.
10. F. S. Holt in R. E. Collin and F. J. Zucker (eds.), *Antenna Theory*, Part 2, McGraw-Hill, New York, 1969.
11. D. J. Struik, *Differential Geometry*, Addison-Wesley, Reading, Mass., 1950, p. 55.
12. R. Kouyoumjian and P. Pathak, "The Dyadic Diffraction Coefficient for a Curved Edge," *NASA CR-2401*, June 1974.
13. A. C. Ludwig, "The Definition of Cross Polarization," *IEEE Trans. Antennas Propagat.*, vol. AP-21, no. 1, January 1973, pp. 116–119.
14. J. R. Cogdell and J. H. Davis, "Astigmatism in Reflector Antennas," *IEEE Trans. Antennas Propagat.*, vol. AP-21, no. 4, July 1973, pp. 565–567.
15. Y. T. Lo, "On the Beam Deviation Factor of a Parabolic Reflector," *IEEE Trans. Antennas Propagat.*, vol. AP-8, May 1960, pp. 347–349.
16. J. Ruze, "Lateral-Feed Displacement in a Paraboloid," *IEEE Trans. Antennas Propagat.*, vol. AP-13, no. 5, September 1965, pp. 660–665.
17. W. V. T. Rusch and A. C. Ludwig, "Determination of the Maximum Scan-Gain Contours of a Beam Scanned Paraboloid and Their Relation to the Petzval Surface," *IEEE Trans. Antennas Propagat.*, vol. AP-21, no. 2, March 1973, pp. 141–147.
18. W. A. Imbriale, P. G. Ingerson, and W. C. Wong, "Large Lateral Feed Displacements in a Parabolic Reflector," *IEEE Trans. Antennas Propagat.*, vol. AP-22, no. 6, November 1974, pp. 742–745.
19. D. K. Cheng, "Effect of Arbitrary Phase Errors on the Gain and Beamwidth Characteristics of Radiation Pattern," *IEEE Trans. Antennas Propagat.*, vol. AP-3, July 1955, pp. 145–147.
20. J. Ruze, "Antenna Tolerance Theory — A Review," *Proc. IRE*, vol. 54, no. 4, April 1966, pp. 633–640.
21 M. S. Zarghamee, "On Antenna Tolerance Theory," *IEEE Trans. Antennas Propagat.*, vol. AP-15, no. 6, November 1967, pp. 777–781.
22. R. C. Hansen, *Microwave Scanning Antennas*, Academic Press, New York, 1964, p. 74.
23. E. U. Condon, "Theory of Radiation from Paraboloid Reflectors," *Westinghouse Rept. No. 15*, September 1941.
24. W. H. Watson, "The Field Distribution in the Focal Plane of a Paraboloidal Reflector," *IEEE Trans. Antennas Propagat.*, vol. AP-12, no. 5, September 1964, pp. 561–569.

25. T. B. Vu, "Optimization of Efficiency of Reflector Antennas: Approximate Method," *Proc. IEE*, vol. 117, January 1970, pp. 30–34.
26. B. MacA. Thomas, "Theoretical Performance of Prime Focus Paraboloids Using Cylindrical Hybrid Modes," *Proc. IEE*, vol. 118, November 1971, pp. 1539–1549.
27. N. Amitay and H. Zucker, "Compensation of Spherical Reflector Aberrations by Planar Array Feeds," *IEEE Trans. Antennas Propagat.*, vol. AP-20, no. 1, January 1972, pp. 49–56.
28. V. Galindo-Israel, S. W. Lee, and R. Mittra, "Synthesis of Laterally Displaced Cluster Feed for a Reflector Antenna with Application to Multiple Beams and Contoured Patterns," *IEEE Trans. Antennas Propagat.*, vol. AP-26, no. 2, March 1978, pp. 220–228.
29. B. Popovich et al., "Synthesis of an Aberration Corrected Feed Array for Spherical Reflector Antennas," *IEEE/APS Symp. Digest*, May 1983.
30. V. Mrstik, "Effect of Phase and Amplitude Quantization Errors on Hybrid Phased-Array Reflector Antennas," *IEEE Trans. Antennas Propagat.*, vol. AP-30, no. 6, November 1982, pp. 1233–1236.
31. W. V. T. Rusch, "Phase Error and Associated Cross Polarization Effects in Cassegrainian-Fed Microwave Antennas," *IEEE Trans. Antennas Propagat.*, vol. AP-14, no. 3, May 1966, pp. 266–275.
32. P. Kildal, "The Effects of Subreflector Diffraction on the Aperture Efficiency of a Conventional Cassegrain Antenna—An Analytical Approach," *IEEE Trans. Antennas Propagat.*, vol. AP-31, no. 6, November 1983, pp. 903–909.
33. A. M. Isber, "Obtaining Beam-Pointing Accuracy with Cassegrain Antennas," *Microwaves*, August 1967, pp. 40–44.
34. W. V. T. Rusch and R. Wohlleben, "Surface Tolerance Loss for Dual-Reflector Antennas," *IEEE Trans. Antennas Propagat.*, vol. AP-30, no. 4, July 1982, pp. 784–785.
35. G. W. Collins, "Noise Temperature Calculations from Feed System Characteristics," *Microwave J.*, vol. 12, December 1969, pp. 67–69.
36. T. Li, "A Study of Spherical Reflectors as Wide-Angle Scanning Antennas," *IEEE Trans. Antennas Propagat.*, vol. AP-7, July 1959, p. 223–226.
37. R. Woo, "A Multiple-Beam Spherical Reflector Antenna," *JPL Quart. Tech. Rev.*, vol. 1, no. 3, October 1971, pp. 88–96.
38. A. W. Love, "Spherical Reflecting Antennas with Corrected Line Sources," *IEEE Trans. Antennas Propagat.*, vol. AP-10, September 1962, pp. 529–537.
39. F. S. Bolt and E. L. Bouche, "A Gregorian Corrector for Spherical Reflectors," *IEEE Trans. Antennas Propagat.*, vol. AP-12, no. 1, January 1964, pp. 44–47.
40. A. S. Dunbar, "Calculation of Doubly Curved Reflectors for Shaped Beams," *Proc. IRE*, vol. 36, no. 10, October 1948, pp. 1289–1296.
41. R. S. Elliott, *Antenna Theory and Design*, Prentice-Hall, Englewood Cliffs, N.J., 1981, p. 500.
42. T. F. Carberry, "Analysis Theory for the Shaped Beam Doubly Curved Reflector Antenna," *IEEE Trans. Antenna Propagat.*, vol. AP-17, no. 2, March 1969, pp. 131–138.
43. V. Galindo, "Design of Dual Reflector Antennas with Arbitrary Phase and Amplitude Distributions," *IEEE Trans. Antennas Propagat.*, vol. AP-12, no. 4, July 1964, pp. 403–408.
44. W. F. Williams, "High Efficiency Antenna Reflector," *Microwave J.*, vol. 8, July 1965, pp. 79–82.
45. G. Collins, "Shaping of Subreflectors in Cassegrainian Antennas," *IEEE Trans. Antennas Propagat.*, vol. AP-21, no. 3, May 1973, pp. 309–313.
46. V. Galindo-Israel and R. Mittra, "Synthesis of Offset Dual Shaped Subreflector Antennas for Control of Cassegrain Aperture Distributions," *IEEE Trans. Antennas Propagat.*, vol. AP-32, no. 1, January 1984, pp. 86–92.
47. J. D. Kraus, *Antennas*, McGraw-Hill, New York, 1950, p. 328.
48. H. M. Elkamchouchi, "Cylindrical and Three-Dimensional Corner Reflector Antennas," *IEEE Trans. Antennas Propagat.*, vol. AP-31, no. 3, May 1983, pp. 451–455.

CHAPTER

9

LENS ANTENNAS

In lenses, as in parabolic reflectors, free space is used as a feed network to excite a large aperture. Because the feed locates behind the aperture, the configuration eliminates aperture blockage and allows the direct connection of the feed to the transmitter or receiver. When frequencies are above microwaves, we must remove lossy transmission lines and establish the receiver noise figure close to the antenna.

Lenses have half the tolerance requirements of reflectors. The wave passes by the anomaly only once in a lens. In a reflector the wave path deviates by twice the distance as the wave travels to and from the reflector. At low microwave frequencies the lens is prohibitively heavy, but zoning and the use of artificial dielectrics reduce the problem. Both zoning and artificial dielectrics present mechanical stability problems and narrow the usable frequency bandwidth.

We will organize lenses by the available degrees of freedom. A single lens with a uniform dielectric has two surfaces. It is equivalent to a dual reflector. Each surface gives us a degree of freedom. We start the discussion with single-surface lenses; that is, we use only one degree of freedom. We make the second surface match either the incoming or outgoing wavefront and remove its possible effects. Shaping both surfaces lets us correct one lens anomaly. We can remove either coma to improve the feed-scanning capability or design to convert a given feed pattern to a required aperture distribution. Bootlace lenses have three possible degrees of freedom. They consist of back-to-back arrays with cables connecting the sides. We use the degrees of freedom to increase the number of focal points. In many designs one of the degrees of freedom is given up to simplify the mechanical layout. Finally, we discuss the use of a variable index of refraction in the Luneburg lens.

We base the design of lenses on geometric optics. Like parabolic reflectors, the antennas have no inherent frequency bandwidth limitation. We are limited by the feeds and mechanical problems of large sizes. Because we can borrow from optics, lenses have great potential for high-frequency use.

9-1 Single Refracting Surface Lenses

Single-surface lenses convert the wave type, such as spherical to planar, at one surface through refraction. The constant-phase surface (eikonal) of the wave type determines the shape of the second surface of the lens. The common lens converts an incident spherical or cylindrical wave to a plane wave. Conversion to a cylindrical wave requires a line source feed and cylindrical surfaces on the lens. Spherical waves use point feeds and axisymmetrical surfaces. Like the reflector which also converts waves from the feed to plane waves by geometric optics (GO), diffraction from an aperture determines the far-field pattern.

Consider the second or nonrefracting surface. If the surface toward the feed converts the wave type, then the wave exits the second surface as a plane wave. The surface is a plane. Likewise, when the surface away from the feed converts the exiting wave to a plane wave, the inner surface toward the feed follows the incident wave eikonal, that is, a cylindrical or spherical surface.

Figure 9-1 shows the two types of single refracting surface lenses. We can determine the refracting surface shape by either of two different approaches. Snell's law can be applied to the refracting surface, and the surface slope can be determined for each feed angle. Equivalently, we can apply Fermat's principle to equalize the optical path length from the feed through the lens to an aperture plane. The results are easily found [1, 2]. For Fig. 9-1*a*

$$\rho(\psi) = \frac{(n-1)f}{n\cos\psi - 1} \tag{9-1}$$

where n is the index of refraction given by

$$n = \sqrt{\epsilon_r \mu_r} \tag{9-2}$$

and ϵ_r and μ_r are the relative permittivity and permeability of the lens medium. When $n > 1$, Eq. (9-1) describes a hyperbola with the feed at one focus. The distance from the feed to the hyperbola along the axis is f.

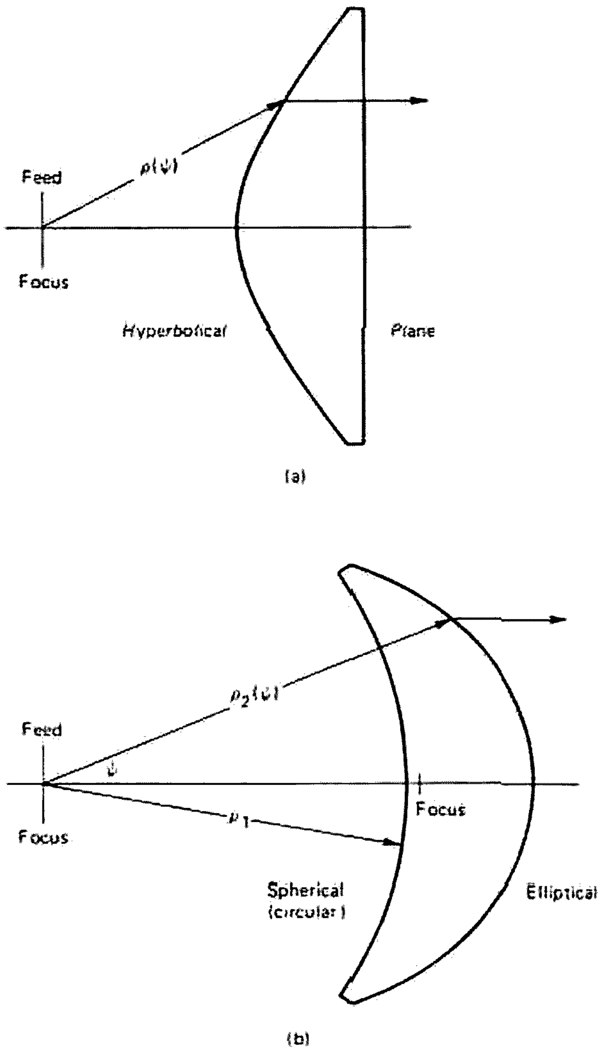

Figure 9-1 Single-surface lenses.

A hyperbola has asymptotes that limit the collimated portion of the feed radiation.

$$\psi_a = \cos^{-1}\frac{1}{n} \tag{9-3}$$

We must limit the lens edge to angles less than that because the asymptotes imply an infinite aperture size. As in the case of the paraboloidal reflector, we have spillover power from the feed normally considered to be lost in sidelobes. Placing the lens at the aperture of a horn eliminates spillover.

We calculate the lens diameter from Eq. (9-1)

$$D = 2\rho \sin \psi_e = \frac{2(n-1)f \sin \psi_e}{n \cos \psi_e - 1} \tag{9-4}$$

where ψ_e is the edge angle subject to the restriction of Eq. (9-3).

The surfaces of the lens in Fig. 9-1*b* have the polar equations

$$\rho_1 = \text{constant} \qquad \rho_2(\psi) = \frac{(n-1)f}{n - \cos \psi} \tag{9-5}$$

The inner surface must either be a circular cylinder (cylindrical lens) or be spherical (axisymmetrical lens). The outer surface $\rho_2(\psi)$ is elliptical for $n > 1$. The junction of the circle and ellipse can determine the feed limitation.

$$\cos\psi_e = n - \frac{(n-1)f}{\rho_1} \tag{9-6}$$

We can, of course, truncate the lens before the two curves meet. Equation (9-6) gives the limitation on ρ_1 at the lens edge as well

$$\rho_1 \le \frac{(n-1)f}{n - \cos\psi_e} \tag{9-7}$$

Example Find f and ρ_1 at the edge for an elliptical lens (Fig. 9-1*b*) with $D = 10\lambda$, $n = 1.6$ (polystyrene), and $\psi_e = 50°$. Solve Eq. (9-5) for f/D

$$\frac{f}{D} = \frac{n - \cos\psi_e}{2\sin\psi_e(n-1)} \qquad f = 10.41\lambda \tag{9-8}$$

$$\rho_1 \le \frac{D}{2\sin\psi_e} = 6.53\lambda \tag{9-9}$$

If ρ_1 remained constant to the center of the lens, it would be 3.88λ thick. In narrowband applications we could remove the multiple wavelength thicknesses by zoning and reduce weight and dielectric material loss.

The lenses change the amplitude distribution of the feed in the aperture plane. We relate the feed pattern to the aperture distribution through the conservation of power in differential areas. For an axisymmetrical lens

$$\begin{array}{ccc} \text{Feed power} & & \text{Aperture power} \\ F(\psi,\phi)\sin\psi\, d\psi\, d\phi & = & A(r,\phi)r\, dr\, d\phi \end{array} \tag{9-10}$$

where ψ is the feed angle and $r, \rho\sin\psi$, is the aperture radial distance. $F(\psi,\phi)$ is the feed power pattern, and $A(r,\phi)$ is the aperture power distribution.

$$\frac{A(r,\phi)}{F(\psi\phi)} = \frac{\sin\psi}{r}\frac{d\psi}{dr} \tag{9-11}$$

For a cylindrical lens, we also equate differential areas times differential powers:

$$F(\psi,y)\, d\psi\, dy = A(r,y)\, dr\, dy$$

$$\frac{A(r,y)}{F(\psi,y)} = \frac{d\psi}{dr} \tag{9-12}$$

We substitute Eqs. (9-11) and (9-12) into Eq. (9-1) for the hyperbolical lens to find the aperture distribution relative to the feed power pattern.

Axisymmetrical / Cylindrical

$$\frac{A(r,\phi)}{F(\psi,\phi)} = \frac{(n\cos\psi - 1)^3}{f^2(n-1)^2(n-\cos\psi)} \qquad \frac{A(r,y)}{F(\psi,y)} = \frac{(n\cos\psi - 1)^2}{f(n-1)(n-\cos\psi)} \tag{9-13}$$

The field distribution is the square root of Eq. (9-13).

We substitute Eqs. (9-11) and (9-12) into Eq. (9-5) for the elliptical lens:

Axisymmetrical

$$\frac{A(r,\phi)}{F(\psi,\phi)} = \frac{(n-\cos\psi)^3}{f^2(n-1)^2(n\cos\psi - 1)}$$

Cylindrical (9-14)

$$\frac{A(r,y)}{F(\psi,\phi)} = \frac{(n-\cos\psi)^2}{f(n-1)(n\cos\psi - 1)}$$

The hyperbolical and elliptical lenses concentrate the aperture power in different ways. The hyperbolical lens reduces the feed power toward the edges and produces an additional aperture taper. On the other hand, an elliptical single-surface lens increases the power toward the edges as compared with the center.

Example For axisymmetrical lenses with $\psi_e = 40°$ and $n = 1.6$, find the edge taper due to the lenses.

We divide Eq. (9-13*a*) with $\psi = \psi_e$ by the same equation with $\psi = 0$ to find the ratio of power at the edge to that at the center of the aperture (assuming an isotropic feed). We do the same thing with Eq. (9-14*a*).

Hyperbolical lens

$$\frac{A_e}{A_c} = \frac{(n\cos\psi_e - 1)^3}{(n-1)^2(n-\cos\psi_e)} \tag{9-15}$$

Elliptical lens

$$\frac{A_e}{A_c} = \frac{(n-\cos\psi_e)^3}{(n-1)^2(n\cos\psi_e - 1)} \tag{9-16}$$

By substituting ψ_e and n, we find the edge taper.

Hyperbolical lens: 0.038 (−14.2 dB)

Elliptical lens: 7.14 (8.5 dB)

The increased taper of the hyperbolical lens reduces sidelobes, and the elliptical lens increases aperture efficiency by compensating for some of the feed antenna pattern taper to make the aperture distribution more uniform.

9-2 Zoned Lenses

Lenses designed by the methods of Sec. 9-1 have bandwidth limitations determined only by the invariability of the dielectric constant with frequency changes. Zoning removes multiples-of-wavelength path lengths in the lens to reduce weight, to reduce the lens-induced amplitude taper, or to thin the lens. The act of changing dimensions by wavelengths implies narrowing the frequency bandwidth.

We can step the lens in either the nonrefracting or the refracting surface. Stepping the nonrefracting surface (Fig. 9-2*a* and *b*) has the least effect. The edges of the steps, parallel with the waves, will diffract waves and cause some change in the aperture fields, but GO predicts no effect. Stepping the

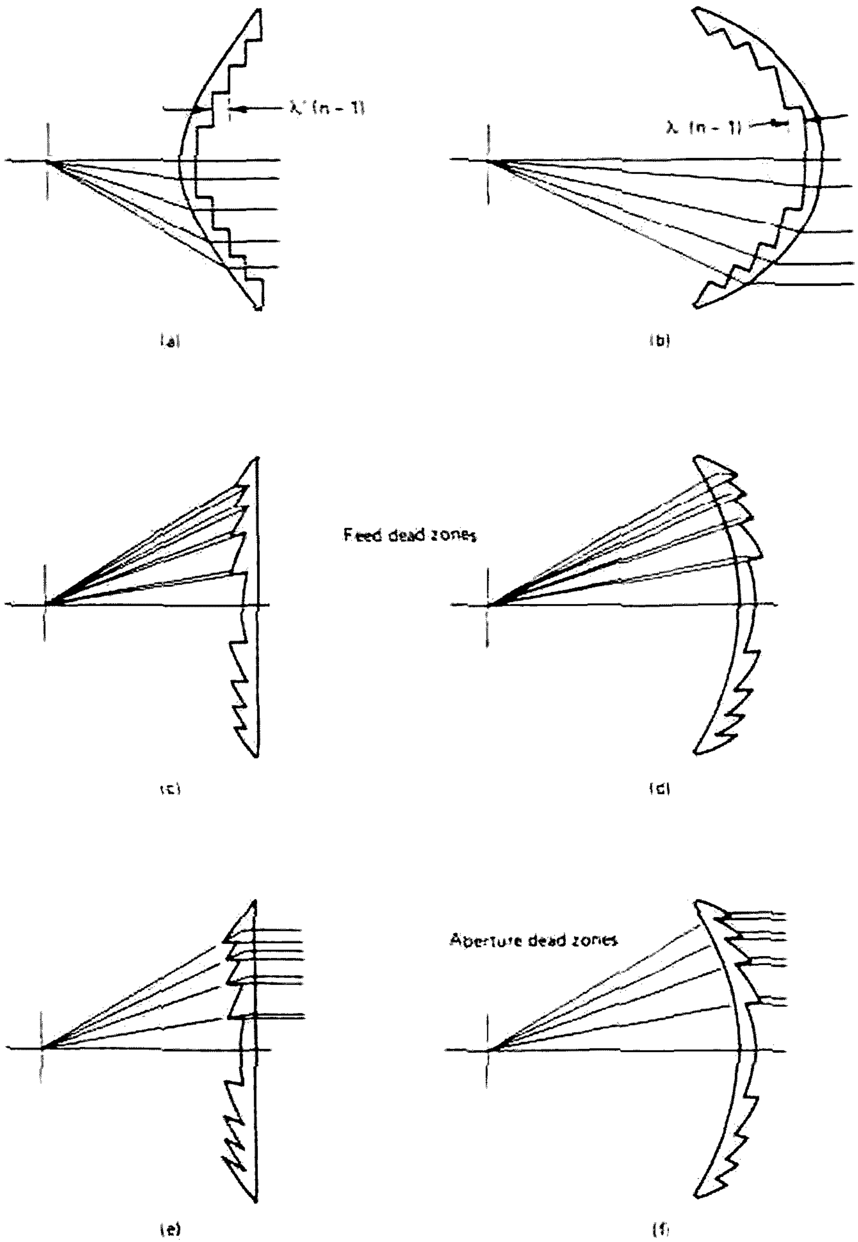

Figure 9-2 Zoning of a single-surface lens.

refracting surface introduces losses either as misdirected feed power (Fig. 9-2*c* and *d*) or as unexcited aperture (Fig. 9-2*e* and *f*). But stepping the *refracting surface reduces the lens-induced aperture taper by changing the* focal lengths in various zones. Figure 9-2 shows the limits in the two types of refracting surface steps, since we could compromise between the directions and have both spilled-over feed power and unexcited aperture.

We can easily find the step dimensions in Fig. 9.2*a* and *b*. We equate the path lengths inside and outside the dielectric along the step with a difference of λ or some integer multiple of λ.

$$\underset{\text{Inside}}{n\Delta} = \underset{\text{Outside}}{\Delta + \lambda}$$

The step Δ becomes

$$\Delta = \frac{\lambda}{n-1} \tag{9-17}$$

In Fig. 9-2*c*, *d*, *e*, and *f* we determine the change in the focal lengths instead of the step dimensions. Zoning affects the optical path lengths in the center of the lens. We calculate the edge focal length from the unzoned case. The focal length increases by Eq. (9-17) for each inner step of hyperbolical lenses and decreases by the same amount for each inner step of elliptical lenses. We find the lens-induced taper relative to the center by using ratios of Eq. (9-13) or (9-14). For axisymmetrical lenses

$$\frac{A(r,\phi)}{A_c} = \frac{f_c^2(n\cos\psi - 1)^3}{f^2(n-1)^2(n-\cos\psi)} \qquad \text{hyperbolical} \tag{9-18}$$

$$\frac{A(r,\phi)}{A_c} = \frac{f_c^2(n-\cos\psi)^3}{f^2(n-1)^2(n\cos\psi - 1)} \qquad \text{elliptical} \tag{9-19}$$

where f_c is the focal length in the center, f is the focal length in the feed direction ψ, and A_c is the central amplitude.

Example Design an axisymmetrical hyperbolical lens ($n = 1.6$) by using the three types of zoning shown in Fig. 9-2. Use an aperture diameter of 30λ and a maximum feed angle of 35° with a 70° 10-dB beamwidth feed. The minimum allowable thickness is 0.5λ with a 0.3λ edge thickness.

By working through the geometry, we obtain the following dimensions: Figure 9-2*a*, nonrefracting surface zoning. Steps = $\lambda/(n-1) = 1.67\lambda$.

Step number	1	2	3	4
Aperture radius, λ	12.418	10.009	7.403	4.256

We estimate the feed spillover loss from Eq. (8-32) for the 10-dB feed edge taper, 0.41 dB. Equation (9-15) gives the edge taper (9.72 dB), since the refracting surface is not zoned. Combined with the feed edge taper of 10 dB, we have a 19.72-dB amplitude taper in the aperture plane. We use Eq. (6-16) to calculate the amplitude taper loss (1.8 dB) for this axisymmetric distribution.

Figure 9-2*c*. Zoning in the refracting surface of the hyperbolical lens (parallel with outgoing waves). We find the following dimensions starting with the edge focal length found from a rearrangement of Eq. (9-4).

Zone	*Focal length, λ*	*Aperture radius of step, λ*	*Thickness*	*Feed dead zone angles, °*
1	20.21	0	1.52	
2	18.54	5.12	2.09	13.57 to 14.62
3	16.87	8.42	1.98	21.64 to 23.10
4	15.21	10.84	1.90	27.06 to 28.68
5	13.54	12.89	1.83	31.28 to 32.95

The changing focal lengths in the zones change the aperture amplitude distribution. The edge taper becomes [Eq. (9-18)] 6.24 dB and reduces the amplitude taper loss [Eq. (6-16)] to 1.19 dB. The portion of the feed directed to the dead zones refracts out of the aperture and forms sidelobes that reduce the aperture efficiency. We consider this as a second spillover loss (0.81 dB).

Figure 9-2*e*. Zoning in the refracting surface of the hyperbolical lens (parallel with the feed wave rays). Again we start with the edge focal length and increase it by $\lambda/(n-1)$ at each step and determine the feed angles where the change in the focal length will give the minimum allowable thickness. The following dimensions were obtained.

Zone	*Focal length, λ*	*Feed angle, °*	*Thickness, λ*	*Aperture dead zones, λ*
1	20.21	0	1.51	0
2	18.54	13.57	2.25	4.70 to 5.12
3	16.87	21.64	2.41	7.66 to 8.42
4	15.21	27.06	2.60	9.77 to 10.84
5	13.54	31.28	2.83	11.48 to 12.89

Since the focal lengths are the same as for Fig. 9-2*c*, the lens-induced edge taper is 6.24 dB. The dead zones in the aperture distribution increase the amplitude taper loss to 3.10 dB. These ring dead zones can be considered as radiating and adding to the fully excited aperture pattern. They radiate patterns with closely spaced lobes that raise the near sidelobes of the total antenna.

The three designs are compared in the following table.

Design, Fig. 9-2	*SPL, dB*	*ATL, dB*	*Sum, dB*
(*a*)	0.41	1.80	2.21
(*c*)	1.22	1.19	2.41
(*e*)	0.41	3.10	3.51

Example Similarly to the above example, we can design zoned elliptical axisymmetrical lenses that have the same problems of feed angle or aperture dead zones. The edge taper of the elliptical lens counteracts some of the feed taper and reduces amplitude taper loss. The following losses were calculated for those designs.

Design, Fig. 9-2	*SPL, dB*	*ATL, dB*	*Sum, dB*
(*b*)	0.41	0.06	0.47
(*d*)	1.43	0.14	1.57
(*f*)	0.41	1.43	1.84

Zoning reduces the frequency bandwidth. At the center frequency the optical path length difference between the central ray and edge ray is $K - 1$ for K zones. A common maximum allowed deviation of feed to aperture path is 0.125λ; it leads to a bandwidth of

$$B \cong \frac{25}{K-1} \quad \% \tag{9-20}$$

For the five zone lenses of the above examples Eq. (9-20) gives a 6 percent bandwidth. We find the loss at band edge by tracing rays from the feeds-to-aperture plane and calculating the phase error loss by using Eq. (6-17). The loss at band edge is about 0.3 dB for all the designs. Bandwidth is greatly underestimated by Eq. (9-20) if a greater phase error loss is allowed. The 1-dB phase error loss bandwidth becomes $45\%/(K - 1)$.

9-3 Metal-Plate Lenses

The phase velocity of a wave in waveguide exceeds that of a wave in free space and produces a medium with an effective refractive index less than 1. We can make a microwave lens by spacing parallel metal plates and feeding the lens with a wave polarized in the direction of the plates. For plates spaced a distance a the index of refraction becomes

$$n = \sqrt{1 - \left(\frac{\lambda}{2a}\right)^2} \tag{9-21}$$

where λ is the wavelength in the medium between the plates. The index of refraction is frequency-dependent. The lens can be made polarization-independent by forming an egg crate of orthogonal plates. We divide an arbitrary polarization into orthogonal polarizations normal to the plates.

If we substitute n from Eq. (9-21) into Eq. (9-1), we obtain the equation of a front single-surface lens.

$$\rho(\psi) = \frac{(1-n)f}{1 - n\cos\psi} \tag{9-22}$$

Equation (9-22) is an ellipse with f as the distance from the far focus of the ellipse to the center of the lens front surface. This surface refracts waves parallel with the axis and determines the second surface: a plane. The parallel plates constrain the waves parallel with the axis and prevent the design of an outer single-surface lens.

The cutoff wavelength $2a$ and the possibility of higher-order modes restrain the range of n. The second-order-mode cutoff occurs when $\lambda = a$, and it limits n to 0.866 [Eq. (9-21)]. At cutoff $\lambda = 2a$, n equals zero. Reasonable values lie between 0.3 and 0.7.

The variation of n with frequency changes limits the frequency bandwidth. When the phase variation in the aperture is limited to $\lambda/8$, the bandwidth is approximately [1]

$$\text{Bandwidth }(\%) = \frac{25n}{1-n}\,\frac{\lambda}{(1-n)t} \tag{9-23}$$

where n is the center-frequency index of refraction and t is the maximum thickness. An acceptable bandwidth is underestimated by Eq. (9-23) through restriction of the band edge phase error.

The elliptical surface increases the aperture distribution toward the edges. When we substitute Eq. (9-22) into Eqs. (9-11) and (9-12), we obtain the aperture amplitude distribution relative to the feed pattern.

Axisymmetrical

$$\frac{A(r,\phi)}{F(\psi,\phi)} = \frac{(1 - n\cos\psi)^3}{f^2(1-n)^2(\cos\psi - n)}$$

Cylindrical (9-24)

$$\frac{A(r,y)}{F(\psi,y)} = \frac{(1 - n\cos\psi)^2}{f(1-n)(\cos\psi - n)}$$

Example Design an axisymmetric parallel-plate lens with a diameter of 30λ, maximum feed angle of 35°, $n = 0.625$, and minimum thickness of λ.

$$\rho(35^\circ) = \frac{30}{2\sin 35^\circ} = 26.15\lambda$$

Rearrange Eq. (9-22) to find the focal length at the edge.

$$f = \frac{(1 - n\cos 35^\circ)\rho(35^\circ)}{1-n} = 34.03\lambda$$

Equation (9-21) gives us the plate separation with a slight rearrangement.

$$a = \frac{1}{2\sqrt{1-n^2}} = 0.64\lambda$$

The amplitude variation from the center to the edge caused by the ellipse is given by [Eq. (9-24a)]

$$\frac{A(\psi_e)}{A(0)} = \frac{(1 - n\cos\psi_e)^3}{(1 - n)^2(\cos\psi_e - n)} = 4.26 \quad (6.3\text{ dB})$$

A feed with its 10-dB beamwidth equal to the subtended angle of the lens at the feed produces a −3.7-dB edge taper in the aperture.

The edge thickness is given by

$$t = f + 1 - \rho(35^\circ)\cos 35^\circ = 13.61\lambda$$

Equation (9-23) predicts a bandwidth of 1.9 percent. A detailed analysis using ray tracing through the lens and varying n with changes in frequency predicts a 0.2-dB loss at this band edge. The 1-dB bandwidth is about 4.5 percent.

Zoning a parallel-plate lens increases the frequency bandwidth by limiting the maximum thickness, since the variation of the optical path length due to the varying n exceeds that due to the zoning. Figure 9-3 gives the central curve of the three possible types of zoning. The lens in Fig. 9-3*a* only suffers loss due to diffractions from edges. The other two zoned lenses (Fig. 9-3*b* and *c*) have dead zones in the aperture. These dead zones produce additional amplitude taper loss and high close-in sidelobes.

The feed side zoning has different focal lengths in each zone. The outer zone remains the same as the unzoned lens. The focal lengths of the inner zones are reduced by $\lambda/(1 - n)$ at each step. The stepping reduces the amplitude taper of the lens by varying f:

$$\frac{A(\psi)}{A(0)} = \frac{f_c^2(1 - n\cos\psi)^3}{f^2(1 - n)^2(\cos\psi - n)} \tag{9-25}$$

where f_c is the central focal length and f is the focal length of the ellipse at ψ.

The zoned lens bandwidth is approximately [1]

$$\text{Bandwidth} = \frac{25\%}{K - 1 + [(1 + n)(1 - n)t/n]} \tag{9-26}$$

where K is the number of zones and t is the maximum thickness.

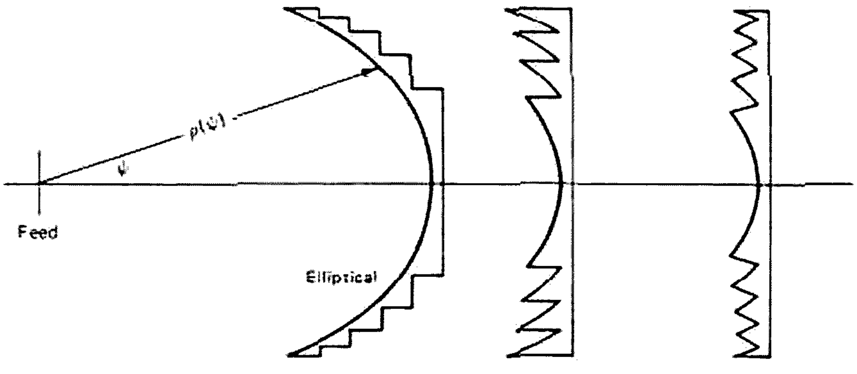

(a) (b) (c)

Figure 9-3 Central section of zoned parallel-metal-plate lenses.

Equation (9-26) also is an underestimation of an acceptable loss level bandwidth.

Example The lens of the above example was zoned as in Fig. 9-3*a* and *c* with five zones. The maximum thickness is 3.4λ. Equation (9-26) predicts a bandwidth of 3.4 percent. By tracing rays through the lens and applying Eq. (6-17) to find the phase error loss, we predict a 10 percent bandwidth for a 1-dB loss.

Zoning the nonrefracting surface has no effect on the aperture distribution except for edge diffractions that modify the fields slightly. Zoning the refracting surfaces causes aperture dead zones and reduces the lens-induced amplitude taper. The focal length of the ellipse at the edge remains at 34.03λ. The focal length of the center ellipse is reduced by $4\lambda/(1-n)$ from the edge ellipse to 23.36λ. The edge taper [Eq. (9.25)] becomes 2.01 (3 dB). The aperture dead zones increase the loss by 2 dB.

The bandwidth of a parallel-plate lens can be increased by a method of compounding lenses into a doublet [3]. We can make a lens by using a uniform waveguide length between the input and output surfaces and placing a phase shifter in each line to compensate for the optical path length differences and produce an eikonal at the aperture plane. If we combine a refracting surface waveguide plate lens with a differential phase shift lens, we can match the aperture phase at two frequencies. This matching broadbands the antenna as an optical achromatic doublet would.

9-4 Surface Mismatch and Dielectric Losses

The reflection coefficient of a wave normally incident on a dielectric is

$$\Gamma = \frac{1-n}{1+n} \tag{9-27}$$

which is valid for both dielectric and metal lenses. The actual reflection coefficient of any ray depends on the angle of incidence and the polarization. Both surfaces of the lens have reflections, and these interact to produce the actual reflection. With plane surfaces, such as those assumed for radomes, we can analyze the combination of reflections as mismatched transmission line equivalences. Since the reflections from second surfaces may not return to the same point as the incident waves and may have their caustic distances changed by the curved surfaces, transmission line models of the two surfaces have limited use for lenses. Equation (9-27) gives us a reasonable approximation to expected mismatch, since one surface of the single refracting surface lens will be normal to the wave incident from the feed and reflect into the feed. The other surface fails to focus power back to the feed and has a secondary effect.

Example A lens with $n = 1.6$ or $n = 0.625$ has a reflection coefficient magnitude of 0.23 [Eq. (9-27)] at one surface that focuses into the feed. This gives a feed mismatch

$$\text{VSWR} = \frac{1 + 0.23}{1 - 0.23} = 1.6$$

or the same as n ($n > 1$) or $1/n$ ($n < 1$). The mismatch loss becomes

$$1 - |\Gamma|^2 = 0.95 \quad (0.2\ \text{dB})$$

The wave may be matched to the surface by a quarter-wavelength transformer with an index of refraction $n^{1/2}$. Adding matching transformers will narrowband the antenna. The surface, which reflects power back to the feed, should be matched first, since the second surface has a minor effect on feed mismatch. Also, the primary reflecting surface has normally incident waves and does not suffer from the need to vary the thickness to match waves off normal incidence. Transformers to match waves off normal incidence are polarization-sensitive.

Simple methods can be used to reduce lens-caused feed mismatch [2]. The lens can be tilted to cause the reflection to miss the feed. Offsetting half the lens by $\lambda/4$ causes the cancellation of the reflection from the two halves. Tilting does not reduce the mismatch loss but does produce backlobe power in the pattern. Similarly, the reflected power from the hyperbolical surface forms backlobes. These reflections reduce the antenna efficiency below that predicted by aperture theory alone.

Cohn and Morita [2, 4] developed methods of matching the surface of the lenses by removing some of the dielectric for a quarter wavelength. The surfaces are either corrugated, have arrays of holes, or have arrays of rods. With this method, the lens can be made from a single dielectric slab. The design depends on the angle of incidence and the polarization of the waves.

The lens dissipates power by the attenuation constant of the material

$$\alpha = \frac{27.3\, n \tan \delta}{\lambda} \quad \text{dB/length} \tag{9-28}$$

where $\tan \delta$ is the loss tangent of the dielectric. Waveguide losses reduce the power transmitted through metal plate lenses. Zoning eliminates material and its associated loss to improve efficiency. For most materials, this loss is small.

Artificial dielectrics [2] are used to reduce the problems of excessive weight and material losses of lenses. We make them by embedding metal particles in a foam with a dielectric constant near 1. The metal parts may be strips or disks made from metal foil. Similarly, solid metal parts can be hollow. Since the effective dielectric constant depends on the size of the metal particles in wavelengths, the lenses made from artifical dielectrics will be narrowband.

9-5 Feed Scanning of Hyperboloidal Lens [5]

The hyperboloidal lens has no cross-polarization when fed from an electric dipole source. Kreutel [5] analyzed the effects of off-axis dipole sources on the pattern of the hyperboloidal lens. The coma increases more rapidly for the lens than for a paraboloidal reflector for the same scanning.

Like the paraboloidal reflector, the hyperboloidal lens beam scans less than the deviation angle of the feed relative to the vertex and axis and has a beam deviation factor (Table 9-1). The scanning loss (Table 9-2) decreases with increasing n. The peak coma lobe (Table 9-3) limits the possible scan before unusable patterns are obtained. The paraboloidal reflector can be scanned further (Table 8-2) for the same coma.

9-6 Dual-Surface Lenses

The second surface of the lens offers an additional degree of freedom that can be used to control the pattern characteristics. Ruze [6] developed methods to reduce coma for feed-scanned cylindrically shaped metal-plate lenses, which constrain the wave parallel with the axis. Both surfaces are used to satisfy focusing requirements. We will develop a method for axisymmetrical dielectric lenses to eliminate coma for small feed displacements. We can also choose to control the amplitude distribution in the aperture plane as another use of the second surface.

Coma-free Axisymmetric Dielectric Lens [7] The design of the coma-free axisymmetric antenna reduces to the numerical solution of a differential equation with side conditions to produce a collimated beam and satisfy the Abbe sine condition [8]. Successful designs require a number of iterations, since the ultimate lens shape depends heavily on the initial conditions. The

TABLE 9-1 Beam Deviation Factor for Feed-Scanned Hyperboloidal Lens

	Refractive index			Refractive index	
f/D	$n = \sqrt{2}$	$n = 2$	f/D	$n = \sqrt{2}$	$n = 2$
0.8	0.75	0.84	1.8	0.92	0.94
1.0	0.80	0.87	2.0	0.93	0.95
1.2	0.83	0.89	2.5	0.95	0.96
1.4	0.86	0.91	3.0	0.97	0.98
1.6	0.89	0.92			

TABLE 9-2 Scanning Loss for a Hyperboloidal Lens

Refractive index:	$n = \sqrt{2}$	$n = \sqrt{2}$	$n = 2$	$n = 2$
Focal length/ diameter:	$f/D = 1$	$f/D = 2$	$f/D = 1$	$f/D = 2$
Beamwidths of scan	Scanning loss, dB			
0.5	0.03	0	0.01	0
1.0	0.06	0.01	0.04	0.01
1.5	0.12	0.03	0.07	0.02
2.0	0.23	0.05	0.12	0.04
2.5	0.36	0.09	0.20	0.06
3.0	0.51	0.13	0.28	0.08
3.5	0.69	0.19	0.37	0.11
4.0	0.90	0.24	0.49	0.14
4.5	1.09	0.31	0.60	0.18
5.0		0.38	0.75	0.22
5.5		0.44		0.25

TABLE 9-3 Coma Sidelobe Level for Scanned Hyperboloidal Lens

Refractive index:	$n = \sqrt{2}$	$n = \sqrt{2}$	$n = 2$
Focal length/ diameter:	$f/D = 1$	$f/D = 2$	$f/D = 1$
Beamwidths of scan	Coma sidelobe level, dB		
0	20.9	18.5	19.5
1	17.6	17.5	17.6
2	15.2	16.5	15.7
3	13.1	15.5	14.2
4	11.3	14.8	12.9
5	9.8	14.0	11.5
6	8.8	13.3	10.4

solution of the differential equation will sometimes diverge into unrealizable designs or fail to continue to satisfy the side conditions.

A lens satisfying the Abbe sine condition is free of coma aberrations for small deviations of the feed from the axis. The deviations produce higher-order aberrations that eventually distort the beam with continued scanning, but coma is removed. For a lens focused at infinity, the Abbe sine condition requires that the surface which refracts the waves parallel with the axis must be spherical with its center on the effective focus of the lens. The dielectric lens refracts waves parallel with the axis on the outer surface (away from the feed). Given the aperture radial component r,

$$r = f_e \sin \psi \tag{9-29}$$

where f_e is the effective focus and ψ is the feed angle. A waveguide plate lens satisfies the Abbe sine condition by having a spherical inner surface [4], since the waves are parallel with the axis in the lens. The waveguide plates constrain the wave parallel with the axis.

The second surface must produce the conditions for a uniform phase in the aperture plane. The waveguide plate lens only has to equalize the path lengths. In the dielectric lens, the inner surface must refract the waves in the proper direction to satisfy the Abbe sine condition, and it must be so placed as to equalize the path lengths from the feed to the aperture plane. The locations of both surfaces along the axis are varied to equalize the path lengths.

Figure 9-4 shows the coordinates of the coma-free dielectric lens. The polar equation $\rho(\psi)$ describes the inner surface and ψ' is the angle of the refracted wave with the axis. The distance from the feed to the center of the lens inner surface is f, and T is the thickness. The coordinates (r, z) describe the outer lens surface, where z is axis dimension and r is the aperture radial component.

Snell's law reduces to a differential equation at the inner surface

$$\frac{d\rho}{d\psi} = \frac{n \sin(\psi - \psi')\rho}{n \cos(\psi - \psi') - 1} \tag{9-30}$$

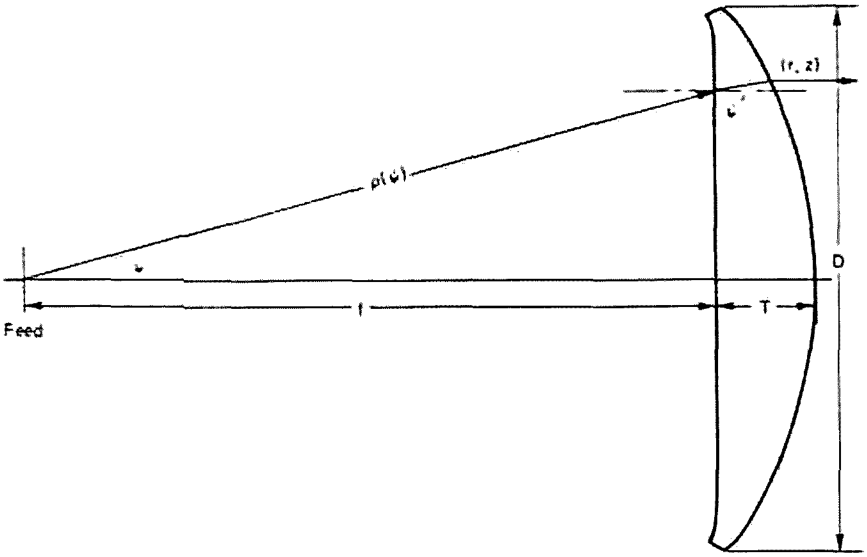

Figure 9-4 Coma-corrected dual-surface axisymmetric lens; $n = 1.6$, $D = 35$, $f = 45$, $T = 6.5$, $f_e = 49$.

where

$$\tan \psi' = \frac{r - \rho \sin \psi}{z - \rho \cos \psi} \tag{9-31}$$

By use of Eq. (9-29), this is reduced to

$$\tan \psi' = \frac{(f_e - \rho) \sin \psi}{z - \rho \cos \psi} \tag{9-32}$$

The requirement for equal optical path lengths to the aperture determines a quadratic equation in z:

$$Az^2 + Bz + C = 0 \tag{9-33}$$

where

$$A = n^2 - 1$$

$$B = 2(\rho - K) - 2n^2\rho \cos \psi$$

$$C = n^2\rho^2 \cos^2 \psi + n^2(f_e - \rho)^2 \sin^2 \psi - (\rho - K)^2$$

$$K = T(n - 1)$$

$$z = \frac{-B + \sqrt{B^2 - 4AC}}{2A}$$

The design consists of the numerical solution of the differential equation (9-30) subject to the conditions of Eqs. (9-32) and (9-33). Realizable solutions depend on the initial conditions. Most failures occur in Eq. (9-33), which satisfies the requirement of equal aperture phase.

Example Figure 9-4 shows a scale drawing of a realizable design for $n = 1.6$, focal distance $f = 45$, diameter $D = 35$, center thickness $T = 6.5$, and effective focal length $f_e = 49$. Table 9-4 lists a few points of the solution obtained by a Runge-Kutta numerical method for the differential equation (9-30).

The example contains only relative dimensions. The solution is size and frequency-independent, since it is obtained by geometric optics.

We can zone the lens for a given frequency by cutting along ray paths. Each step is $\lambda/(n - 1)$ as before. Table 9-4, as in the above example, establishes the ray paths through the lens. Zoning will produce either feed or aperture dead zones. The reduction of weight must be balanced with the loss in efficiency to achieve some compromise.

We used the degree of freedom of the second surface to satisfy the Abbe sine condition. We lose control of the aperture distribution through the lens surfaces. Most practical designs produce an amplitude taper near that of the feed antenna. We must achieve low sidelobes, if required, through a tapered illumination from the feed. The feed pattern plays no part in the design and leaves us with a degree of freedom.

TABLE 9-4 Design of Fig. 9-4 for a Coma-Free Lens*

		Outer surface		
Feed angle ψ,°	Inner surface $\rho(\psi)$	Horizontal distance z	Radius r	Thickness along ray T
0	45.00	51.50	0	6.5
5	45.18	51.19	4.27	6.20
10	45.70	50.27	8.51	5.29
15	46.59	48.71	12.68	3.77
20	47.63	46.28	16.76	1.59
20.92	47.61	45.40	17.50	1.06

*$n = 1.6$; diameter = 35; focal length = 45, effective focal length = 49; central thickness = 6.5.

An antenna designed and built with a diameter of 32 wavelengths [7] showed no coma in a scanning of ±2 beamwidths. Like the paraboloidal reflectors, increasing the focal length for a given diameter allows greater scanning without significant coma.

Specified Aperture Distribution Axisymmetric Dielectric Lens [9] We use the required aperture amplitude distribution to specify the relation between the aperture radius r, and the feed angle ψ. Earlier, the Abbe sine condition established this relation.

Given a feed power pattern $F(\psi)$ and a required aperture distribution $A(r)$, we relate the two through differential areas:

$$F(\psi)\sin\psi\, d\psi = A(r) r\, dr$$

where an axisymmetrical pattern is assumed. We find the relation between ψ and r through normalized integrals as in Sec. 8-18 for shaped reflectors.

$$\frac{\int_0^{\psi} F(\psi)\sin\psi\, d\psi}{\int_0^{\psi_m} F(\psi)\sin\psi\, d\psi} = \frac{\int_0^{r} A(r) r\, dr}{\int_0^{r_m} A(r) r\, dr} \tag{9-34}$$

In any particular design we generate a table, such as Table 8-5, of the feed angle versus its normalized feed pattern integral and the aperture radius versus its normalized aperture distribution integral. For a given feed angle ψ we equate the normalized integrals to find the corresponding aperture radius. We calculate a table of aperture radius versus feed angle, such as Table 8-6, using interpolation techniques. The design is very dependent on feed pattern, because changing the feed pattern will change the table. Low sidelobe aperture distributions require close tolerances, and a good specification of the feed pattern will be needed.

Once we have the relation between ψ and r, the design follows steps similar to those taken in designing the lens for the Abbe sine condition. We solve the differential equation (9-30) numerically. We specify the aperture radius by the table generated for the transformation of the feed pattern into the aperture distribution. The requirement for equal path length through the lens determines the axis location z of the outer surface.

$$\begin{aligned}
&Ax^2 + Bx + C = 0 \qquad x = z - f\\
&A = n^2 - 1\\
&B = 2[n^2(f - \rho\cos\psi)] + \rho - K - f\\
&C = [n(\rho\cos\psi - f)]^2 + (r - \rho\sin\psi)^2 - (f + K - \rho)^2\\
&K = T(n - 1) \qquad z = f + \frac{-B + \sqrt{B^2 - 4AC}}{4A}
\end{aligned} \tag{9-35}$$

where T is the central thickness and f is the axis focal length.

A successful design requires a number of iterations with different initial conditions. The differential equation solution will diverge to shapes unable to satisfy the equal-path-length requirement with poor initial conditions. Each design has a narrow range of satisfactory initial conditions. In most cases increasing the thickness will increase the chance for a successful design.

Example A lens was designed to transform the feed pattern of a conical corrugated horn into a circular Taylor distribution with 40-dB sidelobes ($\bar{n} = 8$). The initial conditions were $n = 1.6$, diameter $D = 32$, focal distance $f = 35$, central thickness $T = 9$, and maximum feed angle $\psi_m = 20°$.

A table of the feed angle and its normalized power pattern integral, along with the aperture radius and its normalized power distribution integral, was generated. A table of feed angle and the corresponding aperture radius follows from equating normalized integrals. This table is independent of the lens thickness but not the feed pattern.

A Runge-Kutta numerical method is used to solve the differential equation (9-30) subject to the conditions imposed by the aperture radius table and Eq. (9-35) for equal optical path lengths. Figure 9-5 shows a design for a 36° 10-dB beamwidth feed horn (12-dB feed edge taper). The horn dimensions are aperture radius = 1.90λ and slant radius = 9λ for a maximum quadratic phase deviation S of 0.2 cycle. A few points of the design are listed in Table 9-5.

Other antennas designed with small changes in the feed pattern beamwidth showed large changes in the lens shape near the edges for a constant center thickness.

Axisymmetric dielectric lenses can be designed to be independent of frequency because only relative sizes are specified. The lenses tend to be thick to allow room to satisfy the equal optical path length requirement.

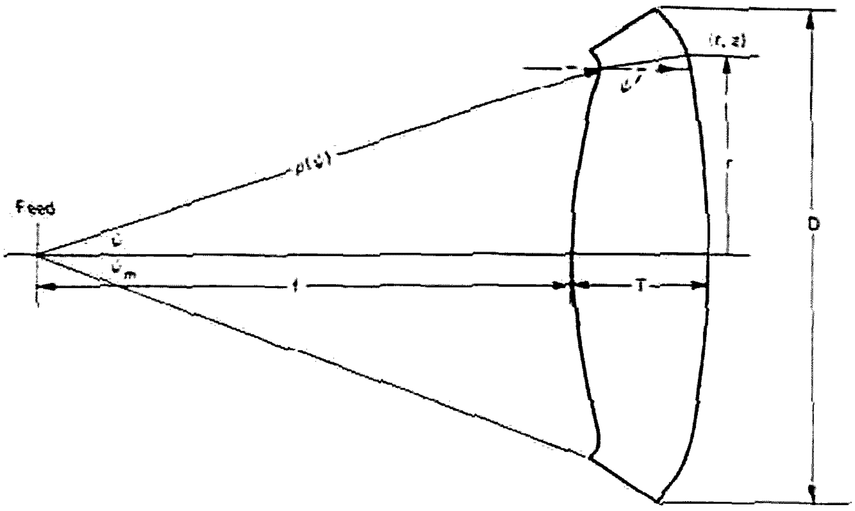

Figure 9-5 Dual-surface axisymmetric lens for circular Taylor aperture distribution (40 dB, $\bar{n} = 8$). Lens: $n = 1.6$, $D = 32$, $f = 35$, $T = 9$, $\psi_m = 20°$. Feed: conical corrugated horn, 36° 10-dB beamwidth. $S = 0.2$.

Zoning the lens will reduce the weight while decreasing the frequency bandwidth. Low-sidelobe designs will be inherently narrowband, since small changes in the beamwidth of the feed change the aperture distribution and sidelobe levels. Zoning may not reduce the bandwidth significantly.

An antenna designed and tested by using the above technique revealed a number of requirements on the design [10]. The sidelobe levels exceeded the design specification for three main reasons. First, the feed pattern was specified as $\sin(\pi U)/(\pi U)$, an oversimplification of the actual feed pattern. Realistic feed patterns must be used because small changes of the feed pattern require new designs. Second, the surfaces must be matched with quarter-wavelength sections to prevent reflections, unaccounted for in the design, from changing the aperture distribution. Third, diffractions from the

TABLE 9-5 Design of Fig. 9-5 for a Specified Aperture Distribution Axisymmetric Dielectric Lens*

		Outer surface		
Feed angle ψ,°	Inner surface $\rho(\psi)$	Horizontal distance z	Radius r	Thickness along ray T
0	35.00	44.00	0.00	9.00
5	35.31	43.95	3.27	8.78
10	36.14	43.67	6.59	8.08
15	37.69	43.25	10.11	6.86
20	38.71	40.58	16.00	5.03

*40-dB ($\bar{n} = 8$) circular Taylor distribution from a conical corrugated-horn feed.

edges will affect the distribution. Increasing the aperture diameter or using a low edge illumination from the feed will reduce these effects.

As designed, the antenna exhibits severe coma when scanned by feed lateral offset. Since most lenses are quite thick, zoning can be used to approximate the Abbe sine condition on the inner surface. The lens refracts most of the rays parallel with the axis by the inner surface. If the zones approximate a spherical surface on the average, coma is reduced for the scanned beams. These coma-corrected lenses can be useful for multibeam applications when each beam is fed from an offset feed.

9-7 Bootlace Lens

The bootlace lens consists of a set of receiving antennas on a surface connected by cables to a set of transmitting antennas on a second surface (Fig. 9-6). The cables constrain the path of the waves through the lens. We have three degrees of freedom with this lens: (1) input surface, (2) output surface, and (3) cable length. We can dynamically change the lens characteristics by placing phase shifters and/or attenuators in the lines between the input and output radiators and scan one or more beams. The input and output surfaces are arrays, and we can generate multiple beams by placing more than one feed on a focal arc determined by the lens geometry.

The simplest bootlace lens consists of a spherical input surface connected to a plane output surface by equal-length cables. The lens converts spherical waves radiated from a feed at the center of the spherical input surface into plane waves at the output surface. The lens uses true time delay that removes bandwidth limitations.

Most bootlace lenses are line sources or two-dimensional lenses fed by line sources. The general lens can have four focal points [11] placed sym-

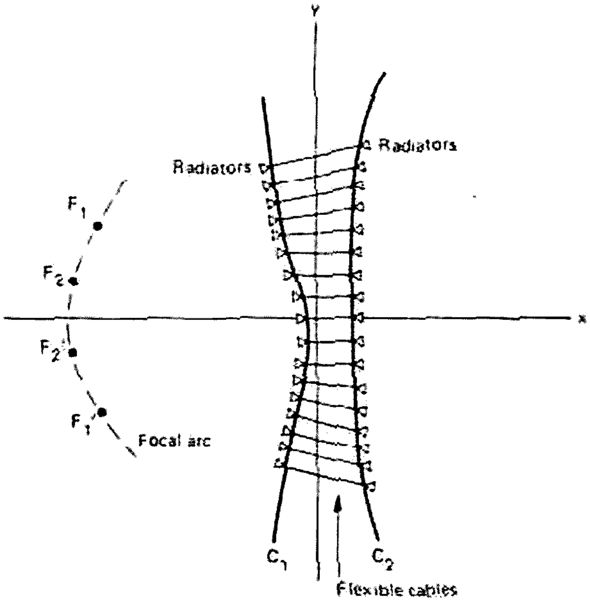

Figure 9-6 Bootlace lens. (Source: M. L. Kales and R. M. Brown, "Design Considerations for Two-Dimensional Symmetric Bootlace Lenses," *IEEE Trans. Antennas Propagat.*, vol. AP-13, no. 4, July 1965, pp. 521–528. © 1965 IEEE.)

metrically about the axis of the symmetric structure. The focal arc is chosen on a curve through the focal points to minimize defocusing when feeds are placed off the focal points. A feed at each point along the focal arc produces an output beam in a different direction. Each feed uses the full aperture and has the full gain less the loss of projection of the aperture length in the direction of the beam.

The number of focal points reduces to three when the lens is further restrained. The Ruze design for a metal plate lens [6] has three focal points, since the waveguides between the surfaces travel in straight lines. There is one central axis focal point, and there are two symmetrically placed focal points. The Rotman [12] lens loses one possible focal point because the output surface is limited to a straight line. A parallel-plate structure in the Rotman lens leads from the possible feed locations to the feed side surface, which normally is excited by probes in the parallel-plate guide. The lens becomes a feed network that produces multiple beams whose directions depend on the location of the feed on the focal arc. Although perfect focusing is achieved at only three points, the phase error loss associated with points between them is small. Because the Rotman lens feed network is a true time delay array feed network, we can achieve bandwidths greater than an octave from it.

Rao [13] extends the design of bootlace lenses to three dimensions. He shows that the number of focal points cannot be extended beyond four. The lens is not axisymmetric and has different scanning capabilities in the orthogonal planes. Rao designs lenses with two, three, and four focal points on a focal line. Decreasing the number of focal points in one plane will increase the scanning capability in the orthogonal plane for a given phase error level.

9-8 Luneburg Lens [14]

The Luneburg lens, a spherically symmetric lens with a variable index of refraction, will radiate a beam in any direction for a feed located opposite the beam. We can place the feed phase center either on the surface of the lens or a short distance away. We form multiple beams by feeding the lens at a number of places. Our only restriction is the blockage due to other feeds or support structures. We can rapidly scan a beam by moving a lightweight feed around the sphere.

When we place the feed on the outer surface of the sphere, the required index of refraction is

$$n = \sqrt{2 - \left(\frac{r}{a}\right)^2} \tag{9-36}$$

where a is the lens outer radius and r is the inner radius. The dielectric constant n^2 must vary between 2 in the center and 1 on the outer surface.

Few feeds have their phase centers on a surface which can be mounted against a sphere. We can move the feed away from the surface by changing the variation of the index of refraction from that given by Eq. (9-36). The required center index of refraction decreases as we move the feed away from the lens surface. We must find the variation of the index of refraction from an integral equation. The curves follow the general shape of the curve specified by Eq. (9-36). For the feed-to-sphere radius of 1.1, the proper center dielectric constant is 1.83 and varies smoothly to 1 at the lens surface. Similarly, the center dielectric constant starts at 1.68 for the feed-to-sphere radius of 1.2.

The lens changes the amplitude distribution in the aperture compared with the feed. Given the ratio of feed radius to lens radius r_1, the aperture plane power distribution becomes

$$A(r) = \frac{F(\psi)}{r_1^2 \cos \psi} \tag{9-37}$$

where ψ is the feed angle, $F(\psi)$ is the feed power pattern, and $A(r)$ is the aperture power distribution. Equation (9-37) shows that the lens refracts power toward the edge of the aperture.

Lenses have been made by using a series of concentric spherical shells each with a constant dielectric. A minimum of 10 shells is needed for an adequate approximation of the required variation of the dielectric constant.

REFERENCES

1. J. R. Risser in S. Silver (ed.), *Microwave Antenna Theory and Design*, McGraw-Hill, New York, 1948, chap. 11.
2. S. B. Cohn in H. Jasik (ed.), *Antenna Engineering Handbook*, McGraw-Hill, New York, 1961, chap. 14.
3. A. R. Dion, "A Broadband Compound Waveguide Lens," *IEEE Trans. Antennas Propagat.*, vol. AP-26, no. 5, September 1978, pp. 751–755.
4. T. Morita and S. B. Cohn, "Microwave Lens Matching by Simulated Quarter-Wave Transformers," *IEEE Trans. Antennas Propagat.*, vol. AP-4, no. 1, January 1956, pp. 33–39.
5. R. W. Kreutel, "The Hyperboloidal Lens with Laterally Displaced Dipole Feed," *IEEE Trans. Antennas Propagat.*, vol. AP-28, no. 4, July 1980, pp. 443–450.
6. J. Ruze, "Wide-Angle Metal-Plate Optics," *Proc. IRE*, vol. 38, no. 1, January 1950, pp. 53–59.
7. J. J. Lee, "Numerical Methods Make Lens Antennas Practical," *Microwaves*, vol. 21, no. 9, September 1982, pp. 81–84.
8. R. Kingslake, *Lens Design Fundamentals*, Academic Press, New York, 1978, p. 157.
9. J. J. Lee, "Dielectric Lens Shaping and Coma-Correcting Zoning, Part I: Analysis," *IEEE Trans. Antennas Propagat.*, vol. AP-31, no. 1, January 1983, pp. 211–216.
10. J. J. Lee and R. L. Carlise, "A Coma-Corrected Multibeam Shaped Lens Antenna, Part II: Experiments," *IEEE Trans. Antennas Propagat.*, vol. AP-31, no. 1, January 1983, pp. 216–220.

11. M. L. Kales and R. M. Brown, "Design Considerations for Two Dimensional Symmetric Bootlace Lenses," *IEEE Trans. Antennas Propagat.*, vol. AP-13, no. 4, July 1965, pp. 521–528.
12. W. Rotman and R. F. Turner, "Wide-Angle Microwave Lens for Line Source Applications," *IEEE Trans. Antennas Propagat.*, vol. AP-11, no. 6, November 1963, pp. 623–632.
13. J. B. L. Rao, "Multifocal Three-Dimensional Bootlace Lenses," *IEEE Trans. Antennas Propagat.*, vol. AP-30, no. 6, November 1982, pp. 1050–1056.
14. R. S. Elliott, *Antenna Theory and Design*, Prentice-Hall, Englewood Cliffs, N.J., 1981, p. 545.

CHAPTER

10

ARRAY SYNTHESIS

We can consider an array as a sampled aperture. Of course, an array has more freedom than an aperture. We can, for example, form multiple beams by using the whole size of the aperture for each beam, since phase and amplitude can be varied between elements in any manner. We can also dynamically change the pattern of the array to change the beam direction or form multiple seemingly independent beams. An array has great potential. For large arrays we sample continuous distributions to avoid the mathematical difficulties of the large number of operations needed to find the feeding coefficients. Second, a large Dolph-Chebyshev array has limited possible gain because of the constant sidelobe level. A sampled Taylor line source has no theoretical gain limitation.

We find applications for small arrays to which the methods discussed in this chapter can be conveniently applied. The unit circle method of Schelkunoff allows the design of a linear array, usually broadcast towers, to specified null directions. We describe all linear arrays in terms of the unit circle representation, which we can use in a hand search for a required pattern. The equal sidelobe level designs of Dolph give the minimum possible beamwidth for a given sidelobe level. Both the Dolph and Schelkunoff methods can be extended to planar arrays to design for either a given sidelobe level or specified pattern nulls. Finally, we can design shaped beams by either sampling Woodward line sources or through a Fourier series expansion of the desired array pattern. Each pair of elements added on the ends adds another harmonic to the design.

10-1 Schelkunoff's Unit Circle Method [1]

Schelkunoff's unit circle method consists of the manipulation of the zeros (nulls) of the array pattern to achieve a desired pattern for a linear array. We can use the representation to describe any uniformly spaced array. The method is similar to designing networks by specifying the placement of poles and zeros in the complex plane, but the array has only zeros to manipulate.

Consider a uniformly spaced array along the z axis with the pattern angle θ measured from the axis. The array response will be symmetrical about the z axis. If we define the variable

$$\psi = kd \cos \theta + \delta$$

where δ is a fixed progressive phase shift between elements, d is the element spacing, and k is the wave number $(2\pi/\lambda)$, then the pattern of the array is given by

$$E = I_0 + I_1 e^{j\psi} + I_2 e^{j2\psi} + I_3 e^{j3\psi} + \cdots \tag{10-1}$$

where I_i, a phasor, is the excitation of the ith element in the array. We will further simplify the notation by defining

$$W = e^{j\psi} \tag{10-2}$$

We then write Eq. (10-1) as

$$E = I_0 + I_1 W + I_2 W^2 + I_3 W^3 + \cdots + I_{N-1} W^{N-1} \tag{10-3}$$

where N is the number of elements in the array. We have taken our phase reference point on the first element. This array factor (isotropic elements) is a polynomial with $N - 1$ roots (zeros) for N elements.

We denote the roots W_i, and we can then write Eq. (10-3) as

$$E = E_0(W - W_1)(W - W_2)\cdots(W - W_{N-1})$$

We can ignore the normalization E_0 and find the array pattern magnitude as

$$E(W) = |W - W_1|\,|W - W_2|\cdots|W - W_{N-1}|$$

where $|W - W_i|$ is the distance from the root W_i to W in the complex plane. W is limited to the unit circle [Eq. (10-2)] because it always has unit value.

The spacing of the elements and the progressive phase shift δ determines the limits of the phase of W.

$$\begin{aligned} \theta &= 0^\circ & \psi_s &= kd + \delta & &\text{start} \\ \theta &= 180^\circ & \psi_f &= -kd + \delta & &\text{finish} \end{aligned} \tag{10-4}$$

As θ increases, ψ decreases and W progresses in a clockwise direction on the unit circle (Fig. 10-1). We have no 2π limitation on either ψ_s or ψ_f. The element spacing determines the number of times W cycles the unit circle as θ varies from 0° to 180°. If $\psi_s - \psi_f$, $2kd$, exceeds 2π, there is a possibility of more than one main beam (grating lobes).

The zeros W_i suppress the pattern when W moves close to one or more of them. The pattern rises to form a lobe when W is removed from the zeros. The main beam peak occurs at the point with the maximum product of the distances from the zeros. Whenever W passes through that point, another main beam forms.

A uniformly fed array has the W space polynomial

$$f(W) = \frac{1 - W^N}{1 - W} \qquad \text{for } N \text{ elements}$$

The zeros of $f(W)$ are the N zeros of $W^N = 1$ with the zero at $W = 1$ removed.

$$W_i = e^{j2\pi i/N}$$

These are uniformly spaced on the unit circle.

Figure 10-2 shows the unit circle diagram of a 10-element array fed with uniform phase and amplitude. W starts at -1, since $d = \lambda/2$, and it progresses clockwise around the unit circle one revolution to the same point as θ varies from 0° to 180°. At $\theta = 90°$, the product of the distances from the zeros is a maximum. A lobe forms within the space between each pair of zeros. As W moves from the start to the main beam at $W = 1$, it starts at a zero and passes through four additional zeros. These zeros W_i correspond to the nulls in the pattern from $\theta = 0°$ to $\theta = 90°$. An equal number of nulls occur as W moves through the range $\theta = 90°$ to 180°.

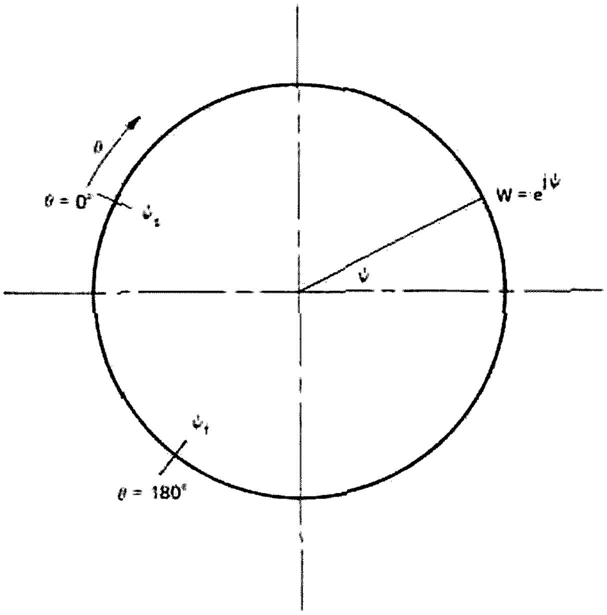

Figure 10-1 Unit circle in W plane.

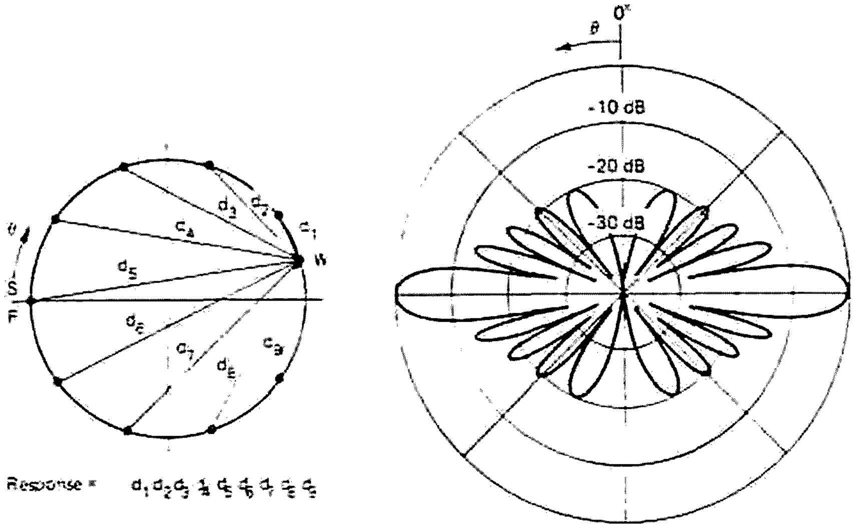

Figure 10-2 Unit circle representation of 10-element array with $\lambda/2$ spacings.

A uniform-amplitude end-fire array can be represented on the same unit circle diagram. With antenna elements spaced $\lambda/4$, the excursion from start ψ_s to finish ψ_f is only π ($2kd$). A progressive phase shift δ of $-kd$ through the array forms an end-fire pattern. From Eq. (10-4), $\psi_s = 0$ and $\psi_f = 180°$. The end-fire array pattern has only five nulls including the null at $\theta = 180°$ as θ ranges from 0° to 180°, since only five zeros occur in the visible region.

The Hansen and Woodyard increased directivity end-fire array corresponds to a shift in the start and stop locations on the unit circle. The excursion from start to finish remains π determined only by element spacing. Equation (10-4) calculates the start: $\psi_s = 90° - 108° = -18°$. The pattern has five nulls from $\theta = 0°$ to 180°.

A binomial array has all its zeros at $W = -1$ and has no sidelobes, since they occur for points on the unit circle between zeros. Only one beam forms as W traverses the unit circle. The W-space polynomial is

$$f(W) = (W + 1)^{N-1}$$

For an array of given size we can manipulate the location of the nulls to either reduce sidelobes or place pattern nulls. We reduce a sidelobe by moving the zeros on both sides of it closer together. When we do that, either the main-lobe beamwidth increases or the other sidelobes rise. We form a null in the array pattern by moving one of the zeros to that point on the unit circle corresponding to W at the null angle. Given a desired null θ_n

$$W_i = e^{j(kd\cos\theta_n - \delta)} \tag{10-5}$$

Equation (10-5) gives the phase angle $kd\cos\theta_n + \delta$ of the required zero on the unit circle in W space.

In the case of an end-fire array in which the spacing between elements is less than $\lambda/2$, we can shift zeros from invisible space into visible space to narrow the beam and reduce sidelobes. We thereby form large lobes in invisible space that represent energy storage in the array. The large energy storage reduces the bandwidth and efficiency of the array. This superdirectivity method has limited success, although we can produce beautiful patterns on paper.

Example Design a four-element array of broadcast towers to give nearly uniform coverage for $\theta = \pm 45°$ with nulls at $\theta = 270°$ and 135° [2].

We will align the array with $\theta = 0°$ to obtain symmetry for the $\pm 45°$ requirement. We actually need only three elements, since only two nulls are specified. Using $\lambda/4$ spacings, we set $\delta = -90°$ to get an end-fire array. Equation (10-5) gives the required zeros of the polynomial for the pattern nulls.

$$W_1: \qquad \psi = \frac{360°}{\lambda}\frac{\lambda}{4}\cos(270°) - 90° = -90°$$

$$W_2: \qquad \psi = \frac{360°}{\lambda}\frac{\lambda}{4}\cos(135°) - 90° = -153.64°$$

We find the polynomial from the roots:

$$f(W) = (W - e^{-j90°})(W - e^{-j153.64°})$$

$$= W^2 + 1.6994We^{j53.18°} + e^{j116.36°}$$

We will normalize the phase to the first element of the array [constant term of $f(W)$].

$$f(W) = W^2e^{-j116.36°} + W1.6994e^{-j55.18°} + 1$$

At this point the polynomial representation of the array $f(W)$ does not include the progressive phase factor $\delta = -90°$. We add the factor to the polynomial by adding $-90°$ to the phase of the second element (W term) and $-180°$ to the third element (W^2 term).

$$f(W) = W^2e^{-j296.36°} + W1.6994e^{-j145.18°} + 1$$

The coefficients of the polynomial are the voltage (or current) components of the array. No null develops at $\theta = 180°$ because the two available nulls ($N - 1$) were used. Adding the fourth element gives us the freedom to improve the response flatness in the $\pm 45°$ region of θ. Figure 10-3 shows a unit circle representation and pattern to give a nearly equal ripple response between $\pm 45°$ and the required nulls. We increase the spacing to 0.35λ and place the pattern nulls at 90°, 135°, and 180°. W starts at $+1$ on the unit circle or $\psi_s = 0°$ and determines δ.

$$\psi_s = 0 = kd + \delta \qquad \text{or} \qquad \delta = -kd = -\frac{360}{\lambda}0.35\lambda = -126°$$

We find the phase of the zeros from Eq. (10-5)

$$\psi_1 = 360°(0.35)\cos(90°) - 126° = -126°$$

$$\psi_2 = 360°(0.35)\cos(135°) - 126° = -215.1° \quad (144.9°)$$

$$\psi_3 = 360°(0.35)\cos(180°) - 126° = -252° \quad (108°)$$

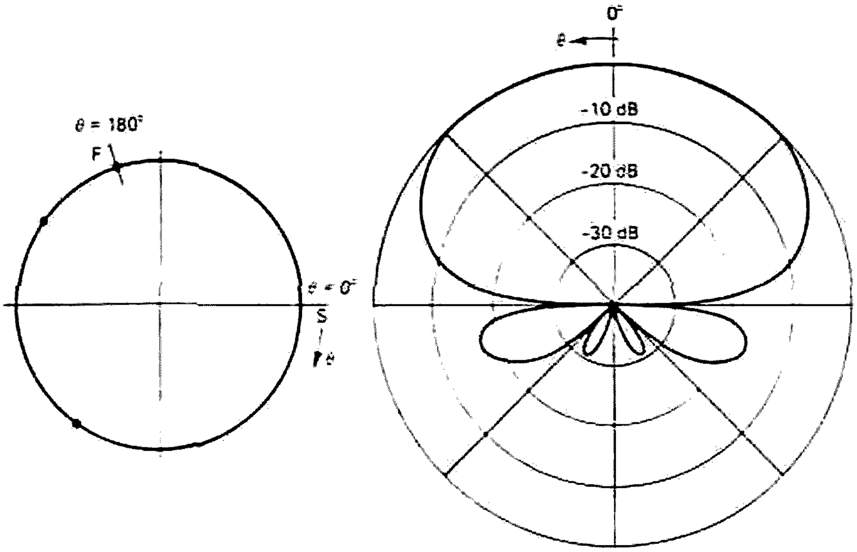

Figure 10-3 Four-element linear array with pattern nulls at $\theta = 90°$, 135°, and 150°. The elements are spaced at 0.35 λ to give flat response ±45°.

By following the same steps as above, we find the phase and amplitudes of the array elements.

No.	Amplitude, dB	Phase, °
1	−9.50	0
2	−4.11	−103.31
3	−4.11	138.41
4	−9.50	35.10

10-2 Dolph-Chebyshev Linear Array [3]

The Chebyshev polynomials have equal ripples in the region $x = \pm 1$, and the amplitude varies between $+1$ and -1. Outside that region the polynomial value rises exponentially.

$$T_m(x) = \begin{cases} (-1)^m \cosh(m \cosh^{-1}|x|) & x < -1 \\ \cos(m \cos^{-1} x) & -1 \le x \le 1 \\ \cosh(m \cosh^{-1} x) & x > 1 \end{cases}$$

The order of the polynomial m equals the number of roots.

Dolph devised a method of relating the Chebyshev polynomials to the array factor polynomial for a broadside array. We scale the polynomial to make the equal-ripple portion the sidelobes while the exponential increase beyond $x = 1$ becomes the main beam. Take an array that is fed symmetrically about the centerline and has either $2N + 1$ or $2N$ elements. We expand the array factor in a polynomial with factors $\cos(\psi/2)$, where $\psi = kd \cos\theta + \delta$. The beam peak occurs when $\psi = 0$. If we make this correspond to a value x_0, where the Chebyshev polynomial has a value R, the sidelobes will be equal ripple at a level $1/R$. By substituting $x = x_0 \cos(\psi/2)$, we can use the Chebyshev polynomial for the array polynomial with

$$T_m(x_0) = R \qquad \text{or} \qquad x_0 = \cosh \frac{\cosh^{-1} R}{m} \tag{10-6}$$

where $20 \log R$ is the desired sidelobe level in dB.

The zeros of $T_m(x)$ are given by

$$x_p = \pm \cos \frac{(2p - 1)\pi}{2m} \tag{10-7}$$

By using the equation $x_p = x_0 \cos(\psi/2) = x_0(e^{j\psi/2} + e^{-j\psi/2})$, we find the angles of the symmetrical zeros in the W plane:

$$\psi_p = \pm 2 \cos^{-1} \frac{x_p}{x_0} \tag{10-8}$$

Both values of x_p [Eq. (10-7)] give the same ψ_p pair. Given the zeros in the W plane, we multiply out the root form of the polynomial to find the feeding coefficients of the array.

Example Design a 10-element array with 25-dB sidelobes. The array has nine nulls, so we pick $m = 9$ for the Chebyshev polynomial.

Eq. (10-6) $\quad R = 10^{25/20} = 17.7828 \quad x_0 = 1.0797$

We need only the first five zeros, since they are symmetrical about zero. We find them from Eq. (10-7), divide them by x_0, and use Eq. (10-8) for their angles on the unit circle of the W plane.

p	x_p	ψ_p, °
1	0.9848	±48.41
2	0.8660	±73.34
3	0.6428	±106.93
4	0.3420	±143.06
5	0	180

We multiply out the root form of the polynomial and convert the voltage magnitude of the coefficients to dB for the feeding coefficients of the array. Because the roots are symmetrical about the real axis, all phase angles are zero. We obtain the following coefficients when we normalize to the total power.

Number	*1 and* 10	*2 and* 9	*3 and* 8	*4 and* 7	*5 and* 6
Coefficient, dB	−15.46	−13.31	−10.23	−8.31	−7.39

Figure 10-4 shows the unit-circle representation and pattern of the array with $\lambda/2$ spacings.

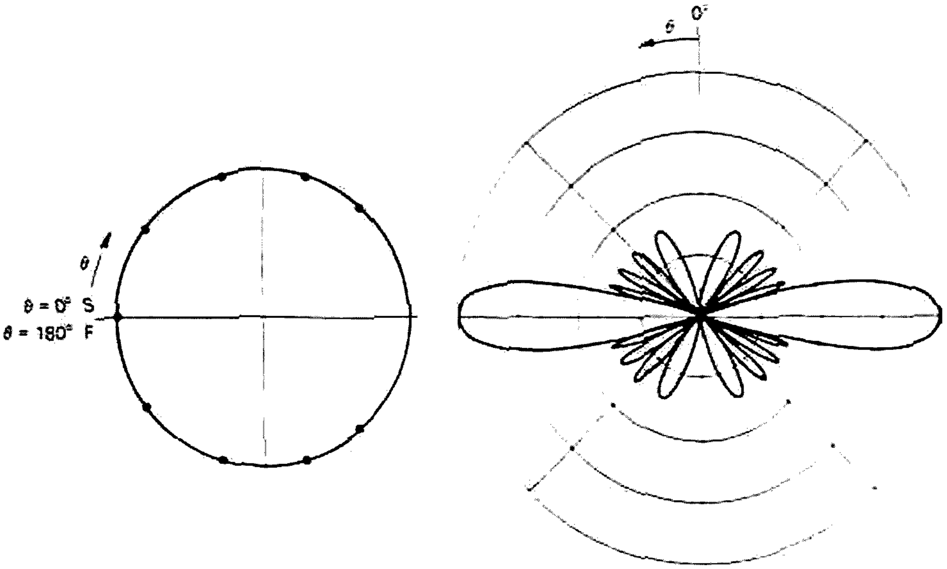

Figure 10-4 Ten-element Dolph-Chebyshev array with 25-dB sidelobes.

We can estimate the beamwidth of a Chebyshev array by using a beamwidth broadening factor and the beamwidth of the same length uniformly fed array [4]. The beamwidth broadening factor is given by

$$f = 1 + 0.632\left[\frac{2}{R}\cosh\sqrt{(\cosh^{-1}R)^2 - \pi^2}\right]^2 \tag{10-9}$$

Equation (10-9) is valid in the range of sidelobe levels from 20 to 60 dB and for scanning near broadside.

Example Find the broadside beamwidth of a Dolph-Chebyshev array with 61 elements, a 30-dB sidelobe level, and $\lambda/2$ spacings.
Equation (10-9) gives the value 1.144 for f using $R = 10^{30/20}$. We estimate the beamwidth of the uniform array from $\text{HPBW} = 50.76°\lambda/Nd = 1.66°$, where d is the element spacing.

$$\text{HPBW}_{\text{array}} = (f)\text{HPBW}_{\text{uniform}} = 1.144(1.66°) = 1.90°$$

We use the beam-broadening factor to estimate the array directivity.

$$D = \frac{2R^2}{1 + \dfrac{(R^2 - 1)f\lambda}{Nd}} \tag{10-10}$$

Example We find the directivity of the above 61-element array from Eq. (10-10). $D = 52.0$ (17.2 dB).

If we take its limit as $Nd \to \infty$, Eq. (10-10) becomes $2R^2$. An infinite Dolph-Chebyshev array has a gain 3 dB more than the sidelobe level.

10-3 Other Chebyshev Array Techniques [5, 6]

We will use the Chebyshev polynomials to arrive at other equal-sidelobe designs. The method of the preceding section fails to give optimum designs for spacings less than $\lambda/2$. We need to restrict the designs to an odd number of elements to use the following methods. Start with the array factor for an odd number of elements symmetrically fed about the centerline. We will relate the array factor to the Chebyshev polynomial by using the transformation

$$x = a\cos\psi + b \tag{10-11}$$

and a polynomial order of $(N-1)/2$ for N elements. The visible region ranges from x_0 [Eq. (10-6)] at the beam peak to $x=-1$. Each root of the polynomial is used twice: once on the positive portion of the unit circle and once on the negative portion.

The beam peak occurs at $\psi = 0$ on the unit circle, which gives us

$$x_0 = a + b \tag{10-12}$$

We set both the pattern start and finish points on the unit circle to correspond to $x=-1$ of the Chebyshev polynomial; that is,

$$\psi_s = -kd + \delta \qquad \text{and} \qquad \psi_f = kd + \delta$$

transform into the point $x=-1$.

Suppose $\delta = 0$ and $kd < \pi$ (less than $\lambda/2$ spacings), then

$$-1 = a\cos(kd) + b \tag{10-13}$$

Between Eq. (10-12) and Eq. (10-13), we solve for a and b.

$$a = \frac{1+x_0}{1-\cos kd} \qquad b = \frac{-(1+x_0\cos kd)}{1-\cos kd} \tag{10-14}$$

Example Design a Chebyshev array with nine elements at 0.375λ spacings and 25-dB sidelobes.

We use the order $(N-1)/2 = 4$ for the Chebyshev polynomial. Eq. (10-6) gives us x_0:

$$x_0 = \cosh\frac{\cosh^{-1} 10^{25/20}}{4} = 1.426$$

Substitute this x_0 and $kd = 360°(0.375) = 135°$ into Eq. (10-14) to find the constants of the transformation: $a = 1.4209$ and $b = 0.0047$. We use Eq. (10-7) to find the roots of the Chebyshev polynomial and the transformation Eq. (10-11) to find the angles of the zeros

$$\psi_p = \pm\cos^{-1}\frac{x_p - b}{a} \tag{10-15}$$

We substitute a, b, and the values of x_p found from Eq. (10-7) into Eq. (10-15) and obtain the following table, in which we obtain different zero locations ψ_p for both the positive and negative solutions of Eq. (10-7) (x_p).

P	x_p	ψ_p, °	ψ_p, °
1	±0.9239	±49.69	±130.81
2	±0.3827	±74.57	±105.82

Given the zeros, we multiply out the polynomial to find the array coefficients. Figure 10-5 shows the unit circle representation and pattern of this design.

Drane [7] gives an approximate formula for the directivity of these arrays with spacings less than $\lambda/2$.

$$D = \frac{2R^2}{1 + (\lambda/L)R^2\sqrt{(\ln 2R)/\pi}\,\sin(kd/2)} \tag{10-16}$$

Equation (10-16) gives good estimates for 10 or more elements. An estimate for the beamwidth of a scanned array is given by

$$\mathrm{BW} \cong 10.3°\frac{\lambda}{L}\sqrt{S + 4.52}\,\csc\theta_0 \tag{10-17}$$

where L is the length of the array (Nd), S is the sidelobe level (dB), and θ_0 is the scan angle from the axis. Equation (10-16) is also an estimate of the directivity of arrays with spacings greater than $\lambda/2$, but less than the appearance of grating lobes, if we remove the sin $(kd/2)$ factor in the denominator.

If kd is greater than or equal to π, the pattern will extend to or further than once around the unit circle in the W plane. We use the following transformation

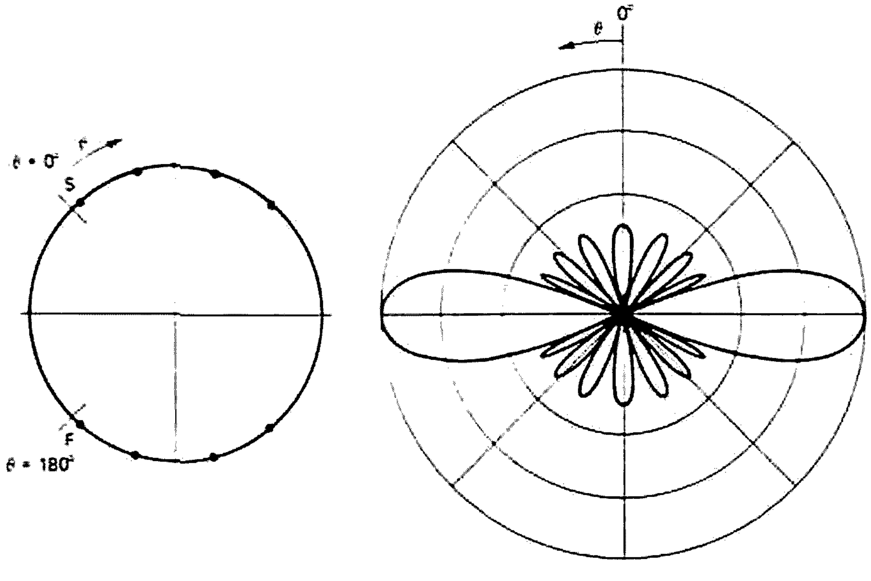

Figure 10-5 Nine-element Chebyshev array with 0.375λ spacings and 25-dB sidelobes.

$$a = \frac{1 + x_0}{2} \quad \text{and} \quad b = \frac{x_0 - 1}{2} \tag{10-18}$$

When we use this transformation, we obtain the same zeros ψ_p as found in Sec. 10-2.

Suppose $\delta \neq 0$; then the beam will be scanned. We must adjust the zeros in the W plane to still give an equal-sidelobe response. We consider two cases. *In the first case the point $W = -1$ is excluded from the visible region.* We modify Eq. (10-14) to include δ in the transformation.

$$a = \frac{1 + x_0}{1 - \cos(kd - \delta)} \qquad b = \frac{-[1 + x_0 \cos(kd - \delta)]}{1 - \cos(kd - \delta)} \tag{10-19}$$

Example Design a nine-element array with 0.25λ spacings scanned to 45° with 25-dB sidelobes.

To scan to 45° the progressive phase shift between elements δ is $-kd \cos \theta_m = -63.64°$. We use Eq. (10-6) to find $x_0 = 1.4256$ for $m = (N - 1)/2 = 4$. Substitute δ, kd, and x_0 into Eq. (10-19) to find a and b.

$$a = 1.2793 \qquad b = 0.1463$$

The combination of Eq. (10-7) for the roots x_p and Eq. (10-15) gives us the phase angles of the zeros on the unit circle.

P	x_p	ψ_p, °	ψ_p, °
1	±0.9239	±52.57	±146.77
2	±0.3827	±79.35	±114.42

In the second case the point $W = -1$ is in the visible region. We use Eq. (10-18) for a and b of the transformation. This method gives an equal-sidelobe design for an end-fire array, but it is not optimum.

End-Fire Design We let the beam maximum correspond to $-x_0$ [Eq. (10-6)], and we make the progressive phase shift between elements δ greater than that necessary for end fire.

$$-x_0 = a \cos(kd + \delta) + b \tag{10-20}$$

The pattern at $\psi = 0$ is at a maximum of the ripple. When $x = 1$,

$$a + b = 1 \tag{10-21}$$

The other end of the visible region corresponds to $x = -1$:

$$-1 = a \cos(kd - \delta) + b \tag{10-22}$$

We find the unknowns, a, b, and δ, from Eqs. (10-20), (10-21), and (10-22).

$$a = \frac{x_0 + 3 + 2\cos(kd)\sqrt{2x_0 + 2}}{2\sin^2 kd}$$

$$b = 1 - a$$

$$\delta = \sin^{-1} \frac{x_0 - 1}{2a \sin kd} \tag{10-23}$$

Example Design a nine-element end-fire array with 0.25λ spacings and 25-dB sidelobes by using the expressions of Eq. (10-23).

From Eq. (10-6) $x_0 = 1.4256$ for $m = 4$. Substitute into Eq. (10-23) to find $a = 2.2128$, $b = -1.2128$, and $\delta = 5.52°$. Equations (10-7) and (10-15) give us the angles of the zeros on the unit circle. The ψ_p values are

$$\psi_p\!: \pm 15.07°,\ \pm 43.86°,\ \pm 67.97°,\ \text{and } \pm 82.50°$$

Figure 10-6 is a plot of the W-space representation and array pattern. All the zeros have been moved into the visible region and produce a design with a large lobe in the invisible region representing a large amount of stored energy in the aperture. *We find array coefficients with alternating phases and a nearly* 180° phase difference. This superdirective array will be narrowband and have low efficiency.

10-4 Planar Arrays

We design planar arrays with nearly circular boundaries by sampling circular distributions. Given enough sample points in the array, a distribution such as the circular Taylor will be adequately modeled to produce a similar pattern. We can use pattern multiplication to combine the designs for linear arrays into a planar array, but in the special case of a square array a true Chebyshev design can be obtained in all planes. A technique has been developed to allow the synthesis from pattern nulls provided some of the

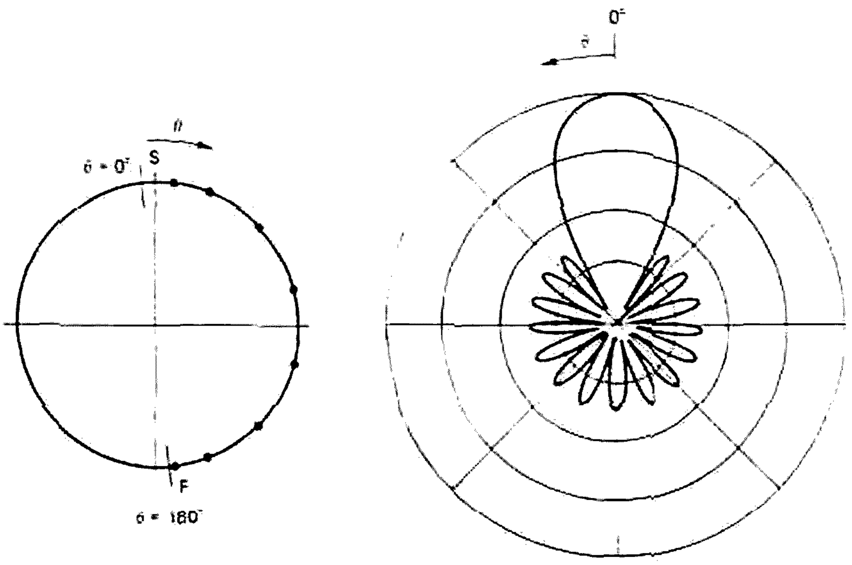

Figure 10-6 *Nine-element Chebyshev array with λ/4 spacings* and 25-dB sidelobes.

possible nulls are not specified. We are still left with the problem of picking the large number of nulls possible with a planar array.

Chebyshev Array [8] Combining two Dolph-Chebyshev linear arrays through pattern multiplication produces patterns with lower sidelobes than specified in all planes except the principal ones along the axes. These designs give wider than necessary beamwidths in the diagonal planes. The pattern deviates from the optimum because sidelobes are suppressed further than necessary.

We will use a technique on a square array to produce equal sidelobes in all constant ϕ cuts around the array. The array is square in the number of elements, but different spacings along the axes can produce a rectangular array. *We expand the pattern in a single Chebyshev polynomial*

$$T_{L-1}(x_0 \cos \psi_1 \cos \psi_2) \qquad (10\text{-}24)$$

where $\psi_1 = kd_x \cos \theta \cos \phi + \delta_1$ and $\psi_2 = kd_y \cos \theta \sin \phi + \delta_2$ and $L = 2N$ or $L = 2N + 1$ for L^2 elements in the array. We find x_0 from Eq. (10-6) for a given sidelobe level. The pattern for an odd number of elements in each row and column is

$$E(\theta, \phi) = \sum_{m=1}^{N+1} \sum_{n=1}^{N+1} \varepsilon_m \varepsilon_n I_{mn} \cos 2(m-1)\psi_1 \cos 2(n-1)\psi_2 \qquad L = 2n + 1$$

where $\varepsilon_m = 1$ for $m = 1$ and $\varepsilon_m = 2$ for $m \neq 1$. Similarly,

$$E(\theta, \phi) = 4 \sum_{m=1}^{N} \sum_{n=1}^{N} I_{mn} \cos (2m-1)\psi_1 \cos (2n-1)\psi_2 \qquad L = 2N$$

The element excitations I_{mn} are given by

$$I_{mn} = \left(\frac{2}{L}\right)^2 \sum_{p=1}^{N+1} \sum_{q=1}^{N+1} \varepsilon_p \varepsilon_q T_{L-1}\left[x_0 \cos \frac{(p-1)\pi}{L} \cos \frac{(q-1)\pi}{L}\right] \times \cos \frac{2\pi(m-1)(p-1)}{L} \cos \frac{2\pi(n-1)(q-1)}{L} \qquad L = 2N + 1 \qquad (10\text{-}25)$$

or

$$I_{mn} = \left(\frac{4}{L}\right)^2 \sum_{p=1}^{N} \sum_{q=1}^{N} T_{L-1}\left[x_0 \cos \frac{(p-\frac{1}{2})\pi}{L} \cos \frac{(q-\frac{1}{2})\pi}{L}\right] \times \cos \frac{2\pi(m-\frac{1}{2})(p-\frac{1}{2})}{L} \cos \frac{2\pi(n-\frac{1}{2})(q-\frac{1}{2})}{L} \qquad L = 2N \qquad (10\text{-}26)$$

Convolution Technique We can synthesize a desired pattern through multiplication of two or more simpler patterns. Because patterns derive from Fourier transforms of distributions in space, the distribution to produce the product of two simpler patterns is the convolution of the simpler distributions [9]. We find it easier to synthesize by using a few elements and then build up patterns through multiplication.

Consider the convolution of a linear array with another linear array on the same axis. We describe the array as a distribution consisting of weighted impulse functions, $\delta(x - x_i)$

$$A_1(x) = \sum_{i=1}^{N_1} a_{1_i}\delta(x - x_i)$$

where a_{1_i} are the feeding coefficients and x_i are the locations for an N_1 element array. To find the array which gives the product of two array patterns, we convolve the second array, $A_2(x)$, with the first.

$$A_1(x) * A_2(x) = \int_{-\infty}^{\infty} A_1(\tau)A_2(x - \tau)\,d\tau \tag{10-27}$$

We evaluate a function at the argument of the impulse function when we convolve the two arrays [10]. Equation (10-27) reduces to

$$A_1(x) * A_2(x) = \sum_{i=1}^{N_1}\sum_{j=1}^{N_2} a_{1_i}a_{2_j}\,\delta(x - x_i - x_j) \tag{10-28}$$

Example Consider the two 2-element arrays in Fig. 10-7 and the graphical solution of the convolution. Figure 10-7*a* shows the location of the elements in the arrays on the x axis. To perform the convolution, we reflect the x axis of one array and move it across the other array while performing the integral at each location x, the coordinate of the convolution. We have a net result of the integral only when two impulse functions are aligned, that is, $x = x_i + x_j$. We have four elements in the resulting array (Fig. 10-7*c*). If the elements are equally spaced in the two arrays, then two elements will sum into one.

Patterns are the result of a three-dimensional Fourier transform. For a general array with element locations $\mathbf{r}_i$, we must perform a convolution along all three axes to find the distribution which gives the product of the patterns of two simpler distributions. For the general array, Eq. (10-28) becomes

$$A_1(\mathbf{r}) * A_2(\mathbf{r}) = \sum_{i=1}^{N_1}\sum_{j=1}^{N_2} a_{1_i}a_{2_j}\,\delta(\mathbf{r} - \mathbf{r}_i - \mathbf{r}_j) \tag{10-29}$$

where $\mathbf{r}$ is the location vector and $\mathbf{r}_i$ and $\mathbf{r}_j$ are the locations of elements in the two arrays.

A rectangular array can be described as the convolution of a linear array on the x axis with a linear array on the y axis. When $y = y_j$, there is a string of values $x = x_i$ which satisfy the impulse argument [Eq. (10-29)]. These are

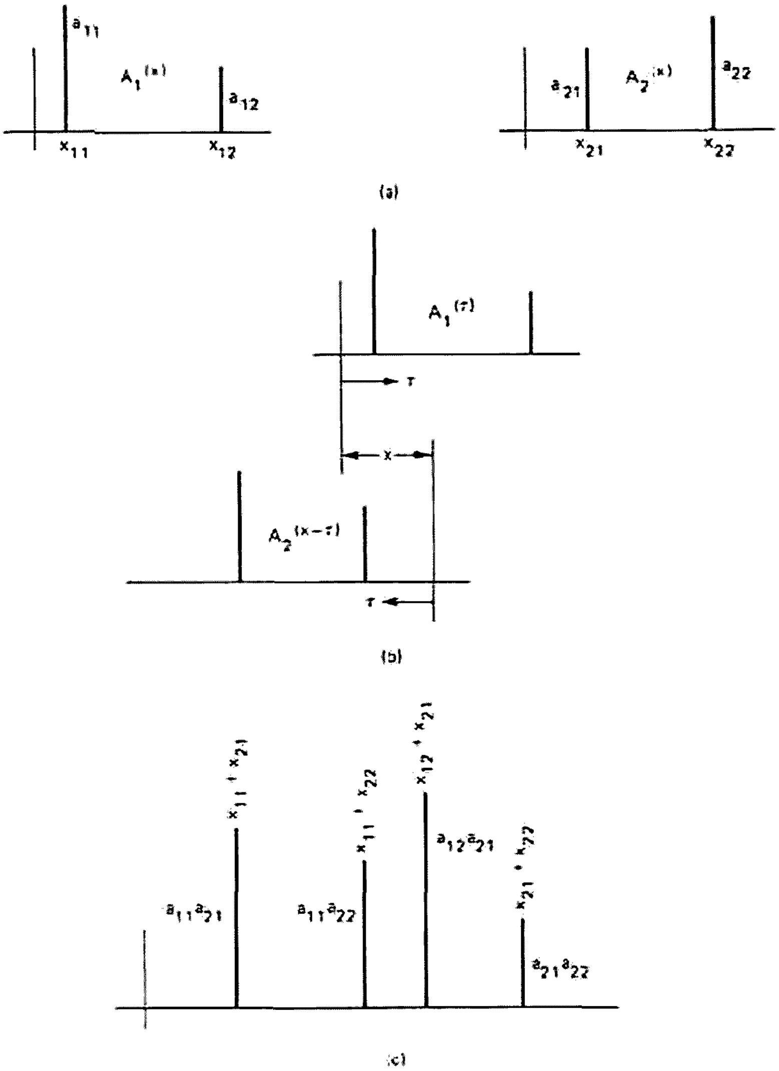

Figure 10-7 Convolution of two linear arrays: (*a*) separate arrays; (*b*) graphical convolution; (*c*) convolution.

the locations of the elements. We step through all values of y_j until the whole array is formed. Equation (10-29) gives the feeding coefficient of each element $a_{1i}a_{2j}$, since no two elements of the convolution are in the same place. The pattern of the rectangular array is the product of the linear array patterns along the axes.

Given an array, we find the pattern from a Fourier transform containing N terms each of which corresponds to one element. Ignoring the element pattern, we have

$$E = \sum_{i=1}^{N} a_i e^{j\mathbf{k}\cdot\mathbf{r}_i} \tag{10-30}$$

The array has $N - 1$ independent nulls (zeros) in the pattern. Given the set of nulls $\mathbf{k}_j$, we can substitute them into Eq. (10-30) to form a matrix equation in $N - 1$ unknowns a_i. We must normalize one coefficient, $a_1 = 1$, to solve the set of equations for the feeding coefficients.

$$[B]\begin{bmatrix} a_2 \\ a_3 \\ \cdot \\ \cdot \\ \cdot \\ a_N \end{bmatrix} = -\begin{bmatrix} e^{jk_1\tau_1} \\ e^{jk_2\tau_1} \\ \cdot \\ \cdot \\ \cdot \\ e^{jk_{N-1}\tau_1} \end{bmatrix} \tag{10-31}$$

where $b_{ij} = e^{jk_i\tau_{j-1}}$.

We find the direct solution of Eq. (10-31) unwieldy for a large array. We can subdivide the array into smaller arrays whose convolution is the total array and use pattern multiplication. We reduce the number of nulls we need to specify in the synthesis of an array.

Convolution can be used in the synthesis of planar arrays by using a rhombic array (four elements) as the basic building block [11] (Fig. 10-8). If we convolve two identically shaped rhombic arrays, we obtain a nine-element (three on a side) array (Fig. 10-8*b*). By continuing to convolve the resulting array with other rhombic arrays, we can build up a large array in the shape of the rhombus.

Each rhombic array has three pattern nulls without the symmetry of the linear array about some axis. The rhombic array has symmetry only about the plane of the rhombus. We build up an array of $N + 1$ by $N + 1$ elements through the convolution of N rhombic arrays. The original array has $N + 1$ by $N + 1$ minus 1 independent nulls. The convolution of N rhombic arrays reduces the number of independent nulls to $3N$. Similarly, when we use the convolution of two linear arrays to form a square array, $N + 1$ by $N + 1$, the number of independent nulls is $2N$, or N for each array.

We denote a single rhombic array as RA_1 and the convolution of two rhombic arrays as RA_2. The number of elements on each side of an RA_N array is $N + 1$. We can convolute a rhombic array with a linear array to form an $M \times N$ array ($M > N$). Denote the linear array by L_N, where the array has $N + 1$ elements. The planar array $PA_{M,N}$ becomes

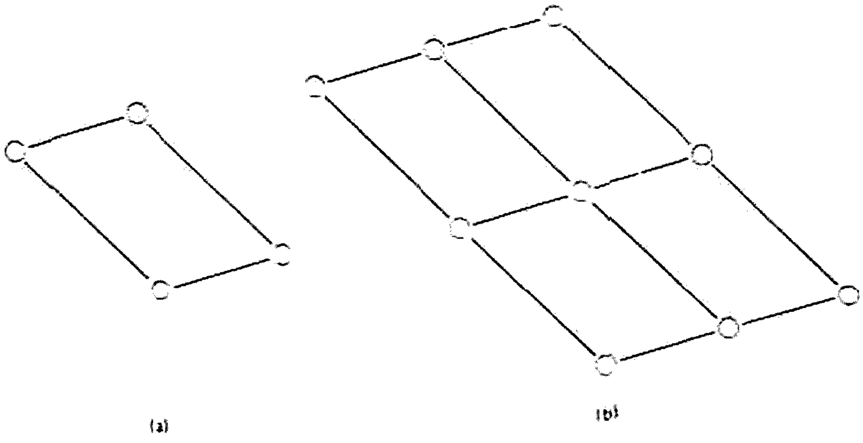

Figure 10-8 Rhombic array with its convolution: (*a*) rhombic array RA_1; (*b*) convolution of two rhombic arrays RA_2.

$$PA_{M,N} = L_{M-N} * RA_{N-1} \tag{10-32}$$

We specify $3(N - 1)$ nulls in space for the rhombic arrays and $M - N$ nulls about the axis of the array. Like all convolutions, the pattern is the product of the individual array patterns.

This method allows the specification of nulls in space with other than linear symmetry. Second, it reduces the required specification of nulls. Third, it provides a method for synthesis of triangularly or hexagonally spaced elements.

Example Consider the six-element rectangular array shown in Fig. 10-9*a*. It can be broken down into the convolution of a four-element rectangular array (rhombic) and a two-element linear array from Eq. (10-32)

$$PA_{3,2} = L_1 * RA_1$$

Pick the three nulls of the rhombic array at

θ	90°	90°	90°
ϕ	110°	−60°	180°

We measure the pattern nulls from the normal of the plane containing the rhombus and the x axis (ϕ). For an array of broadcast towers, the nulls point toward the horizon. We restrict θ to less than or equal to 90°. We substitute the positions of the elements (Fig. 10-9*b*) and the nulls into Eq. (10-31) to solve for the feeding coefficients of the rhombic array.

Element	*Amplitude, dB*	*Phase*
1	0.00	0.0°
2	4.12	−79.2°
3	0.00	−109.2°
4	4.12	−30.1°

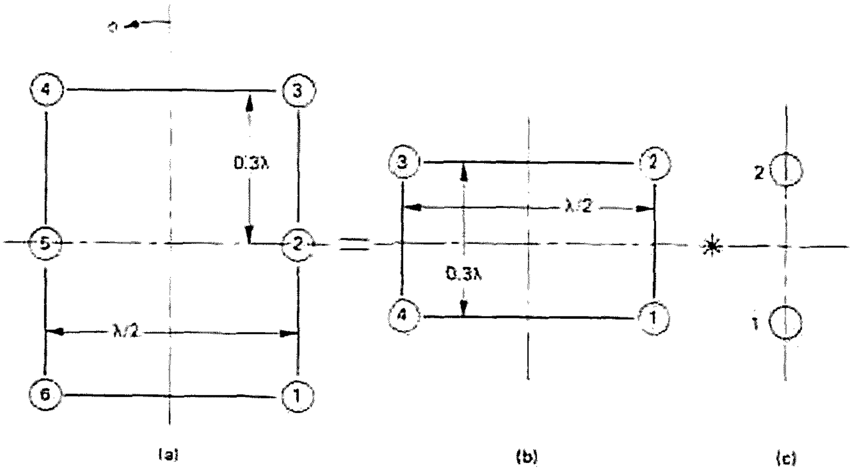

Figure 10-9 Rectangular array from convolution of rhombic and linear arrays: (*a*) six-element rectangular array; (*b*) rhombic array; (*c*) linear array.

We pick the single null of the two-element array at 135°. This null has symmetry about the axis of the array. With the first element at zero phase, we pick the element phase to cancel the first element voltage when $\theta = 135°$:

$$\text{Phase} = 180° - 360°(0.3)\cos 135° = 256.37°$$

When we convolute the two arrays, we obtain the feeding coefficients from Eq. (10-29). The elements in the center that result from two convolutions have summed feeding coefficients producing a six-element array.

Element	*Amplitude, dB*	*Phase, °*
1	0.00	0.0
2	8.13	−88.5
3	4.12	177.2
4	0.00	147.2
5	8.13	−124.3
6	4.12	−30.1

Figure 10-10 shows the patterns of the convolution. We obtain the six-element array pattern (Fig. 10-10*b*) by multiplication of the patterns of the individual subarrays (Fig. 10-10*a*).

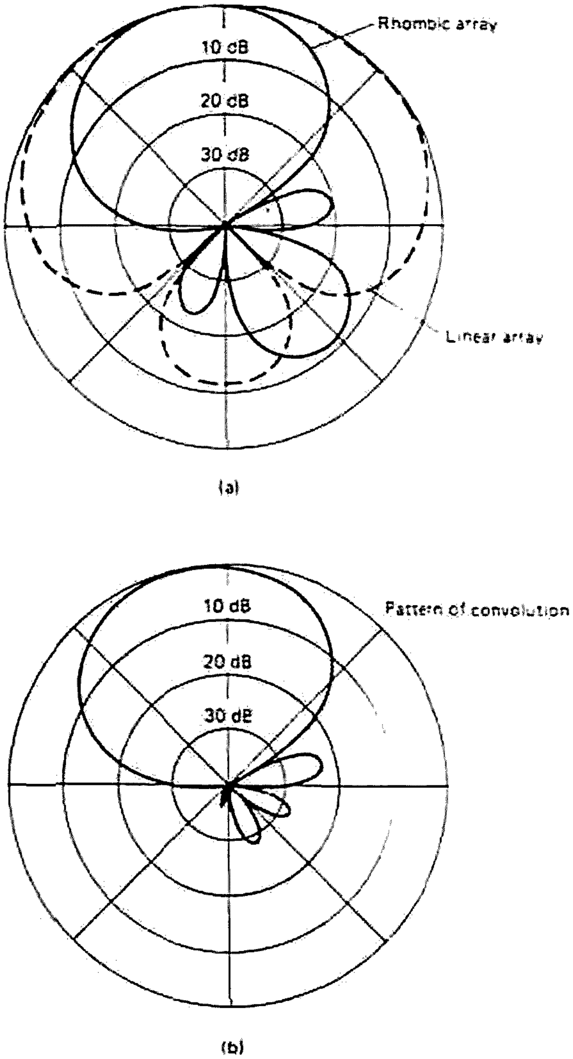

Figure 10-10 Patterns of the convolution of a rhombic and a linear array to form the six-element rectangular array of Fig. 10-9.

10-5 Zero Sampling of Continuous Distributions [12]

We sample continuous distributions, such as the Taylor line source, for large arrays. By using that method, we avoid the numerical difficulties of multiplying out long polynomials. When a small array samples an aperture distribution, its pattern fails to follow the pattern of the distribution. We improve the pattern by matching the zeros of the array to the distribution nulls.

The array ψ-space pattern repeats at 2π intervals, but the k-space pattern of the aperture has no repeat. We space elements by $\lambda/2$ to span the total ψ-space nonrepeating region. We then equate an array with $\lambda/2$ spacings to an aperture of the same length regardless of the actual spacings between elements. Since the array samples a continuous distribution, the aperture is Nd long, where d is the distance between array elements. That is, we consider the array element to be sampling $d/2$ on both sides of its location.

Consider the U-space pattern of a uniform aperture distribution

$$\frac{\sin \pi U}{\pi U}$$

The aperture zeros occur at integer values of U. The corresponding zeros of the uniformly fed array are

$$W_i = e^{j2\pi i/N} \qquad \text{where } i = 1, 2, \ldots, N-1$$

The Taylor distribution modifies the location of the zeros of the uniform distribution to U_i, and the sampled zeros of the array must move to follow this pattern.

$$W_i = e^{j2\pi U_i/N} \tag{10-33}$$

Example Given a Taylor line source with 30-dB sidelobes and $\bar{n} = 6$. Find the zeros of an array with 12 elements to sample the distribution.

The array spans 12/2 in U space. We find the zeros of the distribution from Sec. 6-5 and the angles of the array zeros from Eq. (10-33).

U_i	±1.473	±2.1195	±2.9989	±3.9680	±4.9747	6
ψ_i	±44.19°	±63.58°	±89.97°	±119.04°	±149.24°	180°

We multiply out the root form of the polynomial to find the array feeding coefficients.

The array has 30-dB first sidelobes. A straight sampling of the distribution gives an array whose sidelobes exceed 30-dB.

10-6 Shaped Beam Methods

The preceding methods seek the narrowest beamwidths for a given sidelobe level. Arrays can also produce shaped beams. We discussed the Woodward line source method for shaped beams in Sec. 6-9. We obtain good approximations by sampling the line source distribution with an array. Beyond sampling a line source, we can apply Fourier series to design an array directly. An array for a shaped beam must be much larger than is required for the beamwidth. The extra size of the array gives us the degrees of freedom necessary for beam shaping. Increasing the array size increases the match between the specified and the actual beam shape.

Because the array pattern is periodic in k space, we can expand the pattern in a Fourier series. The array pattern for a symmetrically fed array is given by either

$$f(\psi) = 1 + 2\sum_{n=1}^{m} \frac{I_n}{I_0} \cos \frac{2n\psi}{2} \qquad N \text{ odd} \tag{10-34}$$

or

$$f(\psi) = 2\sum_{n=1}^{m} \frac{I_n}{I_0} \cos \frac{(2n-1)\psi}{2} \qquad N \text{ even} \tag{10-35}$$

where $m = (N-1)/2$ (odd) or $m = N/2$ (even) with $\psi = kd \cos\theta + \delta$. Equations (10-34) and (10-35) are Fourier series expansions of the pattern in ψ space. The elements farthest from the centerline produce the highest harmonics in the series.

In an asymmetrically fed array, we express Eqs. (10-34) and (10-35) as a sum of exponential terms.

$$\begin{aligned} f(\psi) &= \sum_{n=-m}^{m} a_n e^{jn\psi} && N \text{ odd} \\ f(\psi) &= \sum_{n=1}^{m} a_n e^{j(2n-1)\psi/2} + a_{-n} e^{-j(2n-1)\psi/2} && N \text{ even} \end{aligned} \tag{10-36}$$

Suppose we have a desired pattern in k space given by $f_d(\psi)$. We expand it in an infinite Fourier series of the same form as Eq. (10-36) with $m = \infty$. We equate the first m coefficients of the two Fourier series to approximate the desired pattern. As by any Fourier series method, we solve for the coefficients by using the orthogonality of the expansion functions when integrated over a period.

$$a_n = \frac{1}{2\pi}\int_{-\pi}^{\pi} f_d(\psi) e^{-jn\psi}\, d\psi \qquad N \text{ odd} \tag{10-37}$$

$$\begin{aligned} a_n &= \frac{1}{2\pi}\int_{-\pi}^{\pi} f_d(\psi) e^{-j(2n-1)\psi/2}\, d\psi \\ & && N \text{ even} \\ a_{-n} &= \frac{1}{2\pi}\int_{-\pi}^{\pi} f_d(\psi) e^{j(2n-1)\psi/2}\, d\psi \end{aligned} \tag{10-38}$$

We find the array coefficients directly from the Fourier series coefficients.

Example Design a 21-element array with $\lambda/2$ spacings with a constant beam $2b$ wide centered in ψ space.
We use Eq. (10-37) to find the coefficients a_n

$$a_n = \frac{1}{2\pi}\int_{-b}^{b} e^{-jn\psi}\,d\psi = \frac{\sin nb}{\pi n}$$

Suppose the constant beam is 45° at broadside: $67.5^\circ \le \theta \le 112.5^\circ$. Then

$$b = \frac{360^\circ}{\lambda}\frac{\lambda}{2}\cos 67.5^\circ = 68.88^\circ$$

We can ignore the constant factor $1/\pi$ and expand to find the array coefficients.

n	a_n	*Amplitude, dB*	*Phase,* °
0	1.0000	0.00	0
±1	0.9328	− 0.60	0
±2	0.3361	−9.47	0
±3	−0.1495	−16.50	180
±4	−0.2488	−12.08	180
±5	−0.0537	−25.40	180
±6	0.1336	−17.48	0
±7	0.1209	−18.35	0
±8	−0.0240	−32.40	180
±9	−0.1094	−19.22	180
±10	−0.0518	−25.72	180

The method fails to some extent when we try it on arrays with spacings greater than $\lambda/2$. The integral does not cover the total visible region. We can, however, use it with spacings less than $\lambda/2$ with good results. As we increase the number of elements in the array, the match to the desired pattern improves. Of course, tapering the desired pattern reduces the higher harmonics and the subsequent need for more elements.

Example Suppose we want to scan the beam of the 21-element array with $\lambda/2$ spacings to 60° with a 45° beamwidth.
The beam edges are 37.5° and 82.5°. We could find the coefficients by directly integrating Eq. (10-37) with this requirement, but we can use δ, the progressive phase shift between elements, to simplify the problem. The beam edges in ψ space are

$$180^\circ\cos(37.5^\circ) + \delta \qquad \text{and} \qquad 180^\circ\cos(82.5^\circ) + \delta$$

$$142.8^\circ + \delta \qquad\qquad 23.49^\circ + \delta$$

We pick δ to center the beam in ψ space.

$$b = 142.8^\circ + \delta \qquad -b = 23.49^\circ + \delta$$

On solving, we have $\delta = -83.15^\circ$ and $b = 59.65^\circ$. We use the formula $\sin(nb)/\pi n$ to find the coefficients of the array and then add the progressive phase shift through the array. Figure 10-11 shows the array pattern.

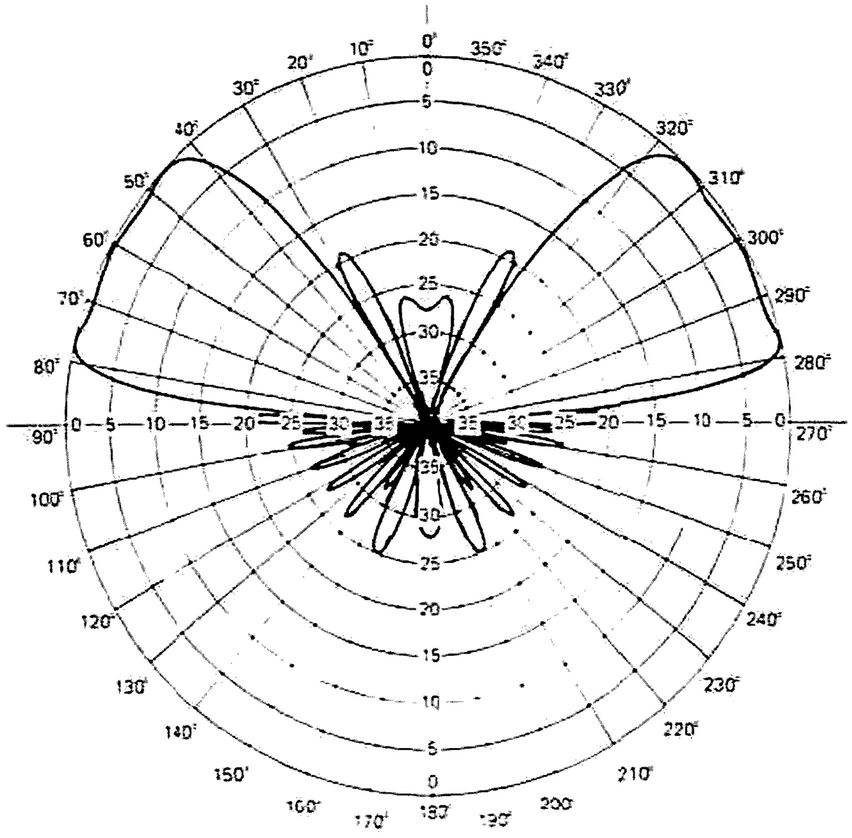

Figure 10-11 Twenty-one-element array designed by the Fourier series method to scan to 60° with a 45° beamwidth.

When we scan the beam to end fire, we must account for the symmetry about $\theta = 0°$. Because we limit the spacings to less than $\lambda/2$ to prevent grating lobes, we have an unspecified region of ψ space that we can choose in any convenient manner.

Example Design a 21-element end-fire array with a 90° beamwidth and 0.30λ spacings.

For an end-fire array we pick $\delta = -kd = -108°$. This places the edge of the visible region on the ψ-space origin. We are free to specify the invisible region that will be included in the integral [Eq. (10-37)]. We specify the invisible region as the mirror image of the portion in the visible region. We solve for b.

$$-b = 360°(0.3)\cos(45°) - 108° = -31.63°$$

We use the sin $(nb)/\pi n$ formula to find the array coefficients. We must then apply the progressive phase shift δ to the coefficients obtained to get the proper phase to scan to end fire.

REFERENCES

1. S. A. Schelkunoff, "A Mathematical Theory of Linear Arrays," *Bell System Tech. J.*, vol. 22, 1943, pp. 80–107.
2. J. Kraus, *Antennas*, McGraw-Hill, New York, 1950, p. 69.

3. C. L. Dolph, "A Current Distribution for Broadside Arrays which Optimizes the Relationship between Beamwidth and Sidelobe Level," *Proc. IRE*, vol. 34, no. 6, June 1946, pp. 335–348.
4. R. S. Elliott, "Beamwidth and Directivity of Large Scanning Arrays," *Microwave J.*, vol. 6, no. 12, December 1963, pp. 53–60.
5. R. H. DuHamel, "Optimum Patterns for Endfire Arrays," *Proc. IRE*, vol. 41, no. 5, May 1953, pp. 652–659.
6. W. L. Weeks, *Antenna Engineering*, McGraw-Hill, New York, 1968, p. 101.
7. C. J. Drane, "Useful Approximations for the Directivity and Beamwidth of Large Scanning Dolph-Chebyschev Arrays," *Proc. IRE*, vol. 56, no. 11, November 1968, pp. 1779–1787.
8. F. I. Tseng and D. K. Cheng, "Optimum Scannable Planar Arrays with an Invariant Sidelobe Level," *Proc. IRE*, vol. 56, no. 11, November 1968, pp. 1771–1778.
9. B. D. Steinberg, *Principles of Aperture & Array System Design*, Wiley, New York, 1976, p. 30.
10. D. K. Cheng, *Analysis of Linear Systems*, Addison-Wesley, Reading, Mass., 1959, p. 237.
11. S. R. Laxpati, "Planar Array Synthesis with Prescribed Pattern Nulls," *IEEE Trans. Antennas Propagat.*, vol. AP-30, no. 6, November 1982, pp. 1176–1183.
12. R. S. Elliott, "On Discretizing Continuous Aperture Distributions," *IEEE Trans. Antennas Propagat.*, vol. AP-25, no. 5, September 1977, pp. 617–621.

CHAPTER 11

TRAVELING WAVE ANTENNAS

Line sources dominate the study of traveling wave antennas. We use surface wave structures to radiate end-fire beams and leaky wave structures to radiate beams at an angle to the axis of the line source. In both cases there are planar configurations that have their uses. We combine leaky wave line source radiators, such as slotted rectangular waveguides, into planar arrays, but the line source remains the building block.

We make traveling wave antennas from structures that guide waves. Surface wave structures bind the power near the transmission line and radiate from discontinuities such as bends or dimensional changes. In some cases we analyze the surface wave as radiating throughout its extent on the transmission line. Both methods provide insight. Leaky wave antennas carry waves internally, as a waveguide does, and radiate at openings that allow power to escape. The radiation mechanism differs in the two cases, but we use similar mathematics to describe antennas of both types. We may have trouble distinguishing the radiation mode because the structures may be similar. With small changes in structure, some antennas can radiate in either mode. We separate traveling wave antennas from other antennas by the presence of a wave that is traveling along the structure and has most of its power propagating in a single direction.

We divide antennas by their structure: line and planar. We usually analyze planar structures as being infinite in the direction normal to the wave propagation. Similarly, we usually ignore the diameter of line sources in a first-order analysis. The diameter is important for determining the mode structure, but we calculate patterns based on a thin line source. The width of a planar structure determines the pattern beamwidth in that plane. Increasing the diameters of the rods of line sources will decrease the pattern beamwidth and increase gain, but the effect is secondary. Only when we include the diameter can we make the transition to aperture-type structures considered to be radiating from the end.

We must consider unusual transmission line structures in this chapter. Properly designed dimensions provide the proper phase velocity to establish a single end-fire beam for slow wave antennas or to point the beam of a leaky wave antenna. We calculate some of the dimensions by analysis (an ever-expanding list), but we can also measure the velocities and leakage and proceed to design.

11-1 General Traveling Waves

A wave traveling in a single direction has a field representation

$$E = E_0(z)e^{-jkPz} \tag{11-1}$$

where z is the direction of propagation, k is the free-space propagation constant (wave number) $2\pi/\lambda$, and P is the relative propagation constant. $E_0(z)$ describes the amplitude variation.

$$\begin{aligned} &P > 1 \qquad \text{surface waves} \\ &P < 1 \qquad \text{leaky waves} \end{aligned} \tag{11-2}$$

For a planar structure in the YZ plane, we consider separable distributions.

$$E = E_0(z)E_1(y)e^{-jkPz}$$

We find the pattern from

$$f = \int_0^L \int_{-a}^{a} E_0(z)E_1(y)e^{-jkPz}e^{jk_z z}e^{jk_y y}\,dz\,dy \tag{11-3}$$

where $k_z = k\cos\theta$. Similarly, for circular distributions we have

$$E = E_0(z)E_1(\phi_c)e^{-jkPz}$$

and

$$f = \int_0^L E_0(z)e^{-jkPz}e^{jk_z z}\,dz \int_0^{2\pi} E_1(\phi_c)ae^{jka\sin\theta\cos(\phi-\phi_c)}\,d\phi_c \tag{11-4}$$

where a is the radius. The second integral must include vector dot products to project the ring aperture fields onto the far-field polarizations (see Sec. 7-2). We consider only the term along the z axis, and we can consider the effect of the other coordinate separately. The pattern response becomes

$$f = \int_0^L E_0(z) e^{-jkz(P-\cos\theta)}\,dz \tag{11-5}$$

We use the results of Chap. 6 with these separable distributions. Maximum gain comes from a uniform distribution reduced by the amplitude taper efficiency for tapered distributions. In Eq. (11-3) the y-axis distribution and size determine the gain factor of the product for aperture area. Equation (11-4) has a separable ϕ distribution that separates directivity into a product. We will ignore these factors for now and concentrate on the z-axis pattern and associated directivity. Linear-rod antennas have increased directivity for dipole ϕ distributions and increased radii.

A traveling wave with a uniform distribution has a pattern response

$$\frac{\sin(\psi/2)}{\psi/2} \qquad \text{where } \psi = kL(P - \cos\theta) \tag{11-6}$$

for θ measured from the z axis. The y or ϕ distribution determines the pattern in the other coordinate. For $P > 1$, a slow wave, the beam peak approaches $\theta = 0$ for $P \to 1$. The length bounds P for an end-fire pattern maximum. Leaky waves, $P < 1$, have a pattern peak when $P = \cos\theta$ or

$$\theta_{\max} = \cos^{-1} P \tag{11-7}$$

The pattern peak approaches end fire ($\theta = 0$) as $P \to 1$. By increasing P beyond 1, the directivity increases and reaches maximum value for a given P depending on the length [1]

$$P = 1 + \frac{0.465}{L} \tag{11-8}$$

Equation (11-8) is the Hansen and Woodyard criterion for increased directivity of a long end-fire structure commonly approximated by [2]

$$P = 1 + \frac{1}{2L} \tag{11-9}$$

The phase increase of 180° [Eq. (11-9)] along the length gives the maximum directivity for a long structure with a uniform distribution. The amplitude distribution for most surface wave devices ($P > 1$) peaks near the input. The tapered distribution reduces the gain by the amplitude taper efficiency [Eq. (6.14)]. We must reduce the relative propagation constant from that given by Eq. (11-8) depending on the length [3]

$$P = 1 + \frac{1}{RL} \tag{11-10}$$

where $R = 6$ at $L = \lambda$, diminishing to 3 from $L = 3\lambda$ to $L = 8\lambda$ and tapering to 2 [Eq. (11-9)] at $L = 20\lambda$. Zucker [4] uses $R = 6$ for the amplitude, which peaks by 3 dB at the input for all lengths. Equations (11-8) and (11-10) give designs with only small differences in gain.

The value of P controls one edge of the visible region. Setting $P = 0$ centers the visible region about $\psi = 0$. End fire occurs at $P = 1$. As we increase P beyond 1, the beam peak of the distribution in ψ space moves into invisible space and the sidelobe level increases. A progression of sidelobes become the beam peaks as P increases. Since the amplitude difference between sidelobes decreases as the sidelobe number increases, the sidelobe level of the pattern increases as the pattern degrades because P increases beyond the value given by Eq. (11-9).

Figure 11-1 shows the effects on directivity of varying P on an axisymmetrical traveling wave antenna with a uniform amplitude distribution. For

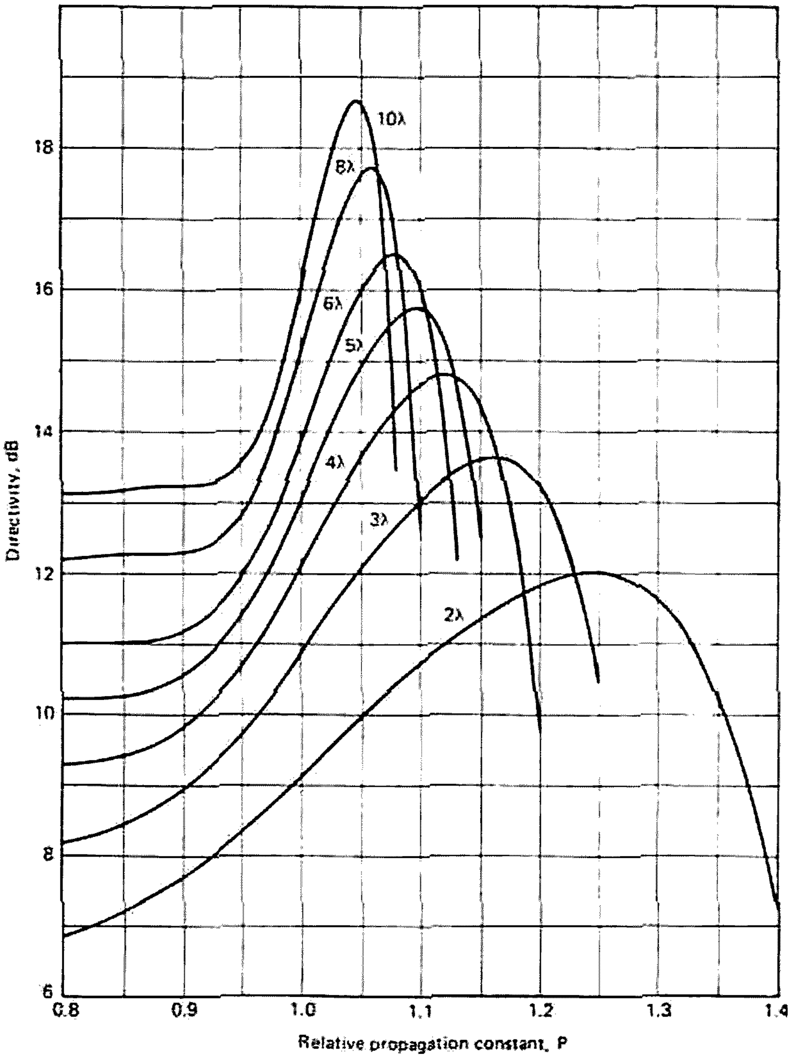

Figure 11-1 Directivity of axisymmetrical uniform distribution traveling wave.

broadside radiation ($P = 0$) and for P near end fire the directivity is a constant value with scan:

$$\text{Directivity} = \frac{2L}{\lambda} \tag{11-11}$$

When the broadside conical beam is scanned until the cone joins into a single end-fire beam, the directivity increases. For end fire, $P = 1$:

$$\text{Directivity} = \frac{4L}{\lambda} \qquad \text{end fire} \tag{11-12}$$

The directivity peaks for P given by Eq. (11-8):

$$\text{Directivity} = \frac{SL}{\lambda} \tag{11-13}$$

L/λ	2	4	6	10	20
S	7.92	7.58	7.45	7.33	7.25

Figure 11-2 is a plot of the maximum directivity of end-fire structures versus length. For the case $P = 1$, Eq. (11-12) gives the directivity on the curve. The Hansen and Woodyard criterion increases the directivity shown in Fig. 11-2 for an infinitesimal-diameter structure. The finite diameter of the helical wire antenna in the axial mode increases the directivity over that for the Hansen and Woodyard increased directivity criterion. The hybrid mode with its linear polarization has a dipole null normal to the traveling

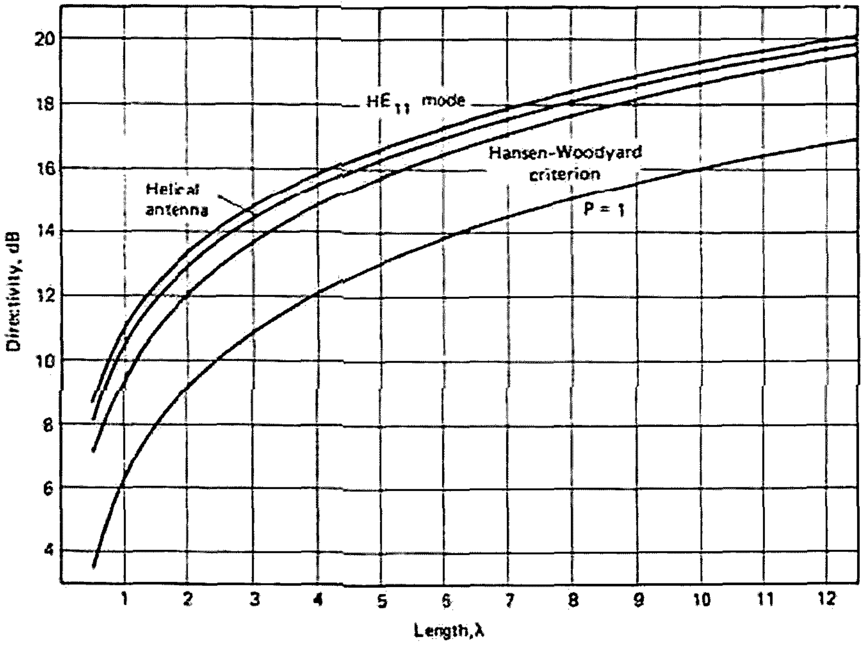

Figure 11-2 Directivity of end-fire traveling wave antenna.

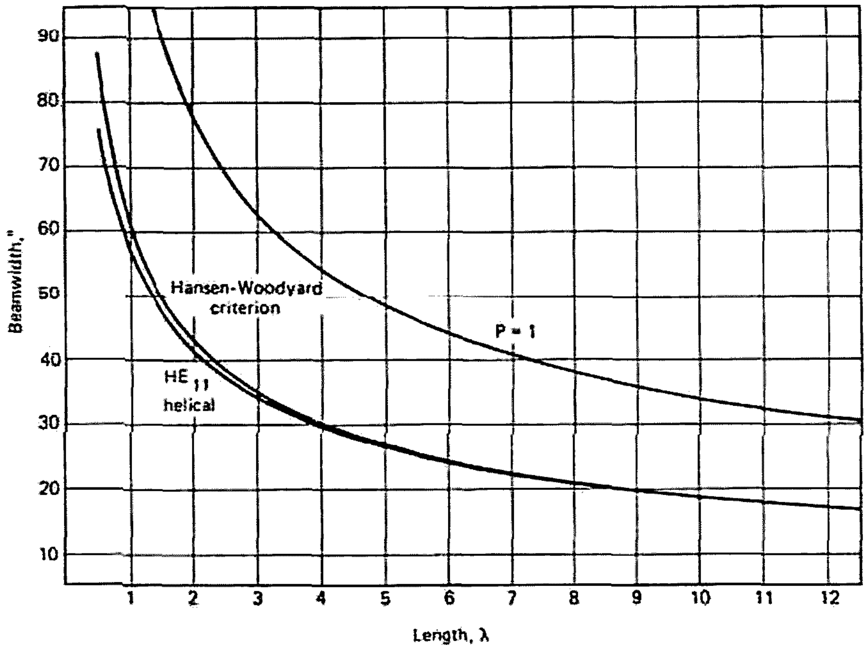

Figure 11-3 Beamwidth of traveling wave end-fire antenna.

wave axis whose elemental pattern increases directivity. Figure 11-3 is a plot of the corresponding beamwidths of those structures. Figure 11-2 establishes an upper bound to the possible directivity of a small-diameter end-fire traveling wave structure of given length.

Slow Wave A slow wave exists on an open transmission line structure. It binds the wave by slowing a passing wave and bending it in the direction of the structure. In the same manner a lens bends waves toward regions of higher index of refraction (increased slowing). We designate x as the direction normal to a planar structure and the radial coordinate ρ as the direction normal to the cylindrical slow wave structure. The relation between propagation constants in various directions is found in any electromagnetics text [5].

$$k_z^2 + k_x^2 = k^2 \qquad \text{or} \qquad k_z^2 + k_\rho^2 = k^2 \tag{11-14}$$

Since x (or ρ) is unbounded, the waves must attenuate exponentially from the surface.

$$\alpha = jk_x \qquad \text{or} \qquad \alpha = jk_\rho \tag{11-15}$$

The z-directed propagation constant becomes

$$k_z^2 = k^2 + \alpha^2 = P^2k^2$$

where

$$P = \sqrt{1 + \frac{\alpha^2}{k^2}} = \sqrt{1 + \left(\frac{\lambda\alpha}{2\pi}\right)^2} \tag{11-16}$$

P, the relative propagation constant, becomes a measure of the wave binding to the surface. We rearrange Eq. (11-16):

$$\alpha = \frac{2\pi}{\lambda}\sqrt{P^2 - 1}\ (\text{nepers}/\lambda) = 8.63\frac{2\pi}{\lambda}\sqrt{P^2 - 1}\,(\text{dB}/\lambda)$$

As P increases, the wave is more closely bound to the surface. Figure 11-4 is a plot of the distances of constant-field contours versus P. The fields fall off rapidly from the surface. For $P \rightarrow 1$, the slow-wave structure only diffracts passing plane waves without capturing the power. This is the sense of a cutoff frequency for the structure.

Most surface wave antennas consist of three regions. The feed region launches the wave on the structure with P between 1.2 and 1.3 [4]. The structure tapers until P suitable for the length is reached. We design for a given phase shift along the entire length. For example, a long antenna would be designed so that the wave on the structure has an excess phase shift of 180° [Eq. (11-9)] over the traveling wave in free space. Near the end we sometimes taper the structure to reduce the end reflection given approximately by [4]

$$P^2 - 1 \qquad \text{power}$$

This end taper can be quite short, and good results will be achieved with it.

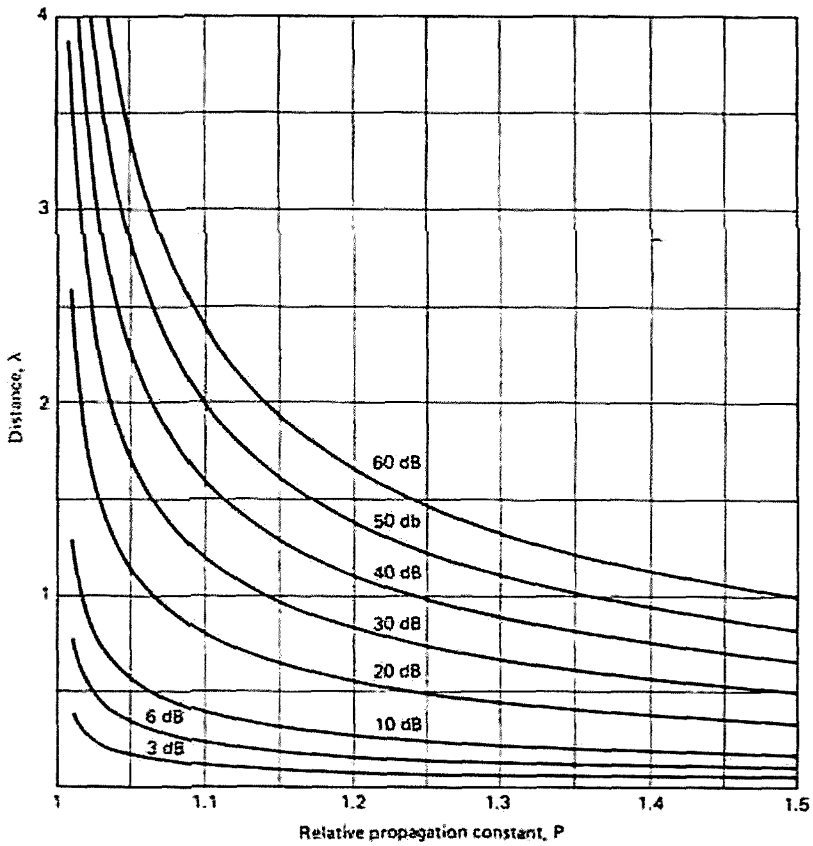

Figure 11-4 Constant-field contours off the surface of a surface wave structure.

Fast Waves (Leaky Waves Structure) Only closed structures, such as waveguides, support fast waves. An open structure requires a negative α [Eq. (11-16)] for fast waves, which implies an exponentially increasing wave away from the structure. The structure soon radiates all its power and no longer guides the wave. By limiting α, the leakage, we can extend the length of the radiating structure. We include the attenuation due to leakage in the z-axis propagation constant, in general, but we ignore it when α is small.

$$\theta_{\max} = \cos^{-1}\frac{k_z}{k}$$

Example A rectangular waveguide has $k_x = 2\pi/2a$ for the TE_{10} mode, where a is the guide width. We find the z-directed propagation constant

$$k_z = \sqrt{k^2 - \left(\frac{\pi}{a}\right)^2}$$

which gives us

$$P = \sqrt{1 - \left(\frac{\lambda}{2a}\right)^2} = \cos\theta_{\max}$$

The waveguide propagation constant determines the direction of radiation from a traveling wave leaking out of the guide at a slow rate. We find the guide width to give radiation in a given direction from

$$a = \frac{\lambda}{2\sqrt{1-\cos^2\theta_{\max}}}$$

11-2 Long Wire Antennas

One of the simplest traveling wave antennas consists of a terminated wire antenna. A standing wave can be divided into two waves traveling in opposite directions. By terminating the wire, we eliminate or reduce the reflected wave and its radiation. The uniform current traveling on a wire is given by

$$I = I_0 e^{-jkPz}$$

We insert this current into Eq. (2-4) to find the magnetic vector potential, and we use Eq. (2-1) to find the electric field. The resulting radiation intensity is

$$U = \frac{\eta|I_0|^2}{(2\pi)^2}\sin^2\theta\left[\frac{\sin\left[kL(P-\cos\theta)/2\right]}{P-\cos\theta}\right]^2 \tag{11-17}$$

Equation (11-17) has two pattern factors: $\sin^2\theta$ is the pattern of an incremental current element, and the second pattern is Eq. (11-6) for the uniform distribution. The null at $\theta = 0$ due to the current element pushes the beam peak off the axis of the traveling wave. Figure 11-5 shows the

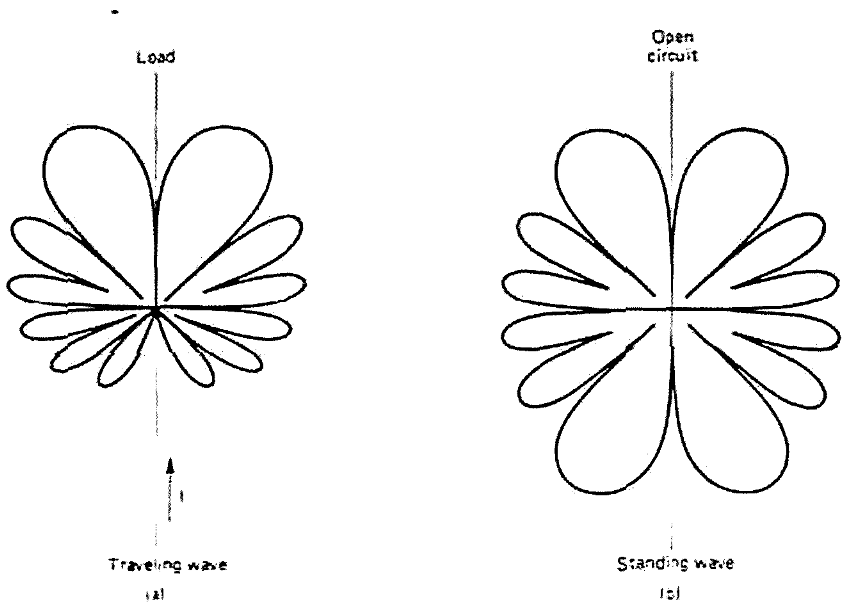

Figure 11-5 Patterns of long wire antennas (3λ): (*a*) traveling wave: (*b*) standing wave.

patterns of traveling wave and standing wave currents using a 40-dB scale for $L = 3\lambda$. The patterns are axisymmetrical about the wire. Table 11-1 gives the beam peak direction and the directivity of the pattern for various lengths. The beam peak approaches the wire as the length increases.

If we remove the termination, a wave reflects from the end and forms a beam in the other direction (Fig. 11-5*b*). The small backlobes that are due to the forward traveling wave have little effect on the main beam from the backward traveling wave.

Beverage Antenna [6] The Beverage antenna consists of a wire strung horizontally a fraction of a wavelength over ground (Fig. 11-6). The antenna must be fed relative to ground, and the ground plane image of the horizon-

TABLE 11-1 Characteristics of a Traveling Wave Current on a Straight Wire

Length, λ	Directivity, dB	Beam peak, °	Length, λ	Directivity, dB	Beam peak, °
0.5	3.55	64.3	5.5	11.32	20.2
1.0	5.77	47.2	6.0	11.61	19.4
1.5	7.06	38.9	6.5	11.88	18.7
2.0	8.00	33.7	7.0	12.13	17.9
2.5	8.71	30.1	7.5	12.37	17.4
3.0	9.30	27.5	8.0	12.59	16.8
3.5	9.81	25.2	8.5	12.80	16.3
4.0	10.25	23.8	9.0	13.00	15.8
4.5	10.64	22.3	9.5	13.18	15.4
5.0	11.00	21.3	10.0	13.35	15.0

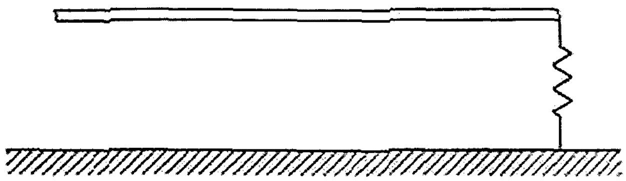

Figure 11-6 Beverage antenna.

tally polarized antenna cancels much of the far-field pattern of the antenna. Table 11-1 gives the length for a given takeoff angle for sky waves. The antenna can have good directivity but poor efficiency, since a great deal of the power is absorbed by the load.

We make a vertically polarized Beverage antenna by elevating the feed point on a tower and tilting the wire to the load on the ground. The beam due to the wire and its image adds to a horizontal beam when the wire tilt equals the beam direction given by Table 11-1 for a given length. The vertically polarized antenna needs a better ground plane than the horizontally polarized antenna because the ground (earth) reflects horizontally polarized waves better than it reflects vertically polarized waves. We may vary the tilt angle to produce takeoff angle, but the beams of the wire and its image may no longer add. The tilted antenna presents a feed problem because it is fed relative to ground at an elevated point.

V Antenna We separate two Beverage antennas by an angle and feed from a balanced line to form a V antenna. When the separation angle is twice that given by Table 11-1, the beam peaks of the individual wires add. The balanced line input eases the feed problem of the Beverage antenna, since the antenna does not feed against ground.

We place the input on a single insulating tower and stretch sloping wires to ground (Fig. 11-7) to produce a beam. The beam is horizontal when the tilt angle equals the beam peak angle of Table 11-1. By varying the tilt angle, we change the elevation angle of the beam. The balanced feed produces horizontal polarization and reduces the requirement for a ground

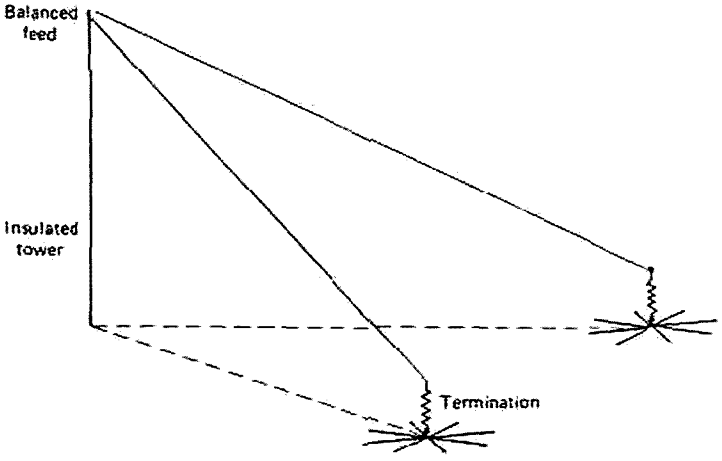

Figure 11-7 Sloping V antenna.

screen. The antenna impedance is about 800 Ω. The pattern contains high sidelobes with an overall low efficiency. The bandwidth of the terminated antenna approaches an octave.

We can also make an unterminated V antenna. One method is to connect λ/4 rods, which extend in the same direction as the V elements, to the normally grounded end of the loads on the V antenna [7]. The open-circuited quarter-wavelength lines reflect a short circuit to the loads over a limited bandwidth. The terminating resistors reduce the backlobe from that of the unterminated V antenna while eliminating the need for grounding the loads. In a second design a moment method solution is used to find the angle between the elements to optimize directivity of a beam halfway between the directions of the expanding elements [8]. The angle between the elements is fitted to a polynomial

$$\alpha = -149.3\left(\frac{L}{\lambda}\right)^3 + 603.4\left(\frac{L}{\lambda}\right)^2 - 809.5\left(\frac{L}{\lambda}\right) + 443.6 \quad \text{(degrees)}$$

for $0.5 \le L/\lambda \le 1.5$

or

$$\alpha = 13.36\left(\frac{L}{\lambda}\right)^2 - 78.27\left(\frac{L}{\lambda}\right) + 169.77 \qquad (11\text{-}18)$$

for $1.5 \le L/\lambda \le 3.0$

where L is the length of each arm. The maximum directivity at α given by Eq. (11-18) is

$$\text{Directivity} = 2.94\left(\frac{L}{\lambda}\right) + 1.15 \quad \text{dB} \qquad (11\text{-}19)$$

Rhombic Antenna [9] The rhombic antenna consists of two V antennas. The second V antenna brings the two sides back together and makes possible the connection of the balanced lines through a single terminating resistor (Fig. 11-8). Using a single terminating resistor eliminates the grounding

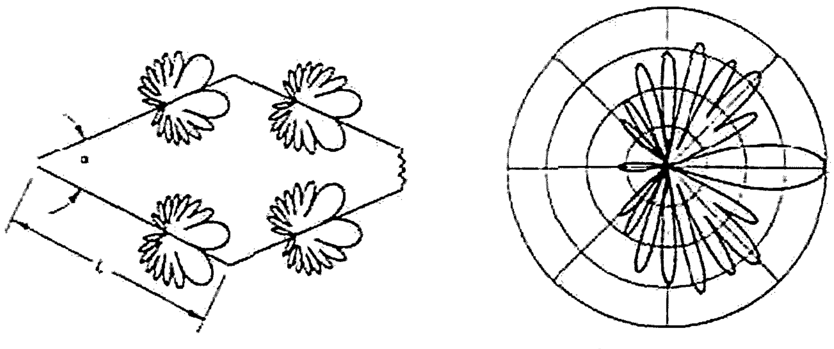

Individual patterns

Composite pattern

Figure 11-8 Rhombic antenna.

problem of V antenna loads when the antenna transmits. The load absorbs up to one-half of the transmitter power.

Figure 11-8 shows the patterns of the individual wire radiators on the elements and the combined pattern in the horizontal plane for the antenna in free space. The pattern has high sidelobes. The peak pattern output occurs when the angle α is approximately twice the peak radiation angle of the individual wires. Table 11-2 lists the angle α for the maximum output for a given elevation angle when we mount the antenna parallel with the earth.

We raise the antenna a height H over ground to control the beam elevation angle

$$H = \frac{\lambda n}{4 \sin \Delta} \qquad n = 1, 3, 5, \ldots \tag{11-20}$$

where Δ is the elevation angle measured from the horizon and n is an odd integer. The elevated beam forms from the combination of the antenna and its ground image radiations. Because the antenna radiates horizontal polarization, the requirement for a ground plane screen is minimal.

The terminating resistor should be about 600 Ω. The input impedance varies from 600 to 900 Ω over an octave bandwidth, and the actual value depends on frequency, height, and load resistor. We can use multiple wires that spread apart at the corners to reduce the impedance variation over the band and increase the power-handling capability of smaller wires.

We can build an inverted V antenna by mounting half a rhombic antenna over a ground plane. We use a single insulated tower; and by controlling the

TABLE 11-2 V Angle α for Maximum Output of a Rhombic Antenna [9]

Arm length, L/λ	Elevation angle, °						
	0	5	10	15	20	25	30
	V angle for maximum radiation, °						
1.5	90	89	88	86	84	80	76
2.0	77	76	75	73	70	66	60
2.5	69	68	66	64	60	56	48
3.0	62	61	60	57	52	48	40
3.5	58	57	55	52	47	42	34
4.0	54	53	50	47	42	36	28
4.5	51	50	47	43	38	32	24
5.0	48	47	44	40	35	28	20
6.0	44	43	40	36	30	22	14
7.0	41	38	36	32	25	18	8
8.0	38	37	34	28	22	14	
10.0	34	32	29	23	16		
15.0	28	26	22	15			
20.0	24	22	17				

wire tilt angle with respect to ground, we combine the beams for the wire and its ground image into a horizontal beam. The inverted V places both the input and the terminating load on the ground. Because the antenna is vertically polarized, we must provide a good ground screen. In outdoor applications we ground and feed the antenna through a transformer to give some lightning protection and to match the high input impedance of the antenna.

11-3 Yagi-Uda Antennas [10]

The Yagi-Uda antenna uses mutual coupling between standing wave current elements to produce a traveling wave unidirectional pattern. It uses parasitic elements around the feed element for reflectors and directors to produce an end-fire beam. Because the antenna can be described as a slow structure [11], the directivity of a traveling wave antenna (Fig. 11-2) is bounded when we include the directivity due to the element pattern. Maximum directivity depends on length along the beam direction and not on the number of elements.

Consider two broadside coupled dipoles. We describe the circuit relation between them by a mutual impedance matrix

$$\begin{bmatrix} V_1 \\ V_2 \end{bmatrix} = \begin{bmatrix} Z_{11} & Z_{12} \\ Z_{12} & Z_{22} \end{bmatrix} \begin{bmatrix} I_1 \\ I_2 \end{bmatrix} \tag{11-21}$$

where the diagonal elements of the matrix are equal from reciprocity. If we feed one element and load the other, we can solve for the input impedance of the feed antenna

$$Z_{in} = \frac{V_1}{I_1} = Z_{11} - \frac{Z_{12}^2}{Z_{22} + Z_2} \tag{11-22}$$

where Z_2 is the load on the second antenna. We short the second antenna ($Z_2 = 0$) to maximize the induced standing wave current and eliminate power dissipation:

$$Z_{in} = Z_{11} - \frac{Z_{12}^2}{Z_{22}} \tag{11-23}$$

The mutual impedance between broadside coupled dipoles (Z_{12}) approaches the self-impedance (Z_{11}) as we move the dipoles close together and cause the input impedance [Eq. (11-23)] to approach zero.

The second equation of Eq. (11-21) for a shorted antenna relates the currents in the two dipoles:

$$0 = Z_{12} I_1 + Z_{22} I_2 \qquad \text{or} \qquad I_2 = -\frac{Z_{12} I_1}{Z_{22}} \tag{11-24}$$

Since $Z_{12} \approx Z_{22}$, the current in the shorted dipole is opposite the current in the feed element. The radiation from the induced current reduces the fields around the dipoles.

Given the current on the parasitic element, we solve for the far field by array techniques. When the elements are spaced a distance d, with the parasitic element on the z axis and the feed element at the origin, the normalized pattern response is

$$E = 1 + I_r e^{j(kd\cos\theta+\delta)}$$

where $I_r e^{j\delta} = I_2/I_1$ is the current of the parasitic element relative to the feed element. If we take the power pattern difference between the pattern at $\theta = 0$ and $\theta = 180°$, we get

$$|\Delta E|^2 = -2I_r \sin\delta \sin kd \tag{11-25}$$

Case 1. $\delta = 180°$, $\Delta E = 0$, and we have equal pattern levels in both directions with a null at $\theta = 90°$.

Case 2. $180° < \delta \le 360°$, $\Delta E > 0$. The parasitic element is a director, and the pattern in its direction will be higher ($\theta = 0$) than at $\theta = 180°$.

Case 3. $0° \le \delta < 180°$, $\Delta E < 0$. The parasitic element is a reflector because the pattern away from it ($\theta = 180°$) is higher than at $\theta = 0°$. We look at the phase of the relative currents to determine whether a parasitic element is a director or reflector.

The mutual impedance between dipoles has been reduced to equations for a variety of configurations [12–16]. By use of these equations, Fig. 11-9 was generated to show the phasing between a half-wavelength dipole and a parasitic dipole as the length and spacing are varied. A parasitic dipole of given length can be either a director or reflector for different element spacings. Generally, a director is somewhat shorter and a reflector somewhat longer than the feed element. If we reduce the length of the feed element or increase the element's diameter, the dividing line between a director and reflector shifts upward. Figure 11-9 also shows the decreased element length at the transition point for further spaced elements.

Figure 11-10 illustrates a three-element Yagi-Uda dipole antenna having one reflector and one director around the feed element. The design is a compromise between various characteristics. With a 50-Ω source its response is as follows:

Gain = 7.6 dB
Front/back = 18.6 dB
Input impedance = $33 - j7.5$
VSWR = 1.57 (50-Ω system)
E-plane beamwidth = 64°
H-plane beamwidth = 105°

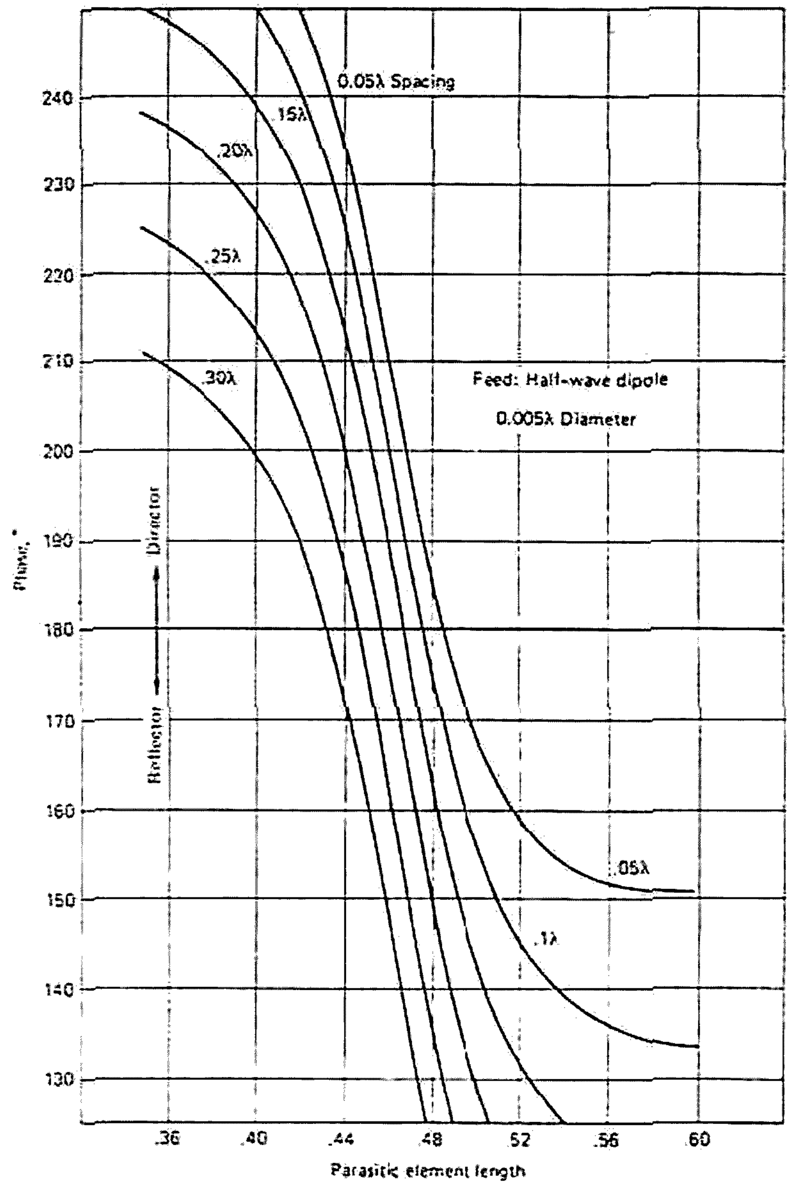

Figure 11-9 Phase of current on parasitic dipole relative to current on driven dipole.

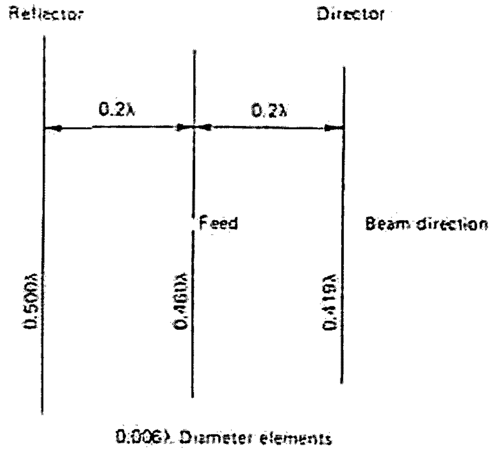

Figure 11-10 Three-element Yagi-Uda dipole antenna.

With input matching we could increase the gain by 0.2 dB. The 3-dB gain bandwidth is 15 percent and a 1-dB gain bandwidth is 10 percent. At the 3-dB band edges the F/B drops to 5.5 dB. As in many designs, the peak gain does not occur at the peak F/B. The gain rises by 0.2 dB to a 50-Ω source at a point 3 percent higher in frequency than the point of maximum F/B. The maximum gain with input impedance matching (8.6 dB) occurs at a point 7 percent above the center frequency. The dipole element pattern narrows the E-plane beamwidth and produces a null at 90° from boresight. The traveling wave alone forms the H-plane beam. A design to optimize the gain would have a phase progression along the elements to match Eq. (11-10) for short traveling wave antennas. The array of dipoles samples an aperture 0.6λ long. Figure 11-3 gives an H-plane beamwidth of about 80° for this optimum design. With only three elements we find difficulty in matching the phase distribution required and will produce a design with low F/B.

We analyze Yagi-Uda antennas by using the moment method [17]. Calculate the mutual impedance matrix

$$[V] = [Z][I] \tag{11-26}$$

The input voltage vector $[V]$ has only one nonzero term (the feed). By solving the linear equations (11-26), we find the currents at the base of each element. We assume a sinusoidal current distribution on each element, Eq. (4-1), and solve for the pattern response from the array of dipoles. We find the input impedance of the array by using the moment method; and by retaining the current levels on the dipoles for a known input power, we can calculate gain directly.

The moment method allows reasonably quick calculation of the antenna characteristics so that optimization techniques can be applied. Cheng and Chen [18, 19] use a perturbation technique that alternates between element spacings and lengths to find an optimum design with rapid convergence. One iteration of each produces the design. No optimization technique can assure that a global optimum can be found. Designs will converge to local maximums. By limiting the search variables, the method of Cheng and Chen avoids some local optimums. Most optimizations work at a single frequency and produce designs with high gains that fall off rapidly with increasing frequency. The wave relative propagation constant increases with frequency. The gain curves in Fig. 11-1 decrease rapidly after the peak point as the sidelobes increase. All traveling wave end-fire antennas follow this pattern.

Kajfez [20] developed a method for optimizing over a band of frequencies. His method is to reduce the peak gain while increasing the bandwidth and reducing some of the tolerance requirements. We fix the band limits at frequencies f_1 and f_2 and optimize a composite cost function containing both the average directivity and the ripple or deviation from the average. Maximize

$$C = D_{\text{avg}} - wd \tag{11-27}$$

where D_{avg} is the average directivity and d is the rms deviation of the directivity from D_{avg} over the band weighted by w.

$$D_{\text{avg}} = \frac{1}{f_2 - f_1}\int_{f_1}^{f_2} D(f)\,df$$

$$d = \left\{\frac{1}{f_2 - f_1}\int_{f_1}^{f_2}[D(f) - D_{\text{avg}}]^2\,df\right\}^{1/2} \tag{11-28}$$

$D(f)$ is the directivity function (a ratio, not dB). We vary w to stress either high directivity or design flatness. If w is made two or more times greater than the expected directivity, an optimization routine will design an antenna with a flat response. We calculate the integrals by using Gauss-Legendre quadrature, which requires only a few evaluations of the pattern response (5 to 8).

We usually use only one reflector element. More elements can be used, but they add little. The gain of a two-element pair—a feed dipole and a reflector dipole—rises with increasing separation in a broad peak starting about 0.15λ, peaking about 0.20λ, and falling slowly with greater spacing. The reflector primarily affects F/B. As we move it closer to the feed element, the impedance level of the antenna drops. The response of the antenna is less sensitive to the diameter of the reflectors compared with the director diameters, and it requires smaller adjustments to the length to compensate the design for the change.

We add length to the antenna to increase gain by adding director elements. Length along the axis, not the number of elements, produces gain provided element currents are phased correctly. Beyond 0.3λ to 0.4λ spacings, the coupling drops and reduces possible control of the current phasings on the directors. Changing the diameters of directors requires changing the element lengths to retune the antenna.

In one design method computer optimization routines are used to vary the dimensions to optimize some cost function. The lengths of the feed and first director elements have the greatest effect on gain. If we use a gradient-type search, we find most of the design concentrated on varying those element lengths. In long antennas with many directors the elements far from the feed will be changed little from initial lengths by a gradient search. We can also adjust the lengths to match the current phasing of the elements to a distribution such as that given by Eq. (11-10). Manual tuning requires a retuning of the two elements closest to the feed and the feed element after tuning each director.

When adjusting the lengths to maximize bandwidth [Eqs. (11-27) and (11-28)], we should optimize gain to a given source impedance. We can optimize a single-frequency antenna to any reasonable impedance level and design a matching network, but broadband antennas may produce difficult matching network problems to achieve the design gain. A moment method gives us the peak gain to a conjugate matched source. To find the gain to a given source impedance Z_s, multiply the voltage gain by

$$\frac{2\sqrt{\mathrm{Re}\,(Z_l)\ \mathrm{Re}\,(Z_s)}}{|Z_l + Z_s|} \tag{11-29}$$

where Z_l is the antenna input impedance. Equation (11-29) allows optimizations to a given source impedance.

Table 11-3 gives the dimensions of an antenna designed by using Eqs. (11-27) and (11-28) for a maximum gain to a 50-Ω source [Eq. (11-29)]. The normalized frequency limits are 0.95 to 1.05 with a weighting w of 15 on the rms deviation d. Table 11-4 lists the calculated response of the antenna. Like many designs, gain falls off more rapidly on the high-frequency end. In this case maximum gain occurs at maximum F/B.

TABLE 11-3 Six-Element Yagi-Uda Dipole Antenna with 0.01λ-Diameter Elements

Element type	Element length, λ	Location along boom, λ
Reflector	0.484	0
Feed	0.480	0.250
Director	0.434	0.400
Director	0.342	0.550
Director	0.416	0.700
Director	0.400	0.850

TABLE 11-4 Normalized Frequency Response of Yagi-Uda Dipole Antenna of Table 11-3

Normalized frequency	Gain, 50-Ω source, dB	Max. gain, dB	F/B, dB	Input impedance, Ω		VSWR, 50-Ω source
0.90	4.8	6.3	1.4	29.6	−j45.2	3.36
0.92	7.0	7.7	3.6	32.5	−j30.8	2.29
0.94	8.4	8.7	6.5	39.3	−j19.6	1.65
0.96	9.0	9.2	9.9	42.7	−j13.2	1.39
0.98	9.4	9.5	14.4	39.5	−j 7.6	1.34
1.00	9.7	10.0	22.7	31.2	+j 2.8	1.61
1.02	9.5	10.6	21.1	22.0	+j19.8	2.70
1.04	8.1	11.1	12.2	15.2	+j42.5	5.79
1.06	5.5	10.8	7.2	12.9	+j69.1	11.41
1.08	2.5	8.9	3.7	16.0	+j97.2	15.20

Higher gains can be attained for six elements. Chen and Cheng [19] achieved 13.4 dB, but for a restricted bandwidth. We achieve bandwidth by limiting gain, and with each added element we can improve flatness at a higher gain level. Kajfez shows a nearly constant gain-bandwidth product for different designs. The gradient search method used in the design in Table 11-3 is sensitive to initial conditions. The search method will converge to a local maximum and miss the global maximum. The normal gradient search cannot escape a local optimum. A better design may be achieved by using another initial condition.

Table 11-5 lists the design of a 16-element Yagi-Uda dipole antenna. In this case the optimization routine was to manipulate elements 4 through 16 as a group to reduce the number of different-sized elements to four. This reduces the tooling cost and causes little loss in possible performance. Since the size of the last few directors has only a minor effect on the total gain, most of the time in an optimization routine is spent changing the elements around the driven dipole and only slowly changing those elements. We adjust the reflector, feed element, and first director to match into the uniform surface wave structure of equally spaced elements.

The frequency response, Table 11-6, has a peak gain equal to the value given by Fig. 11-2 for the hybrid mode and at this overall length. Like many Yagi-Uda dipole antennas, this antenna matches best to a low input impedance (30 Ω). The gain rises slowly below the resonant frequency of the antenna and falls rapidly for higher frequencies as predicted by Fig. 11-1, which shows gain versus relative propagation constant along a uniform surface wave structure.

The element diameter affects the optimum length of the Yagi-Uda dipole elements. A number of optimum Yagi-Uda dipole antennas of various overall lengths were built with different-diameter elements and adjusted to regain optimum performance [21]. Table 11-7 summarizes the length changes required of directors when their diameters are changed. Similarly, Table 11-8 lists the changes required for reflectors. Tables 11-7 and 11-8 require little or no change in the feeder element length to regain the optimum design. We can use the tables to modify element lengths when changing diameters.

TABLE 11-5 Sixteen-Element Yagi-Uda Dipole Antenna with 0.006λ-Diameter Elements

Element	Element length, λ	Element spacing, λ
Reflector	0.4836	0.2638
Feed	0.4630	0.2168
Director 1	0.4448	0.2390
Directors 2 to 13	0.4228	0.2838

TABLE 11-6 Normalized Frequency Response of 16-Element Yagi-Uda Dipole Antenna

Normalized frequency	Gain, 30-Ω source, dB	F/B, dB	Input impedance, Ω		VSWR, 30-Ω source
0.95	12.1	12.2	26.7	−j36.1	3.34
0.96	13.4	12.2	28.4	−j26.4	2.40
0.97	14.4	12.2	31.6	−j17.7	1.77
0.98	15.0	13.3	34.3	−j12.1	1.49
0.99	15.5	17.3	32.2	−j 7.3	1.28
1.00	15.9	35.1	27.0	j 3.4	1.17
1.01	15.2	15.6	27.3	j20.8	2.05
1.02	14.0	10.6	40.4	j33.0	2.61
1.03	13.7	11.8	36.0	j23.5	2.06
1.04	8.2	16.4	22.8	j51.5	5.77
1.05	5.4	4.7	54.1	j68.2	5.03

TABLE 11-7 Length Changes of Directors in a Yagi-Uda Dipole Antenna for Different Diameters [21]

Dipole diameter, λ	Dipole length change, λ	Dipole diameter, λ	Dipole length change, λ
0.001	0.030	0.008	0.006
0.0012	0.029	0.009	0.002
0.0015	0.027	0.010	0.000
0.002	0.025	0.012	−0.004
0.0025	0.023	0.015	−0.010
0.003	0.021	0.020	−0.018
0.004	0.017	0.025	−0.024
0.005	0.014	0.030	−0.029
0.006	0.011	0.040	−0.038
0.007	0.008		

TABLE 11-8 Length Changes of Reflectors in a Yagi-Uda Dipole Antenna for Different Diameters [21]

Dipole diameter, λ	Dipole length change, λ	Dipole diameter, λ	Dipole length change, λ
0.001	0.011	0.008	0.002
0.002	0.008	0.010	0.000
0.003	0.006	0.020	−0.003
0.004	0.005	0.030	−0.005
0.006	0.003	0.040	−0.006

TABLE 11-9 Length Changes to Increase Elements of a Yagi-Uda Dipole Antenna to Account for Boom Diameter [21]

Boom diameter, λ	Dipole length change, λ	Boom diameter, λ	Dipole length change, λ
0.002	0.0010	0.022	0.0158
0.004	0.0022	0.024	0.0173
0.006	0.0034	0.026	0.0189
0.008	0.0048	0.028	0.0205
0.010	0.0064	0.030	0.0220
0.012	0.0084	0.032	0.0236
0.014	0.0095	0.034	0.0252
0.016	0.0111	0.036	0.0265
0.018	0.0127	0.038	0.0283
0.020	0.0142	0.040	0.0299

Building these antennas established a required tolerance on the element lengths at 0.003λ. The boom supporting the elements also affects element length for optimum designs. Table 11-9 lists the required element length increases for a given boom diameter.

Example Find the length adjustment necessary when building the design of Table 11-5 with 0.002λ elements.

From Table 11-7 the length adjustment for 0.006λ is 0.010λ and the adjustment for 0.002λ-diameter elements is 0.025λ. We increase the lengths of the directors by the difference, 0.015λ. Similarly, from Table 11-8 we increase the reflector length by 0.005λ. For a boom diameter of 0.02λ we also increase the lengths of all the elements by 0.0142λ (Table 11-9).

Multiple-Feed Yagi-Uda Antennas We will further improve the response of Yagi-Uda antennas by direct feeding of more than one element. The convenience of Yagi-Uda antennas lies in the single feed point. With many feed points a log-periodic dipole antenna (Sec. 12-7) produces a wider band design. Figure 11-11 illustrates a four-element design with a crisscross feeder.

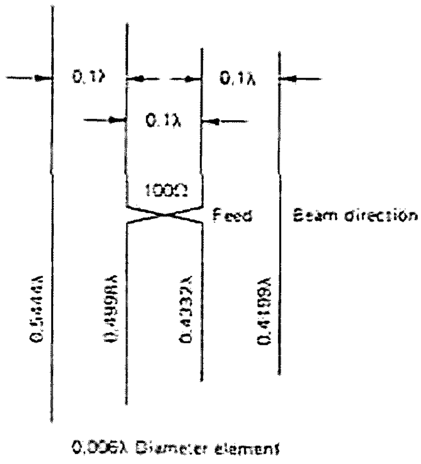

Figure 11-11 Multiple-feed Yagi-Uda dipole antenna.

TABLE 11-10 Normalized Frequency Response of Four-Element Yagi-Uda Dipole Antenna with a Crisscross Feeder between Two Elements (Fig. 11-11)

Normalized frequency	Gain, 50-Ω source, dB	F/B, dB	Input impedance, Ω		VSWR, 50-Ω source
0.90	7.0	12.1	30.1	$+j14.0$	1.82
0.92	7.1	17.5	42.6	$+j\ 4.0$	1.20
0.94	7.0	21.9	44.0	$-j\ 3.0$	1.15
0.96	6.9	25.9	43.9	$-j\ 5.8$	1.20
0.98	7.0	31.3	44.4	$-j\ 7.3$	1.22
1.00	7.0	53.0	45.2	$-j\ 9.4$	1.25
1.02	7.1	30.7	44.8	$-j13.5$	1.35
1.04	7.2	23.6	40.0	$-j18.8$	1.60
1.06	7.0	19.0	29.0	$-j20.5$	2.12
1.08	6.5	15.3	16.5	$-j14.2$	3.29
1.10	5.0	11.9	8.0	$-j\ 2.3$	6.30

Table 11-10 lists the calculated response of the antenna. The gain response is flat with good F/B and input VSWR over the band for a short antenna (0.3λ long). The crisscross feeder adds an additional 180° phase shift along the length to produce a backfire pattern from a fast wave.

The simple antenna of Fig. 11-12 uses only two dipole elements with a crisscross feed. This antenna, like many Yagi-Uda dipole antennas, matches best to a low-impedance (25-Ω) source. Although its gain and bandwidth (Table 11-11) are less than those of the four-element multiple-feed antenna, its bandwidth is better than that of a singly fed equivalent antenna. The length along the boom still determines the ultimate gain of the antenna, but the backfire crisscross feed improves the front-to-back ratio.

We can no longer use just Eq. (11-26), the matrix equation of mutual impedances, to analyze a multiple-feed antenna. We invert the mutual impedance matrix and add the 2 by 2 admittance matrices of the transmission line feeders between the dipole center point nodes.

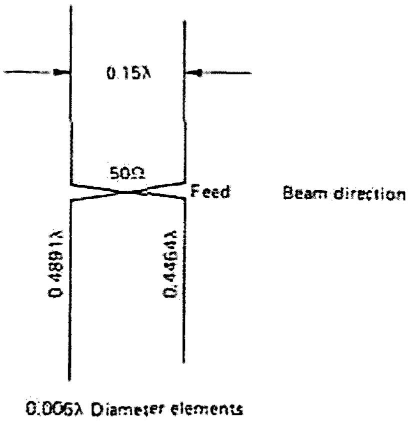

Figure 11-12 Dipole two-element backfire antenna.

TABLE 11-11 Normalized Frequency Response of Two-Element Crisscross-Fed Antenna

Normalized frequency	Gain, 25-Ω source, dB	F/B, dB	Input impedance, Ω	VSWR, 25-Ω source
0.95	5.0	13.1	12.8 $-j$ 1.6	1.96
0.96	5.2	14.8	13.6 $-j$ 0.5	1.84
0.97	5.4	17.0	14.4 $+j$ 0.8	1.74
0.98	5.6	20.0	15.2 $+j$ 2.3	1.67
0.99	5.8	24.6	16.0 $+j$ 3.9	1.62
1.00	5.9	34.1	17.0 $+j$ 5.9	1.61
1.01	6.0	29.0	18.2 $+j$ 8.2	1.64
1.02	6.1	22.0	19.7 $+j$10.8	1.71
1.03	6.1	18.1	21.7 $+j$14.0	1.84
1.04	6.1	15.3	24.3 $+j$17.6	2.02
1.05	6.1	13.2	27.9 $+j$22.0	2.26

$$[I] = [Y_c + Y_f][V] \qquad (11\text{-}30)$$

where Y_c is the dipole mutual admittance matrix and Y_f is the feeder admittance matrix. Since most of the elements are short-circuited, we reduce the matrix [Eq. (11-30)] to only the terms involving unshorted dipoles and solve for the input voltages for a current vector with one nonzero term (the input). We return to Eq. (11-26) and use the voltage vector obtained from the solution of Eq. (11-30) to find the dipole base currents.

Multiple feeds can also be used to reduce sidelobes. A backward-wave excited array (crisscross feeder) feeding a Yagi-Uda dipole antenna reduced the antenna sidelobes [22]. The extra feed points add degrees of freedom for design independently of the number of elements.

Resonant Loop Yagi-Uda Antennas We can make Yagi-Uda arrays by using the resonant loop element (Sec. 4-11). The loop radiates its maximum signal normal to the plane of the loop (along the axis) and has a linearly polarized wave in the direction of the voltage across the feed. A two-element-loop parasitic array, reported in 1942, was built to eliminate corona problems at high altitudes in Ecuador [23]. The maximum standing wave voltage points occur a quarter wavelength from the feed along the loop and not at the rod ends, where air breakdown can occur. The symmetry of the loop reduces the effects of nearby structures on the antenna. The loops can be mounted at the voltage null opposite the feed along a metal rod in a coaxial array with little effect.

The loop shape has only a minor effect on input impedance at the resonant perimeter length of about 1.1λ. The larger size (and gain) of the basic element raises the gain of a parasitic (Yagi-Uda) array from one made with dipoles.

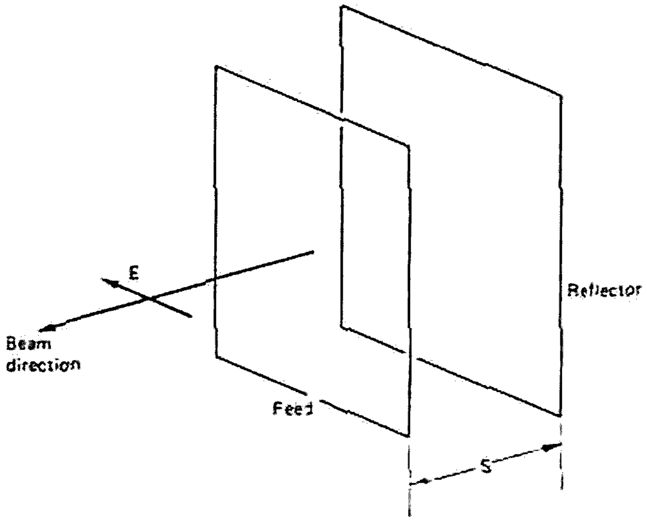

Figure 11-13 Cubic-quad traveling wave resonant loop antenna.

A simple antenna consists of two square loops (Fig. 11-13) with a feed element and a parasitic reflector. The reflector perimeter is somewhat larger than the feed loop. The antenna is commonly called a cubic-quad, and it is usually made by stretching wires on a frame. The feed point location determines the polarization. The antenna of Fig. 11-13 radiates horizontal polarization as fed.

Table 11-12 lists the dimensions of antennas designed to be resonant (zero reactance) at the maximum F/B with a wire radius of 0.0002λ. The maximum F/B occurs for a spacing of 0.163λ. Table 11-13 lists the frequency response of the antenna spaced at 0.15λ. Like the Yagi-Uda dipole antenna, the design must be adjusted as the wire radius changes to obtain the same design response. Table 11-14 lists the design changes on a logarithmic scale. The greater change occurs to the reflector perimeter. When close to the final design, we adjust the reflector for maximum F/B and the feed loop for resonance independently. Each has little effect on the other.

We approach the design of coaxial loop arrays from traveling wave phasing. Table 11-15 lists the traveling wave relative propagation constant along an infinite array of loops [24]. For a given array length we use Eq. (11-8)

TABLE 11-12 Characteristics of Resonant Cubic-Quad Antennas; 0.0002λ-Diameter Wire

Element spacing, λ	Feed perimeter, λ	Reflector perimeter, λ	Gain, dB	F/B, dB	Input resistance, Ω
0.10	1.000	1.059	7.2	17.5	76
0.15	1.010	1.073	7.1	32.8	128
0.16	1.013	1.075	7.1	46.1	137
0.163	1.014	1.0757	7.1	59.6	140
0.17	1.016	1.077	7.1	38.1	145
0.18	1.018	1.079	7.0	31.0	153
0.20	1.025	1.082	6.9	24.6	166

TABLE 11-13 Normalized Frequency Response of a Cubic-Quad Antenna Resonant at a Spacing of 0.15λ

Normalized frequency	Gain, dB	F/B, dB	Input Impedance, Ω	
0.96	7.3	2.9	38.5	$-j140.9$
0.98	7.8	11.0	72.9	$-j\ 55.4$
0.99	7.5	17.9	100.5	$-j\ 22.4$
1.00	7.1	32.8	128.0	
1.01	6.8	19.9	150.7	$+j\ 13.3$
1.02	6.8	14.8	167.0	$+j\ 24.2$
1.03	6.2	12.1	178.0	$+j\ 35.1$
1.04	6.0	10.4	185.4	$+j\ 47.3$
1.06	5.7	8.2	195	$+j\ 77$
1.08	5.5	6.8	202	$+j113.4$

TABLE 11-14 Cubic-Quad Antenna Adjustments for Changed Wire Diameter

Wire diameter, λ	Reflector perimeter, λ	Feeder perimeter, λ
0.00005	−0.013	−0.002
0.0001	−0.007	−0.001
0.0002	0	0
0.0004	0.009	0.002
0.0008	0.019	0.003
0.0016	0.033	0.005
0.0032	0.052	0.008

or (11-10) to find the required mode relative propagation constant to maximize gain.

Example Find the loop size for an array 2λ long with the ratio of loop spacing to loop radius = 0.5 for maximum gain.

We use Eq. (11-10) with $R = 4.5$ to find $P = 1 + \frac{1}{9} = 1.111$. By using Table 11-15, we have

$$\frac{2\pi b}{\lambda} = 0.84 \qquad b = 0.134\lambda$$

The spacing between loops is 0.5(0.134) = 0.0668λ, and 30 loops are required for an antenna length of 2λ.

Table 11-15 suggests closely spaced elements. With further tabular data [25] designs with spacings up to 0.3λ are possible. The reflector element is spaced 0.1λ away from the exciter with a perimeter of 1.05λ. We adjust the perimeter of the feed element to resonate the antenna.

TABLE 11-15 Relative Propagation Constant along Coaxial Array of Circular Loops [24]

Circumference $2\pi b/\lambda$	Spacing ratio S/b		
	0.25	0.50	1.00
	Relative propagation constant P		
0.74	1.05	1.03	1.01
0.76	1.06	1.04	1.016
0.78	1.08	1.05	1.02
0.80	1.09	1.06	1.03
0.82	1.12	1.08	1.04
0.84	1.14	1.11	1.06
0.86	1.17	1.13	1.07
0.88	1.20	1.16	1.09
0.90	1.24	1.20	1.12
0.92	1.30	1.26	1.16
0.94	1.37	1.32	1.23
0.96	1.47	1.40	1.32
0.98	1.60	1.55	1.44

In the above design example the Hansen and Woodyard criterion for maximum gain for the relative propagation constant was not used. The gain in Fig. 11-1 falls rapidly for an increase in P (increased frequency). We obtain a better pattern bandwidth by designing with less than the maximum gain value of P. The possible gain bandwidth shrinks (Fig. 11-1) as we increase length to obtain more gain. This is a general property of all traveling wave end-fire structures. Similarly, the beam of a leaky wave antenna ($P < 1$) scans toward end fire with increasing frequency because P increases.

We can combine loops and dipoles in the same array. In some designs dipoles are used for far-out directors in front of loops. A parasitic loop can provide an effective reflector element for a dipole or crossed dipoles. A loop spaced 0.25λ from a resonant dipole (0.47λ long) increased gain to 5.9 dB with an F/B of 21.7 dB for a loop circumference of 1.15λ.

11-4 Corrugated-Rod, or Cigar, Antenna

The corrugated-rod traveling wave structure consists of disks placed on a central metal rod (Fig. 11-14). The rod supports a TM axisymmetrical mode with readily calculable parameters [2]. The TM mode has a pattern null on axis. The hybrid mode HE_{11} (Sec. 7-4) propagates on the rod to produce a pattern with its peak on axis with linear polarization. The hybrid mode is the sum of the TE_{11} and TM_{11} modes. The surface wave mode has exponentially decaying radial fields.

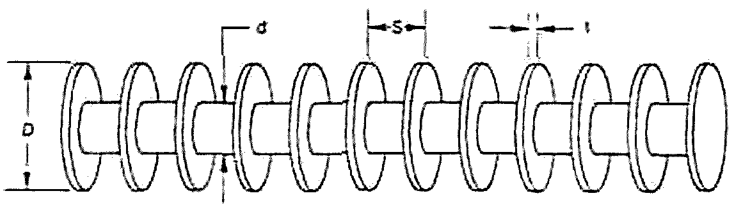

Figure 11-14 Corrugated-rod (cigar) traveling wave structure.

We design this antenna empirically by measuring phase velocities along an excited structure. The gain increases slightly for an increased diameter, but it is determined primarily by length. Table 11-16 lists measured data for the range of disk spacings from 0.15λ to 0.21λ [26]. In this range the spacing has negligible effect on the wave velocity. We use this table with a given length to determine the necessary relative propagation constant P.

We can excite the corrugated rod from a number of feeding structures. A circular waveguide propagating the TE$_{11}$ mode will excite the rod in the hybrid HE$_{11}$ mode [26] when tapered into the guide. A resonant ring will excite the rod when backed by a suitable reflector ring or disk. Wong and King [27] excite the rod from an open-sleeve dipole in a cavity (Fig. 5-14). The length of the rod controls the pattern beamwidth, and the feed structure controls the impedance band. Each may be adjusted somewhat separately.

11-5 Dielectric Rod (Polyrod) Antenna

A dielectric rod will support the HE$_{11}$ hybrid mode. Inside the rod we describe the fields with Bessel function J_n. Outside the rod the fields fall off exponentially and we use the modified Bessel functions K_n. The hybrid mode consists of the sum of TE$_{11}$ and TM$_{11}$ modes. To determine the mode velocity, we equate the propagation constants of the internal and external waves. This equation contains two constants. We eliminate one constant by equating

TABLE 11-16 Measured Relative Propagation Constant on Corrugated-Rod (Cigar) Antenna [26]

$(D-d)/\lambda$	P	$(D-d)/\lambda$	P
0.15	1.03	0.275	1.23
0.175	1.05	0.30	1.31
0.20	1.08	0.325	1.47
0.225	1.12	0.35	1.67
0.25	1.16	0.375	1.92

$0.15 \leq$ disk spacing/$\lambda \leq 0.21$
$0.15 \leq$ central rod diameter/$\lambda \leq 0.21$
$0.018 \leq$ disk thickness/$\lambda \leq 0.025$

TABLE 11-17 Diameter of Dielectric Rod Supporting HE_{11} Mode

P	Dielectric constant				
	2.08	2.32	2.55	3.78	10
	Diameter, λ				
1.01	0.345	0.316	0.296	0.240	
1.02	0.378	0.345	0.322	0.257	0.1780
1.03	0.403	0.366	0.340	0.270	0.1824
1.04	0.425	0.384	0.356	0.279	0.1860
1.05	0.444	0.400	0.369	0.287	0.1888
1.06	0.462	0.414	0.381	0.294	0.1912
1.07	0.479	0.427	0.393	0.300	0.1933
1.08	0.495	0.440	0.404	0.306	0.1951
1.10	0.527	0.465	0.424	0.317	0.1983
1.12	0.559	0.489	0.444	0.327	0.2010
1.14	0.592	0.513	0.463	0.336	0.2034
1.16	0.627	0.538	0.482	0.344	0.2055
1.18	0.663	0.563	0.501	0.353	0.2074
1.20	0.703	0.590	0.521	0.361	0.2092
1.25	0.823	0.664	0.575	0.381	0.2133
1.30	0.994	0.758	0.638	0.402	0.2170
1.35	1.283	0.885	0.716	0.424	0.2205
1.40		1.081	0.820	0.448	0.2238

the radially directed wave impedance at the boundary. The result is a transcendental equation that must be solved by graphical or numerical methods [2]. Table 11-17 summarizes the results of these calculations for common dielectrics.

Figure 11-15 shows a common feeding arrangement for the polyrod antenna. The rod protrudes from a circular waveguide supporting the

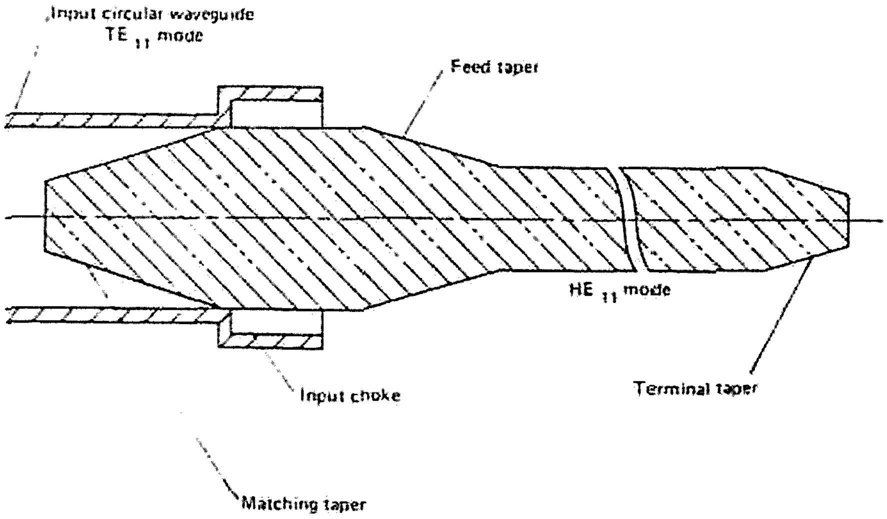

Figure 11-15 Dielectric rod (polyrod) antenna.

TE_{11} mode. This waveguide mode excites the hybrid mode HE_{11} on the rod. At the waveguide exit we use a rod diameter to give P from 1.2 to 1.3 so that the wave will be closely bound to the rod. The feeding guide (Fig. 11-15) has a quarter-wavelength choke to reduce the backfire lobe due to direct radiation from the transition [28]. The choke region can also be flared in a short horn [29].

The second region of the rod tapers either to a uniform diameter section to produce maximum gain or to a tapered section to reduce sidelobes. At the end of the antenna we taper the rod rapidly in a terminating section to bring the surface wave relative propagation constant near 1. This reduces the wave reflection from the end. We find P along the guide and adjust the uniform section diameter or tapered section length to satisfy the total extra phase shift condition for maximum end-fire radiation.

11-6 Helical Wire Antenna [30]

We can excite a single wire wound in a helix to radiate an end-fire pattern on its axis for a circumference around one wavelength. The axial beam is circularly polarized in the same sense as the helix. In low-gain applications the antenna works over a 1.7:1 bandwidth that reduces as gain increases. We see this result from Fig. 11-1 for any traveling wave antenna.

Figure 11-16 illustrates the parameters of the helical antenna. The helix has a pitch angle α with spacing S on a diameter D. These parameters are interdependent.

$$C = \pi D \qquad \text{circumference}$$

$$\tan \alpha = \frac{S}{C} = \frac{S}{\pi D} \tag{11-31}$$

$$L = \sqrt{S^2 + C^2} = \frac{\pi D}{\cos \alpha} \qquad \text{length of turn}$$

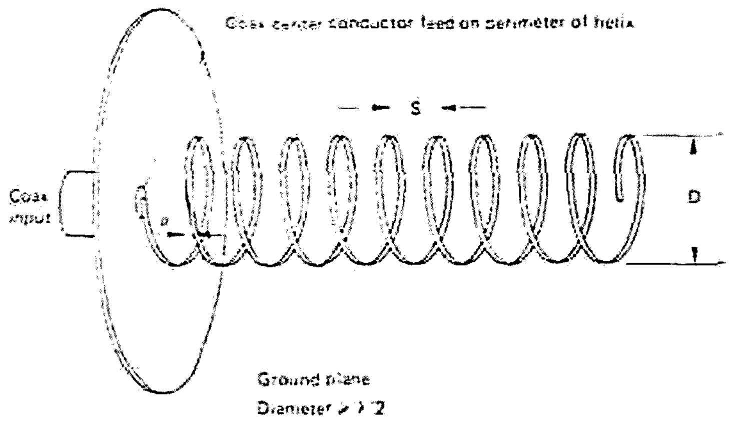

Figure 11-16 Axial mode helical wire antenna (RHC).

Helical Modes We arrive at an understanding of the antenna operation by considering the modes of the helical transmission line. For diameters small in wavelengths the wave travels along the wire at the free-space velocity in the T_0 mode. This mode has equal phase points occurring on separate turns. Traveling wave tube amplifiers use this mode to couple power from an electron beam. The helix slows the axial velocity of the wave by sin α.

The second mode, T_1, occurs when the circumference of the helix approaches one wavelength. The whole phase variation cycles on one turn. The velocity on the wire adjusts for the circumference in this mode. The adjustment gives a velocity whose axial component closely matches the Hansen and Woodyard criterion for increased end-fire directivity over a range of pitch angles.

The third helical transmission line mode, T_2, has two cycles on each turn. The wave slows as compared with the T_1 mode. Near a circumference of one wavelength, the T_1 mode predominates. We express the general mode distribution by

$$I_m e^{\pm jm\phi} \tag{11-32}$$

where m is an integer, ϕ is the polar angle of the developing helix, and the sign determines the polarization sense ($-$ = right hand).

The T_1 mode radiates its beam peak on the helix axis. The T_0 mode radiates the normal mode a combination of patterns from small loops and short dipoles arrayed along the axis. It produces circular polarization over a narrow band of frequencies. The T_2 mode radiates a pattern with a shape like that of the traveling wave current (Fig. 11-5*a*) with a null on the axis.

Axial Mode Antennas radiating from the T_1 mode have good axial ratio, bandwidth, and the possibility of high gains over narrow bandwidths. Transitions such as the feed and helix end excite other helical transmission line modes detected in the antenna patterns, but proper construction can reduce these anomalies.

We analyze the pattern response from a linear array of single-turn helical antennas spaced at the pitch S. Each loop is a traveling wave current element

$$I_1 e^{\pm j\phi}$$

from Eq. (11-32). We calculate the total pattern from pattern multiplication of the single-turn helical antenna and a uniform-amplitude linear array with pattern

$$E_0 \frac{\sin (N\psi/2)}{N\psi/2}$$

where $\psi = kS \cos \theta + \delta$, δ is the phase shift between array elements, and N is the number of turns. The antenna currents satisfy the Hansen and

Woodyard criterion in the range of circumferences from 0.78λ to 1.33λ. We can excite the T_1 mode over that whole band for short helices (lengths less than 2λ), but we can obtain it cleanly for only a limited bandwidth on long helices. The Hansen and Woodyard criterion determines the axial phase shift.

$$-\delta = kS + \frac{\pi}{N}$$

Since the wave travels around the wire, we add 2π to match the T_1 mode. Along the wire we have

$$PkL = Pk\sqrt{C^2 + S^2} = kS + \frac{\pi}{N} + 2\pi$$

or

$$\frac{PL}{\lambda} = \frac{S}{\lambda} + 1 + \frac{1}{2N} \qquad (11\text{-}33)$$

Given $L = \pi D/\cos\alpha = C/\cos\alpha$, define $C_\lambda = C/\lambda$ and substitute into Eq. (11-33) to obtain the relative propagation constant along the wire

$$PC_\lambda/\cos\alpha = C_\lambda \tan\alpha + \frac{2N+1}{2N}$$

$$P = \sin\alpha + \frac{[(2N+1)/2N]\cos\alpha}{C_\lambda} \qquad (11\text{-}34)$$

a result verified by experiments with helical antennas.

A single-turn pattern establishes the polarization of the antenna. The array determines most of the pattern shape, but not the polarization. Figure 11-17 gives the pattern of a single turn of a helical antenna with the T_1 traveling wave current. The whole antenna has five turns. We see a cross-polarization level on boresight of less than 25 dB but little front to back when we consider both polarizations. The end-fire array provides the formed beam to produce the total pattern (Fig. 11-18). The five-turn helical antenna has the same boresight polarization as the single turn. The boresight axial ratio improves for more turns by

$$\text{Axial ratio} = \frac{2N+1}{2N} \qquad (11\text{-}35)$$

for current that follows the increased directivity criterion. The current wave rotates on the helix at nearly the radian frequency. A circularly polarized wave electric field also rotates at the radian frequency. The rotating currents match the rotating electric field of the circularly polarized wave. The helical antenna radiates the same sense of polarization as its screw sense. When

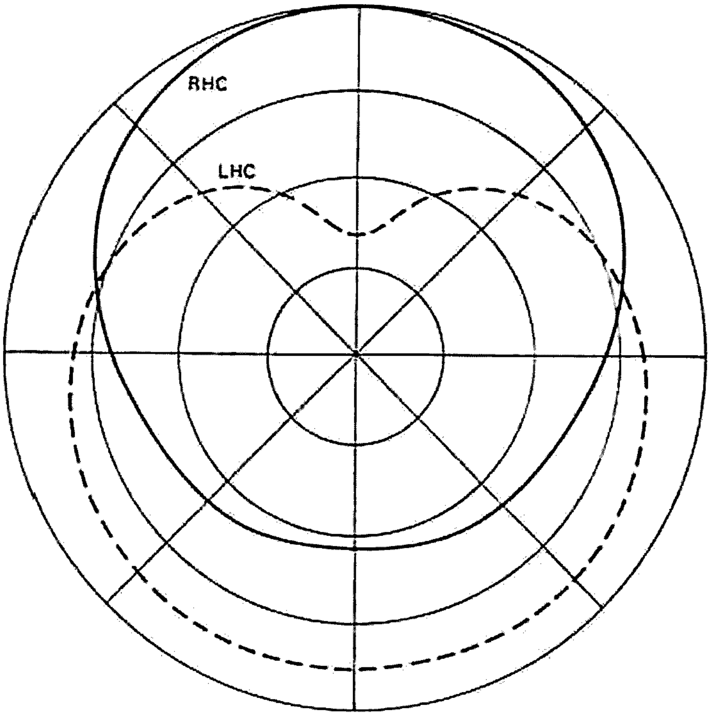

Figure 11-17 Single turn of helical wire antenna with a circumference of 0.9λ and $\alpha = 13°$. Relative propagation constant $P = 1.416$ on wire.

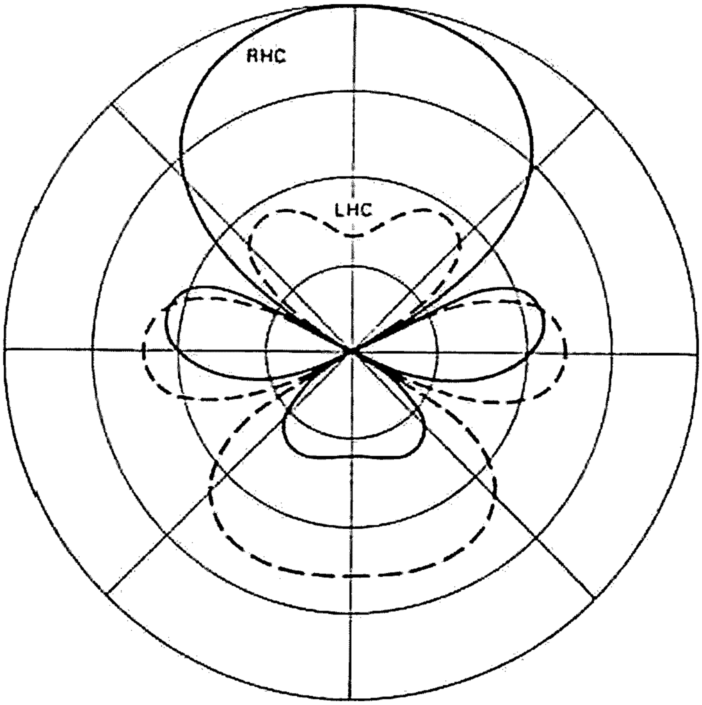

Figure 11-18 Five-turn helical wire antenna with a circumference of 0.9λ and $\alpha = 13°$. Relative propagation constant $P = 1.416$ on wire.

looking into (from the beam peak) a helical antenna radiating RHC, the currents rotate counter clockwise.

The helical antenna operates over the usual following limits:

Pitch angle	$12^\circ \le \alpha \le 18^\circ$
Circumference/λ	$0.78 \le C_\lambda = 1.33$

Helical antennas can be successfully built outside the limits of α. The diameter affects the possible directivity slightly, but we determine the directivity of the T_1 mode from the helix length. Figure 11-2 is a plot of that directivity. Exciting only the T_1 mode becomes a problem as the length increases. The feed excites the other helical transmission line modes.

Feed of Helical Antenna We feed short helical antennas from a coax mounted on a ground plane. The ground plane should be at least $\lambda/2$ in diameter to achieve a good transition. The pattern does not depend on the ground plane to achieve good F/B. Figure 11-18 for the five-turn helical antenna is without a ground plane. The antenna can be fed successfully from a coax twisted in a helix and the outer conductor tapered away in the manner of the balun (Sec. 4-7) until the center conductor alone feeds the helical antenna [31]. We place the coax feed on the edge of the helix and not on the axis where a long transition must be made. When the wire bends to the axis, it generates additional modes on the helix.

Kraus [30] gives the approximate formula for the helical antenna impedance: $R = 141C_\lambda$. The actual value varies about it. We reduce the input impedance by soldering a flat strip on the wire from the feed of the helix [32]. The strip and the ground plane form a parallel-plate line brought close together to form a tapered impedance transformer that provides a broadband low-impedance input. Empirical adjustments, by distorting the last half to quarter turn to bring the line close to the ground plane, can also match the antenna to 50 Ω.

For narrowband applications a gamma match feed (Sec. 4-12) improves the overall system performance. The long helical antenna is grounded and shunt-fed. This will prevent static charge buildup on the antenna and discharge through the receiver. The gamma match narrowbands the antenna that would receive signals from nearby bands that reduce receiver sensitivity. The antenna acts as a filter.

The feed generates modes other than the T_1 to satisfy the boundary conditions. Similarly, conditions on the end of the helical antenna also generate extra modes. Tapering the last two turns to a diameter 65 percent of the helix diameter reduces the mode generation from the end [33]. This tapering in the middle of the antenna can also control the antenna's characteristics as other degrees of freedom are added.

Long Helical Antenna A long helical antenna can achieve the directivity predicted in Fig. 11-2 over a limited bandwidth. The limited bandwidth comes not so much from the restrictions of Fig. 11-1 (because the velocity on the helical transmission line adjusts to the length through coupling) as from the feed structure. The feed structure generates extra modes whose radiation greatly reduces directivity. The normal flat ground plane feed is limited to lengths of about 2λ. Beyond that length the feed generates the T_0 mode that radiates a broad pattern at $\theta = 90°$.

A circular cup around the feed point (Fig. 11-19) will greatly reduce the excitation of unwanted modes. We determine the cup dimensions empirically. The following have been built or reported.

N	α	*C*	*L*	*Cup diam.*	*Cup height*	
35	12.8°	1.07λ	8.5λ	0.82λ	0.40λ	[34]
50	14°	0.90λ	11.2λ	0.97λ	0.85λ	

In both cases the directivity fell by 0.2 dB from the curve for the Hansen and Woodyard criterion of Fig. 11-2. The cup cannot fully eliminate the generation of extra modes on the helical antenna, since the pattern has dropped by about 0.5 dB from prediction because of the radiation of the extra modes. The 35-turn helical antenna has a 15 percent bandwidth, and the 50-turn antenna has only a 10 percent bandwidth.

The helical transmission line fails to maintain the Hansen and Woodyard phase criterion over the total range of C_λ as the length increases. The lower values of C_λ retain this property, and the range of acceptable values shrinks as the number of turns increases. As the helix approaches infinite length, the range of acceptable C_λ approaches 0.78 [35]. At 50 turns on a 13° pitch helical wire antenna the proper phase velocity is maintained over the range $0.78 \leq C_\lambda \leq 1.0$.

Short Helical Antenna [36] We can mount a short helical wire in a square cavity to make a conformal antenna. As shown in Fig. 11-20, the helix has only two turns and the cavity depth is just sufficient for the helix height. The

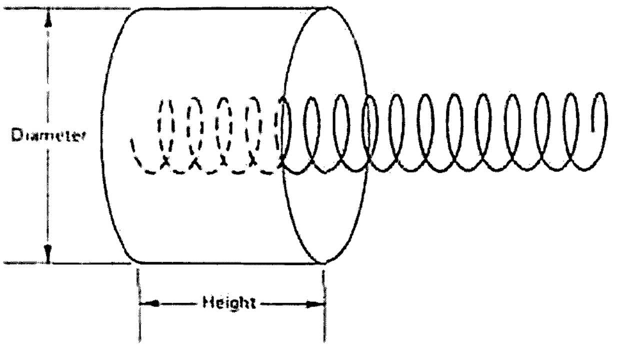

Figure 11-19 Cup feed for long axial mode helical wire antenna.

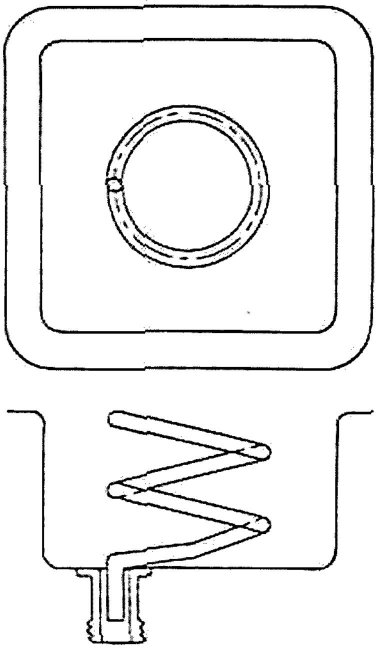

Figure 11-20 Two-turn helical wire antenna in a cavity. (Source: A. Bystrom and D. G. Berntsen, "An Experimental Investigation of Cavity-Mounted Helical Antennas," *IRE Trans. Antennas Propagat.*, vol. AP-4, no. 1, January 1956, p. 54. © 1956 IRE; now IEEE.)

number of turns has minor effects on the pattern, which is determined primarily by the cavity width. Helices with pitch angles from 12° to 14° give the best results when the cavity width is at least 0.5λ. The pattern axial ratio improves for larger cavities, and the best results are obtained with an antenna on a flat ground plane. A cavity width of 0.75λ gives good results with its beamwidths ranging from 45° to 60°.

In the last quarter turn we reduce the pitch angle to between 2° and 6° to form the tapered transformer to match the feed to 50 Ω. As with the longer helical antennas, we place the feed connection on the perimeter of the helix. Both the impedance match and pattern axial ratio improve compared with the central axis feed. The VSWR and pattern band extend from 0.9 to about 1.7 times the design frequency when the helix circumference is one wavelength.

A two-turn helical antenna with a pitch angle of 12° has a cavity depth given by

$$2\lambda \tan 12° = 0.425\lambda$$

for a one-wavelength helix circumference. This antenna is somewhat thicker than the antennas of Chap. 5, but the increased volume increases the bandwidth to nearly an octave.

11-7 Planar Surface Wave Structures

We mount planar slow wave structures on ground planes to shape the pattern of a feed antenna. The slow wave structure bends the power toward the ground plane. We will discuss a corrugated surface and a grounded dielectric, both of which are TM structures with the electric field normal to the slab. The dielectric slab also supports a TE mode with its electric field parallel with the slab for an increased thickness.

Corrugated Ground Plane (Fig. 11-21) The corrugated surface supports surface waves (TM) when the slot depth is less than $\lambda/4$ (inductive). As with the corrugated horn, we assume many slots per wavelength along the direction of propagation. The fields attenuate exponentially above the ends of the corrugations in a surface wave. We derive the fields from a potential function

$$A_1 \exp\left(\frac{-2\pi bx}{\lambda}\right) \exp(-jk_z z) \tag{11-36}$$

above the corrugations, where A_1 is an amplitude constant, x is the distance out of the corrugations, and $\alpha(= 2\pi b/\lambda)$ is the attenuation constant of the fields above the corrugations. We expand the fields and take the ratio of the z-directed electric field to the y-directed magnetic field to find the wave impedance into the corrugated surface.

$$Z_{-x} = \frac{E_z}{H_y} = jb\eta \tag{11-37}$$

where η is the impedance of free space and b is related to α [Eq. (11-36)]. The structure must present this impedance to the wave.

The corrugated surface is a parallel-plate transmission line to E_z, and it presents a per unit length impedance of

$$Z_c = j\eta \tan kd \tag{11-38}$$

where d is the corrugation depth. We equate Eqs. (11-37) and (11-38) to find the constant b

$$b = \tan kd \tag{11-39}$$

We use Eq. (11-39) in Eq. (11-16) for the relative propagation constant.

$$P = \sqrt{1 + b^2} = \sqrt{1 + \tan^2 kd} \tag{11-40}$$

We include the effect of the corrugation thickness by averaging between the parallel-plate impedance and the zero impedance along the corrugation edges. Equation (11-40) becomes

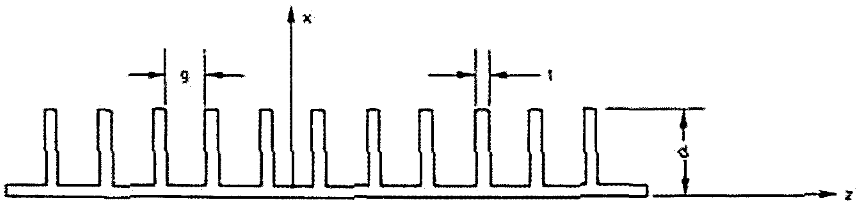

Figure 11-21 Corrugated ground plane.

$$P = \sqrt{1 + \left(\frac{g}{g+t}\right)^2 \tan^2 kd} \tag{11-41}$$

where g is the gap distance and t is the corrugation thickness. P increases without bound as the depth d approaches $\lambda/4$. The fields become tightly bound to the surface and attenuate rapidly to zero above the corrugations—the normal electric field vanishes as in a corrugated horn E-plane wall.

We design the depth of the corrugations by using

$$d = \frac{\lambda}{2\pi} \tan^{-1} \frac{g+t}{g\sqrt{P^2 - 1}} \tag{11-42}$$

Dielectric Slab A grounded dielectric slab will support TM modes when thin and TE modes when thick. The TM mode is polarized normal to the slab surface. The TE mode is polarized parallel to the slab surface. A TM mode needs an inductive surface like the corrugated ground plane. The corrugations prevent propagation between the slots, but the wave can propagate in the dielectric slab as well as in the space above it. We must equate not only the wave impedances at the boundary but the propagation constants in the two regions.

We deduce the grounded dielectric slab solution from a slab that is twice as thick in free space and has an odd-mode electric field excitation on the slab sides. The center becomes a virtual short circuit. We divide the space around the slab into three regions—1 above the slab, 2 in the slab, and 3 below the slab—and derive the fields from the potential functions [5, p. 129].

$$\begin{aligned}
\psi_1 &= A_1 \exp\left(\frac{-2\pi bx}{\lambda}\right) \exp(-jk_z z) \\
\psi_2 &= A_2 \begin{Bmatrix} \sin \dfrac{2\pi p_x x}{\lambda} \\ \cos \dfrac{2\pi p_x x}{\lambda} \end{Bmatrix} \exp(-jk_z z) \qquad (11\text{-}43) \\
\psi_3 &= \pm A_1 \exp\left(\frac{2\pi bx}{\lambda}\right) \exp(-jk_z z)
\end{aligned}$$

where the sign of ψ_3 depends on satisfying continuous tangential fields across the lower slab boundary. The center of the coordinate normal to the slab (x) is the slab center. Equating the propagation constants and x-directed wave impedances gives us transcendental equations in the transverse propagation constant in the slab p_x.

$$\sqrt{\left(\frac{\omega a}{2}\right)^2 (\epsilon_1\mu_1 - \epsilon_0\mu_0) - \left(\frac{\pi p_x a}{\lambda}\right)^2} = \pm B_0 \frac{\pi p_x a}{\lambda} \begin{Bmatrix} \tan \dfrac{\pi p_x a}{\lambda} \\ \cot \dfrac{\pi p_x a}{\lambda} \end{Bmatrix} \tag{11-44}$$

where $B_0 = \mu_0/\mu_1$ for TE waves, $B_0 = \epsilon_0/\epsilon_1$ for TM waves, ω is the radian frequency ($2\pi f$), a is the slab thickness, and ϵ_1 and μ_1 are the permittivity and permeability of the slab. We solve for p_x [Eq. (11-44)] numerically or graphically and use

$$\frac{\pi b}{\lambda} a = \sqrt{\left(\frac{\omega a}{2}\right)^2 (\epsilon_1\mu_1 - \epsilon_0\mu_0) - \left(\frac{\pi p_x}{\lambda}\right)^2} \tag{11-45}$$

to find the attenuation constant b and the relative propagation constant of the slab [Eq. (11-40)].

Equation (11-44) has an infinite number of solutions corresponding to the multiple values of the tangent and cotangent functions. Order 0 corresponds to the tangent function from 0° to 90°; Order 1 corresponds to the cotangent function from 90° to 180°; and so on. Even-mode orders use the tangent function, and odd-mode orders use the cotangent function. We define the cutoff frequency as the point where $\alpha = 0$, the transition between bonded and unbonded waves.

$$\lambda_c = \frac{2a}{n} \sqrt{\frac{\epsilon_1\mu_1}{\epsilon_0\mu_0} - 1} \tag{11-46}$$

The lower cutoff frequency for the zeroth order mode is zero. Only the TM_0 mode has odd symmetry required for the grounded slab. The grounded slab supports even-order TM modes and odd-order TE modes. Equation (11-44) coupled to Eq. (11-45) has been solved numerically to generate Tables 11-18 and 11-19. Table 11-18 lists the thicknesses of a slab in free space supporting the TM_0 mode for a given P. The grounded slab is one-half the thickness of the values in Table 11-18. Similarly, Table 11-19 lists the thicknesses for the TE_1 mode. Equation (11-46) can be solved for the minimum thickness to support the TE_1 mode. Below that thickness the waves do not bind to the surface.

We feed these surfaces from either a small horn or a parallel-plate transmission line. We must match the feed polarization to the mode on the slab. The slab only binds part of the power. The rest radiates directly from the feed or reflects to the feed input.

We can feed an ungrounded slab by centering it in a waveguide. The TE_{10} waveguide mode excites the TE_0 slab mode when the mode velocity determining thickness is in the H plane. Like the grounded slab with the TM_0 mode, the TE_0 mode has no cutoff frequency for a free-space slab. Table 11-20 lists the slab thicknesses for a given relative propagation constant for the TE_0 mode.

11-8 Leaky Wave Structures

A leaky wave structure allows for the separate specification of the amplitude distribution and beam direction. We position the beam direction by adjust-

TABLE 11-18 Thickness of Dielectric Slab Supporting TM_0 Mode*

	Dielectric constant				
	2.08	2.32	2.55	3.78	10
P	Thickness, λ				
1.01	0.086	0.078	0.073	0.060	0.047
1.02	0.122	0.110	0.102	0.083	0.063
1.04	0.171	0.154	0.142	0.113	0.081
1.06	0.209	0.186	0.172	0.134	0.093
1.08	0.242	0.214	0.196	0.150	0.101
1.10	0.272	0.239	0.217	0.164	0.107
1.12	0.300	0.262	0.237	0.175	0.112
1.14	0.328	0.283	0.255	0.186	0.116
1.16	0.356	0.304	0.272	0.196	0.120
1.18	0.385	0.326	0.289	0.204	0.123
1.20	0.416	0.347	0.306	0.213	0.126
1.25	0.504	0.405	0.350	0.232	0.132
1.30	0.624	0.473	0.398	0.251	0.137
1.35	0.821	0.563	0.454	0.269	0.141
1.40		0.696	0.527	0.288	0.145

*Use half thickness for slab on ground plane.

TABLE 11-19 Thickness of Dielectric Slab Supporting TE_1 Mode*

	Dielectric constant				
	2.08	2.32	2.55	3.78	10
P	Thickness, λ				
1.01	0.528	0.474	0.433	0.318	0.172
1.02	0.551	0.492	0.449	0.326	0.174
1.04	0.589	0.521	0.474	0.338	0.178
1.06	0.624	0.548	0.495	0.348	0.180
1.10	0.692	0.598	0.536	0.367	0.185
1.15	0.786	0.665	0.587	0.390	0.190
1.20	0.900	0.742	0.644	0.412	0.195
1.25	1.052	0.835	0.710	0.436	0.200
1.30	1.273	0.954	0.790	0.461	0.204

*Use half thickness for slab on ground plane.

ing the relative propagation constant [Eq. (11-7)]. The surface wave structure permits only small modifications of the amplitude distribution for the pattern scanned to end fire. The uniform distribution on an axisymmetrical leaky wave structure has a directivity of $2L/\lambda$ that is independent of the scan angle

TABLE 11-20 Thickness of Dielectric Slab Supporting the TE$_0$ Mode

	Dielectric constant				
	2.08	2.32	2.55	3.78	10
P	Thickness, λ				
1.01	0.042	0.034	0.029	0.016	0.005
1.02	0.061	0.050	0.042	0.023	0.007
1.04	0.089	0.072	0.061	0.033	0.010
1.06	0.112	0.090	0.076	0.042	0.012
1.10	0.156	0.124	0.104	0.055	0.016
1.15	0.211	0.165	0.136	0.071	0.021
1.20	0.275	0.209	0.170	0.085	0.024
1.25	0.357	0.260	0.207	0.100	0.028

until the pattern approaches end fire. Near end fire the cone beamwidths join to produce higher directivities. Figure 11-1 shows the modification of directivity as these join ($P \to 1$). The directivity is nearly constant below $P = 0.9$ for the lengths of 8λ and 10λ.

Tapered amplitude distributions reduce the directivity by the amplitude taper efficiency [Eq. (6-14)]. The relative propagation constant along the structure determines the beam direction [Eq. (11-7)] for small values of attenuation per unit length. We use Eq. (6-40) for the phase error efficiency due to the varying P along the antenna by replacing $\sin\theta_{\max}$ by $\cos\theta_{\max}$

$$\text{PEL} = \frac{\left|\int_0^L E(z)e^{jk\cos\theta_{\max} z}\,dz\right|^2}{\left(\int_0^L |E(z)|\,dz\right)^2} \tag{11-47}$$

where $E(z)$ is the voltage distribution along the line source. We can use values other than $\theta_{\max}$ in Eq. (11-47) and evaluate the pattern at any θ. When we join a number of leaky wave line sources into a planar array, scanning the beam causes a reduction in the effective aperture length. We reduce the gain by the projection of the length in the scan direction.

Fast wave structures have cutoff frequencies that modify the relative propagation constant

$$P = \sqrt{1 - \left(\frac{f_c}{f}\right)^2} = \sqrt{1 - \left(\frac{\lambda}{\lambda_c}\right)^2} \tag{11-48}$$

where f_c is the cutoff frequency and λ_c is the cutoff wavelength. As frequency increases, P approaches 1 and scans the beam toward end fire.

A waveguide can be made into a leaky wave antenna by openings that cut the wall currents. For example, a slot in the center of the broadwall of a rectangular waveguide does not radiate because it cuts no net current. If we vary the distance of a continuous slot from the centerline, we can control the leakage rate. We form other leaky wave antennas by cutting closely spaced holes or slots. We analyze these discrete radiators as continuous structures whose radiation rate is controlled by the size of the holes or the placement of the slots.

As the wave propagates along the antenna, it continuously loses power. The slots or holes must radiate more and more of the remaining power if the distribution is to be uniform. In general, the holes or slots must increasingly load the waveguide as the wave travels to the termination. The power at any point in the guide is

$$P(z) = P_0 \exp\left[-2\int_0^z \alpha(z)\,dz\right] \tag{11-49}$$

where P_0 is the power at $z = 0$ and $\alpha(z)$ is the attenuation distribution (nepers/length). Suppose we have a desired amplitude distribution: $A(z)$ (voltage).

$$P_{\text{in}} = \int_0^L |A(z)|^2\,dz + \int_0^L \rho_L(z)\,dz + P_{\text{load}} \tag{11-50}$$

where P_{load} is the power lost in the termination, $|A(z)|^2$ is the radiated power distribution, and $\rho_L(z)$ is the ohmic loss in the walls. Let the power into the termination be a ratio of the input power $P_{\text{load}} = RP_{\text{in}}$; then

$$P_{\text{in}} = \frac{1}{1-R}\int_0^L [|A(z)|^2 + \rho_L(z)]\,dz \tag{11-51}$$

The power anywhere along the leaky wave antenna is

$$P(z) = P_{\text{in}} - \int_0^z |A(z)|^2 + \rho_L(z)\,dz \tag{11-52}$$

We differentiate this to get

$$\frac{dP(z)}{dz} = -[|A(z)|^2 + \rho_L(z)] \tag{11-53}$$

We differentiate Eq. (11-49) to relate $\alpha(z)$ to $P(z)$

$$\frac{1}{P(z)}\frac{dP(z)}{dz} = -2\alpha(z) \tag{11-54}$$

We substitute Eq. (11-51) into Eq. (11-52) for P_{in}. By combining Eq. (11-52) and Eq. (11-53) into Eq. (11-54), we find the required attenuation distribution [2, p. 153].

$$\alpha(z) = \frac{\frac{1}{2}|A(z)|^2}{\dfrac{1}{1-R}\displaystyle\int_0^L |A(z)|^2 + \rho_L(z)\,dz - \int_0^z |A(z)|^2 + \rho_L(z)\,dz} \tag{11-55}$$

If we assume a lossless transmission line, then $\rho_L(z) = 0$ and Eq. (11-55) simplifies.

Example Find the attenuation distribution for a uniform distribution along a lossless transmission line leaky wave antenna.

Substitute $A(z) = 1$ and $\rho_L(z) = 0$ into Eq. (11-55) and perform the integrations.

$$\alpha(z) = \frac{\frac{1}{2}}{[L/(1-R)] - z} = \frac{\frac{1}{2}(1-R)}{L[1 - z(1-R)/L]}$$

Given $R = 0.05$ (5 percent of the power into the load) for a structure length of 10λ. The initial and final attenuation constants are

$$\alpha_i(0) = \frac{0.95}{20} = 0.0475 \text{ nepers}/\lambda, \text{ or } 0.413 \text{ dB}/\lambda$$

$$\alpha_f(L) = \frac{0.95}{2LR} = 0.95 \text{ Np}/\lambda, \text{ or } 8.25 \text{ dB}/\lambda$$

We reduce the variation between the initial and final values by dissipating more power in the termination. Given $R = 0.1$

$$\alpha_i(0) = 0.045 \text{ Np}/\lambda, \text{ or } 0.39 \text{ dB}/\lambda$$

$$\alpha_f(L) = 0.45 \text{ Np}/\lambda, \text{ or } 3.9 \text{ dB}/\lambda$$

If we take the ratio of the attenuations at the ends, we have $\alpha(L)/\alpha(0) = 1/R$.

We can normalize Eq. (11-55) to the interval $\pm\frac{1}{2}$ and use the distributions of Chap. 6.

$$\alpha(x)L = \frac{\frac{1}{2}|A(x)|^2}{\dfrac{1}{1-R}\displaystyle\int_{-1/2}^{1/2} |A(x)|^2\,dx - \int_{-1/2}^{x} |A(x)|^2\,dx} \tag{11-56}$$

where $x = z/L$ and $\rho_L(z) = 0$. Figure 11-22 shows the attenuation distribution for a Taylor distribution with 30-dB sidelobes and $\bar{n} = 8$ for various levels of power dissipation in the load. Table 11-21 lists the bounds on $\alpha(x)L$ for some Taylor distributions. Changing the number of modified zeros has only a minor effect on the bounds. A $\cos^2$ on a pedestal distribution with a 30-dB sidelobe level has very similar bounds on the attenuation. The 40-dB sidelobe level design requires a greater variation of attenuation than the 30-dB cases. Long structures may not be able to provide the low levels of radiation above the ohmic losses for an effective design. In all cases we decrease the range on α by decreasing the antenna efficiency by absorbing more power in the termination.

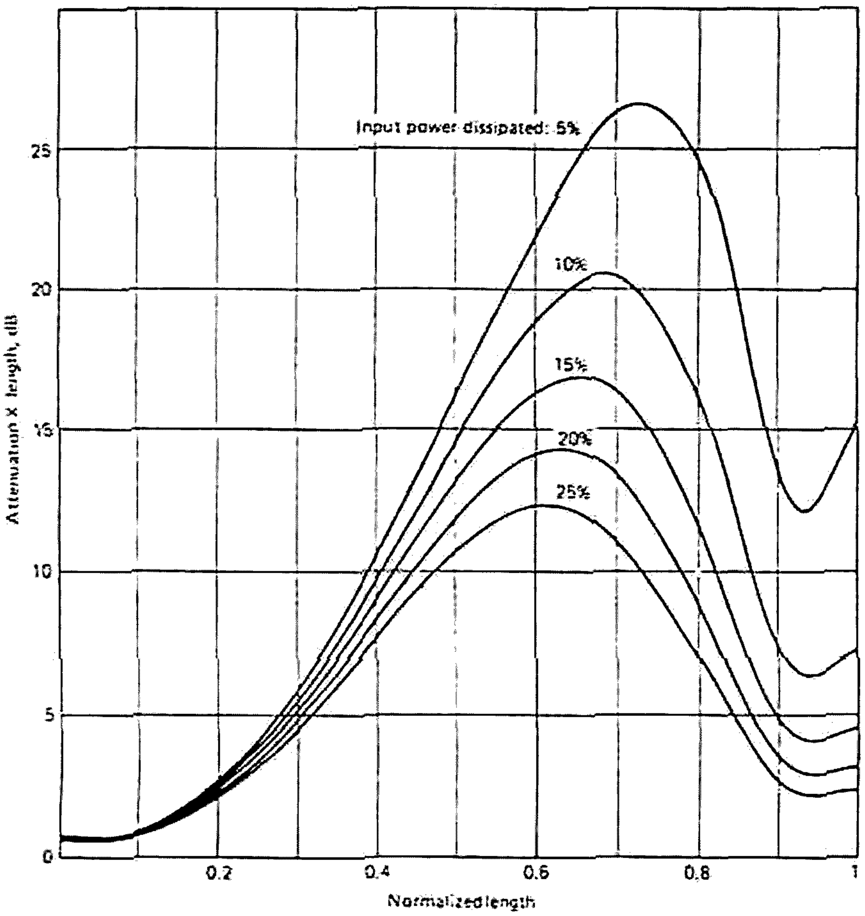

Figure 11-22 Leaky wave attenuation distribution for Taylor distribution with 30-dB sidelobes, $\bar{n}$ = 8.

TABLE 11-21 Maximum and Minimum Normalized Attenuation $\alpha(z)L$ of a Leaky Wave Taylor Distribution

Termination power, %	Design					
	30 dB, $\bar{n}$ = 6		30 dB, $\bar{n}$ = 12		40 dB, $\bar{n}$ = 8	
	Attenuation					
	Max., dB	Min., dB	Max., dB	Min., dB	Max., dB	Min., dB
5	27.08	0.59	26.04	0.63	31.61	0.12
6	25.38	0.58	24.54	0.63	29.63	0.12
8	22.70	0.57	22.06	0.61	26.52	0.12
10	20.66	0.56	20.08	0.60	24.12	0.11
12	19.00	0.55	18.46	0.59	22.18	0.11
15	17.00	0.53	16.52	0.57	19.81	0.11
20	14.42	0.50	14.04	0.53	16.78	0.10
25	12.42	0.46	12.09	0.50	14.44	0.10

Goldstone and Oliner [37] use a transverse resonance method to find the characteristics of waveguides with slots or holes on the narrow wall of the waveguide. The network consists of a shorted parallel-plate transmission line with a conductance and susceptance connected on the other end. The shunt conductance represents the power lost from the opening; the shunt susceptance is due to the wall perturbation. Goldstone and Oliner use this equivalent circuit to find the complex propagation constant. The holey waveguide is one of the most useful structures.

The holey waveguide leaky wave antenna consists of a series of round holes in the sidewall of a rectangular waveguide propagating the lowest-order mode (TE_{10}). The holes control the attenuation over a large range with only minor changes occurring in P. The smooth edges enable higher powers in the holey guide compared with a continuous slot. Given a series of equally spaced S holes of diameter h in a waveguide with width a and height b, the leaky wave characteristics are

$$\alpha = \frac{\lambda_{g0}}{2a^2}\frac{G'}{G'^2 + B'^2} \tag{11-57a}$$

$$P = \frac{\lambda\left[1 + \dfrac{\lambda^2_{g0}}{2a^2}\dfrac{B'}{G'^2 + B'^2}\right]}{\lambda_{g0}} \tag{11-57b}$$

where

$$G' = \frac{\pi b}{2a} \qquad B' = \frac{6abS}{\pi h^3} \qquad \text{and} \qquad \lambda_{g0} = \frac{\lambda}{\sqrt{1 - (\lambda/2a)^2}}$$

We use an average value for P as we vary the hole size to fit the leakage.

Elliott [38] and Hyneman [39] consider a leaky wave antenna made with a series of transverse slots in the broad wall of a waveguide. The transverse slots cut series currents, and we make the slots shorter than necessary for resonance to reduce loading. Honey [40] cuts a series of slots in what is the narrow wall of a waveguide. The wall parallel with the E field is widened to form a wide somewhat flat antenna. By varying the spacing between the strips of the metal grid, we control the leakage rate from the waves reflecting from the two narrow walls of the waveguide. Like surface wave structures, the list of possible leaky wave antennas is large.

11-9 Measurement of Traveling Wave Parameters [2]

We must not be bound to shapes which coincide with separable coordinate systems. Calculated results save time, but we can design antennas based on the measurement of the parameters. Of course, analysis does not always account for every part of the antenna, and measurement is necessary to verify calculations. In many cases we assume an infinitely thin dimension to simplify the analysis. Some measurement and adjustment of almost any antenna will be required. The measurement techniques divide into near- and far-field measurements.

For near-field measurements we need a probe and a carriage to move the probe along the antenna or, equivalently, the antenna by the probe. We connect the probe to a vector network analyzer or to a phase-amplitude receiver. The relative propagation constant P will modify the normal free-space phase shift for a given length along the uniform traveling wave structure. The presence of a reflected wave causes ripple in the phase distribution as the presence of the second traveling wave produces a standing wave on the antenna. We expect a linear phase distribution: $360° P/\lambda$. In the case of a leaky wave structure the field amplitude decreases along the antenna. The near-field amplitude variation measures α directly. We probe by using a small dipole, loop, or open-ended waveguide [41]. The probe and structure of the measuring equipment reflect signals back into the antenna and limit the measurement accuracy. Using absorber around the equipment will reduce these problems to some extent.

Near-field probing of a completed design can separate problems. Many problems can be detected in far-field measurements, but only near-field measurements separate the possible causes. We use the measurement of standing waves as an indication of reflections from the termination. We adjust the terminal taper of a surface wave antenna to minimize the standing wave. We obtain direct measurement of P along the antenna that points to the needed direction of adjustment, and possibly the magnitude also if good design equations are available.

We use far-field measurements for the final check of any traveling wave antenna, but measurements on a uniform structure can serve for the antenna's design parameters. If we remove the termination of a leaky wave antenna, the reflected power produces a backfire beam as it travels back along the antenna. The main-beam direction (Fig. 11-23) determines P from Eq. (11-7). Our ability to locate the main beam limits the accuracy. Antenna range reflections produce pattern ripple. We use the front-to-back ratio of the two beams (Fig. 11-23) to determine α. The wave travels along the antenna and reduces its amplitude by

$$e^{-\alpha L}$$

the open- or short-circuit termination reflects this power and produces the second beam. Given the difference in dB

$$\alpha = \frac{(F/B)_{dB}}{8.68\,L}$$

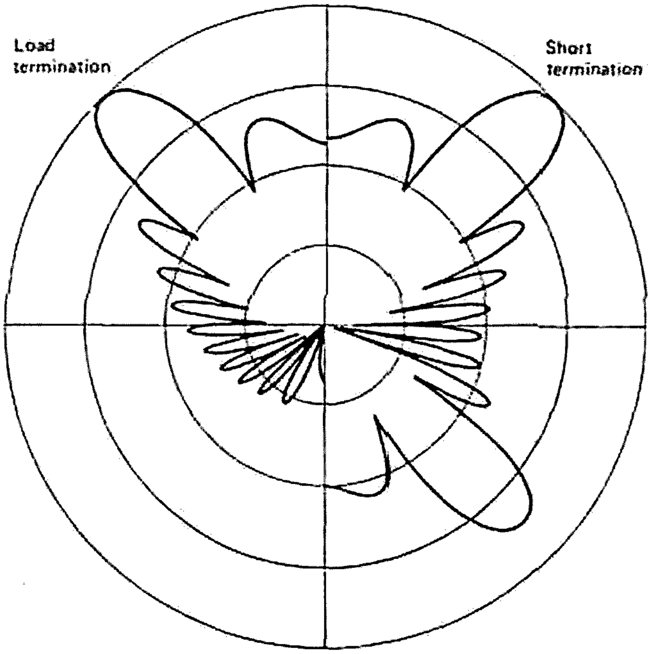

Figure 11-23 Leaky wave structure measurement using a short-circuited termination, $P = 0.71$ and $\alpha L = 5$ dB.

Longer structures improve the measurement of $\theta_{\max}$, but receiver sensitivity and accuracy with large differences in signals limit the measurement of α.

11-10 Waveguide Slot Array

We can design resonant and nonresonant waveguide slot arrays. Both use resonant length slots. We space the slots at $\lambda_g/2$ in the resonant array. We place the slots in alternating positions about the centerline of the broadwall or at alternating tilt angles in the sidewall to give the additional 180° phase shift to produce a broadside beam. The admittances of the slots of the resonant array add at the input. In nonresonant arrays a traveling wave is used to excite the slots. We space the slots at other than $\lambda_g/2$ and terminate the waveguide with a load. We assume a matched system throughout the antenna in a first-order analysis suitable for most designs. The beam of the nonresonant slot array is designed to backfire at an angle to broadside.

Nonresonant Array In the nonresonant waveguide slot array resonant-length slots are used in a traveling wave antenna terminated at the end with a load. The antenna radiates at an angle to the normal of the waveguide face determined by wave velocity and the slot spacing. We must vary the slot loading along the waveguide so that each slot radiates the proper amount of the remaining power. A termination absorbs the power remaining after the last slot. With a mismatched termination the reflected power radiates a second lower-amplitude beam as the wave travels to the source.

We design with either shunt- or series-loading slots. A shunt slot radiates $\frac{1}{2}|V|^2 g_i$, where g_i is the normalized slot conductance. Similarly, a series slot radiates $\frac{1}{2}|I|^2 r_i$, where r_i is the normalized slot resistance. We normalize the conductance or resistance to a per unit length function: $g(z)$ or $r(z)$. The attenuation equation [Eq. (11-54)] becomes

$$\frac{1}{P(z)}\frac{dP}{dz} = -g(r) \qquad \text{or} \qquad -r(z) \tag{11-58}$$

Equation (11-58) modifies the normalized attenuation equation [Eq. (11-56)] [42]

$$g(z)L = \frac{|A(z)|^2}{\dfrac{1}{1-R}\displaystyle\int_{-1/2}^{1/2}|A(z)|^2\,dz - \int_{-1/2}^{z}|A(z)|^2\,dz} \tag{11-59}$$

where the aperture runs $\pm L/2$ and R is the ratio of the input power absorbed by the termination. $A(z)$ is the normalized aperture distribution on $\pm\frac{1}{2}$. We use $r(z)L$ in Eq. (11-59) for series-loading slots.

Equation (11-59) assumes light loading by the slots so that the waveguide transmission line is matched at all points. The approximation improves as the length increases. Equation (11-59) is the same as Eq. (11-56) except for a constant. We divide the values in Table 11-21 or Fig. 11-22 by 4.34 to find the normalized conductances (resistances) of shunt (series) slots times the array length. Each slot provides the loading over the spacing between slots.

$$g_i = \int_{-d/2}^{d/2} g(z)\,dz \simeq g(z_i)d$$

where d is the spacing of the slot at z_i.

We must space the slots at other than $\lambda_g/2$. At $\lambda_g/2$ spacings all reflections from the mismatches (slots) add in phase at the input. The small mismatches add with various phase angles for spacings off $\lambda_g/2$ and cancel each other to give a good input match over a reasonable bandwidth.

As we increase the array length, we can no longer ignore the waveguide losses. The conductances become very small and radiate power of the order of the losses. We must modify Eq. (11-59) to include the losses as in Eq. (11-55). The conductances increase to compensate for the ohmic losses in the walls. Small conductances are difficult to achieve with longitudinal broadwall slots when one edge of the slot must be over the centerline of the waveguide wall. The results become unpredictable.

If we specify the radiating power of each slot in a discrete sequence P_i, we modify Eq. (11-59). The integrals become summations, since

$$|A(z)|^2 = \delta(z - id)P_i$$

where d is the slot spacing, $\delta(x)$ is the Dirac delta (impulse) function, and P_i is the power coefficient of the ith slot. The radiated power is

$$\sum_{i=1}^{N} P_i = P_{\text{in}}(1 - R) = \int_0^L |A(z)|^2\,dz$$

The integral

$$\int_0^z |A(z)|^2\,dz$$

is the power radiated by the preceding slots. Equation (11-59) reduces to

$$g_i = r_i = \frac{P_i}{1 - \sum_{n=1}^{i-1} P_n} \tag{11-60}$$

Dissipating more power in the termination decreases each P_i and the required conductance (resistance) of all the slots.

We alternate the locations of longitudinal slots about the centerline of the broadwall to add 180° phase shift between elements. Similarly, sidewall slot directions are alternated along the array. The additional phase shifts cause backfire of the beam in most cases. The element spacing, as well as the traveling wave phase velocity, determines the beam direction. The phasing equation in the array factor for beam peak becomes $kd\cos\theta + 2n\pi = Pkd - \pi$, where θ is measured from the array axis and n is an arbitrary integer. We solve for the beam peak direction and the necessary spacing to get a particular beam direction:

$$\theta = \cos^{-1}\left[P - \frac{(n + \frac{1}{2})\lambda}{d}\right] \tag{11-61}$$

$$\frac{d}{\lambda} = \frac{n + \frac{1}{2}}{P - \cos\theta_{\max}} \tag{11-62}$$

We usually work with $n = 0$ because using $n > 0$ produces multiple beams.

Example Find the slot spacings to produce a beam at $\theta = 135°$ in a waveguide of width 0.65λ.

Calculate the relative propagation constant from Eq. (11-48) ($\lambda_c = 2a$)

$$P = \sqrt{1 - \left(\frac{1}{1.3}\right)^2} = 0.640 = \frac{\lambda}{\lambda_g}$$

From Eq. (11-62), using $n = 0$, we find the spacing in free space.

$$\frac{d}{\lambda} = 0.371$$

The waveguide spacing is given by $(d/\lambda)(1/P) = 0.581(\lambda_g)$. If we use $n = 1$, then $d/\lambda = 1.11$, which gives an additional beam at $\theta = 79°$ for $n = 0$ [Eq. (11-61)].

Beams enter visible space at $\cos\theta = -1$ (180°) and move toward end fire ($\theta = 0$) as the spacings increase. We find the region of single-beam operation from Eq. (11-62). The minimum d/λ occurs when $\theta = 180°$ for $n = 0$, and the maximum occurs when $\theta = 180°$ for $n = 1$.

$$\frac{0.5}{1+P} \le \frac{d}{\lambda} \le \frac{1.5}{1+P} \tag{11-63}$$

We substitute the upper bound into Eq. (11-61) and use $n = 0$ to find the minimum angle of single-beam operation.

$$\theta_{\min} = \cos^{-1}\left(P - \frac{1+P}{3}\right) \tag{11-64}$$

Example Find the minimum scan angle (toward end fire) for $P = 0.6, 0.7, 0.8$, and 0.9 that has a single beam.
Substitute into Eq. (11-64) to find:

P	0.6	0.7	0.8	0.9
$\theta_{\min}$	86.2°	82.3°	78.5°	74.5°

If we scan to $\theta = 90°$, the spacings become $\lambda_g/2$ and the mismatches from each slot add to the input and produce a resonant array. The nonresonant array has a backfire beam that scans toward broadside as frequency P increases. Hansen [43] gives the slope of the beam shift with frequency change:

$$f\frac{d \sin\theta}{df} = \frac{1}{P} - \sin\theta \tag{11-65}$$

where f is the frequency.

Resonant Array We space the slots at $\lambda_g/2$ and terminate the waveguide end with a short circuit either $\lambda_g/4$ or $3\lambda_g/4$ from the last slot. The beam radiates broadside to the array. The 2:1 VSWR bandwidth of the array is approximately 50%/N for N elements in the array. The antenna is narrowband.

The admittances of all elements add at the input. To have a matched input

$$\sum_{i=1}^{N} g_i = 1$$

where g_i are the normalized conductances. If we define P_i as the normalized power radiated by the ith slot, then

$$g_i = P_i \qquad \text{where} \qquad \sum_{i=1}^{N} P_i = 1$$

Improved Design Methods The methods given above ignore the interaction of slots and their effect on the transmission line. We can describe the array as a loaded transmission line and consider the interactions of the slots by accounting for the transmission line mismatches [44]. We ignore the mutual coupling for longitudinal broadwall slots because it is small. Sidewall slots have high mutual couplings and require an adjustment of the effective slot impedance. We use an incremental admittance, found from the measured change in admittance, when one slot is added to the array. This accounts somewhat for the mutual coupling.

Elliott and Kurtz [45] relate the self-admittance of a longitudinal broadwall slot, measured or calculated, to the mutual admittance of the array of slots found from equivalent dipoles. They use Babinet's principle and the mutual impedance of equivalent dipoles. The method requires a solution of a set of $2N$ equations in the location and length of the slots to give the desired excitation while accounting for mutual coupling. Their formulation ignores slot interaction in the waveguide beyond the first-order mode. Elliott [46] extends this method to the analysis and design of nonresonant arrays.

Dielectric loaded waveguide arrays require additional analysis because the approximation of a piecewise sinusoidal distribution, such as dipole current, fails to model the slot distribution adequately. Elliott [47] uses a slot distribution

$$E(x) = \cos\frac{\pi x}{2b}$$

where b is the length. Mutual impedances between dipoles that have the wrong distribution are not used; instead, the active admittances are found from forward and back scattering between the slots directly. The method still requires the solution of $2N$ equations for the slot lengths and locations.

REFERENCES

1. W. W. Hansen and J. R. Woodyard, "A New Principle in Antenna Design," *Proc. IRE*, vol. 26, no. 3, March 1938, pp. 333–345.
2. C. H. Walters, *Traveling Wave Antennas*, Dover, New York, 1970.
3. H. W. Ehrenspeck and H. Poehler, "A New Method for Obtaining Maximum Gain from Yagi Antennas," *IRE Trans. Antennas Propagat.*, vol. AP-7, 1959, p. 379.
4. F. J. Zucker in H. Jasik (ed.), *Antenna Engineering Handbook*, McGraw-Hill, New York, 1961, chap. 16.
5. R. F. Harrington, *Time-Harmonic Electromagnetic Fields*, McGraw-Hill, New York, 1961.
6. H. H. Beverage, C. W. Rice, and E. W. Kellogg, " The Wave Antenna—A New Type of Highly Directive Antenna," *AIEE Trans.*, vol. 42, 1923, p. 215.
7. K. Iizuka, "The Traveling-Wave V-Antenna and Related Antennas," *IEEE Trans. Antennas Propagat.*, vol. AP-15, no. 2, March 1967, pp. 236–243.
8. G. A. Thiele and E. P. Ekelman, "Design Formulas for Vee Dipoles," *IEEE Trans. Antennas Propagat.*, vol. AP-28, no. 4, July 1980, pp. 588–590.
9. A. E. Harper, *Rhombic Antenna Design*, Van Nostrand, New York, 1941.
10. H. Yagi, "Beam Transmission of Ultra Short Waves," *Proc. IRE*, vol. 26, June 1928, pp. 715–741.
11. R. J. Mailloux, "Antenna and Wave Theories of Infinite Yagi-Uda Arrays," *IEEE Trans. Antennas Propagat.*, vol. AP-13, no. 4, July 1965, pp. 499–506.
12. P. S. Carter, "Circuit Relations in Radiating Systems and Applications to Antenna Problems," *Proc. IRE*, vol. 20, 1932, p. 1004.

13. J. D. Kraus, *Antennas*, McGraw-Hill, New York, 1950, p. 254.
14. R. C. Hansen (ed.), *Microwave Scanning Antennas*, Vol. 2, Academic Press, New York, p. 162.
15. H. E. King, "Mutual Impedance of Unequal Length Antennas in Echelon," *IRE Trans. Antennas Propagat.*, vol. AP-5, July 1957, pp. 306–313.
16. J. H. Richmond, "Coupled Linear Antennas with Skew Orientation," *IEEE Trans. Antennas Propagat.*, vol. AP-18, no. 5, September 1970, pp. 694–696.
17. G. A. Thiele, "Analysis of Yagi-Uda Type Antennas," *IEEE Trans. Antennas Propagat.*, vol. AP-17, no. 1, January 1969, pp. 24–31.
18. D. K. Cheng and C. A. Chen, "Optimum Element Spacings for Yagi-Uda Arrays," *IEEE Trans. Antennas Propagat.*, vol. AP-21, no. 5, September 1973, pp. 615–623.
19. C. A. Chen and D. K. Cheng, "Optimum Element Lengths for Yagi-Uda Arrays," *IEEE Trans. Antennas Propagat.*, vol. AP-23, no. 1, January 1975, pp. 8–15.
20. D. Kajfez, "Nonlinear Optimization Extends the Bandwidth of Yagi Antenna," *IEEE Trans. Antennas Propagat.*, vol. AP-23, no. 2, March 1975, pp. 287–289.
21. P. P. Viezbicke, "Yagi Antenna Design," *NBS Tech. Note 688*, U.S. Dept. of Commerce/National Bureau of Standards, December 1976.
22. W. K. Kahn, "Double Ended Backward-Wave Yagi Hybrid Antenna," *IEEE Trans. Antennas Propagat.*, vol. AP-29, no. 3, May 1981, pp. 530–532.
23. J. E. Lindsay, "A Parasitic End-fire Array of Circular Loop Elements," *IEEE Trans. Antennas Propagat.*, vol. AP-15, no. 5, September 1967, pp. 697–698.
24. L. C. Shen and G. W. Raffoul, "Optimum Design of Yagi Array of Loops," *IEEE Trans. Antennas Propagat.*, vol. AP-22, no. 6, November 1974, pp. 829–831.
25. A. Shoamanesh and L. Shafai, "Design Data for Coaxial Yagi Array of Circular Loops," *IEEE Trans. Antennas Propagat.*, vol. AP-27, no. 5, September 1979, pp. 711–713.
26. S. A. Brunstein and R. F. Thomas, "Characteristics of a Cigar Antenna," *JPL Quarterly Tech. Rev.*, vol. 1, no. 2, July 1971, pp. 87–95.
27. J. L. Wong and H. E. King, "A Wide-Band Low-Sidelobe Disc-o-Cone Antenna," *IEEE Trans. Antennas Propagat.*, vol. AP-31, no. 1, January 1983, pp. 183, 184.
28. V. C. Smits, "Rear Gain Control of a Dielectric Rod Antenna," *Microwave J.*, vol. 11, no. 12, December 1968, pp. 65–67.
29. S. Kobayashi, R. Mittra, and R. Lampe, "Dielectric Tapered Rod Antennas for Millimeter Applications," *IEEE Trans. Antennas Propagat.*, vol. AP-30, no. 1, January 1982, pp. 54–58.
30. J. D. Kraus, *Antennas*, McGraw-Hill, New York, 1950, chap. 7.
31. B. A. Munk and L. Peters, "A Helical Launcher for the Helical Antenna," *IEEE Trans. Antennas Propagat.*, vol. AP-16, no. 3, May 1968, pp. 362–363.
32. J. D. Kraus, "A 50-ohm Input Impedance for Helical Beam Antennas," *IEEE Trans. Antennas Propagat.*, vol. AP-25, no. 6, November 1977, p. 913.
33. J. L. Wong and H. E. King, "Broadband Quasi-taper Helical Antennas," *IEEE Trans. Antennas Propagat.*, vol. AP-27, no. 1, January 1979, pp. 72–78.
34. H. E. King and J. L. Wong, "Characteristics of 1 to 8 Wavelength Uniform Helical Antennas," *IEEE Trans. Antennas Propagat.*, vol. AP-28, no. 3, March 1980, pp. 291–296.
35. T. S. M. Maclean and R. G. Kouyoumjian, "The Bandwidth of Helical Antennas," *IRE Trans. Antennas Propagat., Sympos. Suppl.*, vol. AP-7, December 1959, pp. S379–S386.
36. A. Bystrom and D. G. Berntsen, "An Experimental Investigation of Cavity-Mounted Helical Antennas," *IRE Trans. Antennas Propagat.*, vol. AP-4, no. 1, January 1956, pp. 53–58.
37. L. O. Goldstone and A. A. Oliner, "Leaky-Wave Antennas I: Rectangular Waveguides," *IRE Trans. Antennas Propagat.*, vol. AP-7, October 1959, pp. 307–319.
38. R. S. Elliott, "Serrated Waveguides—Part I: Theory," *IRE Trans. Antennas Propagat.*, vol. AP-5, July 1957, p. 270.
39. R. F. Hyneman, "Closely-Spaced Transverse Slots in Rectangular Waveguide," *IRE Trans. Antennas Propagat.*, vol. AP-7, October 1959, pp. 335–342.
40. R. C. Honey, "A Flush-Mounted Leaky-Wave Antenna with Predictable Patterns," *IRE Trans. Antennas Propagat.*, vol. AP-7, October 1959, pp. 320–329.
41. J. H. Richmond and T. E. Tice, "Probes for Microwave Near-Field Measurements," *IRE Trans. Microwave Theory Tech.*, vol. MTT-3, April 1955, pp. 32–34.

42. A. Dion, "Nonresonant Slotted Arrays," *IRE Trans. Antennas Propagat.*, vol. AP-7, October 1959, pp. 360–365.
43. R. C. Hansen in A. W. Rudge et al. (eds.), *The Handbook of Antenna Design*, vol. 2, Peregrinus, London, 1983, p. 90.
44. M. J. Ehrlich in H. Jasik (ed.), *Antenna Engineering Handbook*, McGraw-Hill, New York, 1961, pp. 9–11.
45. R. S. Elliott and L. A. Kurtz, "The Design of Small Slot Arrays," *IEEE Trans. Antennas Propagat.*, vol. AP-26, no. 2, March 1978, pp. 214–219.
46. R. S. Elliott, "On the Design of Traveling-Wave-Fed Longitudinal Shunt Slot Arrays," *IEEE Trans. Antennas Propagat.*, vol. AP-27, no. 5, September 1979, pp. 717–720.
47. R. S. Elliott, "An Improved Design Procedure for Small Arrays of Shunt Slots," *IEEE Trans. Antennas Propagat.*, vol. AP-31, no. 1, January 1983, pp. 48–53.

CHAPTER

12

SELF–SCALING ANTENNAS

We derive the idea of self-scaling or frequency-independent antennas from the principle of frequency scaling used in model measurements. As we decrease the wavelength (increase frequency), we decrease the model size in the same proportion. We need structures that can be their own scale models. One approach to getting them is to remove any characteristic length by specifying the antenna only in terms of angles [1]. This method leads to the continuously scaled antennas: spirals. A second approach is to include antenna parts that scale the antenna exactly at discrete frequency intervals. We scale these parts logarithmically so that the intervals between frequencies of perfect scaling grow with frequency. The log-periodically scaled antennas have varying characteristics between the points of scaling. We decrease the ripple as the scaling constant approaches 1 (continuous scaling), but also increase the number of parts.

A continuous or log-periodically scaled structure has no ends. We must be able to truncate a successful frequency-independent antenna. A self-scaling antenna must be a transmission line structure that delivers the power to an active region. We feed the high-frequency end, and the high-frequency portion of the antenna serves as a transmission line for the lower-frequency portion. The currents must decay after a radiating active region so that the structure can be stopped without adversely affecting the antenna properties.

We identify the finite active region by truncation constants that we use for sizing the design.

The active region radiates most of the power of a given frequency. A true self-scaling antenna has a constant beamwidth with changing frequency, although we expect small variations between the frequencies of exact scalings (log periodic). We obtain constant beamwidths only if the active region dimensions scale with wavelength.

The truncation requirement affects the pattern. A self-scaling antenna cannot radiate in the direction of the expanding structure. If the antenna did radiate in those directions, portions of the structure would be excited in higher-order modes beyond the normal truncation point. A self-scaling antenna backfires toward the feed point.

We can make a structure with logarithmically scaled radiating parts along a transmission line and still not achieve a successful broadband antenna. The parts must couple power directly and not just through the connection of the feeder. The interaction of the various modes, used to describe the fields, produces cancellation and the rapid attenuation of currents after the active region. We cannot account for the rapid attenuation of currents through loss of power in radiation by considering a single mode. We place dipoles of the log-periodic dipole antenna close together to produce the coupling needed for rapid attenuation. Similarly, we expand a spiral logarithmically to excite the higher-order helix modes and direct interaction between turns.

A successful self-scaling antenna structure satisfies these requirements [2]:

1. The antenna contains its own scale model parts — continuous or discrete — that can be scaled to an infinitesimal size.
2. The antenna radiates most of the power in a finite active region so that it can be terminated with minimal effect.
3. Fed from the high-frequency end, the antenna must be a transmission line to carry power to the low-frequency end.
4. The dimensions of the active region must scale with wavelength.
5. The antenna must not radiate in the direction of expanding structure.
6. The parts must have significant direct coupling outside the transmission line feeder.

12-1 Archimedian Spiral [3, 4]

The Archimedian spiral radiates over a large frequency band, but it is not a true self-scaling antenna because it fails to satisfy the truncation requirement. Since the currents do not decrease sufficiently after the active region, the spiral cannot be truncated without affecting the pattern response. We must load the ends to prevent reflections.

An Archimedian spiral radius increases uniformly with angle

$$r = r_0 + a\phi \tag{12-1}$$

where r_0 is the initial radius and a is the growth rate. We cannot scale the structure to an infinitesimal size by using Eq. (12-1), a requirement of frequency-independent antennas. Figure 12-1 shows two shapes of Archimedian spirals. We usually make the antenna complementary—the uniform metal stripwidth equals the spacing between strips. A two-arm infinite structure has an impedance of 188 Ω from the Babinet-Booker principle (Sec. 4-3) for a self-complementary structure.

A balanced line feeds the spiral from the center. The radiations from the nearly equal and opposite currents at the feed point cancel in the far field. The growing spiral arms separate the currents. When the perimeter of the turn approaches one wavelength, the out-of-phase currents at P and Q (Fig. 12-1) become in phase at points P and P', and radiations from the currents no longer cancel in the far field. This condition starts before the one-wavelength perimeter point and continues for some distance after it. The antenna must have a perimeter of 1.25λ at the lowest operating frequency. The upper frequency truncation size is determined by a requirement to limit the spacing between feed points to less than λ/4.

Beyond the last turn we load a few turns with lossy material, which prevents reflections from the ends. A spiral radiates circular polarization from helical modes of traveling wave currents. Power reflected from the ends travels toward the feed and radiates the opposite sense of polarization from the helical mode with currents traveling in the opposite direction.

We expand the currents in the fundamental modes

$$e^{\mp jm\phi} \tag{12-2}$$

of the helix. The $|m| = 1$ mode (T_1) radiates normal to the spiral plane. Coupling between turns modifies the wave velocity on the structure to fit the

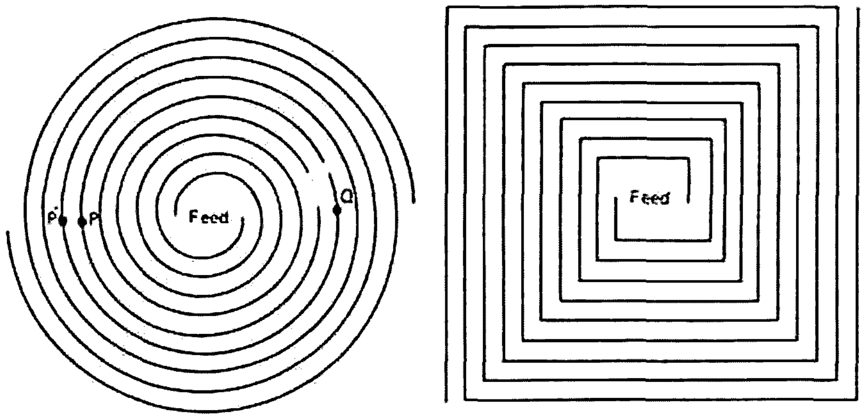

(a) LHC (b) RHC

Figure 12-1 Archimedian spirals: (*a*) LHC; (*b*) RHC.

fundamental modes. Because the spiral increases uniformly, the higher-order modes (T_2, T_3, etc.) attenuate the currents slowly and significant currents remain at the spiral ends.

A spiral radiates RHC polarization on one side and LHC polarization on the other side. We mount the antenna in a cavity to eliminate the unwanted polarization. The balun producing the balanced feed can be mounted in the cavity. It prevents pattern squint and allows for a coaxial input. Hand rules determine the sense of circular polarization. Let the fingers roll in the direction of the spiral (tips toward increasing radius). The thumb points to the pattern maximum for the proper sense of polarization (hand).

12-2 Equiangular Spiral

Rumsey [2] states that an antenna shape determined entirely by angles will be frequency-independent because it is invariant to a change of scale. The biconical antenna satisfies the angle requirement but fails the truncation requirement for frequency independence. The current remains constant along the length. An equiangular spiral antenna (Fig. 12-2) defined by

$$r = r_0 e^{a\phi} \tag{12-3}$$

is defined only by angles, since

$$r_0 = e^{a\phi_0}$$

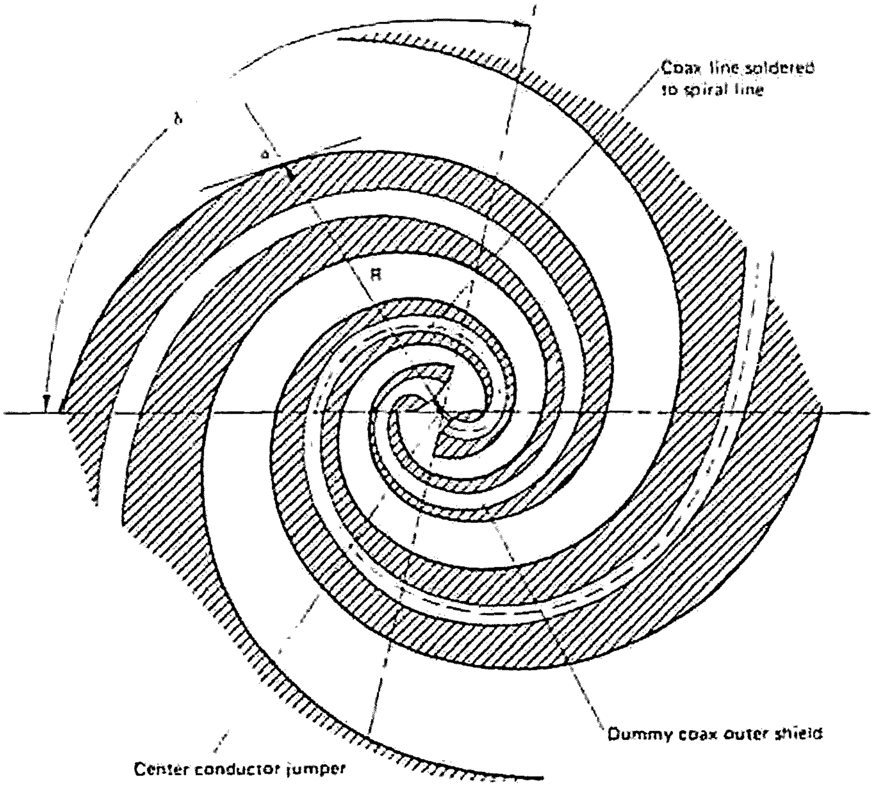

Figure 12-2 Equiangular spiral (RHC) with infinite balun feeder.

satisfies the truncation requirement. The wrap angle α (Fig. 12-2) relates to the growth rate a of the spiral by

$$a = \frac{1}{\tan \alpha} \tag{12-4}$$

Angles also determine the width of the arms. We rotate the spiral by δ to generate the other boundary of the spiral arm. We shift the angle ϕ by 180° (π) to generate the second arm.

The antenna has a finite active region. The currents do not follow the windings [2] but vary in direction throughout the spiral with rapid attenuation as power couples into higher-order modes (T_n, $n > 1$).

Dyson [5] measured these antennas extensively. He found the minimum length to be $1\frac{1}{2}$ turns before the antenna had reasonable patterns. Second, he found the length along the arms necessary for a 3-dB axial ratio on boresight (normal to the plane of the spiral). We integrate Eq. (12-3) to find the arm length

$$L = (r - r_0)\sqrt{1 + \tan^2 \alpha} = (r - r_0)\sqrt{1 + \frac{1}{a^2}} \tag{12-5}$$

The minimum length is a function of the wrap angle and the stripwidth angle δ. Define

$$K = e^{-a\delta} \tag{12-6}$$

Table 12-1 gives the mimimum arm length as a function of K. The initial radius should be at most $\lambda/8$ at the highest frequency.

Example Design an equiangular spiral to operate from 1 to 12 GHz with a wrap angle of 70° and self-complementary arms.

The highest frequency determines the initial radius

$$r_0 = \frac{\lambda}{8} = 0.3 \text{ cm}$$

Self-complementary arms require $\delta = \pi/2$ (90°). We use Eqs. (12-4) and (12-6) to find K.

TABLE 12-1 Minimum Arm Length of Equiangular Spiral as a Function of $K = e^{-a\delta}$ for Wrap Angles between 66° and 79° [5]

K	Arm length, L	K	Arm length, L
0.40	0.86 λ	0.70	1.26 λ
0.45	0.90	0.75	1.37
0.50	0.96	0.80	1.47
0.55	1.03	0.85	1.60
0.60	1.11	0.90	1.76
0.65	1.18		

$$K = e^{-\pi/(2\tan 70^\circ)} = 0.56$$

From Table 12-1 we find the necessary arm length: 1.05λ. We use the lowest frequency (1 GHz) to find the length of the arms: 31.5 cm. We rearrange Eq. (12-5) to find the outer radius

$$r = r_0 + \frac{L}{\sqrt{1 + \tan^2 \alpha}} = 11.07 \text{ cm}$$

Use Eq. (12-3) to find the number of turns:

$$T = \frac{\ln r/r_0}{2\pi a} = \ln \left(\frac{r}{r_0}\right) \frac{\tan \alpha}{2\pi} = 1.58$$

The antenna is at the lower limit for the number of turns. We can compare this design to a circular Archimedian spiral 1.25λ in circumference at 1 GHz: $r = 5.97$ cm. Increasing the wrap angle of the equiangular spiral will decrease the outer radius to a more competitive size.

The antenna has a broad pattern with its peak on the normal of the plane containing the spiral. It radiates RHC polarization on one side and LHC polarization on the other side. Because the antenna satisfies the truncation requirement, we have a pattern null in the direction of the expanding spiral ($\theta = 90°$). We can mount the spiral over a cavity to eliminate the radiation of one polarization sense.

12-3 Infinite Balun

We feed the spiral from a balanced line. We can make a balun by using the truncation property because the current attenuates rapidly beyond the active region. A balun prevents currents excited on the outside of a coax from reaching the input. In Fig. 12-2 we solder the coax feeder to one of the arms. The antenna does not radiate in the direction of the expanding arms. The spiral will not excite currents on the structure after the active region; conversely, no currents excited on the structure beyond the active region will reach the input. The coax feeder outer shield becomes part of the antenna. We solder a dummy coax on the second arm to maintain symmetry.

Because the balun uses the active region limitation on currents of the antenna, its bandwidth matches that of the antenna. We use the same balun structure for log-periodic dipole antennas when similar truncation requirements can be used to form the balun.

12-4 Conical Log Spiral Antenna [6, 7]

When we form the equiangular spiral on a cone, the antenna radiates predominantly toward the vertex. We gain some control of the beamwidth. The antenna projected on a cone continues to satisfy the truncation condition:

radiation is reduced along the structure. We control the beamwidth by varying both the cone angle θ_0 and the wrap angle δ (Fig. 12-3).

The antenna is a slow wave structure from the feed on the upper diameter to the active region. In the active region the antenna changes to a fast wave structure to radiate a backfire pattern toward the cone vertex. Because the spiral on the cone radiates a unidirectional pattern, it reduces the radiation of one circular polarization sense. The flat spiral radiates equally on both sides, but because the pattern has a null in the direction of increasing structure, the null decreases the radiation of one sense of circular polarization.

We describe the spiral arms by the radius from the cone apex,

$$\rho = \rho_0 e^{b\phi} \qquad \text{where } b = \frac{\sin\theta_0}{\tan\alpha} \tag{12-7}$$

We measure the angle of the spiral α with respect to the radius ρ along the cone. The angle δ determines the stripwidth, since Eq. (12-7) describes every edge of the spiral within an offset angle of ϕ. The length of the spiral strip edge is

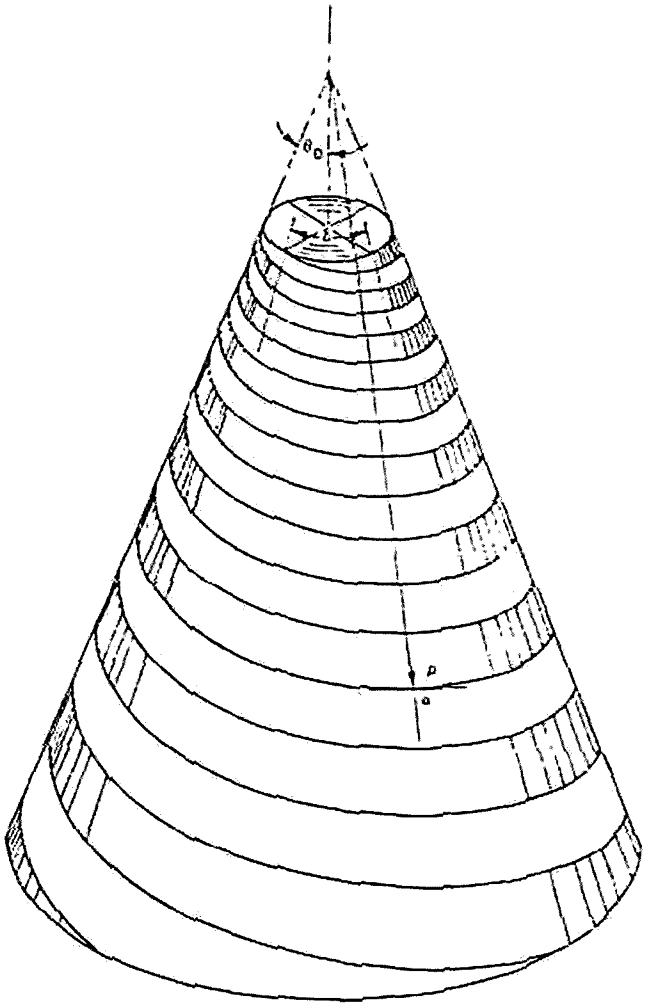

Figure 12-3 Two-arm conical log spiral antenna (RHC).

$$L = (\rho - \rho_0)\sqrt{1 + \frac{1}{b^2}} = (\rho - \rho_0)\sqrt{1 + \frac{\tan^2 \alpha}{\sin^2 \theta_0}} \qquad (12\text{-}8)$$

As θ_0 approaches $\pi/2$ (90°) we have the flat equiangular spiral.

Dyson [7] measured a large number of antennas to determine their properties. We reduce the results to design tables. Table 12-2 gives the average beamwidth of the conical spiral. If we increase the wrap angle (tighter spiral) or decrease the cone angle (longer antenna), the beamwidth decreases and directivity increases. As we decrease the wrap angle to increase the beamwidth, the variation in beamwidth of various pattern cuts through the cone vertex increases. There are too few turns to maintain pattern symmetry.

Diameters of cuts through the cone primarily determine the location of the active region. Dyson found a correlation between the band edges and the level of near-field probed currents. The current peaks in the active region, and we can remove those portions of the antenna where the current drops by 3 dB on the high-frequency (small) end and 15 dB on the lower-frequency (large) end without affecting performance. These near-field current points give us upper and lower truncation diameters to scale the design. If we allow small changes in the beamwidth at the low-frequency end, we can use the 10-dB point to determine the lower diameter from the lowest operating frequency. Tables 12-3 and 12-4 list the radii of the circles truncating the cone at the end of the active region as functions of wrap angle and cone angle.

Example Design a conical log spiral with cone angle of 10° and wrap angle of 75° from 1 to 3 GHz.

$$2\theta_0 = 20°$$

TABLE 12-2 Average Half-Power Beamwidth of Two-Arm Conical Log Spiral Antenna ($\delta = 90°$)

	$2\theta_0$ (twice cone angle)					
	2°	5°	10°	15°	20°	30°
Wrap angle, α, °	Average half-power beamwidth, °					
90	36	49	55	60	65	70
85	37	50	58	64	68	74
80	38	53	63	70	74	81
75	41	56	70	78	83	90
70	44	60	79	88	95	103
65	47	65	89	100	108	119
60	52	71	102	114	127	139
55	57	79	115	132		
50	63	89				
45	69	106				

TABLE 12-3 Two-Arm Conical Log Spiral Antenna Upper Radius of Active Region (a_3^-/λ), Where the Current Drops 3 dB from the Peak

Wrap angle α, °	$2\theta_0$ (twice cone angle)						
	2°	5°	10°	15°	20°	30°	45°
	Upper radius (a_3^-/λ)						
85	0.119	0.111	0.106			0.091	
80	0.101	0.096	0.090	0.084	0.080	0.071	0.067
75	0.089	0.084	0.078	0.074	0.069	0.067	
70	0.078	0.074	0.069	0.066	0.060	0.057	
65	0.071	0.067	0.062	0.058	0.052	0.053	
60	0.063	0.059	0.054	0.050	0.045	0.046	
55	0.057	0.053	0.049	0.043	0.039		
50	0.052	0.048	0.043	0.035	0.036		
45	0.046	0.043		0.031	0.032		

TABLE 12-4 Two-Arm Conical Log Spiral Antenna Lower Radius (a_{10}^+/λ) of Active Region (Slightly Degraded Pattern), Where the Current Drops 10 dB from the Peak

Wrap angle α, °	$2\theta_0$ (twice cone angle)						
	2°	5°	10°	15°	20°	30°	45°
	Lower radius (a_{10}^+/λ)						
85	0.136	0.144	0.150			0.174	
80	0.117	0.128	0.136	0.147	0.156	0.164	
75	0.106	0.120	0.132	0.144	0.156	0.172	
70	0.100	0.118	0.130	0.144	0.159	0.185	
65	0.096	0.117	0.131	0.145	0.168	0.215	
60	0.095	0.116	0.132	0.150	0.178	0.250	
55	0.095	0.116	0.134	0.156	0.186		
50	0.096	0.116		0.166	0.200		
45	0.098	0.117		0.180	0.215		

From Table 12-3, upper truncation constant: $a_3^-/\lambda = 0.069$
From Table 12-4, lower truncation constant: $a_{10}^+/\lambda = 0.156$
We use the radius a_3^-/λ with 3 GHz to determine the upper cone diameter and use the radius a_{10}^+/λ with 1 GHz to determine the lower cone diameter.

Upper diameter = 1.38 cm   Lower diameter = 9.36 cm

We find the cone height from the projected central trapezoid:

$$\text{Height} = \frac{D_L - D_U}{2\tan\theta_0} = 22.63 \text{ cm}$$

We determine the sense of circular polarization from the projection of the spiral on a plane ($\theta_0 = 90°$) and by using hand rules with radiation toward the vertex. We use the same mode theory as the helical antenna to describe the radiation modes. The two-arm conical spiral radiates from the T_1 mode with its peak on boresight (on axis). Rumsey [2] suggests that coupling into higher-order modes causes the rapid attenuation of currents after the active region. The changing curvature of the windings produces this coupling. Because the Archimedian spiral has nearly uniform curvature, the antenna fails to couple sufficient power into higher-order modes to limit the active region.

12-5 Mode 2 Conical Log Spiral Antenna

We use the modal expansion of helical modes to gain insight into possible radiations [8]. The second-order mode T_2 radiates an axisymmetrical circularly polarized pattern with a null on boresight. We achieve this mode by using four arms in the spiral. The T_2 mode function is

$$e^{\pm j2\phi} \tag{12-9}$$

for circular polarization. When we rotate the antenna, its phase changes at twice the rate of rotation [Eq. (12-9)]. A normal circularly polarized antenna radiating on boresight, T_1 mode, changes phase at the same rate as rotation (Sec. 1-9). Of course, we must measure the mode 2 spiral off boresight to be out of the null. Figure 12-4*a* shows the feeding phases for the mode 2 on a four-arm spiral. These match Eq. (12-9). We can feed the four-arm spiral to achieve the T_1 mode (Fig. 12-4*b*). The antennas of Fig. 12-4 radiate RHC polarization. A feed network with a separate input to each of the four arms can excite both the T_1 and T_2 modes [9].

Conical log spiral antennas have limited available design information [10]. The beams off boresight have half-power beamwidths ranging from 48° to 60°. Higher wrap angles and smaller cone angles decrease the beamwidth, but within this limited range. We cannot increase the axial length of the active region beyond a certain point which limits the achievable gain. Although we have limited control of beamwidth, we can control the beam direction by the wrap angle. Table 12-5 lists the approximate beam peak given wrap angle on a 10° cone log spiral. Antennas built with other cone angles follow Table 12-5 closely.

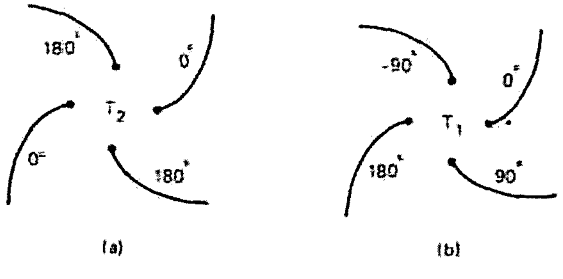

Figure 12-4 Feed phasing of four-arm conical log spiral antenna: (*a*) mode 2; (*b*) mode 1.

TABLE 12-5 Beam Direction of Mode 2 Conical Log Spiral Antenna for $2\theta_0 = 20°$ [10]

Wrap angle α, °	Beam peak θ, °	Wrap angle α, °	Beam peak θ, °
38	82	62	58
42	80	66	52
46	76	70	46
50	74	74	41
54	70	78	38
58	64		

We must increase the diameters of the bottom and top of the four-arm mode 2 spiral from those calculated for the two-arm mode 1 conical log spiral. We obtain a suitable lower truncation constant from Dyson's results (Tables 12-3 and 12-4) if we multiply the lower truncation diameter by 1.42. The upper truncation constant multiplier varies linearly from 4 at $\alpha = 65°$ to 2.3 at $\alpha = 80°$. Since a little extra length on the top of the antenna will not degrade the pattern or increase the height significantly, we use the lower value for all designs.

Example Design a four-arm mode 2 conical log spiral antenna to point the beam at 30° over the frequency range 500 to 1500 MHz on a 10° cone.
Table 12-5 determines the wrap angle to scan the beam to 50°, $\alpha = 67°$.
Table 12-3 gives us the upper truncation radius of the two-arm mode 1 spiral (0.055). Multiply by 2.3 for the mode 2 spiral.

$$\frac{a_{\bar{3}}}{\lambda} = 2.3(0.055) = 0.126 \qquad \text{mode 2}$$

Similarly, Table 12-4 gives us the 10-dB lower truncation radius (0.165). We multiply it by 1.42 to find the lower truncation radius of the mode 2 spiral.

$$\frac{a_{\bar{10}}}{\lambda} = 1.42(0.165) = 0.234 \qquad \text{mode 2}$$

We use $a_{\bar{3}}/\lambda$ with the highest frequency (1500 MHz) to determine the upper radius and use $a_{\bar{10}}/\lambda$ with the lowest frequency (500 MHz) to determine the lower radius of the truncated cone of the antenna.

$$D_U = 5.04 \text{ cm} \qquad D_L = 28.08 \text{ cm}$$

$$\text{Height} = \frac{D_L - D_U}{2 \tan \theta_0} = 65.33 \text{ cm}$$

12-6 Feeding Conical Log Spirals

We must feed the two-arm mode 1 spiral with a balanced line. The infinite balun consisting of coax soldered to the windings uses the truncation properties of the antenna to prevent currents induced on the outside of the coax from reaching the input. On the top we connect the center conductor of the coax to the second winding that contains a dummy coax to maintain symmetry. The coax length and associated loss become prohibitive for many spirals. We shorten the coax length by using a split tapered coax balun along the cone axis. Its bandwidth matches the antenna bandwidth.

It is difficult to tell if the four-arm mode 2 conical spiral antenna needs a balun. The null on axis reduces the induced currents on the outside of a coax along the axis. We can achieve suitable patterns without a balun. In some cases we see narrowband pattern distortion caused by the interaction of the outer-shield currents and higher-order modes: T_3, T_4, etc. These cause pattern ripple in roll plane patterns (constant θ) near the beam peak. We can feed the antenna from four coax lines along the axis. We feed each winding separately and obtain cancellation of currents among the four shields soldered together.

Dyson says that we obtain the best patterns from complementary antennas—spacing equal stripwidth. The Babinet-Booker principle (Sec. 4-3) predicts an impedance of 188 Ω for a flat two-arm complementary spiral and 95 Ω for the four-arm spiral. Forming the spiral on a cone lowers the input impedance to about 150 Ω for the two-arm spiral and 85 Ω for the four-arm spiral. We can vary the stripwidth to impedance-match the antenna with minor effects on the pattern.

LOG-PERIODIC ANTENNAS

All continuously scaled antennas radiate circular polarization. The point of constant beamwidth rotates with frequency. We can build linearly polarized self-scaling antennas only with structures that scale at discrete frequency intervals. The pattern characteristics will ripple between exact scaling frequencies. With closely spaced scalings the antenna is practically frequency-independent.

Every log-periodic structure has a basic scaling cell. We scale every dimension throughout the antenna by a constant

$$\frac{f_1}{f_2} = \frac{\lambda_2}{\lambda_1} = \tau \qquad \text{scaling constant} \quad \tau < 1$$

The antenna will scale exactly at the sequence of frequencies:

$$f_n = \frac{f_0}{\tau^n}$$

We make the antenna periodic in the logarithm of frequency with every dimension scaled by τ from element to element.

Log-periodic antennas were developed in the late 1950s out of modifications to the conical spiral concept of an antenna specified by angles. We will depart from an historical development and discuss the log-periodic dipole antenna first.

12-7 Log-Periodic Dipole Antenna [11–14]

The design of a log-periodic antenna proceeds in two parts. The desired pattern characteristics determine the required number of elements in the active region and the element spacing. We find truncation points from the current levels on the antenna to establish the number of elements required for a given frequency range. As is true of the conical spiral, only a limited range of gains is possible because the aperture length is limited.

Figure 12-5 shows the log-periodic dipole antenna with a crisscross feeder line. We denote the longest dipole length by L_1. The element ends lie on lines that meet at the virtual apex. We measure the distance from the virtual apex to the dipole by R_n. The distance between elements is d_n. Given the initial dimensions L_1, R_1, and d_1, we find all other dimensions by using the scaling constant τ.

$$L_2 = \tau L_1 \qquad R_2 = \tau R_1 \qquad d_2 = \tau d_1 \qquad L_3 = \tau L_2 = \tau^2 L_1 \qquad \text{etc.}$$

In general,

$$L_n = \tau^{n-1} L_1, \qquad R_n = \tau^{n-1} R_1 \qquad d_n = \tau^{n-1} d_1 \tag{12-10}$$

Note: d_n is not an independent variable, since

$$d_n = R_n - R_{n+1} = R_n(1 - \tau) \tag{12-11}$$

The angle between the dipole end points and the centerline—α, the half

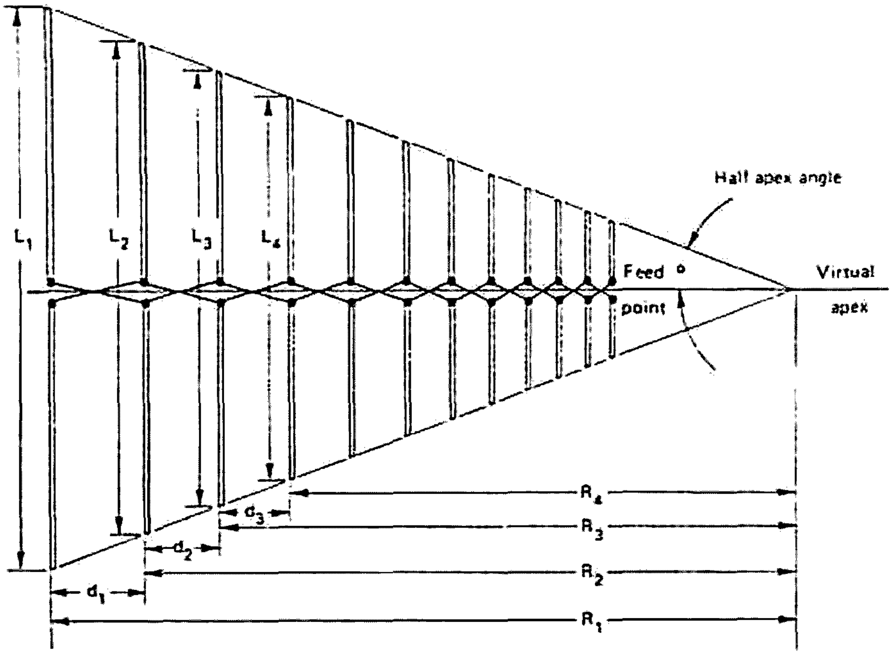

Figure 12-5 Log-periodic dipole antenna.

apex angle—is given by

$$\alpha = \tan^{-1}\frac{L_n}{2R_n} \tag{12-12}$$

Carrel introduced a spacing constant σ as a second constant to describe the antenna.

$$\sigma = \frac{d_n}{2L_n} \tag{12-13}$$

We specify the log-periodic dipole antenna by the constants τ and σ. We can find α, the half apex angle, from τ and σ.

$$\alpha = \tan^{-1}\frac{1-\tau}{4\sigma} \tag{12-14}$$

Tables 12-6 and 12-7 list the E- and H-plane average beamwidths over a suitable range of parameters τ and σ [14]. The beamwidths will vary between scaled frequency points. Carrel [12] used Kraus's directivity estimate Eq. (1-12) with calculated beamwidths to produce Fig. 12-6. This plot overestimates directivity slightly, but it does show an optimum gain line relating τ and σ. We use Tables 12-6 and 12-7 and Fig. 12-6 to determine suitable design constants.

We use the frequency range with upper and lower truncation constants to design the length of the lower element and determine the number of required elements. The greatest element length is given by

$$L_1 = K_1\lambda_L \tag{12-15}$$

where λ_L is the longest operating wavelength and K_1 is the lower truncation

TABLE 12-6 Calculated *E*-Plane Beamwidth of a Log-Periodic Dipole Antenna [14]

	Scaling constant τ				
	0.80	0.875	0.92	0.95	0.97
Spacing constant σ	E-plane beamwidth, °				
0.06		51.3	50	49	47
0.08	51.5	50.3	49	48.3	46.3
0.10	50.5	49.5	48.2	47.4	45.4
0.12	50	48.7	47.5	46.5	44.3
0.14	50	48.3	46.8	45.5	42.7
0.16	51	48.2	46.5	44	41
0.18	53	49.6	46.7	43.5	40
0.20	57	52.5	48.3	44.5	41
0.22	62	56.4	50.4	46.6	43

TABLE 12-7 Calculated *H*-Plane Beamwidth of a Log-Periodic Dipole Antenna [14]

Spacing constant σ	Scaling constant τ				
	0.80	0.875	0.92	0.95	0.97
	H-plane beamwidth				
0.06			110	101	91
0.08	153	128	105	98	88
0.10	145	124	102	93	82
0.12	132	120	100	88	75
0.14	123	111	97	80	70
0.16	125	104	89	72	64
0.18	136	104	87	69	61
0.20	155	113	94	72	63
0.22	185	125	98		

constant. We find K_1 from the empirical equation [13]

$$K_1 = 1.01 - 0.519\tau \tag{12-16}$$

Equation (12-16) overestimates K_1 for $\tau > 0.95$, and the lower band edge will be extended slightly. We find the upper truncation constant from

$$\begin{aligned} K_2 = {} & 7.10\tau^3 - 21.3\tau^2 + 21.98\tau - 7.30 \\ & + \sigma(21.82 - 66\tau + 62.12\tau^2 - 18.29\tau^3) \end{aligned} \tag{12-17}$$

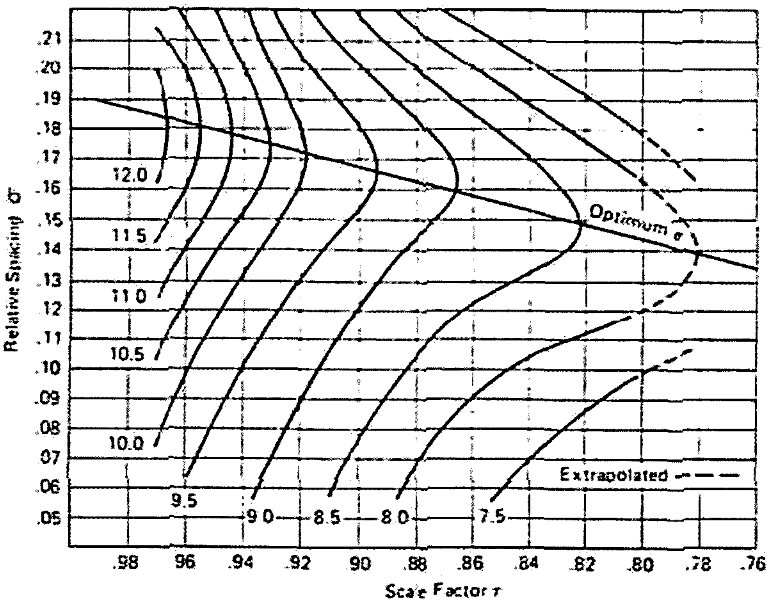

Figure 12-6 Constant-directivity contours in dB versus τ and σ of log-periodic dipole antenna. (Source: R. L. Carrel, "The Design of Log-Periodic Dipole Antennas," *1961 IRE Natl. Conv. Record*, pt. 1, p. 70, © 1961 IRE; now IEEE.)

another empirical equation. The shortest element length is

$$L_U = K_2\lambda_U$$

where λ_U is the shortest operating wavelength. We use the truncation constants and the frequency band edges to find the number of dipoles in the antenna.

$$N = 1 + \frac{\log (K_2/K_1) + \log (F_L/F_U)}{\log \tau} \tag{12-18}$$

For a given frequency, $F_L = F_U = F$, and we find the number of elements in the active region from Eq. (12-18).

$$N_a = 1 + \frac{\log (K_2/K_1)}{\log \tau} \tag{12-19}$$

When we increase the number of elements in the active region, the gain increases. We combine Eqs. (12-11) and (12-13) to find the virtual apex distance.

$$R_n = \frac{2L_n\sigma}{1 - \tau} \tag{12-20}$$

The axial length of the antenna is the difference between R_1 and R_N.

$$\text{Length} = R_1 - R_N = R_1(1 - \tau^{N-1}) = \frac{2L_1\sigma(1 - \tau^{N-1})}{1 - \tau} \tag{12-21}$$

We find the dimensions of the antenna from the equations above by using an integer number of dipoles [Eq. (12-18)].

Example Design a log-periodic dipole antenna to operate from 100 to 1000 MHz. Use $\tau = 0.9$ and $\sigma = 0.15$.

We estimate the E- and H-plane average beamwidths from Tables 12-6 and 12-7.

E-plane beamwidth = 47.8° H-plane beamwidth = 100°

And we use Eqs. (12-16) and (12-17) to find the truncation constants

$$K_1 = 0.54 \qquad K_2 = 0.32$$

We calculate the length L_1 by using K_1 and the lowest operating wavelength [Eq. (12-15)]

$$L_1 = K_1\lambda_{100\text{ MHz}} = 162 \text{ cm}$$

We find the number of elements from Eq. (12-18), $N = 28$, and substitute N into Eq. (12-21) to find the total length, 457.7 cm. We rearrange Eq. (12-13) to find the first spacing

$$d_1 = 2\sigma L_1 = 48.6 \text{ cm}$$

We find the virtual apex distance from Eq. (12-20):

$$R_1 = \frac{2L_1\sigma}{1-\tau} = 486 \text{ cm}$$

We use these dimensions and the scaling constant to find the rest of the antenna dimensions by using Eq. (12-10). For example,

$$L_2 = \tau L_1 = 145.8 \text{ cm} \qquad R_2 = \tau R_1 = 437.4 \text{ cm} \qquad d_2 = \tau d_1 = 43.74 \text{ cm}$$

We can estimate the gain from the length of the active region. We find the half apex angle from Eq. (12-14): 9.46°. The axial length of the active region is $(K_1 - K_2)/\tan\alpha = 1.32\,\lambda$. We use Eq. (11-12) for the directivity of a linear end-fire antenna.

$$\text{Directivity} = \frac{4L}{\lambda} = 5.28 \quad (7.2 \text{ dB})$$

The dipole pattern of the elements will decrease the average radiation intensity in a separable integral and increase the directivity by that of the dipole.

$$\text{Directivity} = 9.4 \text{ dB}$$

This value is close to Carrel's estimate of 9.5 dB.

Feeding the Log-Periodic Dipole Antenna The antenna of Fig. 12-5 must be fed from a balanced line; antennas designed for HF frequencies use that type of feed. If we can run a coax along the center of the antenna, we can use an infinite balun. We alternate the direction of the elements (Fig. 12-7) on the outer shield of the coax feeder and a dummy coax to achieve the crisscross. A two-wire transmission line feeds the elements. The truncation property of the antenna inhibits the flow of induced current on the feeder beyond the active region from reaching the input.

We use a crisscross feed to increase the phase velocity on the feeder in the active region. If we used straight feeders between dipoles, the phase delay would equal that necessary for end-fire in the direction of the feeder currents. This would produce a pattern in the direction of increasing structure and violate the truncation requirement. The extra 180° phase shift between elements produces a backfiring fast wave in the active region.

The region before the active region is a transmission line loaded with small open-circuited stubs (the dipoles). These capacitively load the line and reduce the characteristic impedance. Each dipole has capacitance

$$Z = -jZ_a \cot\frac{kL_i}{2} \tag{12-22}$$

where L_i is the total dipole length, k is the wave number $(2\pi/\lambda)$, and Z_a is the average characteristic impedance of the dipole

$$Z_a = 120\left[\ln\left(\frac{L_i}{2a}\right) - 2.25\right] \tag{12-23}$$

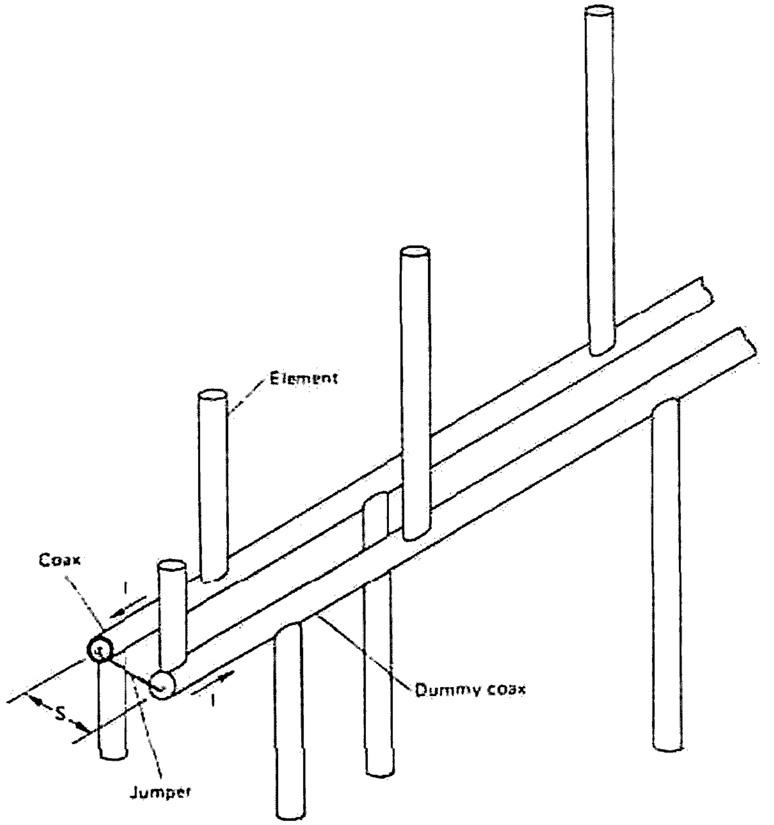

Figure 12-7 Log-periodic dipole antenna feed with an infinite balun.

for a dipole radius a. We use Eq. (12-23) with a constant length-to-diameter ratio in Eq. (12-22) to find an effective added capacitance per unit length along the feeder due to the nonresonant dipoles. With a little manipulation we reduce this to an expression in terms of the log-periodic dipole antenna parameters. The effective feeder impedance R_0 is related to the unloaded two-wire impedance Z_0 by

$$R_0 = \frac{Z_0}{\sqrt{1 + (\sqrt{\tau} Z_0)/(\sigma Z_a)}} \tag{12-24}$$

If the length-to-diameter ratio of the dipoles remains constant, then R_0 is constant along the antenna length. Even with a changing Z_0 or Z_a the feeder acts as a tapered transmission line transformer. We may expect impedance variations about the nominal value of Eq. (12-24) with a cycle of τ.

The currents on the feeder radiate; but because they are close together and nearly equal and opposite, they cancel in the far field. The feeder currents and the jumper at the feed limit the cross-polarization response to about 20 dB that ripples with frequency changes.

The jumper between the center conductor of the coax feeder and the dummy coax line will squint the beam toward the dummy coax at high frequencies. We can represent the jumper as a series inductor in the transmission line. The construction difficulties of this jumper connection limit the high-frequency design of log-periodic dipole antennas.

Phase Center We expect the antenna phase center to be in the middle of the active region. If the antenna were made from many half-wavelength dipoles each resonant at a single frequency, we would look to the one $\lambda/2$ long at a given frequency to be the phase center. In the preceding example the active region ranged from 0.32 to 0.54. These numbers are element lengths measured in wavelengths. We expect the phase center to be in front of the $\lambda/2$ element (or location of a possible element), since a great deal of the active region has elements less than $\lambda/2$.

Table 12-8 lists the approximate E- and H-plane phase center locations measured from the virtual apex relative to a $\lambda/2$ element. We may not have a $\lambda/2$ element at a given frequency; but given the envelope of elements defined by the apex angle, we find the location of a possible element. Table 12-8 shows the astigmatism of the antenna with the H-plane phase center behind the E-plane phase center. The phase center distance from the virtual apex increases linearly with frequency.

Example Find the E- and H-plane phase centers of the antenna designed above for the 100- to 1000-MHz range ($\tau = 0.9$) at 600 MHz.

The half apex angle is 9.46°. The apex distance of the half-wavelength element is

$$R_g = \frac{\lambda}{4\tan\alpha} = \frac{50}{4\tan 9.46^\circ} = 75.02 \text{ cm}$$

From Table 12-8 we find R_p/R_g (E plane) = 0.862 and R_p/R_g (H plane) = 0.874. The phase center distances from the virtual apex are

$$R_p\ (E \text{ plane}) = 64.67 \text{ cm} \qquad R_p\ (H \text{ plane}) = 65.57 \text{ cm}$$

This astigmatism of 0.018λ gives an insignificant loss as a paraboloidal reflector feed (Fig. 8-5).

Elevation Angle The dipole elements must be alternately connected to the coax feeder and the dummy coax, but the feeder lines can diverge (Fig. 12-8).

TABLE 12-8 Log-Periodic Dipole Antenna Phase Center R_p Measured from the Virtual Apex Relative to the Location of a $\lambda/2$ Element $R_g = \lambda/(4\tan\alpha)$ [13]

Scaling constant τ	E-plane R_p/R_g	H-plane R_p/R_g	Scaling constant τ	E-plane R_p/R_g	H-plane R_p/R_g
0.80	0.959	0.997	0.90	0.862	0.874
0.82	0.939	0.968	0.92	0.849	0.859
0.84	0.928	0.941	0.94	0.842	0.849
0.86	0.897	0.916	0.96	0.840	0.844
0.88	0.878	0.893			

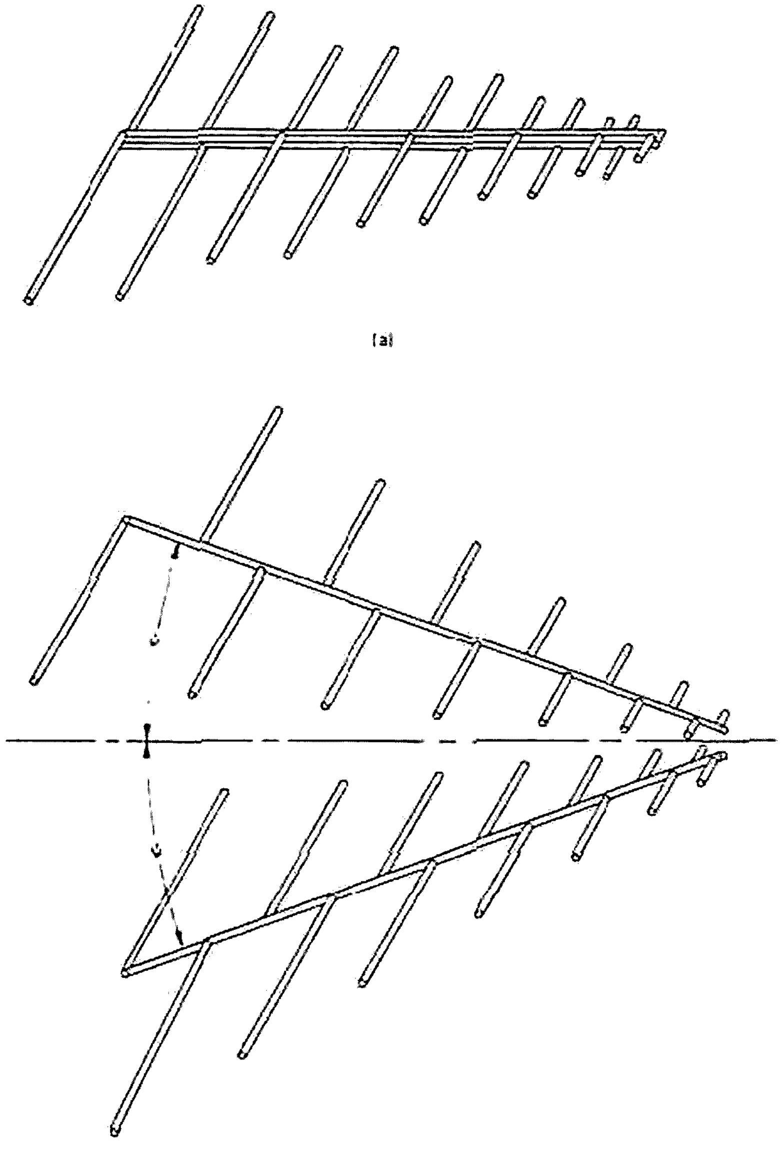

Figure 12-8 Log-periodic dipole antenna with feeder diverged by elevation angle.

We direct the feeder lines at angles $\pm\psi$ from the antenna axis. For the antenna to remain frequency-independent it is necessary for the projection of the two feeders to intersect at the virtual apex.

Spacing the sides at angles $\pm\psi$ decreases the H-plane beamwidth, since the aperture size increases in that plane. The elevation angle moves the antenna phase center toward the virtual apex and reduces movement with frequency changes. We must analyze the feeder line as a tapered transmission line. Moving the sides apart will increase the backlobe of the pattern because, in the limit of $\psi = 90°$, the front and back lobes are equal.

Arrays of Log-Periodic Dipole Antennas [15] We can make broadband arrays with log-periodic antennas. Like the elevation angle of the single antenna, we have frequency-independent arrays only if the virtual apexes of

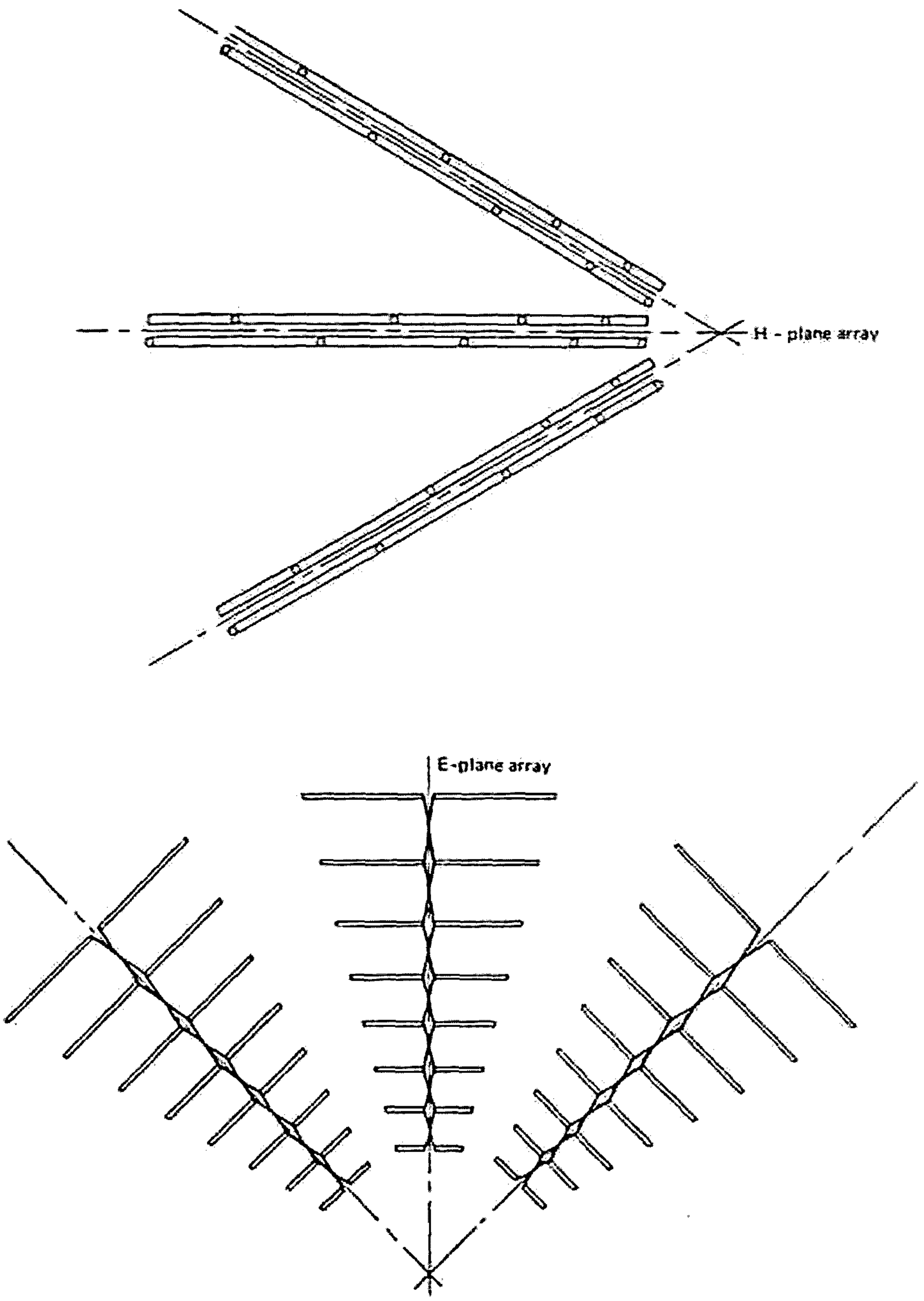

Figure 12-9 Arrays of log-periodic antennas.

all the elements of the array are coincident. The elements must also have the same τ and σ. Figure 12-9 shows E- and H-plane arrays.

The relative phasing between elements can be changed in a frequency-independent manner. If an antenna is turned over, its far-field phase changes by 180°. In an array of two elements this will produce a null on the axis between them, the effect of placing a horizontally polarized antenna over a ground plane. Given a particular antenna, if we multiply every element by the scaling constant, then the far-field phase shifts by 180°. Multiplying every element by τ is equivalent to turning the antenna over (somewhere in the middle of the frequency band). Adding elements at the feed end does not change the location of the phase center. We can change the phase arbitrarily by multiplying the antenna dimensions by

$$\tau^{\gamma/180^\circ} \tag{12-25}$$

where γ is the phase shift. Changing the phase by Eq. (12-25) has meaning only in an array.

We can build a frequency-independent circularly polarized antenna from two log-periodic antennas. Locate the antennas at right angles with one of them scaled by $\tau^{1/2}$. When fed in phase, the pair combines 90° out of phase and radiates circular polarization.

When we array log-periodic antennas, they may develop narrowband gain dropouts [16]. These dropouts occur in a sequence of frequencies with the scaling constant τ of the antenna. Antennas arrayed in either the E or the H plane show these dropouts, as well as antennas arrayed orthogonally. If we change the scaling constants between the antennas in the array, each has dropouts scaled by its own scaling factor. Single antennas also can develop gain dropouts, although they seldom occur in a sequence of frequencies.

The phenomenon points to the importance of swept gain measurements. The location of the frequencies of dropouts remains somewhat unpredictable except for the sequence. Moment method models of the antenna will predict dropouts, but a large number of cases must be run to find the location. Unbalanced currents on the feeder lines interact with the elements to produce cross-polarization and large amounts of off-boresight radiation that lowers gain. These unwanted currents on the feeder are produced by either asymmetry in the antenna or interactions between antennas.

12-8 Other Log-Periodic Types [17, 18]

Many different types of log-periodic antennas have been built. If we can find a structure that satisfies the self-scaling antenna requirements and has the desired polarization, we will have a new frequency-independent antenna.

The first log-periodic antennas were teeth cut into the sides of bifin antennas. These radiated equally on both sides with the polarization rotated parallel to the teeth instead of the normal dipole pattern polarization in the direction of the feed voltage. Isbell folded the sides at elevation angles to produce a unidirectional pattern. DuHamel and Ore straighten the teeth to form the trapezoidal tooth antenna (Fig. 12-10). We separate the sides by an angle 2Ψ, and they project to the virtual apex. This is a good high-frequency antenna because it can be largely self-supporting. Figure 12-10 shows the teeth the same width as the spacings. We can reduce the width of the teeth, but we continue to measure the distances R_n to the bottom of the teeth. As we continue to reduce the width of the teeth, the antenna transforms into a log-periodic dipole antenna.

Removing material to form the teeth of a wire outline trapezoidal tooth antenna (Fig. 12-11) has only minor effects on the pattern response. The shape of the teeth is not too important as long as the teeth scale. The triangular tooth wire outline antenna (Fig. 12-12) also works well. The tooth

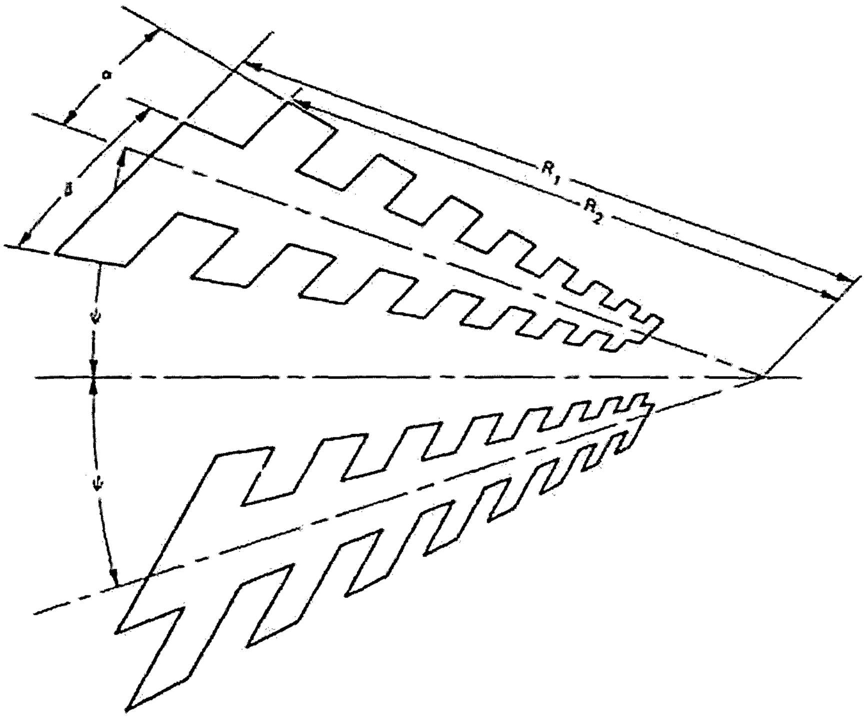

Figure 12-10 Trapezoidal tooth log-periodic antenna.

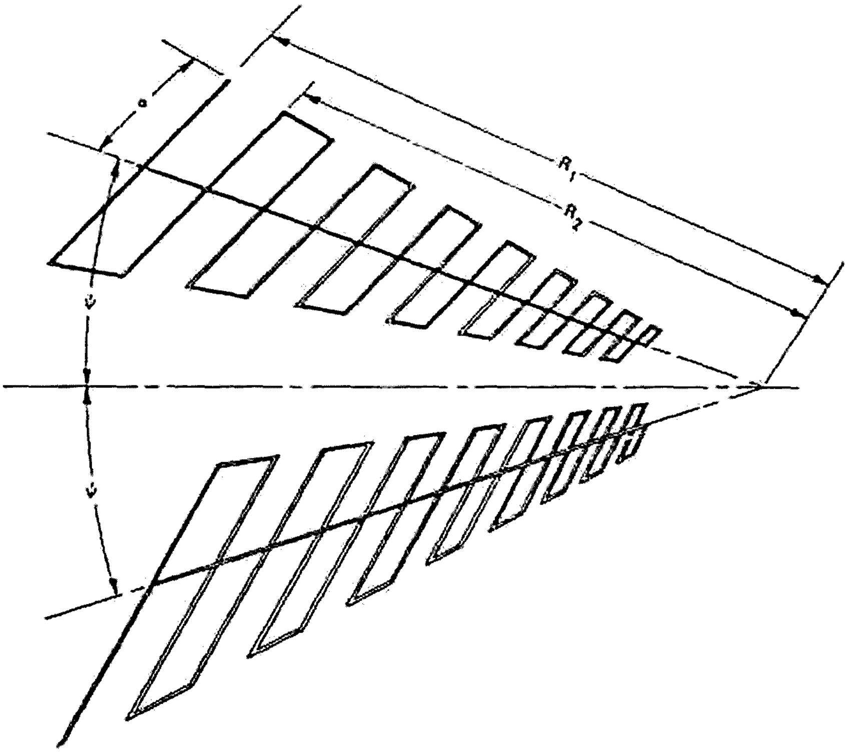

Figure 12-11 Trapezoidal tooth wire outline log-periodic antenna.

shape reduces some of the construction problems of the trapezoidal tooth design, especially at low frequencies. Because the wider teeth have greater coupling than dipoles, we can use smaller scaling constants τ and achieve good designs. Antennas have been built with $\tau = 0.63$, and the log-periodic

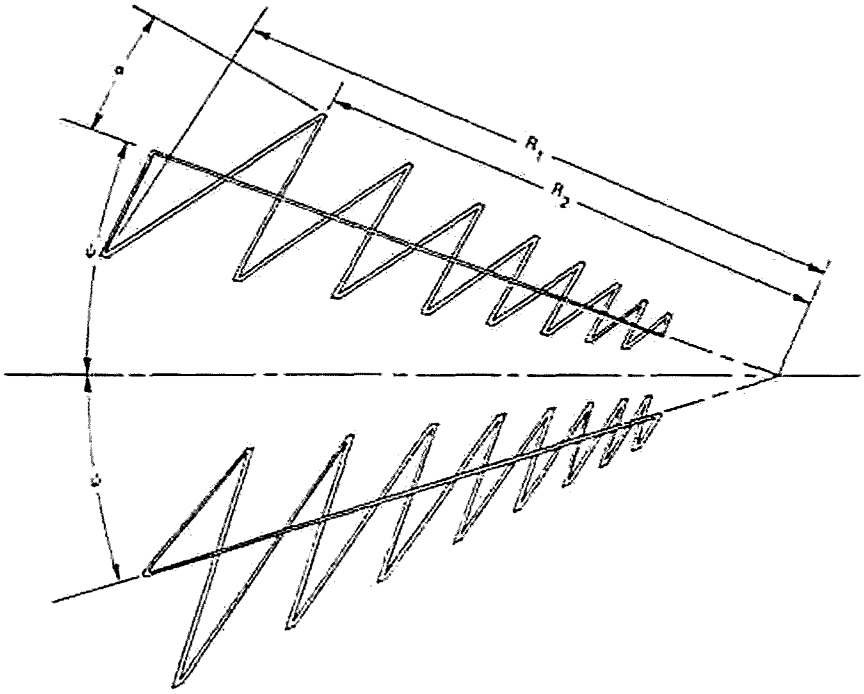

Figure 12-12 Triangular tooth wire outline log-periodic antenna.

TABLE 12-9 Trapezoidal Tooth Wire Outline Log-Periodic Antenna Designs [18]

Scaling constant τ	Elevation angle ψ	Half apex angle α	E-plane beamwidth	H-plane beamwidth	Directivity, dB	Sidelobes, dB
0.63	15	30	85	153	5.0	12
0.63	15	37.5	74	155	5.6	12.4
0.71	15	30	70	118	7.0	17.7
0.71	15	37.5	66	126	7.0	17.0
0.63	22.5	30	86	112	6.3	8.6
0.63	22.5	37.5	72	125	6.6	11.4
0.71	22.5	30	71	95	7.9	14.0
0.71	22.5	37.5	67	106	7.6	14.9
0.77	22.5	30	67	85	8.6	15.8
0.84	22.5	22.5	66	66	9.8	12.3
0.84	22.5	30	64	79	9.1	15.8
0.63	30	30	87	87	7.4	7.0
0.63	30	37.5	73	103	7.4	8.6
0.71	30	30	71	77	8.8	9.9
0.71	30	37.5	68	93	8.1	12.8

dipole has a lower limit of about 0.80 for a good response. Table 12-9 lists the parameters of successful trapezoidal tooth wire outline antennas [18] in terms of log-periodic dipole parameters. Increasing the elevation angle decreases the H-plane beamwidth and raises the sidelobes. The E-plane beamwidth decreases as we increase the half apex angle, but the dipole type pattern of the E plane is the predominant factor. In the range of scaling constants given, the directivity increases with increasing scaling constant.

REFERENCES

1. V. H. Rumsey, "Frequency Independent Antennas," *1957 IRE National Convention Record*, pt. 1, pp. 114–118.
2. V. H. Rumsey, *Frequency Independent Antennas*, Academic Press, New York, 1966.
3. E. M Turner, "Spiral Slot Antenna," Wright Air Dev. Center, Dayton, Ohio, *Tech. Note WCLR-55-8*, June 1955.
4. J. A. Kaiser, "The Archimedian Two-Wire Spiral Antenna," *IRE Trans. Antennas Propagat.*, vol. AP-8, May 1960, pp. 312–323.
5. J. D. Dyson, "The Equiangular Spiral Antenna," *IRE Trans. Antennas Propagat.*, vol. AP-7, April 1959, pp. 181–186.
6. J. D. Dyson, "The Unidirectional Equiangular Spiral Antenna," *IRE Trans. Antennas Propagat.*, vol. AP-7, October 1959, pp. 329–334.
7. J. D. Dyson, "The Characteristics and Design of the Conical Log-Spiral Antenna," *IEEE Trans. Antennas Propagat.*, vol. AP-13, no. 4, July 1965, pp. 488–498.
8. C. S. Liang and Y. T. Lo, "A Multiple-Field Study for the Multiarm Log-Spiral Antennas," *IEEE Trans. Antennas Propagat.*, vol. AP-16, no. 6, November 1968, pp. 656–664.
9. G. A. Deschamps and J. D. Dyson, "The Logarithmic Spiral in a Single-Aperture Multimode Antenna System," *IEEE Trans. Antennas Propagat.*, vol. AP-19, no. 1, January 1971, pp. 90–96.
10. A. E. Atia and K. K. Mei, "Analysis of Multiple-Arm Conical Log-Spiral Antennas," *IEEE Trans. Antennas Propagat.*, vol. AP-19, no. 3, May 1971, pp. 320–331.
11. D. E. Isbell, "Log Periodic Dipole Arrays," *IRE Trans. Antennas Propagat.*, vol. AP-8, May 1960, pp. 260–267.
12. R. L. Carrel, "The Design of Log-Periodic Dipole Antennas," *1961 IRE National Convention Record*, pt. 1, pp. 61–75.
13. C. E. Smith, *Log Periodic Design Handbook*, Smith Electronics, Cleveland 1966.
14. R. L. Carrel, "Analysis and Design of the Log-Periodic Dipole Antenna," *Antenna Lab. Tech. Rept. 52*, University of Illinois, October 1961.
15. R. H. DuHamel and D. G. Berry, "Logarithmically Periodic Antenna Arrays," *1958 IRE National Convention Record*, pt. 1, pp. 161–174.
16. K. G. Balmain and J. N. Nkeng, "Asymmetry Phenomenon of Log-Periodic Dipole Antennas," *IEEE Trans. Antennas Propagat.*, vol. AP-24, no. 4, July 1976, pp. 402–410.
17. R. H. DuHamel and D. E. Isbell, "Broadband Logarithmically Periodic Antenna Structures," *1957 IRE National Convention Record*, pt. 1, pp. 119–128.
18. R. H. DuHamel and F. R. Ore, "Logarithmically Periodic Antenna Designs," *1958 IRE National Convention Record*, pt. 1, pp. 139–151.

INDEX

Amitay, N., 272
Atia, A. E., 396

Bahl, I. J., 127, 128
Bailey, M. C., 23
Balanis, C. A., 65, 93
Balmain, K. G., 396
Barrow, W. L., 179, 213
Bayliss, E. T., 144, 148, 166, 178
Beck, F. J., 179, 213
Berntsen, D. G., 354, 370
Berry, D. G., 396
Beverage, H. H., 369
Bhartia, P., 127
Blass, J., 65
Bock, E. L., 94
Boersma, J., 213
Bolt, F. S., 272
Booker, H. G., 37, 70, 93
Bouche, E. L., 272
Braun, E. H., 213
Brown, R. M., 293, 296
Brunstein, S. A., 370
Butler, J. L., 65
Bystrom, A., 354, 370

Carberry, T. F., 265, 272
Carlise, R. L., 295
Carrel, R. L., 385, 386, 396
Carter, P. S., 369
Carver, K. R., 127
Chen, C. A., 335, 338, 370
Cheng, D. K., 232, 271, 319, 335, 338, 370
Cheston, T. C., 65
Chow, F. V. M., 116, 127
Chu, L. J., 179, 213
Chu, T. S., 213
Clarricoats, P. J. B., 213
Clayton, L., 17
Coffey, E. L., 127
Cogdell, J. R., 271
Cohn, S. B., 285, 295
Collin, R. E., 271
Collins, G. W., 248, 265, 272
Condon, E. U., 235, 271
Craig, A. D., 271
Croswell, W. F., 23

Davis, J. H., 271
Derneryd, A. G., 107, 127
Deschamps, G. A., 396
Dicke, R. H., 23
Dion, A. R., 295, 371
Dolph, C. L., 141, 178, 297, 302, 304, 319
Dorne, A., 94, 128
Doundoulakis, G., 178
Drane, C. J., 306, 319
DuHamel, R. H., 319, 393, 396
Dunbar, A. S., 272
Duncan, J. W., 94
Dyson, J. D., 376, 379, 383, 396

Ehrenspeck, H. W., 369
Ehrlich, M. J., 371
Ekelman, E. P., 369
Elkamchouchi, H. M., 271, 272
Elliott, R. S., 93, 127, 128, 153, 178, 265, 272, 296, 319, 363, 369, 370, 371
English, W. J., 213

Farrar, F. G., 128
Frank, J., 65
Friis, H., 23, 179, 184, 213

Galindo-Israel, V., 265, 271, 272
Gethin, S., 178
Goldstone, L. O., 363, 370

Hacker, P. S., 178
Hammerstad, E. O., 127
Hansen, R. C., 94, 127, 163, 178, 234, 271, 370, 371
Hansen, W. W., 39, 47, 59, 65, 322, 369
Harper, A. E., 369
Harrington, R. F., 23, 25, 47, 93, 101, 127, 178, 369
Hollis, J. S., 17
Holt, F. S., 271
Honey, R. C., 363, 370
Hueber, D. A., 128
Hyneman, R. F., 153, 178, 363, 370

Iizuka, K., 369
Imbriale, W. A., 271
Ingerson, P. G., 271
Isbell, D. E., 393, 396
Isber, A. M., 272

James, G. L., 207, 213
Jasik, H., 23, 213, 295, 369, 371
Johnson, R. C., 23
Jones, B. B., 116, 127

Kahn, W. K., 370
Kaiser, J. A., 396
Kajfez, D., 335, 338, 370
Kales, M. L., 293, 296
Kay, A. F., 201, 213
Kelleher, K. S., 184, 213
Kellogg, E. W., 369
Kerr, J. L., 115, 127
Kildal, P., 246, 272
King, H. E., 123, 124, 128, 346, 370
Kingslake, R., 295
Kobayashi, S., 370
Kouyoumjian, R., 218, 271, 370
Krall, A. D., 128
Kraus, J. D., 10, 23, 33, 94, 269, 272, 318, 352, 370
Kreutel, R. W., 286, 295
Kumer, A., 207, 213
Kurtz, L. A., 369, 371

Lampe, R., 370
Laxpati, S. R., 319
Lazarno, D., 128
Lee, J. J., 295
Lee, S. W., 271, 272
Legg, W. E., 213
Li, T., 272
Liang, C. S., 396
Lind, A. G., 127
Lindberg, C. A., 123, 128
Lindsay, J. E., 370
Lo, Y. T., 127, 271, 396
Lochner, O., 213
Love, A. W., 178, 179, 202, 213, 214, 271, 272
Ludwig, A. C., 21, 172, 178, 223, 235, 271
Lyon, T. J., 17

Maclean, T. S. M., 370
Mailloux, R. J., 369
Marchand, N., 94
Mattes, H., 213
Matthaei, G. L., 120
Mayes, P. E., 94
Mei, K. K., 396
Mentzer, C. A., 271
Metzler, T., 115, 127
Minerva, V. P., 94
Mittra, R., 265, 271, 272, 370
Montgomery, C. G., 23
Morita, T., 285, 295
Mrstik, V., 272
Muehldorf, E. I., 190, 213
Munk, B. A., 370
Munson, R. E., 127

Nelson, J. A., 94
Newman, E. H., 125, 126, 128
Nkeng, J. N., 396

Oliner, A. A., 127, 363, 370
Ore, F. R., 393, 396

Park, P. K., 127
Pathak, P., 218, 271
Peters, L., 271, 370
Poehler, H., 369
Poggio, A. J., 94
Popovich, B., 272
Potter, P. D., 213, 214, 271
Purcell, E. M., 23

Raffoul, G. W., 370
Ramakrishna, S., 172, 178
Rao, J. B. L., 294, 296
Rao, J. S., 127
Ras, B. N., 127
Rhodes, D. R., 146, 178
Rice, C. W., 369
Richmond, J. H., 370
Risser, J. R., 295
Rotman, W., 294, 296
Rudge, A. W., 213, 271, 371
Rumsey, V. H., 71, 93, 375, 396
Rusch, W. V. T., 214, 245, 271, 272
Russo, P. M., 213
Ruze, J., 232, 271, 294, 295

Sachidananda, M., 172, 178
Saha, P. K., 213
Satoh, T., 211, 213
Schaubert, D. H., 128
Schelkunoff, S. A., 23, 179, 184, 213, 297, 298, 318
Schneider, M. V., 109, 127
Schorr, M. G., 179, 213
Schrank, H. E., 178
Seeto, A. W., 127
Shafai, L., 370
Shen, L. C., 127, 370
Shoamanesh, A., 370
Silver, S., 94, 178, 213, 214, 235, 266, 271, 295
Simmons, A. J., 201, 213
Simms, P. D., 271
Smith, C. E., 396
Smits, V. C., 370
Solbach, K., 128
Steinberg, B. D., 319
Stern, G. J., 128
Struik, D. J., 271
Stutzman, W. L., 94

Taylor, T. T., 141, 164, 178
Thiele, G. A., 94, 125, 126, 128, 369, 370
Thomas, B. MacA., 201, 213, 272
Thomas, R. F., 370
Tice, T. E., 370
Tou, S., 94
Tseng, F. I., 153, 178, 319
Tsukiji, T., 94
Turner, E. M., 396
Turner, R. F., 296

Van Bladel, J., 127
Viezbicke, P. P., 370
Vu, T. B., 272

Walters, C. H., 369
Watson, W. H., 271
Weeks, W. L., 94, 319
Williams, W. F., 265, 272
Wohlleben, R., 213, 272
Wong, J. L., 123, 124, 128, 346, 370
Wong, W. C., 271
Woo, R., 272
Wood, P. J., 214, 237, 239, 271
Woodward, P. M., 154, 178, 315
Woodyard, J. R., 39, 47, 59, 65, 322, 369

Yagi, H., 332, 369

Zarghamee, M. S., 234, 271
Zucker, F. J., 271, 369
Zucker, H., 272

SUBJECT INDEX

Abbe sine condition, 286–293
Active impedance, 53–55, 120
Airy function, 236
Amplitude taper efficiency, 33, 42, 134–136
  axisymmetrical apertures, 136, 199
  end fire, 322
  lens dead zones, 278–281, 283–284, 289
  overmoded circular horns, 199
  paraboloidal reflector, 222–226
  separable linear apertures, 135
Apertures, 31–35, 129–178
  amplitude taper efficiency, 134–136
  arbitrary sidelobes, 153
  axisymmetrical, 136
  Bayliss circular distribution, 166–169
  Bayliss line source, 144, 148–153
  blocked, 169–172, 223
  circular distributions, 157–177
  cosine distributions, 139–141, 174, 182–185
  cylindrical, 211–212
  edge condition, 140
  efficiency, 32, 42
  gaussian circular distribution, 161–163, 174, 225
  Hansen distribution, 163–164, 171, 175, 225
  leaky wave, 360–362
  linear distributions, 137–157
  parabolic distribution, 158–161, 171, 175
  phase error efficiency, 134–136
  quadratic phase error, 173–176, 179–185, 190–194
  random phase error, 232–234
  sampled, 57–59, 297, 315
  scanned, 133, 154–157
  separable linear, 31, 135
  sidelobes, 140
  superdirectivity, 141, 153
Apertures (*Cont.*):
  Taylor circular distribution, 164–166, 171, 174–175, 291–292
  Taylor line source, 141–148, 297, 315, 361–362
  triangular distribution, 139
  uniform distribution, 32–35, 137–139, 158–160, 171, 173–177, 182–185
  varying polarization, 191, 199, 322
  Woodward line source synthesis, 154–157
Archimedian spiral antenna, 41, 373–377, 381
Arrays, 48–65, 297–319
  active impedance, 53–55, 120
  bandwidth, 62–63
  beamwidth, 57–59
  binomial, 300
  Chebyshev, 141, 297, 302–309
  circular, 108
  density tapering, 119
  directivity, 51–54
  end-fire, 50, 58–60, 300–302, 307–308, 318
  even-mode, 50, 72
  factor, 49, 298
  feed networks, 107–109, 119–122
  Fourier series expansion synthesis, 316–318
  Franklin, 120–122
  grating lobes, 56, 299
  Hansen and Woodyard criterion, 59–60, 300
  linear, 55–60, 298–308, 315–318
  log-periodic dipole, 391–393
  microstrip, 99, 107–109
  multiple beams, 63–65
  nonresonant, 88, 117, 365–368
  odd-mode, 50, 73
  paraboloidal reflector feed, 237, 266
  phased, 56–65, 99
  planar, 308–314
  polynomial representation, 298–302
  progressive phase shift, 55, 298

Arrays (*Cont.*):
  resonant, 88, 117, 368
  scanned, 56–62
  series-fed, 115–117
  shaped beam synthesis, 315–318
  superdirectivity, 300–301, 308
  synthesis, 297–318
  traveling wave (*see* nonresonant, *above*)
  two-element, 49–53
  uniform, 53–60, 299–300
  unit circle, 298–302
  visible region, 55–59, 298–299
  waveguide slot, 40, 88–93, 365–369
  Woodward synthesis, 315–316
  zero sampling, 315
Astigmatic ray, 217–220
Astigmatism, 190, 195–196, 201, 390
Axial defocusing, 173, 226–228
Axial ratio, 15–18

Babinet-Booker principle, 37, 70–71, 369, 374, 383
Balanced line, 74–75
Balanced mode, 74–83
Baluns, 74–83, 377, 388–390
Bandwidth limitations, 38, 62–63, 95–96
Bandwidth relation, 115
Bayliss distribution:
  circular-aperture, 166–169
  line source, 144, 148–153
Bazooka balun, 77, 80
Beam deviation factor, 228–232, 251, 286
Beam efficiency, 14, 175–177
Beamwidth, 4–5
  circular-aperture, 159–169
  circular horn, 192–194
  corrugated horn, 202–204
  paraboloid reflector, 44, 225–226
  rectangular horn, 184–189
  relation between, 46–47, 185
  scalar horn, 204–205
  uniform distribution, 33, 138–139, 159–160, 184–189, 192–194
Beamwidth factor, 138, 159
Beverage antenna, 328–329
Biconical horn, 2, 211–212
Bifin log-periodic antenna, 393
Binomial array, 300
Blockage efficiency, 169–172, 223, 243–246
Bootlace lens, 293–294
Box horn, 208–210
Boxed stripline slot array, 98–99
Branch-line hybrid, 111–112
Butterfly patterns, 12–13, 262, 381

Candelabra balun, 79–81
Cassegrain reflector antenna, 44, 239–249
  diffraction loss, 245–246
  effective focal length, 241–242
  feed blockage, 243–246
  feed scanning, 247
  G/T, 248–249
  minimum blockage, 243–246
  shaped, 265–266
  tolerances, 246–247
Caustics, 217–220, 239, 252
Chebyshev array, 141, 297, 302–309
  beamwidth broadening, 304, 306
  directivity, 304, 306
  end-fire, 307–308
  planar, 308–309
  scanned, 306–307
Chebyshev polynomials, 302–303
Choke horn antenna, 43, 206–207
Cigar antenna, 39, 345–346
Circular-aperture distributions, 157–177
Circular horn antenna, 42–43, 190–201
  beamwidth, 192–194
  gain, 194–195
  multimoded, 210–211
  optimum, 195
  overmoded, 196–201
  phase center, 195–196
Circular microstrip patch antenna, 105–107
Circular polarization, 16–22
  hand rules, 375
  phase response, 22
  standards, 39
Circular-waveguide slots, 92
Coax wall slots, 92
Coaxial horn antenna (*see* Choke horn antenna)
Coma, 228–232, 237, 286–293
Compound lens, 284
Condon lobes, 235, 251
Conformal antennas, 38, 95–128
Conic section reflectors, 239–243

Conical equiangular spiral antenna, 41, 377–383
Conical pattern, 4
Convolution array synthesis, 310–314
Corner reflector antenna, 45, 267–271
Corrugated horn antenna, 42–44, 201–208, 356
  circular (conical), 201–207, 237
  phase center, 204–207
  rectangular, 207–208
Corrugated-rod antenna, 39, 345–346
Corrugated wall, 202–206, 354–356
Cosecant-squared pattern, 155–157
Cosine distributions, 139–141, 174, 182–185
Crisscross feeder, 340–342, 384
Cross-polarization efficiency, 223–224
Crossed-slot antenna, 123–124
Currents, radiation from, 25–29, 66–74
Cylindrical reflector, 45, 258
Cylindrical waves, 218–220, 274–277, 282

Dielectric losses, 284–285
Dielectric rod antenna, 39, 346–348
Dielectric slab, 354–357
Diffraction loss, 245–246
Dipole, 36–37, 66–78, 83–87
  average impedance, 388
  cavity-mounted, 126–127, 346
  coupled, 332–335
  directivity, 6, 68
  efficiency, 28
  feeding, 74–78, 83–87
  folded, 85–86
  Franklin array, 120–122
  gamma match, 86
  half-wavelength, 6
  incremental, 27–29, 70, 235
  input impedance, 69–71
  magnetic, 29–31, 235
  microstrip, 119–120
  mutual coupling, 332–335, 341–342
  offset feed, 83–84
  over ground plane, 72–74, 266–267
  pattern, 67
  radiation resistance, 28, 68
  shunt feeding, 86–87
  sleeve, 37, 84–85, 126, 346
  T match, 86–87
  turnstile, 112–115, 126
Directional antenna, 36
Directivity, 9–14
  aperture, 34, 134–136
  array, 51–54
  axisymmetrical leaky wave, 40
  end-fire pattern, 38, 322–325
  rectangular horn, 183–184
Discontinuity radiation, 35, 320
Dolph-Chebyshev array (*see* Chebyshev array)
Dual-reflector antennas, 44, 239–249, 254–256
  corrector for spherical reflector, 254–256
  effective focal length, 242
  feed blockage, 243–246
  shaped, 45, 265
Dual-surface lenses, 286–293

Effective area, 6, 133
Efficiency, 5, 9, 28
Eikonal, 217, 221, 274
Electric vector potential, 29–31, 130–132
Electric wall, 75, 99
Elliptical reflector, 239–243
End-fire antennas, 38–40, 320–325, 332–354
  array, 50, 58–60, 300–302, 307–308, 318
  bandwidth, 345
  directivity, 38, 322–325
  peak gain, 324
Equiangular spiral antenna, 41, 375–377
Equivalent parabola, 241–243
Even mode, 50

Fan-beam pattern, 36
Fast waves (*see* Leaky wave)
Fermat's principle, 215, 219–220, 254, 274
Ferrite core baluns, 80–82
Flat-plate reflectors, 45, 266–271
Focal length, 218–221
Focal plane fields, 236–237
Folded balun, 76–77, 84
Folded dipole, 85
Four-to-one balun, 79–81
Fourier series synthesis, 316–318
Fourier transform, 31, 129–133
  axisymmetric, 157–158
  varying polarization, 191

Franklin array, 120–122
Fraunhofer region, 130–132
Fresnel region, 130–132

Gain, 4–6, 29, 32
Gamma match, 86–87, 352
Gaussian distribution, 161–163, 174, 225
Geometric optics, 215–220, 257
Geometric theory of diffraction (GTD), 35, 45, 201, 215, 245, 266–270
Grating lobes, 56, 299
Great circle pattern, 4
Gregorian reflector antenna, 44, 239–247
  effective focal length, 242–243
  feed blockage, 243–246
  tolerances, 246–247
G/T (gain/noise temperature), 248–249

Half apex angle, 384–385
Half-patch antenna, 117–119
Half-wavelength balun, 79
Hansen circular distribution, 163–164, 171, 175, 225
Hansen and Woodyard criterion, 39, 59–60, 300, 322–325, 349–350
Helical wire antenna, 39, 348–354
  axial mode, 349–352
  axial ratio, 350
  feed, 352–354
  long, 353
  short, 353–354
Helical wire modes, 349, 374–375, 381–383
Holey waveguide antenna, 363
Horn antennas, 42–44, 179–213
  axial length, 187
  biconical, 2, 211–212, 375
  box, 44, 208–210
  choke, 43, 206–207
  circular, 42–43, 190–201
  corrugated, 42–44, 201–208
  design to beamwidths, 188–189, 194, 202–204
  multimoded, 43–44, 208–211
  optimum, 186–188, 195, 205
  overmoded, 196–201
  phase center, 189–190, 195–196, 204
  rectangular, 42–43, 181–190, 207–210
  scalar, 201–207
  sectoral, 179

Horn antennas (*Cont.*):
  small, 181, 207
  stepped, 208–211
Huygens source, 31, 132–134, 181–183, 223, 235–236
Hybrid mode, 202–206, 237
Hyperbolical reflector, 239–243

Images, 72, 266–271
Impedance, 22–23
  active, 53–55, 120
Incremental admittance, 369
Index of refraction, 215–216, 274, 281, 294
Infinite balun, 375–377, 382–383, 388–390
Inverted V antenna, 331–332
Isotropic antenna, 4, 49–60
  mutual impedance, 53–55

k space, 26, 31–33, 129–133

Leaky wave, 320–322, 327
Leaky wave antennas, 40–41, 320–322, 327, 357–365
  aperture distribution, 360–362
  directivity, 40, 323–324, 358–359
  frequency scanning, 359
  measurement, 363–365
  pattern peak, 40, 322
  phase error efficiency, 359
  rectangular waveguide, 327
  relative propagation constant, 327, 359
Lens antennas, 45–46, 273–296
  aperture distribution synthesis, 290–293
  artificial dielectrics, 285
  bandwidth, 274, 281–284, 292–294
  bootlace, 293–294
  coma-free, 286–293
  compound, 284
  dielectric losses, 284–285
  dual-surface, 286–293
  feed scanning of, 286
  Luneburg, 294–295
  metal-plate, 281–284, 294
  quarter-wavelength transformer, 285
  single-surface, 274–281
  surface mismatch, 284–285

- Lens antennas (*Cont.*):
  - tolerances, 273
  - zoning, 278–281, 283–284, 289, 292–293
- Linear distributions, 137–157
- Linear polarization, 15
- Log-periodic antennas, 41–42, 384–395
- Log-periodic dipole antennas, 384–393
  - active region, 385–388
  - arrays, 391–393
  - beamwidth, 385–386
  - directivity, 386–388
  - elevation angle, 390–391
  - feeder impedance, 389
  - feeder radiation, 389, 393
  - feeding, 388–390
  - half apex angle, 384–385
  - phase center, 390
  - phasing, 392–393
  - spacing constant, 385
  - squint, 389
  - truncation constants, 385–387
- Long wire antennas, 327–332
  - beverage, 328–329
  - rhombic, 330–332
  - V, 329–330
- Longitudinal waveguide slots, 90–91, 359–360, 365–369
- Loop, 29–31
  - parasitic, 345
  - resonant, 37, 86, 342–345
  - Yagi-Uda array, 343–345
- Luneburg lens, 294–295

- Magnetic currents, 29–31, 67–68, 105, 119
- Magnetic dipole, 235
- Magnetic vector potential, 25–27, 130–132
- Magnetic wall, 75, 85, 99, 102, 108
- Magnification factor, 242
- Metal-plate lens, 281–284, 294
- Microstrip, 99, 109–111
  - coupled, 109
  - effective dielectric constant, 101
- Microstrip balun, 82
- Microstrip dipole, 119–120
- Microstrip Franklin array, 120–122
- Microstrip patch antenna, 38, 99–119
  - bandwidth, 103–107
  - cavity model, 99, 103, 106
- Microstrip patch antenna (*Cont.*):
  - circular, 105–107
  - circularly polarized, 111–115
  - coax feed, 102, 106–107
  - continuous strip, 108
  - cross-polarization, 104–105
  - effective radius, 105
  - efficiency, 104
  - feed networks, 107–111, 115–117
  - gain, 38, 105
  - half-patch, 117–119
  - impedance, 101–107
  - mechanical properties, 122–123
  - radomes, 122
  - rectangular, 100–105
  - series-fed array, 115–117
  - transmission line model, 100–102
  - tuning, 122
- Mismatch loss, 23, 112
- Mode matching, 208–211
- Mode 2 conical spiral antenna, 381–383
- Moment method, 29, 332–335, 341–342
- Monopole, 37, 72, 84
- Monopulse, 149–150, 166
- Multimode horn antenna, 43–44, 208–211
- Multiple beams, 63–65, 297
- Mutual impedance, 51–55, 332–342

- Near fields, 3, 27, 130–132
- Noise temperature, 248–249

- Obliquity factor, 132, 138, 183–186, 189, 192–194
- Odd mode, 50
- Offset-fed dipole (slot), 83–84, 97
- Offset-fed reflector, 45, 249–251
  - beam deviation factor, 251
  - pattern squint, 251
- Omnidirectional pattern, 36
- Optical path length, 215
- Optimization over band, 335–338
- Overmoded horns, 196–201

- Parabolic circular-aperture distribution, 158–161, 171, 175
- Paraboloidal reflector, 44, 220–239
  - amplitude taper efficiency, 222–226
  - aperture efficiency, 7–8, 44

Paraboloidal reflector (*Cont.*):
  array feed, 237, 266
  astigmatism, 228–229
  axial defocusing, 173, 226–228
  beam deviation factor, 228–232, 247, 251
  beamwidth, 44, 225–226
  Cassegrain, 44, 239–249
  central blockage, 223, 243–246
  coma, 228–232, 237
  Condon lobes, 235, 251
  cross-polarization efficiency, 223–224
  edge taper, 221
  feed mismatch, 237–239
  feed scanning, 228–232, 247, 251
  focal plane fields, 236–237
  gain, 222–229, 236
  geometry, 220–221
  Gregorian, 44, 239–247
  offset-fed, 45, 249–251
  phase error efficiency, 222–234
  physical optics, 234–239
  random phase errors, 232–234
  rms, 232–233
  shaped, 256–266
  spherical aberration, 252–254
  spillover loss, 223–225, 237
  subtended angle at feed, 221
  surface error, 233
Parallel plate radiator, 101
Paraxial focus, 252–253
Path loss, 6–9
Pattern, 4–5, 36
  butterfly, 12–13, 262, 381
  multiplication, 49, 309–314
  pencil beam, 10–12, 36
  squint, 75–76, 83
Phase center, 189–190, 195–196, 204–205, 226, 267
Phase convention, 2, 22, 50
Phase error efficiency, 34, 134–136
  astigmatism, 228–229
  axisymmetrical aperture, 136
  difference pattern, 152–153, 169–170
  leaky wave, 359
  paraboloidal reflector, 222–234
  quadratic, 173–175
  random phase errors, 232–234
  scanned aperture, 135, 152, 169, 230, 359
  separable linear apertures, 135–136
Phase response, 21–22
Phased array, 56–65, 99
Physical optics, 234–239
Planar array synthesis, 308–314
  Chebyshev, 309
  convolution, 310–314
Plane waves, 2, 15, 218
Polarization, 15–22, 48, 223
  efficiency, 19–21, 112
  orthogonal, 20, 223
  varying direction in aperture, 191, 199, 322
Polyrod antenna (*see* Dielectric rod antenna)
Poynting vector, 3
Principal plane patterns, 4
Propagation constant, 2
  relative, 40, 321
  vector, 31, 48, 131
Pyramidial horn (*see* Rectangular horn)

Quad antenna, 86, 342–344
Quadratic phase distribution, 131, 173–176, 179–185, 190–194, 226–228

Radiation approximation, 25–26, 48
Radiation intensity, 4
Radiation resistance, 28, 68–70
Radius of curvature, 217–219
Radome, 121–122, 284
Random phase errors, 93, 232–234
Ray-fixed coordinates, 216–219
Ray tracing, 219–220
Reactive power divider, 108–109
Reciprocity, 7, 52, 76
Rectangular horn, 42–43, 181–190, 207–210
  axial length, 187
  beamwidth, 184–186
  corrugated-wall, 207
  design to beamwidths, 188–189
  directivity, 183–184
  optimum, 186–188
  phase center, 189–190
Rectangular microstrip patch antenna, 100–105
Reflection coefficient, 22, 238, 284–285
Reflection differential equation, 257
Reflections, surface, 218–220
Relative propagation constant, 40, 321
Retarded potential, 1–2, 25, 29, 130

Return loss, 23
Rhombic antenna, 330–332
Rhombic array, 312–314
Ridged horn antenna, 44
Robieux's theorem, 237
Rotman lens, 294

Scalar horn, 201–207
Scaling constant, 383
Schelkunoff's unit circle method, 298–302
Shaped reflectors, 45, 256–266
  axisymmetrical synthesis, 258–262
  cylindrical reflector synthesis, 258
  doubly curved, 263–265
  dual, 45, 265–266
  reflection differential equation, 257
Shunt-fed dipole, 86–87
Sidelobe, 5, 129–130, 140
Sidewall slots, 90–92
Slant radius, 180
Sleeve balun, 77, 80
Sleeve dipole, 37, 84–85, 126, 346
Sleeve monopole, 84
Slot, 29–30, 36–37, 66–72, 87–93, 96–99, 123–126
  annular, 38
  array, 88–93, 98–99, 365–369
  cavity-backed, 37, 72, 96–99
  coax feed, 83, 92–93
  crossed-slot, 123–124
  dielectric loaded, 96–97, 369
  directivity, 68
  incremental admittance, 369
  input conductance, 69–71
  mutual coupling, 368–369
  offset-feed, 83, 97
  pattern, 68
  polarization, 30, 37, 88, 91
  probe-coupled, 91–92
  radiation conductance, 68–71
  short, 70, 96
  stripline, 38, 96–99
  T-bar-fed, 124–126
  waveguide-fed, 40, 87–93, 365–369
Slow wave (*see* Surface wave)
Snell's laws, 215–216, 254, 274, 288
Spacing constant, 385
Spherical aberration, 252
Spherical reflectors, 45, 252–256
  aperture distribution, 256
Spherical reflectors (*Cont.*):
  corrector subreflector, 254–256
  line source feed, 253–254
  point source feed, 254
Spherical waves, 2, 15, 26, 218
Spillover loss, 223–225, 237, 275
Spiral antennas, 41, 372–383
Spiral slot antenna, 118–119
Split coax balun, 77–79
Split tapered coax balun, 82–83, 383
Standing wave currents, 23, 66–67, 88–89, 327–328
Stationary point, 215, 238
Stepped horn (*see* Box horn)
Stripline series slots, 96–99
Superdirectivity, 141, 153, 300–301, 308
Surface wave, 321–326
Surface wave radiation, 35, 38–40, 320
  axisymmetric, 345–354
  planar, 354–359
Symmetry, 26–27, 49–50, 196, 211

Taylor distribution:
  circular, 164–166, 171, 174–175, 291–292
  leaky wave, 361–362
  line, 141–148, 297, 315
  line with edge nulls, 146–148
T match, 86–87
T-bar-fed slot antenna, 124–126
Three-wire transmission line, 74–75
Tilt of polarization ellipse, 15–18
Transformer balun, 82
Transverse resonance, 363
Transverse top-wall slots, 90–93
Trapezoidal tooth log-periodic antenna, 393–395
Traveling waves, 88–89, 321–327
  measurement, 363–365
Triangular distribution, 139
Triangular tooth log-periodic antenna, 393–395
Truncation constants, 373, 379–382, 385–387
Turnstile dipole antenna, 112–115, 126

Unbalanced line, 74–75
Unbalanced mode, 74–83
Uniform distribution, 32–35, 137–139, 158–160, 171, 173–177, 182–185

Universal pattern, 55, 182, 183, 192, 193, 198, 199, 203

V antenna, 329–332
Vector potential, 25–31, 130–132
Vertex plate, 239
Vestigial lobe, 4–5, 228–229
Visible region, 55–59, 137–138, 298–299
VSWR (voltage standing wave ratio), 23

Waveguide-fed slots, 87–93
Waveguide slot arrays, 40, 88–93, 365–369
  amplitude distribution, 365–368
  bandwidth, 368
  beam direction, 367–368
  cross-polarization, 91, 98
  dielectric loaded, 369
Waveguide slot arrays (*Cont.*):
  frequency scanning, 368
  nonresonant, 40, 88–89, 365–368
  resonant, 40, 88–89, 368
  transmission line model, 368–369
Waveguide wall currents, 88–93
Woodward line source synthesis, 154–157, 315–316

Yagi-Uda antenna, 39, 332–344
  band optimization, 335–338
  boom adjustments, 340
  diameter adjustments, 338–339
  dipole, 332–342
  gain-bandwidth product, 338
  maximum element spacings, 336
  multiple-feed, 340–342
  optimization, 335–338
  resonant loop, 342–345
  source match optimization, 337